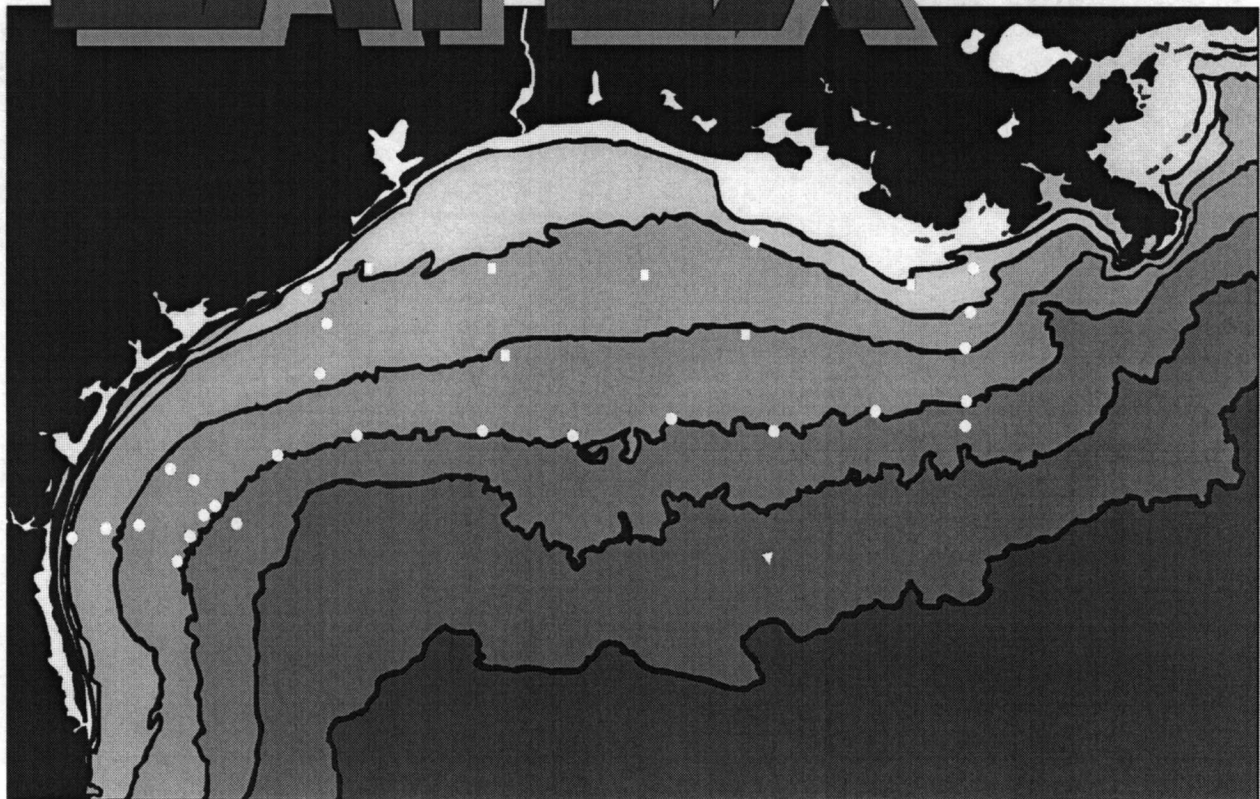


Texas-Louisiana Shelf Circulation and Transport Processes Study: Synthesis Report

Volume I: Technical Report

LATEX

Volume 1



Texas-Louisiana Shelf Circulation and Transport Processes Study: Synthesis Report

Volume I: Technical Report

Authors

W.D. Nowlin, Jr.
A.E. Jochens
R.O. Reid
S.F. DiMarco

Prepared under MMS Contract
14-35-0001-30509
by
Texas A&M University
College Station, Texas 77843-3146

Published by

**U.S. Department of the Interior
Minerals Management Service
Gulf of Mexico OCS Region**

**New Orleans
September 1998**

DISCLAIMER

This report was prepared under contract between the Minerals Management Service (MMS) and the Texas A&M Research Foundation. This report has been technically reviewed by the MMS and approved for publication. Approval does not signify that the contents necessarily reflect the views and policies of the Service, nor does mention of trade names or commercial products constitute endorsement or recommendation for use. It is, however, exempt from review and compliance with MMS editorial standards.

REPORT AVAILABILITY

Extra copies of the report may be obtained from the Public Information Office (Mail Stop 5034) at the following address:

U.S. Department of the Interior
Minerals Management Service
Gulf of Mexico OCS Region
Public Information Office (MS 5034)
1201 Elmwood Park Boulevard
New Orleans, Louisiana 70123-2394

Telephone Number: 1-800-200-GULF or
504-736-2519

CITATION

Suggested citation:

Nowlin, W.D. Jr., A.E. Jochens, R.O. Reid, and S.F. DiMarco. 1998. Texas-Louisiana Shelf Circulation and Transport Processes Study: Synthesis Report, Volume I: Technical Report. OCS Study MMS 98-0035. U.S. Dept. of the Interior, Minerals Mgmt Service, Gulf of Mexico OCS Region, New Orleans, LA. 502 pp.

ABOUT THE COVER

The cover art, by Karen Glenn, shows the LATEX study area, with LATEX A's mooring locations superimposed over the bathymetry.

DEDICATION

In Memoriam

John D. Cochrane

November 28, 1920 - September 21, 1997

He contributed much to every facet of this study.

And may there be no sadness of farewell when I embark;
for tho' from out our bourne of time and place
The flood may bear me far, I hope to see my pilot face to face
when I have crossed the bar.

"Crossing the Bar"
Alfred Lord Tennyson

SUMMARY OF FINDINGS

INTRODUCTION

The Texas-Louisiana Shelf Circulation and Transport Processes Study (LATEX A) had four principal objectives:

1. To identify key dynamical processes governing circulation, transport, and cross-shelf mixing on the Texas-Louisiana shelf.
2. To (a) improve the data base available for study of the processes in objective 1, (b) synthesize the data into a scheme of circulation, and (c) quantify transports and mixing rates.
3. To develop conceptual models of meso- to large-scale processes and circulation features and of large-scale shelf circulation on event to seasonal scales.
4. To provide physical and chemical information needed for synthesis with biological data into a broader ecological characterization of the region.

To what extent has LATEX A achieved these four objectives?

1. The key governing processes of wind, topography, freshwater runoff, surface heating and cooling, bottom friction, stratification, and influence of offshelf circulation have been identified and described.
2. The data base for studying key governing processes over the Texas-Louisiana shelf has been massively extended; based on the data, an empirical circulation scheme was developed; and first estimates have been made of budgets and transports.
3. The conceptual model for shelfwide circulation of Cochrane and Kelly (1986) has been examined and modified to give a tested conceptual model of meso- to large-scale circulation over the shelf on scales from major atmospheric events to seasonal.
4. The new physical and chemical data bases have been supplemented by data on light transmission, particle distributions, and pigments, resulting in a generalized ecological characterization of the region.

The remainder of this summary presents in concise statements the principal scientific findings conveyed by the body of this synthesis report.

PHYSICAL BOUNDARY CONDITIONS

Surface meteorological fields. A high quality set of hourly surface winds and wind stress, sea level atmospheric pressure, air temperature, and sea surface temperature (SST) was produced on a 0.5° latitude and longitude grid for the LATEX region for the period April 1992 through November 1994. They are adequate for the study of the effects of atmospheric events (from frontal passage to seasonal variation) on the Texas-Louisiana shelf from meso- to shelf-scale. These LATEX surface fields are available via the Department of Oceanography, Texas A&M University.

The seasonal surface meteorological patterns showed the lower atmosphere over the LATEX shelf region in summer to be different than in other seasons. In summer, the atmosphere is relatively stable; only one to two fronts per month pass through this region. Average summer winds are to the northwest with very strong northward components (about $6 \text{ m}\cdot\text{s}^{-1}$) over the western area. Alongshore wind components are upcoast (in a direction from Mexico toward the Mississippi) on average. Air temperatures are the highest (28.2°C) in the annual cycle and spatially quite uniform. Air-sea temperature differences are small (only of order 0.5°C).

In other seasons, winds are generally directed downcoast. In spring, they are toward the west or northwest; in fall and winter, they are directed west or southwest. In fall through spring, the lower atmosphere is more variable than in summer due to more frequent frontal passages. The wind speed and direction fluctuations in other seasons are larger than in summer, especially in winter. These differences are important to forcing the shelf circulation. Surface air temperature as well as SST in these three seasons show that isotherms basically follow isobaths, with values increasing toward the open Gulf. Cross-shelf gradients for both air temperature and SST are largest in winter. Fall air-sea temperature differences reach maximum values of about 4°C near the coast. Seasonal values of SST are always higher than for surface air temperature, with differences smallest in spring (0.5°C) and largest in fall (3°C).

Time series of river discharge from the beginning of such recording through 1994 were assembled for the Mississippi and Atchafalaya rivers and the fourteen next largest (based on annual average discharge) U.S. rivers to the west. The long-term mean discharge rates of the Mississippi and Atchafalaya have a rather smooth annual cycle with a peak in April and a broad minimum during September and October. However, year-to-year variability is large. Discharge during nearly all of 1993 exceeded the long-term mean by two or more standard deviations; the same was true for 1994 during the late winter and spring; while discharge rates fell well below the mean during flood season in 1992.

The total average annual discharge rate for the 14 lesser rivers is $1,113 \text{ m}^3\cdot\text{s}^{-1}$, an order of magnitude less than the average discharge rate for the Mississippi River alone. However, year-to-year variability is again large. During October 1994 (normally a low discharge period for the lesser rivers) the combined discharge for the lesser rivers exceeded that of the Mississippi-Atchafalaya—emphasizing the potential impact of the discharge of these rivers on the circulation and ecology of the Texas-Louisiana shelf.

Bottom stress parameterization. A linear plus quadratic representation of the low frequency (40-hr low-passed) bottom stress in terms of the low frequency current is shown to be superior to a commonly employed linear approximation in subtidal models. The suggested new parameterization is based on an analysis using near-bottom current meter data from 30 LATEX A moorings where the basic hypothesis is that the bottom boundary layer is fully turbulent and the *unfiltered* bottom stress is quadratically related to the *unfiltered* near bottom current.

Eddy-shelf interactions. Loop Current eddies observed adjacent to the Texas-Louisiana shelf during the LATEX field program were tracked; their motions and interactions with the shelf and other eddies are briefly described. A special case study was made of Eddy Vazquez (Appendix D).

Impacts of the eddies on shelf currents in LATEX are described. In summary, the Loop Current eddies are major drivers of shelf edge currents and frequently affect the outer shelf

through exchanges of mass, energy, and water properties. Their impact on the inner shelf circulation is episodic. During such episodes, however, they can cause substantial exchanges between shelf and deep Gulf waters.

WATER MASS CHARACTERIZATION AND BUDGETS

Salinity and temperature distributions. CTD measurements at each station of the ten LATEX A hydrographic cruises led to an excellent characterization of temperature and salinity distribution over the Texas-Louisiana shelf. Data are available from NODC, and a data report with complete graphic portrayal of distributions is available. Of the subsurface water masses of the Gulf of Mexico, only Subtropical Underwater, characterized by a salinity maximum between 100 and 150 m, can penetrate onto the shelf. The high salinities of this water characterize anticyclonic Loop Current eddies, with salinities often exceeding 36.6 even in the western Gulf. The very tight temperature-salinity relations for waters at the shelf edge below the Subtropical Underwater are evidence of the high quality of the observations. Vertical sections of temperature and salinity along the 200-m isobath characterize the outer boundary conditions for the shelf, especially effects of cyclonic and anticyclonic eddies; cross-shelf sections describe general seasonal differences.

Heat and freshwater budgets. Relative to a reference ocean with uniform temperature of 0°C and uniform salinity of 37, heat energy and freshwater components were calculated for data from the ten LATEX A hydrographic cruises. Cruise-to-cruise differences yielded time rates of change of heat and freshwater. Estimates of air-sea exchanges were made from contemporaneous data and atmospheric numerical model output; measurements of river discharge were obtained. These terms were compared to climatological baselines, which first were updated.

Comparisons of the computed heat budget terms with the baseline climatologies generally showed good agreement. The eight values of the rate of oceanic heat storage agreed well with the climatic baseline. This suggests that the rate of change for heat storage follows a predictable pattern, particularly when using shelfwide averages that tend to dampen the effects of transient phenomena. The baseline values showed heat storage maxima in April and minima in November-December.

In general, the component parameters of the freshwater budget agreed well with the corresponding climatic baselines. The eight values of the rate of freshwater storage were consistent with climatic baseline. The rate of freshwater storage generally followed the pattern of the monthly climatology, although there was notable interannual variability. This was not unexpected in view of the interannual variability of the river discharge. Values of precipitation departed from the baseline, but these departures were verified using coastal station data rates.

Time sequences of heat and freshwater flux divergences were formed from the other terms as residuals to the heat and freshwater budgets. These divergences agreed reasonably well with climatological envelopes.

Examining freshwater storage from cruise to cruise, values for the eastern shelf tended to increase with increasing river discharge. However, factors other than river discharge must be introduced to explain changes in the freshwater storage over the western shelf. It is suggested that much of the fresh water discharged from the Mississippi and Atchafalaya Rivers is exported off shelf before reaching the western shelf; this is consistent with particle distributions as well.

Volumetric temperature-salinity census. The circulation regime over the inner shelf strongly influences the volumetric distribution of salinity over both the eastern and western shelf. The discharge from the Mississippi-Atchafalaya rivers leads to low salinity waters (minimum salinities seen in the census) over the inner regions of both eastern and western shelves in spring. However, this discharge is not correlated with the total volume of fresh water over the eastern shelf. That volume is at a maximum in summer when the wind-driven circulation over the inner shelf is upcoast and maintains a surface layer of fresh water in that region. Over the western shelf, the volume of fresh water is at annual maximum in spring and minimum in summer. The spring maximum results from combined enhanced river discharge and downcoast flow; the summer minimum results from upcoast transport of salty water from off Mexico by the summer upcoast flow regime.

Annual heating and cooling cycles and the wind mixing of surface layers principally control the distribution of the temperature versus time over this shelf. This leads to the most voluminous temperature classes exhibiting a continuous temperature range (from 15° to 24°C) in winter and spring, but splitting into several modes, separated by the vertical temperature ranges of the thermoclines, in summer and fall.

The interaction of Loop Current eddies with the shelf results in the exchange of waters between the eddies and the shelf. The presence of anticyclonic rings near the shelf break and water saltier than 36.6 on the shelf seem well correlated. Salinities greater than 36.6 associated with the core of Subtropical Underwater are found near 200 m in anticyclonic eddies detached from the Loop Current; salinities this high are not generally present at the Subtropical Underwater core depth outside eddies in the western Gulf.

SHELFWIDE CIRCULATION AND TRANSPORTS

The Cochrane-Kelly schema. At the outset of the LATEX study, the leading (and generally accepted) hypothesis regarding the shelf-scale, low-frequency circulation over the Texas-Louisiana shelf was that espoused by Cochrane and Kelly (1986). The principal features of that circulation pattern and its forcing, here referred to as the CK schema, are:

- During nonsummer (approximately September through June) winds with a generally downcoast component drive downcoast currents over the inner shelf. Due to the concave orientation of the coast, a convergence of alongshelf winds occurs over the south Texas coast, resulting in a convergence of currents over the inner shelf and an offshore, a cross-shelf flow that contributes the southwest limb of a cyclonic circulation gyre with upcoast flow near the shelf break. This gyre is closed by shoreward, cross-shelf flow over the Louisiana shelf west of the Mississippi River mouth.
- During spring the prevailing winds over the inner shelf develop an upcoast component, beginning over the Mexican shelf and moving northward. Consequently, in spring the area of coastal current convergence migrates, under the influence of the wind, upcoast. This phenomenon reaches Louisiana by July. Thus, prevailing currents over the inner shelf are upcoast during summer.
- Downcoast winds generally are reestablished in August-September, at which time the nonsummer circulation gyre is reestablished.
- Shelf break currents are thought to be directed upcoast all year.

- Low-salinity surface water from the Mississippi-Atchafalaya rivers is advected down the shelf near the coast by downcoast currents over the inner shelf in nonsummer. On average, low salinity is enhanced during the period of maximum Mississippi-Atchafalaya discharge in spring.
- During summer brackish surface water is held over the Louisiana shelf by upcoast currents and results in a pool of low-salinity water distributed broadly across the shelf.
- The low-salinity surface waters distributed along the coast during nonsummer should contribute buoyancy forcing to enhanced shear flow downcoast, although this is not specifically stated as part of the CK schema.

Using historical, LATEX, and collateral data we examined the meso- and shelfwide scales of circulation and property distributions over the Texas-Louisiana shelf. We examined mean and synoptic patterns of low-frequency, shelf-scale circulation and its forcing, with one objective being to confirm, deny, or modify the CK schema. A circulation model for the inner shelf was developed as well as a box model for estimates of mass, freshwater, and heat fluxes during the LATEX period. Based on this work, we formulate a new set of hypotheses regarding the low-frequency, shelf-scale circulation of the Texas-Louisiana shelf.

The results are summarized in the subsections which follow.

Seasonal mean hydrographic fields. For the Texas-Louisiana continental shelf we prepared and examined mean fields, with standard deviations, of surface and bottom temperature and salinity and of geopotential anomaly representing spring, summer, and fall. The mean fields verify a bimodal cycle of geopotential anomaly and circulation patterns, although the patterns differ somewhat from those inferred by CK, who used only a subset of these data. Unlike the schema of CK, our mean fields indicate that upcoast flow occurs only weakly over the outer eastern shelf in spring and only very weakly over the outer shelf from 94°-95°W in fall. Based on the standard deviations, we have quantified the interannual spatial variations in geopotential anomaly, salinity, and temperature. Though we believe our mean fields are a significant improvement over previous descriptions of the shelfwide circulation and property distributions, it should be remembered that the estimates of variability are based on small samples.

Mean hydrographic patterns for the inner Texas-Louisiana shelf imply downcoast flow during both spring and fall. Differences in shelf-scale distributions of salinity and temperature as well as year-to-year variability are as might be expected considering the forcing mechanisms of air-sea heat exchange, Mississippi-Atchafalaya discharge, and wind patterns over the inner shelf. A model study by Oey (1995) examines the relative effects of wind stress, river discharge, and interactions of offshore circulation eddies on the Texas-Louisiana shelf. His results support the inner shelf patterns seen here and in CK.

Using the hydrographic data assembled for the seasonal study, we examined the effects of forcing mechanisms on the patterns of circulation and property distributions. We began by describing and discussing several anomalous fields in relation to anomalous forcing by wind stress, river discharge, and offshore eddy activity. Then, we prepared for individual cruises the residuals of surface salinity and geopotential anomaly from the appropriate seasonal mean fields. Residuals of surface salinity were shown to be significantly correlated with residuals of geopotential anomaly in a negative sense, as expected. The variability of geopotential anomaly, and thus baroclinic flow, is believed to be governed

primarily by variability of salinity. The interannual variability of temperature is believed to play only a minor role in interannual variability of the circulation, though there is a large, regular seasonal variation in temperature, as well as in associated steric water level anomaly.

We also prepared residuals of Mississippi-Atchafalaya discharge related to the long-term mean and averaged them over the periods April-May, June-August, and October-November in years for which we have residuals from individual cruises of surface salinity from seasonal means. For spring, summer, and fall we regressed the river discharge residuals onto the surface salinity residuals. For all seasons there is significant negative correlation, as expected, with stronger correlation over the eastern and central than over the southwestern part of the shelf. Similarly we defined an alongshelf wind index that estimated the strength and direction of alongshelf winds for five days before and during each cruise period relative to the 30-year mean alongshelf wind for the same time period. This index was related to surface salinity residuals. For spring and fall cases, downcoast wind strength was significantly related to negative salinity residuals, as expected if more low salinity water is advected downcoast by anomalously large wind-driven downcoast currents. For the summer case, anomalously large upcoast winds, and thus expected upcoast advection of salty water, was significantly correlated with positive salinity residuals.

Temporal and spatial scales of variability. Data used to remove shelf-scale background fields and estimate scales of the residual or anomaly fields were obtained by subtracting the background fields from synoptic data were obtained from the first seven LATEX A cruises. The hydrographic stations had 5- to 10-km cross-shelf and 20-km alongshelf separations. Computing anomaly fields and estimating their spatial scales based on data from 1-km cross-shelf and 10-km alongshelf separations yields essentially the same results. The resulting analyses led to a general characterization of scales over the Texas-Louisiana shelf.

The cross-shelf scales of geopotential anomaly, surface salinity, and surface temperature over the western shelf are shorter (order 15 km) than those in the eastern and central shelf regions (order 20 km). Alongshelf scales (order 35 km) are essentially the same over the western and eastern regions of the shelf, over the mid-shelf (50-m isobath), along the shelf break (200-m isobath), and at different water depths along the 200-m isobath. It is shown that the spacing of observations along the LATEX hydrographic transects was adequate to resolve the mean anomaly scales, ranging from about 12 to 38 km for the different transects.

The results were subjected to several statistical tests. For a given transect (cross-shelf or alongshelf), there are no significant differences between the anomaly scales obtained for the three variables, for estimates at three levels (surface, mid-depth, and bottom), or for the four seasons. Moreover, the standard deviation of sample estimates of scale, when normalized by the transect average, are not significantly different among transects. There is, however, a significant relationship between the transect-average anomaly scale and the length of the transect (cross- or alongshelf)—shorter transects having smaller anomaly scales.

Preliminary analysis of the horizontal scales associated with the detrended ADCP data seems to support the analysis based on the geopotential anomaly using CTD data, with cross-shelf scales of order 20 km on average and alongshelf scales of order 35 km. Also, like the scales determined from the hydrographic residual fields, there was not a significant variation between summer and fall.

It is clear that variances of the shelf-scale (reference) fields of observed salinity and temperature and calculated geopotential anomaly are greater across than along shelf. The spatial variance of the cross-shelf anomaly fields is around 10% of the cross-shelf reference fields; that of the alongshelf anomaly is about 35% of that in the alongshelf reference fields. Therefore, most of the spatial variance of the baroclinic circulation and property distributions is in the shelf-scale, which is the principal focus of the LATEX shelf study. Nevertheless, significant variance is found at mesoscales in the anomaly fields.

The range of anomaly scales over the Texas-Louisiana shelf seems consistent with values of the baroclinic radius of deformation on this shelf, i.e., 10-25 km as estimated by Nowlin et al. (1991) but perhaps up to 35 km at the shelf-slope break. This radius of deformation is a natural scale of variability. It is expected that a spectrum of processes will excite variability at these scales. Direct forcing of the shelf circulation and thermal structure by the atmosphere at subinertial frequency (weather band and seasonal) tends to be at very large scales (order 400 km) and probably explains a large fraction of the variance of the shelfwide scales of properties (Hsu 1988; Mitchum and Clarke 1986). Mechanisms by which some variance of properties may occur at small scales, of order 10 to 50 km, follow. Interaction of flow with rough bottom topography tends to cause a cascade of variance towards small scales (Rhines and Bretherton 1974); this might occur near the outer region of the Texas-Louisiana shelf (depths greater than 100 m), where canyons and coral reefs produce rugged relief. Another mechanism is the cascade of baroclinic geostrophic turbulence toward the radius of deformation (Rhines 1975, 1977); this is known to occur in deep oceanic realms, but might be suppressed in the shelf domain. The impact of the large freshwater discharge from the Mississippi and Atchafalaya Rivers produces small cross-shelf scales associated with the coastal front (Murray and Donley 1994), but the associated alongshore scales can be very large. Finally, another possible mechanism for generation of small scales (both cross- and alongshelf) is backward scattering of coastal trapped waves due to alongshelf changes in bathymetry (Wilkin and Chapman 1990). The most likely mechanism for producing the anomaly scales found in this study is that of Rhines and Bretherton (1974).

The temporal variability of horizontal current velocity, temperature, and salinity was evaluated by splitting the time series into the recordlength mean, annual signal, and residual signal. Examination of the results shows that shelf circulation is divided into two geographical regimes: the inner shelf inshore of the 50-m isobath and the outer shelf seaward of that isobath. The circulation over the inner shelf is found to be driven mainly by the winds while that over the outer shelf is greatly influenced by mesoscale phenomena such as Loop Current eddies.

The recordlength mean alongshelf currents over the inner shelf are downcoast, while those over the outer shelf are upcoast. The recordlength mean cross-shelf currents over the shelf edge are onshelf at about $1 \text{ cm}\cdot\text{s}^{-1}$ ($2 \text{ cm}\cdot\text{s}^{-1}$ in extreme southwest) except near 94° - 95° W where they are offshelf. The annual signal of 10-m, alongshelf velocity is upcoast during the summer and downcoast for the rest of the year. This pattern is present throughout the water column inshore of the 50-m isobath. The annual cross-shelf velocity amplitudes are much less than those of alongshelf velocity. This annual cycle of currents over the inner shelf is being driven by the annual cycle of the winds, consistent with the CK schema. The annual cycle over the outer shelf is not necessarily consistent with that pattern. The mean and annual signals were removed from the records to obtain residual signals that were band-passed for further examination. The weather band kinetic energy, with periods of 2 to 10 days, dominates over the inner shelf, while mesoscale band kinetic energy, with periods of 10 to 100 days, dominates over the outer shelf and shelf edge. The time scale of the

dominant fluctuations of the residual time series was estimated as the number of days to the first zero-crossing of the sample autocorrelation function. The longest time scales (> 20 days) for 10-m currents are located over the western and eastern shelf edges, regions influenced by the Loop Current eddies. Over the rest of the shelf, the scales are 5-10 days, which is within the weather band forcing period.

The recordlength mean salinity shows fresher waters (< 34 at 10 m) over the inner than over the outer shelf, exhibiting the influence of the Mississippi-Atchafalaya river discharge. The annual signal of salinity responds to the annual cycles of the winds, which drive the currents over the inner shelf, and of the Mississippi-Atchafalaya river discharge. The river system discharges high volumes of fresh water onto the shelf during the spring. The currents carry this fresh water downcoast, resulting in fresher water over both the east and west regions of the inner shelf. This leads to the pattern of springtime freshening seen in the 10-m annual salinity signals over the shelf. In summer, the currents are upcoast, holding fresh water from the river system over the eastern shelf. The upcoast summer currents also move saltier water from the south onto the western shelf. This results in the salinity maxima seen in the annual signal of salinity for the western moorings in late summer. In fall, the downcoast current is reestablished and again carries fresh water to the inner western shelf, resulting in a secondary fall freshening seen in the annual signal of the moorings located there. Variability in the residual signal of 10-m salinity increases from the shelf edge to the innermost moorings, showing the greater influence of the river discharge over the inner shelf. Time scales for 10-m residual salinity are 20 to 50 days over most of the shelf, suggesting salinity is not responsive to forcing in the weather band.

The isotherms of recordlength mean 10-m temperature generally parallel isobaths with cooler waters inshore and warmer offshore; temperatures decrease with depth. Over the entire shelf, the pattern of the annual signal of 10-m temperature shows warming in summer and cooling in winter in response to the annual cycle of insolation. The warmest peaks generally occur earlier in the year in the east than in the southwest; the warm period is longest at the innermost moorings and shortest at the shelf edge moorings. The pattern of the annual signal of bottom temperature over the inner shelf is similar to that of the 10-m pattern, although much less pronounced and with extrema shifted later in time by one to two months. The variability of the residual signal of temperature increases from the shelf edge to the inner shelf. Time scales for 10-m residual temperature are 20 to 60 days over all the shelf. This is greater than the weather band scale, suggesting that residual temperature does not respond to forcing at weather band frequencies. Longest time scales (> 70 days) are at the western shelf edge, showing the influence of the Loop Current eddies there.

Shelf-scale currents observed during LATEX. Using the monthly means of the LATEX A 40-hour subtidal current data at 6-hour intervals from the 10-m instruments, velocity streamfunction fields were computed and examined for the 32 months of observations (Cho 1996). Cho also constructed monthly mean transport streamfunctions. These representations are augmented by monthly mean current fields from objective analysis of the current meter observations and fields of geopotential anomaly for twelve periods of hydrographic surveys.

Based on the velocity streamfunction fields and objectively analyzed velocity fields for the shelf-wide, low-frequency circulation, there is a distinct difference between the nonsummer and summer periods. The nonsummer fields (September-May) generally show downcoast flow over the inner shelf. For the streamfunction fields, strong closure of a cyclone over the shelf (i.e., strong upcoast flow at the shelf edge) was evident in only 7 of 23 months; in 11 months no cyclonic closure was evident. In nonsummer months there is a tendency for

onshore, cross-shelf flow over the eastern shelf and a weaker tendency for off-shelf flow over the southwestern shelf. The summer current fields generally show upcoast flow over outer as well as inner shelf. There is prominent interannual variability in the streamfunction field for given month, and also in the time of reversal of the flow from spring to summer and summer to fall that are well correlated with the alongshelf wind stress variability. A strong upcoast current was dominant in the western shelf break region, and sometimes present in the eastern shelf break region, that seemed to be associated with Loop Current eddies.

The dominant first EOF pattern of variability shows a simple shelf-wide pattern of unidirectional alongshore flow. This single EOF mode accounts for 89% of the monthly variance from the recordlength mean pattern. The amplitude of the first EOF mode is highly correlated with the seasonal variation of wind, while the second mode is not, implying that wind is the primary forcing for seasonal variation of shelf-wide low-frequency circulation on the Texas-Louisiana shelf. Even the interannual variations of the first EOF mode are explained by variations in the wind forcing. Thus the wind forcing serves as a very robust index of low-frequency, wind-induced, shelf-wide upcoast or downcoast flow on the Texas-Louisiana continental shelf.

Although the vertical resolution of horizontal velocity by the moored current meters is not good (only two or three meters were on each mooring), the agreement between vertical shear measured by the moored arrays and that measured by shipboard ADCP seems remarkably good. Examination of vector mean currents with variance ellipses yields some information regarding the vertical current structure. There is relatively strong polarization of both mean flow and variance ellipses for 40-hour, low-pass currents along isobaths. (By contrast, tidal ellipses have major axes across the shelf; see Appendix F.1.) The polarization of variance increases near bottom, as expected. Also, polarization is stronger for nonsummer than for summer, indicating more cross-isobath variability in summer. Along the 20-m isobath, over the inner shelf, there is evidence for cyclonic turning at the near-bottom instrument relative to the 10-m instrument; this is consistent with expected shear for a bottom Ekman layer.

Coherence of winds and currents. Autospectra of hourly surface (10-m) wind components over this shelf show several characteristic features.

- Strong diurnal and semi-diurnal peaks appear in summer and remain, though less pronounced, through autumn. These peaks are not present in winter and fall.
- There is a large seasonal difference in weatherband (2- to 10-day periods) energy. Winter records show considerably more energy, perhaps a factor of five at the nine-day period, than summer records because of the relatively few frontal passages during summer. During fall and into winter the weatherband portion of the energy spectra increases, beginning with shorter and continuing to longer periods.

Autospectra of ocean current components show similar features. Spectral peaks centered at diurnal period in the summer are believed due to diurnal thermal cycling caused by heating and cooling of the upper ocean. The upper ocean then responds strongly to diurnal wind variation, perhaps with energy feedback. In other seasons, the peaks in ocean current spectra around diurnal periods are due in part to inertial oscillations forced by frontal passages. As for winds, weatherband energy in the current spectra is at a minimum in summer and maximum in winter.

In general, coherence between alongshelf weather band (2- to 10-day periods) components of wind and current is greatest near shore and at downcoast moorings. Coherency is least during summer. Offshore from the inner shelf coherency in the weather band is significant only for winter and spring. At the shelf edge there is little coherence in any season. For alongshelf current and cross-shelf wind components in the weather band, coherence is often significant during nonsummer months when frontal passages are frequent. Again, this coherence decreases offshore. For weatherband periods, the phase for significant coherence suggests that winds lead 10-m currents by the order of 1 day or less.

Analysis of cross-shelf currents versus either cross-shelf or alongshelf wind gave no evidence of significant coherence in the weather band during any season.

General shelfwide circulation based on LATEX results.

- The mean currents based on the 32 months of LATEX data are downcoast over the inner shelf and upcoast over the outer shelf.
- The annual (yearly plus three harmonics) signal of currents over the inner shelf is of downcoast flow during nonsummer (September through May) and upcoast flow during summer; over the outer shelf there is no systematic, general pattern to the annual signal although there is general upcoast, near surface flow in summer.
- The kinetic energy of currents in the mesoscale band (periods between 10 and 100 days) is greatest at the shelf edge ($50\text{-}100\text{ cm}^2\cdot\text{s}^{-2}$ at 10 m depth) and decreases toward shore. Such currents are greatest at the shelf break between 94° and 96°W and result largely because of offshore eddies—particularly anticyclonic Loop Current eddies.
- The kinetic energy of currents in the weather band (periods between 2 and 10 days) is greatest near shore ($\sim 100\text{ cm}^2\cdot\text{s}^{-2}$ at 10 m depth) and decreases offshore over the shelf. Currents are well correlated with wind stress in the weather band; they are most energetic in winter and spring and decrease to a minimum in summer with infrequent frontal passages.
- Forcing for circulation over the inner shelf is essentially by wind stress and buoyancy contrast.
- Currents over the inner shelf are largely forced by wind stress. The correlation between monthly averaged, alongshelf current and alongshelf wind stress is positive and highly significant, with the general pattern of downcoast forcing in nonsummer months and upcoast forcing in summer months. Examination of the principal EOF of monthly velocity streamfunction and the monthly alongshelf wind stress give evidence that wind-forced alongshelf currents over the outer shelf are in the same direction as those over the inner shelf though much weaker and may be masked by the effects of offshore eddies.
- The bimodal (summer versus nonsummer) pattern of alongshelf currents over the shelf is interrupted by energetic wind events that alter the direction of alongshelf wind stress—usually for periods of a few days. The region in which alongshelf current direction changes in a statistically significant manner in response to short period, alongshelf wind change extends offshore almost to the shelf break near the Mexican border but is confined to shallower depths upcoast (the 50-m isobath over the central shelf and near the 20-m isobath off the Mississippi Delta). Within this region current

reversals follow wind stress reversals in less than 1 day; response times vary from about 4 hours off south Texas to almost 10 hours off Louisiana.

- The Mississippi-Atchafalaya river discharge is historically maximum in spring, however interannual variability is large. The fresh waters contribute to buoyancy forcing over the inner shelf, thus increasing the downcoast geostrophic shear. The total discharge by U.S. rivers west of the Atchafalaya is very small relative to Mississippi-Atchafalaya discharge on average. However, in cases of extreme discharge, water from Texas rivers may occasionally enhance buoyancy forcing of downcoast flow.
- Because of the sporadic occurrence of current rings adjacent to the shelf, interannual and even intraseasonal variability over the outer shelf is quite large.
- The occurrence of rings seems most frequent off the south Texas shelf, less frequent off the Louisiana shelf, and infrequent off the upper Texas shelf. Perhaps this is due to bathymetric constraints—the slope is wider off the upper Texas shelf.
- The flow near the shelf edge is greatly influenced by the presence of eddies adjacent to the shelf. The upcoast (eastward) flow at the shelf edge envisioned in the CK schema is the result of integrated effects of anticyclonic eddies impinging on the shelf edge.
- Although onshelf and offshelf flow may occur over the shelf break to maintain continuity of the pattern of alongshelf currents over the shelf, large cross-isobath currents due to offshore eddies are frequent and may dominate the property exchange across the shelf break.

ECOSYSTEM STUDIES

Suspended particle distributions. Vertical profiles of light transmission and discrete measurements of suspended particle matter (available from NODC, the National Oceanographic Data Center) were collected during ten LATEX hydrographic cruises and used to describe by cruise and season particle distributions in the surface layer, entire water column, and bottom nepheloid layer. Suspended particle matter distributions in the surface layers commonly extend to or past the shelf edge off Texas south of 27°N. These offshore, cross-shelf transports result from the occurrence and interactions of offshore cyclonic and anticyclonic eddies with the shelf circulation. Over the Louisiana shelf, high surface values of particle beam attenuation coefficients, and, by inference, high surface suspended particle matter, can be related to sustained high discharge rate of the Mississippi-Atchafalaya which are greatly influenced by the circulation. In nonsummer, if the dominant downcoast flow over the inner shelf is diminished, there is more likelihood that the surface particle distributions will extend further seaward than for large downcoast flow which sweeps the surface nepheloid layer away in a coastal boundary layer. These are the mechanisms responsible for the fact that the sedimentary record indicates that fine grained modern sediments blanket the shelf in these areas and can most effectively cross the shelf there.

The pattern of average water column suspended particle matter that emerges presents a maximum in the fall season. This is true for the entire shelf, but is even more striking for the eastern half. Ignoring the one winter realization (cruise H04), each year shows a minimum in summer, maximum in fall, and an intermediate value in spring. Our examination did not reveal a unique relationship between the Mississippi-Atchafalaya discharge rate and average water column suspended particle matter over the shelf on cruise-by-cruise or seasonal bases. However, large interannual variability in suspended particle

matter is present. For each season in 1992 the values were less than those for the corresponding season in 1993 and 1994, which we attribute to the fact that 1992 was a year of less, but 1993 and 1994 higher, than average Mississippi-Atchafalaya discharge.

The LATEX data show a positive correlation between average suspended particle matter in the entire water column and that in bottom nepheloid layers. Thus, the high average water column suspended particle matter may result when the bottom nepheloid layers are transporting more matter. The causal factors for such enhanced bottom nepheloid layer transport include large near bottom currents (e.g., enhanced coastal current or bottom currents over the outer shelf due to current eddies) or enhanced wind wave activity.

Nutrient distributions. Nitrate, nitrite, phosphate, silicate, ammonia, and urea were measured at every water depth sampled at each hydrographic station of the ten LATEX A cruises; data are available via NODC. The space-time distributions of nitrate, phosphate, and silicate over the Texas-Louisiana shelf during the sampling period are presented and discussed. Total nutrient masses in the upper 5 m of the water column increase inshore and upcoast, consistent with riverine sources. The nitrate mass peaks during spring except in the immediate vicinity of the Mississippi-Atchafalaya, where the peak is in summer; this may be attributed to the upcoast wind-driven flow over the inner shelf which helps maintain surface discharge waters over the far eastern shelf area. In nonsummer the downcoast currents over the inner shelf sweep higher nutrient-content waters from major sources in the east toward the west-southwest. In contrast with nitrate, the phosphate and silicate masses peak during summer with two maxima slightly west of the outflows of the Mississippi and Atchafalaya rivers. Silicate and phosphate masses are highest over the inner shelf between 92°W and 94°W during fall. Surface phosphate mass is smallest in spring, silicate in fall.

Photic zone (upper 60 m) inventories of nutrient mass are approximately an order of magnitude greater than for the upper 5 m. For both surface and photic zone distributions the total masses are considerably larger for the eastern (east of 94°W) than for the western shelf. Seasonal variations of photic zone inventories of these three nutrients are essentially the same as variations in the upper 5 m. The distributions suggest that phosphate and silicate inventories may be more strongly controlled by biological processes than are nitrate inventories. Excess nitrate available for primary production during the spring and fall could lead to depletion of water column phosphorus that phytoplankton need for growth. Consumption of silicate by the preponderance of diatoms in eastern shelf surface waters would explain the lower surface silicate levels during spring and fall. Studies of primary production during the LATEX A hydrography cruises showed that primary production rates, and accompanying nutrient consumption rates, are highest in the spring and fall and lowest during summer, as found in previous studies of the Louisiana shelf. Thus, nutrients on the Texas-Louisiana shelf are consumed at a more rapid rate in the spring and fall than during the summer, leading to the peaks in phosphate and silicate seen in the summer. As noted, circulation and riverine sources also play prominent roles in determining silicate and phosphate distributions, but not so much so as for nitrate. We found a positive linear correlation between mass of nitrate input by Mississippi-Atchafalaya and total surface (0-5 m) nitrate mass at the 97.5% significance level for the eastern shelf, but only at a 75% significance level for the western shelf. Clear effects of offshore eddies on the nutrient distributions over the outer shelf are demonstrated.

Dissolved oxygen distributions and hypoxia. Dissolved oxygen concentrations measured on all LATEX A hydrographic cruises are available from the NODC. Surface distributions of dissolved oxygen (% saturation) are presented and discussed for each cruise. In winter

and spring surface waters generally were at saturation or above; summer and fall values were between 90 and 100% saturation almost everywhere. Although phytoplankton blooms can be major oxygen contributors to surface waters, squared correlations between surface oxygen saturation and surface chlorophyll-a examined for all eastern shelf stations are all less than 0.5, with only four cruises at the 95% significance level; significant correlations were positive. A similar result was found for correlations between surface salinity and oxygen saturation; only five of 10 cruises had correlations significant at 95% and these were negative, indicating some correlation between low salinity and high saturation levels.

Cross-shelf vertical profiles of dissolved oxygen were presented and discussed to illustrate seasonal and interannual variability. The distributions along the 200-m isobath reveal the effects of cyclonic and anticyclonic offshore eddies. At a given depth, the waters of an anticyclone generally are higher in dissolved oxygen than those of a cyclone.

Hypoxic conditions (dissolved oxygen concentrations less than $1.4 \text{ ml}\cdot\text{l}^{-1}$) were observed in bottom waters of the eastern shelf in four of ten cruises: summer 1992, spring and summer 1993, and summer 1994. Near-hypoxic conditions were found at the eastern survey boundary in spring 1992.

A stratified water column facilitates the formation of hypoxic bottom waters by restricting the resupply of oxygen from the surface. The Mississippi-Atchafalaya discharge, together with a reduction in wind stress and a seasonal thermocline in summer, contributes to the stratification observed on the continental shelf of the Gulf of Mexico. Water column static stability was estimated as the difference between surface and bottom potential density anomaly divided by water depth. All stations with hypoxia have high stability values. Correlations between stability and bottom oxygen saturation values are positive and significant at the 95% level for all cruises with hypoxia and for the winter cruise. Hypoxic stations all are associated with fresh (< 31) surface waters from river runoff. Thus river discharge that contributes to low surface salinity also contributes to stratification associated with hypoxic conditions. There is evidence of an enhanced flux of organic material to the bottom and resulting oxygen depletion from decomposition of that material. We examined the bottom oxygen saturation levels versus bottom nitrate concentrations. Enhanced bottom nitrate concentrations occurred at the hypoxic and near-hypoxic stations. Correlations for all cruises are negative and significant at 90%; for seven cruises the significance level was above 99%.

Phytoplankton pigments. Chlorophyll-a, accessory pigments, nutrients, salinity, and temperature were analyzed together using principal component analysis to delineate patterns among the variables in sea surface and chlorophyll maximum data sets for each of the ten hydrographic cruises. The low frequency circulation over the inner shelf first described by Cochrane and Kelly (1986) and now substantiated by LATEX data is an important mechanism in the distribution of chlorophyll-a on the Texas-Louisiana shelf. Annual differences in mean concentrations of chlorophyll-a were related to the magnitude of fresh water on the shelf. High mean chlorophyll-a was observed on the shelf in all seasons when Mississippi-Atchafalaya discharge was above average. Winter and spring mean chlorophyll-a levels were highest on the eastern shelf. Spring and fall chlorophyll-a were highest in low salinity inner shelf water carried downcoast by the prevailing circulation.

The distribution of phytoplankton pigments on the Texas-Louisiana shelf reflected the environment in which they were found; the highest overall chlorophyll-a levels were found during highest river flow periods. Areas of high chlorophyll-a followed the circulation and distribution of low salinity water. High levels of chlorophyll-a and fucoxanthin dominated

coastal waters where diatoms thrived in the nutrient-rich inner shelf environment. Algal class distributions were predictable based on the distribution of high and low chlorophyll-a. Diatom pigments were always grouped in low salinity, high chlorophyll-a waters. Cryptophyte pigments (alloxanthin) and peridinin-containing dinoflagellates were usually grouped with diatoms. Prymnesiophytes, chrysophytes, and cyanobacterial pigments were more prevalent where the water column most resembled open ocean conditions on the outer shelf.

SELECTED APPENDICES

Winter Cyclogenesis. There were 8 winter cyclogenesis events in each of the two winter seasons during the LATEX field program. These included one event in March 1993 that was comparable in strength to a category 1 hurricane and was dubbed the "Storm of the Century".

Effects of a hurricane and severe local cyclone. Observations are available to characterize the wave and current regimes over the Texas-Louisiana shelf during the passage across the Gulf of Mexico from south Florida to Louisiana, 25-27 August 1992, of Hurricane Andrew. This hurricane had sustained winds in excess of $61 \text{ m}\cdot\text{s}^{-1}$ crossing the Gulf. Low frequency waves with periods as long as 13-16 s outdistanced the storm center and were recorded in advance of the storm contacting the Louisiana shelf all along the Texas-Louisiana shelf at depths near 10 m. As the eye of the storm passed approximately 30 km from LATEX mooring 16 (located about 20 km south of Terrebonne Bay, Louisiana) peak wave heights exceeding 9 m were observed. Low frequency waves continued to contribute significantly to energy spectra after the storm center passed the area. The current meters at mooring 16 failed or were swept away by Andrew; however, 10-meter currents at the other moorings over the mid and outer shelf along 90.5°W measured maximum speeds exceeding $100 \text{ cm}\cdot\text{s}^{-1}$ —reaching $163.5 \text{ cm}\cdot\text{s}^{-1}$ in one case. The maximum current occurred under the northwest quadrant of the storm and were directed generally to the southwest. The influence of the storm forcing 10-m current speeds of $45\text{-}60 \text{ cm}\cdot\text{s}^{-1}$ extended over most of the mid and outer shelf. As expected, large inertial oscillations were initiated by the storm passage.

Early on 12 March 1993, an intense cyclone (later called "Storm of the Century") formed over northern Mexico near the Texas border, moved over the Gulf where it intensified, then followed an eastward path just offshore of the Texas-Louisiana slope-shelf break, and continued northeastward to make landfall near Pensacola, Florida around 0900 UTC on 13 March. Wind speeds in this storm strengthened to greater than $25 \text{ m}\cdot\text{s}^{-1}$ by 0000 UTC 13 March. Near-surface circulation over the shelf was profoundly affected. A cyclonic, shelf-wide circulation with peak 10-m currents of $80\text{-}120 \text{ cm}\cdot\text{s}^{-1}$ was set up. Its center, located northwest of the storm center, moved eastward along the shelf in seeming synch with the movement of the storm center. Although not as large in absolute value as currents generated by Hurricane Andrew, the currents associated with such local cyclones are large and spatially pervasive, and cyclogenesis is much more frequent than hurricane passages.

Coastal upwelling off south Texas. Mean wind stress is favorable for upwelling along much of the western boundary of the Gulf of Mexico between 20° and 28°N from April through August. Upcoast alongshelf wind components begin sooner further south. Along the south Texas coast June appears to be the transition month for upwelling driven by change from downcoast to upcoast alongshore current components. In the latter half of June or in July of 1992, 1993, and 1994, the inner shelf moorings near 27°N , after a moderate upcoast wind fluctuations, experienced rapid $4\text{-}5^\circ\text{C}$ drops in temperatures at 10-m

depths. These temperatures persisted for more than a month each year, with some short interruptions in 1994. Synoptic hydrographic data sets from LATEX A cruises and historical data confirm this pattern and evidence simultaneous increases in near surface salinities by 2 or more.

Texas flood of October 1994. On October 19, 1994, the combined discharge of Texas rivers, and in particular that of the San Jacinto River, exceeded the discharge of the Mississippi-Atchafalaya for the day. The surface current meter nearest to the Brazos River mouth showed a strong decrease in surface salinity beginning one day after the event. Associated with the decrease is a strong diurnal oscillation. Hydrographic cruise H10 showed that two weeks after the flood significant amounts of low salinity surface water remained off the Texas coast.

Gravity waves. Surface gravity waves were estimated by bottom pressure observations during the LATEX field period; data and estimates are available on CD-ROM from the National Oceanographic Data Center. As a consequence of the low frequency cutoff required to process bottom-mounted wave data, those gauges systematically underestimated actual wave heights. There is an observed alongshelf increase in monthly-averaged wave heights from minima near Atchafalaya Bay to maxima near the Mexican border. Except for extreme episodic atmospheric events, long-period (>10 s) waves are rarely seen over the Texas-Louisiana shelf. During the passage of Hurricane Andrew over the eastern Gulf and Louisiana shelf, wave heights to 9 m and peak spectral periods to 14 s were observed.

Comparisons of currents derived from ADCP and current meters. The agreement between ADCP velocity and measurements from the nearest current meter mooring is surprisingly good. It is shown that minimizing the distance between the mooring and the ship is more critical to getting a good agreement than any other factor.

Were free shelf waves seen in the data? Examination of current, temperature, and salinity time series measurements from moorings along the 200-m isobath did not reveal clear evidence of free (remotely forced) coastal trapped wave propagation in the downcast direction (east to west). There does exist clear evidence of Eddy Vazquez propagating westwards along the upper slope region in April-May of 1993 and then eastwards in August of 1993, but at speeds much smaller than that associated with linear shelf wave theory. On the inner shelf however, evidence of free shelf wave propagation was seen in the current meter records at the downcoast moorings following two forcing events. The first occurred after the landfall of Hurricane Andrew at the upcoast end of the shelf in August of 1992. The second occurred during the exit of the March 1993 "Storm of the Century" from the Texas-Louisiana shelf. In both cases evidence of wave propagation, at speeds comparable to long shelf waves modes, was seen in the downcoast current meter records, at a time when the local winds were nearly calm. Such cases of free shelf wave propagation on the inner shelf are rare because most of the time the shelf waters are under the influence of large scale temporally-varying wind forcing. The phasing of disturbances at adjacent moorings is then strongly dependent on the propagation of the forcing events, whose alongshelf component is often upcoast (opposing that of free wave propagation).

Comparison of observed and modeled currents and sea level on the inner shelf. Application of a nearly barotropic wind-driven shelf model for predicting the subtidal, depth-averaged, alongshelf currents and coastal water level show overall squared correlations between simulated and observed values of these variables of order 0.5, based on comparisons at 12 inner shelf current meters and six coastal tide gauges for the full 32 months of observations. Cross-spectral analysis showed that the maximum squared coherences

between simulated and observed variables at these 18 measurement sites occurred in a frequency band of about 0.03 to 0.1 cpd. The largest squared coherences for alongshelf current comparisons of model and observations were at the downcoast moorings, with maximum values of about 0.8 at mooring 23. Current meters on the three inner shelf moorings at the eastern end of the shelf provided the required specified flow at this upstream open boundary in the model simulations. However, only about 5 percent of the variance of currents and water level variation over the inner shelf is attributed to this forcing, the primary forcing in the model being the local alongshelf component of the wind. At the annual period, the effect of seasonal thermal and river discharge variations on the observed water levels and currents degrade the comparison with the wind-driven model, as should be expected.

Estimates of property exchanges between shelf subregimes using box models. The volume fluxes simulated by this box model are highly consistent in direction and magnitude with currents expected due to seasonal wind stress regimes and the presence of anticyclonic eddies near the shelf break. Although the presence of eddies adjacent to the shelf dramatically affect fluxes on or off the outer shelf, little impact was seen on the inner shelf in the box model results.

The fluxes of volume, freshwater, and heat simulated by the box models are consistent with our understanding of a predominantly alongshelf circulation driven by a two-season (summer versus nonsummer) wind domain.

TABLE OF CONTENTS

VOLUME I

	<u>PAGE</u>
LIST OF FIGURES	xxv
LIST OF TABLES	xxxix
ABBREVIATIONS AND ACRONYMS	xli
ACKNOWLEDGMENTS	xlili
1 INTRODUCTION	1
1.1 LATEX A Program objectives and description	1
1.2 Data collected.....	5
1.3 Report organization.....	15
2 PHYSICAL BOUNDARY CONDITIONS	17
2.1 Wind fields.....	17
2.1.1 Comparisons among LATEX, ERS-1 and NCEP winds	17
2.1.2 Description of LATEX winds	35
2.1.3 Weather events over the Texas-Louisiana shelf	45
2.2 Other surface fields	48
2.3 River discharge	52
2.4 Bottom stress characterization	63
2.5 Eddy-shelf interaction	70
2.5.1 Loop Current eddies during LATEX	70
2.5.2 Influence of Loop Current eddies on current fields	82
3 WATER MASS CHARACTERIZATION AND BUDGETS	97
3.1 Salinity and temperature distributions	97
3.2 Heat and freshwater budgets	118
4 SHELFWIDE CIRCULATION AND TRANSPORTS	135
4.1 Introduction: The Cochrane-Kelly schema for shelf-scale circulation	135
4.2 Seasonal mean hydrographic fields as related to circulation, with estimates of interannual variability	137
4.3 Temporal and spatial scales of variability.....	182
4.3.1 Spatial scales from hydrography.....	182
4.3.2 Temporal scales from current meters.....	191
4.4 Shelf-scale currents observed during LATEX.....	239
4.4.1 Monthly mean streamfunctions from direct observations.....	239
4.4.2 Patterns of variability of velocity streamfunctions	257
4.4.3 Vertical structure of seasonal currents	261
4.5 Coherence of winds and currents	268
4.6 General shelfwide circulation based on LATEX results.....	287
5 ECOLOGICAL STUDIES	323
5.1 Suspended particle distributions	324
5.2 Nutrient distributions	358
5.3 Dissolved oxygen distributions and hypoxia	383
5.4 Phytoplankton pigments.....	416
6 REFERENCES	435

TABLE OF CONTENTS

VOLUME II

<u>APPENDIX</u>	<u>PAGE</u>
A Winter Cyclogenesis	1
A.1 Event analysis	1
A.2 30-year climatology of cyclogenesis events	10
B Examples of Effects on Shelf Circulation by Episodic Atmospheric Forcing	13
B.1 Hurricane Andrew (25-27 August 1992)	13
B.2 The Storm of the Century (March 1993)	27
B.3 Coastal upwelling off south Texas	42
C Effects of the Texas Flood of October 1994	55
D Case Study of Eddy Vazquez	63
E A Volumetric Temperature-Salinity Census for the Texas-Louisiana Shelf	89
F Inertial and Superinertial Motions	107
F.1 Deterministic tides	107
F.2 Non-deterministic 40-hr high-passed signals	119
G Comparison of Observed and Modeled Surface Gravity Waves	129
H Realizations of Current Fields	147
H.1 Geopotential anomaly fields	147
H.2 Monthly average LATEX current fields	158
I Current, Temperature, and Salinity Statistics	165
J Comparisons of Currents Derived from ADCP, Current Meter, and Hydrographic Observations	195
J.1 Comparison of vertical shear from ADCP and hydrography	195
J.2 Comparison of current meter and ADCP velocities	209
K Wave Propagation Along the Shelf and Slope	217
L Model and Observations of Wind-Driven Circulation Over the Inner Shelf	227
M Estimates of Property Exchanges Between Shelf Subregimes Using Box Models	245
REFERENCES	275

LIST OF FIGURES

<u>FIGURE</u>	<u>DESCRIPTION</u>	<u>PAGE</u>
1.1-1	Study area and bathymetry for the LATEX A program over the Texas-Louisiana shelf and slope.....	3
1.2-1	Locations for LATEX A current meter moorings and meteorological buoys.	6
1.2-2	Typical locations for LATEX A hydrographic survey stations during field year 1, April 1992 to March 1993.....	9
1.2-3	Typical locations for LATEX A hydrographic survey stations during field year 2, April 1993 to March 1994.....	10
1.2-4	Typical locations for LATEX A hydrographic survey stations during field year 3, April 1994 to November 1994.....	11
2.1.1-1	Locations of observing stations in the construction of the LATEX surface meteorological fields.....	18
2.1.1-2	LATEX mean winds, NCEP mean winds, and the mean difference field for the period April 1992 through November 1994.....	23
2.1.1-3	Mean seasonal difference between LATEX and NCEP wind fields.....	24
2.1.1-4	The LATEX and NCEP winds at 0600 UTC 4 November 1992.....	26
2.1.1-5	Histograms of speed difference between LATEX and NCEP winds for each season.....	27
2.1.1-6	Histograms of direction difference between LATEX and NCEP winds for each season.....	28
2.1.1-7	Histograms of difference between LATEX and NCEP winds, angles measured positive in counterclockwise sense.....	29
2.1.1-8	Histograms of difference between LATEX and ERS-1 winds, angles measured positive in counterclockwise sense.....	31
2.1.1-9	ERS-1 minus LATEX wind speeds and directions as functions of LATEX wind speeds.....	32
2.1.1-10	LATEX, ERS-1, and NCEP winds at 1700 UTC 18 March 1993.....	33
2.1.2-1	Vector mean winds and variance ellipses constructed from LATEX winds for the period April 1992 through November 1994.	36
2.1.2-2	Vector mean wind stress field constructed from LATEX winds for the period April 1992 through November 1994.....	37
2.1.2-3	Mean field of wind stress curl constructed from LATEX winds for the period April 1992 through November 1994.....	38
2.1.2-4	Seasonal vector mean wind and variance fields constructed from LATEX wind fields for period April 1992 through November 1994.	40
2.1.2-5	Daily wind vectors, zonal wind component, and meridional wind component from daily gridded winds at 28.5°N, 95.5°W, based on LATEX winds.....	41
2.1.2-6	Seasonal mean wind stress fields constructed from LATEX winds during April 1992 through November 1994.....	43
2.1.2-7	Seasonal mean wind stress curl fields constructed from LATEX winds during April 1992 through November 1994.	44
2.2-1	Mean seasonal sea level atmospheric pressure fields constructed from LATEX fields for April 1992 through November 1994.....	49
2.2-2	Mean seasonal surface air temperature fields constructed from LATEX fields for April 1992 through November 1994.	50

LIST OF FIGURES

<u>FIGURE</u>	<u>DESCRIPTION</u>	<u>PAGE</u>
2.2-3	Mean seasonal SST fields constructed from LATEX fields for April 1992 through 1994.....	51
2.3-1	Annual cycle of discharge rates from daily averages for the combined Mississippi-Atchafalaya Rivers based on the 64-year average and for the years of 1992, 1993, and 1994.....	54
2.3-2	Long-term time series of the ratio of Atchafalaya River discharge to the combined Mississippi-Atchafalaya River discharge.....	55
2.3-3	Annual cycle of discharge rates based on daily means for the combined Mississippi-Atchafalaya Rivers bounded by an envelope of one rms deviation based on a 64-year record.....	56
2.3-4	Time series of discharge rates from daily means for combined lesser rivers for years 1992-1994.	58
2.3-5	1992-1994 discharge rates from daily means for the Mississippi-Atchafalaya Rivers and the lesser rivers.	60
2.3-6	1994 time series of discharge rates from daily averages for the Trinity, Brazos, Sabine, Neches, and San Jacinto rivers.	61
2.3-7	Annual cycle of combined mean discharge for 13 Texas rivers plus the Calcasieu River bounded by an envelope of one rms deviation based on record lengths of daily discharge rates for each river.	62
2.4-1	Hourly values of 40-hr low-passed alongshelf wind stress at meteorological station PTAT2 for the 32 months of LATEX measurements.....	64
2.4-2	Typical dependence of 40-hr low-pass pseudo bottom stress on 40-hr low-pass bottom current, using data from all deployments of mooring 25.....	67
2.4-3	Linear fit to water depth of mean speed of 40-hr high-pass current v_h in $\text{cm}\cdot\text{s}^{-1}$ at individual bottom current meter locations employed in the estimation of bottom stress parameters.	69
2.5.1-1	Sea surface height anomaly with respect to alongtrack corrected Rapp 95 mean surface (a) TOPEX cycle 2, 3 to 12 October 1992, including ERS-1 35-day repeat centered on the mid-point of the T/P cycle; the track of LATEX A drifter 2447 is shown and (b) identification of eddies by the 4-cm SSHA contour in (a).....	72
2.5.1-2	Approximate locations of the center of remnant of Eddy T based on sea surface height anomaly maps from ERS-1 cycles and NOAA ocean features analyses maps between 14 April and 6 October 1992, and sea surface height anomaly maps from TOPEX/Poseidon cycles between 3 October and 1 November 1992.	75
2.5.1-3	Approximate locations of the center Eddy U based on sea surface height anomaly maps from ERS-1 cycles between 14 April and 6 October 1992, and sea surface height anomaly maps from TOPEX/Poseidon cycles between 3 October and 1 December 1993.	76
2.5.1-4	Approximate locations of Eddy V centers based on the drifter 2447 track from 12 September to 3 October 1992, and sea surface height anomaly maps for TOPEX/Poseidon cycles between 3 October 1992 and 4 October 1993.....	77

LIST OF FIGURES

<u>FIGURE</u>	<u>DESCRIPTION</u>	<u>PAGE</u>
2.5.1-5	Approximate locations of the center of Eddy W based on sea surface height anomaly maps of TOPEX/Poseidon cycles between 7 June and 23 December 1993.	79
2.5.1-6	Approximate locations of the center of Eddy X based on sea surface height anomaly maps from TOPEX/Poseidon cycles of 26 August 1993 to 3 September 1994.	80
2.5.1-7	Approximate locations of the center of Eddy Y based on sea surface height anomaly maps of TOPEX/Poseidon cycles between 25 August and 8 December 1994.	81
2.5.2-1	Monthly averages of 10-m, 40-hr low-pass current velocity along the shelf edge for April 1992 through July 1993.	83
2.5.2-2	Monthly averages of 10-m, 40-hr low-pass current velocity along the shelf edge for August 1993 through November 1994.	84
2.5.2-3	Monthly averages of 100-m, 40-hr low-pass current velocity along the shelf edge for April 1992 through July 1993.	85
2.5.2-4	Monthly averages of 100-m, 40-hr low-pass current velocity along the shelf edge for August 1993 through November 1994.	86
2.5.2-5	Monthly averages of 190-m/490-m, 40-hr low-pass current velocity along the shelf edge for April 1992 through July 1993.	87
2.5.2-6	Monthly averages of 190-m/490-m, 40-hr low-pass current velocity along the shelf edge for August 1993 through November 1994.	88
3.1-1	Potential temperature-salinity diagram for stations along the 200-m isobath during cruise H05.	99
3.1-2	Potential temperature and salinity profiles for stations along the 200-m isobath during cruise H05.	100
3.1-3	Composite plots of potential temperature versus salinity for the LATEX A 1993 hydrographic cruises H04, H05, H06, and H07.	102
3.1-4a	Contours of temperature in vertical section along the 200-m isobath for LATEX A cruises in spring.	103
3.1-4b	Contours of temperature in vertical section along the 200-m isobath for LATEX A cruises in summer.	104
3.1-4c	Contours of temperature in vertical section along the 200-m isobath for LATEX A cruises in fall.	105
3.1-4d	Contours of temperature and salinity in vertical section along the 200-m isobath for LATEX A cruises in winter.	106
3.1-5a	Contours of salinity in vertical section along the 200-m isobath for LATEX A cruises in spring.	107
3.1-5b	Contours of salinity in vertical section along the 200-m isobath for LATEX A cruises in summer.	108
3.1-5c	Contours of salinity in vertical section along the 200-m isobath for LATEX A cruises in fall.	109
3.1-6	Salinity in vertical sections on lines 8, 4, and 1 from LATEX A cruise H05, 25 April-11 May 1993.	111
3.1-7	Potential temperature in vertical sections on lines 8, 4, and 1 from LATEX A cruise H05, 25 April-11 May 1993.	112
3.1-8	Salinity in vertical sections on lines 8, 4, and 1 from LATEX A cruise H06, 25 July-7 August 1993.	114

LIST OF FIGURES

<u>FIGURE</u>	<u>DESCRIPTION</u>	<u>PAGE</u>
3.1-9	Potential temperature in vertical sections on lines 8, 4, and 1 from LATEX A cruise H06, 25 July-7 August 1993.....	115
3.1-10	Salinity and potential temperature in vertical sections on line 4 from LATEX A cruise H07, 6-22 November 1993.	116
3.1-11	Salinity and potential temperature in vertical sections on line 4 from LATEX A cruise H04, 4-13 February 1993.....	117
3.2-1	Basemap showing LATEX A CTD stations for typical full-shelf cruise and coverage areas for GOES GPI precipitation estimates and for NCEP estimates of surface fluxes.	119
3.2-2	Monthly march of the net oceanic heat gain as determined from the NCEP data set.....	122
3.2-3	The radiation balance at the sea surface and its components—the net absorbed solar radiation and the effective back radiation as determined from the NCEP data set.....	123
3.2-4	Monthly march of the net turbulent heat flux and its components—the turbulent flux of latent heat and the turbulent flux of sensible heat as determined from the NCEP products.	125
3.2-5	Rate of oceanic heat storage determined from the LATEX A hydrography compared to climatological baseline computed by Etter et al. (1985) using the temperature census of Ulm (1983).....	126
3.2-6	Heat flux divergence due to currents determined as a residual in the heat budget equation.....	127
3.2-7	Freshwater flux divergence as determined using the LATEX A hydrography data.....	128
3.2-8	Seasonal march of precipitation derived from the GPI data set.	129
3.2-9	Combined monthly river input from the Mississippi River, Atchafalaya River, and rivers in Texas.....	130
3.2-10	Seasonal march of the evaporation rate as determined from the NCEP data set.	131
3.2-11	Reduced freshwater thickness as determined using LATEX A hydrographic data compared with the baseline climatology computed using Ulm's (1983) salinity census.	132
3.2-12	Rate of freshwater storage as determined using the LATEX A data and from the monthly baseline climatology.	133
4.1-1	Monthly mean fields of surface geopotential anomaly relative to 70 db from Cochrane and Kelly (1986) representing their proposed pattern of annual variability of the shelfwide circulation.....	136
4.2-1	Locations of 745 hydrographic stations from ten May cruises, 822 hydrographic stations from nine July-August cruises, and 615 stations from six November cruises.	140
4.2-2	Average spring sea surface salinity and its standard deviation for eight May cruises.	142
4.2-3	Average spring geopotential anomaly of sea surface relative to 70 db and its standard deviation for eight May cruises.....	143
4.2-4	Average spring sea surface temperature and its standard deviation for eight May cruises.	144
4.2-5	Average spring bottom salinity and its standard deviation for eight May cruises.	146

LIST OF FIGURES

<u>FIGURE</u>	<u>DESCRIPTION</u>	<u>PAGE</u>
4.2-6	Average spring bottom temperature and its standard deviation for eight May cruises.	147
4.2-7	Average spring bottom potential density anomaly and its standard deviation for eight May cruises.	148
4.2-8	Average summer sea surface salinity and its standard deviation for seven July-August cruises.	151
4.2-9	Average summer geopotential anomaly of sea surface relative to 70 db and its standard deviation for seven July-August cruises.	152
4.2-10	Average summer sea surface temperature and its standard deviation for seven July-August cruises.	153
4.2-11	Average summer bottom salinity and its standard deviation for seven July-August cruises.	154
4.2-12	Average summer bottom temperature and its standard deviation for seven July-August cruises.	155
4.2-13	Average summer bottom potential density and its standard deviation for seven July-August cruises.	156
4.2-14	Average fall sea surface salinity and its standard deviation for six November cruises.	159
4.2-15	Average fall geopotential anomaly of sea surface relative to 70 db and its standard deviation for six November cruises.	160
4.2-16	Average fall sea surface temperature and its standard deviation for six November cruises.	161
4.2-17	Average fall bottom salinity and its standard deviation for six November cruises.	162
4.2-18	Average fall bottom temperature and its standard deviation for six November cruises.	163
4.2-19	Average fall bottom potential density and its standard deviation for six November cruises.	164
4.2-20	Histograms of residual fields, i.e., differences between gridded values of surface salinity, surface temperature, and geopotential anomaly for individual cruise fields and those for mean fields.	166
4.2-21	Surface salinity for the nine individual July and August cruises used to construct the summer mean fields.	167
4.2-22	Geopotential anomaly relative to 70 db for the ten individual May cruises used to construct the spring mean fields.	168
4.2-23	Geopotential anomaly of sea surface relative to 70 db for GUS III cruise 5 and corresponding residual field after subtracting the May mean geopotential anomaly field.	171
4.2-24	Sea surface salinity for GUS III cruise 5.	172
4.2-25	30-year average daily alongshelf wind component at Victoria airport, located on the coastal plain of central Texas.	173
4.2-26	Sea surface salinity and residuals of sea surface temperature relative to May mean for LATEX cruise H05.	174
4.2-27	Geopotential anomaly of sea surface relative to 70 db and sea surface salinity for GUS III cruises 32.	176

LIST OF FIGURES

<u>FIGURE</u>	<u>DESCRIPTION</u>	<u>PAGE</u>
4.2-28	Residuals of sea surface salinity in May versus: alongshelf wind index at Port Arthur; residuals of daily river discharge from the Mississippi and Atchafalaya Rivers in April and May; and residuals of geopotential anomaly of sea surface relative to 70 db in May.....	178
4.2-29	Residuals of sea surface salinity in July-August versus: alongshelf wind index at Port Arthur; residuals of daily river discharge from the Mississippi and Atchafalaya Rivers in June-August, and residuals of geopotential anomaly of sea surface relative to 70 db in July-August.....	179
4.2-30	Residuals of sea surface salinity in November versus: alongshelf wind index at Port Arthur; residuals of daily river discharge from the Mississippi and Atchafalaya Rivers in October and November, and residuals of geopotential anomaly of sea surface relative to 70 db in November.....	180
4.3.1-1	Surface salinity observed at each station on transect 4 during LATEX cruise H01; surface salinity from mean May field interpolated to H01 station positions.....	184
4.3.1-2	Average correlation of geopotential anomaly along transect 4 for the first seven LATEX cruises.....	187
4.3.2-1	Illustration of moorings included on each line.....	192
4.3.2-2	Recordlength mean temperature of top, middle, and bottom current meters.....	196
4.3.2-3	Recordlength means of temperature from moorings on line 4 and line 9. ...	197
4.3.2-4	Recordlength mean salinity of top, middle, and bottom current meters.....	198
4.3.2-5	Recordlength means of salinity from moorings on line 4 and line 9.	200
4.3.2-6	Recordlength mean alongshelf velocity component of top, middle, and bottom current meters.....	201
4.3.2-7	Recordlength means of alongshelf velocity component from moorings on line 4 and line 9.....	202
4.3.2-8	Recordlength mean cross-shelf velocity component of top, middle, and bottom current meters.....	203
4.3.2-9	Recordlength means of cross-shelf velocity component from moorings on line 4 and line 9.....	204
4.3.2-10	Annual signal of 10-m, alongshelf current velocity in groupings of alongshelf lines.....	206
4.3.2-11	Annual signal of bottom, alongshelf current velocity in groupings of alongshelf lines.....	207
4.3.2-12	Amplitude of the annual signal of alongshelf velocity from 10-m and bottom current measurements.....	209
4.3.2-13	Amplitude of the annual signal of alongshelf velocity from moorings on line 4 and line 9.....	211
4.3.2-14	Annual signal of 10-m, cross-shelf current velocity in groupings of alongshelf lines.....	212
4.3.2-15	Annual signal of bottom, cross-shelf current velocity in groupings of alongshelf lines.....	213
4.3.2-16	Tendency toward positive or negative correlation between the annual signal of 10-m, alongshelf velocity and the annual signal of top, middle, or bottom depth cross-shelf velocity.....	214

LIST OF FIGURES

<u>FIGURE</u>	<u>DESCRIPTION</u>	<u>PAGE</u>
4.3.2-17	Amplitude of the annual signal of cross-shelf velocity from 10-m and bottom current measurements.....	217
4.3.2-18	Amplitude of the annual signal of cross-shelf velocity from moorings on line 4 and line 9.....	218
4.3.2-19	Weatherband kinetic energy with period between 2 and 10 days from 10-m and combination middle/bottom mooring measurements.....	219
4.3.2-20	Mesoscale band kinetic energy with period between 10 and 100 days from 10-m and combination middle/bottom mooring measurements.....	221
4.3.2-21	Ratio of weatherband to mesoscale band kinetic energy from 10-m and combination middle/bottom residual current measurements.....	222
4.3.2-22	Kinetic energy of the residual time series on line 9 in the weatherband and the mesoscale band.....	224
4.3.2-23	First zero crossing of average autocorrelations for 10-m residual alongshelf and cross-shelf velocity.....	225
4.3.2-24	Annual signal of 10-m salinity in groupings of alongshelf lines.....	227
4.3.2-25	Amplitude of the annual signal of salinity from 10-m and bottom measurements.....	228
4.3.2-26	Amplitude of the annual signal of salinity from moorings on line 4 and line 9.....	230
4.3.2-27	Standard deviation of residual salinity from 10-m and bottom measurements.....	231
4.3.2-28	Annual signal of 10-m temperature in groupings of alongshelf lines.	232
4.3.2-29	Annual signal of bottom temperature in groupings of alongshelf lines.	234
4.3.2-30	Amplitude of the annual signal of temperature from 10-m and bottom measurements.....	235
4.3.2-31	Amplitude of the annual signal of temperature from moorings on line 4 and line 9.....	236
4.3.2-32	Standard deviation of residual temperature from 10-m and bottom measurements.....	238
4.4.1-1	The orthogonal, boundary-fitted curvilinear coordinate system used for calculating streamfunction.....	241
4.4.1-2	Shelfwide 10-m velocity streamfunction fields from recordlength means, nonsummer means, and summer means.....	242
4.4.1-3	Shelfwide monthly mean 10-m velocity streamfunction field for January of 1993 and 1994.....	244
4.4.1-4	Shelfwide monthly mean 10-m velocity streamfunction field for February of 1993 and 1994.....	245
4.4.1-5	Shelfwide monthly mean 10-m velocity streamfunction field for March of 1993 and 1994.....	246
4.4.1-6	Shelfwide monthly mean 10-m velocity streamfunction field for April of 1992, 1993, and 1994.....	247
4.4.1-7	Shelfwide monthly mean 10-m velocity streamfunction field for May of 1992, 1993, and 1994.....	248
4.4.1-8	Shelfwide monthly mean 10-m velocity streamfunction field for June of 1992, 1993, and 1994.....	250
4.4.1-9	Shelfwide monthly mean 10-m velocity streamfunction field for July of 1992, 1993, and 1994.....	251

LIST OF FIGURES

<u>FIGURE</u>	<u>DESCRIPTION</u>	<u>PAGE</u>
4.4.1-10	Shelfwide monthly mean 10-m velocity streamfunction field for August of 1992, 1993, and 1994.....	252
4.4.1-11	Shelfwide monthly mean 10-m velocity streamfunction field for September of 1992, 1993, and 1994.....	253
4.4.1-12	Shelfwide monthly mean 10-m velocity streamfunction field for October of 1992, 1993, and 1994.....	254
4.4.1-13	Shelfwide monthly mean 10-m velocity streamfunction field for November of 1992, 1993, and 1994.....	255
4.4.1-14	Shelfwide monthly mean 10-m velocity streamfunction field for December of 1992 and 1993.....	256
4.4.2-1	Structure of the first two EOFs calculated from the 32 monthly mean 10-m velocity streamfunction fields.....	258
4.4.2-2	The amplitude time series of the first two EOFs for the monthly mean 10-m velocity streamfunctions.....	259
4.4.2-3	Sequence of monthly mean alongshelf wind stress characterizing the Texas-Louisiana inner shelf for the period April 1992 through November 1994.....	260
4.4.3-1	Alongshelf and cross-shelf current components and vector plots averaged for nonsummer and summer periods at moorings along the 20-m isobath..	262
4.4.3-2	Nonsummer mean vectors and their principal variability ellipses at the 10-m, mid-depth, and near-bottom instruments of the LATEX A moorings....	264
4.4.3-3	Summer mean vectors and their principal variability ellipses at the 10-m, mid-depth, and near-bottom instruments of the LATEX A moorings.....	265
4.4.3-4	Alongshelf and cross-shelf current components and vector plots averaged for nonsummer and summer periods at moorings along the 50-m isobath..	266
4.4.3-5	Alongshelf and cross-shelf current components and vector plots averaged for nonsummer and summer periods at moorings along the 200-m isobath.....	267
4.5-1	Gridded and observed alongshelf and cross-shelf winds at L50, L53, 42020, 42019, and BUSL1 from 1 April 1992 to 1 June 1992.	269
4.5-2	Autospectra of alongshelf and cross-shelf gridded and observed winds at BUSL1.	270
4.5-3a	Squared coherency and phase for alongshelf components of gridded and observed winds by season at BUSL1.....	272
4.5-3b	Squared coherency and phase for cross-shelf components of gridded and observed winds by season at BUSL1.....	273
4.5-4	Transfer functions of alongshelf and cross-shelf components of gridded and observed winds by season at BUSL1.....	274
4.5-5a	Autospectra of alongshelf components of current and gridded wind at mooring 23 by season.	276
4.5-5b	Autospectra of cross-shelf components of current and gridded wind at mooring 23 by season.	277
4.5-6	Squared coherency and phase between alongshelf current and alongshelf gridded wind by season at mooring 23.....	278
4.5-7	Squared coherency and phase between alongshelf current and alongshelf gridded wind by season at mooring 24.....	279
4.5-8	Squared coherency and phase between alongshelf current and alongshelf gridded wind by season at mooring 25.....	280

LIST OF FIGURES

<u>FIGURE</u>	<u>DESCRIPTION</u>	<u>PAGE</u>
4.5-9	Squared coherency and phase between alongshelf current and alongshelf gridded wind by season at mooring 07.....	282
4.5-10	Squared coherency and phase between alongshelf current and alongshelf gridded wind by season at mooring 01.....	283
4.5-11	Squared coherency and phase between alongshelf current and alongshelf gridded wind by season at mooring 20.....	284
4.5-12	Squared coherency and phase between alongshelf current and alongshelf gridded wind by season at mooring 17.....	285
4.5-13	Squared coherency and phase between alongshelf current and alongshelf gridded wind by season at mooring 16.....	286
4.6-1	30-year average daily alongshelf wind component observed at Victoria, TX.....	288
4.6-2	Locations of meteorological stations from which wind observations were available including gridded winds determined at locations shown by stars and of moorings from which current observations were available from April 1992 through November 1994.....	289
4.6-3a	Monthly averaged current vectors for 10-m instruments and for mid-depth or near-bottom instruments for 1992.....	292
4.6-3b	Monthly averaged current vectors for 10-m instruments and for mid-depth or near-bottom instruments for 1993.....	293
4.6-3c	Monthly averaged current vectors for 10-m instruments and for mid-depth or near-bottom instruments for 1994.....	294
4.6-4	Average sea surface salinity in fall for six November cruises, in spring for ten May cruises, and in summer for nine July-August cruises.....	297
4.6-5	Average surface geopotential anomaly relative to 200 db based on the seven LATEX A nonsummer cruises and on the three summer cruises.	299
4.6-6a	Monthly averaged 10-m current vectors and surface wind stress vectors for 1992 at current meter moorings and offshore meteorological sites shown in Figure 4.6-2.....	301
4.6-6b	Monthly averaged 10-m current vectors and surface wind stress vectors for 1993 at current meter moorings and offshore meteorological sites shown in Figure 4.6-2.....	302
4.6-6c	Monthly averaged 10-m current vectors and surface wind stress vectors for 1994 at current meter moorings and offshore meteorological sites shown in Figure 4.6-2.....	303
4.6-7a	The annual cycle of daily mean alongshelf wind stress components for six locations along the 20-m isobath.	304
4.6-7b	The annual cycle of daily mean alongshelf wind stress components constructed from long-term records from airport stations located, from north to south along the Texas and Louisiana coastal plains, at: Lake Charles, Port Arthur, Victoria, Corpus Christi, and Brownsville.....	305
4.6-8	Average daily alongshelf component of 10-m current over the period April 1992 through November 1994 from five moorings located near the 20-m isobath.	307
4.6-9	Daily alongshelf surface wind stress averaged over the six locations shown in Figure 4.6-2 and alongshelf current component at 10 m below the sea surface averaged for the five 20-m isobath moorings shown in Figure 4.6-8 during the period April 1992 through November 1994.	308

LIST OF FIGURES

<u>FIGURE</u>	<u>DESCRIPTION</u>	<u>PAGE</u>
4.6-10	Objectively analyzed surface wind stress and 10-m currents from monthly averaged observations for May 1992.	309
4.6-11	Objectively analyzed surface wind stress and 10-m currents from monthly averaged observations for June 1992.	310
4.6-12	Objectively analyzed surface wind stress and 10-m currents from monthly averaged observations for August 1992.	311
4.6-13	Objectively analyzed surface wind stress and 10-m currents from monthly averaged observations for September 1992.	312
4.6-14	Alongshelf component of wind from NDBC buoy 42020 plotted with alongshelf components of 10-m currents measured at moorings 1, 2, and 3 for the period 1-10 November 1992.	314
4.6-15	Cross-correlations of alongshelf wind and current for the cases shown in Figure 4.6-14.	315
4.6-16	Maximum cross-correlations between alongshelf component of surface wind and alongshelf component of 10-m current contoured for values of correlations greater than or equal to 0.4.	316
5.1-1	Linear correlations between PBAC and SPM for the LATEX A hydrographic cruises; crosses represent data points.	327
5.1-2	Depth profile of percent transmission for station 42 on cruise H01, taken along line 2 on 4 May 1992.	330
5.1-3	Particle distributions during cruise H01.	332
5.1-4	Particle distributions during cruise H05.	333
5.1-5	Particle distributions during cruise H08.	335
5.1-6	Particle distributions during cruise H02.	336
5.1-7	Summer particle beam attenuation coefficient distributions for cruises H02 in August 1992, H06 in August 1993, and H09 in August 1994.	338
5.1-8	Particle distributions during cruise H09.	339
5.1-9	Particle distributions during cruise H03.	341
5.1-10	Particle distributions during cruise H07.	342
5.1-11	Particle distributions during cruise H10.	343
5.1-12	Particle distributions during cruise H04.	345
5.1-13	Particle beam attenuation coefficient at 3 m during cruise H05.	349
5.1-14	Vertical profiles of particle beam attenuation coefficient taken on 9 and 10 May 1993 on cruise H05.	351
5.1-15a	Particle beam attenuation coefficient at 3 m depth for the eastern LATEX A study area in 1992 for the May cruise H01, August cruise H02, and November cruise H03.	352
5.1-15b	Particle beam attenuation coefficient at 3 m depth for the eastern LATEX A study area in 1993 for the February cruise H04, May cruise H05, and August cruise H06.	353
5.1-16	Average water column SPM.	356
5.1-17	Average SPM in BNL.	357
5.2-1	Box model diagram of processes affecting nutrient concentrations on the Texas-Louisiana continental shelf.	359
5.2-2	Nitrate concentration versus salinity in all water samples collected below 150 m depth for LATEX A cruises H01, H05, and H10.	360
5.2-3	Texas-Louisiana shelf study area divided into boxes for nutrient data comparisons.	362

LIST OF FIGURES

<u>FIGURE</u>	<u>DESCRIPTION</u>	<u>PAGE</u>
5.2-4	Seasonal average surface nitrate inventories plotted by box number for spring, summer, and fall for all LATEX A hydrography cruises.....	363
5.2-5	Seasonal average surface phosphate inventories plotted by box number for spring, summer, and fall for all LATEX A hydrography cruises.....	364
5.2-6	Seasonal average surface silicate inventories plotted by box number for spring, summer, and fall for all LATEX A hydrography cruises.....	365
5.2-7	Surface inventories of nitrate on the eastern shelf during all LATEX A cruises and western shelf during the six full-shelf cruises.	367
5.2-8	Surface inventories of phosphate on the eastern shelf during all LATEX A cruises and western shelf during the six full-shelf cruises.	368
5.2-9	Surface inventories of silicate on the eastern shelf during all LATEX A cruises and western shelf during the six full-shelf cruises.	369
5.2-10a	Spring surface nitrate concentrations for LATEX A hydrographic cruises H01 in May 1992, H05 in May 1993, and H08 in May 1994.	372
5.2-10b	Summer surface nitrate concentrations for LATEX A hydrographic cruises H02 in August 1992, H06 in August 1993, and H09 in August 1994.	373
5.2-10c	Fall surface nitrate concentrations for LATEX A hydrographic cruises H03 in November 1992, H07 in November 1993, and H10 in November 1994.....	374
5.2-10d	Winter surface nitrate concentrations for LATEX A hydrographic cruise H04 in February 1993.	375
5.2-11	Daily and monthly average Mississippi and Atchafalaya River discharge and nitrate flux from Atchafalaya River, 50% of Mississippi River, and their sum during January 1992 through December 1994.	376
5.2-12	East shelf surface nitrate versus two-month average river nitrate for each LATEX A hydrographic cruise.....	377
5.2-13	West shelf surface nitrate versus two-month average river nitrate for LATEX A full-shelf hydrographic cruises.	377
5.2-14	Depth profiles of nitrate, phosphate, and silicate at hydrographic stations 81, 205, and 209 during hydrographic cruise H05.	379
5.2-15	Vertical contours of bottle nitrate along 200-m isobath during hydrographic cruise H05.	380
5.2-16	Vertical contours of bottle phosphate along 200-m isobath during hydrographic cruise H05.	381
5.2-17	Vertical contours of bottle silicate along 200-m isobath during hydrographic cruise H05.	382
5.3-1a	Surface saturation of dissolved oxygen for winter cruise H04.	384
5.3-1b	Surface saturation of dissolved oxygen for spring cruises H01, H05, and H08.	385
5.3-1c	Surface saturation of dissolved oxygen for summer cruises H02, H06, and H09.	386
5.3-1d	Surface saturation of dissolved oxygen for fall cruises H03, H07, and H10.	387
5.3-2	Surface dissolved oxygen saturation versus surface salinity for all samples for the spring, summer, and fall of 1992, 1993, and 1994.	388
5.3-3	Surface dissolved oxygen saturation versus surface chlorophyll-a concentration for all samples for the spring, summer, and fall of 1992, 1993, and 1994.....	391

LIST OF FIGURES

<u>FIGURE</u>	<u>DESCRIPTION</u>	<u>PAGE</u>
5.3-4	Contours of bottle dissolved oxygen along line 1 during cruise H01, 30 April-9 May 1992.	392
5.3-5	Contours of bottle dissolved oxygen along line 1 during cruise H02, 31 July-9 August 1992.	393
5.3-6	Contours of bottle dissolved oxygen along line 1 during cruise H03, 4-13 November 1992.	394
5.3-7	Contours of bottle dissolved oxygen along line 1 during cruise H04, 4-13 February 1993.	395
5.3-8	Contours of bottle dissolved oxygen along line 1 during cruises H05, H06, and H07.	397
5.3-9	Contours of bottle dissolved oxygen along line 1 during cruises H08, H09, and H10.	398
5.3-10	Contours of bottle dissolved oxygen along line 4 during cruises H01, H02, and H03.	399
5.3-11	Contours of bottle dissolved oxygen along line 4 during cruises H05, H06, and H07.	400
5.3-12	Contours of bottle dissolved oxygen along line 4 during cruises H08, H09, and H10.	401
5.3-13	Contours of bottle dissolved oxygen along line 7 during cruises H05, H06, and H07.	402
5.3-14	Contours of bottle dissolved oxygen along line 7 during cruises H08, H09, and H10.	403
5.3-15	Bottom bottle dissolved oxygen for spring cruise H01 and summer cruise H02.	406
5.3-16	Bottom bottle dissolved oxygen for spring cruise H05 and summer cruise H06.	407
5.3-17	Bottom bottle dissolved oxygen for summer cruise H09.	408
5.3-18	Bottom dissolved oxygen saturation versus stability over the shelf to the west of 94°W for the spring, summer, and fall of 1992, 1993, and 1994... ..	409
5.3-19	Bottom dissolved oxygen saturation versus stability over the east shelf of and including 94°W for the spring, summer, and fall of 1992, 1993, and 1994.	410
5.3-20	Bottom dissolved oxygen saturation versus bottom nitrate over the full shelf sampled for the spring, summer, and fall of 1992, 1993, and 1994. .	413
5.3-21	Dissolved oxygen profiles using bottle data for stations along the 200-m isobath during LATEX A cruise H05.	414
5.3-22	Dissolved oxygen from bottle data on line 9 along the 200-m isobath on LATEX A cruise H05.	415
5.4-1	Spring distributions of chlorophyll maximum for LATEX A hydrographic cruises H01 in May 1992, H05 in May 1993, and H08 in May 1994.	423
5.4-2	Principal component groups for the chlorophyll maximum H01, 1-8 May 1992; H05, 26 April-11 May 1993; and H08, 24 April-7 May 1994.	424
5.4-3	Summer distributions of chlorophyll maximum for LATEX A hydrographic cruises H02 in August 1992, H06 in August 1993, and H09 in August 1994.	426
5.4-4	Principal component groups for the chlorophyll maximum H02, 1-8 August 1992; H06, 26 July-7 August 1993; and H09, 27 July-7 August 1994.	427

LIST OF FIGURES

<u>FIGURE</u>	<u>DESCRIPTION</u>	<u>PAGE</u>
5.4-5	Fall distributions of chlorophyll maximum for LATEX A hydrographic cruises H03 in November 1992, H07 in November 1993, and H10 in November 1994.	429
5.4-6	Principal component groups for the chlorophyll maximum of cruise H03, 5-13 November 1993; H07, 7-21 November 1993; and H10, 2-13 November 1994.	430
5.4-7	Winter distributions of chlorophyll maximum for LATEX A hydrographic cruise H04 in February 1993.	432
5.4-8	Principal component groups for the chlorophyll maximum of cruise H04, 6-13 February 1993.	432

LIST OF TABLES

<u>TABLE</u>	<u>PAGE</u>
1.1-1	LATEX A program tasks. 2
1.1-2	Identifiers and schedules for LATEX A cruises. 4
1.2-1	Typical mooring configurations; depths are averages of the field program. 7
1.2-2	Summary of data collected and scientific participation in the LATEX A hydrography surveys. 12
1.2-3	Dates and locations for deployment and end of transmission for LATEX A drifters. 14
2.1.1-1	Ranges, accuracies, and resolutions of meteorological sensors on LATEX buoys. 19
2.1.1-2	Ranges, accuracies, and resolutions of meteorological sensors used at NDBC and C-MAN measurement sites..... 19
2.1.1-3	Heights of wind and temperature recorders for NDBC and C-MAN sites from which measurements were used to construct meteorological fields..... 20
2.1.1-4	Comparison of speed and direction differences among LATEX, ERS-1, and NCEP winds averaged over all grid points for the 41 selected ERS-1 swaths. 32
2.1.3-1	Number of frontal passages over the Texas-Louisiana shelf during each field year and resulting averages of frontal passages; "—" means not a LATEX field period..... 46
2.1.3-2	Average interval between fronts, where "n" means no meaningful interval..... 46
2.1.3-3	Winter cyclogenesis events over the northwestern Gulf of Mexico from November 1992 through December 1994..... 47
2.3-1	Annual average discharge rates for principal rivers west of the Atchafalaya that flow onto the Texas-Louisiana shelf. 57
2.4-1	Squared correlations of alongshelf bottom stress with alongshelf bottom current for all deployments at 30 LATEX A mooring locations for linear and nonlinear implementations..... 68
2.5.1-1	Anticyclonic Loop Current eddies during LATEX. 71
2.5.1-2	Presence of Loop Current eddies adjacent to the Texas-Louisiana shelf, April 1992-November 1994..... 74
2.5.2-1	Identification of Loop Current eddies present in the geopotential anomaly fields. 82
2.5.2-2	Identification of Loop Current eddies influencing the 10-m shelf edge currents based on the monthly average velocity. 89
2.5.2-3	Identification of Loop Current eddies influencing the 100-m shelf edge currents based on the monthly average velocity. 90
2.5.2-4	Identification of Loop Current eddies influencing the 190-m/490-m shelf edge currents based on the monthly average velocity. 91
4.2-1	Hydrographic cruises on the Texas-Louisiana continental shelf from which data were used. 138
4.3.1-1	Spatial scales of surface anomaly fields of salinity, geopotential anomaly, and temperature along selected transects..... 186

LIST OF TABLES

<u>TABLE</u>	<u>PAGE</u>
4.3.1-2	Spatial scales of anomaly fields of salinity and potential temperature along selected transects at depths of 3 m, 0.5D, and D, where D is water depth.188
4.3.1-3	Spatial scales for anomaly fields of salinity and potential temperature at 3, 30, and 60 m depths on the eastern part of transect 9.188
4.3.1-4	Mean variance estimates for the observed data and the anomaly fields of surface salinity, surface geopotential anomaly relative to 70 db, and surface potential temperature for selected transects based on data from the first seven LATEX cruises.189
4.3.2-1	Along- and cross-shelf orientations of LATEX A current measurement moorings relative to the local bathymetry.193
4.3.2-2	Recordlength means and variances of temperature, salinity, and along- and cross-shelf velocity from 40-hr low-pass current meter data.194
4.3.2-3	Periods and frequencies of the fundamental and first four harmonics of the annual signal.205
4.3.2-4	Average percent contribution of each period to the total variance of the annual signal for temperature, salinity, and along and cross-shelf velocities at the top current meters.208
4.3.2-5	Cross-correlation of the annual signal of 10-m, alongshelf velocity with the annual signal of cross-shelf velocity at the top and bottom or middle depths.216
4.4.1-1	The root mean square speed of monthly current and rms error of the velocity streamfunction fit.243
4.6-1	Period ranges for which currents on the same moorings were coherent at the 95% significance level.296
5.1-1	Summary of water column SPM and percentage of SPM in BNL for each cruise.346
5.3-1	Squared correlation coefficients for surface oxygen saturation with surface salinity and surface chlorophyll-a values over the eastern inner shelf.390
5.3-2	Bottom bottle dissolved oxygen measurements.405
5.3-3	Squared correlation coefficients for bottom oxygen saturation with west shelf stability, east shelf stability, and east shelf bottom nitrate.411
5.4-1	Percent variance accounted for by the first and second principal components for the chlorophyll maximum and the sea surface for cruises H01-H10.418
5.4-2	Characteristics of PCA groups I, II, III, and IV for cruises H01-H10.418
5.4-3	Number and percentage of chlorophyll maxima observed at the surface and the number of stations per line at which pigments samples were taken, with averages for cruises and eastern and western shelves.420
5.4-4	Mean chlorophyll-a calculated at the chlorophyll maximum by cross-shelf transect line by cruise.421
5.4-5	Mean chlorophyll at the chlorophyll maximum ranked by cruise for the eastern and western shelves.422

ABBREVIATIONS AND ACRONYMS

ADCP	acoustic Doppler current profiler
AVHRR	advanced high resolution radiometer
BNL	bottom nepheloid layer
C-MAN	coastal-marine automated network
CTD	conductivity-temperature-density instrument
GOES	Geosynchronous Operational Environmental Satellite
GPI	GOES precipitation index
HPLC	high performance liquid chromatography
IES	inverted echo sounder
LATEX	Louisiana-Texas Shelf Physical Oceanography Program
LATEX A	a LATEX study unit, "Texas-Louisiana Shelf Circulation and Transport Processes Study", carried out by Texas A&M University, College Station
LATEX B	a LATEX study unit, "Mississippi River Plume Hydrography", carried out by Louisiana State University, Baton Rouge
LATEX C	a LATEX study unit, "Eddy Circulation Study", carried out by Science Applications International Corporation, Raleigh, NC
MBKE	mesoscale band kinetic energy
MMS	Minerals Management Service, Dept of the Interior
MRF	medium-range forecast model
NCEP	National Center for Environmental Prediction, a division of NOAA
NDBC	National Data Buoy Center, a division of NOAA
NOAA	National Ocean and Atmospheric Administration, Dept of Commerce
NODC	National Ocean Data Center, a division of NOAA
NOS	National Ocean Service, a division of NOAA
NWS	National Weather Service, a division of NOAA
PBAC	particle beam attenuation coefficient
PCA	principal component analysis
ROV	remotely operated vehicle
SPM	suspended particulate matter
USGS	United States Geological Survey
UTC	universal coordinated time
WAM	wave model
WBKE	weather band kinetic energy
XBT	expendable bathythermograph

ACKNOWLEDGMENTS

This report and the six years of effort it represents would not be possible without the contributions of many people at Texas A&M University, Evans-Hamilton Inc., Louisiana State University, Maine Maritime Academy, and the University of Southern Mississippi. The scientists, technicians, staff, and students listed below deserve more recognition and thanks than can be expressed adequately in so little space.

Chuck Abbott	Mike Fredericks	Eric Noah
Jackie Abert	Rod Fredericks	Chris Nugent
Bob Albers	Ann Galloway	Rick O'Neill
Barbara Allen	Mark Garner	Lisa Ouellette
Les Bender	Francesca Giancristofaro	Brad Pederson
Sarah Benedict	Billy Green	Carl Perkins
Dawn Bennett	Sandy Green	R.V. Pittman
Doug Biggs	Paul Griffin	Erik Quiroz
Wendell Binion	Dennis Guffy	Beau Ratloff
Brian Blanchard	Norman Guinasso	Maureen Reap
Marty Bohn	Bob Hamilton	Bob Reid
Paula Bontempi	Thomas Hamilton	Desmond Rolf
Ken Bottom	Troy Horton	Steve Rutz
Nick Carter	Dan Howard	Lauren Sahl
Joel Chaky	Matt Howard	Alan Schmidt
Changsheng Chen	Mary Howley	John Shannon
Hsien-Wen Chen	S.A. Hsu	Pat Sharrard
Xiaogang Chen	Jodi Hughes	Mindy Smith
Kwangwoo Cho	Woody Isenhardt	Terry Sullivan
John Cochrane	Kayli Jackson	J Svalberg
Carol Coomes	Jim Jobling	Mark Spears
Jeff Cox	Ann Jochens	Prasad Suravarapu
Carole Current	Mike Kelley	Kelly Thornton
Agatha Davis	Frank Kelly	Gert Van Dijken
Roy Davis	Keith Kurrus	Anton Vos
Debz DeFreitas	Sherry Kuttner	Nan Walker
Steve DiMarco	Ken Leder	Wensu Wang
Srinivas Donthireddy	Woody Lee	Denise Warren
Dana Dyre	Dean Letzring	Eddie Webb
Curt Ebbesmeyer	Honghai Li	Bob Whitaker
Paul Etter	Yongxiang Li	Denis Wiesenburg
Doug Evans	Carrie Lyons	Jennifer Wong
Roger Fay	Dave Martin	Hyungmoh Yih
Mike Field	Susan Martin	
Ken Fitzgerald	Rani Nathaniel	

While four names are listed as authors of this report, substantial contributions from other writers deserve acknowledgement. I thank Matt Howard, Yongxiang Li, Les Bender, Wensu Wang, Maureen Reap, Lauren Sahl, Carrie Neuhard Lyons, S.A. Hsu, Denis Wiesenburg, Debz DeFreitas, and Carole Current for their work on this synthesis.

The Texas A&M Research Foundation has provided unflagging administrative support to this project from the proposal stage through its closure. We especially owe to Phyllis Bonifazi and Charlene Miller our deepest gratitude for their careful management of this complex contract. RF staff often work anonymously in service to the research conducted at Texas A&M. We would like to correct that in this case by naming those individuals who have served the LATEX cause: Nadine Abrego, Janice Blum, Pat Branham, Rhonda Briles, Phyllis Brysch, Shirley Budnik, Pat Clark, Dorothy Coppinger, Phyllis Crowder, Steve Garrett, Nate Green, Sherry Havard, Darcy Hensley, Liz Hughes, Toni Jacques, Linda Jeffress, Becky Jones-Pruitt, Nancy Livengood, Ruth Manning, Jennifer Newsom, Teresa O'Brien, Tanya Oplinger, Judy Owens, Pam Pantel, Linda Pitchford, Tracie Robertson, and Cassandra Russell.

At the MMS Gulf of Mexico OCS Region office in New Orleans, we thank Alexis Lugo-Fernandez, the contracting officer's technical representative, whose enthusiasm and thoughtful oversight of our project have been much appreciated. Murray Brown was the first COTR on this project, and we thank him for his contributions to its success.

Worth D. Nowlin, Jr.
LATEX A Program Manager

1 INTRODUCTION

1.1 LATEX A Program objectives and description

The Louisiana-Texas Shelf Physical Oceanography Program (LATEX) was supported by the Minerals Management Service (MMS) of the U.S. Department of the Interior. LATEX comprised three study units: Study Unit A, Texas-Louisiana Shelf Circulation and Transport Processes Study (LATEX A), conducted by the Texas A&M University System; Study Unit B, Mississippi River Plume Hydrography Study (LATEX B), conducted by Louisiana State University; and Study Unit C, Gulf of Mexico Eddy Circulation Study (LATEX C), conducted by Science Applications International Corporation. LATEX A was the largest of the three LATEX study units and covered the Texas-Louisiana continental shelf from the 10-m isobath to the continental slope between the Mississippi River and the Rio Grande. It consisted of five field components: moored ocean measurements, drifting buoys, hydrography, acoustic Doppler current profiling (ADCP), and meteorological measurements. Historical and concurrent data sets were assembled. This report provides a synthesis of the data collected during the LATEX field program.

Impetus for the LATEX program stemmed from responsibilities of MMS in management of the nation's Outer Continental Shelf Leasing Program, including oil and gas leases in federal waters of the Texas-Louisiana shelf. To provide effective management, MMS seeks to understand the physical processes and circulation of the shelf water that influence the stability of structures, the transport of pollutants, and the ecosystem of regions that may be affected by oil and gas operations. Additionally, knowledge of the circulation on the shelf supports MMS oil spill risk analysis models. It was to further the base of knowledge in these areas that MMS sponsored LATEX.

The four objectives for the LATEX A study were:

1. To identify key dynamical processes governing circulation, transport, and cross-shelf mixing on the Texas-Louisiana shelf.
2. To (a) improve the data base available for study of the processes in objective 1, (b) synthesize the data into a scheme of circulation, and (c) quantify transports and mixing rates.
3. To develop conceptual models of meso- to large-scale processes and circulation features and of large-scale shelf circulation on event to seasonal scales.
4. To provide physical and chemical information needed for synthesis with biological data into a broader ecological characterization of the region.

Objectives 2a and 4 were met by the submittal of the LATEX A data set to the National Oceanographic Data Center (NODC) of the National Oceanic and Atmospheric Administration (NOAA). The LATEX A data set has been assigned the NODC code number 0212. Remaining objectives are met in this synthesis report and its supporting documentation.

The LATEX A study area encompassed the Texas-Louisiana shelf and portions of the slope (Figure 1.1-1). The program had 12 named tasks plus Program Management and Data Management tasks. Tasks fell into four types: general management activities; field work and data collection; data processing; information transfer to the MMS, other federal and state agencies, and the public; and analysis and synthesis. The tasks, the Principal Investigators, and the task type are given in Table 1.1-1. Each of the tasks is fully described in the three LATEX A annual reports (Jochens and Nowlin 1994, 1995; Reap et al. 1996). The field components are briefly described in Section 1.2 of this report.

Twenty-eight cruises were conducted during the LATEX A field program; 18 were mooring deployment or maintenance cruises, 10 were hydrographic/ADCP cruises. Table 1.1-2 lists the cruise dates and vessels used. This report will use the three-character cruise designator in the first column of Table 1.1-2 for identification purposes.

Table 1.1-1. LATEX A program tasks.

Task	Description	Task Type	Principal Investigator*
	Program Management	Management	W. D. Nowlin, Jr. ¹ , Program Manager; A. E. Jochens ¹ , Deputy Program Mgr
	Data Management	Management	N. L. Guinasso, Jr. ¹
A-1	Current Measurement Moorings	Field Work	R. C. Hamilton ²
A-2	ARGOS-Tracked Drifting Buoys	Field Work	W. D. Nowlin, Jr.
A-3	Standard Grid Hydrography	Field Work	D. A. Wiesenburg ³
A-4	Acoustic Doppler Current Profiling	Field Work	R. C. Hamilton (year 1) D. C. Biggs ¹ (years 2 & 3)
A-5	Collateral Data Assembly	Data	N. L. Guinasso, Jr.
A-6	Winter Northers/Cyclogenesis	Field/Analysis	S. A. Hsu ⁴
A-7	Data Quality Control	Data	N. L. Guinasso, Jr.
A-8	Analyses and Reports	Analysis/ Information	W. D. Nowlin, Jr. A. E. Jochens
A-9	Field Measurements/Model Comparison	Analysis	R. O. Reid ¹
A-10	Information Transfer	Information	N. L. Guinasso, Jr.
A-11	Public Notification, Cooperation	Information	N. L. Guinasso, Jr.
A-12	GFE Capital Equipment	Field Work	R. C. Hamilton

* affiliations:

¹ Texas A&M University (TAMU)

² Evans-Hamilton, Inc.

³ TAMU (now with University of Southern Mississippi)

⁴ Louisiana State University

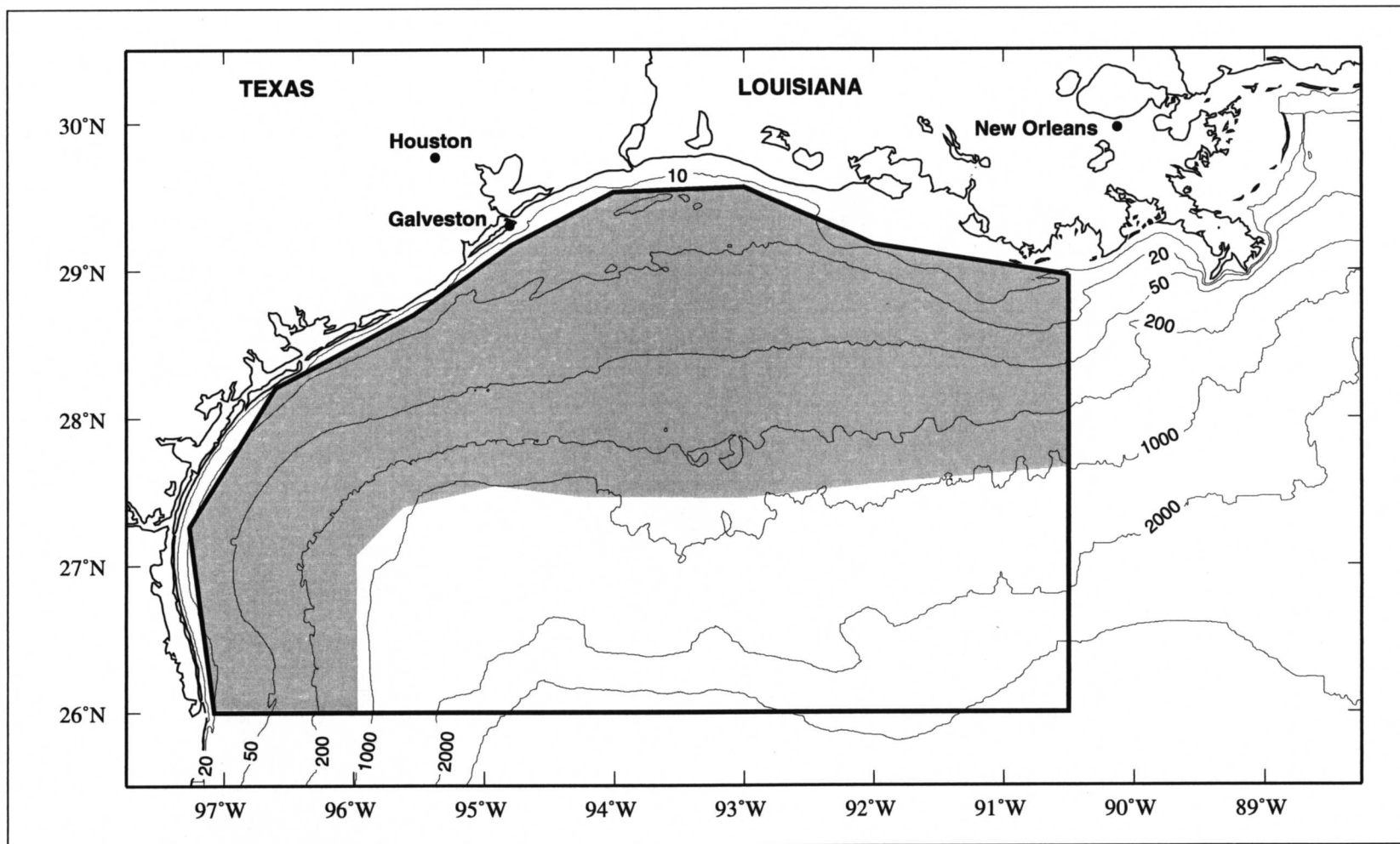


Figure 1.1-1. Study area and bathymetry for the LATEX A program over the Texas-Louisiana shelf and slope. LATEX A hydrography stations and moorings were located over the shelf region within the shaded area. LATEX A used data obtained mostly from other studies to examine the slope regime.

Table 1.1-2. Identifiers and schedules for LATEX A cruises.

Cruise #	MMS ID	Cruise Dates	Vessel & Comments
<i>Task A-1 Mooring Maintenance</i>			
M01	M01CPW9203	7 - 16 April 1992	<i>R/V J. W. Powell</i>
M02	M02CPW9205	26 May - 4 June 1992	<i>R/V J. W. Powell</i>
M03	M03CPW9206	13 - 27 July 1992	<i>R/V J. W. Powell</i>
M04	M04CPW9208	28 August - 6 September 1992	<i>R/V J. W. Powell</i>
M05	M05CPW9209	13 - 23 October 1992	<i>R/V J. W. Powell</i>
M06	M06CPW9212	8 - 18 December 1992	<i>R/V J. W. Powell</i>
M06B	M06CPW9212	28 November - 6 December 1992	<i>M/V Aloha (ROV work)</i>
M07	M07CPW9301	9 - 21 January 1993	<i>R/V J. W. Powell</i>
M08	M08CPW9304	16 - 24 March 1993	<i>R/V J. W. Powell</i>
M09	M09CPW9307	18 - 28 May 1993	<i>R/V J. W. Powell</i>
M10	M10CPW9310	13 - 19 July 1993	<i>R/V J. W. Powell</i>
M10B	M10CPW9310	22 - 26 July 1993	<i>M/V Erica Tide (IES)</i>
M11	M11CPW9312	21 September - 1 October 1993	<i>R/V J. W. Powell</i>
M12	M12CPW9315	3 - 13 December 1993	<i>R/V J. W. Powell</i>
M13	M13CPW9402	9 - 16 February 1994	<i>R/V J. W. Powell</i>
M14	M14CSS9414	21 March - 1 April 1994	<i>M/V Seis Surveyor</i>
M15	M15CPW9406	26 May - 1 June 1994	<i>R/V J. W. Powell</i>
M16	M16CSS9413	23 July - 2 August 1994	<i>M/V Seis Surveyor</i>
M17	M17CUS9413	27 September - 4 October 1994	<i>M/V Universal Surveyor</i>
M18	M18CGY9411	29 November - 7 December 1994	<i>R/V Gyre</i>
<i>Task A-3 Hydrography</i>			
H01	H01CGY9205	30 April - 9 May 1992	<i>R/V Gyre</i>
H02	H02CGY9208	31 July - 9 August 1992	<i>R/V Gyre</i>
H03	H03CPW9210	4 - 13 November 1992	<i>R/V J. W. Powell</i>
H04	H04CGY9302	4 - 13 February 1993	<i>R/V Gyre</i>
H05	H05CPW9306	25 April - 11 May 1993	<i>R/V J. W. Powell</i>
H06	H06CPW9311	25 July - 7 August 1993	<i>R/V J. W. Powell</i>
H07	H07CPW9314	6 - 22 November 1993	<i>R/V J. W. Powell</i>
H08	H08CGY9401	24 April - 7 May 1994	<i>R/V Gyre</i>
H09	H09CPW9410	26 July - 7 August 1994	<i>R/V J. W. Powell</i>
H10	H10CGY9409	2 - 13 November 1994	<i>R/V Gyre</i>

ROV = Remotely Operated Vehicle

IES = Inverted Echo Sounder

1.2 Data collected

The LATEX A field program was conducted from April 1992 to December 1994. The data collected under each of the field tasks are briefly described below.

Data associated with mooring cruises (Tasks A-1 and A-6)

Task A-1, Current Measurement Moorings, included the maintenance of 33 moorings with current meters, wave gauges, meteorological buoys, and inverted echo sounders. These moorings provided a shelfwide network of current, temperature, and salinity time series with which to identify, describe, and study circulation processes. Task A-6, Winter Northers/Cyclogenesis, included the maintenance of four meteorological buoys for six months a year; they were removed during the hurricane season, June to November. These buoys enhanced the meteorological data set for the study of cyclogenesis resulting from cold air outbreaks.

Figure 1.2-1 shows the locations of the moorings and identifies them by number. The mooring deployment consisted of a boundary array along the shelf edge (moorings 4-11, 13, and 48), cross-shelf arrays for study of alongshelf transports (moorings 1-4; 7, and 23-25; 8 and 20-22; 11 and 17-19; and 12-16), a wild card array located in the southwestern portion of the region to study the onshore migration of rings and smaller-scale phenomena (moorings 44-47 in conjunction with moorings 4, 5, and 49), two deep-water inverted echo sounders to monitor the westward passage of rings into the study area (moorings 42 and 43), and eight meteorological buoys to allow study of the wind fields and, specifically, wind-current relationships (moorings 17, 19, 20, and 22) and winter cyclogenesis (moorings 50-53).

The instrumentation initially consisted of 83 current meters, five directional wave gauges, eight meteorological buoys, and two inverted echo sounders. As equipment failed or was lost, wild card array moorings were removed to maintain the other arrays as intact as possible. Table 1.2-1 gives the locations, average water depths, and typical mooring configurations for each mooring. Moorings were maintained on different schedules, with moorings in shallower water being visited more frequently than moorings in deeper water, as indicated in the table.

Details regarding instrumentation, data returns, and data processing are provided in data reports on the current meters (DiMarco et al. 1997), wave gauges (DiMarco 1996; DiMarco and Kelly 1995; DiMarco et al. 1995; Kelly et al. 1993), and meteorological buoys (Wang et al. 1996). These reports contain a variety of data products, including basic statistics, plots of time series, spectra, current and wind roses, and wind fields.

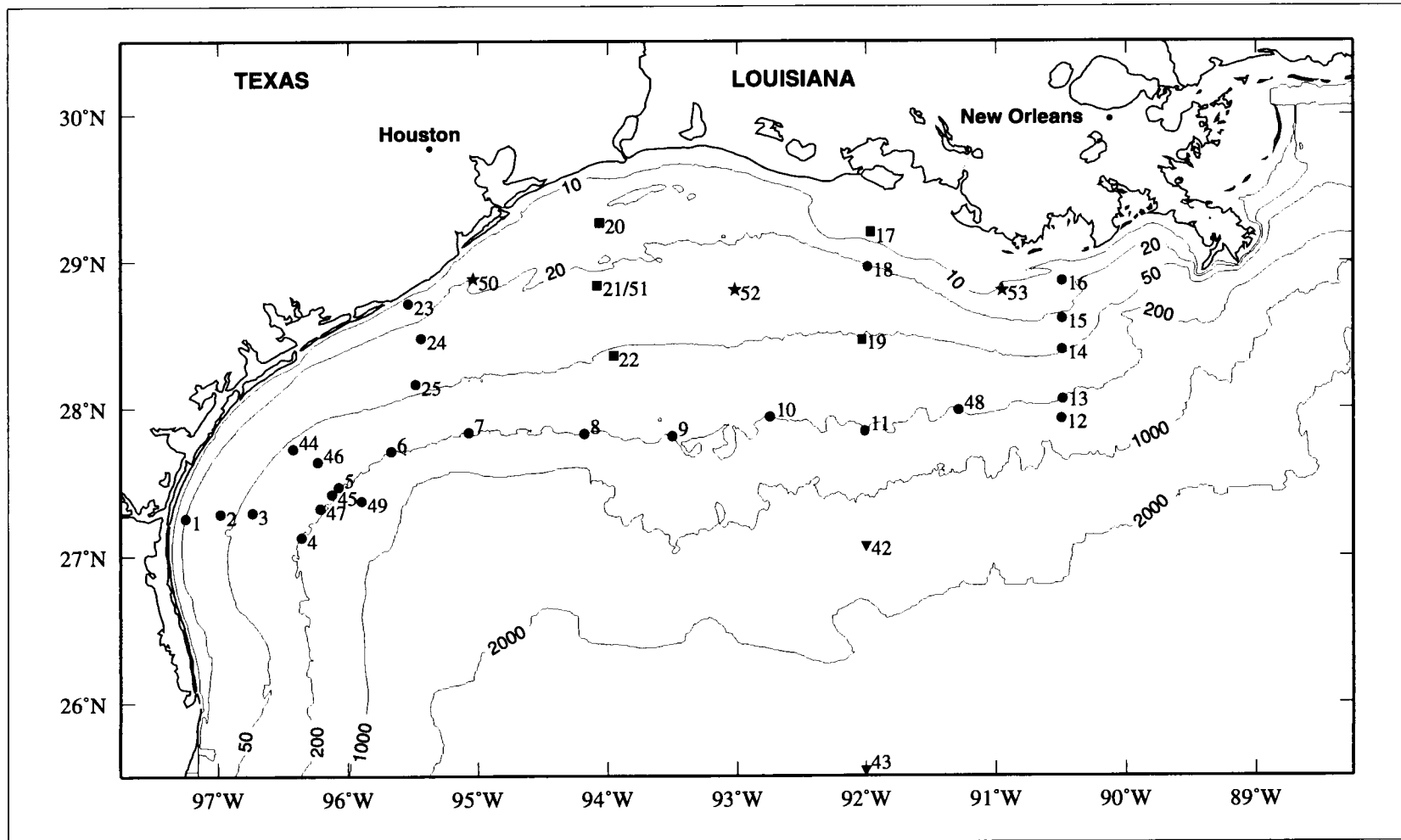


Figure 1.2-1. Locations for LATEX A current meter moorings and meteorological buoys (solid circle denotes a current mooring, star a meteorological buoy, square a current mooring with meteorological buoy attached, and triangle an inverted echo sounder).

Table 1.2-1. Typical mooring configurations; depths are averages over the field program.

Mooring Number	Water Depth	Latitude (°N)	Longitude (°W)	Comments	Top Meter	Middle Meter	Bottom Meter	Maintenance Interval (days)
1	20	27.256	97.246	Platform	174-12m T,C	None	Mini-12m T	45/120
2	37	27.284	96.980	Platform	174-12m T,C	None	174-33m T,C	45/120
3	65	27.290	96.736	Platform	174-13m T,C	174-32m T,C	174-57m T,C	90/120
4	200	27.126	96.358	Surface Marker Buoy after December 1992	174-14m T,C	Aand-100m T,C	Aand-190m T,C	90/120
5	200	27.468	96.073	Surface Marker Buoy after December 1992	174-13m T,C	Aand-100m T,C	Aand-190m T,C	90/120
6	201	27.708	95.664	Surface Marker Buoy after December 1992	174-14m T,C	Aand-101m T,C	Aand-191m T,C	90/120
7	200	27.834	95.069	Surface Marker Buoy after December 1992	174-13m T,C	Aand-100m T,C	Aand-190m T,C	90/120
8	200	27.825	94.179	Surface Marker Buoy after December 1992	174-13m T,C	Aand-100m T,C	Aand-190m T,C	90/120
9	200	27.808	93.503	Surface Marker Buoy after December 1992	174-14m T,C	Aand-101m T,C	Aand-191m T,C	90/120
10	201	27.936	92.745	Surface Marker Buoy after December 1992	174-13m T,C	Aand-101m T,C	Aand-191m T,C	90/120
11	200	27.842	92.009	Surface Marker Buoy after December 1992	174-14m T,C	Aand-99m T,C	Aand-189m T,C	90/120
12	504	27.924	90.495	Surface Marker Buoy after December 1992	174-18m T,C	Aand-105m T,C	Aand-495m T,C	180/180
13	200	28.058	90.486	Surface Marker Buoy after December 1992	174-14m T,C	Aand-100m T,C	Aand-190m T,C	90/120
14	47	28.395	90.493	Platform	174-10m T,C	174-26m T,C	174-40m T,C	45/60
15	27	28.608	90.492	Platform	174-10m T,C	None	174-25m T,C	45/60
16	18	28.867	90.491	Platform	174-10m T,C	None	Mini-17m T	45/60
17	8	29.196	91.965	Platform & Met Buoy	S4-3m T,C	None	Mini-6m T	45/60
18	22	28.963	91.983	Platform	174-11m T,C	None	174-18m T,C	45/60
19	53	28.465	92.035	Platform & Met Buoy	S4-3m T,C	174-21m T,C	174-46m T,C	45/60
20	14	29.261	94.064	Platform & Met Buoy	S4-3m T,C	None	Mini-12m T	45/60
21/51	24	28.837	94.080	Platform & Met Buoy	174-14m T,C	None	174-22m T,C	45/60
22	55	28.356	93.956	Platform & Met Buoy	S4-3m T,C	174-21m T,C	174-48m T,C	45/60
23	15	28.713	95.536	Platform	174-9m T,C	None	Mini-13m T	45/60
24	28	28.474	95.437	Witness Buoy; Platform	174-10m T,C	None	174-22m T,C	45/60
25	37	28.162	95.476	Platform	174-11m T,C	174-20m T,C	174-30m T,C	45/60
42	1890	27.069	92.001	Deployed July 1992	None	None	IES-1889m T	1360/360
43	3130	25.542	92.000	Deployed July 1992	None	None	IES-3129m T	1360/360
44	57	27.726	96.424	Witness Buoy; Platform	174-12m T,C	None	174-52m T,C	90/120
45	198	27.418	96.126		174-10m T,C	Aand-82m T	None	90/120
46	91	27.638	96.234	Platform	174-10m T,C	174-50m T	Aand-84m T,C	90/120
47	204	27.322	96.213	Surface Marker Buoy after December 1992	174-19m T,C	Aand-104m T	Aand-194m T	90/120
48	201	27.983	91.283	Surface Marker Buoy after December 1992	174-15m T,C	Aand-101m T	Aand-191m T	90/120
49	502	27.369	95.894	Surface Marker Buoy after December 1992	174-14m T,C	Aand-102m T,C	Aand-493m T,C	180/180
50	20	28.881	95.037	Platform & Met Buoy	None	None	None	45/90
51/21	24	28.837	94.080	Platform & Met Buoy	174-14m T,C	None	174-22m T,C	45/90
52	27	28.804	93.018	Platform & Met Buoy	None	None	None	45/90
53	15	28.801	90.954	Platform & Met Buoy	None	None	None	45/90

Met Buoy = DSI surface meteorological buoy
S4 = InterOcean S4 electromagnetic current meter
174 = Endeco model 174 current meter

Aand = Aanderaa model RCM 7 or 8
RCM = Aanderaa model 4 or 5
Mini = MiniSpec directional wave gauge

IES = inverted echo sounder
T = temperature sensor
C = conductivity sensor

Data collected during hydrographic cruises (Tasks A-2, A-3, and A-4)

The hydrographic/ADCP surveys were designed to characterize the seasonal patterns of circulation and water mass characteristics and to allow initial assessment of interannual variability. Sampling for Task A-3, Standard Grid Hydrography, consisted of 10 surveys on the Texas-Louisiana shelf over three years. During year 1 (April 1992 through March 1993), four surveys of the eastern half shelf were conducted in spring, summer, fall, and winter. Subsequently, it was determined that full shelf surveys should be conducted during observed hydrographic seasons of the circulation.

Data collected in the first field year of LATEX A and the climatological data from the region showed that there are two major circulation regimes on the Texas-Louisiana shelf: a wind-driven regime of upwelling and upcoast inner-shelf flows in the summer months and a wind-driven regime of downwelling and downcoast inner-shelf flow the rest of the year (“nonsummer”). To sample these regimes, six full-shelf surveys were fielded in years 2 and 3: once each year when the downwelling-downcoast flow was expected to be most extensive and the stratification weak (November); once when the upwelling was most extensive (July/August); and once when both regimes and a boundary between them (a coastal convergence) were most clearly marked within the region (April/May). Figures 1.2-2 through 1.2-4 show typical station locations for the hydrographic surveys in each of the three field years. In the third field year, the cruises tracked the full shelf, but no stations along line 10 at the 50-m isobath were sampled (Figure 1.2-4).

The hydrographic survey stations consisted of continuous vertical profiling using a Sea-Bird 911+ CTD system and discrete sampling using a General Oceanics 12-place Rosette with 10-liter Niskin bottles. Continuous profiling of pressure, temperature, salinity, dissolved oxygen, downwelling irradiance, percent transmission, backscatterance, and fluorescence was accomplished at each station. Discrete sampling of nutrients (nitrate, phosphate, silicate, nitrite, ammonium, and urea) was made at every station and of salinity, dissolved oxygen, suspended particulate material (SPM), and pigments at selected stations. Secchi depth readings were taken at all daytime stations. Additionally, a number of complementary sampling programs were conducted by guest scientists. Table 1.2-2 summarizes the data collection by cruise. Specifics of the cruise tracks and station locations, instrumentation, methods, data processing, and additional cruise information are provided in the hydrographic data report (Jochens et al. 1998). That report also contains horizontal and vertical plots of each parameter measured and selected property-property plots.

Task A-4, Acoustic Doppler Current Profiling, was performed on every hydrographic survey. Measurements were made continuously along the survey tracks. Details of the acoustic Doppler current profiler (ADCP) measurements, including data processing returns, horizontal and vertical sections of current velocity, and comparisons of ADCP profiles with nearby, simultaneous current meter velocities, are contained in the ADCP data report (Bender and Kelly 1998).

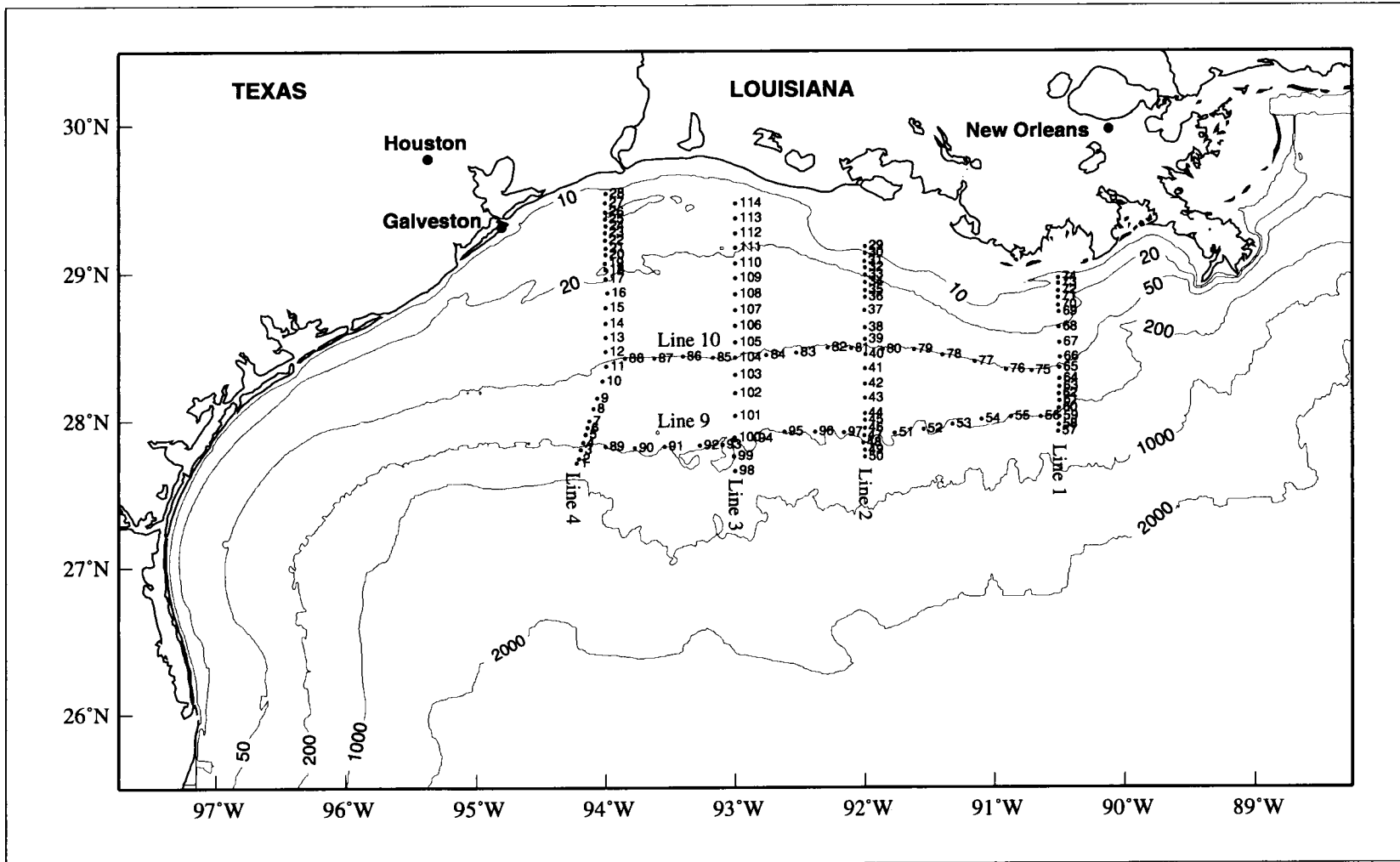


Figure 1.2-2. Typical locations for LATEX A hydrographic survey stations during field year 1, April 1992 to March 1993.

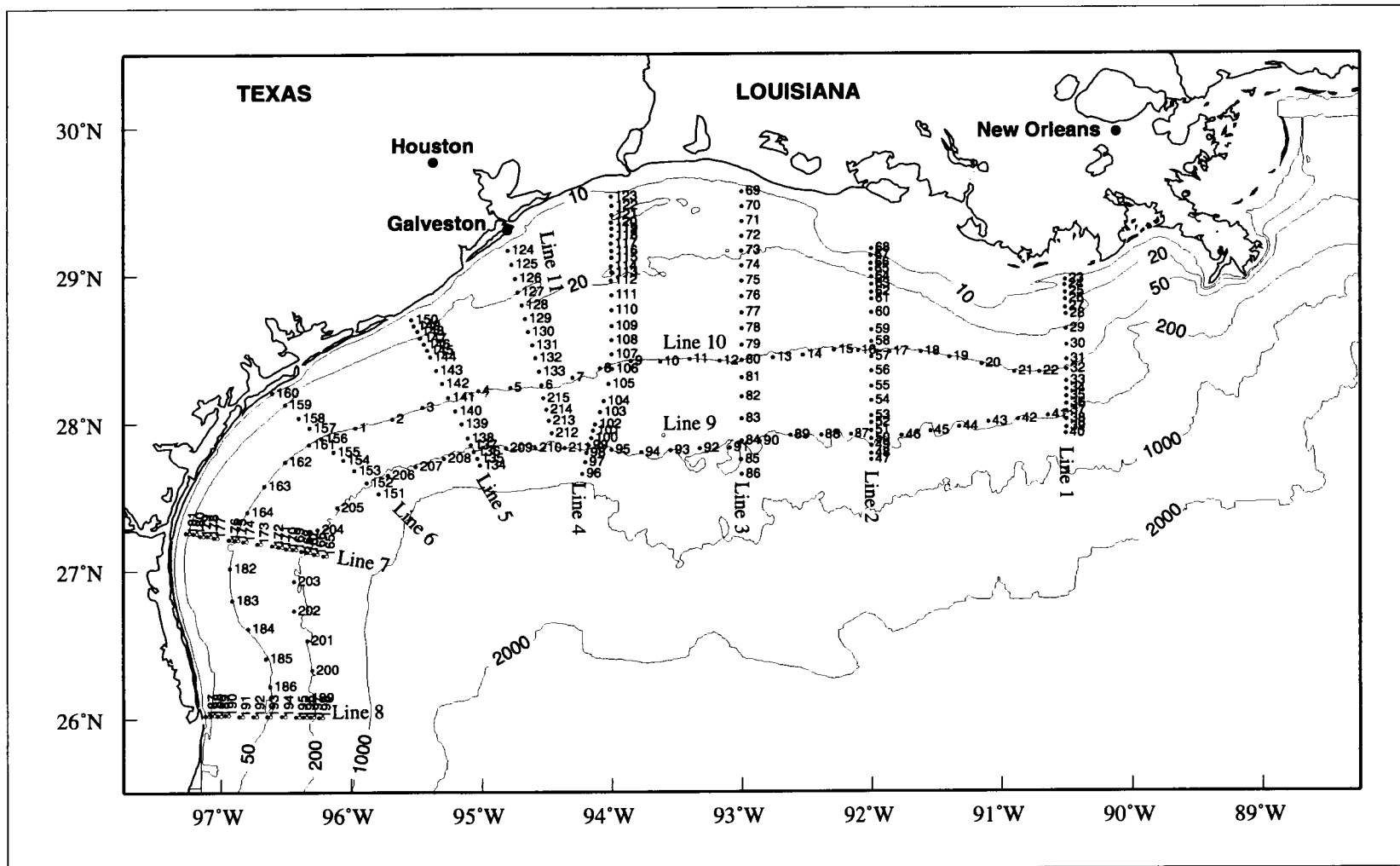


Figure 1.2-3. Typical locations for LATEX A hydrographic survey stations during field year 2, April 1993 to March 1994.

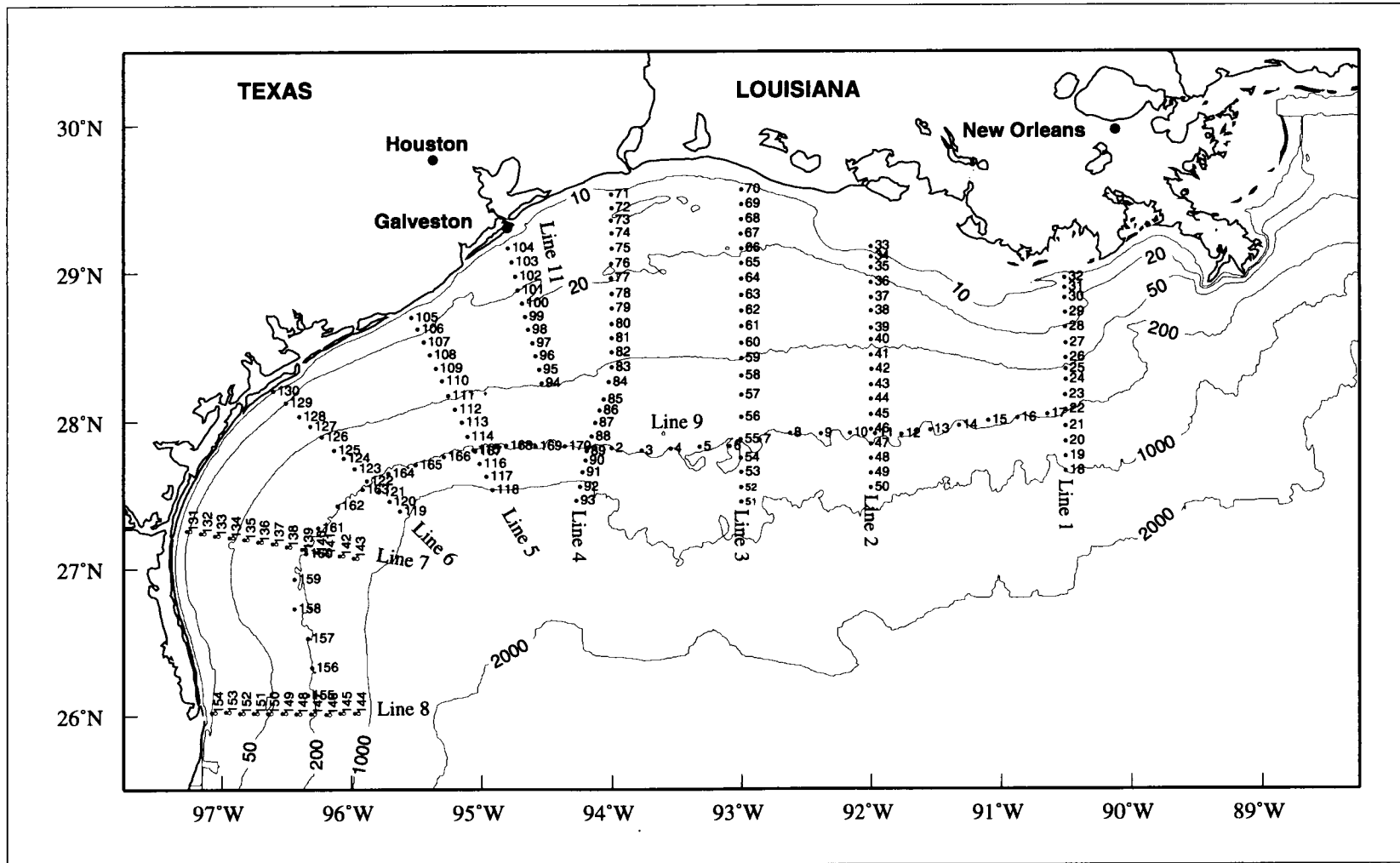


Figure 1.2-4. Typical locations for LATEX A hydrographic survey stations during field year 3, April 1994 to November 1994.

Table 1.2-2. Summary of data collected and scientific participation in the LATEX A hydrography surveys.

Description	H01	H02	H03	H04	H05	H06	H07	H08	H09	H10
	May 1992	Aug. 1992	Nov. 1992	Feb. 1993	May 1993	Aug. 1993	Nov. 1993	May 1994	Aug. 1994	Nov. 1994
Cruise Duration (days)	9	9	9	9	17	13	16	15	12	13
Cruise Track (km)	1117	1050	1050	1080	3680	3632	3720	3393	3393	3393
Total Hydro Stations	114	124	114	119	215	215	238	170	171	170
CTD Stations	114	124	114	118	215	215	238	170	171	170
Nutrient Stations	114	118	114	118	212	215	212	170	171	170
Oxygen Stations	64	72	77	80	145	148	144	153	154	170
Salinity Stations	64	73	68	71	134	133	133	87	88	104
Pigment Stations	83	88	85	87	153	154	152	154	150	154
Particulate Stations	52	50	56	58	107	109	108	118	119	119
Secchi Disk Stations	51	59	45	47	105	115	97	85	103	68
Weather Observations	27	30	32	30	64	48	60	56	40	44
XBT Launches	0	0	0	0	0	0	52	0	0	62
Nutrient Samples	936	1008	955	932	1682	1704	1685	1465	1482	1473
Salinity Samples	485	588	461	556	1058	1044	1054	728	739	940
Oxygen Samples	481	590	544	636	1129	1155	1125	1267	1297	1473
Pigment Samples	644	689	701	900	1204	1211	1217	1266	1235	1279
Particulate Samples	107	93	116	122	214	221	214	235	238	239
Total Scientific Party	20	20	17	23	23	17	20	20	17	19
LATEX Scientists	14	16	14	18	19	15	18	15	15	17
Guest Investigators	6	4	3	5	4	2	2	5	2	2
Graduate Students	5	8	8	9	9	4	6	6	4	5
Complementary Studies	5	4	3	4	4	4	3	7	4	5

Nineteen satellite-tracked drifting buoys under Task A-2, ARGOS-Tracked Drifting Buoys, were launched from five hydrographic cruises (H02, H03, H05, H08, and H10). Three to five drifters were deployed either in cross-shelf lines or along the shelf break at the 200-m isobath. Table 1.2-3 shows the deployment locations and dates for the drifters. Drifter tracks and sea surface temperature were monitored through Service ARGOS. Additional information on the drifting buoys, including plots of the tracks and time series of the velocity and temperature, is provided in the drifter data report (Howard and DiMarco 1998).

Concurrent and historical data (Task A-5)

Under Task A-5, Collateral Data, we assembled data from concurrent programs in the LATEX region, including LATEX B and LATEX C, and from historical sources. Concurrently with LATEX, MMS sponsored the Distribution and Abundance of Marine Mammals in the North-Central and Western Gulf of Mexico program (GulfCet), conducted by Texas A&M University at Galveston. Among the many other concurrent data sources were meteorological data transmitted over the Global Telecommunications System; high-resolution gridded flux data from the NOAA National Meteorological Center; maps of the sea surface height anomaly produced from ERS-1 and TOPEX/Poseidon satellite altimeter data by the Colorado Center for Astrodynamics Research at the University of Colorado; satellite AVHRR sea surface temperature images from the NOAA-COASTWATCH program; and river discharge data from the U.S. Geological Survey and the U.S. Army Corps of Engineers. Examples of the historical data amassed are hydrographic data from the TAMU and NODC archives and river discharge data from the U.S. Geological Survey and the U.S. Army Corps of Engineers. Details are provided in the three annual reports (Jochens and Nowlin 1994, 1995; Reap et al. 1996).

Table 1.2-3. Dates and locations for deployment and end of transmission for LATEX A drifters.

ARGOS ID	Event	Dates (UTC)	Lat (°N)	Long (°W)
03583	Deploy	03-Aug-92	29.080	92.004
	End	11-Aug-92	29.216	92.052
02446	Deploy	03-Aug-92	28.889	91.996
	End	13-Aug-92	28.386	91.454
03582	Deploy	03-Aug-92	28.443	91.997
	End	04-Sep-92	27.980	93.978
02447	Deploy	04-Aug-92	27.997	92.000
	End	07-Feb-93	24.809	97.049
06932	Deploy	11-Aug-92	28.446	91.999
	End	02-Dec-92	28.383	93.857
06934	Deploy	10-Nov-92	28.881	90.512
	End	02-Aug-93	25.771	79.962
06933	Deploy	10-Nov-92	28.773	90.507
	End	08-Jan-93	25.143	97.312
06931	Deploy	12-Nov-92	lost on deployment	
03585	Deploy	12-Nov-92	lost on deployment	
06938	Deploy	02-May-93	27.850	94.175
	End	17-Oct-93	28.342	86.905
06935	Deploy	02-May-93	27.952	94.138
	End	02-Nov-93	26.157	80.038
06937	Deploy	02-May-93	28.150	94.062
	End	08-Jan-94	26.760	83.948
06939	Deploy	02-May-93	28.367	93.995
	End	12-July-93	29.323	94.107
06940	Deploy	01-May-94	27.993	94.035
	End	26-May-94	28.233	93.365
03584	Deploy	01-May-94	27.793	94.198
	End	29-June-94	29.262	93.190
06936	Deploy	01-May-94	27.908	94.168
	End	11-June-94	28.762	91.768
07839	Deploy	03-Nov-94	27.945	91.538
	End	17-April-95	43.833	42.882
07834	Deploy	03-Nov-94	28.043	90.642
	End	15-Nov-94	27.858	90.498
07833	Deploy	03-Nov-94	28.012	91.092
	End	26-Dec-94	26.913	79.948

1.3 Report organization

This report synthesizes the data collected during the LATEX field program and provides a scientific presentation of the results. Section 2 of this report gives a description of the forcing fields that were present during the LATEX A field program. Section 3 characterizes the water masses and describes the heat and freshwater budgets. Analysis of the shelfwide circulation and transports, from current meters, hydrography, and ADCP measurements, is given in Section 4. An empirically-based conceptual model is developed; results of a simple numerical model for wave propagation over the inner shelf is presented. Finally, Section 5 presents a description of the distributions and variability of the ecological parameters—particulates, nutrients, oxygen, and pigments—measured on the hydrographic surveys.

The appendices contain information and results that amplify the principal findings, but may or may not bear directly on the four key LATEX A objectives given in Section 1.1. Appendix A presents a summary of winter cyclogenesis in the region. Brief case studies of several types of atmospheric events and their effects on the circulation and hydrography of the shelf are given in Appendix B. The effects of extremely large river discharge are illustrated by the Texas flood of October 1994 described briefly in Appendix C. A case study of Loop Current Eddy Vazquez, its movements and interactions with bathymetry and other eddies, is presented as Appendix D. Appendix E describes a volumetric temperature-salinity census for the Texas-Louisiana shelf. Smaller scales are considered in Appendix F, which includes analyses of tides and other inertial and superinertial motions. Appendix G compares observed surface gravity waves with wave model results. Appendix H shows two distinct time series of estimated current fields for the LATEX period: geopotential anomaly distributions and monthly average gridded 10-m currents from mooring data. Current, temperature, and salinity statistics are included in Appendix I for completeness. Appendix J includes current comparisons: vertical shear from ADCP versus that from hydrography and current meter versus ADCP velocities. Our search of the LATEX data for wave propagation along the shelf and slope is described in Appendix K, while Appendix L compares observations for the inner shelf with results from a circulation model. Finally, Appendix M summarizes quantitative estimates of monthly fluxes of heat, freshwater, and mass between a series of boxes covering the Texas-Louisiana shelf as well as such transports across the shelf break.

2 PHYSICAL BOUNDARY CONDITIONS

2.1 Wind fields

Hourly fields of 10-m wind, surface wind stress, air temperature, sea level atmospheric pressure, and sea surface temperature for the region of the northwestern Gulf of Mexico including the Texas-Louisiana continental shelf were produced for the period April 1992 through November 1994 using surface wind measurements from a combination of buoys, platforms, and airport weather stations. First, in Section 2.1.1 the data and procedures used to construct these fields are briefly described or referenced. Then, a comparison is described between the resulting wind fields (called here LATEX winds) and two other wind fields for the same region and period: winds derived from scatterometer data collected on the ERS-1 satellite and analyzed winds from the National Center for Environmental Prediction (NCEP).

A description of the LATEX winds, including an annual cycle of monthly winds and seasonal means with variability, is presented in Section 2.1.2. In Section 2.1.3, the monthly frequency of cold fronts passing over the shelf during the LATEX period is presented and compared with the climatology of weather events over the shelf.

The occurrence of atmospheric cyclogenesis over the Texas-Louisiana shelf is reviewed in some detail in Appendix A.

General discussion of the effects of wind forcing on the shelf circulation are given in Section 4. Some examples of the effects of strong episodic wind events, such as hurricanes and other cyclones, are given in Appendix B. Also given in Appendix B is an example of wind-induced upwelling.

2.1.1 Comparisons among LATEX, ERS-1, and NCEP winds

Formulation of LATEX meteorological surface fields

Data. From April 1992 through November 1994, meteorological buoys were maintained as part of the LATEX program over the central area of the Texas-Louisiana shelf (Figure 2.1.1-1). Each buoy had sensors measuring hourly sea surface temperature (SST) and the following surface meteorological properties: wind speed and direction, air temperature, and sea surface barometric pressure. Wind speed and direction were measured at 3.6 m above sea level, air temperature at 3 m, pressure at sea level, and SST at 1 m below sea level. The measurement accuracies and ranges as well as resolutions for each parameter are listed in Table 2.1.1-1. Wind speed and air temperature were adjusted to 10 m above sea level based on marine boundary layer theory (Smith 1988) before further analysis.

Other meteorological measurements used in constructing the LATEX meteorological fields were collected from six National Data Buoy Center (NDBC) buoys, nine Coastal-Marine Automated Network (C-MAN) buoys, and five National Weather Service (NWS) or

Table 2.1.1-1. Ranges, accuracies, and resolutions of meteorological sensors on LATEX buoys.

Sensor	Range	Accuracy	Resolution	Units
Wind Speed	0 to 51	$\pm 10\%$ of reading*	0.2	$\text{m}\cdot\text{s}^{-1}$
Wind Direction	0 to 360	± 20	1.41	deg
Air Temperature	-3.25 to 35.0	± 0.2	0.15	$^{\circ}\text{C}$
Barometric Pressure	900 to 1053.45	± 0.5	0.5	hPa
Sea Surface Temperature	-3.25 to 35.0	± 1.0	0.15	$^{\circ}\text{C}$

* for readings greater than $1 \text{ m}\cdot\text{s}^{-1}$

Table 2.1.1-2. Ranges, accuracies, and resolutions of meteorological sensors used at NDBC and C-MAN measurement sites (Meindl and Hamilton 1992).

Sensor	Range	Accuracy	Resolution	Units
Wind Speed	0 to 62	$\pm 1 \text{ m}\cdot\text{s}^{-1}$ or 10%	0.1	$\text{m}\cdot\text{s}^{-1}$
Wind Direction	0 to 360	± 10	1	deg
Air Temperature	-40 to 50	± 1	0.1	$^{\circ}\text{C}$
Barometric Pressure	900 to 1100	± 1	0.1	hPa
Sea Surface Temperature	-7 to 41	± 1	0.1	$^{\circ}\text{C}$

NWS-sponsored weather stations located on land near the coast. All locations are shown in Figure 2.1.1-1. Details of the variables measured hourly are given in Table 2.1.1-2.

Measurement heights for winds and air temperatures varied on different NDBC and C-MAN buoys. Wind speeds and air temperatures were adjusted by the identical method used in adjusting LATEX winds and air temperatures, thus avoiding bias created by different methods. Reported surface pressures had been adjusted to sea level.

At land weather stations, surface properties were measured hourly. Wind speed in kts and direction were measured at 10 m above local ground level and air temperature in $^{\circ}\text{F}$ at about 1.5 m above ground level. Reported surface pressures were adjusted to sea level. Observed wind speeds were converted to $\text{m}\cdot\text{s}^{-1}$ and air temperature to $^{\circ}\text{C}$; other measurements were used as reported. Positions and sensor heights of wind and air temperature for C-MAN and NDBC stations used in this study are listed in Table 2.1.1-3.

Methodology. The Texas-Louisiana shelf between the coast and the 200-m isobath from 26°N to 90°W encompasses about a 10° square, within which there were fifteen meteorological buoys, giving a mean station separation of about 0.8° . The grid spacing selected for construction of the LATEX meteorological fields is 0.5° in latitude and longitude.

Table 2.1.1-3. Heights of wind and temperature recorders for NDBC and C-MAN sites from which measurements were used to construct meteorological fields.

Station	Anem.* Ht. (m)	Air Temp.* Ht. (m)	Type
42001	10.0	10.0	NDBC
42002	10.0	10.0	NDBC
42007	10.0	10.0	NDBC
42019	5.0	5.0	NDBC
42020	5.0	4.0	NDBC
42035	5.0	4.0	NDBC
BURL	33.8	13.7	C-MAN
BUSL1	93.6	21.3	C-MAN
DPIA1	17.4	9.1	C-MAN
GBCL1	57.6	57.6	C-MAN
GDIL1	17.6	17.0	C-MAN
LNEL1	60.0	34.7	C-MAN
MPCL1	40.2	40.2	C-MAN
PTAT2	14.9	9.1	C-MAN
SRST2	13.4	12.8	C-MAN

* The heights for sea stations are measured from sea level; the heights for land stations are measured from local ground level.

Thus, the spatial resolution of the gridded fields is somewhat greater than half the mean spacing of the meteorological buoys.

Statistical interpolation (also called optimal interpolation) was used in this study to estimate gridded values at grid points using weighted averages of nearby observed data. Introduced as optimal estimation in meteorological data analysis (Gandin 1965), statistical interpolation now is widely used in meteorology and oceanography for both analysis and observing array design (Bretherton et al. 1976; White and Bernstein 1979; McWilliams et al. 1986; Carter and Robinson, 1987; Rienecker et al. 1987; Mariano and Brown 1992). Weights are chosen based on the spatial correlation of the observed data to minimize the error variance of gridded values.

For construction of the LATEX meteorological fields, we used monthly mean values of spatial scales and noise covariance. Details of the analysis used to produce the hourly fields are described and discussed in Wang et al. (1998a). The resulting wind fields are described in Section 2.1.2; other fields in Section 2.2.

Comparisons among wind fields

NCEP made available global analyzed surface wind fields at 10 m above sea level from the Global Data Assimilation System (GDAS) (Dey 1989; Kanamitsu 1989). The GDAS

produces an attractive alternative source of wind data to the operational meteorological forecast and analysis models. Zonal and meridional winds are converted from their original spectral form to 0.93° by 0.93° grids at six-hour intervals. The 6-hourly NCEP wind fields from April 1992 through November 1994 were obtained for use in this study.

The other set of wind fields used in this comparison was constructed from scatterometer data collected aboard the first European Remote Sensing satellite (ERS-1), a multi-mission satellite launched in July 1991 by the European Space Agency. The wind scatterometer carried by ERS-1 observes C-band radar backscatter from Earth's surface (Francis et al. 1991). Three antennae generate radar beams looking 45° forward, sideways, and backward with respect to the satellite's flight direction. These beams continuously illuminate a 500-km wide swath as the satellite moves through its orbit, and each provides independent measurements of radar backscatter from the sea surface on a 25-km square grid. Because the backscatter depends on wind speed and direction, these "triplets" are input to a mathematical model to calculate wind speed and direction at 10-m above sea level. The reported accuracy for ERS-1 scatterometer winds is $2 \text{ m}\cdot\text{s}^{-1}$ or 10 percent (whichever is larger) for wind speeds in the range of 4 to $24 \text{ m}\cdot\text{s}^{-1}$ and 20° for direction. The ERS-1 scatterometer winds used in this study were produced by Freilich and Dunbar (1993) from their CMOFD model.

The purpose of our comparison of NCEP and ERS-1 wind products with LATEX wind products was to assess how well the former products represent the true wind regime, at least for this area.

Bear in mind that LATEX, NCEP, and ERS-1 wind fields were produced differently. LATEX winds were produced from in situ measurements using an objective analysis method. ERS-1 winds are instantaneous, model-derived, spatial averages (over 50-km squares) based on observations independent from LATEX or NCEP winds. NCEP winds are based on a blend of data with a numerical forecast—using both temporal and spatial smoothing.

It is not possible to make quantitatively estimated accuracies independently for the three data sets. Being from in situ measurements from discrete points, the LATEX wind fields have several potential biases and random errors arising from such factors as instrument errors, platform interference effects, and interpolation procedure. The scatterometer winds are also based on in situ (wave) conditions, but remotely sensed, and have inherent biases and random errors related to the measurement procedure and model function. Since the spatial resolution of ERS-1 scatterometer winds far exceeds that of LATEX wind data, more detailed information might be available from the ERS-1 winds, although there are large spatial and temporal gaps in that coverage. The NCEP winds, which are the model forecast results blended with in situ observations, have the coarsest resolution among the three data sets. Thus, larger differences were expected between LATEX and NCEP winds than between LATEX and ERS-1 winds.

LATEX versus NCEP winds

Six-hour averaged LATEX winds were estimated at NCEP grid points using statistical interpolation, and differences between the two fields at those points were calculated. The 32-month mean, seasonal, and monthly difference fields were estimated by averaging the six-hour differences at each grid point over the appropriate periods.

The mean and variability of a vector variable over some period can be described by its vector mean and a variance ellipse. The major and minor axes of the ellipse are orthogonal and are called principal axes, along which the maximum and minimum variances occur. The covariance between the components along the two principal axes is null. Differences between the LATEX and NCEP winds will be described using vector means and variance ellipses.

Mean differences for the LATEX period. The LATEX wind field vector-averaged over the 32-month period, April 1992 through November 1994, at NCEP grid points is pictured in the upper panel of Figure 2.1.1-2; NCEP winds averaged over the same period are shown in the middle panel. Though generally consistent, NCEP winds are somewhat stronger than LATEX winds and have larger northward components, especially over the inner shelf. The variances of NCEP winds are somewhat larger than those of the LATEX winds. The ratios of the major to minor variability axes for NCEP winds tend to be close to unity; for the LATEX field, the north-south variances are larger than those east-west, particularly over the western shelf.

The mean 6-hr vector difference field between NCEP and LATEX wind fields (Figure 2.1.1-2, lower panel) shows speed differences generally less than $1.5 \text{ m}\cdot\text{s}^{-1}$. The differences are larger in the central region where LATEX A maintained a set of buoys for meteorological measurements. Those data were not used in producing the NCEP winds. This seems the major reason for the larger differences in this area. We note that differences are also larger near the coast.

Fluctuations of the differences between the two sets of winds over the 32-month period are represented by principal axis ellipses, showing a preferred north-south orientation over the inner shelf from New Orleans to central Texas. The magnitudes of the fluctuations exceed the mean values by factors of three to four. Note that the variability of the difference is less by a factor of two than the variability of the individual winds.

Seasonal differences. Seasonal patterns of the LATEX and NCEP wind fields also are basically alike, but with differences in detail. The mean seasonal difference fields between LATEX and NCEP wind sets, as well as their fluctuations, are shown in Figure 2.1.1-3. The maximum differences in these means occur during summer, with values near $2 \text{ m}\cdot\text{s}^{-1}$ over the inner, eastern shelf. Minimum values near $0.1 \text{ m}\cdot\text{s}^{-1}$ occur over the outer shelf during winter. Fluctuations are much smaller in summer than in winter. The maximum major axis (standard deviation along that axis) is less than $3 \text{ m}\cdot\text{s}^{-1}$ in summer but more than $4 \text{ m}\cdot\text{s}^{-1}$ in

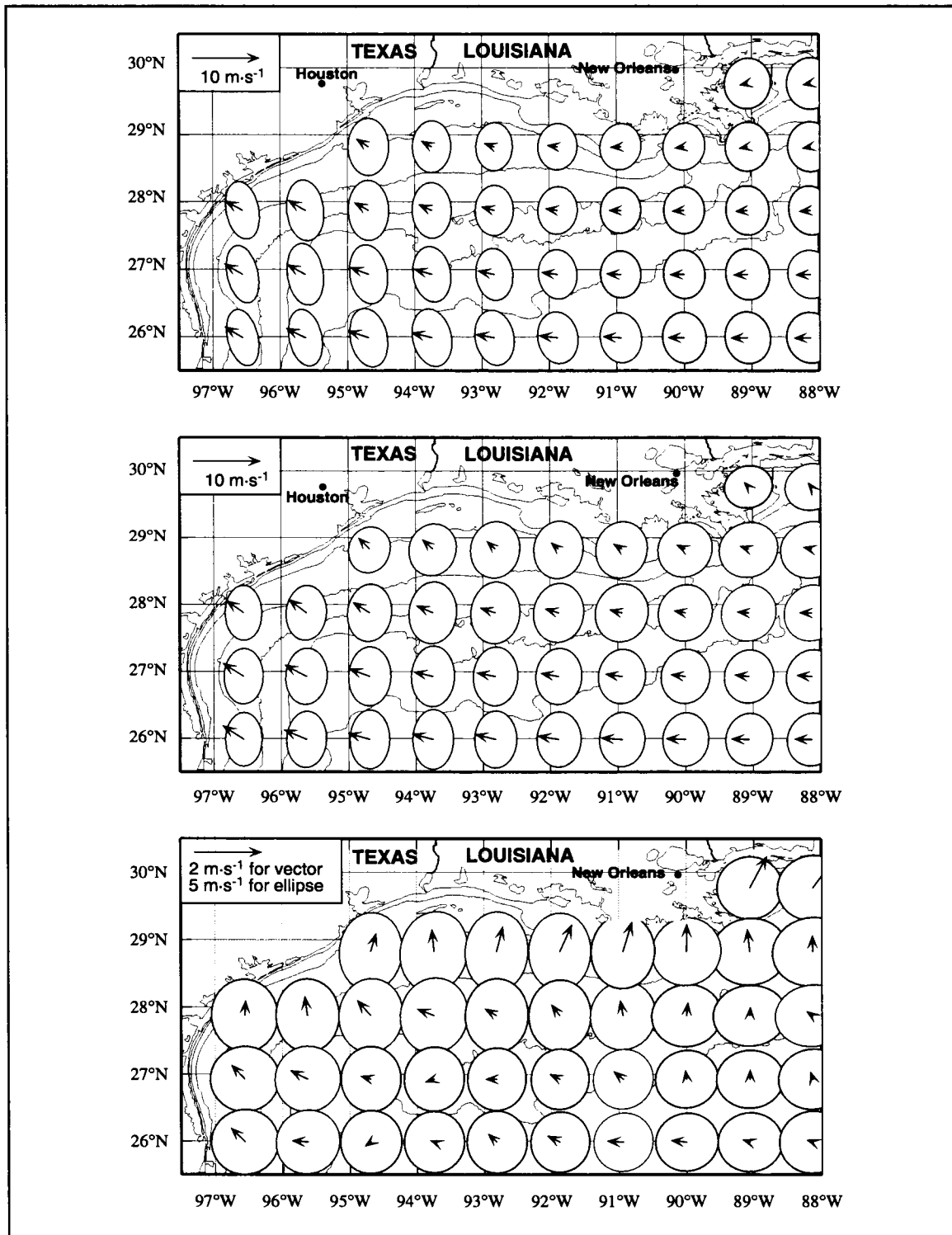


Figure 2.1.1-2. LATEX mean winds (upper panel), NCEP mean winds (middle panel), and the mean difference field (NCEP minus LATEX) (lower panel) for the period April 1992 through November 1994.

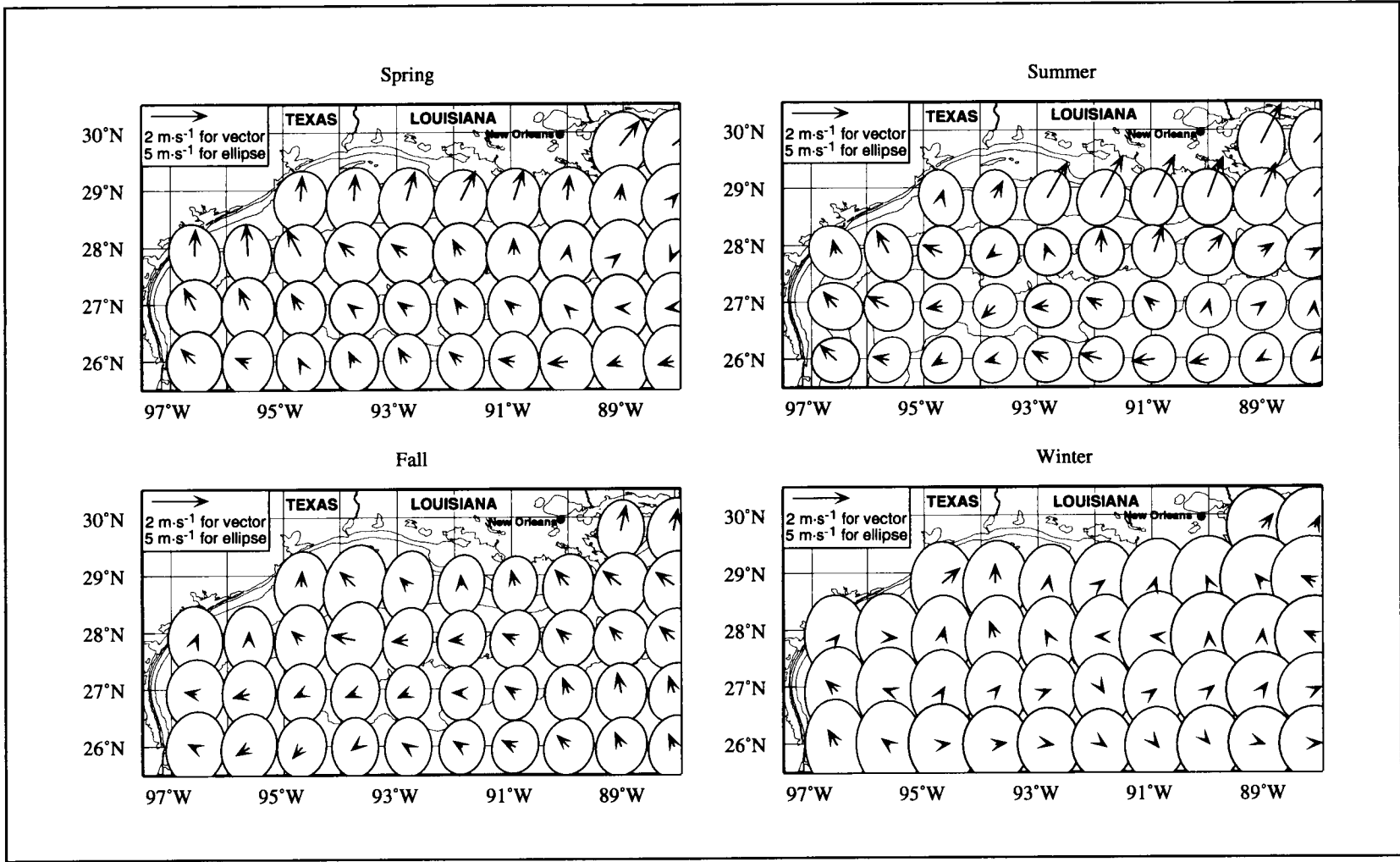


Figure 2.1.1-3. Mean seasonal difference between LATEX and NCEP wind fields (NCEP minus LATEX).

winter. Speed differences in spring and fall generally lie between those of summer and winter. As to direction differences, NCEP appears to have a more northerly component over the inner shelf; in spring that bias seems to extend over most of the shelf.

The larger fluctuations of the differences in winter can be explained by the fact that there are many frontal incursions in this season (see Section 2.1.3 for detail), together with the fact that frontal positions in the NCEP and LATEX fields do not agree well, causing differences of wind speeds and directions near the fronts. Figure 2.1.1-4 illustrates the observed disagreements between these two wind fields for frontal passages. NCEP and LATEX wind vectors are pictured at the time of a frontal passage (0600 UTC on 4 November 1992). The frontal location over the inner shelf was one degree further east (just east of 92°W) in the NCEP field.

For each season, histograms of speed differences and direction differences between the two set winds were examined (Figures 2.1.1-5 and 2.1.1-6). Direction differences were taken as positive if NCEP wind was directed counterclockwise relative to LATEX wind. The histograms of speed differences are centered on 0 for all seasons. However, the wind direction histograms are centered on -10° in summer and fall and on -20° in spring and winter, indicating a clockwise bias of NCEP winds relative to LATEX winds.

Instantaneous differences. Wind vectors vary rapidly in time. Averaging NCEP and LATEX wind fields results in smooth fields with similar patterns for the 32-month mean and seasonal fields, although the instantaneous fields may have large differences. To examine instantaneous differences, all 6-hourly NCEP and LATEX winds were compared. Speed differences were divided into $1 \text{ m}\cdot\text{s}^{-1}$ bins ranging from -16 to $16 \text{ m}\cdot\text{s}^{-1}$, and direction differences into 10° bins from -180 to 180° . Figure 2.1.1-7 shows the histogram of speed and direction differences between the two data sets. For wind speed, there is no systematic difference. For wind direction, the difference peak centered at 10° , not at 0° , which means there is a clockwise bias of NCEP winds relative to LATEX winds. Overall, 70% of the speed differences are less than $2 \text{ m}\cdot\text{s}^{-1}$, and 50% of the direction differences are less than 20° .

LATEX versus ERS-1 winds

We examined winds from 41 ERS-1 orbits that passed over the Texas-Louisiana shelf during five selected months: March 1992 representing spring, July 1992 and 1993 representing summer, November 1992 representing fall, and February 1993 representing winter. If either speed or direction was missing from the ERS-1 data at a grid point, data from that point were omitted from the comparison. LATEX winds were interpolated to ERS-1 grid points using statistical interpolation at the beginning of an hour; thus, there is less than one hour time difference between the ERS-1 and LATEX winds at any point. NCEP winds during these orbit times also were interpolated to the ERS-1 grid points using a bi-cubic spline method. Therefore, comparisons among the three wind fields were possible during the times and areas covered by the 41 selected ERS-1 orbits, amounting to a total of 7259 grid points.

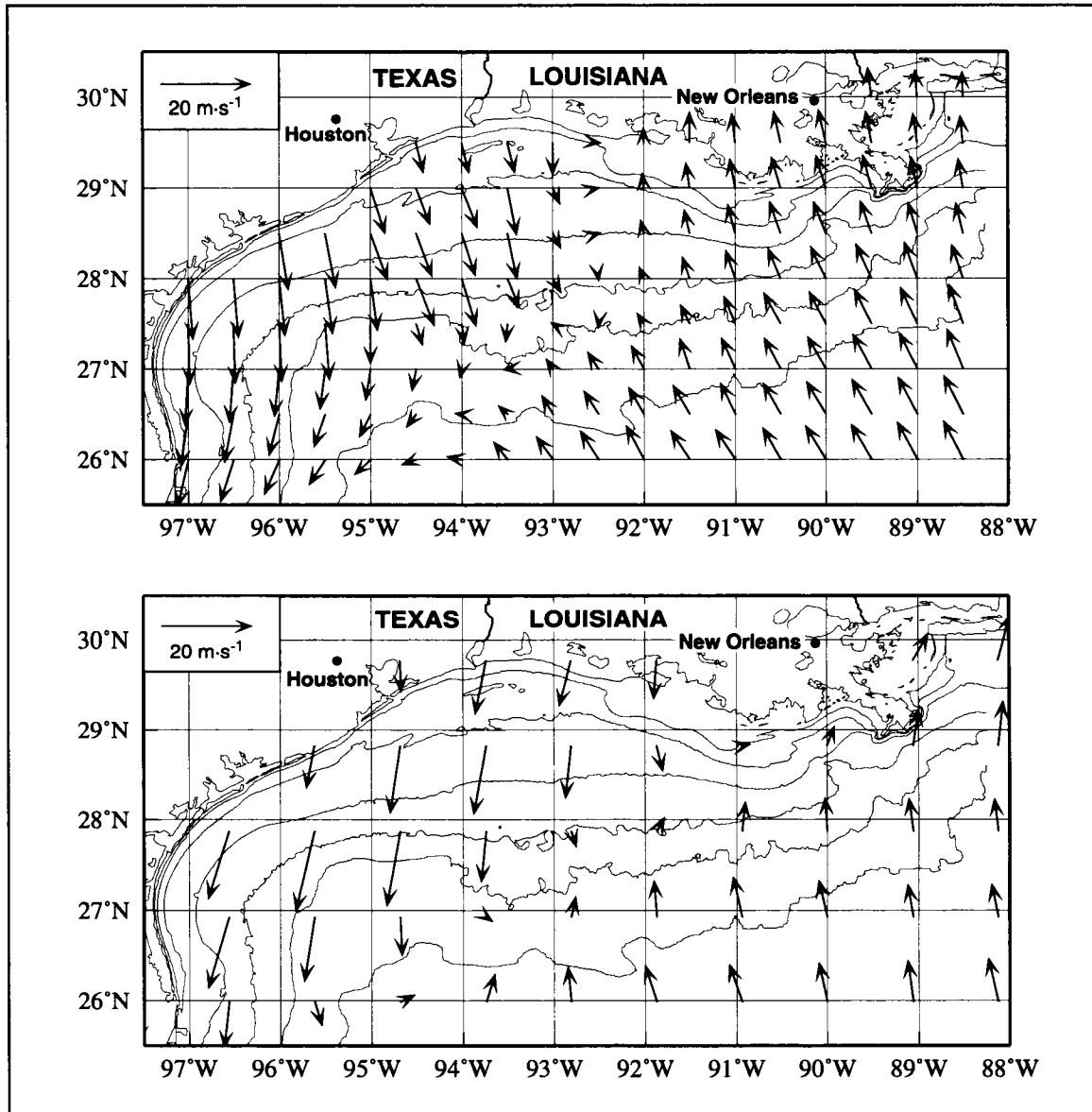


Figure 2.1.1-4. The LATEX (upper panel) and NCEP (lower panel) winds at 0600 UTC 4 November 1992.

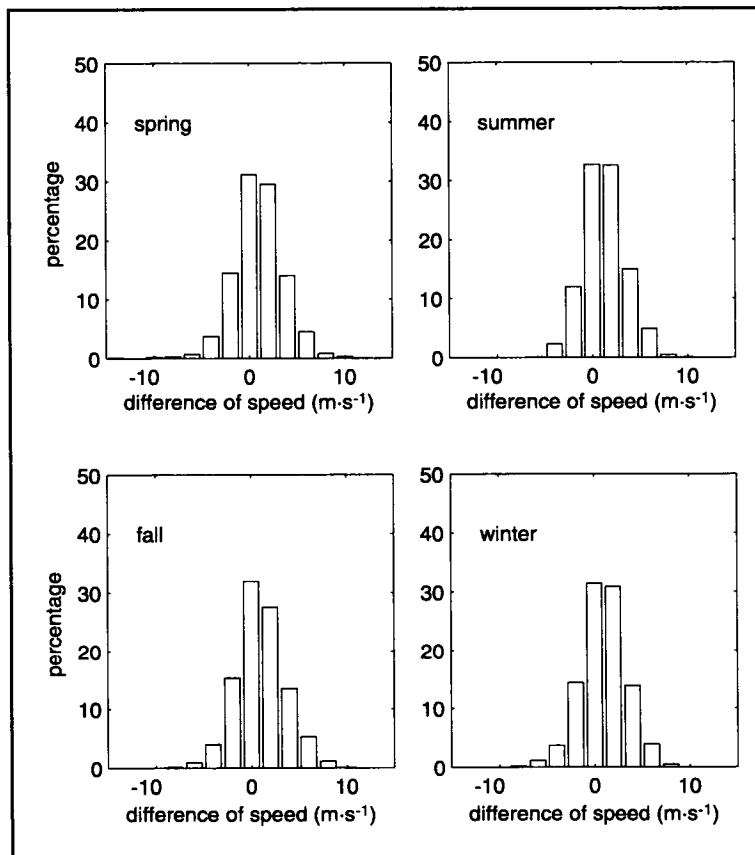


Figure 2.1.1-5. Histograms of speed difference between LATEX and NCEP winds (NCEP minus LATEX) for each season.

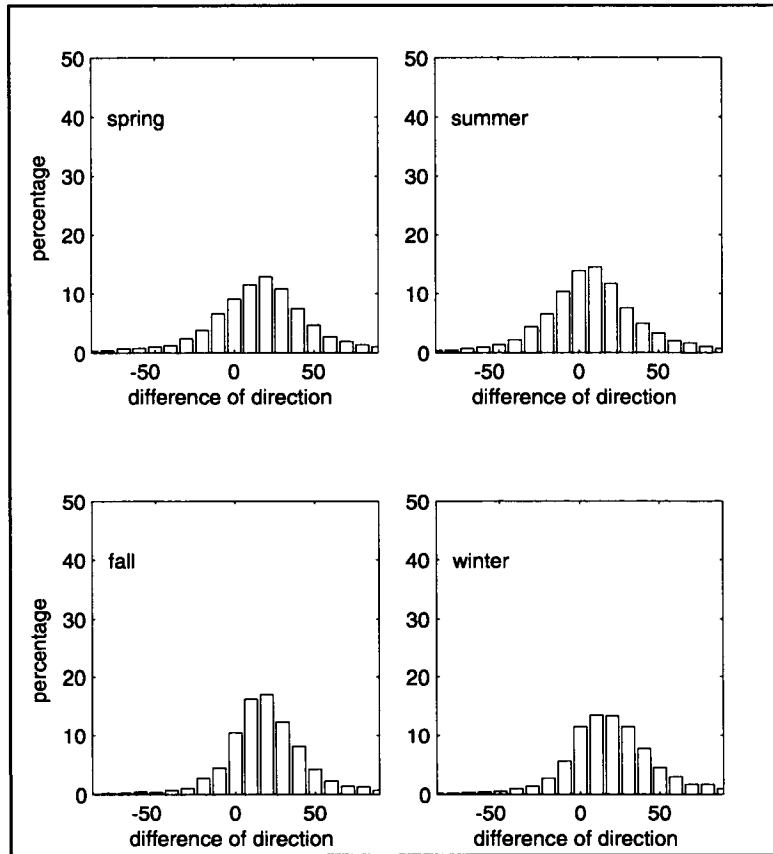


Figure 2.1.1-6. Histograms of direction difference between LATEX and NCEP winds (NCEP minus LATEX) for each season.

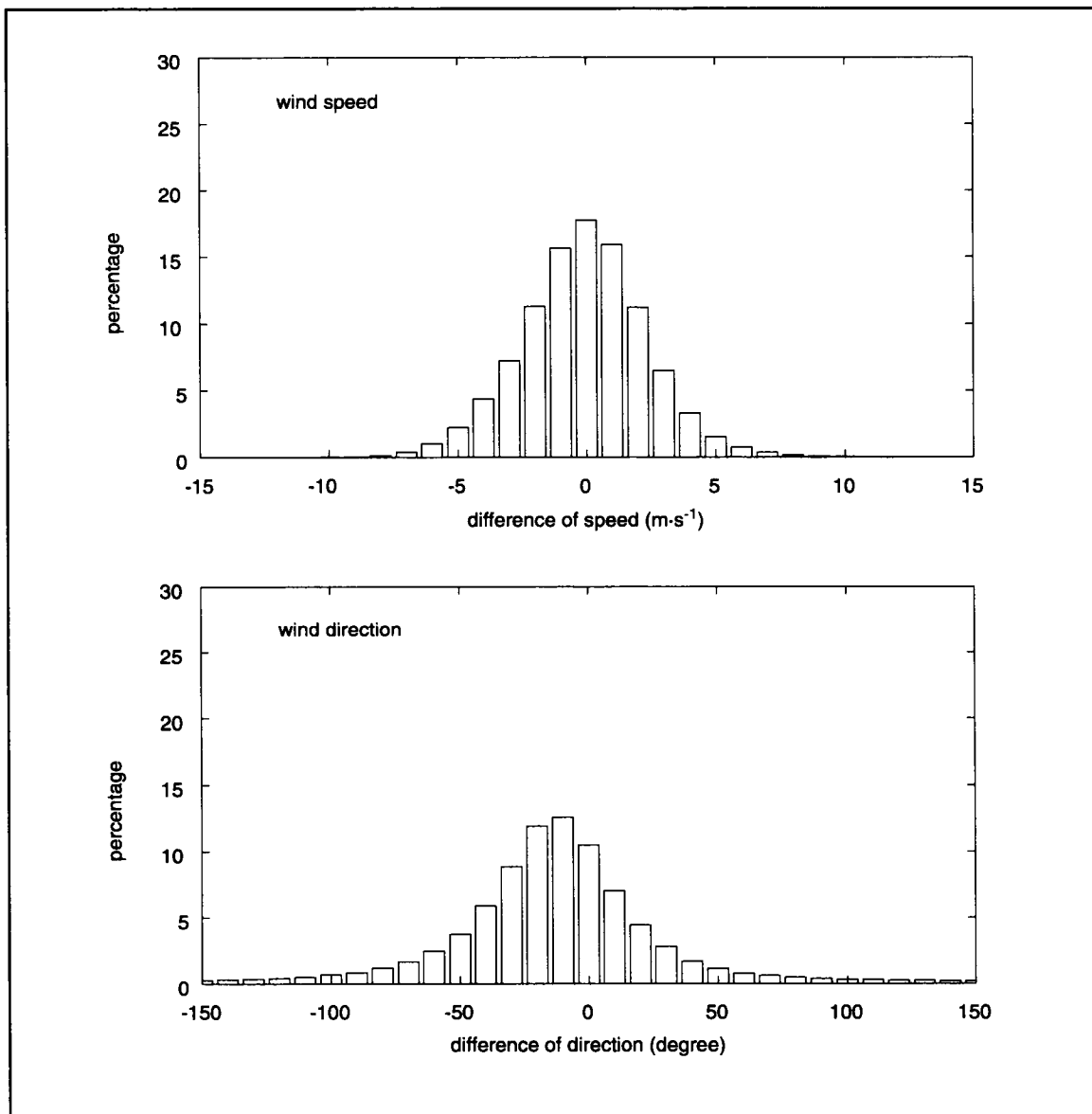


Figure 2.1.1-7. Histograms of difference between LATEX and NCEP winds (NCEP minus LATEX), angles measured positive in counterclockwise sense.

Differences in ERS-1 and LATEX wind speed and direction can be examined from the histograms in Figure 2.1.1-8. Speed differences were divided into $1 \text{ m}\cdot\text{s}^{-1}$ bins ranging from -16 to $16 \text{ m}\cdot\text{s}^{-1}$, and direction differences into 10° bins from -90 to 90° . For wind speed, the difference peak is centered at $0 \text{ m}\cdot\text{s}^{-1}$, and for direction it is at 0° , which illustrates the good overall agreement between these two wind fields.

Dependence of speed and direction differences on wind speeds was examined for bias and scatter between ERS-1 and LATEX winds. Scatter plots of the speed and direction differences between ERS-1 and LATEX winds as a function of LATEX wind speed for the 41 ERS-1 swaths are shown in Figure 2.1.1-9. Also shown are linear regressions and 95% confidence intervals for the regressions. The LATEX wind speed range examined varies from 0 to $13 \text{ m}\cdot\text{s}^{-1}$. At moderate speeds (around $9 \text{ m}\cdot\text{s}^{-1}$) mean differences (i.e., bias) for both speed and direction are small, close to zero. On average, ERS-1 slightly overestimates speed for values lower than about $9 \text{ m}\cdot\text{s}^{-1}$ and underestimates high speeds; as examples: at $2 \text{ m}\cdot\text{s}^{-1}$ the ERS-1 wind is greater than the LATEX wind by about $1.2 \text{ m}\cdot\text{s}^{-1}$ and directions differ by some 10° ; at $13 \text{ m}\cdot\text{s}^{-1}$, the ERS-1 wind is less than the LATEX wind by about $0.7 \text{ m}\cdot\text{s}^{-1}$ and directions differ by some 11° . As seen here, individual differences between ERS-1 and LATEX wind vectors can be rather large; from Table 2.1.1-4 the rms speed difference was $1.9 \text{ m}\cdot\text{s}^{-1}$ and the rms direction difference was 26° .

During the LATEX field period, there were many extreme weather conditions that would test the speeds at the upper limits of the ERS-1 instrument. We examined such situations, e.g., during the 12 March 1993 cyclone called the Storm of the Century. ERS-1 winds clearly do not well represent the physical situation in some extreme conditions, such as wind speeds in excess of $15 \text{ m}\cdot\text{s}^{-1}$ and intense rainfall as occurred near the eye of the Storm of the Century.

Synoptic three-way comparisons

Global statistics provide a good general characterization of differences between these wind fields, but fail to give a complete picture. We compared LATEX, ERS-1, and NCEP wind fields for numerous atmospheric situations to gain more insight into differences. Figure 2.1.1-10 shows one example of the three-way comparison. Both the LATEX and ERS-1 fields show a sharp shift of the wind direction over the eastern part of the swath; speeds are comparable for these two fields. However, the NCEP field is smoother than the others because of the larger spatial scales used in the NCEP analysis. The NCEP speeds are larger than LATEX or ERS-1 speeds.

Summary and conclusions

The LATEX wind fields, prepared from surface observations using an optimal interpolation technique, were compared with two other surface wind fields for the same time and location: an analyzed field from NCEP and fields derived by Freilich and Dunbar (1993) using data from the ERS-1 scatterometer. The LATEX winds extend throughout the period from April

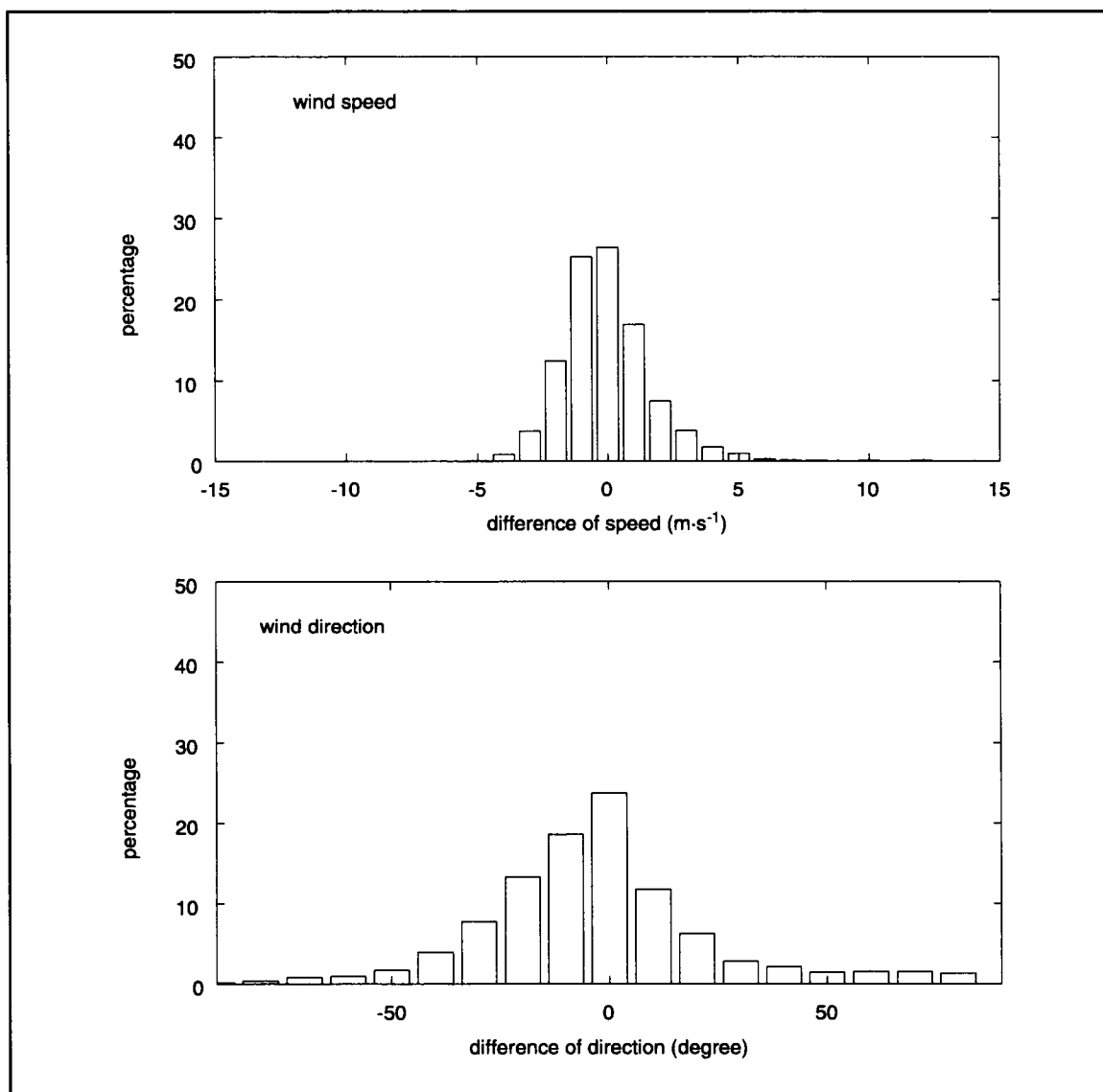


Figure 2.1.1-8. Histograms of difference between LATEX and ERS-1 winds (ERS-1 minus LATEX), angles measured positive in counterclockwise sense.

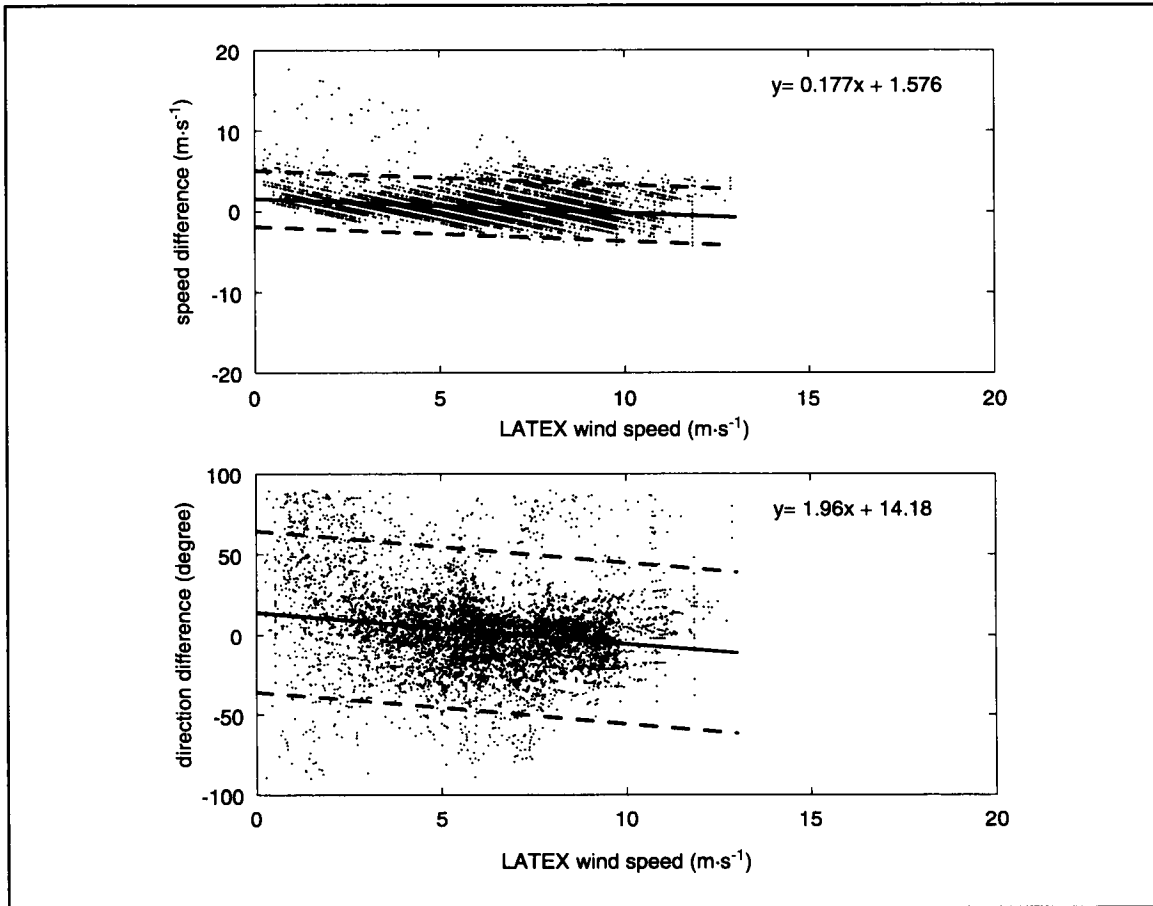


Figure 2.1.1-9. ERS-1 minus LATEX wind speeds and directions (positive counterclockwise) as functions of LATEX wind speed.

Table 2.1.1-4. Comparison of speed and direction differences among LATEX, ERS-1, and NCEP winds averaged over all grid points for the 41 selected ERS-1 swaths.

	ERS-1 vs. LATEX	ERS-1 vs. NCEP	NCEP vs. LATEX
mean speed difference ($\text{m}\cdot\text{s}^{-1}$)	0.5	-0.7	1.2
rms speed difference ($\text{m}\cdot\text{s}^{-1}$)	1.9	2.3	2.6
mean direction difference ($^{\circ}$)	2.6	8.6	-4.4
rms direction difference ($^{\circ}$)	26.1	27.8	38.3
std. deviation ΔU ($\text{m}\cdot\text{s}^{-1}$)	2.2	2.7	3.0
std. deviation ΔV ($\text{m}\cdot\text{s}^{-1}$)	2.5	2.7	3.2
correlation (U)	0.8	0.7	0.6
correlation (V)	0.9	0.9	0.8

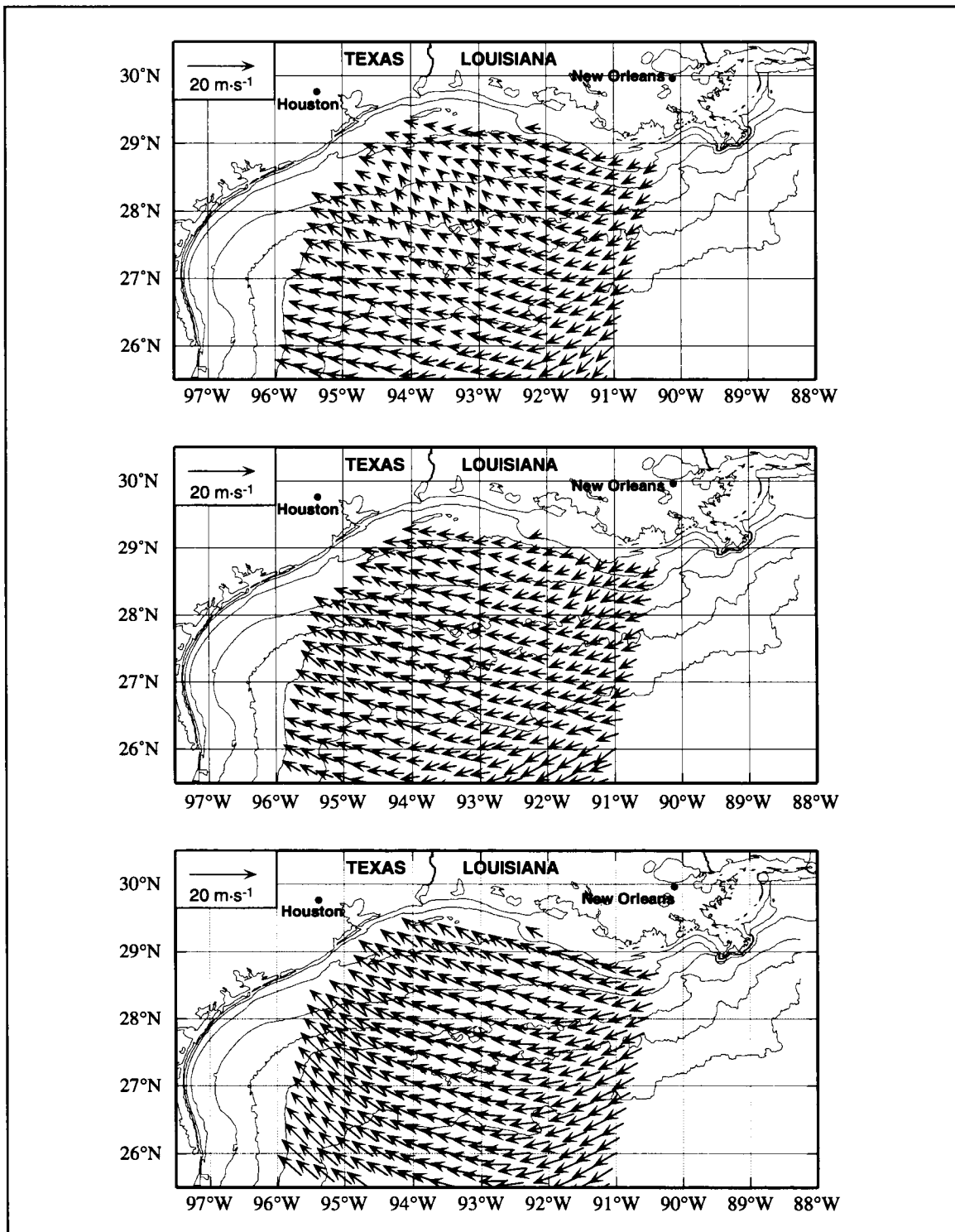


Figure 2.1.1-10. LATEX (upper panel), ERS-1 (middle panel), and NCEP winds (lower panel) at 1700 UTC 18 March 1993.

1992 to November 1994, and provide realistic and detailed surface wind fields for use in the study of mesoscale processes and forcing numerical models over the Texas-Louisiana shelf. Either the gridded LATEX wind fields or the controlled measurements from which they were prepared are available from the Department of Oceanography, Texas A&M University.

Differences between the LATEX winds and NCEP winds were largest near the coast. Statistics showed that there was no significant bias for wind speed between the two wind sets, but the direction of the NCEP winds were biased approximately 10° clockwise relative to LATEX winds. The average standard deviations of differences in both u and v components between LATEX and NCEP winds were approximately $3 \text{ m}\cdot\text{s}^{-1}$ (Table 2.1.1-4). Comparing fields during frontal passages showed that fronts were propagated unrealistically faster and spatial scales were larger in NCEP fields than in LATEX fields.

Comparisons with ERS-1 scatterometer winds indicated that there was no significant bias for either wind speed and direction between the LATEX and ERS-1 winds. Comparing u and v components between LATEX and ERS-1 winds yielded standard deviations of $2.2\text{-}2.5 \text{ m}\cdot\text{s}^{-1}$ (Table 2.1.1-4). The ERS-1 wind fields appear not to represent the physical situation very well in cases of extreme atmospheric events and for swaths very near shore.

Further details of the comparison are given in Wang et al. (1996), Wang (1996), and especially in Wang et al. (1998b).

Acknowledgment

The authors thank M. H. Freilich and R. S. Dunbar who provided, from the NASA Physical Oceanography Distributed Active Archive Center at the Jet Propulsion Laboratory, California Institute of Technology, the ERS-1 scatterometer estimates of winds used in this study.

2.1.2 Description of LATEX winds

Based on the hourly LATEX wind fields described in Section 2.1.1, monthly distributions of wind, wind stress, and wind stress curl are shown in Wang et al. (1996), the LATEX A meteorological data report. We present in this section the mean fields of wind, wind stress, and wind stress curl for the 32-month period of observations and analyzed fields, including variance estimates. Then, seasonal means for wind, wind stress, and wind stress curl are presented and described. Oceanographic convention is used when describing wind direction.

Of course, there are many analyses of wind, wind stress, and other marine meteorological variables (e.g., those discussed in Section 2.2) for the Gulf of Mexico. Examples include Florida A&M University (1988) that includes statistical, climatological descriptions at observation sites and Velasco and Winant (1996) that describes fields for the Gulf of Mexico. The advantages of the LATEX analyzed fields are that they: (1) are of relatively fine resolution, (2) provide fields for the space and times of interest to this study, and (3) are based totally on observations.

Mean fields for the observing period

Thirty-two-month vector mean winds with their variance ellipses are presented in Figure 2.1.2-1. The ellipses are plotted at every other grid point (1° separation) to avoid clutter. The mean wind vectors are generally westward, with stronger winds and larger northward components in the west. We believe this results because the winds are blocked somewhat to the west by land forms and thus are channeled northward. The mean speeds range from less than $1 \text{ m}\cdot\text{s}^{-1}$ over the northeastern region to $3 \text{ m}\cdot\text{s}^{-1}$ in the west. Winds over the open Gulf (off the shelf) have more uniform vector mean speeds, around $2 \text{ m}\cdot\text{s}^{-1}$, but also increase westward. Winds are relatively weaker near the northern coast, probably due to the larger friction over land.

Fluctuations relative to the mean are much larger than the mean speeds—by some 2-3 times over the eastern area, where ratios between minor and major axes are close to unity. Over the western area, the fluctuations show a preferred north-south orientation, again possibly due to the effects of encountering the land mass.

The mean wind stress field is shown in Figure 2.1.2-2. The spatial pattern is, of course, quite similar to the mean wind field pattern. Directions generally are toward the west or northwest, with magnitudes from 0.01 to 0.04 Pa. The area of notable exception is east of 92°W over the shelf, where mean wind stress is directed to the west-southwest.

Figure 2.1.2-3 shows the mean wind stress curl field. The mean curl is negative (anticyclonic) over the region with largest values located between 93° and 95°W ; the maximum occurs near the shelf edge where absolute values reach $1 \times 10^{-4} \text{ Pa}\cdot\text{km}^{-1}$. Minimum absolute values of $0.2 \times 10^{-4} \text{ Pa}\cdot\text{km}^{-1}$ are found in the extreme southwestern corner of the area. Gradients are largest over the central Texas shelf.

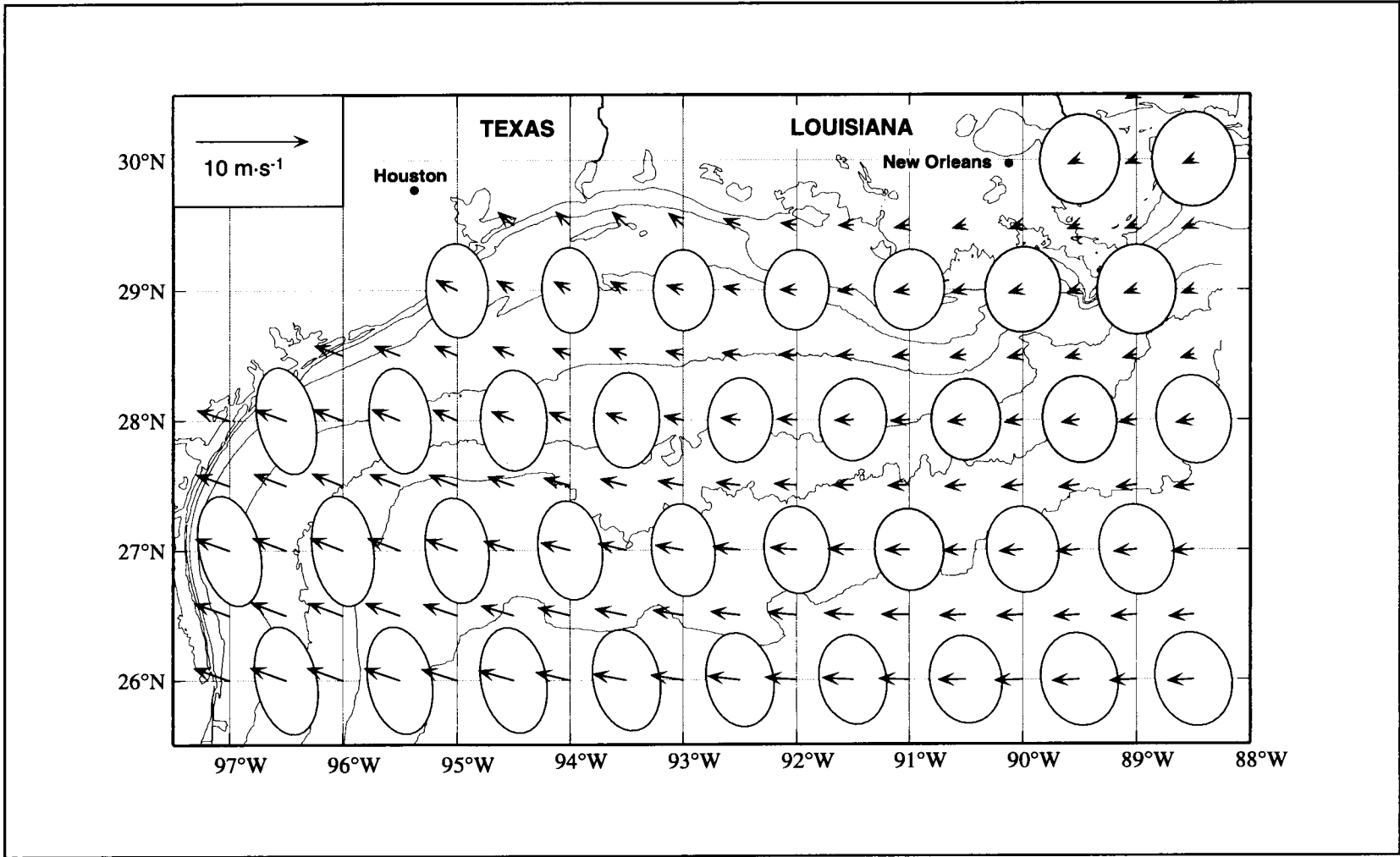


Figure 2.1.2-1. Vector mean winds and variance ellipses constructed from LATEX winds for the period April 1992 through November 1994.

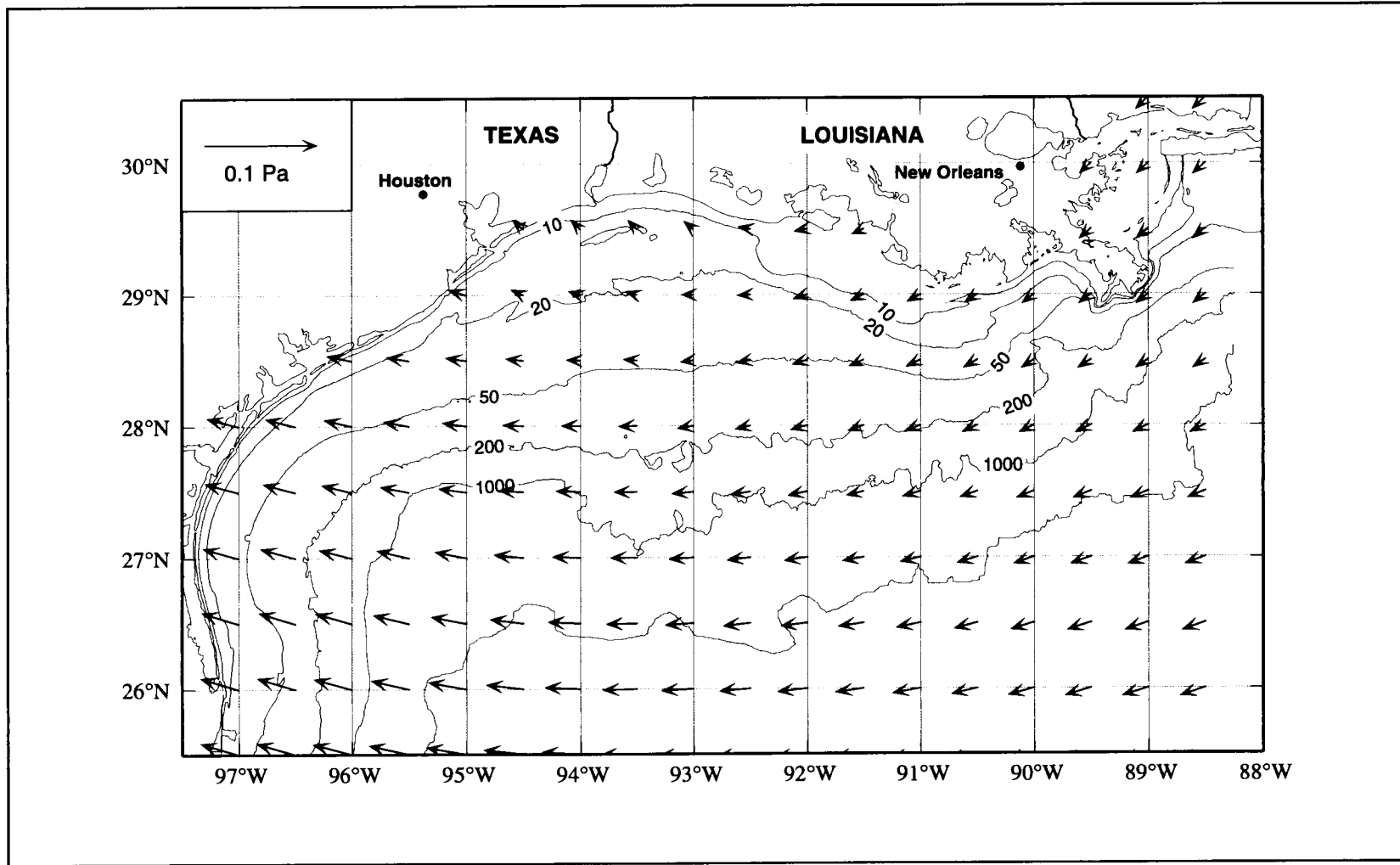


Figure 2.1.2-2. Vector mean wind stress field constructed from LATEX winds for the period April 1992 through November 1994.

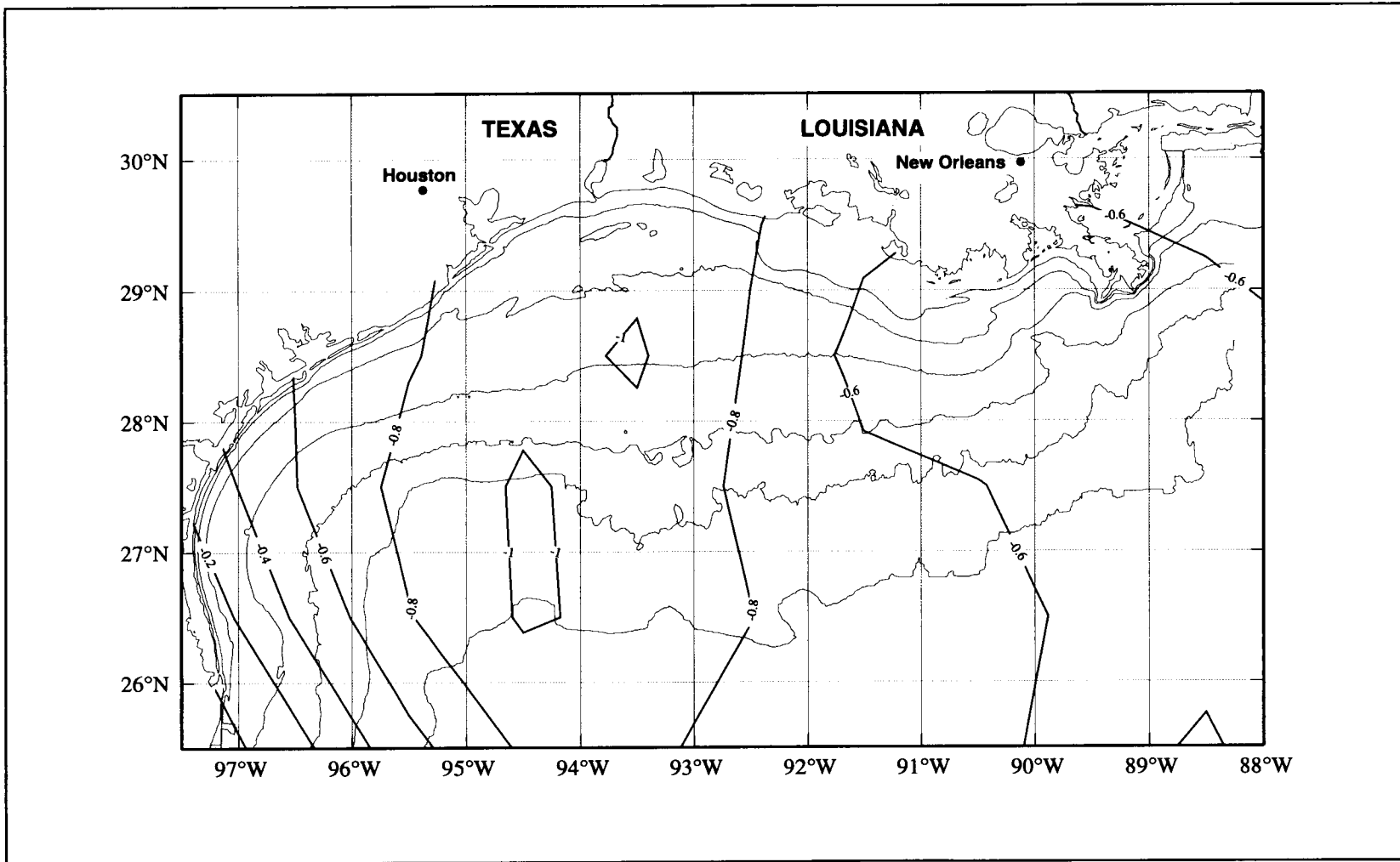


Figure 2.1.2-3. Mean field of wind stress curl constructed from LATEX winds for the period April 1992 through November 1994. Contour units are $10^4 \text{ Pa}\cdot\text{km}^{-1}$.

Seasonal fields of wind and wind stress

Wind fields. Spring is taken as March, April, and May; other seasons are set accordingly. Seasonal vector averages with variance ellipses for the LATEX winds are shown in Figure 2.1.2-4. In spring, wind speeds range from 1 to 4 m·s⁻¹, with strongest winds in the west and weakest in the northeastern corner. East of 92°W, winds are directed to the west; west of 92°W they gradually shift toward the northwest. The variance ellipses indicate that northwest-southeast fluctuations dominate in this season. All fluctuations are larger than means, especially in the east where winds are weak. The large fluctuations are due to frequent frontal passages during this season. As seen in Section 2.1.3, 35 fronts passed over this shelf during the three spring seasons included in the study period.

The summer (June, July, and August) wind field is characterized by the largest northward wind component over the western region, and the smallest fluctuations over the entire study region. Winds are directed northwest except in the northeastern corner where they are directed northward. Speeds range from 1 m·s⁻¹ in the northeast to 6 m·s⁻¹ in the west. East of 92°W the major axes of variance ellipses are comparable to the mean wind speeds, but west of 92°W the mean wind speeds far exceed the major axes. Variances show no strongly preferred direction. The small fluctuations are attributed to the fact that frontal passages occur infrequently in summer. Only six fronts occurred during these summer seasons (see Section 2.1.3).

In contrast to summer and spring, when winds over the eastern shelf are significantly weaker than those to the west, wind speeds in fall (September, October, and November) are nearly uniform over the entire region, with values near 3 m·s⁻¹. The mean wind vectors are to the southwest over the eastern shelf and to the west over the western shelf. The magnitudes of fluctuations are generally the same as those during spring. In fall seasons, 41 fronts passed through this region during the observing period (Section 2.1.3). It is seen from the principal axes of the variance ellipses that the winds shifted frequently from northward to southward.

The mean winter winds are out of the east or northeast; they are stronger over the eastern shelf, with mean vector speeds near 4 m·s⁻¹. The fluctuations in winter are greater than for other seasons. In the west, the mean vector speeds are smaller than for summer, but instantaneous winds in winter and summer are comparable in magnitude. As an example, Figure 2.1.2-5 displays the time series of daily gridded wind at 28.5°N, 95.5°W (see Figure 2.1.1-1). Winds in winter (December, January, February; Figure 2.1.2-4) are seen to be generally much more variable in direction than winds in summer; this is also seen by examining large variance ellipses in winter. Consequently, the vector-averaged winds have much smaller magnitudes than do averaged speeds for that season.

Comparing the four seasons, the summer pattern is distinguished from the other seasons by the fact that summer winds have an upcoast (Brownsville to the Mississippi Delta) component and fluctuations are small. Winds in spring, fall, and winter have downcoast components and greater variability. Monthly mean fields (Wang et al. 1996) also show that the annual

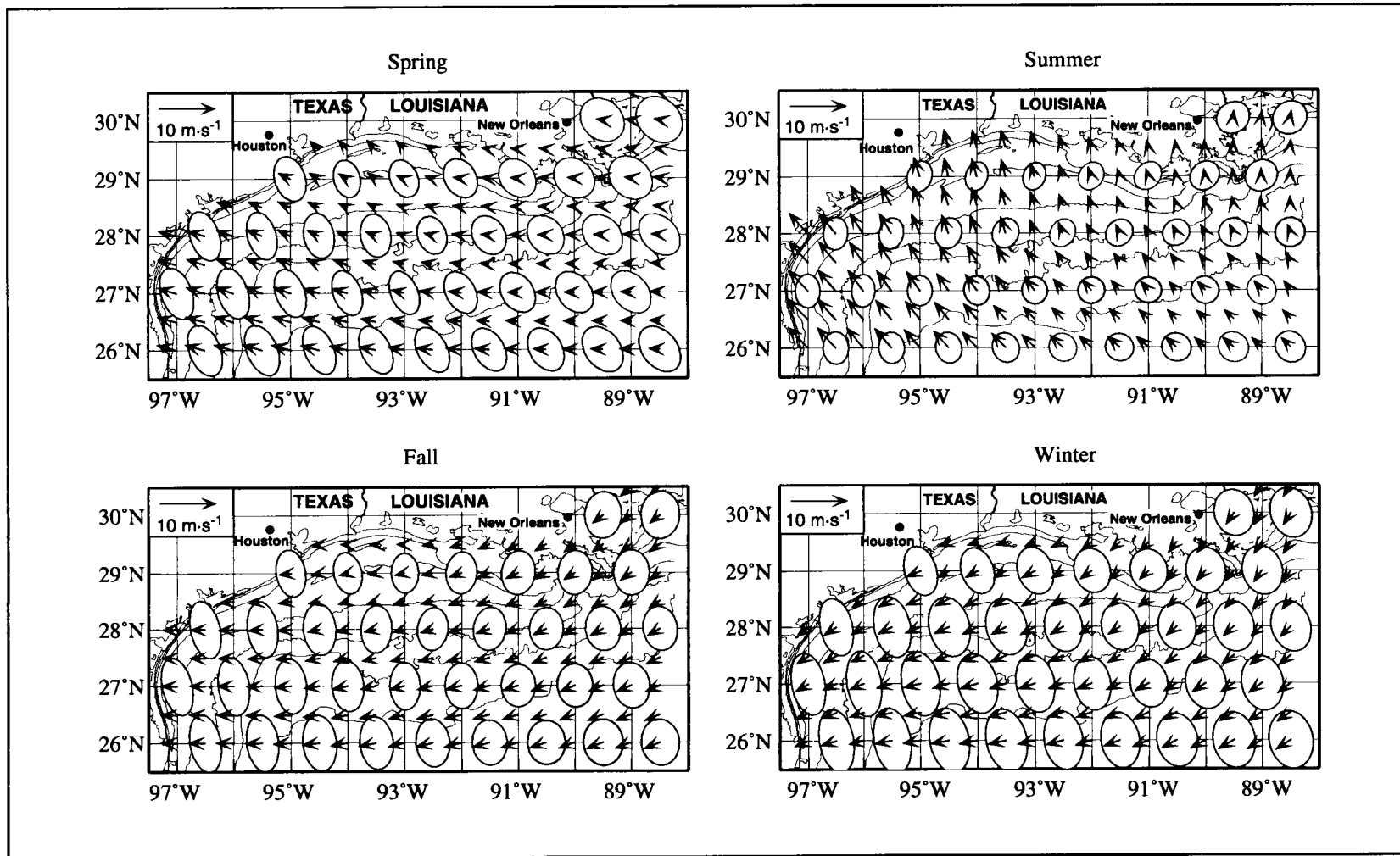


Figure 2.1.2-4. Seasonal vector mean wind and variance fields constructed from LATEX wind fields for period April 1992 through November 1994.

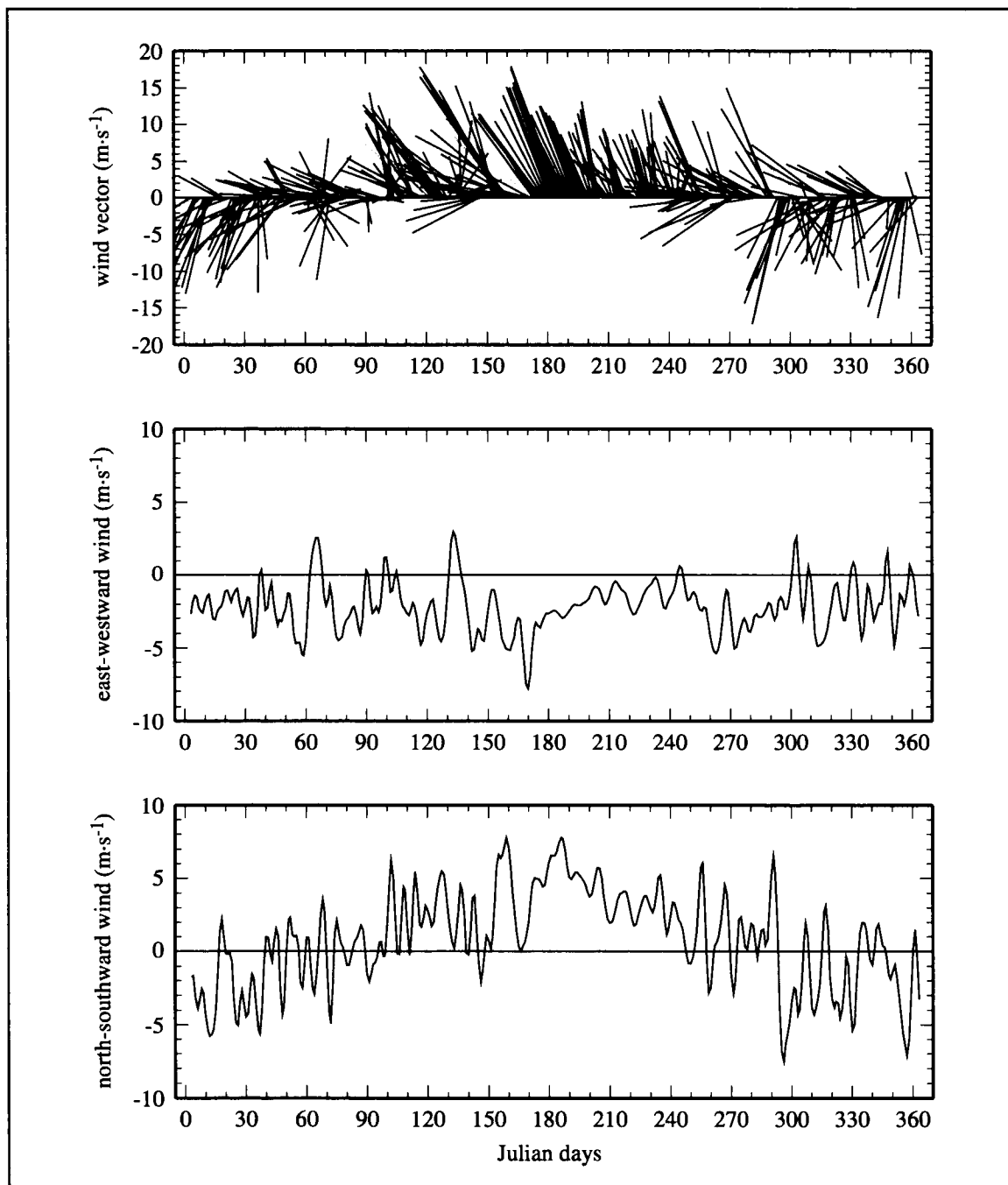


Figure 2.1.2-5. Daily wind vectors (north oriented up), zonal wind component (positive east), and meridional wind component (positive north) from daily gridded winds at 28.5°N, 95.5°W, based on LATEX winds.

cycle can be divided into two “seasons”. One is the summer from June or July through August. The other is the nonsummer period from September through May or June. Near the Mexican border (26°N), the winds begin to change from the nonsummer to the summer pattern, as evidenced by upcoast components, in April. This shift moves northward and eastward along the coast as a function of time. The upcoast wind component increases until July and then decreases. Toward the end of August or early September the winds shift back to a downcoast component. This is shown and discussed further in Sections 4.2, 4.4, and 4.6.

Wind stress and wind stress curl fields. Fields of wind stress and wind stress curl also were produced. Hourly wind stress was estimated by applying bulk aerodynamic formula to hourly gridded 10-m winds with Hsu’s (1994) drag coefficient estimated for the outer Texas-Louisiana shelf. Hourly values of wind stress curl were calculated using centered differences of hourly wind stress at grid points (consistent with Stokes theorem for a quadrangle domain). Finally, hourly values, for the period April 1992 to November 1994, of wind stress and wind stress curl were averaged at each grid point to form 32-month, seasonal means, and monthly means.

Seasonal wind stresses without variance ellipses are shown in Figure 2.1.2-6. The magnitudes of stresses in spring are small, between 0.01 and 0.03 Pa, with directions generally toward the west. In summer, wind stresses are directed northward or northwestward. Maximum values near 0.06 Pa are found over the western shelf. The magnitudes of fall wind stresses are spatially rather uniform (about 0.03 Pa), with directions toward the west or southwest. Winter wind stresses are somewhat larger than in fall, directed southwest, with maximum values near 0.05 Pa in the southern part of the region. The magnitudes of mean stresses in winter are smaller than in summer, however.

Figure 2.1.2-7 shows seasonal wind stress curl fields. In spring, an anticyclonic pattern with low values of $-1 \times 10^{-4} \text{ Pa}\cdot\text{km}^{-1}$ is centered near 26°N, 94°W. Values decrease to about -0.2 to $-0.4 \times 10^{-4} \text{ Pa}\cdot\text{km}^{-1}$ near the south Texas coast. By summer, the low center has shifted north and is located over the shelf edge; values in this center have intensified to $-1.4 \times 10^{-4} \text{ Pa}\cdot\text{km}^{-1}$. In the southwestern and northeastern corners, the curl magnitudes are only about 0.2 to $0.4 \times 10^{-4} \text{ Pa}\cdot\text{km}^{-1}$. Fall wind stress curl has a center located somewhat southwest of the summer position, and central values (about $-1.2 \times 10^{-4} \text{ Pa}\cdot\text{km}^{-1}$) and gradients are weaker than for summer. In winter, the center is diffuse, with the lowest values near $-1.0 \times 10^{-4} \text{ Pa}\cdot\text{km}^{-1}$ located near the coast off the Texas-Louisiana border. East of 92°W, the curl magnitude increases to the east, reaching values of $-0.8 \times 10^{-4} \text{ Pa}\cdot\text{km}^{-1}$ in the southeastern corner of the study region.

Statistics of weather events occurring over the Texas-Louisiana shelf, as well as a summary during the LATEX A field period, are presented in Section 2.1.3. A brief summary of other surface meteorological and SST patterns is included in Section 2.2. Considerable additional information on surface winds and other meteorological variables is presented in Wang et al. (1998a).

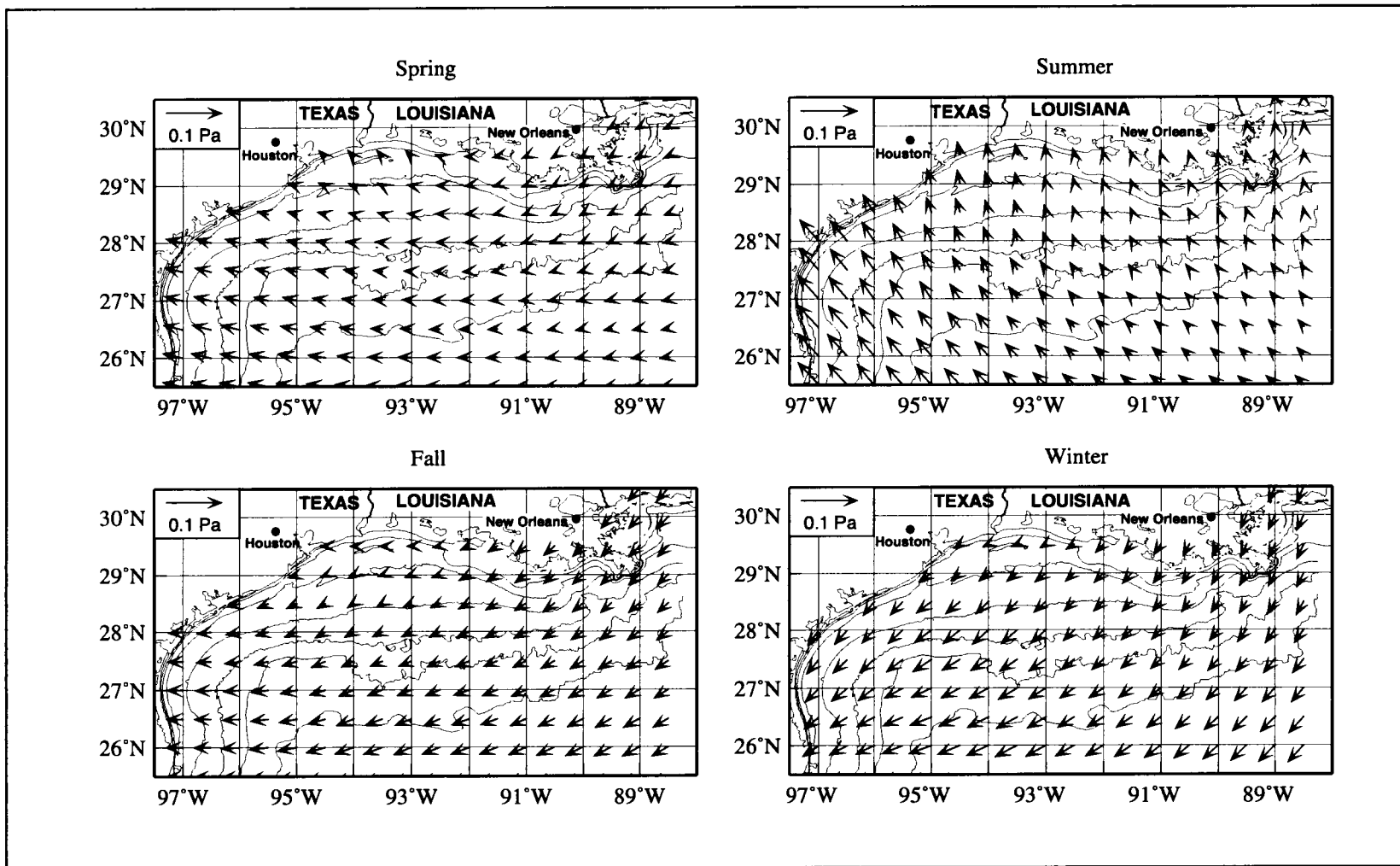


Figure 2.1.2-6. Seasonal mean wind stress fields constructed from LATEX winds during April 1992 through November 1994.

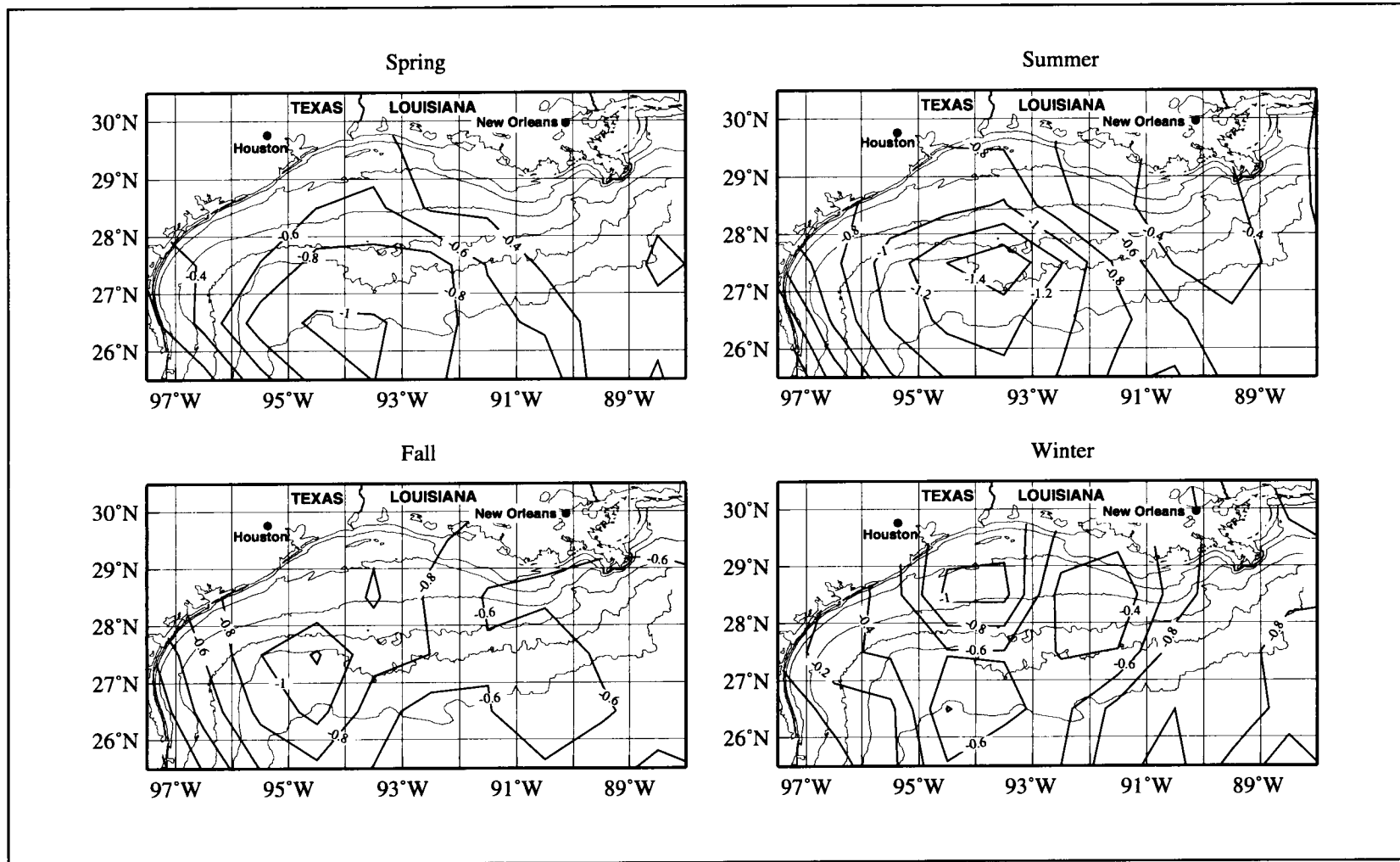


Figure 2.1.2-7. Seasonal mean wind stress curl fields constructed from LATEX winds during April 1992 through November 1994. Contour units are $10^{-4} \text{ Pa} \cdot \text{km}^{-1}$.

2.1.3 Weather events over the Texas-Louisiana shelf

Cold fronts passing over the Texas-Louisiana shelf during the LATEX field program were tracked using the *Daily Weather Maps* of the Climate Analysis Center of NOAA. These weather maps reflect conditions at 7:00 am EST each day. The maps for 30 March 1992 through 11 December 1994 were reviewed. The appearance of cold front symbols over all or part of the shelf and their progress through the LATEX region were counted as frontal passages. Table 2.1.3-1 shows the number of frontal passages by month and includes the average number for periods in the 1960s and 1970s as given by DiMego et al. (1976) and Henry (1979).

The surface weather charts used by DiMego et al. (1976) and Henry (1979) covered six-hour intervals, rather than a daily interval as in the maps used in this analysis. DiMego et al. (1976) used NOAA's six-hourly Northern Hemisphere Surface Charts for 1965-1972 and Henry (1979) used NOAA's six-hourly Northern Hemisphere Surface Charts for 1967-1977 and the NMC Tropical Section from 1973-1977. DiMego et al. (1976) followed the passage of all fronts (warm, cold, stationary, and occluded) through $2\ 1/2^\circ$ latitude-longitude squares. Henry (1979) considered a frontal passage to have occurred if a cold front moved from land onto the Gulf and remained in the Gulf at least 6 hours. LATEX considered only cold fronts that moved through the LATEX region. Differences in data sources and in criteria used to identify fronts likely account for the differences in summer frontal conditions between the three analyses. Because the study by DiMego et al. (1976) included fronts other than cold fronts, it has a higher number of fronts in the summer than either this or the Henry (1979) analysis.

The average number of passages was used to determine the typical number of days between fronts. These are given in Table 2.1.3-2. In summer, June through August, fronts rarely passed over the LATEX shelf; the average three-month interval was 57 days. In nonsummer, September through May, a front passed over the LATEX shelf every 6.4 days on average, comparable to the 5-day interval computed from DiMego et al. (1976) and the 7-day interval from Henry (1979).

Table 2.1.3-3 lists the dates of winter cyclogenesis events. These events were identified by the indications of pressure lows on the *Daily Weather Maps*. The other major weather event was Hurricane Andrew (see Appendix B.1).

Table 2.1.3-1. Number of frontal passages over the Texas-Louisiana shelf during each field year and resulting averages of frontal passages; "—" means not a LATEX field period.

Month	1992	1993	1994	Total	Average	DiMego ¹	Henry ²
Jan	—	6	7	13	6.5	8.5	5.5
Feb	—	5	5	10	5.0	9.0	5.7
Mar	—	6	7	13	6.5	7.5	6.2
Apr	4	5	5	14	4.7	6.5	4.5
May	3	3	2	8	2.7	4.5	3.0
Jun	2	1	0	3	1.0	2.0	2.0
Jul	0	0	1	1	0.3	2.0	0.8
Aug	2	0	0	2	0.7	2.0	0.9
Sep	3	4	5	12	4.0	3.0	2.4
Oct	3	5	6	14	4.7	6.0	3.7
Nov	6	4	5	15	5.0	7.0	5.2
Dec	7	7	—	14	7.0	9.0	6.6

¹ DiMego et al. (1976) considered the years 1965-1972; values interpreted from their Figure 1.

² Henry (1979) considered the years 1967-1977; values given are from his Table 1.

Table 2.1.3-2. Average interval between fronts (days), where "n" means no meaningful interval.

Month	LATEX	DiMego	Henry
January	4.8	3.6	5.6
February	5.6	3.1	4.9
March	4.8	4.1	5.0
April	6.4	4.6	6.7
May	11.6	6.9	10.3
June	30.0	15.0	15.0
July	n	15.5	n
August	n	15.5	n
September	7.5	10.0	12.5
October	6.6	5.2	8.4
November	6.0	4.3	5.8
December	4.4	3.4	4.7

Table 2.1.3-3. Winter cyclogenesis events over the northwestern Gulf of Mexico from November 1992 through December 1994.

Year	Month	Day ¹	Intensity ²
1992	November	4	2
	November	24	3
	December	9	2
	December	15	3
1993	February	22	2
	March	12	4
	April	8	3
	May	12	1
	November	9	1
	December	13	3
	December	19	1
1994	December	22	2
	January	11	1
	February	5	1
	February	10	2
	March	1	2
	March	27	4
	April	19	1
	April	22	2
	May	2	1
	May	14	2
	June	2	2
	June	21	1
	September	9	0
	September	14	0
	September	15	2
	September	22	2
	October	1	3
	October	8	2
	October	29	2
	November	29	1
December	3	2	
December	28	2	
December	31	2	

¹ The beginning date listed marked the first appearance over the northwestern Gulf of either the letter "L" or the word "Low" or a closed isobar on the 0700 EST NOAA Daily Weather Map.

² Intensity classification based on Hsu (1993). Data source is *Daily Weather Maps*.

2.2 Other surface fields

The same statistical interpolation methodology used to produce the LATEX wind fields described in Section 2.1.2 was used for producing hourly gridded fields of sea level atmospheric pressure, surface air temperature, and SST during the period April 1992 through November 1994 (Wang et al. 1998a). Hourly values were produced on a 0.5° latitude by 0.5° longitude grid. These hourly values were averaged at each grid point to form 32-month means, seasonal means, and monthly means. Contoured fields of these averaged values are shown in the LATEX A meteorological data report (Wang et al. 1996). The seasonal patterns are presented here and in Wang et al. (1998a).

Sea level atmospheric pressure

The annual cycle of seasonal mean pressure fields is shown in Figure 2.2-1. In spring, the isobars are almost normal to the coast; in summer, they are oriented generally north-south, associated with the large north (and upcoast) components of surface winds; in fall and winter, the isobars are directed northwest-southeast. (See Figure 2.1.2-4 for seasonal wind fields.) Pressures increase toward the west or southwest for all seasons. Naturally, values decrease from winter to spring and summer. The spring and summer pressure gradients are more intense in the west than in the east, corresponding with stronger winds in the west than in the east for these two seasons. The fall and winter pressure gradients are more nearly uniform over the field. However, it is noted that gradients in winter are somewhat stronger than in fall, which results in larger wind speeds in winter than in fall.

Surface air temperature

Figure 2.2-2 shows mean surface air temperature fields for each season. Spring temperatures vary from 20.8°C near the northern coast to 22.4°C over the open Gulf. Isotherms are oriented east-west except near and south of the Mississippi Delta. In summer, air temperatures are almost uniform, with values near 28.2°C. In fall, the isotherm configurations conform to isobaths, with a range from 22.4 to 25.6°C. Over the western shelf, winter isotherms correspond well in configuration to isobaths, but over the eastern shelf, there are markedly colder temperatures nearshore than are found in the west. The winter pattern shows stronger gradients than in other seasons. The winter temperature range is as large as 7°C from near coast to the open sea, with maximum values located over the open Gulf between 93° and 94°W.

Sea surface temperature

SST fields (Figure 2.2-3) are quite similar to surface air temperature fields for all seasons. Spring SST is about 0.8°C higher than air temperature. In summer, SST is about 1°C higher than surface air temperature but shows more spatial variation. SST increases from west to east. This may reflect the fact that upcoast summer winds drive upcoast currents over the

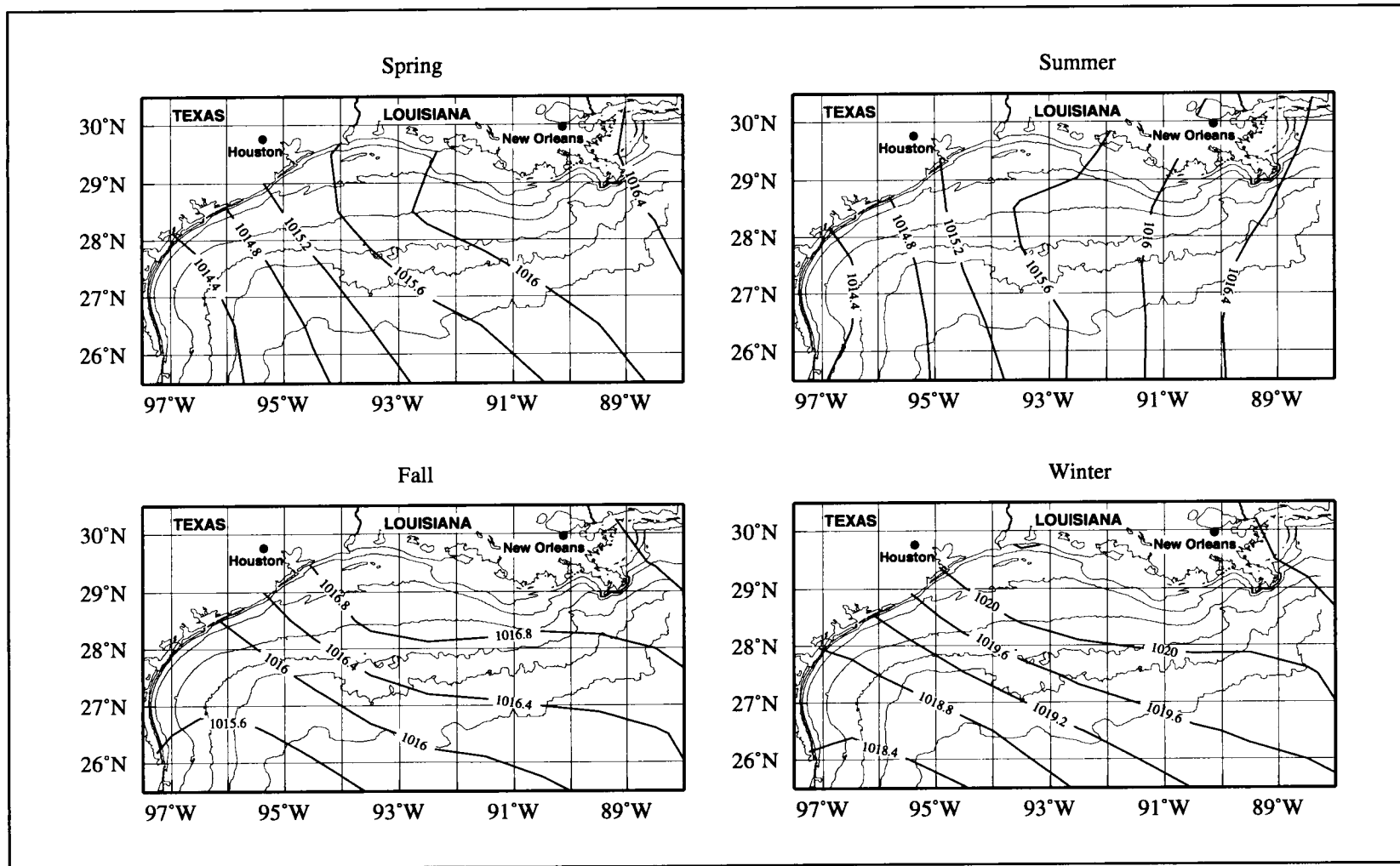


Figure 2.2-1. Mean seasonal sea level atmospheric pressure fields constructed from LATEX fields for April 1992 through November 1994. Units are hPa.

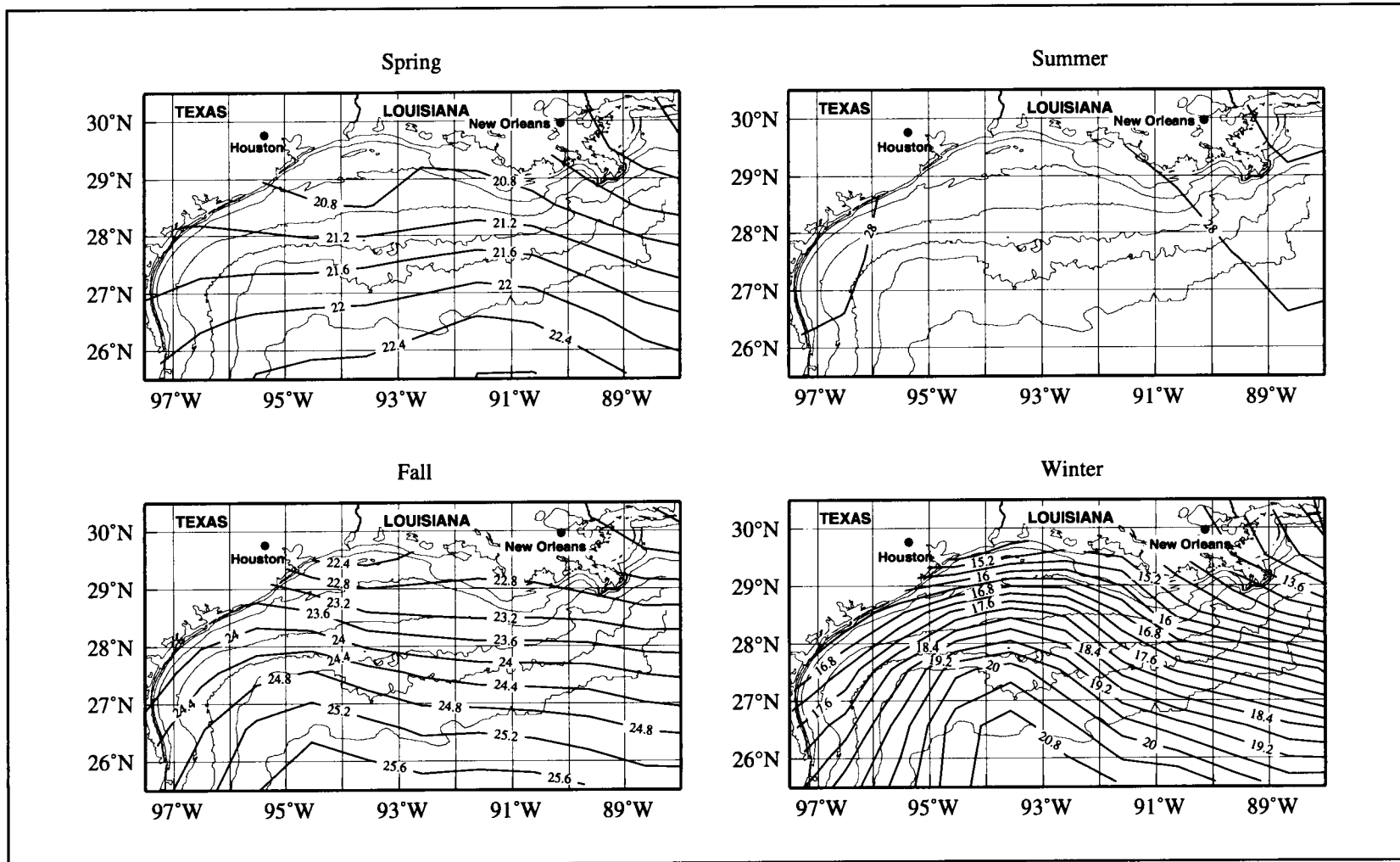


Figure 2.2-2. Mean seasonal surface air temperature fields constructed from LATEX fields for April 1992 through November 1994. Units are °C.

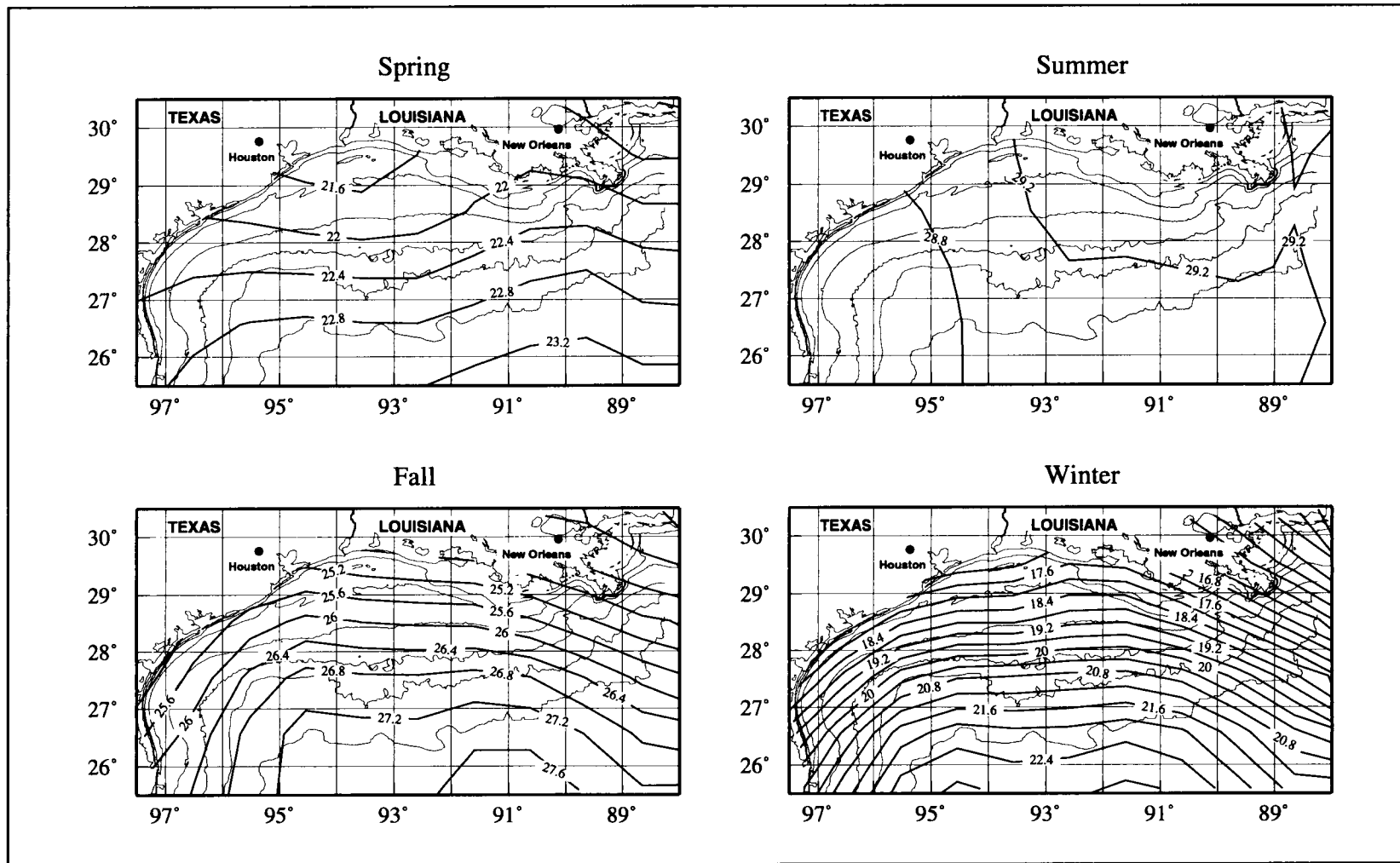


Figure 2.2-3. Mean seasonal SST fields constructed from LATEX fields for April 1992 through 1994. Units are °C.

inner shelf, causing coastal upwelling in that season (Cochrane and Kelly 1986). The upcoast currents carry the colder surface water produced by upwelling.

Fall temperature differences between sea and air are larger than for other seasons as expected; fall is the season of maximum cooling of the surface ocean, associated with outbreaks of cold air masses. Values of air-sea temperature differences exceed 3°C in the coastal region and 2°C over the open Gulf. Winter SST is higher than air temperature by about 2.5°C in the coastal region and 1.5°C over the open Gulf. The range of SST is 5°C , which is less than the range of air temperature. As for air temperatures, the winter SST field has the largest cross-shelf gradients among all seasons. We see that SST is always higher than air temperature, which has the smallest differences in spring (0.5°C) and largest in fall (3°C).

Summary

The seasonal surface meteorological patterns showed the lower atmosphere over the LATEX shelf region in summer to be different than in other seasons. In summer, the atmosphere is relatively stable; only six fronts passed through this region in summer during the observing period of April 1992 to November 1994. Summer winds (Figure 2.1.2-4) were directed northwestward with very strong northward components (about $6\text{ m}\cdot\text{s}^{-1}$) over the western area. Alongshore wind components were upcoast, driving upcoast currents over the inner shelf. Air temperatures were the highest (28.2°C) in the annual cycle and were spatially quite uniform. Air-sea temperature differences were small (only of 0.5°C).

In other seasons, the lower atmosphere was more variable due to more frequent frontal passages. In spring, winds were directed to the northwest or west; in fall and winter, winds were directed to the southwest or west. The fluctuations for other seasons, especially in winter, were larger than for summer. Surface air temperature as well as SST in these three seasons showed that isotherms basically followed isobaths, with values increasing toward the open Gulf. Cross-shelf gradients for both air temperature and SST were the largest in winter. Fall air-sea temperature differences reached maximum values of about 4°C near the coast. SST was always larger than air temperature throughout the year.

2.3 River discharge

Freshwater discharge from rivers has major impact on the property distributions and circulation over the Texas-Louisiana continental shelf. Property distributions affected include, among others, salinity, suspended particle material and turbidity, nutrients, and various manmade chemical compounds. Such properties affect, in turn, the marine ecosystem over the shelf. The circulation is influenced by the buoyancy of the freshwater. Even air-sea fluxes may respond to changes in surface temperature or salinity associated with the river discharge. This section presents an overview of the discharge rates of the Mississippi and Atchafalaya rivers, which are the major providers of fresh water to the shelf, and of the rivers entering the Gulf from Louisiana and Texas west of the Atchafalaya. Time series of

daily discharge for the years 1992 through 1994 also are given. Some statistics of variability are considered.

Mississippi-Atchafalaya river discharge

Based on the 64-year mean, combined discharge rates of the Mississippi and Atchafalaya rivers have a rather smooth annual cycle, with a peak in April and a broad minimum during the months of September and October (Figure 2.3-1).

During the LATEX field period there was great year-to-year variability in the discharge of these rivers (Figure 2.3-1). 1992 was the year for which discharge most closely followed the long-term mean. Rates were appreciably lower than the norm during late spring and early summer; they were appreciably higher in August and for a period from November to the end of the year. Discharge rates remained high in January 1993. With the exception of a brief period in late February, river discharge remained above average for all of 1993—almost double the norm for about half of the year. In January 1994, discharge rates were near the norm. Then, in February they increased and remained very much above the norm until the end of May. For the remainder of 1994, Mississippi-Atchafalaya discharge remained near the long-term average, though there was a peak in mid-December above the norm.

In Figure 2.3-2 we show the time series of the ratio of the Atchafalaya River discharge to the combined discharge of the Mississippi and Atchafalaya rivers. Since the mid-1970s, the U.S. Army Corps of Engineers has held the long-term ratio constant at 30%. This is useful information because the scientific speculation is that about half of the Mississippi River discharge is advected to the east while the remainder, together with that of the Atchafalaya River, is advected to the west (Dinnel and Wiseman 1986; U.S. Army Corps of Engineers 1974).

In Figure 2.3-3 we show the long-term discharge rates based on daily means for the combined Mississippi-Atchafalaya rivers, with one rms deviation based on the 64-yr record. It is clear that the interannual variability is much larger for large discharge rates than for small. We may conclude that the variation in rainfall and snow melt is larger during high discharge.

Discharge of the lesser Texas and Louisiana rivers

Also shown in Figure 2.3-1 is the cycle of long-term average daily discharge from thirteen principal Texas rivers plus the Calcasieu River in Louisiana. Together these constitute the major discharge from Louisiana and Texas west of the Atchafalaya River; we refer to these as the “lesser rivers” in reference to freshwater discharge onto the shelf. It is clear that on average the discharge of fresh water to the Texas-Louisiana shelf is dominated by the Mississippi-Atchafalaya rivers, and that the influence of other rivers generally must be more limited geographically.

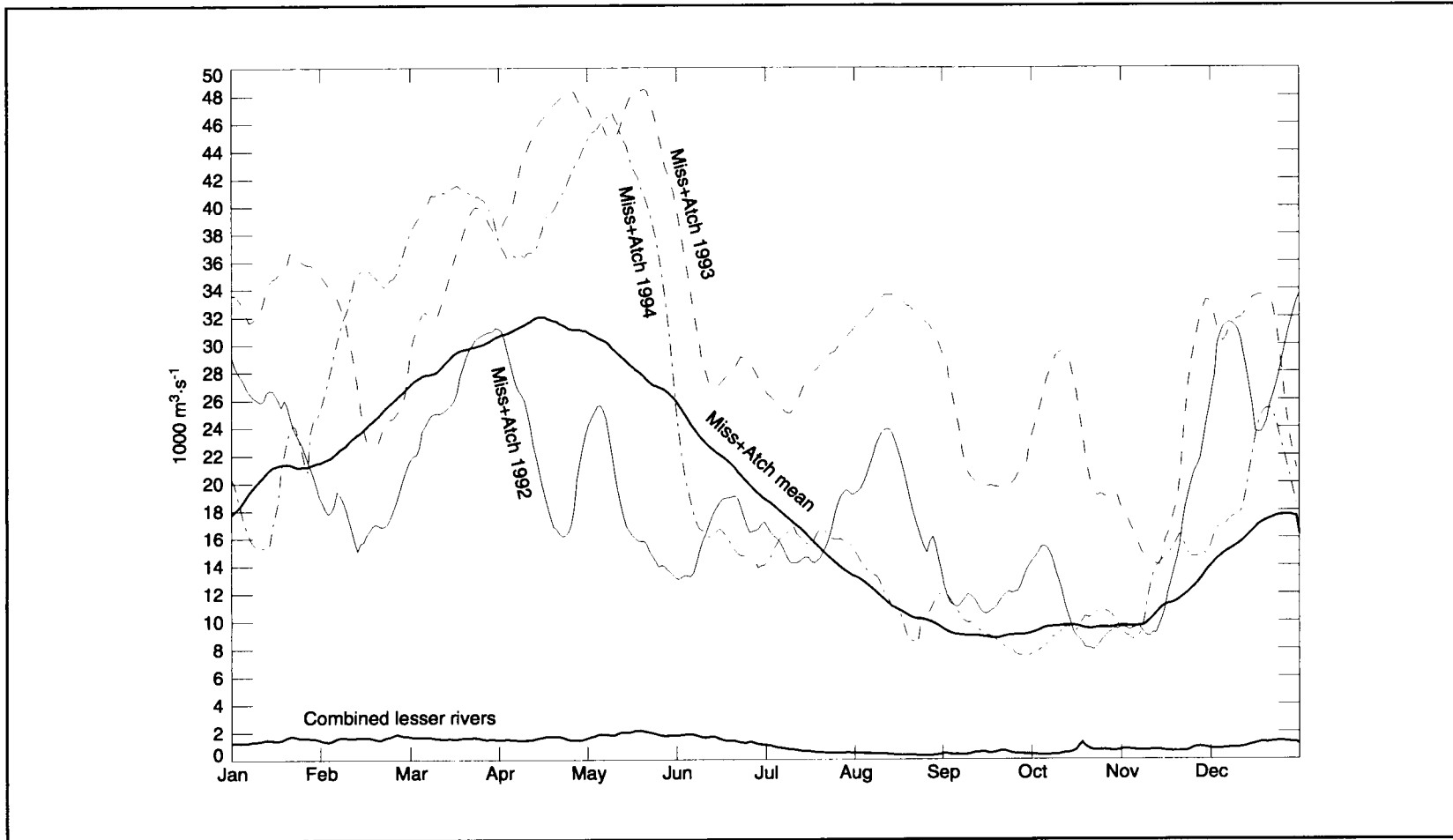


Figure 2.3-1. Annual cycle of discharge rates from daily averages for the combined Mississippi-Atchafalaya Rivers based on the 64-year average and for the years of 1992, 1993, and 1994. Also shown is the annual cycle of average discharge rate for the sum of twelve Texas rivers and the Calcasieu River in Louisiana based on 20 to 77 years of data for the individual rivers.

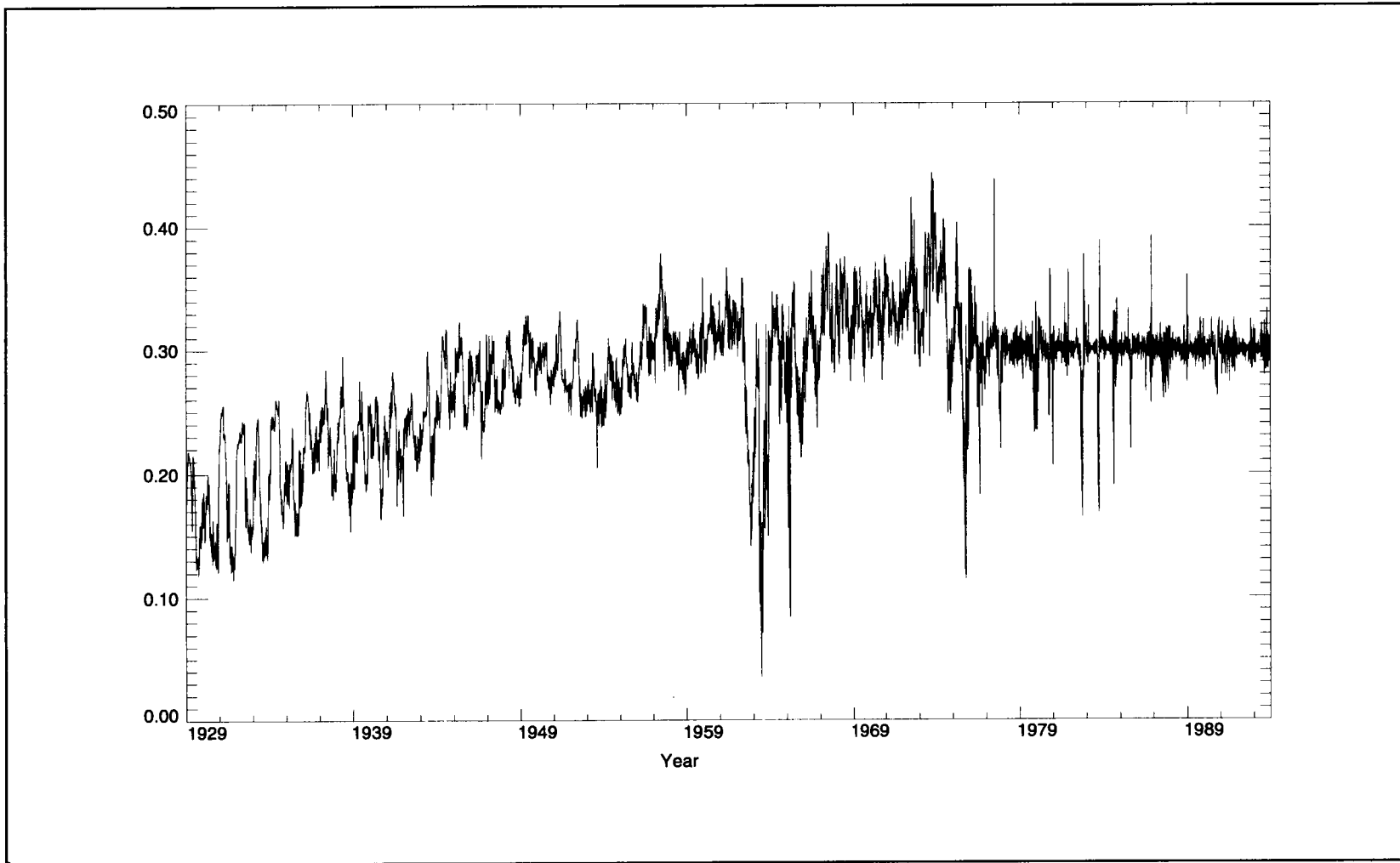


Figure 2.3-2. Long-term time series of the ratio of Atchafalaya River discharge to the combined Mississippi-Atchafalaya River discharge.

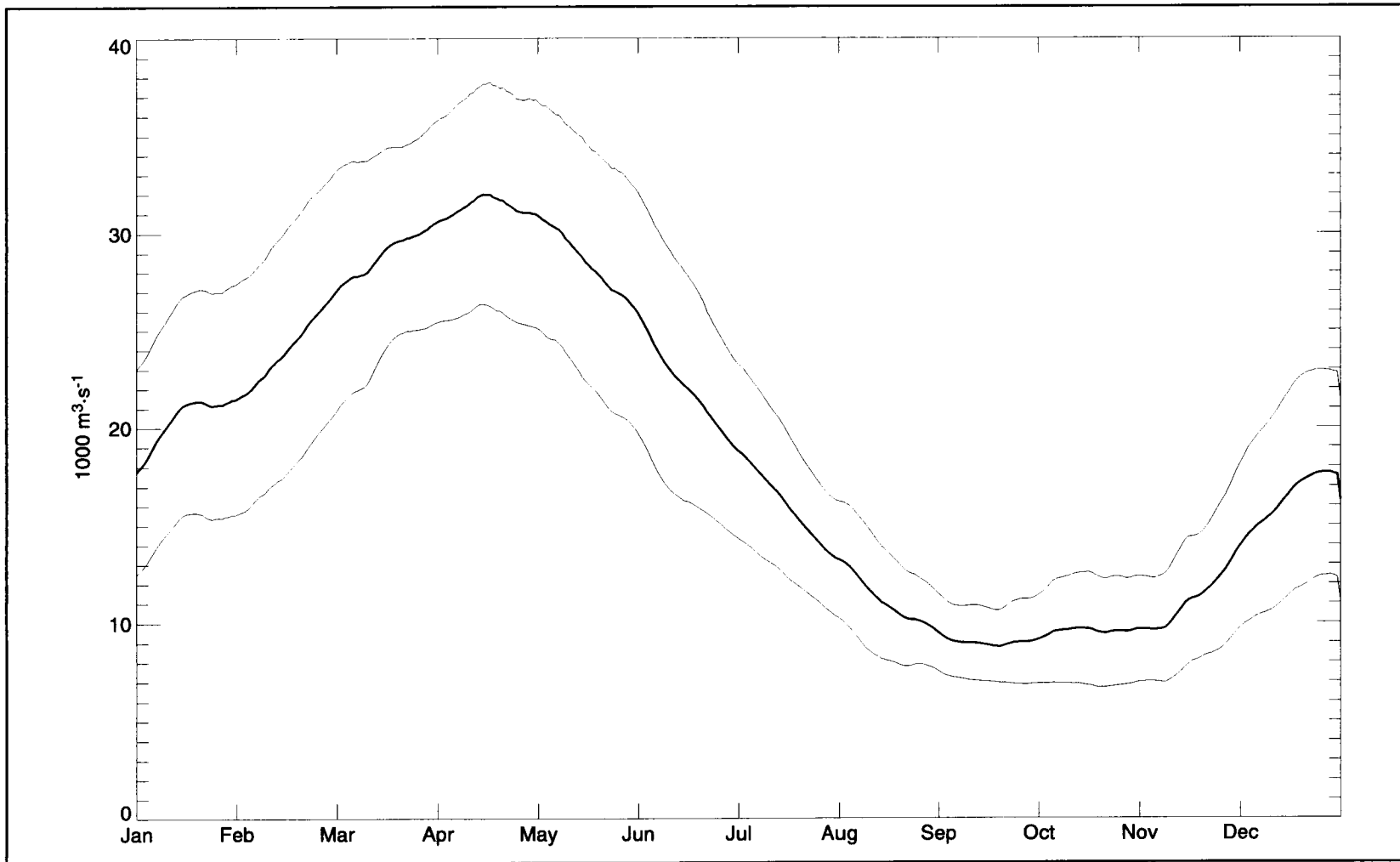


Figure 2.3-3. Annual cycle of discharge rates based on daily means for the combined Mississippi-Atchafalaya Rivers bounded by an envelope of one rms deviation based on a 64-year record.

Table 2.3-1. Annual average discharge rates for principal rivers west of the Atchafalaya that flow onto the Texas-Louisiana shelf. Mississippi and Atchafalaya discharges are included for comparison.

River	Discharge rates ($\text{m}^3 \text{s}^{-1}$)	Record length (yrs)
Mississippi	13,549	64
Atchafalaya	5,489	64
Sabine	238	71
Brazos	236	26
Trinity	218	71
Neches	178	79
Colorado	73	48
Guadalupe	53	61
Calcasieu	33	59
San Jacinto	28	12
San Antonio	20	63
San Bernard	15	41
Lavaca	10	58
Nueces	6	4
Mission	3	57
Aransas	1	32

The lesser rivers, the record lengths over which they have been gauged, and their record-length average annual discharge rates are listed in Table 2.3-1. On average, the Sabine, Brazos, and Trinity rivers alone contribute more than half of the annual discharge of the lesser rivers. The average annual discharge for the 14 lesser rivers is $1113 \text{ m}^3 \cdot \text{s}^{-1}$ —an order of magnitude less than the average annual discharge rate for the Mississippi River.

Time series of discharge rates for the sum of the lesser rivers is shown in Figure 2.3-4 for the years 1992 through 1994. The record-length daily average was computed for each river. These annual cycles were summed to form a long-term mean daily discharge for the lesser rivers, also shown for comparison.

The most striking feature during the LATEX period, and for the long-term mean as well, is the peak in lesser river discharge during October 1994. Referring to Figure 2.3-1, no corresponding peak in discharge occurred in the Mississippi-Atchafalaya discharge in October 1994.

The combined lesser river discharge was much above the norm during the first three months of 1992 and again in May-June. Discharge rates for 1993 peaked above the norm in March-April, May, and June-July. For all three years, discharge rates were above the norm in December. The year 1994, and to a lesser degree 1993, had lower than normal discharge rates during several periods in the first half of the year. 1992 and 1993 seemed drier than average in late summer and early fall. These patterns generally do not correspond with that for Mississippi-Atchafalaya discharge.

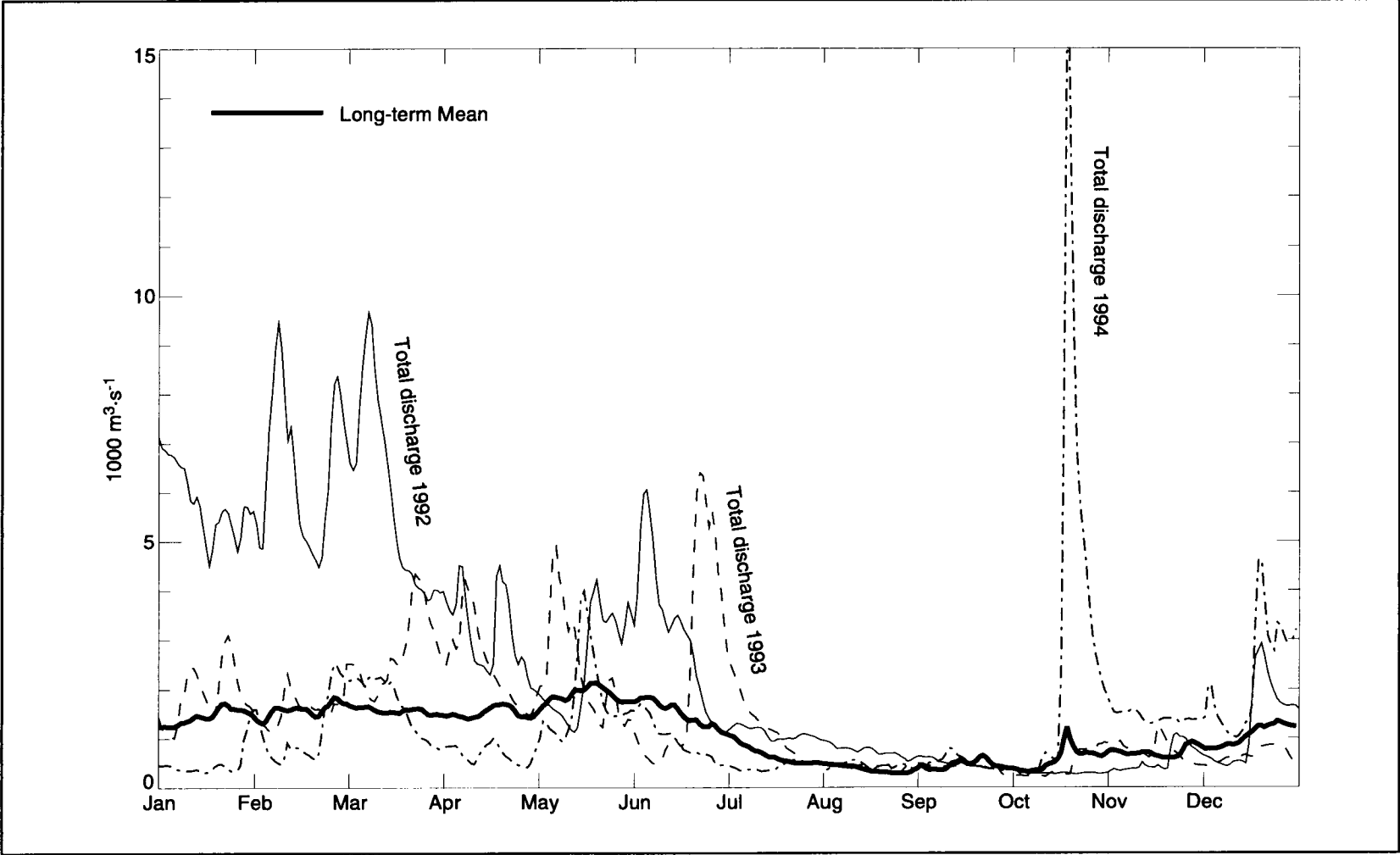


Figure 2.3-4. Time series of discharge rates from daily means for combined lesser rivers for years 1992-1994. The long-term mean discharge for the combined lesser rivers is shown for comparison.

To further illustrate the significance of the 1994 Texas flood, we offer Figure 2.3-5. Shown are the 1992-1994 daily discharge rates for the Mississippi-Atchafalaya rivers and the lesser rivers; also shown is a thrice-repeated cycle of their long-term means. It is remarkable that the October 1994 discharge for the lesser rivers was larger than that for the Mississippi-Atchafalaya—either in October 1994 or their long-term mean for October.

1994 daily time series of discharge rates for the five lesser rivers with highest flow rate are shown in Figure 2.3-6. The maximum October 1994 discharge rate for the San Jacinto River is just over $4000 \text{ m}^3\cdot\text{s}^{-1}$. The San Jacinto record used is from gauged locations upstream from Lake Houston, through which the river flows before entering into Galveston Bay; we used that record because it is relatively long (12 years). Flow leaving Lake Houston is not routinely measured. Ad hoc measurements are sometimes made during significant flow events. On 19 October 1994, the rate of the San Jacinto River outflow from Lake Houston peaked at $10,194 \text{ m}^3\cdot\text{s}^{-1}$ (USGS Station Manuscript for 08072050, San Jacinto River near Sheldon, Texas). This remarkable value exceeds the average combined Mississippi-Atchafalaya river discharge rates during fall!

Appendix C presents a brief description of the effects of the Texas flood of October 1994 on salinity over the shelf.

We show in Figure 2.3-7 the annual cycle of combined mean discharge rate for 13 Texas rivers plus the Calcasieu River bounded by an envelope of one rms deviation. Curves are based on record lengths of daily discharge rates for each river. Again the expected positive correlation between interannual variability and high discharge rates is seen.

Data sources

Texas rivers discharge data from 1904-9/30/1993:

CD-ROM “USGS Daily Values West2 1994”

EarthInfo, Inc.

5541 Central Avenue

Boulder, CO 80301

(303) 938-1788

Texas rivers discharge 10/01/1993-forward:

“US Geological Survey Water Data for Texas”

From the USGS web site

<http://txwww.cr.usgs.gov/cgi-bin/txnwis/>

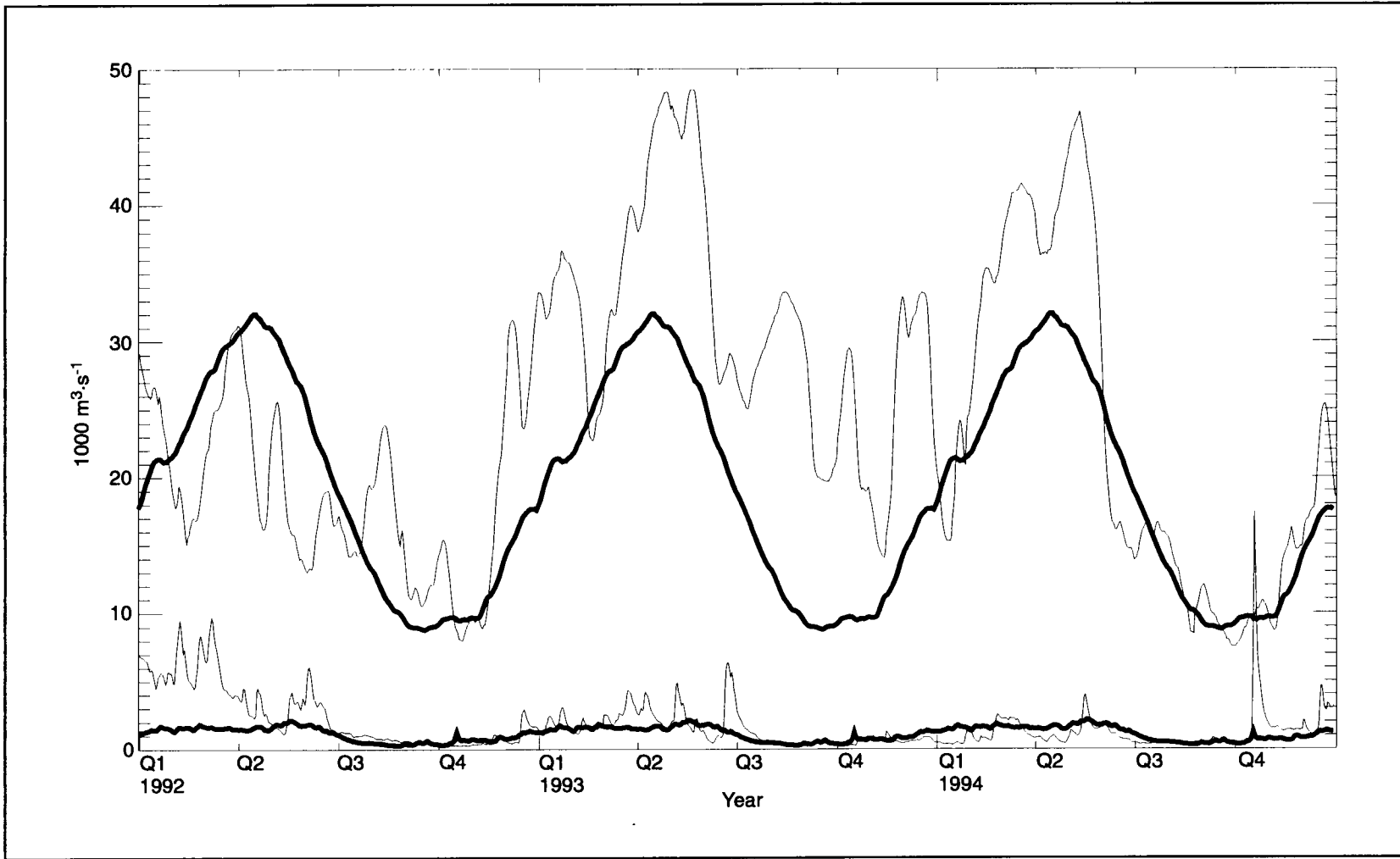


Figure 2.3-5. 1992-1994 discharge rates from daily means for the Mississippi-Atchafalaya Rivers and the lesser rivers. Also shown is a thrice-repeated cycle of their long-term means.

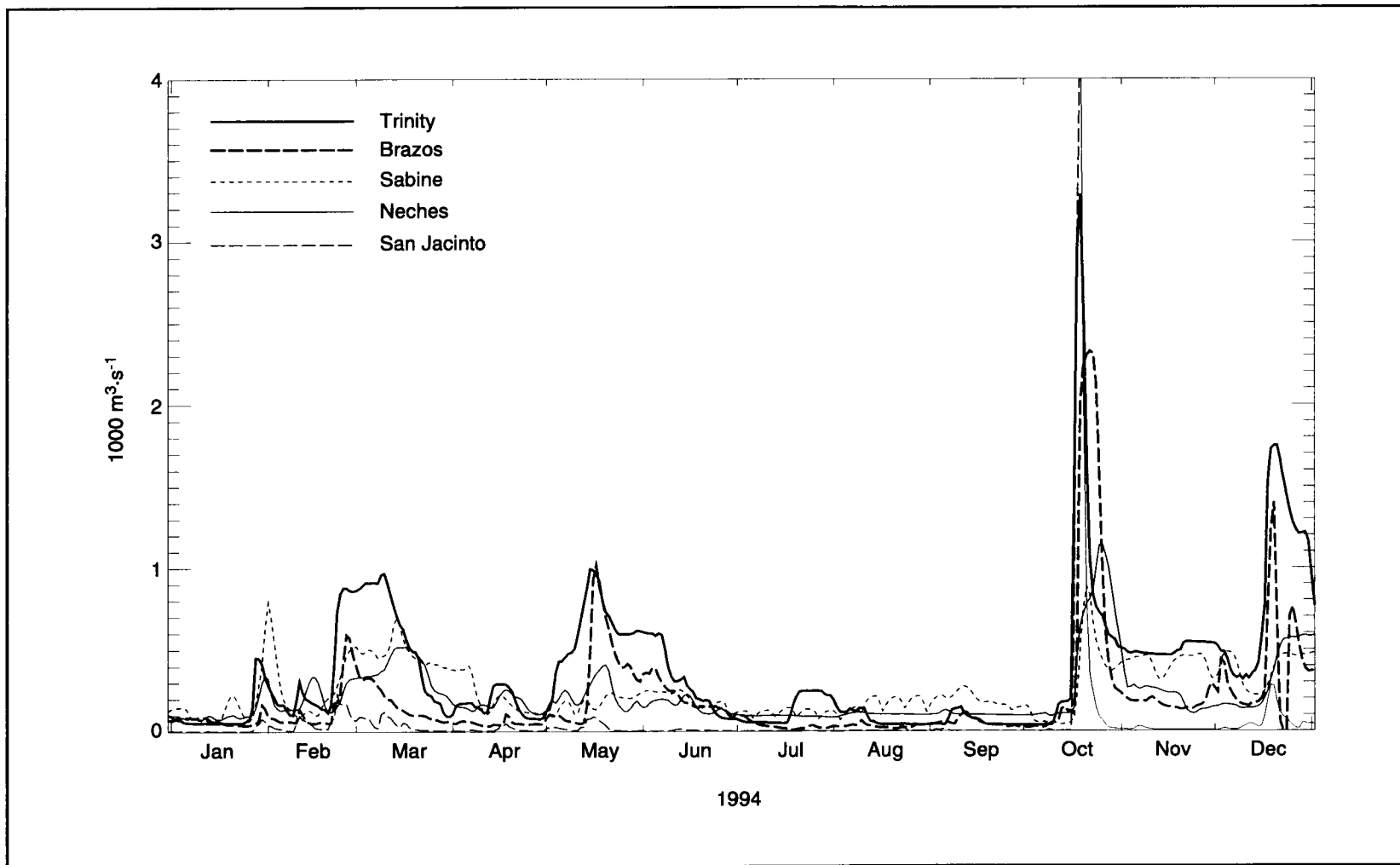


Figure 2.3-6. 1994 time series of discharge rates from daily averages for the Trinity, Brazos, Sabine, Neches, and San Jacinto rivers.

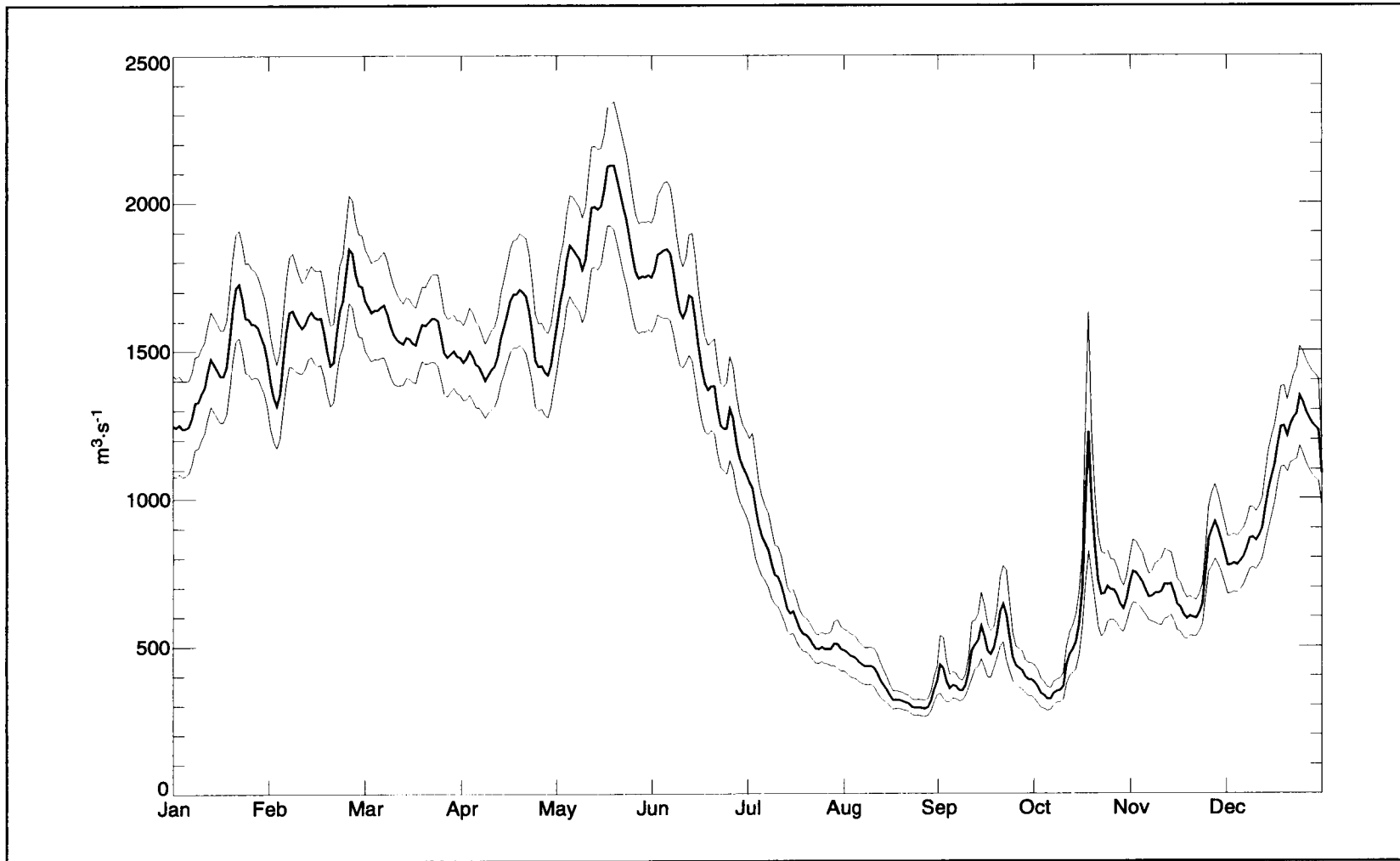


Figure 2.3-7. Annual cycle of combined mean discharge for 13 Texas rivers plus the Calcasieu River bounded by an envelope of one rms deviation based on record lengths of daily discharge rates for each river.

Mississippi and Atchafalaya (all years):

Cecil W. Soileau, P.E.
 Chief, Hydraulics and Hydrologic Branch
 Coastal Engineering Section
 Department of the Army, Corps of Engineers
 New Orleans District
 P.O. Box 60267
 New Orleans, LA 70160-0267

2.4 Bottom stress characterization

Bottom stress is important in the dynamics of the nearshore circulation (Winant and Beardsley 1979; Lentz and Winant 1986; and Lentz 1994). It is also important in sediment suspension and transport (Adams et al. 1982). Like wind stress acting on the sea surface, the shear stress acting on the sea bed is dependent on the flow regime in the boundary layer above. In this section we discuss: (a) the expected thickness of the surface and bottom boundary layers on the inner shelf; (b) the parameterization of the bottom stress as deduced from an analysis of measured near bottom currents; and (c) an evaluation of the bottom stress parameters deduced from optimal tuning of the wind-driven shelf model discussed in Appendix L to the current meter data on the inner Texas-Louisiana shelf.

Surface and bottom Ekman layers

The thickness of the neutral turbulent Ekman layer h_e above the sea bed can be estimated from the relation $h_e = 0.3 u_* / f$ where f is the local Coriolis parameter, u_* is the friction velocity defined by $(\tau_b / \rho)^{.5}$, where τ_b is the stress on the sea bed and ρ is the water density (Tennekes 1973). Jones and Kenney (1977) show that a similar relation applies in the upper turbulent boundary layer beneath the sea surface, but with the surface wind stress taking the place of the bottom stress. Winant and Beardsley (1979) take the thickness of the logarithmic sublayer, where the stress is nearly independent of elevation z , as about $0.1 h_e$. The important point of the above relations is that the boundary layer thicknesses (Ekman and logarithmic sublayer) are strongly dependent on the boundary stress for given latitude.

Typical monthly mean values of wind stress over the Texas-Louisiana shelf are 0.03 Pa (Figure 2.1.2-6). If we regard the monthly mean currents over the inner shelf (water depths of 50 m or less) as having comparable stress, then the upper and lower Ekman layers merge for this region. As seen in Figure 2.1.2-4, the variability of the wind is significantly larger than the monthly means. The associated rms variability of the wind stress is typically of order 0.06 Pa and the maximum 40-hr low-pass filtered alongshelf wind stress can reach 0.3 Pa, as shown in the time sequence Figure 2.4-1 at meteorological station PTAT2 near Port Aransas, Texas, for the 32-month LATEX measurement program. A wind stress of 0.3 Pa will give a logarithmic sublayer thickness of 7 m, that, if matched by an equal bottom stress, would produce merging top and bottom logarithmic layers in a water depth of 14 m. It is thus evident that stress-induced velocity shear can be very important on the inner Texas-

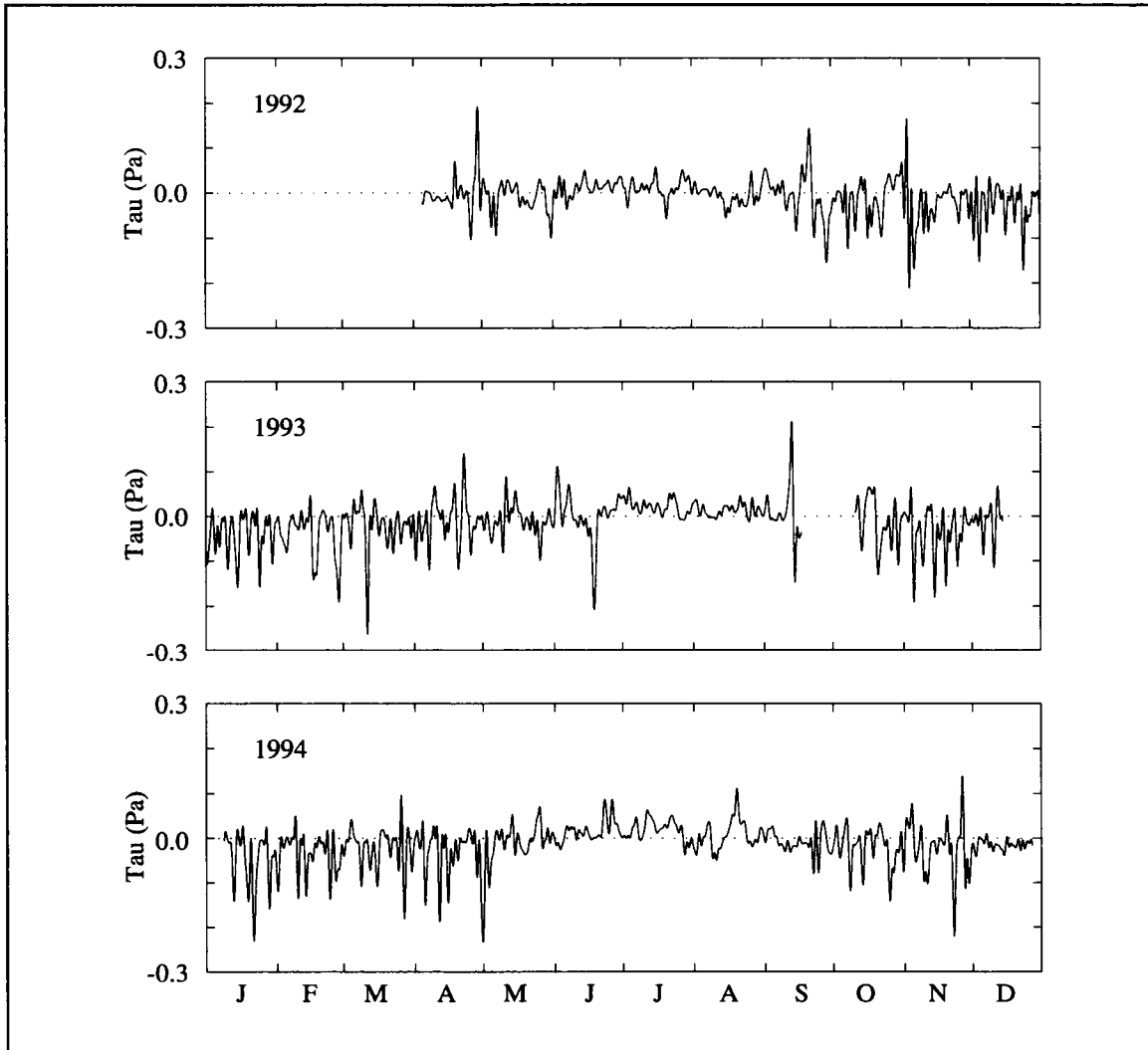


Figure 2.4-1. Hourly values of 40-hr low-passed alongshelf wind stress at meteorological station PTAT2 for the 32 months of LATEX measurements (positive is upcoast). These wind stress estimates approximate the bottom stress for mooring 23.

Louisiana shelf region, particularly in the nonsummer season. We recognize that density stratification effects within the water column can modify the above relations, but a quantitative analysis of such effects is beyond the scope of this report.

Parameterization of bottom stress

Many papers, of which Csanady (1982), Clarke and Brink (1985), and Mitchum and Clarke (1986) are examples, employ a linearized parameterization of bottom stress in studies of subinertial circulation. This is justifiable if there exists a significant background of higher frequency currents, such as tides, inertial motion, internal waves and even surface waves (Grant and Madsen 1979; Winant and Beardsley 1979; Grant et al. 1984). In their 1979 note, Winant and Beardsley addressed the question: Does a nonlinear parameterization of bottom stress give better results than a linear one? They based their analysis on data taken in water depths of 38 m or less and where they had near bottom currents (2.8 to 6.6 m above bottom) as well as simultaneous wind measurements. They assumed that the water was sufficiently shallow that the wind stress represented a reasonable estimate of the bottom stress. Correlations were determined for a quadratic representation of the stress in terms of current and a linear representation of the stress in terms of current. The results from 14 separate data sets indicated that there was essentially no significant difference in correlation for the two representations of a given data set. But there was a large variation in correlation coefficient r among the data sets (from order 0.3 to order 0.9), indicating that the assumption of equating bottom stress to wind stress probably was incorrect at least for those data sets with poor correlation.

A different approach was employed by Current (1996). In her analysis of the LATEX A data the assumption was made that the bottom stress τ_b for a turbulent boundary layer is basically a quadratic function of the near bottom velocity V_b in the form

$$\tau_b = \rho c_b |V_b| V_b, \quad (2.4-1)$$

where c_b is a sea bed drag coefficient that depends on bottom roughness and elevation at which V_b is measured. It is understood that in equation (2.4-1), the time sequence of velocity V_b has a broad band of frequencies, including both subinertial and superinertial (the inertial frequency being the local value of the Coriolis parameter). However, in studies of the subinertial circulation, the subinertial filtered value of bottom stress and that of velocity need to be related. Let \bar{Q} denote the 40-hr low-pass (subinertial) version of an unfiltered time sequence Q . It is then assumed that the 40-hr low-pass filtered version of equation (2.4-1) can be represented by

$$\tau_b = \rho c_b (v_h + \alpha |V_b|) \bar{V}_b, \quad (2.4-2)$$

where v_h is a scalar parameter with dimensions of velocity characterizing the high frequency part of the original velocity time sequence, and α is a dimensionless parameter. If the spectrum

of V_b had no superinertial part (such that $\bar{V}_b = V_b$), then we would expect that $\alpha=1$ and $v_h = 0$. For the more general case, equation (2.4-2) represents a combination of the linear form and the nonlinear form for subinertial bottom stress represented in terms of the subinertial bottom velocity.

Based on LATEX A near-bottom current meter data alone, it is possible to estimate the parameters v_h and α without knowing the actual bottom stress. This is possible because equations (2.4-1) and (2.4-2) imply that

$$\frac{\bar{\tau}_b}{\rho c_b} = \overline{|V_b|V_b} = (v_h + \alpha \overline{|V_b|}) \bar{V}_b, \quad (2.4-3)$$

which we identify as the pseudo stress. The elevation of the near-bottom current meters in the LATEX A mooring array varies from 1.3 m for moorings closest to the coast to 10 m for moorings in depths of 200 m or greater. In Current (1996), estimates of the alongshelf components of the pseudo stress and of \bar{V}_b were calculated from 3-hr low-pass V_b , which includes the dominant part of the high frequency current signals (near inertial motion and tides). Estimates of the parameters v_h and α were then obtained by least squares regression based on equation (2.4-3), with hourly values of $\overline{|v_b|v_b}$ and \bar{V}_b as data. Separate analyses were made for each mooring. An example plot of $\overline{|v_b|v_b}$ versus \bar{V}_b for mooring 25 is shown in Figure 2.4-2. The solid line in this plot is the fitted relation using equation (2.4-3).

As in Winant and Beardsley (1979), it is also possible to estimate the linear regression, in which α is constrained to be zero. The resulting squared correlations for the linear and the nonlinear implementations, along with the fitted α values for the nonlinear case, for 30 LATEX moorings investigated by Current (1996) are shown in Table 2.4-1; note, mooring 12 was not considered. The fitted v_h for each mooring, not shown in table, are much less for the nonlinear regression than for the linear regression, as one should expect. The v_h for the nonlinear case correspond closely to the mean speed of the 40-hr high-pass V_b for a given mooring, as confirmed by calculation from $\overline{|V_b - \bar{V}_b|}$. Current found that the v_h for the nonlinear case tend to be greatest near shore and less off shore (Figure 2.4-3). The solid line in this figure is a linear regression (with v_h in $\text{m}\cdot\text{s}^{-1}$ and depth h in m):

$$v_h = (6.9 - 0.015 h) / 100. \quad (2.4-4)$$

This was employed in the model discussed in Appendix L. The dependency of v_h on water depth is similar to that adopted by Clarke and Brink (1985) in their linear bottom stress parameterization.

It is clear from the results shown in Table 2.4-1 that for the Texas-Louisiana shelf the nonlinear parameterization is significantly better than the linear approximation, based on the comparison of squared correlation coefficients. This is reasonable considering that the rms variability of the subinertial near-bottom current \bar{V}_b is much larger than the mean value of $\overline{|V_b - \bar{V}_b|}$.

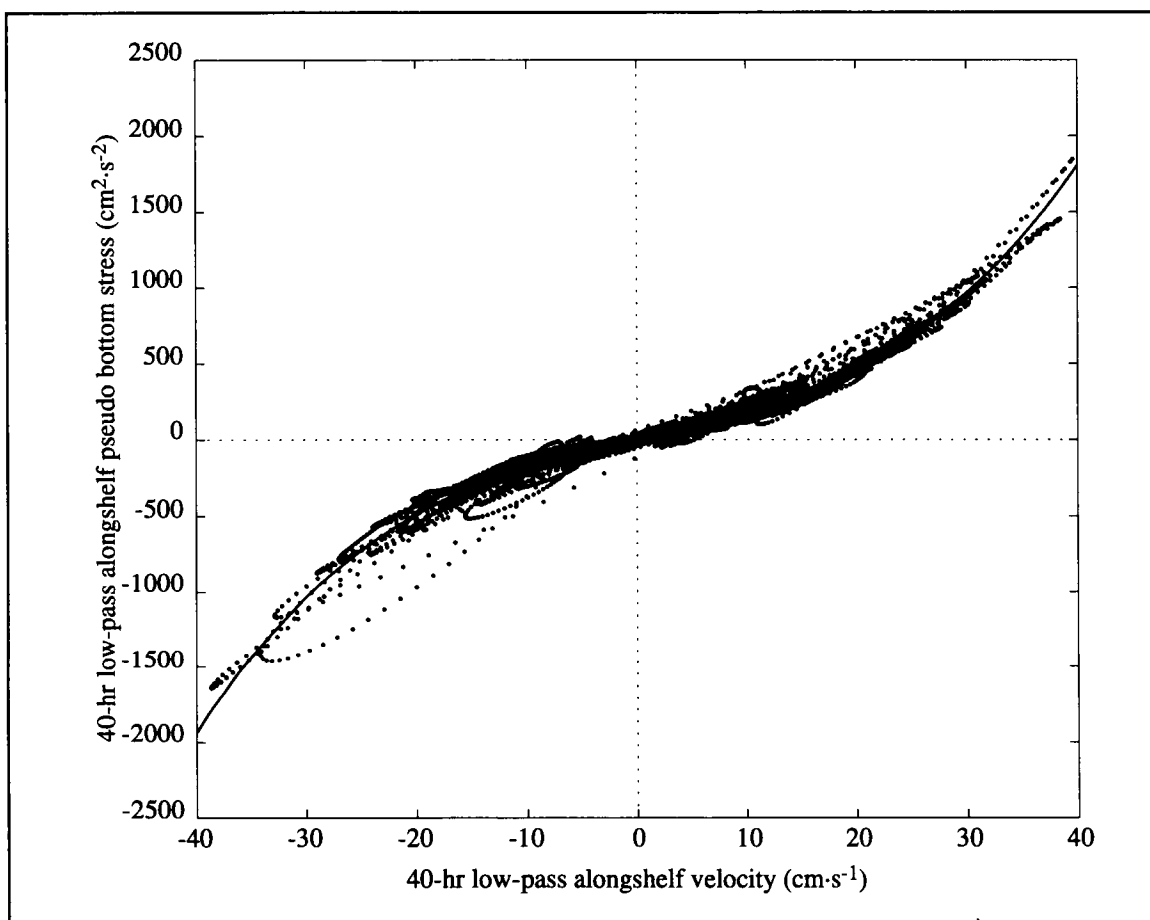


Figure 2.4-2. Typical dependence of 40-hr low-pass pseudo bottom stress on 40-hr low-pass bottom current, using data from all deployments of mooring 25. The root mean square of the fitted (solid) curve is about $58 \text{ cm}^2\cdot\text{s}^{-2}$, a small fraction of the total range in the pseudo stress.

Optimal c_b based on model tuning

A wind-driven model for the subinertial circulation over the inner Texas-Louisiana shelf is described in Appendix L and employed to simulate the alongshelf currents and coastal water level variation. Prior to carrying out extensive simulations, the model was employed to get optimum estimates of c_b and α characterizing the inner shelf (water depths of 50 m or less) as a whole. The shelf model as applied predicts a current that is essentially the depth-averaged value for a given water column. The bottom stress in the model was parameterized by a relation similar to relation (2.4-2), but with the subinertial \bar{V}_b replaced by the predicted local depth-averaged velocity. The parameter v_h was taken as that given by equation (2.4-4), but tuning experiments were carried out to find those c_b and α that maximized the

Table 2.4-1. Squared correlations of alongshelf bottom stress with alongshelf bottom current for all deployments at 30 LATEX A mooring locations (1992-1994) for linear ($\alpha=0$) and nonlinear (α as shown) implementations. Water depth at each mooring varied somewhat for different deployments.

Mooring number	Water depth (m), approx.	α Parameter	r^2 , Linear implementation	r^2 , Nonlinear implementation
1	21	0.8	0.90	0.98
2	37	1.1	0.78	0.98
3	66	0.8	0.86	0.97
4	200	1.5	0.88	0.99
5	200	0.8	0.90	0.99
6	201	0.6	0.87	0.98
7	200	0.8	0.91	0.99
8	200	1.8	0.83	0.96
9	200	1.8	0.92	0.95
10	200	1.4	0.73	0.93
11	200	0.5	0.92	0.92
13	200	0.9	0.83	0.99
14	47	0.5	0.88	0.94
15	27	0.8	0.83	0.92
16	9	0.7	0.85	0.94
17	7	0.8	0.88	0.96
18	22	0.8	0.78	0.95
19	52	0.6	0.86	0.92
20	14	1.0	0.89	0.97
21	10	0.9	0.89	0.96
22	55	1.3	0.89	0.95
23	15	0.9	0.88	0.97
24	29	0.7	0.90	0.98
25	32	0.8	0.90	0.97
44	56	0.8	0.83	0.98
45	198	1.2	0.89	0.99
46	91	0.5	0.91	0.97
47	203	0.8	0.93	0.98
48	201	0.5	0.92	0.94
49	501	0.6	0.89	0.98
Mean \pm standard error		0.90 \pm 0.06	0.87 \pm 0.01	0.96 \pm 0.004
Median		0.8	0.88	0.97

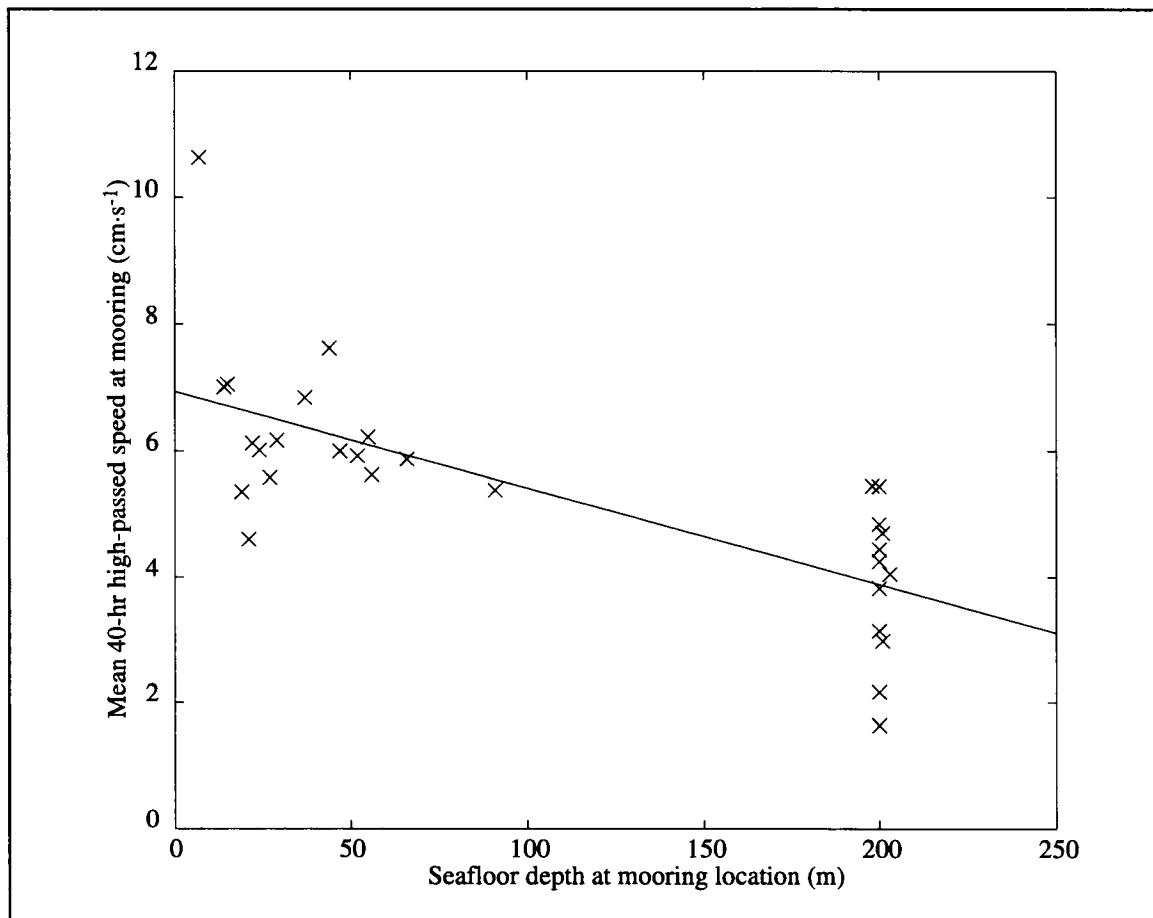


Figure 2.4-3. Linear fit to water depth of mean speed of 40-hr high-pass current v_b in $\text{cm}\cdot\text{s}^{-1}$ at individual bottom current meter locations employed in the estimation of bottom stress parameters. The large variability that exists at given depths (e.g., 200 m) reflects the different results from moorings at different alongshelf positions for the given depth. The alongshelf variability was found not to have any systematic trend.

correlation between the predicted and measured subinertial alongshelf currents for several episodes where adequate shelf coverage of wind and current data existed. The optimum α from these experiments was 0.80, which is the median value of α from Table 2.4-1. The optimum c_b was found to be 0.00065. This is small compared with estimates of c_b that apply within the logarithmic layer near the bottom (Adams et al. 1982). Estimating bottom stress from a depth-averaged current is somewhat analogous to estimating wind stress on the sea surface from winds at the gradient wind level (top of the atmospheric Ekman layer) rather than at the standard 10-m level above the sea surface.

For each mooring, estimates were made of the depth-averaged current from the data and the mean square values of these calculated for the LATEX A measurement period. The mean square values of the near-bottom currents were also determined at each mooring for the same period. The ratios of these for each mooring have a very skewed distribution, from near zero to over 1.0. The median is the best estimate of the central value and was found to be 0.31. This ratio is an estimate of the pseudo stress based on the near-bottom currents to that based on the depth-averaged current. Hence we estimate that the c_b value appropriate to the near-bottom current meter positions is 0.00065 divided by 0.31 or 0.0021, which is about the order one should expect in the logarithmic sublayer over silty to sandy sediments (Rezak et al. 1985) for a low energy wave climatology, typical of the Gulf of Mexico.

As part of the LATEX B study, near-bottom flow profile measurements were made by means of an instrumented tetrapod system (Murray and Donley 1995) on the eastern inner shelf in the spring of 1992 and in spring and summer of 1993 in water depths of less than 21 m. It was found that under low wave activity, the bottom roughness scale is about 0.1 cm or less. A roughness scale of 0.1 cm would correspond to a c_b value of 0.0025 for current measured at an elevation of 3 m above bottom. The latter value is reasonably consistent with the value of 0.0021 inferred for the bottom current levels of the LATEX A moorings, whose elevations above bottom vary from 1 to 10 m, with geometric mean of order 3 m.

2.5 Eddy-shelf interaction

The path of the Loop Current in the Gulf of Mexico is a clockwise (anticyclonic) loop extending northward into the Gulf from the Yucatan Channel and then exiting eastward through the Florida Straits, where it is referred to as part of the Gulf Stream. On the order of once a year, anticyclonic eddies detach from the Loop Current. When newly detached, these eddies can be up to 400 km in diameter. As they decay, they shrink. During their life of approximately one year, the eddies migrate westward, often ending up in the “eddy graveyard” of the northwest corner of the Gulf adjacent to the Texas shelf (Vukovich and Crissman 1986).

In Section 2.5.1, we briefly describe each Loop Current eddy observed adjacent to the shelf during the LATEX field program. A case study of Eddy Vazquez is presented as Appendix D. Section 2.5.2 discusses the impact of the eddies on shelf currents.

2.5.1 Loop Current eddies during LATEX

This section identifies the anticyclonic Loop Current eddies found adjacent to the Texas-Louisiana shelf edge from April 1992 through November 1994. As used here, the term “adjacent” means that a portion of the eddy extended north of 26°N. The primary data source for this identification consists of sea surface height anomaly maps (SSHA) from satellite altimeter data provided by Dr. Robert R. Leben of the Colorado Center for Astrodynamic Research of the University of Colorado in Boulder, Colorado. Jochens (1997)

establishes that the SSHA maps from altimeter data provide a good means for tracking the locations of the Loop Current eddies adjacent to the shelf.

Two altimeter missions were conducted during the LATEX period: the ERS-1 mission of the European Space Agency and the TOPEX/Poseidon (T/P) mission of NASA and the Centre National D'Etudes Spatiales (France). Between April 1992 and December 1993 and from April 1994 through the end of LATEX, ERS-1 was placed, respectively, in a 35-day and a 168-day exact repeat orbit suitable for mapping mesoscale variability. Data from T/P, which was in a 10-day repeat cycle, were available beginning in early October 1992. These two data sets were blended when possible. Preliminary studies showed that blended altimeter-derived SSHA agree with hydrographic estimates of dynamic height anomaly to better than 5 cm rms in the western Gulf (Leben et al. 1993).

The SSHA maps were supplemented with NOAA's ocean features analyses from satellite sea surface temperature data for April to October 1992, and trajectories of drifters deployed by LATEX A and LATEX C. The LATEX A shelf edge current data and composites of the hydrographic and XBT data from LATEX A, LATEX C, and GulfCet also were used. Additional information on the eddies is presented in the LATEX C synthesis report (Berger et al. 1996).

In addition to Loop Current eddies, the shelf edge is influenced by smaller anticyclonic slope eddies and by cyclonic (rotating counterclockwise) eddies. Cyclonic eddies often are associated with Loop Current eddies. A few of these cyclonic and slope eddies will be mentioned here; additional discussion can be found in Berger et al. (1996).

During the period from April 1992 through November 1994, there were six Loop Current eddies or eddy remnants present in the Gulf. Their names are given in Table 2.5.1-1. Each of these eddies was adjacent to the Texas-Louisiana shelf edge for at least a portion of its life.

Loop Current eddies and surrounding cyclones can be seen in the maps of sea surface heights. Figure 2.5.1-1 is an example that shows the locations of three Loop Current eddies and surrounding cyclones adjacent to the Texas-Louisiana shelf in early October 1992. This

Table 2.5.1-1. Anticyclonic Loop Current eddies during LATEX.

Eddy Name	Shorthand Name
Eddy Triton	Eddy T
Eddy Unchained	Eddy U
Eddy Vazquez	Eddy V
Eddy Whopper	Eddy W
Eddy eXtra	Eddy X
Eddy Yucatan	Eddy Y

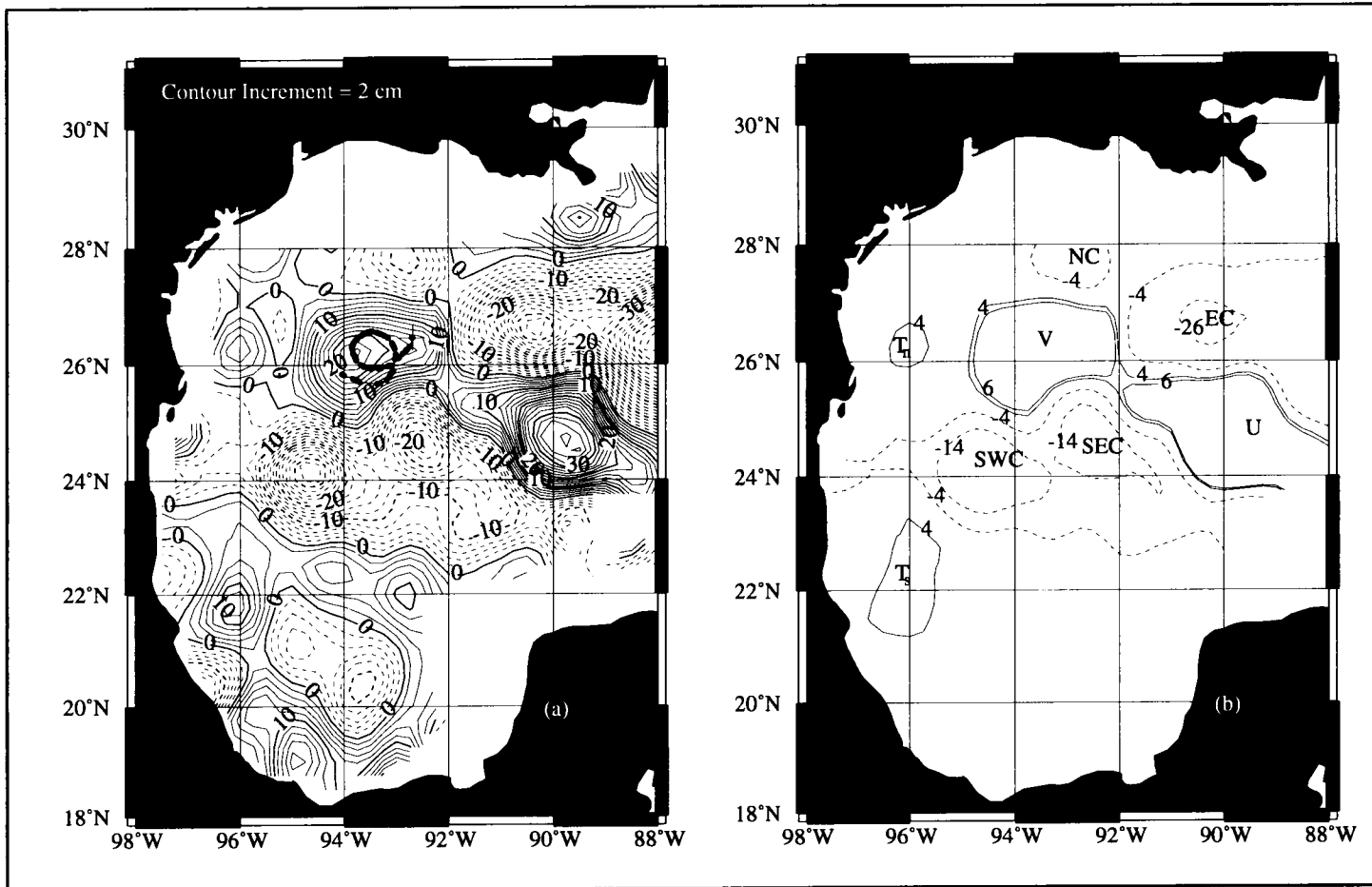


Figure 2.5.1-1. Sea surface height anomaly with respect to alongtrack corrected Rapp 95 mean surface (a) TOPEX cycle 2, 3 to 12 October 1992, including ERS-1 35-day repeat centered on the mid-point of the T/P cycle; the track of LATEX A drifter 2447 (line with solid circles) is shown and (b) identification of eddies by the 4-cm SSHA contour in (a).

figure shows the remnant of Eddy T just before it coalesced with Eddy V. Eddy V is seen to be just attached to Eddy U, which is to its southeast. Cyclones are discernible to the north, east, southwest, and southeast of Eddy V. The centers of the maxima of sea surface height anomalies for each Loop Current eddy determined the nominal center of the eddy. The extent of the 4-cm contour was used to track eddies relative to the Texas-Louisiana shelf. Table 2.5.1-2 identifies when and where a Loop Current eddy was adjacent to the Texas-Louisiana shelf. A brief discussion of the movement of each eddy relative to the Texas-Louisiana shelf is given below.

Eddy T. Eddy T had been shed by the Loop Current in late June 1991 (Biggs et al. 1996). A remnant of Eddy T was adjacent to the LATEX shelf edge from April 1992 through October 1992 (Figure 2.5.1-2). In April and May 1992, Eddy T was splitting apart. Its major portion, Eddy T_S, was centered to the south at about 24°N, 94.5°W, however, a significant part of the eddy was elongated along 26°N. This part had two SSHA maxima: one centered at about 26°N, 95°W (not shown) and the other as shown in Figure 2.5.1-2. By June, the two parts had separated, with the northern portion (Eddy T_N) still elongated along 26°N but beginning to contract and consolidate into a more circular shape. In July and August, Eddy T_N had shifted northwestward into the eddy graveyard. During this time, it may have split into east and west parts, with the east part moving east, becoming centered about 25.8°N, 92.7°W until it coalesced with Eddy V (Jochens 1997). In September, Eddy T_N moved south, away from the Texas-Louisiana shelf edge. In October, it moved back north and was absorbed by Eddy V. Eddy T_S had moved southwest during summer 1992; its early October location is shown in Figure 2.5.1-1. Biggs et al. (1996) provide additional information on Eddy T.

Eddy U. Eddy U was shed from the Loop Current in summer 1992. It moved into the southwestern Gulf and had extremely limited direct interaction with the Texas-Louisiana shelf waters (Figure 2.5.1-3). Its major influence was through its interactions with Eddy V (Appendix D).

Eddy V. Eddy V was a Loop Current eddy that most likely was split from Eddy U in September/October 1992. It was adjacent to the Texas-Louisiana shelf from the time of its formation until it dissipated in September 1993 (Figure 2.5.1-4). From September to November 1992, Eddy V moved westward at the base of the Texas-Louisiana slope. In October, it absorbed Eddy T_N. From November 1992 through March 1993, it was located in the eddy graveyard. In April 1993, Eddy V elongated north-south and developed two SSHA maxima; this began the split of Eddy V into northern and southern parts, Eddy V_N and Eddy V_S, respectively. The track for April shows the locations of the two maxima in SSHA associated with the parts before they fully separated. In mid-May, the two parts separated, and Eddy V_S moved southward out of the area of the Texas-Louisiana shelf as shown in Figure 2.5.1-4. Eddy V_S eventually moved east and coalesced with Eddy W. Eddy V_N remained in the northwest corner and was moved farther up onto the slope than Eddy V had been. Associated with it at this time was a strong cyclonic eddy to its west on the shelf. From May through August, Eddy V_N gradually decayed. In August/September 1993, it

Table 2.5.1-2. Presence of Loop Current eddies adjacent to the Texas-Louisiana shelf, April 1992-November 1994. Each longitude is $\pm 0.5^\circ$. No eddies were adjacent to the shelf from February through June of 1994.

Year	Month	96°W	95°W	94°W	93°W	92°W	91°W	90°W	
1992	April		T	T	T	T	T		
	May		T	T	T	T	T		
	June	T	T	T	T	T			
	July	T	T	T	T	T			
	August	T	T	T	U	U	U	U	
	September	T	T				U	U	
	October	T	T, V	V	V	V			
	November	V	V	V	V	V			
	December	V	V	V					
	1993	January	V	V	V				
		February	V	V	V				
		March	V	V	V				
April		V	V	V					
May		V _n	V _n	V _n					
June		V _n	V _n	V _n			W	W	
July		V _n	V _n	V _n		W	W	W	
August		V _n	V _n	V _n	W _n	W _n	W _n		
September		V _n	V _n	V _n	W _n	W _n , X	X	X	
October				X _w	X _w , X _e	X _e	X _e	X _e	
November				X _w	X _w	X _e	X _e	X _e	
December			X _w	X _w	X _w	X _e	X _e	X _e	
1994	January		X _w	X _w			X _e		
	⋮								
	July		X _n	X _n					
	August		X _n	X _n					
	September							Y	
	October						Y	Y	
November					Y	Y	Y		

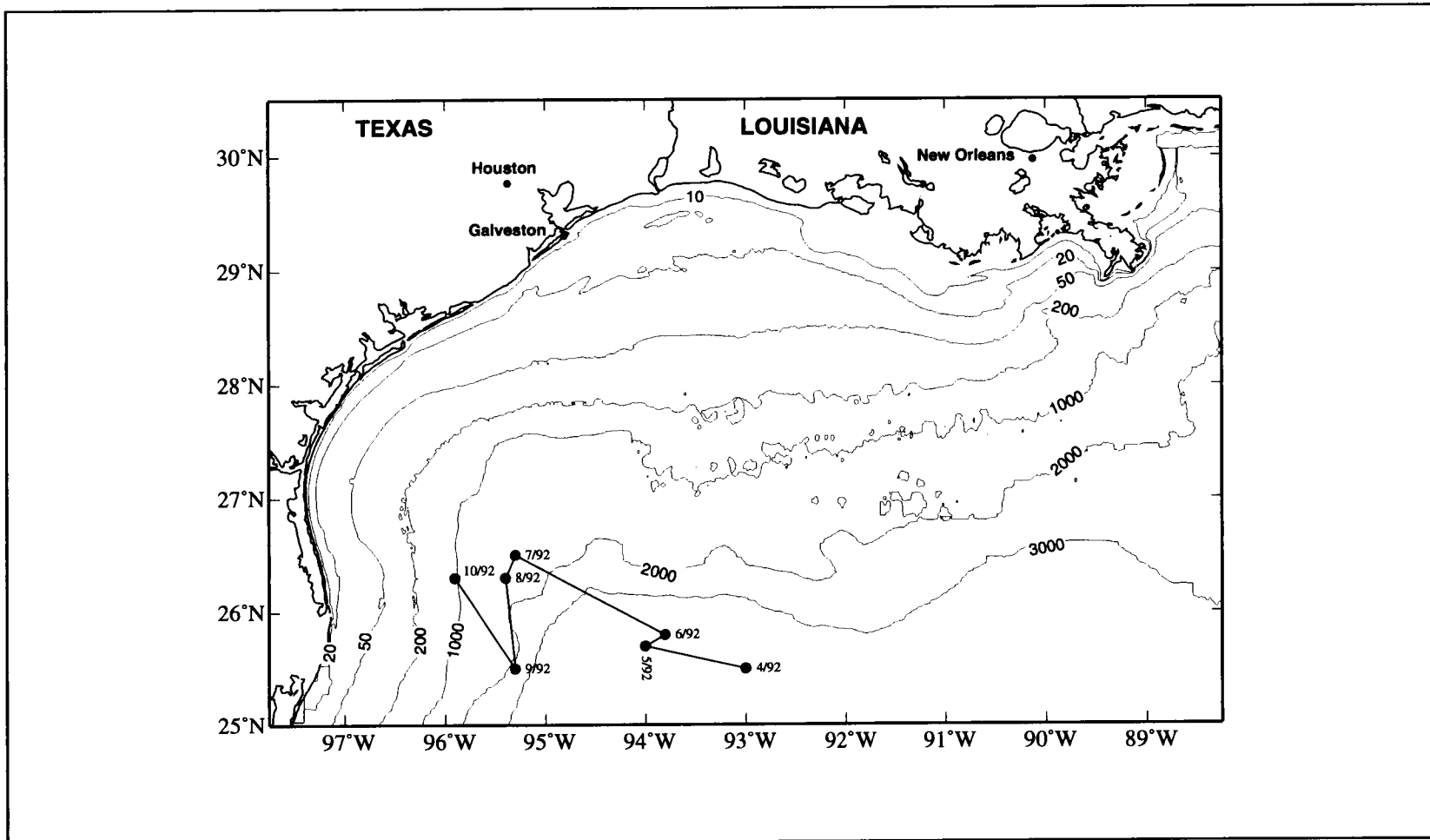


Figure 2.5.1-2. Approximate locations of the center of remnant Eddy T based on sea surface height anomaly maps from ERS-1 cycles and NOAA ocean features analyses maps between 14 April and 6 October 1992, and sea surface height anomaly maps from TOPEX/Poseidon cycles between 3 October and 1 November 1992.

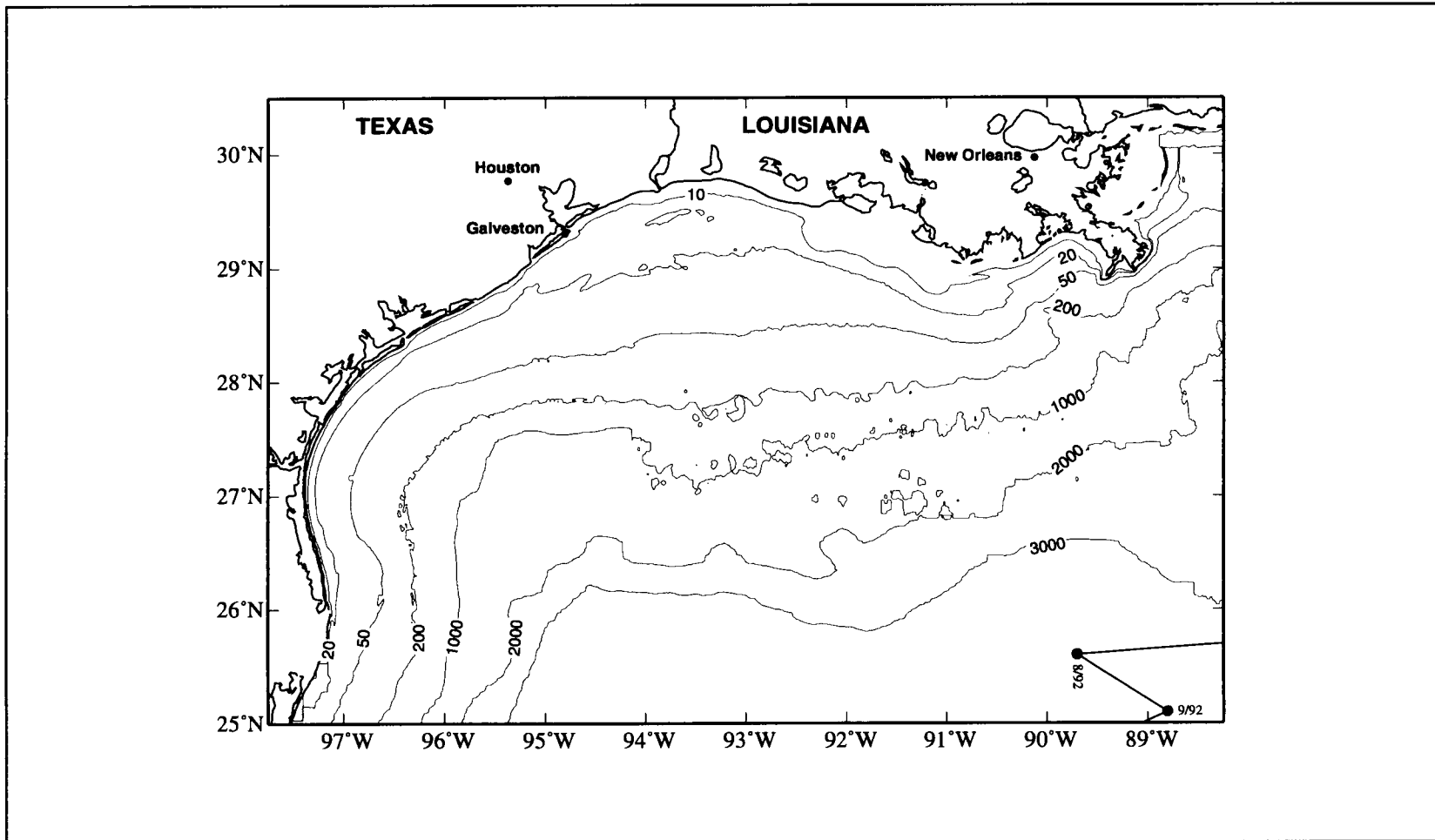


Figure 2.5.1-3. Approximate locations of the center of Eddy U based on sea surface height anomaly maps from ERS-1 cycles between 14 April and 6 October 1992, and sea surface height anomaly maps from TOPEX/Poseidon cycles between 3 October and 1 December 1993.

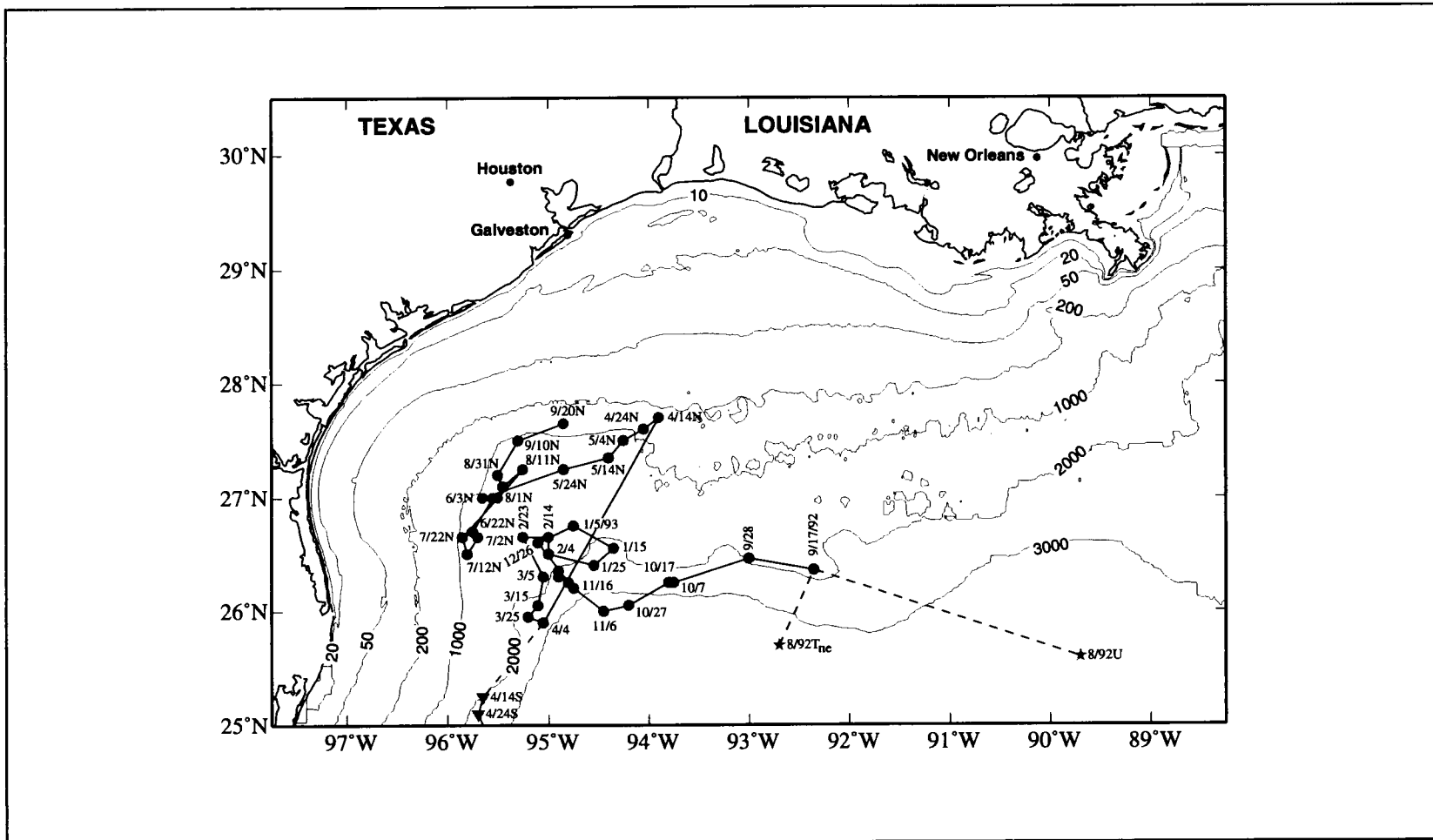


Figure 2.5.1-4. Approximate locations of Eddy V centers based on the drifter 2447 track from 12 September to 3 October 1992, and sea surface height anomaly maps for TOPEX/Poseidon cycles between 3 October 1992 and 4 October 1993. Circles are locations of Eddy V and, after 9 April 1993, of Eddy V_n. Triangles are locations of Eddy V₃; stars are locations of Eddy U and Eddy T as Eddy V was forming.

interacted with Eddy W and then dissipated. Appendix D presents a case history examination of Eddy V.

Eddy W. In June 1993, Loop Current Eddy W formed. Initially it moved westward (Figure 2.5.1-5). In mid-July, it began to split into north and south parts, Eddy W_n and Eddy W_s , respectively. Eddy W_s moved southwestward out of the Texas-Louisiana shelf region in July and eventually coalesced with Eddy V_s . Eddy W_n moved westward for the remainder of July. In August, it moved southwest out of the Texas-Louisiana shelf region and eventually coalesced with Eddy W_s .

Eddy X. Eddy X was shed from the Loop Current in fall 1993. Initially it moved westward (Figure 2.5.1-6). During late September through October 1993, Eddy X interacted with Eddy W_n (Figure 2.5.1-5). This interaction resulted in its split into east and west parts, Eddy X_e and Eddy X_w , respectively. Throughout October 1993, the eastern portion of Eddy X was located at about 26.5°N , 90.5°W , and the western portion at about 26°N , 94°W . The separation was complete in early November 1993. Eddy X_e then moved southwestward, leaving the Texas-Louisiana shelf region in January 1994 and eventually coalescing with Eddy W. Eddy X_w remained at about 26°N , 94°W until late December when it moved west. In early January 1994, it moved southward out of the Texas-Louisiana shelf region. Eddy X_w joined with the coalescence product of Eddy W and Eddy X_e . During summer 1994, the joined Eddy X_w elongated north-south and an extension reached northward into the Texas-Louisiana shelf region in late July and August 1994. In early September, the extension had dissipated.

Eddy Y. Loop Current Eddy Y was shed in summer 1994. From September through November 1994, it moved westward (Figure 2.5.1-7). Throughout December 1994, it was centered about 25.5°N , 91.5°W , after which it moved southwestward out of the Texas-Louisiana shelf region.

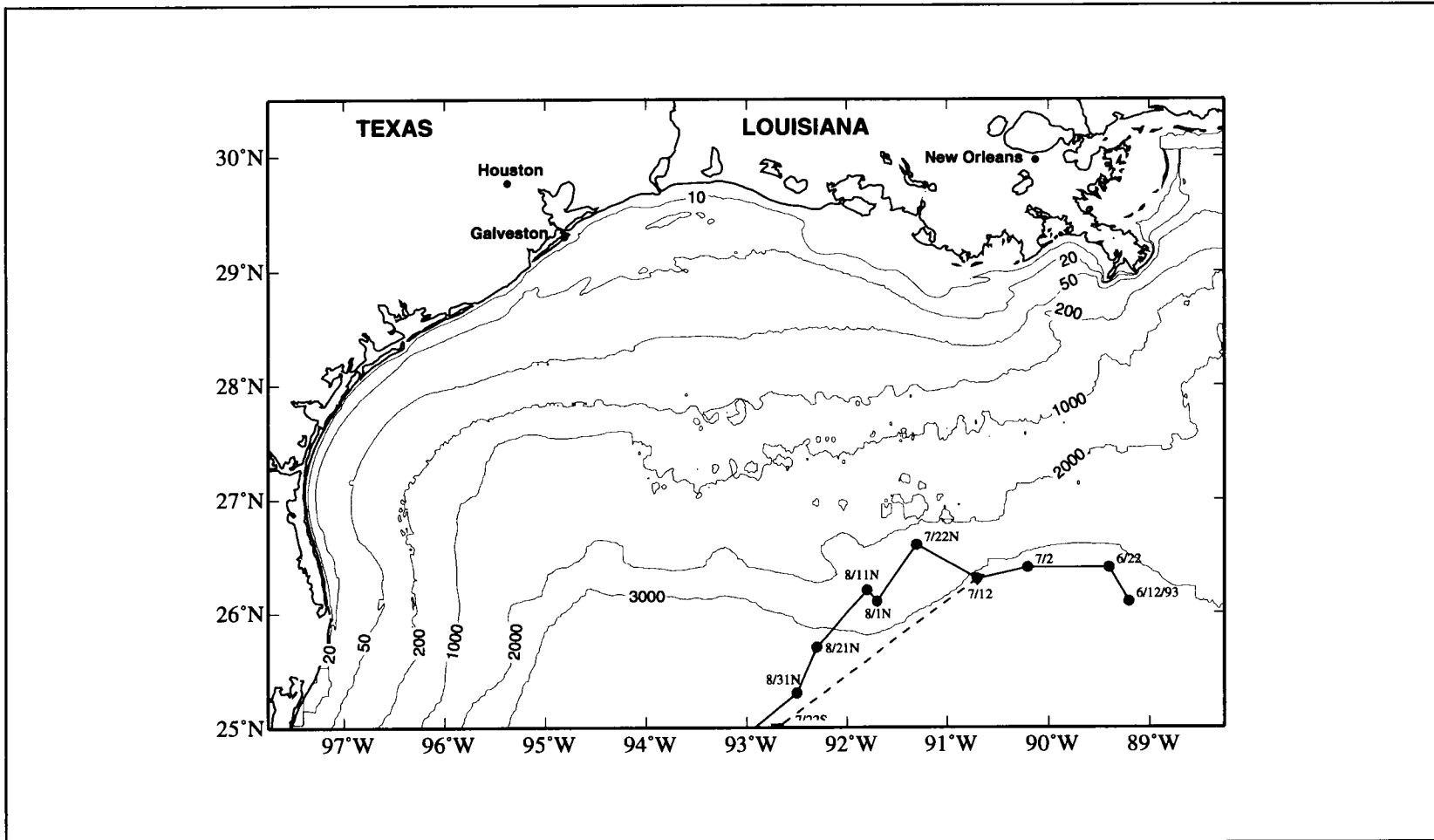


Figure 2.5.1-5. Approximate locations of the center of Eddy W based on sea surface height anomaly maps of TOPEX/Poseidon cycles between 7 June and 23 December 1993. Circles are locations of Eddy W and, after 17 July 1993, of Eddy W_n . Triangle is the center location of Eddy W_s .

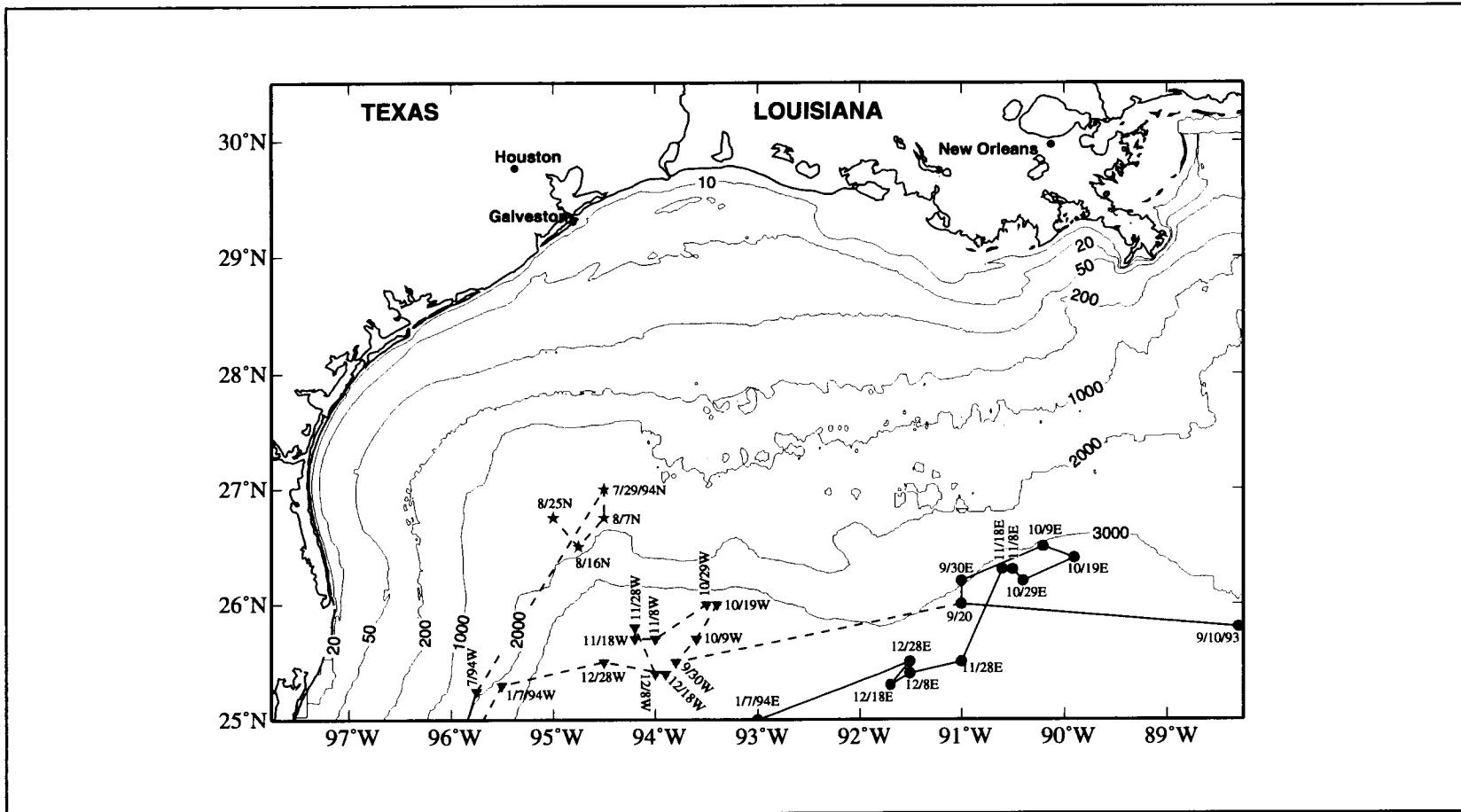


Figure 2.5.1-6. Approximate locations of the center of Eddy X based on sea surface height anomaly maps from TOPEX/Poseidon cycles of 26 August 1993 to 3 September 1994. Circles show the centers of Eddy X and, after 20 September 1993, of Eddy X_c . Triangles show the centers of Eddy X_w and stars show the centers of a northward extension of the remnant of Eddy X_w .

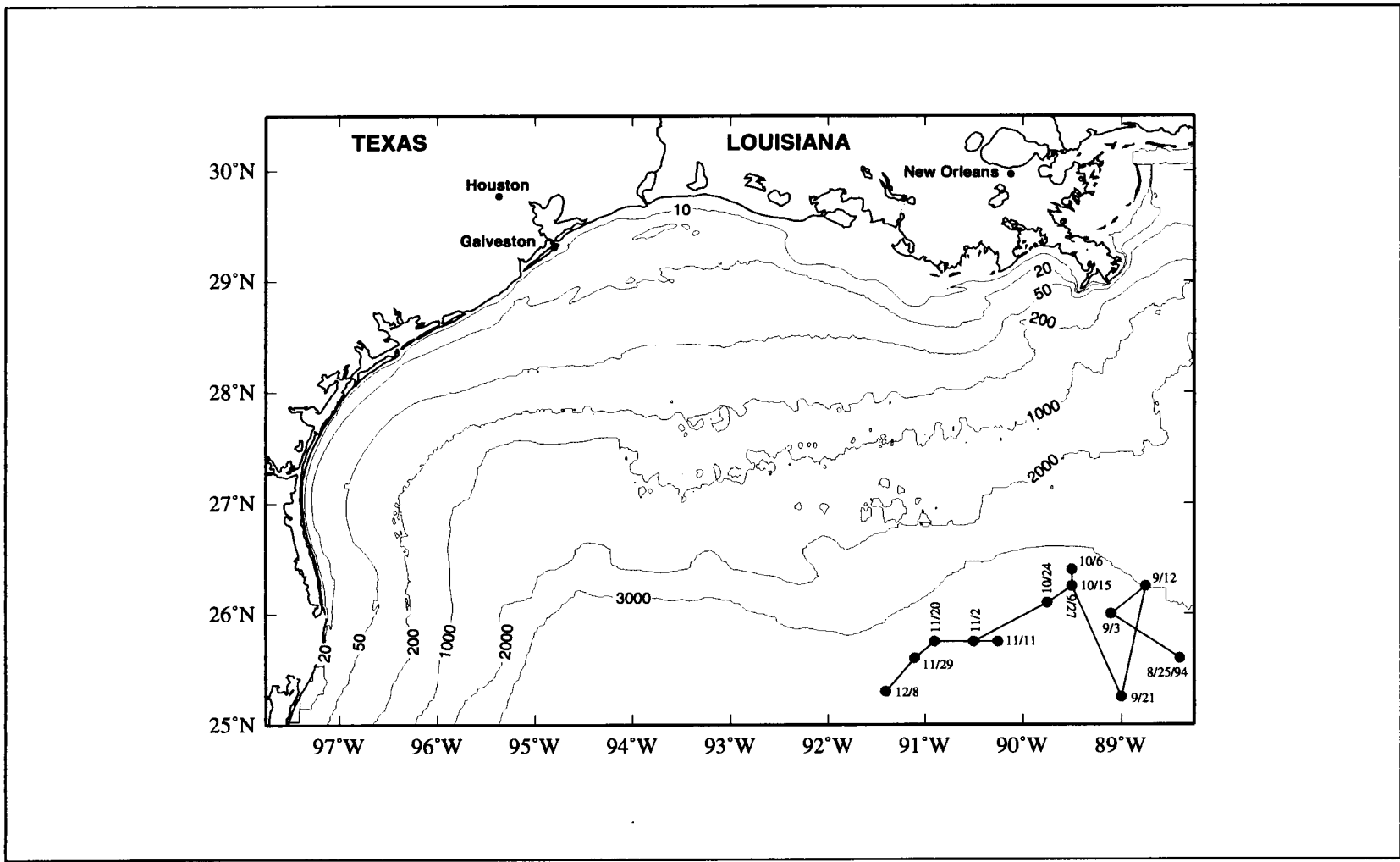


Figure 2.5.1-7. Approximate locations of the center of Eddy Y based on sea surface height anomaly maps of TOPEX/Poseidon cycles between 25 August and 8 December 1994.

2.5.2 Influence of Loop Current eddies on current fields

Using altimeter-derived sea surface height anomalies to map Loop Current eddies in space and time provides a way to determine their influence on currents at the shelf edge. Figures 2.5.1-2 through 2.5.1-7 show locations of the nominal centers of the six Loop Current eddies that were present in the western Gulf during the LATEX field program. Table 2.5.1-2 shows by month the shelf regions to which the eddies were adjacent. To determine when the eddies influenced the currents at the outer shelf requires the additional information of how close the eddy peripheries were to the shelf edge. Although both the SSHA and geopotential anomaly maps extend east of 90.5°W, we limit this discussion to the Texas-Louisiana shelf that is west of 90.5°W. This is the shelf region over which current meter moorings were deployed.

Loop Current eddy influence on the geopotential anomaly fields

Geopotential anomaly fields that extend from the shelf to the slope are presented in Figures H.1-2 through H.1-13 of Appendix H. Loop Current eddies are manifested as highs in geopotential anomaly and are centered well off-shelf of the 200-m isobath. The currents flow anticyclonically or clockwise around these highs. The SSHA maps identified which Loop Current eddies were present in each of the geopotential anomaly fields. The eddies and the portions of the shelf they were adjacent to are identified in Table 2.5.2-1.

Loop Current eddy influence on the shelf edge currents

Figures 2.5.2-1 through 2.5.2-6 show monthly averaged current vectors for the near-surface (10-m), mid-depth (100-m), and bottom-depth (190-m or 490-m) current meters of the shelf

Table 2.5.2-1. Identification of Loop Current eddies present in the geopotential anomaly fields. Each longitude band is approximately $\pm 0.5^\circ$.

Year	Dates	Figure	96°W	95°W	94°W	93°W	92°W	91°W	90°W
1992	15 Apr - 8 May	H.1-2	T	T	T				
	1-11 Aug	H.1-3	T	T	T	U	U	U	U
	5-21 Nov	H.1-4	V	V	V	V			
1993	4-21 Jan	H.1-5	V	V	V				
	5-24 Feb	H.1-6	V	V	V				
	26 Apr - 18 May	H.1-7	V _n	V _n	V _n				
	26 July - 7 Aug	H.1-8	V _n	V _n			W _n	W _n	W _n
	28 Oct - 22 Nov	H.1-9			X _w	X _w	X _e	X _e	X _e
	5-23 Dec	H.1-10			X _w			X _e	X _e
	23 Apr - 24 May	H.1-11							
1994	26 July - 14 Aug	H.1-12	X _n	X _n	X _n				
	1-16 Nov	H.1-13					Y	Y	Y

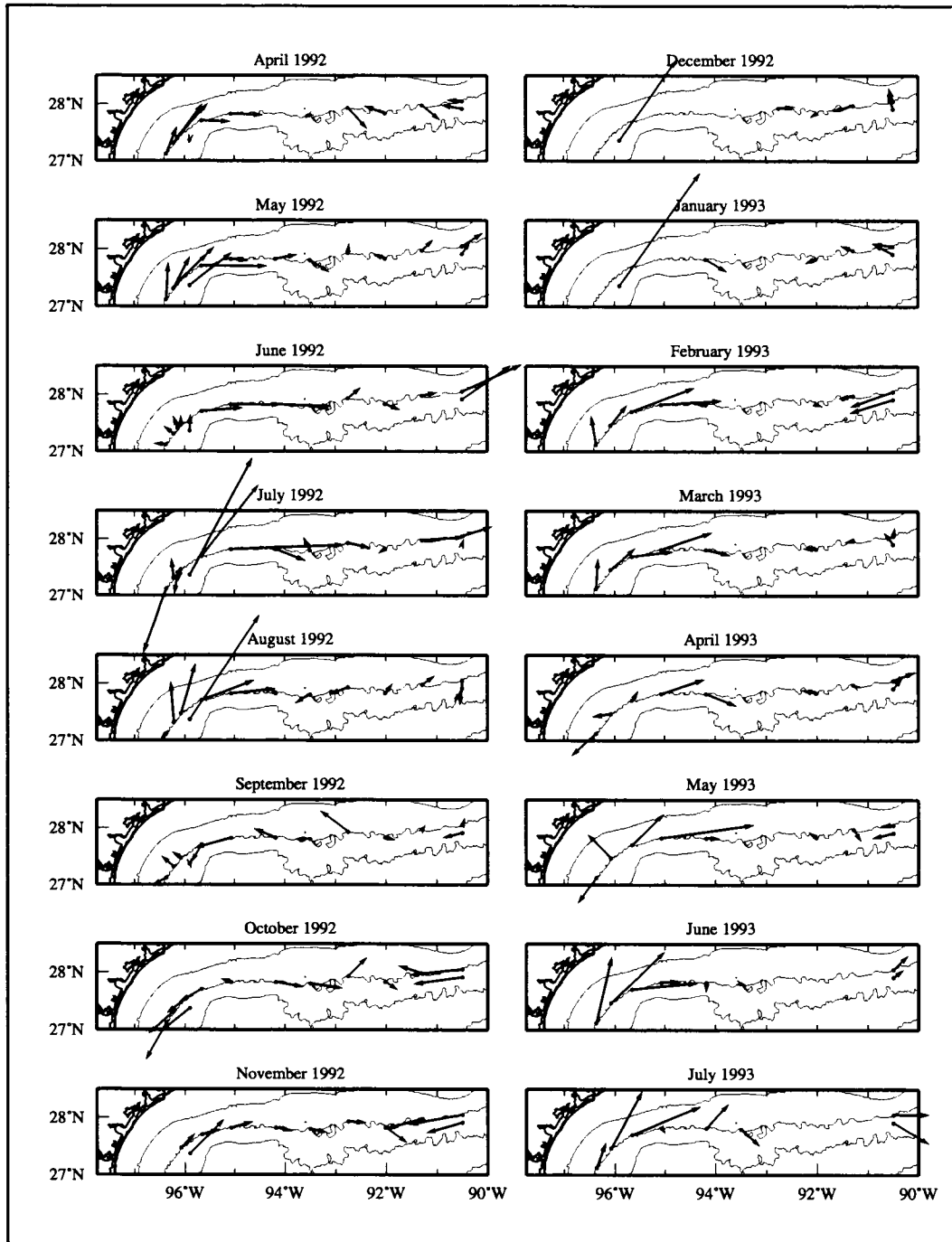


Figure 2.5.2-1. Monthly averages of 10-m, 40-hr low-pass current velocity along the shelf edge for April 1992 through July 1993. Velocity vectors of length \rightarrow represent $10 \text{ cm}\cdot\text{s}^{-1}$. The 50-, 200-, and 1000-m isobaths are contoured.

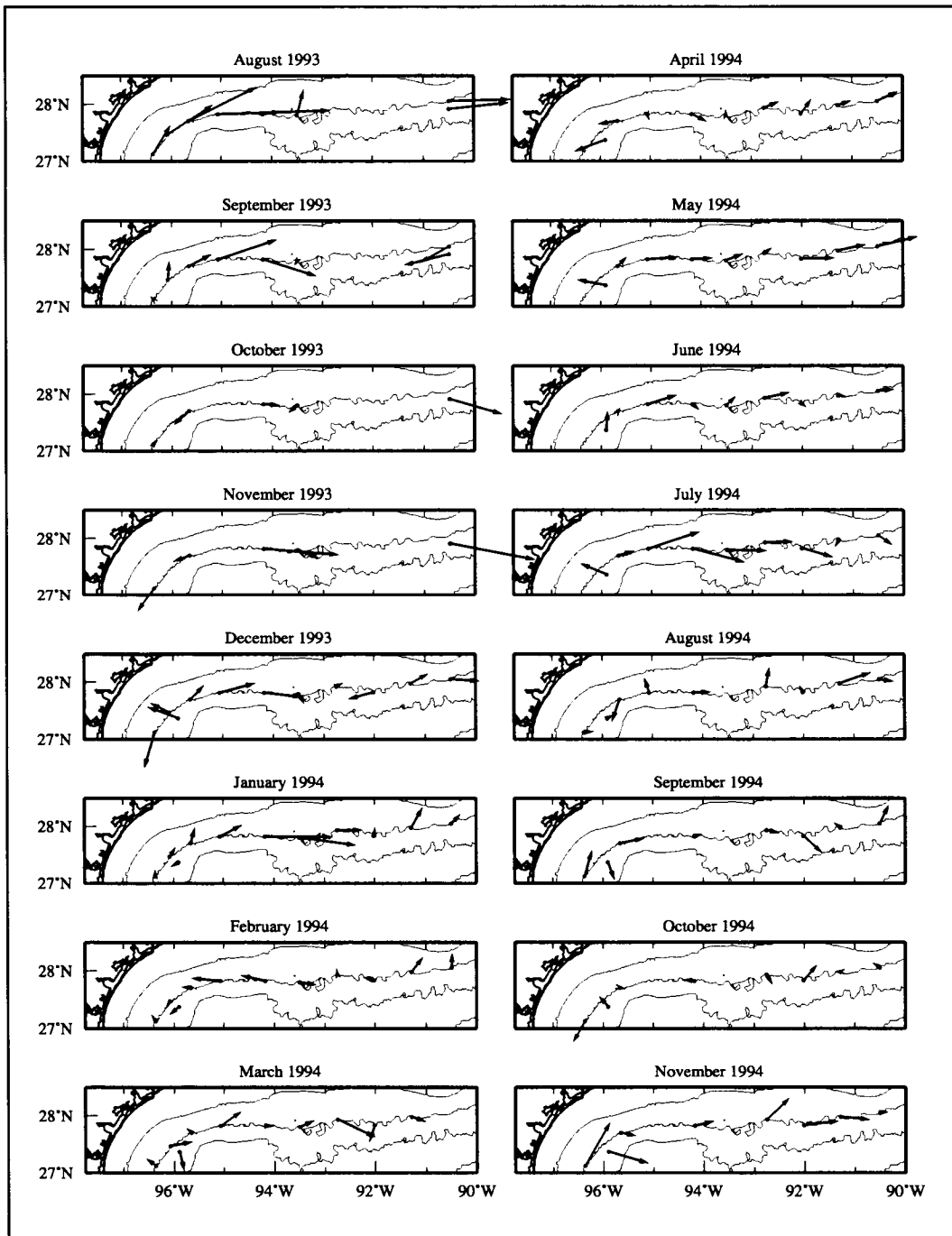


Figure 2.5.2-2. Monthly averages of 10-m, 40-hr low-pass current velocity along the shelf edge for August 1993 through November 1994. Velocity vectors of length \rightarrow represent $10 \text{ cm}\cdot\text{s}^{-1}$. The 50-, 200-, and 1000-m isobaths are contoured.

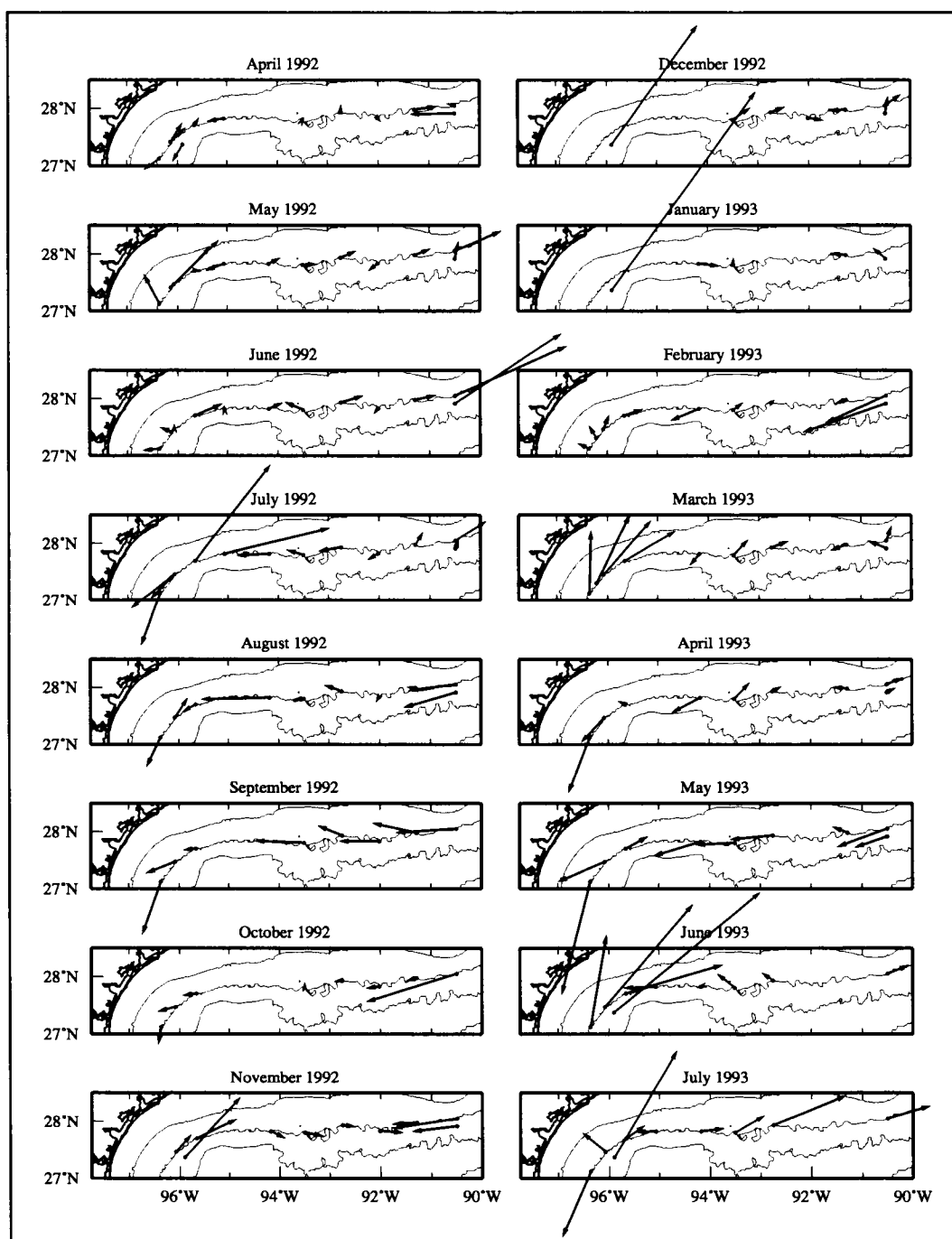


Figure 2.5.2-3. Monthly averages of 100-m, 40-hr low-pass current velocity along the shelf edge for April 1992 through July 1993. Velocity vectors of length \rightarrow represent $5 \text{ cm}\cdot\text{s}^{-1}$. The 50-, 200-, and 1000-m isobaths are contoured.

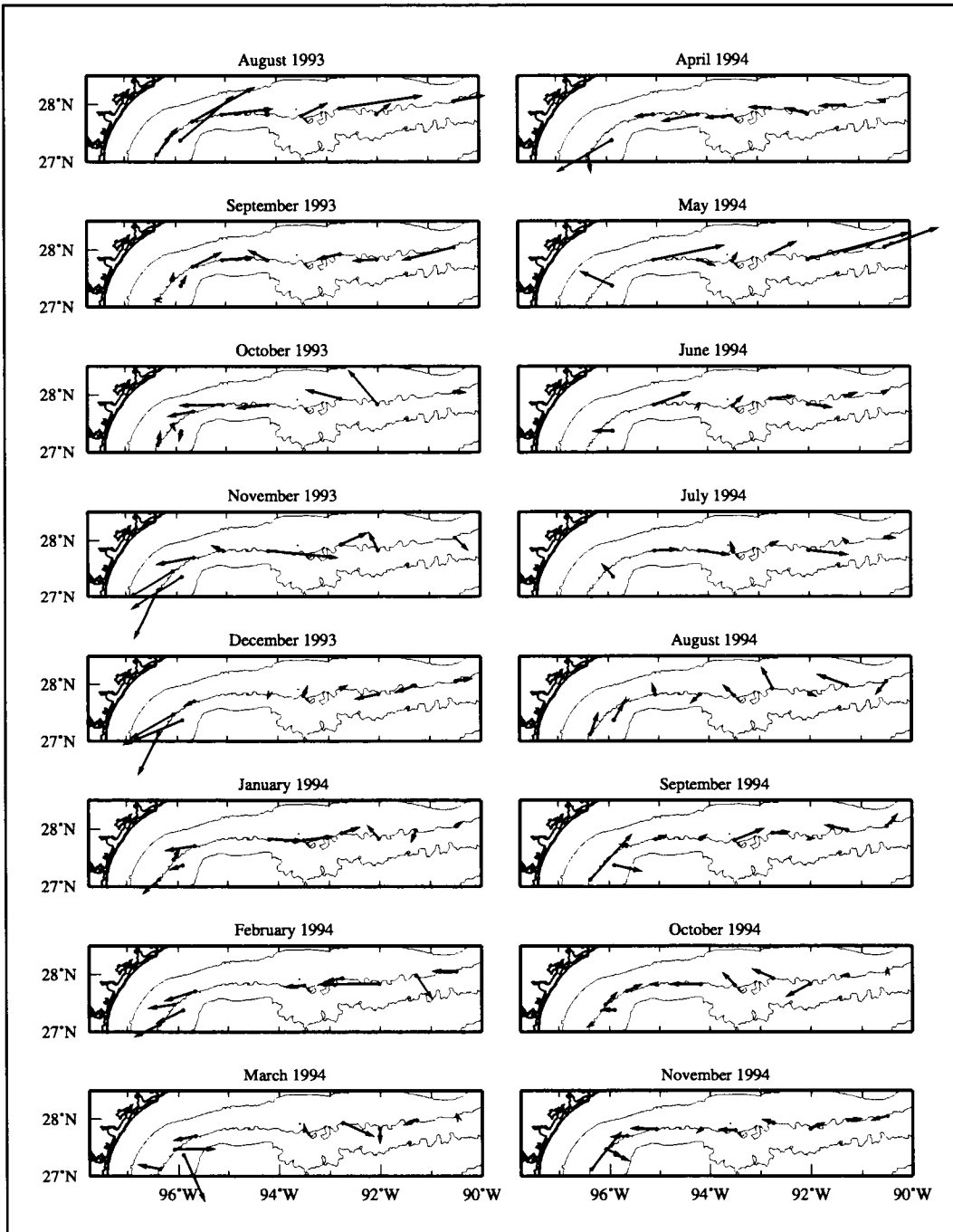


Figure 2.5.2-4. Monthly averages of 100-m, 40-hr low-pass current velocity along the shelf edge for August 1993 through November 1994. Velocity vectors of length \rightarrow represent $5 \text{ cm} \cdot \text{s}^{-1}$. The 50-, 200-, and 1000-m isobaths are contoured.

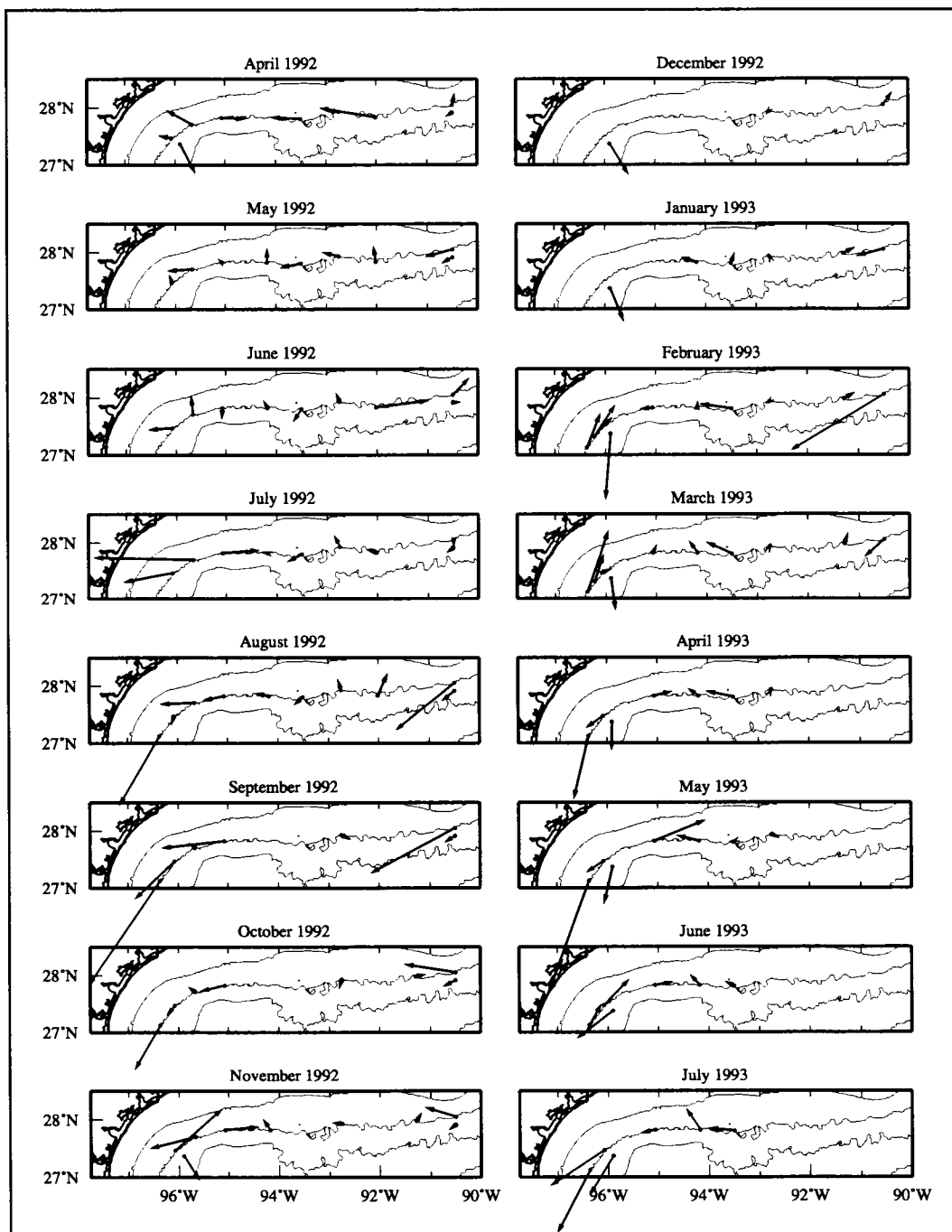


Figure 2.5.2-5. Monthly averages of 190-m/490-m, 40-hr low-pass current velocity along the shelf edge for April 1992 through July 1993. Velocity vectors of length \rightarrow represent $2.5 \text{ cm}\cdot\text{s}^{-1}$. The 50-, 200-, and 1000-m isobaths are contoured.

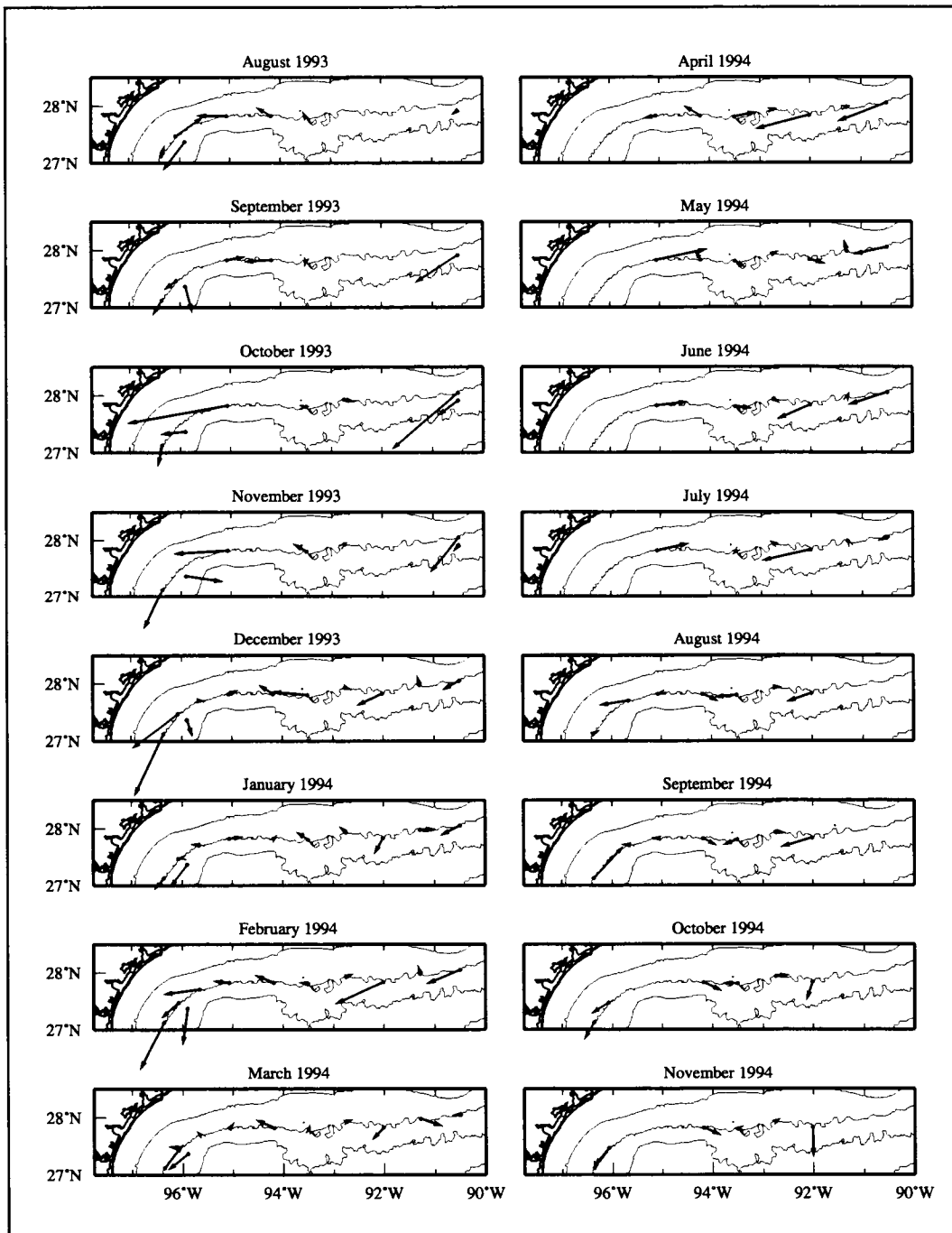


Figure 2.5.2-6. Monthly averages of 190-m/490-m, 40-hr low-pass current velocity along the shelf edge for August 1993 through November 1994. Velocity vectors of length \rightarrow represent $2.5 \text{ cm}\cdot\text{s}^{-1}$. The 50-, 200-, and 1000-m isobaths are contoured.

edge moorings. These moorings are along the 200-m isobath, except moorings 49 and 12, which are along the 500-m isobath in the west and east, respectively (see Figure 1.2-1 for mooring locations). The monthly average currents were based on the 40-hr low-passed time series. For months with less than 10 days worth of data, no average current vector is shown. Note that scales are different for each set of figures.

SSHA maps, supplemented by geopotential anomaly maps and AVHRR images, established which Loop Current eddies influenced shelf edge currents. Eddies are identified by mooring in Tables 2.5.2-2 (for 10-m current meters), 2.5.2-3 (100-m), and 2.5.2-4 (190-m/490-m). Shading denotes months for which there were less than 10 days of data. Many other cyclonic and anticyclonic features are in the velocity maps; several are discussed below.

At 10-m depths, shelf edge currents affected by Loop Current eddies flow in an anticyclonic or clockwise direction. This usually appears in the figures as intensified upcoast flow along the shelf edge with, perhaps, onshelf flow to the west and offshelf flow to the east (e.g., see western moorings 4 and 8 for February 1993 in Figure 2.5.2-1). There may be associated cyclonic eddies giving rise to a bifurcation of currents at the shelf edge (e.g., see moorings 4 - 8 for May 1993 in Figure 2.5.2-1). This pattern shows a counterclockwise flowing cyclone. The bifurcation occurs in the region where the Loop Current eddy and its associated western cyclone meet. For all patterns, the magnitude of the currents depends on how close the eddy is to the shelf edge. In general, the closer the eddy, the stronger the currents. As the eddy encroaches on the shelf, deep ocean waters are moved onto the shelf on the west side of the eddy and shelf waters are moved off on the east side (Appendix D).

The currents at the 100-m depth usually are similar to the 10-m currents, but are of lesser magnitude (Figures 2.5.2-3 and 2.5.2-4). They also may exhibit a shift in the location of the axis of the eddy relative to the moorings. For example, the 100-m currents for July 1993 (Figure 2.5.2-3) show the influence of Loop Current Eddy V on the western shelf edge, as do the 10-m currents (Figure 2.5.2-1). Currents at these levels suggest that Eddy V was tilted toward the west, which would put its center at 100 m to the east of its center at 10 m.

The bottom moorings at the shelf edge were approximately 10 m above the sea floor. Throughout the LATEX period, the 190-m currents were predominantly downcoast, even when a Loop Current eddy was adjacent to the shelf edge (Figures 2.5.2-5 and 2.5.2-6). However, for some cases when an eddy was close to the northern shelf edge, such as were Eddy T and Eddy V, the 190-m currents exhibited flow patterns similar to those of the 10-m and 100-m currents. This occurred, for example, with the July 1992 currents (compare the currents at 10 m and 100 m with those at 190 m in Figures 2.5.2-1, 2.5.2-3, and 2.5.2-5, respectively). Figure 2.5.1-2 shows that, at that time, Eddy T was centered relatively close to the northern shelf edge. In contrast, when a Loop Current eddy was farther from the northern shelf edge, the currents at 190-m had a cyclonic pattern rather than the anticyclonic pattern present in the 10-m and 100-m currents. This occurred with the August 1992 currents (compare the currents in Figures 2.5.2-1, 2.5.2-3, and 2.5.2-5). Figure 2.5.1-2 shows that in August Eddy T had moved southward away from the northern shelf edge.

Table 2.5.2-2. Identification of Loop Current eddies influencing the 10-m shelf edge currents based on the monthly average velocity (see Figures 2.5.2-1 and 2.5.2-2); shading indicates there were insufficient data available to determine a monthly average.

Year	Month	49	04	05	06	07	08	09	10	11	48	13	12	
1992	April	T	T	T	T	T								
	May	T	T	T	T	T								
	June	T	C	T	T	T	T					M	M	
	July	T	C	T	T	T	T							
	August	T	C	T	T	T						U	U	
	September													
	October	C	C	C	C	C	V	V						
	November	V		V	V	V	V							
	December	V												
	1993	January	V					V						
		February		V	V	V	V	V						
		March		V	V	V	V	V						
April			C	C	V	V	V							
May			C	V _n										
June			V _n					W	W					
July			V _n	M	M				W	W				
August			V _n	M				W _n	W _n					
September			V _n											
October														X _e
November			C			C		X _w	X _w					X _e
December		X _w	C	X _w			X _e	X _e						
1994	January				X _w	X _w	X _w	X _w						
	February													
	March								M	M	M			
	April													
	May	M				M	M	M						
	June	M				M	M	M						
	July	X _n				X _n	X _n	X _n						
	August													
	September													
	October													
	November	M	M		M					Y	Y	Y	Y	

- | | |
|--|--|
| T = Remnant of Eddy Triton | X _e = Eddy eXtra East |
| V = Eddy Vazquez | X _w = Eddy eXtra West |
| V _n = Eddy Vazquez North | X _n = Eddy eXtra North |
| W = Eddy Whopper | Y = Eddy Yucatan |
| W _n = Eddy Whopper North | C = Loop Current eddy-associated western cyclone |
| M = Miscellaneous anticyclonic feature | |

Table 2.5.2-3. Identification of Loop Current eddies influencing the 100-m shelf edge currents based on the monthly average velocity (see Figures 2.5.2-3 and 2.5.2-4); shading indicates there were insufficient data available to determine a monthly average.

Year	Month	49	04	05	06	07	08	09	10	11	48	13	12	
1992	April													
	May		T	T	T									
	June											M	M	
	July		C	C	T	T								
	August													
	September													
	October													
	November	V		V	V			V						
	December	V												
	1993	January	V					V						
		February		V	V	V								
		March		V	V	V								
April			C	C	V									
May			C	C	V _n									
June		V _n	V _n	V _n	V _n									
July		V _n	C	V _n	V _n			M	M	M		W		
August		V _n		M	M	M		W _n						
September		V _n		V _n	V _n	V _n								
October														
November		C	C	C	C	C	X _w					X _e		
December		C	C	C	C		X _w							
1994	January						X _w	X _w	X _w					
	February													
	March							M	M	M				
	April													
	May	M				M	M		M	M	M	M		
	June	M				M								
	July	X _n				X _n	X _n							
	August	X _n	X _n											
	September	M	M	M										
	October													
	November	M	M	M										

T = Remnant of Eddy Triton

V = Eddy Vazquez

V_n = Eddy Vazquez North

W = Eddy Whopper

W_n = Eddy Whopper North

M = Miscellaneous anticyclonic feature

X_e = Eddy eXtra East

X_w = Eddy eXtra West

X_n = Eddy eXtra North

Y = Eddy Yucatan

C = Loop Current eddy-associated western cyclone

Table 2.5.2-4. Identification of Loop Current eddies influencing 190-m/490-m shelf edge currents based on monthly average velocity (see Figures 2.5.2-5 and 2.5.2-6); shading indicates there were insufficient data available to determine a monthly average. Moorings 49 and 12 are at 490-m depth.

Year	Month	49	04	05	06	07	08	09	10	11	48	13	12	
1992	April													
	May													
	June			T	T	T								
	July			C	C	T								
	August		C	C	C									
	September		C	C	C	C								
	October		C	C										
	November	V		V	V	V								
	December	V												
	1993	January	V											
		February	V	V	V									
		March	V	V	V									
April		V	C	C		V								
May		V _n	C	C		V _n								
June		V _n	V _n	V _n		V _n								
July		C	C	C										
August		V _n	V _n	V _n										
September		V _n	C	C		V _n								
October		C	C			C								
November		C	C			C								
December		C	C	C	X _w	X _w								
1994	January													
	February	C	C	C	C									
	March													
	April													
	May					M								
	June					M								
	July					X _n								
	August													
	September													
	October													
	November													

T = Remnant of Eddy Triton

V = Eddy Vazquez

V_n = Eddy Vazquez North

W = Eddy Whopper

W_n = Eddy Whopper North

M = Miscellaneous anticyclonic feature

X_e = Eddy eXtra East

X_w = Eddy eXtra West

X_n = Eddy eXtra North

Y = Eddy Yucatan

C = Loop Current eddy-associated western cyclone

The currents at the 490-m depths were much smaller in magnitude than those higher in the water column and often were dissimilar in direction (Figures 2.5.2-5 and 2.5.2-6). At mooring 49, when the 10-m and 100-m currents were moving to the northeast under the influence of a Loop Current eddy, the 490-m currents are moving at about a 90° angle to the southeast; e.g., for November 1992 through January 1993 compare the currents at mooring 49 in Figure 2.5.2-5 to currents at 100-m in Figure D-3. Water moved offshore at this depth.

Cyclonic eddies associated with Loop Current eddies have been mentioned. There are also anticyclonic features that appear associated with the Loop Current eddies. An example is from the 10-m currents for July 1993 (Figure 2.5.2-1). Eddy V caused anticyclonic shelf edge circulation between approximately 94.5°W and 96.5°W. Yet the currents also exhibit anticyclonic flow characteristics between 93°W and 94.5°W. There, the current structure flows northeastward at about 94°W and southeastward at about 93.5°W. The geopotential anomaly map for this time (Figure H.1-8) shows the peanut-shaped Eddy V influencing the flows between 94.5°W and 96.5°W. It also shows a smaller anticyclonic eddy causing the circulation pattern seen between 93°W and 94.5°W. Note also in this geopotential anomaly map a third anticyclonic feature—Loop Current Eddy W—in contact with the shelf edge between 90°W and 93°W. The 10-m currents at the eastern shelf edge show the influence of this eddy.

A brief summary follows of how each Loop Current eddy influenced the shelf edge currents.

Eddy T. A remnant of Eddy T was adjacent to the western shelf edge from April 1992 through October 1992 (Figure 2.5.1-2). In May, it had moved westward to where it influenced the 10-m currents, which flowed roughly parallel to the bathymetry. In June, currents west of 94°W were affected. Flows at the shelf edge west of 96°W were cyclonic. In July and August, Eddy T moved west against the westernmost shelf edge. The anticyclonic currents increased in magnitude and, by August, the cyclonic currents all but disappeared. In September, when Eddy T moved south and away from the LATEX shelf edge, the 10-m current magnitudes diminished substantially and no anticyclonic currents were present. The 100-m currents behaved similarly to the 10-m currents. The bottom currents, however, were mainly cyclonic except in July 1992 when Eddy T was closest to the northern shelf edge. In October 1992, Eddy T was absorbed by Eddy V and no longer influenced the currents at the Texas-Louisiana shelf edge.

Eddy U. During most of its lifetime, Eddy U was too far from the Texas-Louisiana shelf to affect the shelf circulation (Figure 2.5.1-3). Early in its life, however, it was located adjacent to the far eastern shelf edge. In August 1992, it drew water off the shelf, as evidenced by drifter 2447 (Figure D-1). The 10-m currents at 90.5°W flowed southward and offshore at that time (Figure 2.5.2-1).

Eddy V. Eddy V influenced the currents at the Texas-Louisiana shelf edge from October 1992 through September 1993 (see Appendix D and Figure 2.5.1-4). In October, it and an associated cyclonic circulation to its north caused the 10-m currents at the shelf edge between

92°W and 94.3°W to flow eastward (Figure 2.5.2-1). At that time cyclonic eddies were located at the shelf edge to the west and east of Eddy V. Eddy V then moved west where, from November 1992 through March 1993, it caused currents at the shelf edge between 94°W and 96°W to flow mainly in an anticyclonic direction. In April and May, Eddy V split into northern and southern parts. The southern part moved southward away from the Texas-Louisiana shelf and exerted no further influence on the shelf edge currents. The northern part of Eddy V (Eddy V_n), however, affected currents between 94°W and 96°W from April until it dissipated in September 1993. Associated with Eddy V_n was a strong cyclonic eddy located to the west. This associate forced currents to move downcoast in April at the shelf edge at moorings 4 and 5. In May, the cyclone-anticyclone pair induced substantial flows between the shelf and offshore waters (see Appendix D).

Eddy W. Loop Current Eddy W formed in June of 1993 (Figure 2.5.1-5). It began to affect the far eastern portion of the LATEX shelf at about 90.5°W in late June (Figures 2.5.2-1, 2.5.2-3, and 2.5.2-5); currents flowed upcoast in response in June and July. In August, after Eddy W had split into two parts, its northern part, Eddy W_n, continued to drive the easternmost shelf edge currents. In September, Eddy W_n moved southward away from the Texas-Louisiana shelf edge and no longer influenced the currents. The shelf edge currents reversed direction and flowed downcoast at all depths.

Eddy X. Eddy X had split into two parts prior to influencing the shelf edge currents. In October 1993, the eastern part, Eddy X_e, affected the easternmost portion of the Texas-Louisiana shelf edge, causing the currents at 10-m and 100-m to flow upcoast (Figures 2.5.2-2 and 2.5.2-4). In November, the effects of both Eddy X_e and Eddy X_w were seen at the shelf edge, with Eddy X_w influencing the currents between 93.5°W and 94.5°W and Eddy X_e between 90°W and 92°W. By December, Eddy X_e had moved southward; its influence on the eastern shelf edge currents weakened and then ceased in January 1994. In December, Eddy X_w altered currents over the entire western shelf edge. This continued until February 1994, when Eddy X_w moved south and ceased to exert an influence over the shelf edge currents. The SSHA maps suggest that parts of Eddy X coalesced in the southwest Gulf. A remnant of Eddy X then appears to have extended northward in July 1994 to influence the shelf edge currents between 92.5°W and 95°W (Figures 2.5.2-2, 2.5.2-4, and 2.5.2-6).

Eddy Y. Eddy Y was adjacent to the eastern shelf edge in November 1994. It caused the 10-m currents between 90.5°W and 93°W to flow upcoast.

Loop Current eddy influence on shelf circulation

The major impact of the Loop Current eddies is felt at the shelf edge; over the inner shelf, eddies have less effect. This contrast can be seen in the 10-m current velocity fields for the whole shelf (Figures H.2-1 through H.2-3 of Appendix H).

Eddy influence on currents over the eastern shelf generally was limited to the outer shelf regime. For example, in November 1994, Eddy Y was adjacent to the eastern shelf edge

between 90.5°W and 93°W. It was a relatively young and strong eddy at that time. The currents in the region were strongly eastward at the shelf edge, but were weaker and in the opposite direction over the inner shelf regime (Figure H.2-3). Thus, the influence of Eddy Y was limited to the shelf edge.

Loop Current eddies can have effects over the central shelf that extend onto the shelf. One case of this occurred in October 1992. The SSHA maps show a cyclone to the north of and associated with Eddy V when that eddy was adjacent to the shelf between 92°W and 94°W (Figure 2.5.1-1). The 10-m currents show an eastward flow at the shelf edge where the cyclone-anticyclone pair meet and cyclonic circulation associated with the northern cyclone over the outer and inner shelf regimes. This cyclone would have been driven on its north side in part by the winds that are downcoast over the inner shelf at this time.

Over the western shelf, eddy influence often is limited to the shelf edge, but also can extend over the inner shelf. In January 1993, a relatively strong Eddy V occupied the northwest corner of the Gulf adjacent to the western shelf. The 10-m currents for that time show anticyclonic circulation at the western shelf edge (Figure H.2-2). Over the inner shelf, however, the currents were flowing downcoast, probably in response to the downcoast winds. Eddy V_n, however, influenced a larger area of the shelf. In May 1993, it was farther up on the slope than Eddy V had been earlier. It was part of the cyclone-anticyclone pair, discussed in Appendix D, that moved Gulf water onto the shelf and drew fresh water from the inner shelf across and off the shelf both south of the cyclone and east of Eddy V_n.

In summary, the Loop Current eddies are major drivers of shelf edge currents and frequently affect the outer shelf through exchanges of mass, energy, and water properties. Their impact on the inner shelf circulation is episodic. During such episodes, however, they can effect substantial exchanges between shelf and deep Gulf waters.

3 WATER MASS CHARACTERIZATION AND BUDGETS

3.1 Salinity and temperature distributions

Water masses of the upper open Gulf of Mexico

Surface waters of the Gulf of Mexico are greatly modified by heat and freshwater exchanges through the surface, river discharges, and wind mixing, but no subsurface water of consequence is thought to be formed locally. Waters from the global ocean enter the Gulf only through the Yucatan Channel from the Yucatan Basin of the Caribbean Sea. In the Caribbean, extrema in properties label four water masses in the upper 1000 m: Subtropical Underwater, 18°C Sargasso Sea Water (18° Water), Tropical Atlantic Central Water, and Antarctic Intermediate Water; the source regions for these waters are discussed in Morrison and Nowlin (1982). Morrison and Nowlin (1977) described the water masses found in the Loop Current of the eastern Gulf, and Morrison et al. (1983) described the water masses and properties found offshore in the Gulf.

The Subtropical Underwater is identified in the Caribbean Sea and the Loop Current of the eastern Gulf of Mexico by a subsurface salinity maximum at 150-250 m centered about $25.40 \text{ kg}\cdot\text{m}^{-3}$ in $\sigma\text{-}\theta$. In the Loop Current, maximum salinity values in this core are 36.6 to 36.8. Most of the water in the western Gulf of Mexico has a less pronounced upper salinity maximum—typically from 36.4 to 36.5. As the waters of the Loop Current enter the Gulf, those along its western boundary are vertically mixed by the interaction of the current with bathymetry, resulting in a flattening of the pronounced subsurface salinity maximum associated with the Subtropical Underwater source of those waters (Nowlin 1972). Moreover, after separation, Loop Current eddies eventually spin down in the Gulf. That process entails mixing, which likewise reduces the salinity at the maximum and may spread the lesser maximum over a larger range of depths—0-250 m according to Morrison et al. (1983), based on measurements made in the offshore western Gulf north of 22°S and west of 94°W.

Nevertheless, the salinity values usually found at the upper salinity maximum in anticyclonic Loop Current eddies in the western Gulf are normally still great enough to identify the feature. In the region offshore from the Texas-Louisiana shelf maximum salinities in such rings often exceed 36.6 and are found commonly at depths between 100 and 150 m.

In the Caribbean Sea and Loop Current, the water mass below Subtropical Underwater is 18° Water. It is found at depths from 200 to 400 m and is identified by an oxygen maximum centered about $26.5 \text{ kg}\cdot\text{m}^{-3}$ in $\sigma\text{-}\theta$. Oxygen values greater than $4.2 \text{ ml}\cdot\text{l}^{-1}$ are found in the Caribbean near entrances of this water from the greater North Atlantic. Within the Loop Current, oxygen maxima are only between $3.6\text{-}3.8 \text{ ml}\cdot\text{l}^{-1}$. Remnants of this water can be identified by weak relative oxygen maxima with values slightly greater than $3 \text{ ml}\cdot\text{l}^{-1}$ near $\sigma\text{-}\theta$ of $26.5 \text{ kg}\cdot\text{m}^{-3}$ in some western Gulf stations, but oxygen is not a useful tracer there.

Tropical Atlantic Central Water is identified by relative minima in vertical profiles of dissolved oxygen. In the Caribbean Sea and Loop Current, it is found from 400 to 700 m and identified by oxygen values below $3 \text{ ml}\cdot\text{l}^{-1}$ centered about 27.15 in sigma- θ . This water is clearly seen with similar characteristics in the western Gulf of Mexico although at depths closer to 400 m.

Beneath the Tropical Atlantic Central Water and extending over a vertical range of 700 to 1200 m are remnants of the Antarctic Intermediate Water. This water is identified in the Caribbean and Loop Current by a nitrate maximum, a phosphate maximum, a salinity minimum, and a silicate maximum found at increasing depths. This water is clearly seen in the western Gulf, although it is too deep to affect the shelf regime.

Characteristics offshore of the Texas-Louisiana shelf

In Figure 3.1-1 are plotted potential temperature versus salinity for three stations taken during LATEX A spring hydrographic cruise H05. All three were along the 200-m isobath, located as follows:

Station 81	27° 55.1'N	92° 37.5'W,
Station 205	27° 16.8'N	96° 15.2'W, and
Station 209	27° 45.7'N	95° 17.2'W.

Station 81 was removed from any apparent eddy (Figure H.1-7) and in this discussion represents the far field for rings in the western Gulf. Station 209 was in the shoreward limb of an anticyclonic Loop Current eddy (Vazquez), and station 205 was in the shoreward limb of a cyclone associated with the anticyclone.

For potential temperatures (θ) less than about 17°C there is little difference between the characteristics at the three stations. Above that temperature the curves become distinct with decreasing depth. The salinity maximum above 36.6 at station 209 identifies these waters as derived from the Loop Current—and so marks this station as being within a Loop Current eddy. The far field, represented by station 81, has the lowest salinity maximum associated with Subtropical Underwater of the three stations, as expected. Station 205, within a cyclone spun up by Eddy Vazquez, has θ -S characteristics intermediate between the Eddy Vazquez station 209 and the far field station 81. It is likely that waters were mixed between the anticyclone and the far field in the process of forming the cyclone.

In Figure 3.1-2 are vertical profiles of potential temperature and salinity for stations 81 and 209. Comparison of the potential temperature profiles shows that warm water extended deeper into the water column in the anticyclone than in the far field (e.g., waters of 20°C occur at about 60 m in the far field, but at approximately 140 m in the anticyclone). The salinity profiles show the high salinity (≥ 36.6) Subtropical Underwater signature of Loop Current eddies at about 135 m at station 209, while the far field station 81 had a salinity

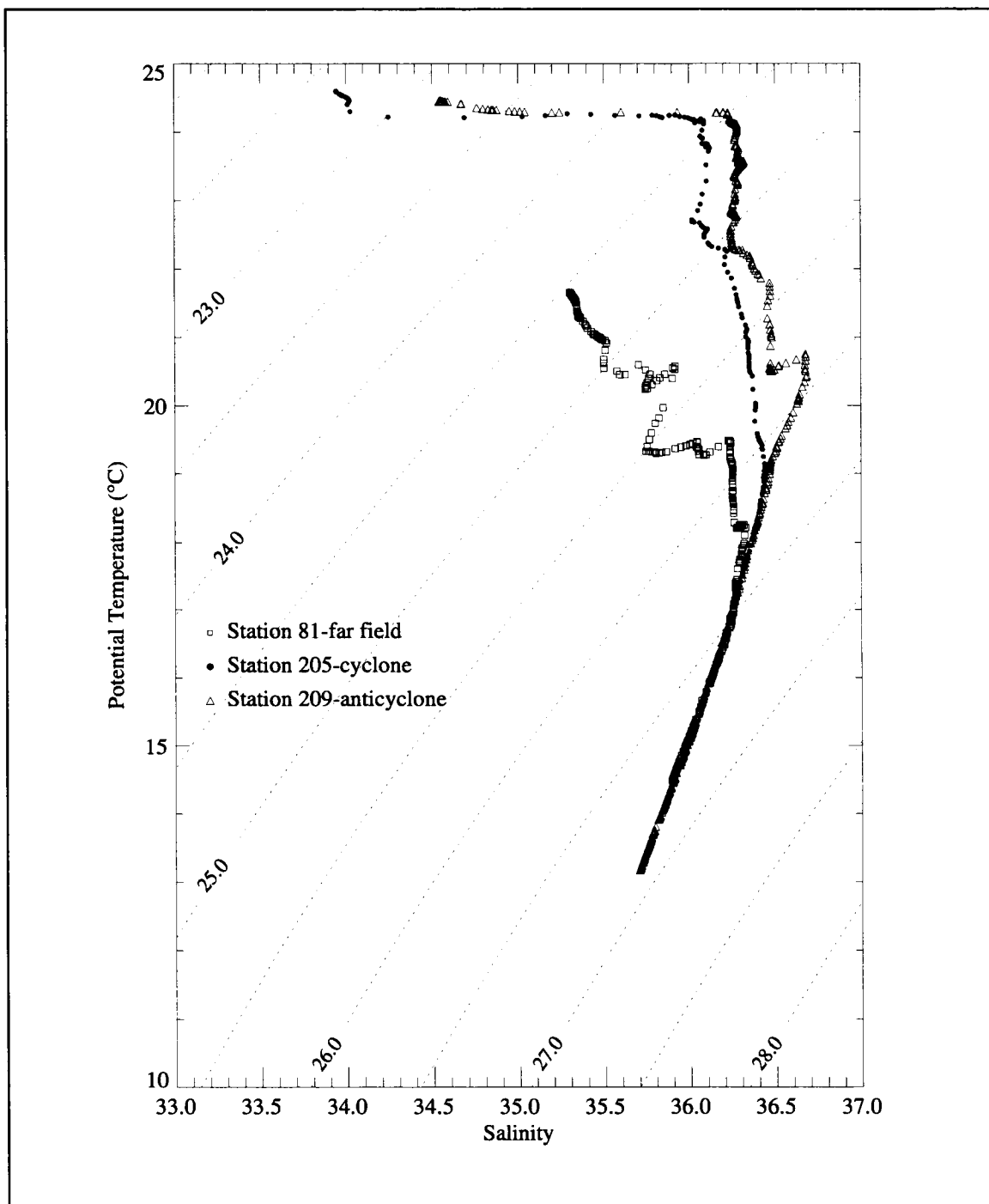


Figure 3.1-1. Potential temperature-salinity diagram for stations along the 200-m isobath during cruise H05. Station 209 (triangle) is in the northern edge of Eddy V_n ; station 205 (circle) is in the western cyclone; station 81 (square) is in the far field.

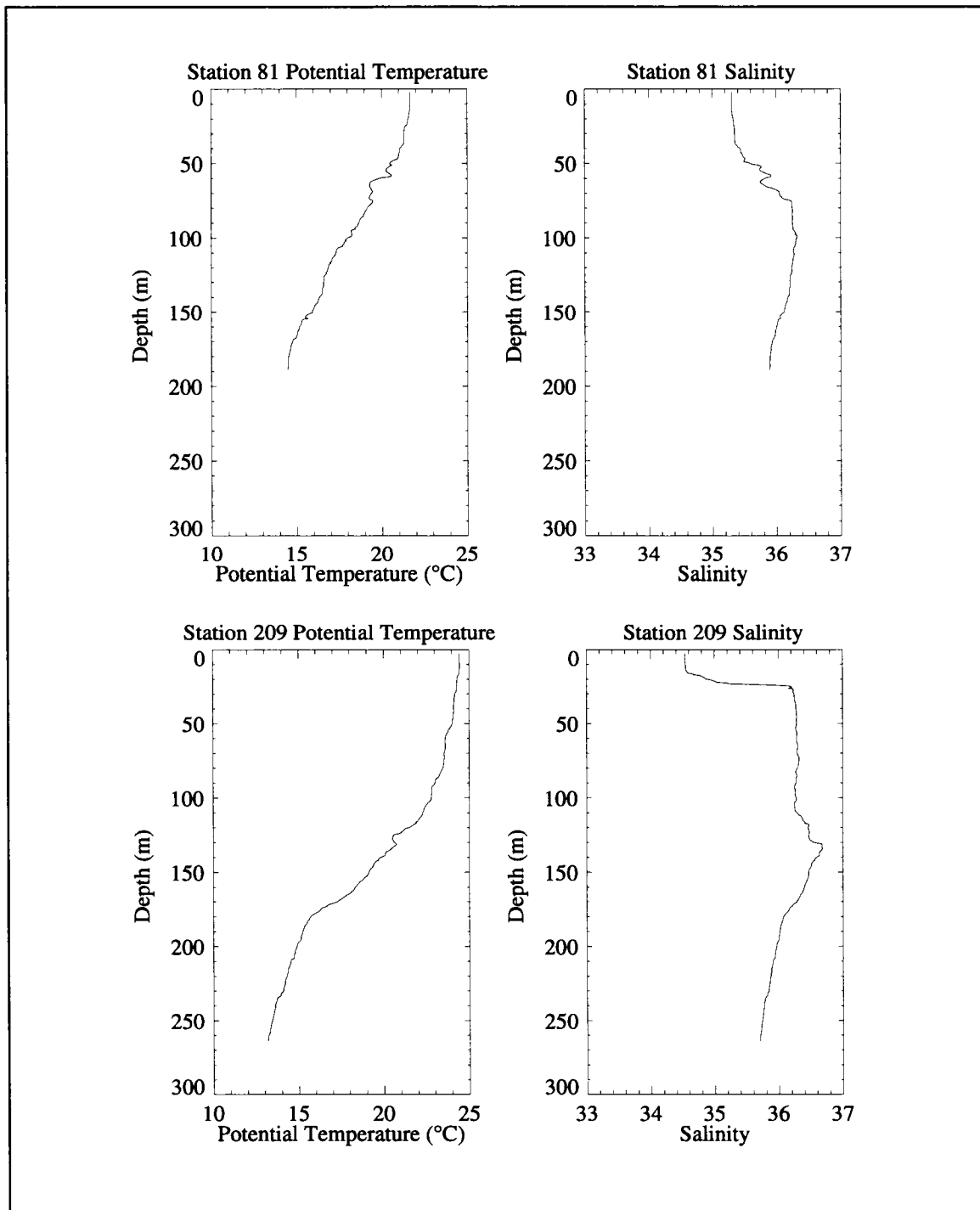


Figure 3.1-2. Potential temperature and salinity profiles for stations along the 200-m isobath during cruise H05. Station 81 is in the far field. Station 209 is in the northern edge of Eddy V_n .

maximum under 36.4. The salinity in the upper 25 m at station 209 was relatively fresh compared to that of the far field. This is evidence of fresh water being drawn off the shelf by the eddy (see Appendix D for more details).

Temperature-salinity relation for the Texas-Louisiana shelf

In Figure 3.1-3 are shown composite potential temperature versus salinity plots for all stations taken during the four LATEX A hydrographic cruises in 1993: H04, 4-13 February; H05, 25 April-11 May; H06, 25 July-7 August; and H07, 7-21 November. There was only one winter cruise, H04, and it covered only the eastern shelf. The other three cruises shown covered the entire shelf and are quite similar to composite plots for other cruises in the same season.

In each of the composite plots in Figure 3.1-3, the temperature-salinity relationship is seen to be very tight for the deeper portion of the water column. Above this level, but starting at depths below the salinity maximum of the Subtropical Underwater remnant, the θ -S relations differ for different stations—more so approaching the sea surface. The differences below the salinity maximum likely result from stations located in different dynamical regimes (e.g., rings or far field as discussed above) and thus in different waters. Note that the relation below the salinity maximum is tighter for cruise H04 than for the other cruises. This probably is because cruise H04 covered only the eastern shelf and there were no rings adjacent to the eastern shelf during this cruise period (see Figure H.1-6).

Above the salinity maximum, the interstation differences are due mostly to changes in the θ -S properties of the surface layers. The trend toward colder and more uniform temperatures during winter is seen from the February cruise H04. By comparison temperatures of the surface layers are all warmer and are less uniform in April-May (H05). They are much warmer and with a trail of salinities less than 20 by summer (H06). The fall distribution (H07) shows marked cooling of the surface waters since summer and much higher minimum surface salinities.

Temperature and salinity at the outer shelf boundary (200-m isobath)

Given in Figures 3.1-4 and 3.1-5 are vertical sections of temperature and salinity along the 200-m isobath for each LATEX A hydrographic cruise. These may be considered the offshore boundary conditions in temperature, salinity, and thus density for the shelf during the times of those cruises. It might be noted that time series show salinity changes typically with time scales of 20-50 days over most of this shelf (Section 4.3.2); thus, the surveys (which lasted only about 10 days) may be considered as representative of a running average of the salinity distribution over a period longer than the sampling period.

In winter (February) cooling and surface mixing produce a relatively deep (order of 100 m) surface mixed layer. This represents the most voluminous temperature class (see

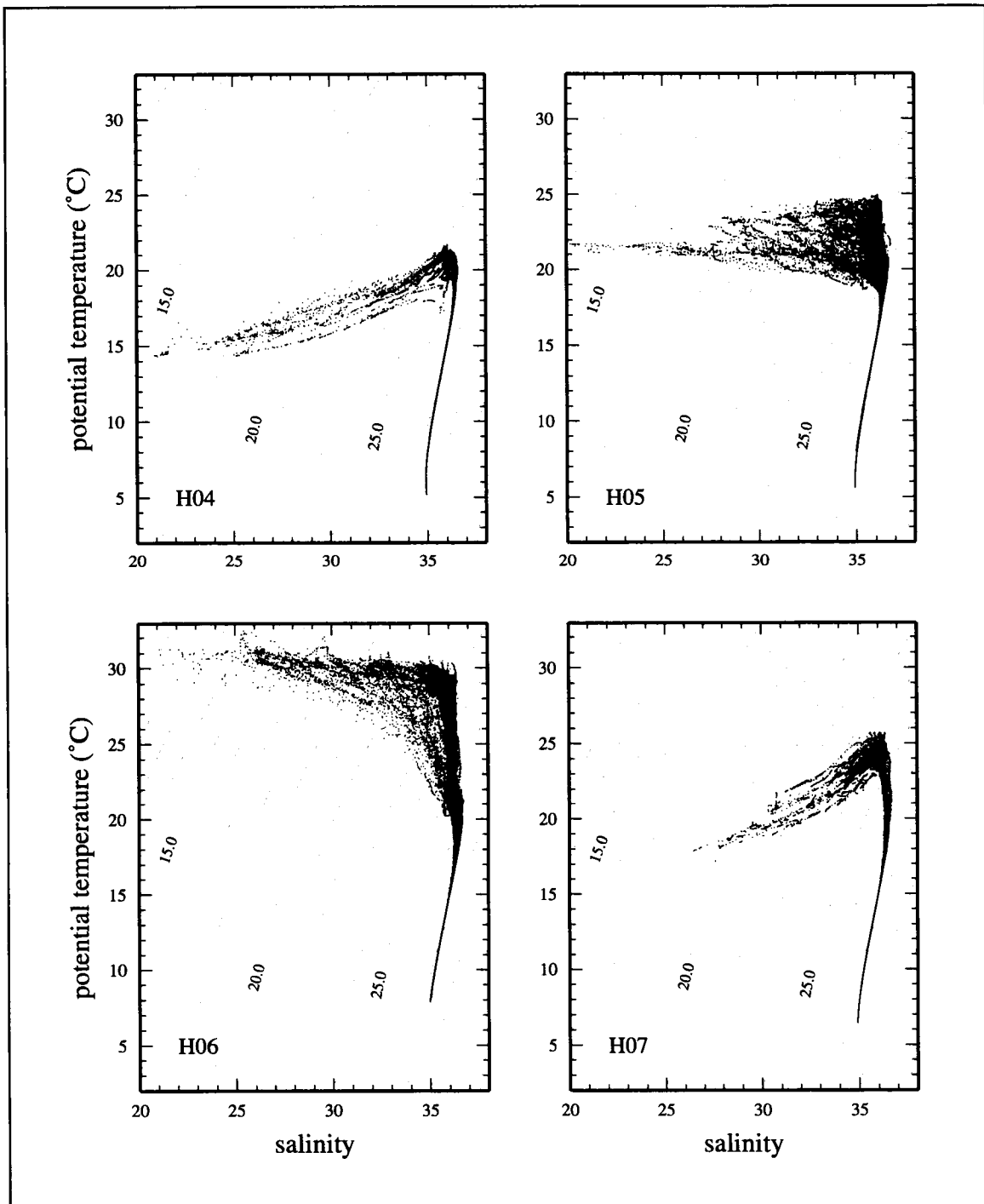


Figure 3.1-3. Composite plots of potential temperature versus salinity for the LATEX A 1993 hydrographic cruises H04 (4-13 February), H05 (25 April-11 May), H06 (25 July-7 August), and H07 (6-22 November).

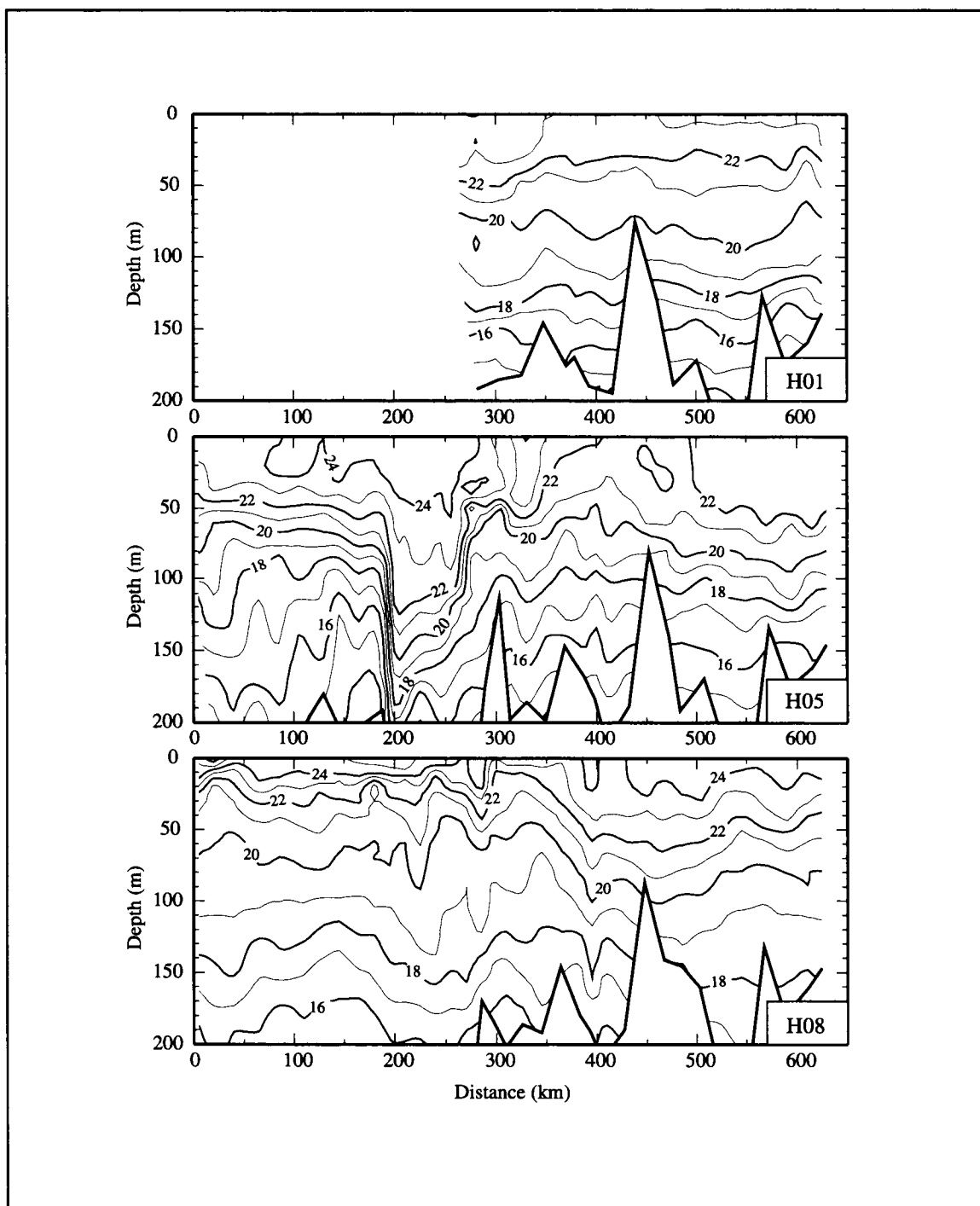


Figure 3.1-4a. Contours of temperature in vertical section along the 200-m isobath for LATEX A cruises in spring (May). Sections are from southwest on the left to east on the right.

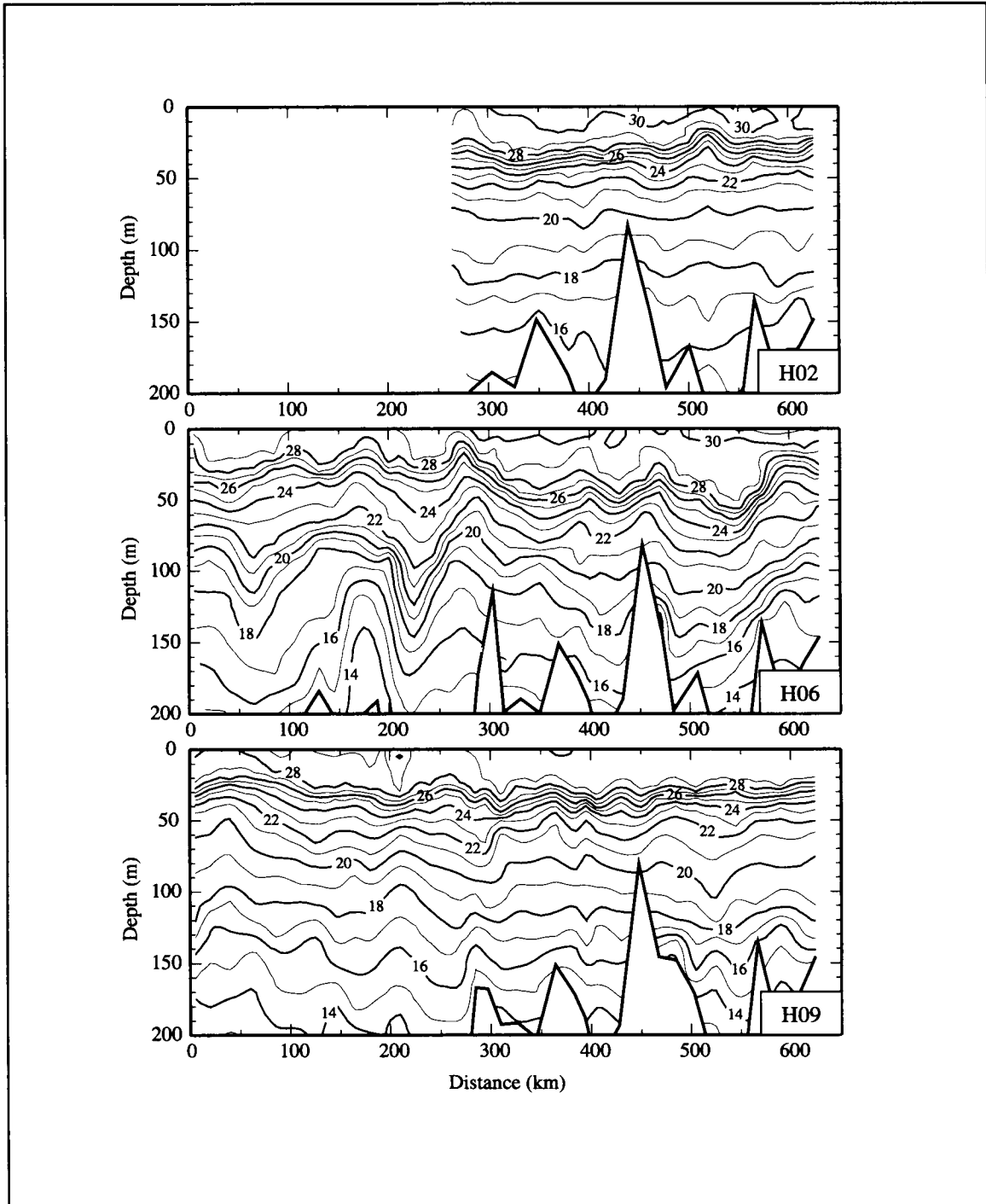


Figure 3.1-4b. Contours of temperature in vertical section along the 200-m isobath for LATEX A cruises in summer (July-August). Sections are from southwest on the left to east on the right.

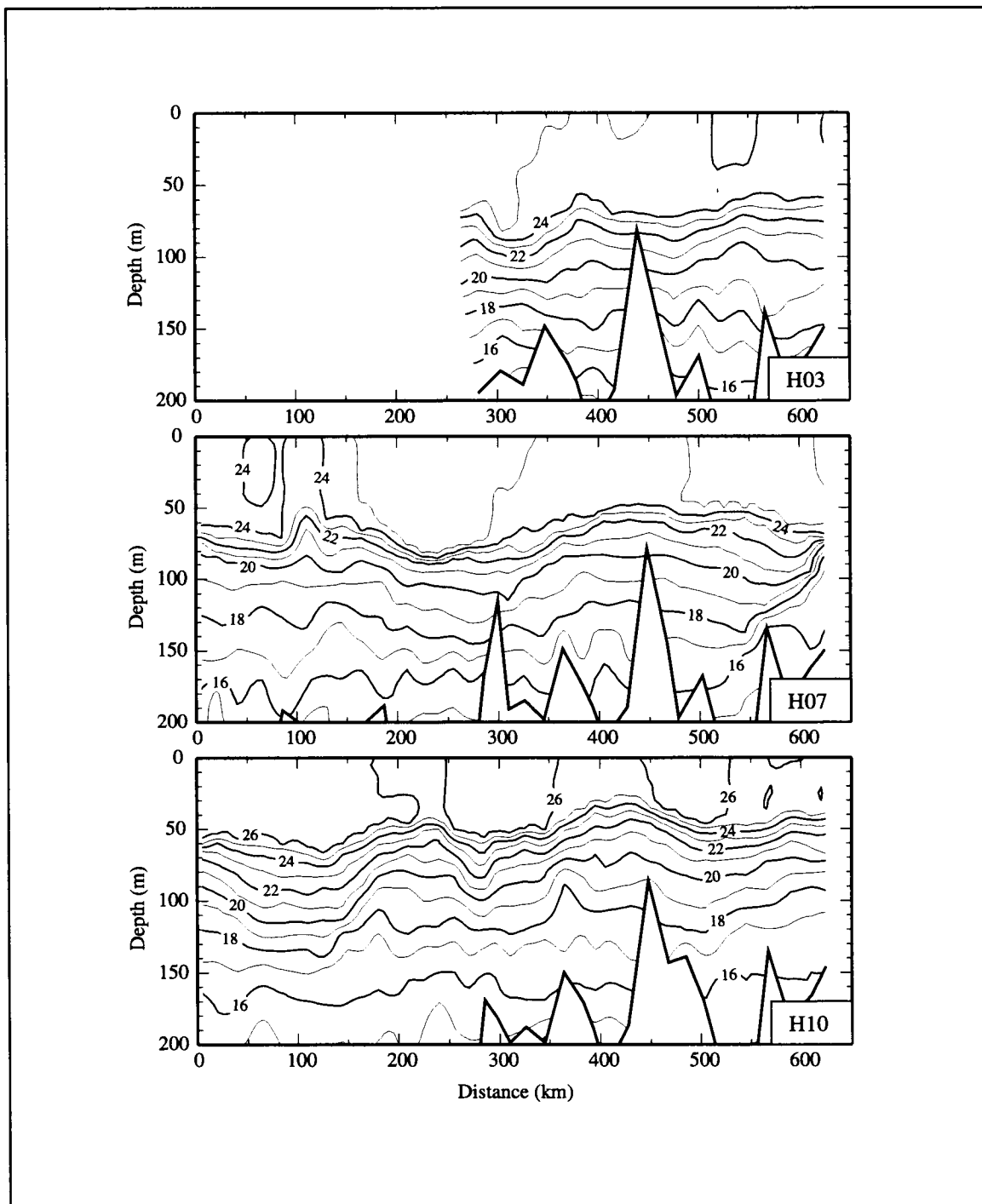


Figure 3.1-4c. Contours of temperature in vertical section along the 200-m isobath for LATEX A cruises in fall (November). Sections are from southwest on the left to east on the right.

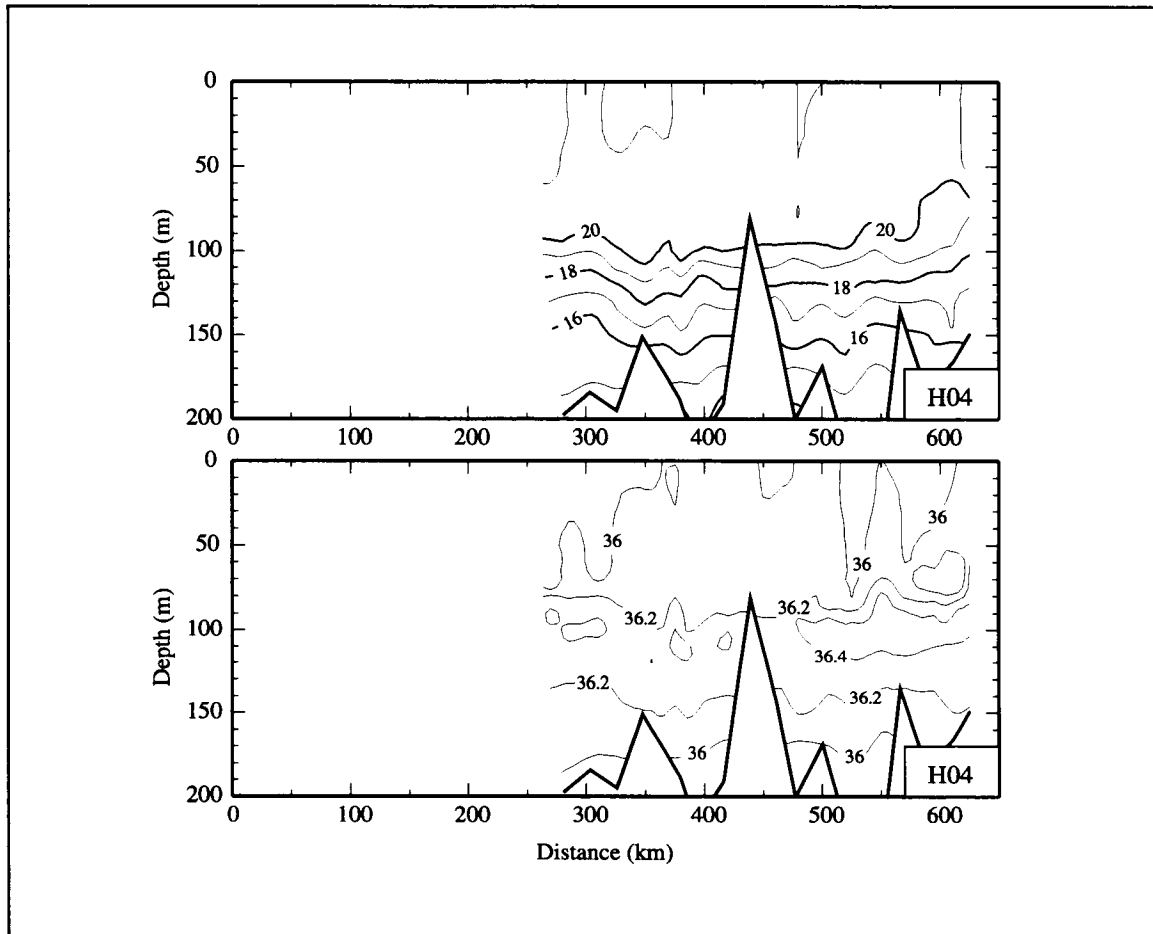


Figure 3.1-4d. Contours of temperature (top) and salinity (bottom) in vertical section along the 200-m isobath for LATEX A cruises in winter (February). Sections are from southwest on the left to east on the right.

Appendix E for a volumetric T-S census based on LATEX A hydrography). Spring (May) heating of this relatively deep surface mixed layer results in the most uniform vertical temperature gradient for any season. Continued spring and summer heating produces thermoclines with large gradients, and the light winds of summer result in a shallow mixed layer. Surface cooling and stronger winds of fall cool and deepen the mixed layer, creating large volumes of surface and sub-thermocline waters.

Anticyclonic rings detached from the Loop Current and their associated cyclonic eddies are often found just offshore from the shelf break (the 200-m isobath). (See Section 2.5.1 for a chronology of anticyclonic eddies near the shelf edge.) As discussed above, these Loop Current eddies have high salinity cores. Thus, the presence of these anticyclonic rings off the Texas-Louisiana shelf may be expected to affect the salinity of the shelf by transfer of

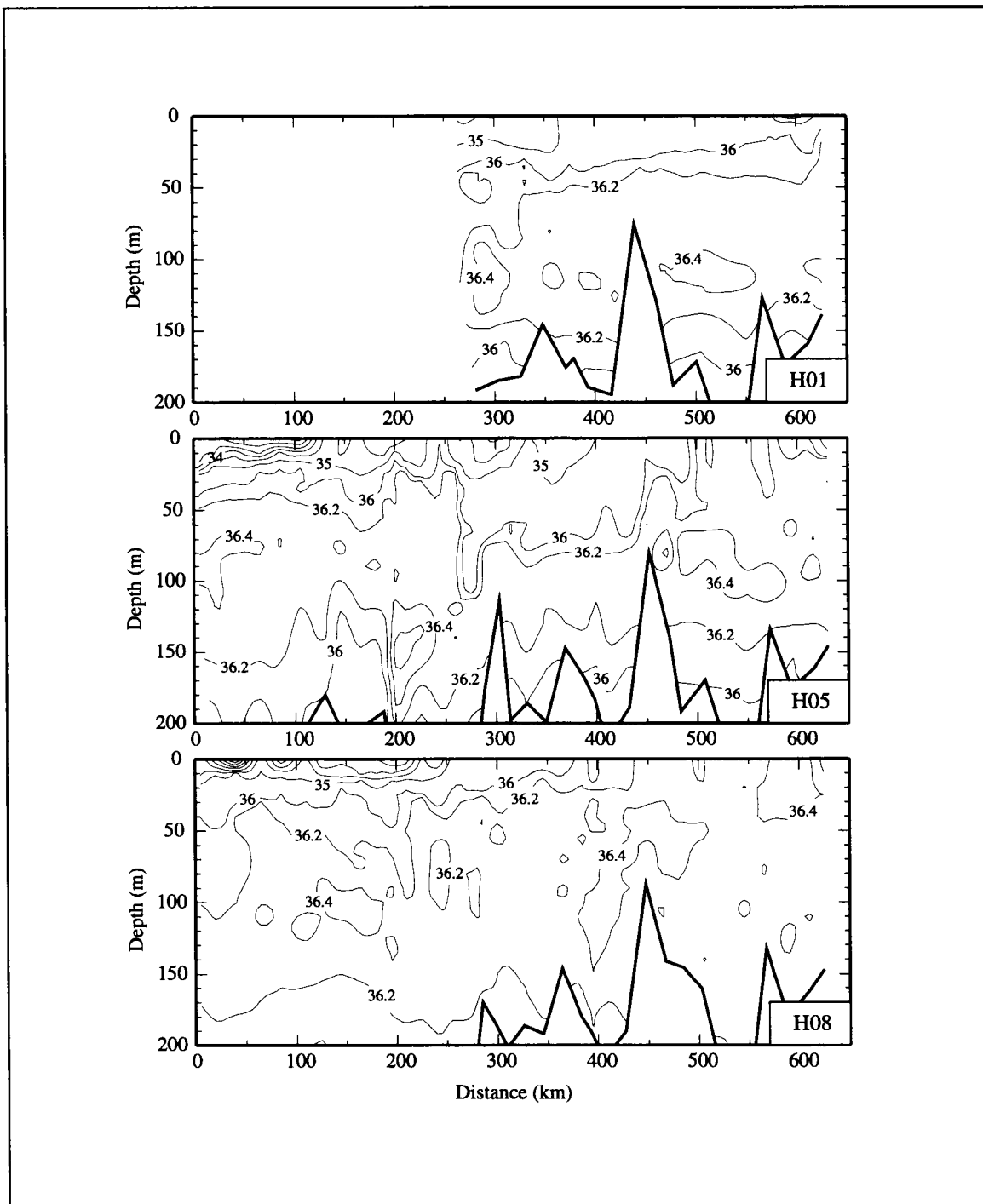


Figure 3.1-5a. Contours of salinity in vertical section along the 200-m isobath for LATEX A cruises in spring (May). Sections are from southwest on the left to east on the right.

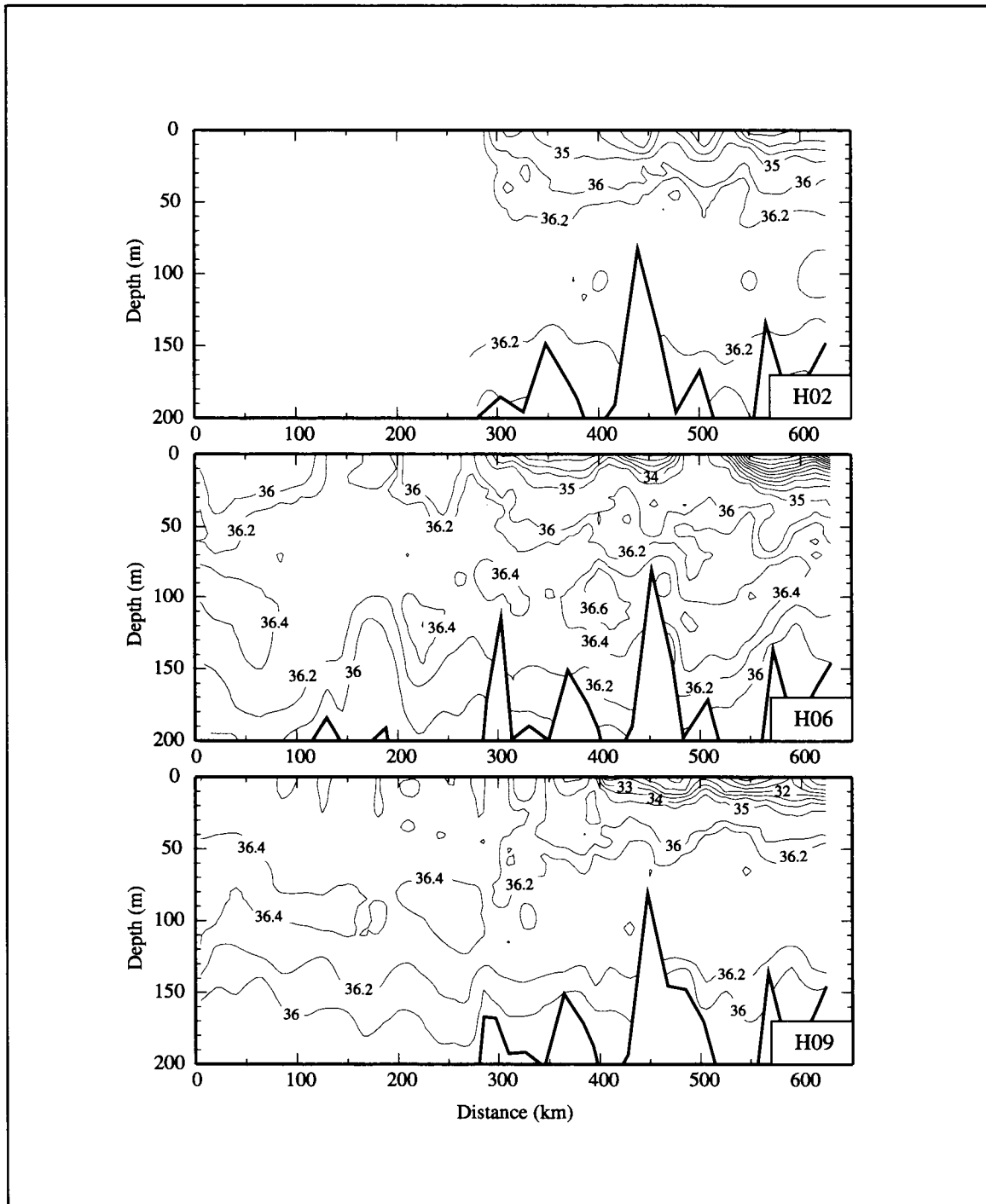


Figure 3.1-5b. Contours of salinity in vertical section along the 200-m isobath for LATEX A cruises in summer (July-August). Sections are from southwest on the left to east on the right.

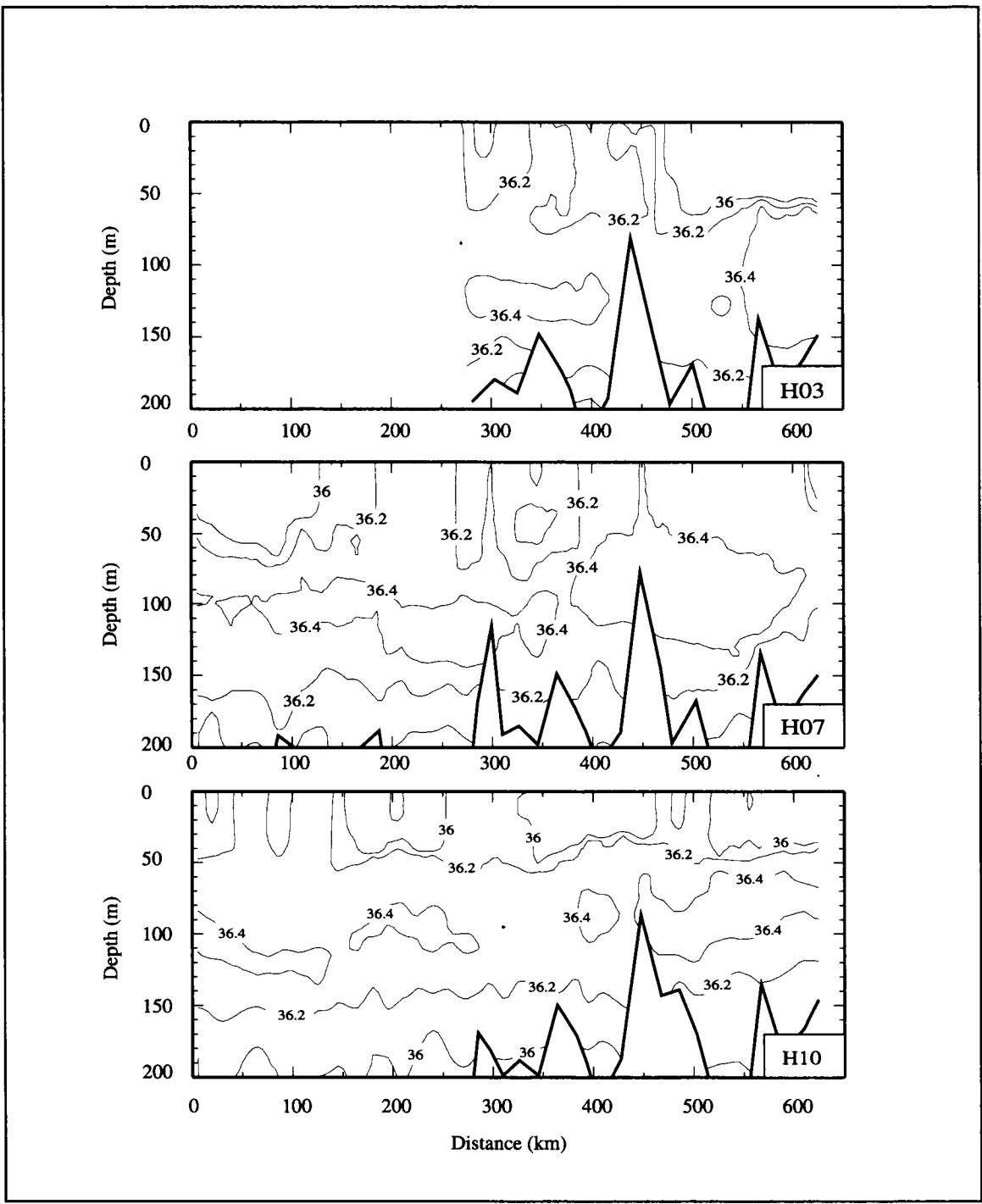


Figure 3.1-5c. Contours of salinity in vertical section along the 200-m isobath for LATEX A cruises in fall (November). Sections are from southwest on the left to east on the right.

waters between the rings and the shelf. Several examples of such intrusions are seen in Figure 3.1-5; one during July-August 1993, cruise H06, is discussed in Appendix E.

Lateral distributions of hydrographic variables over the Texas-Louisiana shelf

Presented in Section 4.2 are mean surface fields of temperature, salinity, and geopotential anomaly relative to 70 db; mean bottom fields of temperature, salinity, and density; and some individual LATEX A horizontal distributions. Fields of surface geopotential anomaly relative to 400 db and of 20°C isotherm depth based on LATEX A and C and GulfCet are given in Appendix H.1. In those sections, as well as throughout Section 4, the circulation and its effects on property distributions are discussed. Surface and bottom distributions are given in the LATEX A hydrographic data report (Jochens et al., 1998). Additional distributions of nutrients and oxygen are shown in Section 5.

Variation of temperature and salinity over the shelf from vertical sections

Here we first describe the salinity and temperature distributions over the shelf during 26 April-11 May 1993 based on vertical sections from cruise H05 along hydrographic survey lines 1 (at approximately 90.5°W), 4 (at approximately 94°W), and 8 (at about 26°N). We believe this sufficiently characterizes the major features to be seen during spring. Then, we describe salinity and temperature distributions along the same lines from cruise H06, 26 July-7 August 1993. Contrasting those distributions makes clear the principal differences between summer and nonsummer, when the flow over the inner shelf is upcoast and downcoast, respectively. Finally we present the temperature and salinity distributions on line 4 for fall cruise H07, 7-21 November 1993, and winter cruise H04, 6-13 February 1993.

The spring salinity and potential temperature distributions are presented in Figure 3.1-6 and 3.1-7. Based on salinity, one can see the extent of the intrusion of Subtropical Underwater onto the edge of the shelf. Salinities greater than 36.2 or 36.4 intrude well past the shelf break at depths of 50 to 150 m. Even higher salinities (> 36.6) were found at the shelf edge between lines 4 and 8 associated with Eddy Vazquez (see Appendix D for details). The influence of the Mississippi-Atchafalaya river system also is seen in the salinity field. Salinities less than 24 were present inshore on line 1, located east of the outflow of the Atchafalaya River. That influence is more strongly seen on line 4, where nearshore values were below 20 and offshore gradients were large—indicative of a narrow coastal plume that extended to the bottom in depths of 10 m or less. Downcoast off Brownsville (line 8) there was little influence by the Mississippi-Atchafalaya river system; nearshore salinities were close to 33.

Figure 3.1-7 shows cross-shelf temperature distributions in spring. Surface water is warmer offshore (lower latitudes) on lines 1 and 4, as expected. Highest temperatures were observed at line 8, which is at considerably lower latitude.

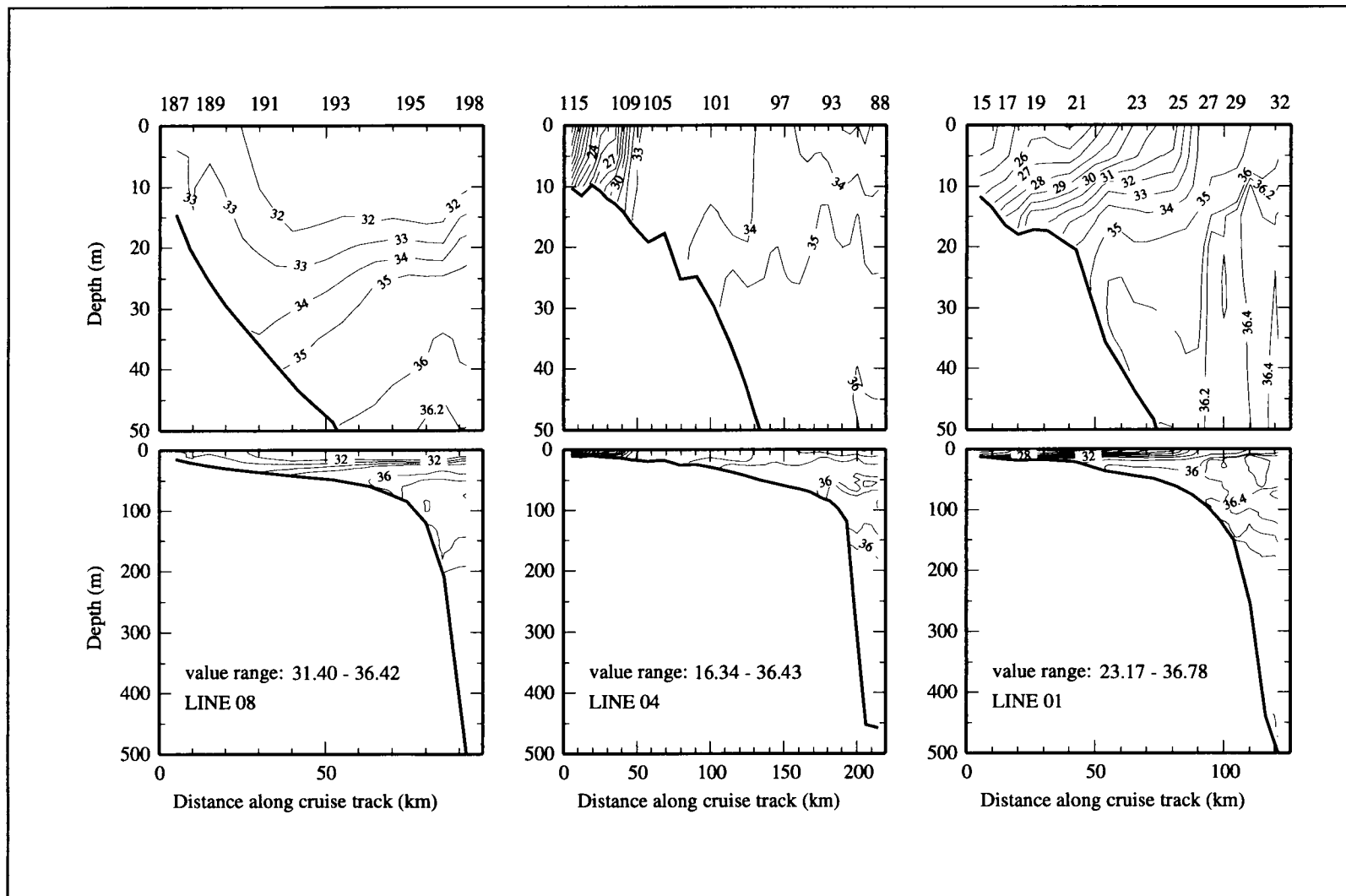


Figure 3.1-6. Salinity in vertical sections on lines 8, 4, and 1 from LATEX A cruise H05, 25 April-11 May 1993.

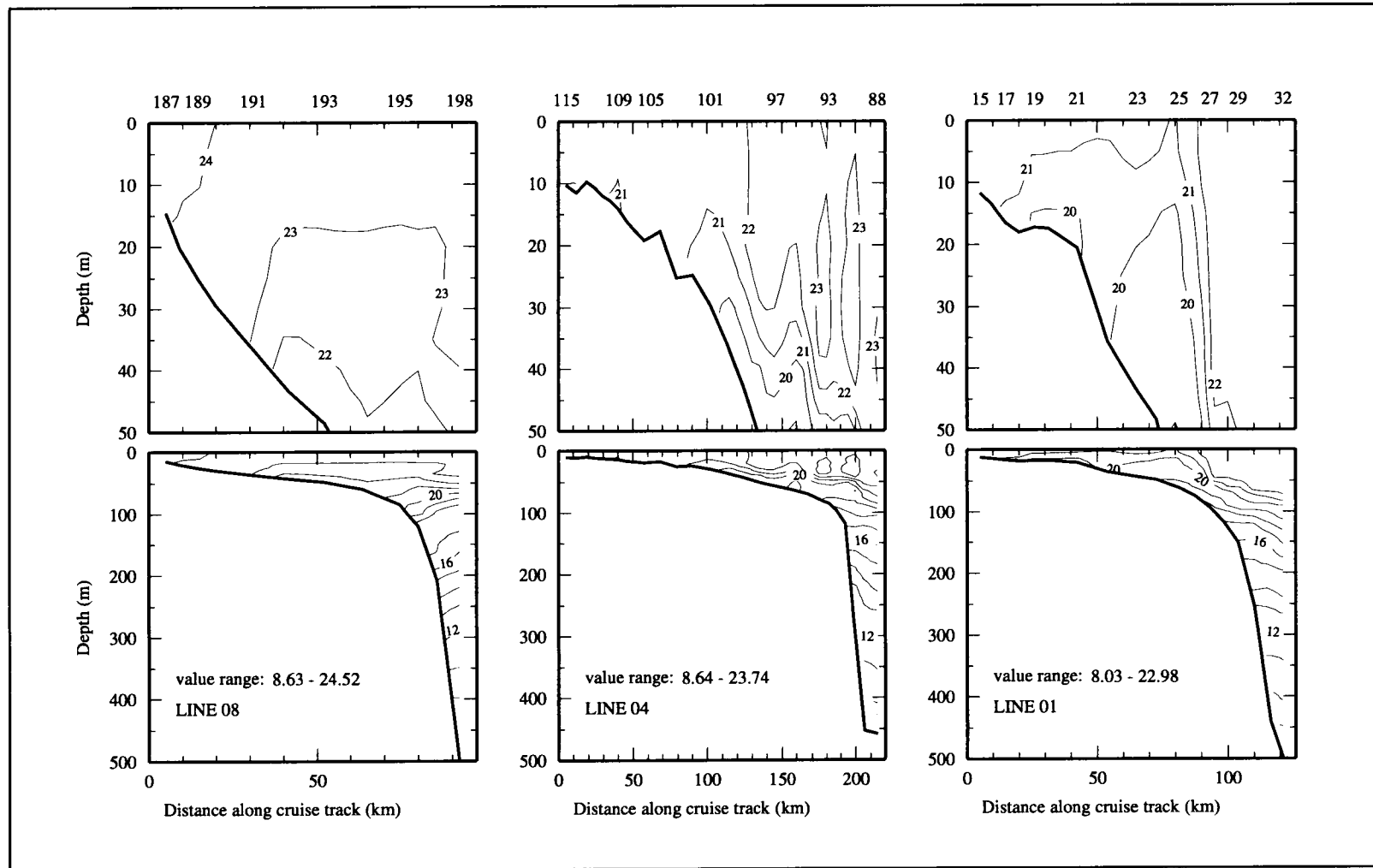


Figure 3.1-7. Potential temperature (°C) in vertical sections on lines 8, 4, and 1 from LATEX A cruise H05, 25 April-11 May 1993.

In Figures 3.1-8 and 3.1-9 are shown the vertical sections of salinity and potential temperature for summer 1993, three months after the sections of Figures 3.1-6 and 3.1-7. Very fresh waters ($S < 15$) were present near surface at the inshore end of line 1. Note that 1993 was a July record high for Mississippi-Atchafalaya river system discharge. In contrast to the spring distribution, there was relatively little fresh water on line 4 during summer of 1993; on line 8 the salinities were above 36. This is attributed to the upcoast flow during the summer, which advects high salinity water from off Mexico and holds freshwater discharge over the extreme eastern shelf (discussed in Section 4 and Appendix E). Remnants of Subtropical Underwater are found over the shelf edge in summer as well as nonsummer.

Summer temperatures show much more vertical stratification than for spring due to continued surface heating. Surface temperatures increased downcoast. Distributions of both salinity and temperature are indicative of strong coastal upwelling. This is stronger at line 8 off south Texas than further upcoast, but seems evident in all sections. For further discussion of summer coastal upwelling, see Appendix B.3.

By November (Figure 3.1-10), the parade of cold air outbreaks from over the continent had completely changed the stratification. Both salinity and temperature gradients had large horizontal components, with lower values of both nearshore. Such changes associated with a cold air outbreak were documented in some detail for the Texas shelf by Nowlin and Parker (1974), and for the Louisiana shelf effects of outbreaks have been reported by Mortimer et al. (1988). Other references related to cold-air outbreaks over the Gulf of Mexico include: Crisp and Lewis (1992), Henry (1979), Henry and Thompson (1976), Huh et al. (1984), Huh et al. (1978), Konrad (1996), Lewis and Crisp (1992), Liu et al. (1992), and Rabin et al. (1993). A pertinent reference is *Journal of Applied Meteorology*, Vol. 31, No. 8 (August 1992) on "Air-sea interaction and air mass modification over the Gulf of Mexico".

February 1993 (Figure 3.1-11) evidenced lower temperatures than November due to increased cooling and mixing attendant on the winter season. Inshore salinities were larger in February than in November. This may be expected on average because the mean Mississippi-Atchafalaya river system discharge is at minimum in October-November. However, it should be noted that there is large interannual variation in the patterns found in any month or season, as discussed in Section 4.2.

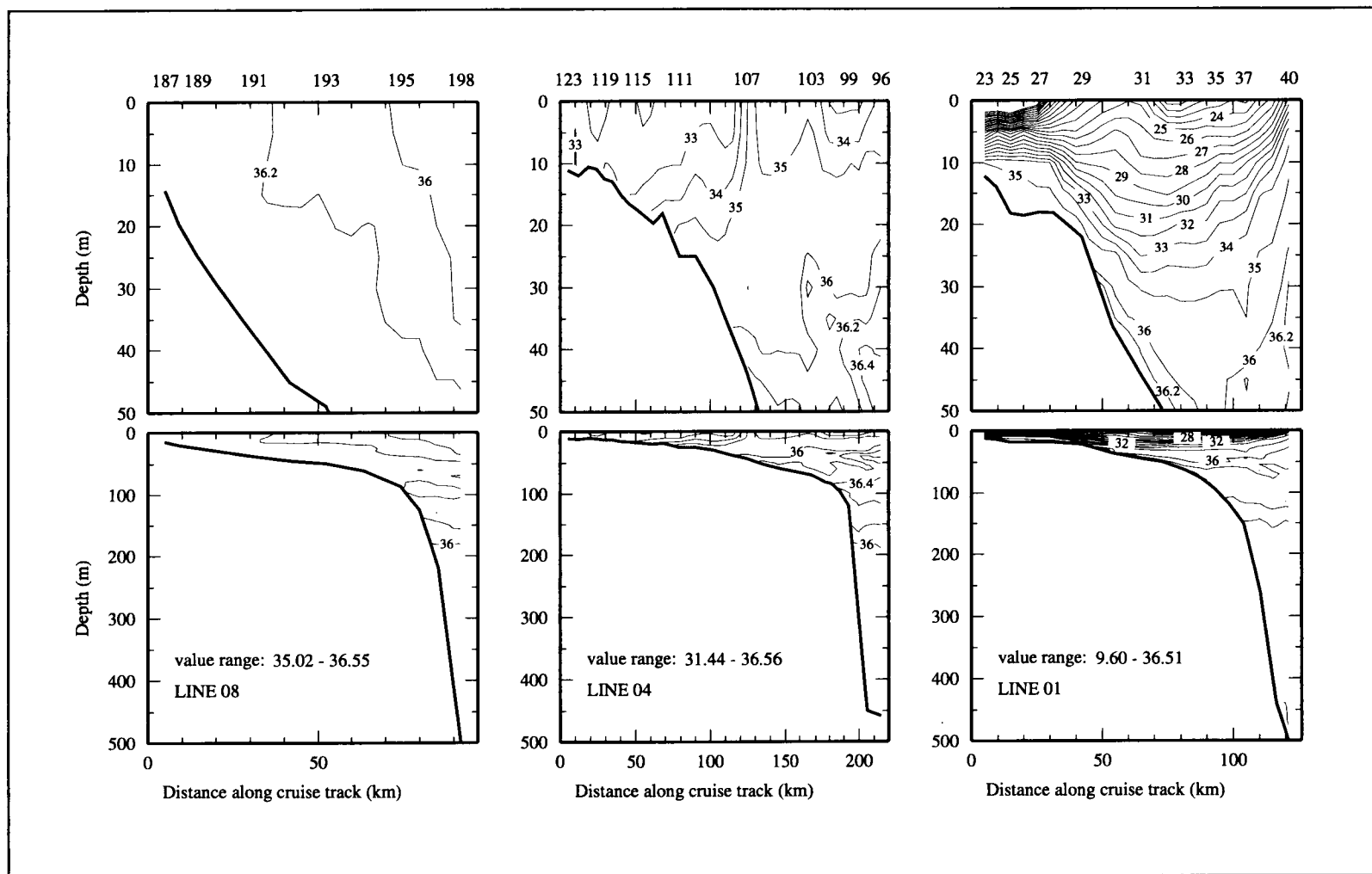


Figure 3.1-8. Salinity in vertical sections on lines 8, 4, and 1 from LATEX A cruise H06, 25 July-7 August 1993.

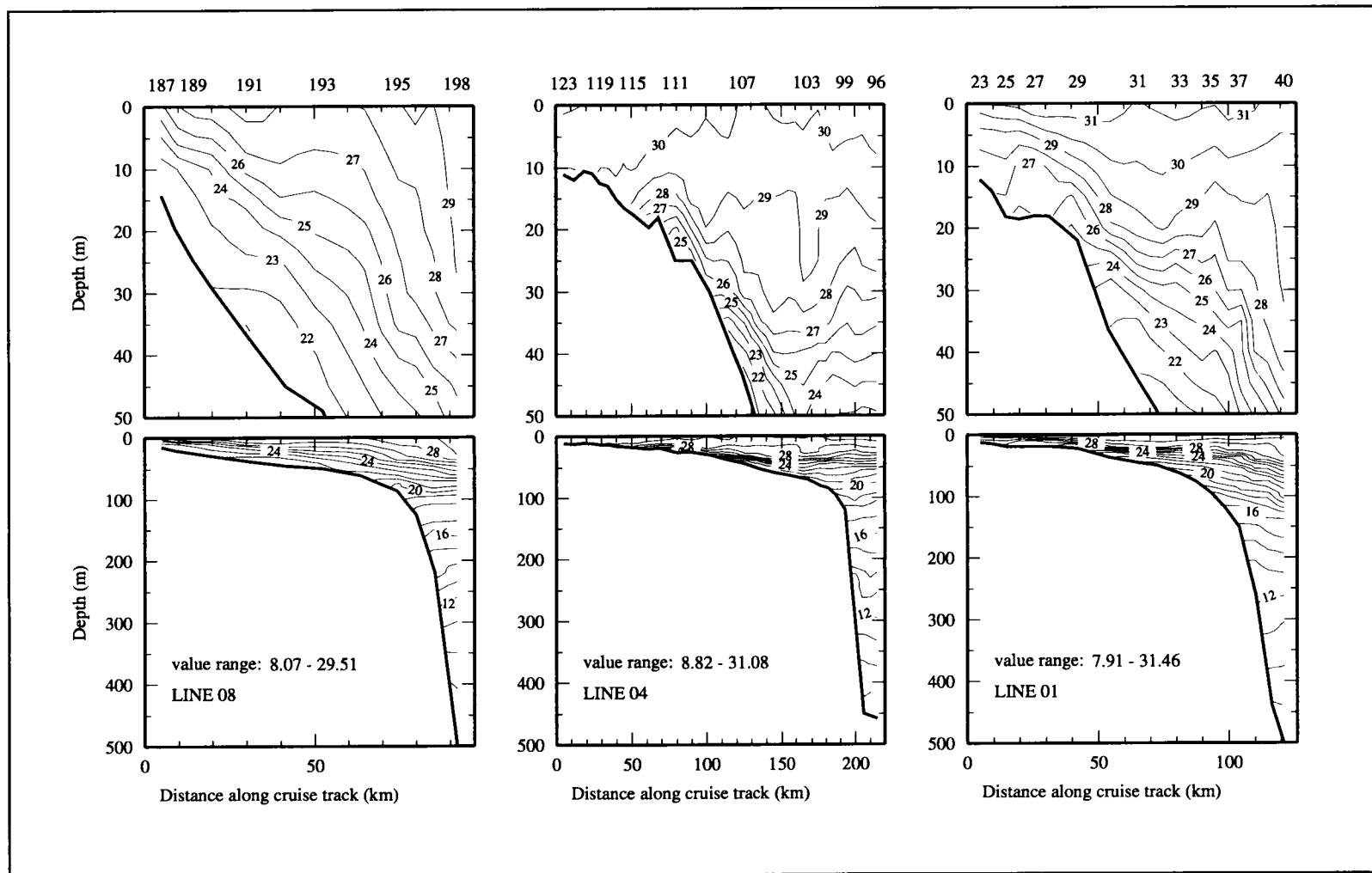


Figure 3.1-9. Potential temperature ($^{\circ}\text{C}$) in vertical sections on lines 8, 4, and 1 from LATEX A cruise H06, 25 July-7 August 1993.

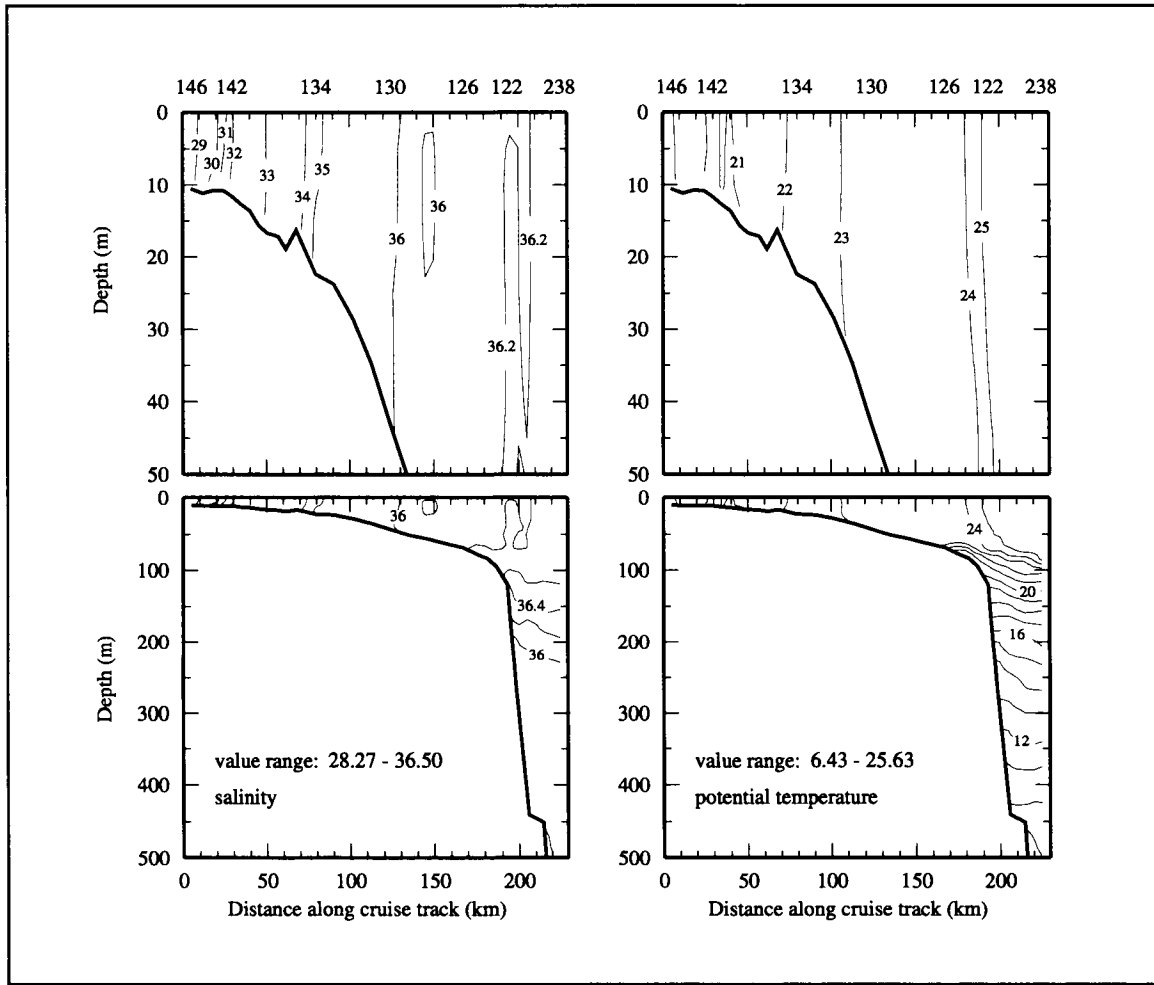


Figure 3.1-10. Salinity and potential temperature ($^{\circ}\text{C}$) in vertical sections on line 4 from LATEX A cruise H07, 6-22 November 1993.

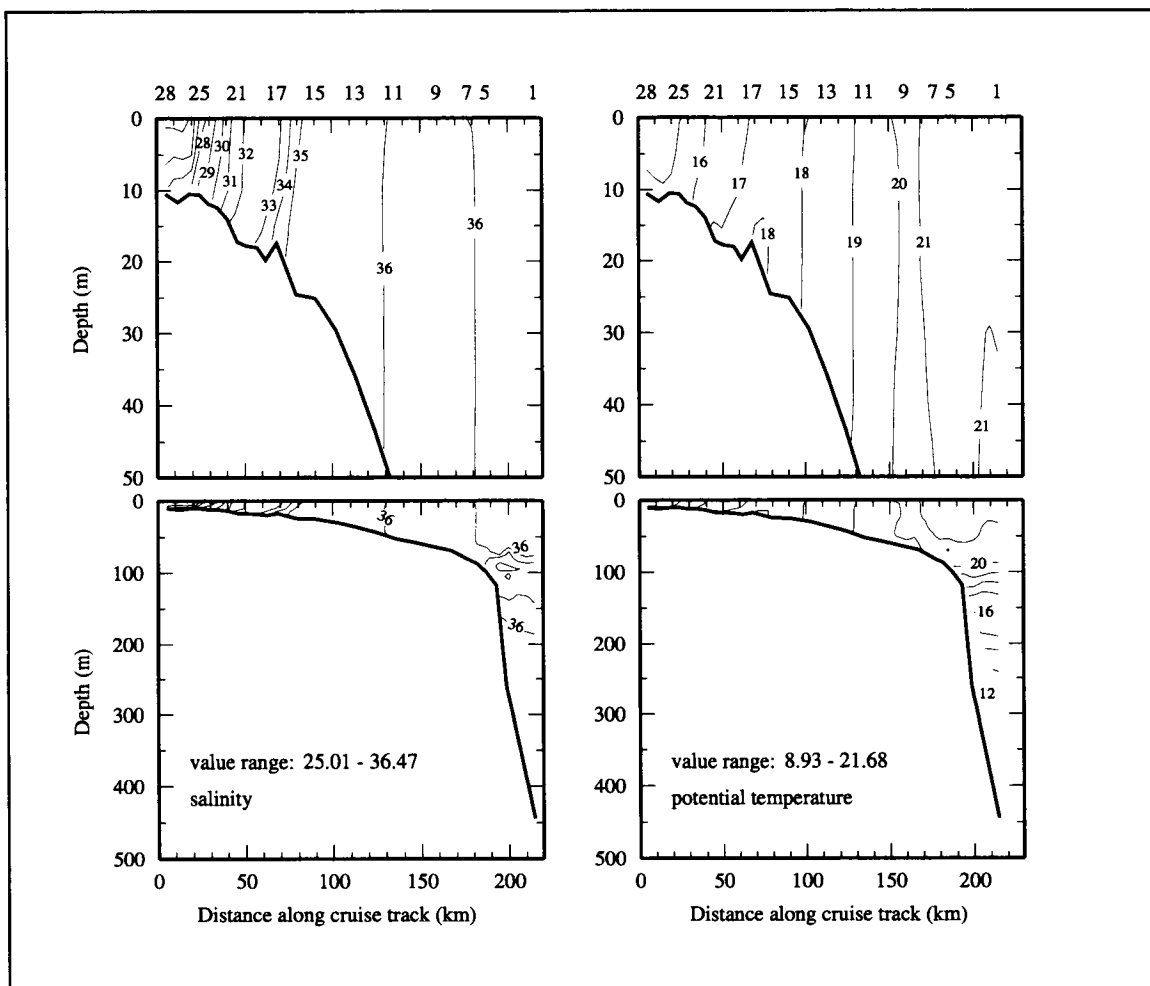


Figure 3.1-11. Salinity and potential temperature ($^{\circ}\text{C}$) in vertical sections on line 4 from LATEX A cruise H04, 4-13 February 1993.

3.2 Heat and freshwater budgets

Oceanic temperatures vary with location and season as a result of a balance between the gain and loss of heat due to a number of variables: solar heating, back radiation, evaporation, condensation, conduction, dissipation, and redistribution by currents. Internal heating due to dissipation of turbulent kinetic energy and exchanges with the sea floor are usually ignored because these effects are relatively small and little is known about their temporal or spatial distributions. Tracking thermal energy in the ocean is called a heat budget study and is based on the principle of conservation of (heat) energy. This analysis entails balancing the thermal energy crossing the sea surface of a hypothetical water column with the energy stored within and transferred through the lateral boundaries of the column. Similarly, salinity is considered to be a conservative quantity and is the result of the addition or removal of freshwater by: precipitation, evaporation, river input, and redistribution by currents. Salinity distributions are best determined by a freshwater budget; i.e., by balancing the fresh water (rather than the salt) crossing the top and sides of the hypothetical water column with the freshwater stored within. The reference ocean in this study is one with a uniform temperature of 0°C and a uniform salinity of 37. The heat energy followed is the energy in excess of that contained in water at 0°C. The freshwater component followed is the freshwater needed to dilute an ocean with a constant salinity of 37 down to the observed salinity.

Heat and freshwater budgets were computed for the Texas-Louisiana shelf for the period April 1992 to November 1994, using vertical profiles of temperature and salinity collected during the LATEX A hydrography cruises and contemporaneous estimates of air-sea exchanges and hydrologic inputs from collateral sources. The budget parameters (heat and freshwater storage and their rates of change) derived from the hydrographic data were computed either as instantaneous fields or as difference fields. The instantaneous fields were computed on the basis of individual cruise data; difference fields entailed computation of the rate of change of conditions between consecutive cruises. The interval between cruises was approximately three months, except for one five-month interval. This permitted the computation of eight difference fields centered on the middle month of each 3-month interval. Computations based on 3-month intervals correspond directly to those used by Etter (1975, 1983) and by Etter et al. (1985, 1987). A ninth difference field centered on the middle month of the 5-month interval is also included. The first four LATEX A hydrography surveys covered only the eastern shelf; the six subsequent cruises covered the whole shelf. The only other data measured directly were daily values of river discharge obtained from the U.S. Geological Survey (USGS) and from the U.S. Army Corps of Engineers. CTD station locations for a typical full-shelf cruise (94J in this case), are shown on the basemap in Figure 3.2-1.

Surface heat flux and precipitation estimates were obtained from other sources. The NOAA National Center for Environmental Prediction (NCEP) medium-range forecast model (MRF) routinely generates surface heat flux parameters on a global grid. MRF estimates of surface fluxes of radiation and latent and sensible heat for 1992-1994 were purchased from the

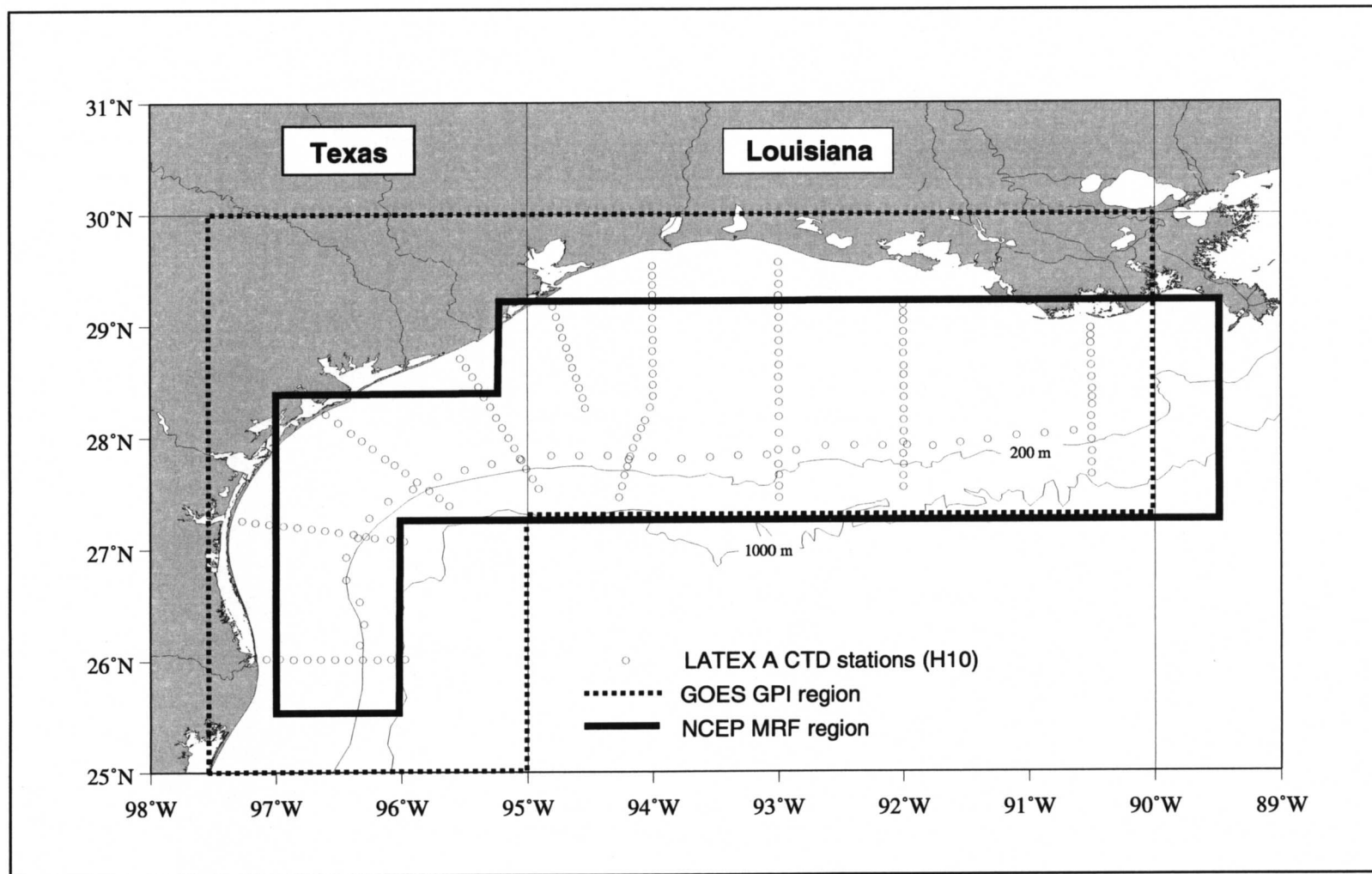


Figure 3.2-1. Basemap showing LATEX A CTD stations for typical full-shelf cruise (circles) and coverage areas for GOES GPI precipitation estimates (dashed line) and for NCEP estimates of surface fluxes (solid line).

National Center for Atmospheric Research. Monthly precipitation estimates were obtained from NOAA's GOES (Geosynchronous Operational Environmental Satellite) Precipitation Index (GPI), which is based on daily infrared satellite imagery. The region for which NCEP and GPI estimates were used is shown in Figure 3.2-1. These supplemental heat flux and precipitation estimates were derived from operational products; they may not be of the same quality as research data. In the absence of direct observations, however, these derived products afforded us the opportunity to complete the heat and freshwater budgets and to obtain flux estimates not possible otherwise.

To assess the derived budget terms, climatological and historical data were assembled for comparison with 1992-1994 estimates. Expanded discussions of the calculations, collateral data products, and historical baseline data appear in Etter (1996). That report also contains maps of the spatial distribution of the heat and freshwater budget terms for the study period which do not appear here. Much of the material here is distilled from Etter (1996) and, on occasion, material from his report appears here verbatim. Etter (1996) built upon the previous heat and freshwater budget investigations of Etter (1975, 1983), Etter and Cochrane (1975), and Etter et al. (1985, 1987).

Heat and freshwater budget equations

The heat and freshwater budget equations used in this study follow.

The heat budget equation is

$$Q_N = Q_R - Q_A = Q_T + Q_V,$$

where:

- Q_N = net oceanic heat gain,
- Q_R = radiation balance at the sea surface ($= Q_S - Q_B$),
- Q_S = net absorbed solar radiation (visual and near infrared) at the sea surface,
- Q_B = effective back (terrestrial) radiation (far infrared) at the sea surface,
- Q_A = net turbulent heat flux from the sea surface ($= Q_E + Q_H$),
- Q_E = turbulent flux of latent heat ($= L \times E$),
- L = latent heat of evaporation,
- E = rate of evaporation,
- Q_H = turbulent flux of sensible heat,
- Q_T = rate of oceanic heat storage, and
- Q_V = heat flux divergence due to currents.

The freshwater budget equation is

$$F_w = (P+R) - E - W,$$

where: F_w = freshwater flux divergence,
 P = rate of precipitation,
 R = rate of river discharge,
 E = rate of evaporation, and
 W = rate of oceanic freshwater storage.

Calculations for the 1992-1994 budgets used Q_T , W , and R values based on direct measurements. Q_R , Q_B , Q_H , Q_E , and E were based on NCEP MRF model output. P was taken from the GOES GPI. Q_V and F_w were calculated as residuals. The historical or climatological baseline values used for comparison with the 1992-1994 results are from various sources as discussed in Etter (1996).

Estimates of heat budget terms

Q_N . The net oceanic heat gain (Q_N) represents the difference between the radiation balance at the sea surface (Q_R) and the net turbulent heat flux from the sea surface (Q_A). Alternatively, Q_N also represents the sum of the rate of oceanic heat storage (Q_T) and the heat flux divergence (Q_V). Q_N was calculated as $Q_R - Q_A$ using estimates obtained from NCEP. The change in Q_N during the field experiment (Figure 3.2-2) indicated Texas-Louisiana shelf experiences a net gain of heat in the spring and summer and a net loss during the fall and winter.

Q_R , Q_S , Q_B . The radiation balance at the sea surface (Q_R) is the difference between the heat gain due to absorbed (short-wave) solar radiation (Q_S) and the loss due to the effective long-wave back radiation (Q_B). The short-wave radiation is the sum of direct solar radiation and diffuse radiation; it depends on the solar constant, latitude, time of day and year, surface albedo, declination of the sun, and atmospheric influences such as scattering, absorption, and clouds. The outgoing effective long-wave radiation consists of the terrestrial radiation and long-wave radiation of the atmosphere. Positive values of Q_R indicate the ocean is gaining heat. Q_R is always positive for the Texas-Louisiana shelf waters when averaged over periods longer than a few days. The monthly march for radiation balance at the sea surface (Q_R) during the LATEX period was constructed using NCEP products. Values derived for Q_R , Q_S , and Q_B are presented in Figure 3.2-3. The NCEP estimates of Q_R closely follow the baseline estimates as shown in figure 2-10 in Etter (1996).

Q_A , Q_E , Q_H . The net turbulent heat flux from the sea surface (Q_A) is composed of the turbulent flux of latent heat due to evaporation or condensation (Q_E) and the turbulent flux of sensible heat due to direct air-sea contact (Q_H). Positive values of Q_A indicate a loss of heat by the ocean to the atmosphere. For a given air-sea temperature difference, more heat is lost by the ocean when it is warmer than the air above it than is gained by the ocean when the air is warmer than the water. When the ocean warms the air, the warmed air rises and the cooled water sinks, thereby maintaining the air-sea temperature difference and the exchange of heat. In the case of a cooler ocean, the heat exchange stabilizes both the air and water

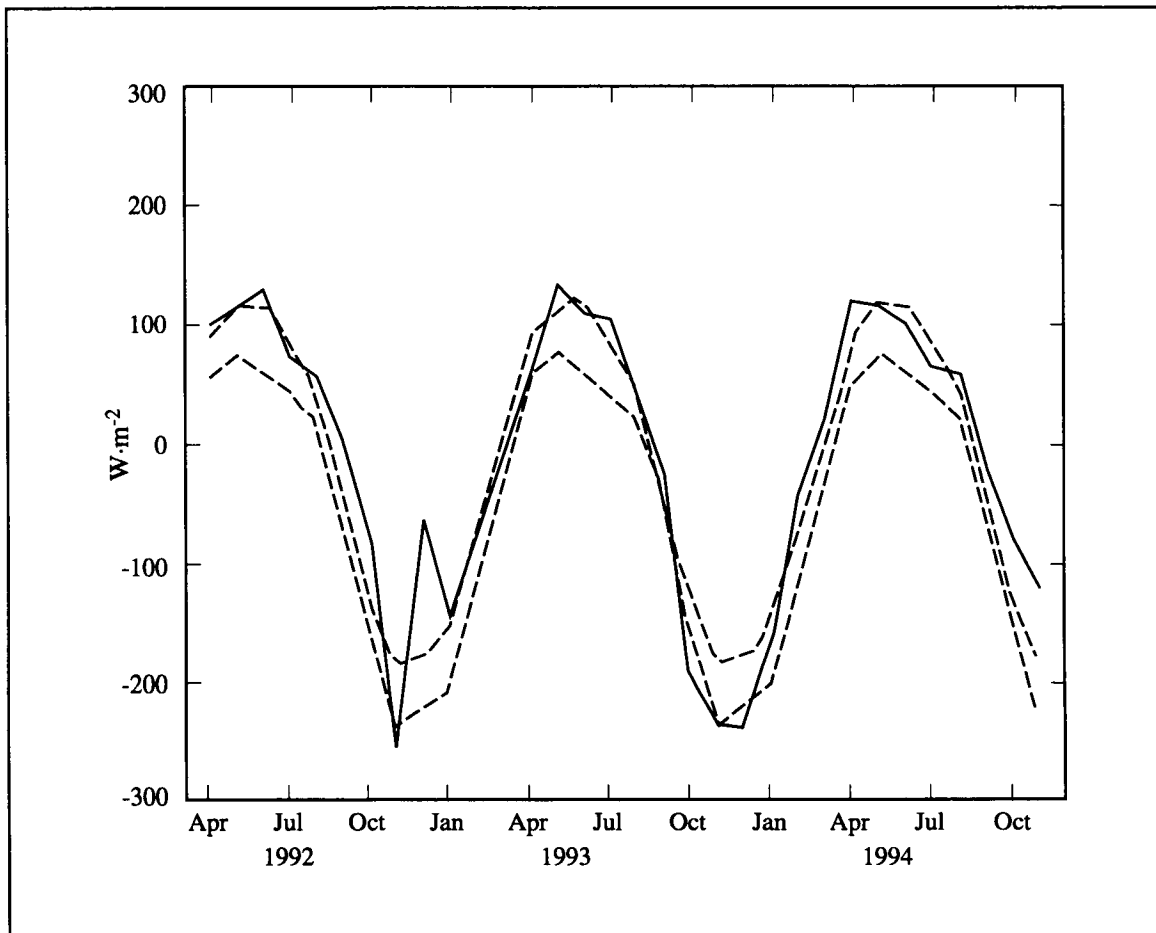


Figure 3.2-2. Monthly march of the net oceanic heat gain (Q_N) as determined from the NCEP data set (solid line). The envelope of dashed lines indicates the spread in monthly, multi-annual mean values derived by Etter (1996) from studies of Bunker (1976), Hastenrath and Lamb (1978), and Isemer and Hasse (1987).

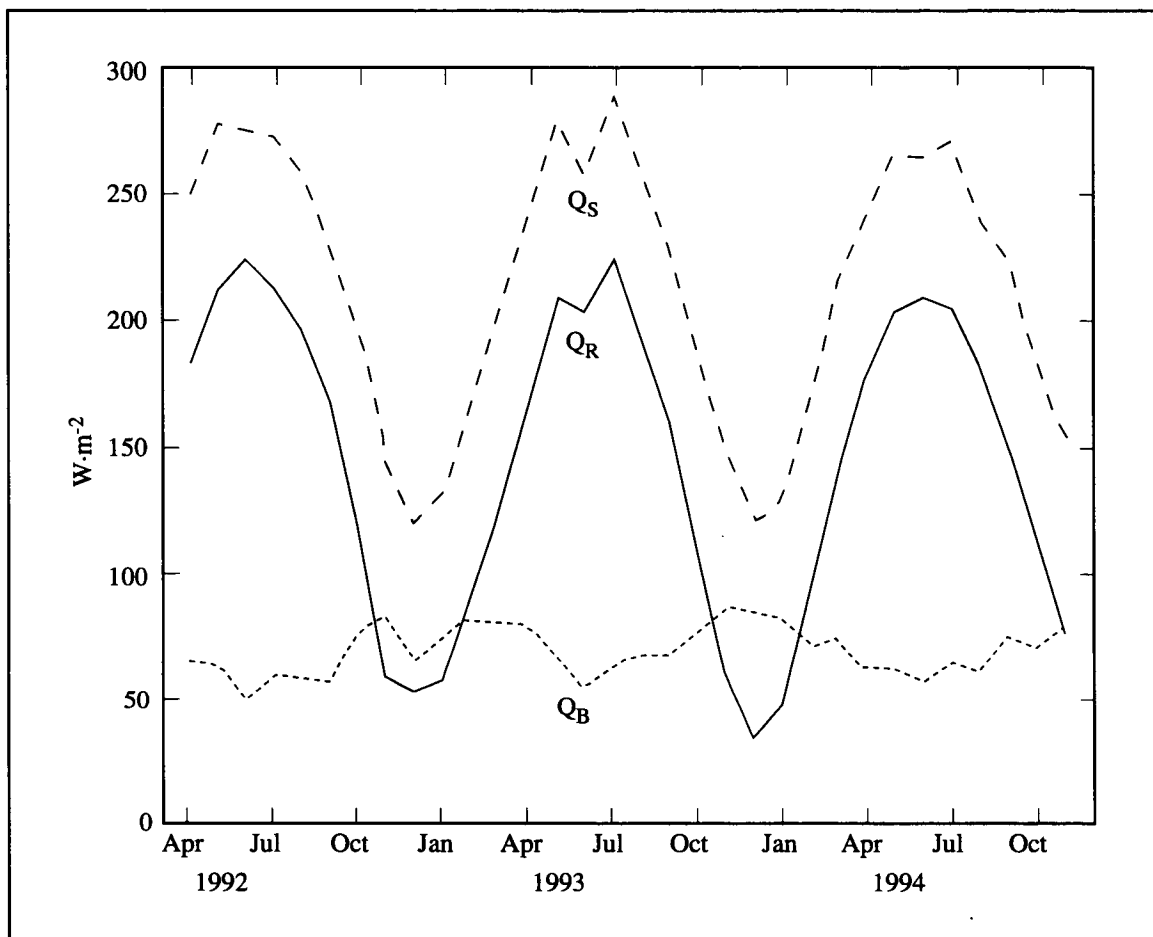


Figure 3.2-3. The radiation balance at the sea surface (Q_R) and its components—the net absorbed solar radiation (Q_S) and the effective back radiation (Q_B) as determined from the NCEP data set.

columns, which inhibits vertical motion and decreases the air-sea temperature difference, thereby suppressing the exchange of heat.

Over the Texas-Louisiana shelf, sea surface temperatures are warmer than air temperatures about 80 percent of the time, irrespective of season. However, the smallest air-sea temperature differences occur in summer and the largest in winter. When averaged over periods of a few days or more, these budget terms almost always indicate a loss of heat by the waters of the Texas-Louisiana shelf. Monthly marches for the net Q_A , Q_H , and Q_E are shown in Figure 3.2-4. Heat loss is greatest in the fall and winter when air-sea temperature differences are greatest. The low Q_A value in December 1992 is due to unusually warm air temperatures over the shelf which resulted from monthly mean winds coming from the east rather than the more usual direction of northeast.

Q_T . The oceanic heat storage term (Q_T) is the rate of change of the oceanic heat content (H), here defined as

$$H = \int_0^D \rho_w C_{pw} T_w dz,$$

where: H = heat content of water column [$J \cdot m^{-2}$],
 ρ_w = density of sea water [$kg \cdot m^{-3}$],
 C_{pw} = specific heat of sea water at constant pressure [$J \cdot kg^{-1} \cdot ^\circ C^{-1}$],
 T_w = water temperature at depth z [$^\circ C$],
 z = depth in water column [m], and
 D = depth of integration (bottom or 200 m, whichever is less) [m].

The long-term mean of Q_T should be zero. The rate of heat storage term was computed as the difference of the mean total heat content of the ocean from cruise to cruise. The total heat content was computed directly by integrating the vertical profiles of temperature measured during the ten LATEX A hydrography cruises. Individual casts were averaged to obtain the mean total content.

Mean values of the nine Q_T fields are compared with the climatological baseline in Figure 3.2-5. The baseline for Q_T , derived from Etter et al. (1985), was based on the temperature census of Ulm (1983). The temporal progression illustrates good agreement between the mean values of Q_T and the baseline.

Q_V . Direct calculation of oceanic heat transport (Q_V) entails a determination of the barotropic, baroclinic, and Ekman transport components across the boundaries of the water body and a knowledge of the temperature distribution across the currents. Though a direct calculation could be attempted with the LATEX data set, for the present study, the Q_V was calculated as a residual from the heat budget equation, $Q_V = Q_N - Q_T$. The temporal progression is presented in Figure 3.2-6 and reveals a pattern similar to that of the climatology, but with generally

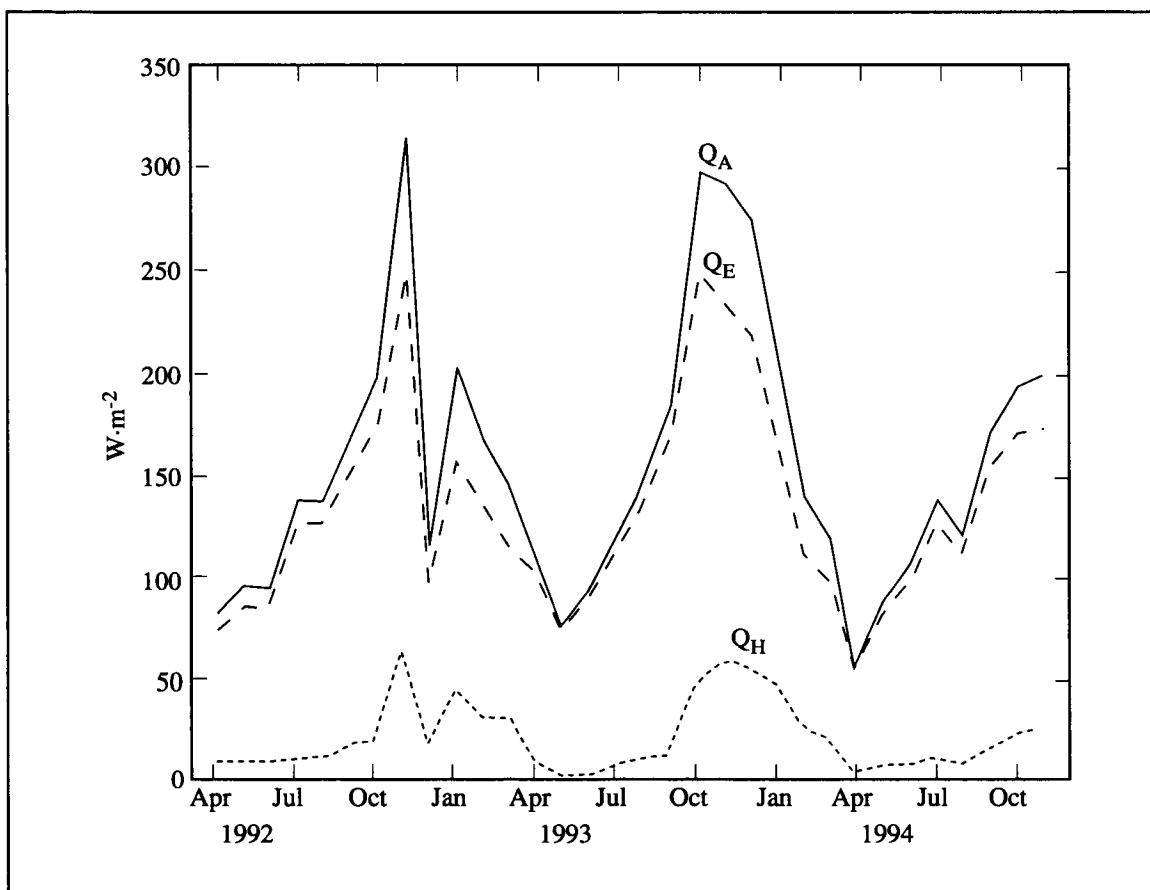


Figure 3.2-4. Monthly march of the net turbulent heat flux (Q_A) and its components—the turbulent flux of latent heat (Q_E) and the turbulent flux of sensible heat (Q_H) as determined from the NCEP products.

higher values especially in the fall of 1992. Positive values represent cases where heat is exported from the region by currents.

Freshwater budget terms

F_w . The freshwater flux divergence is the amount of freshwater entering or leaving through the sides of the region. F_w was computed as a residual in the freshwater budget equation $F_w = (P+R)-E-W$. Values of F_w were computed on the assumption that, in addition to the full discharge of Atchafalaya River and the rivers in Texas, 53% of the Mississippi River discharge was directed to the west (Dinnel and Wiseman 1986). In Figure 3.2-7 the residual values of F_w are compared with the baseline climatology. The computed values of F_w fell within or close to the baseline envelope. This figure implies that freshwater was exported from the Texas-Louisiana shelf throughout the study.

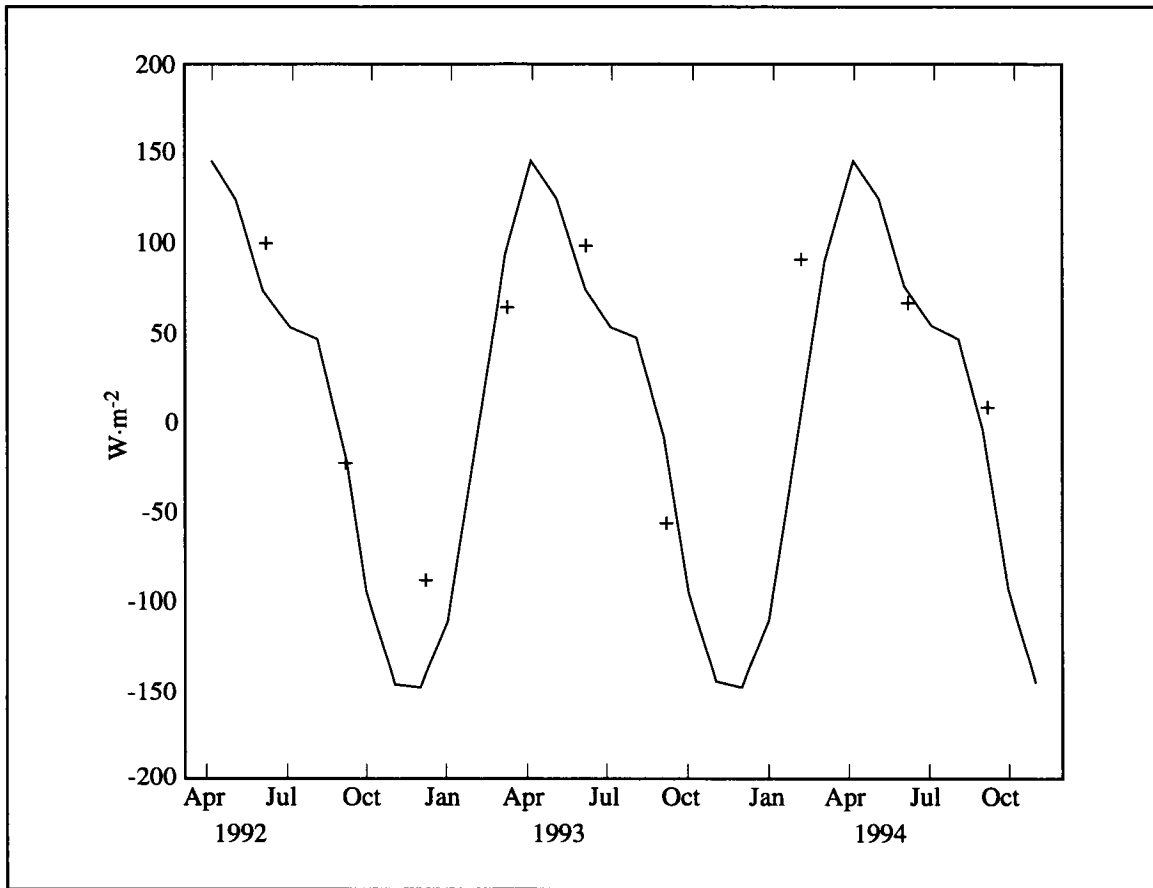


Figure 3.2-5. Rate of oceanic heat storage (Q_T) determined from the LATEX A hydrography (crosses) compared to climatological baseline (solid line) computed by Etter et al. (1985) using the temperature census of Ulm (1983).

P. The freshwater input due to rain was not measured at sea on a regular basis. For the study period, we used precipitation estimates based on the GOES GPI. The GPI method was calibrated over the open ocean during GARP (Global Atmospheric Research Programme) Atlantic Tropical Experiment and thus provides better estimates of precipitation over water than over land. In Figure 3.2-8 seasonal marches of precipitation derived from the GPI data are compared to the climatological baseline. The spring GPI values were consistently higher than the corresponding climatological baseline, but coastal precipitation records from Brownsville, Corpus Christi, Galveston, and Port Arthur, Texas, confirm that high spring rainfall occurred in 1993 and 1994.

R. R is the freshwater input due to river discharge. The Mississippi and Atchafalaya rivers are the major sources of river water to the Texas-Louisiana shelf (Section 2.3). Discharge

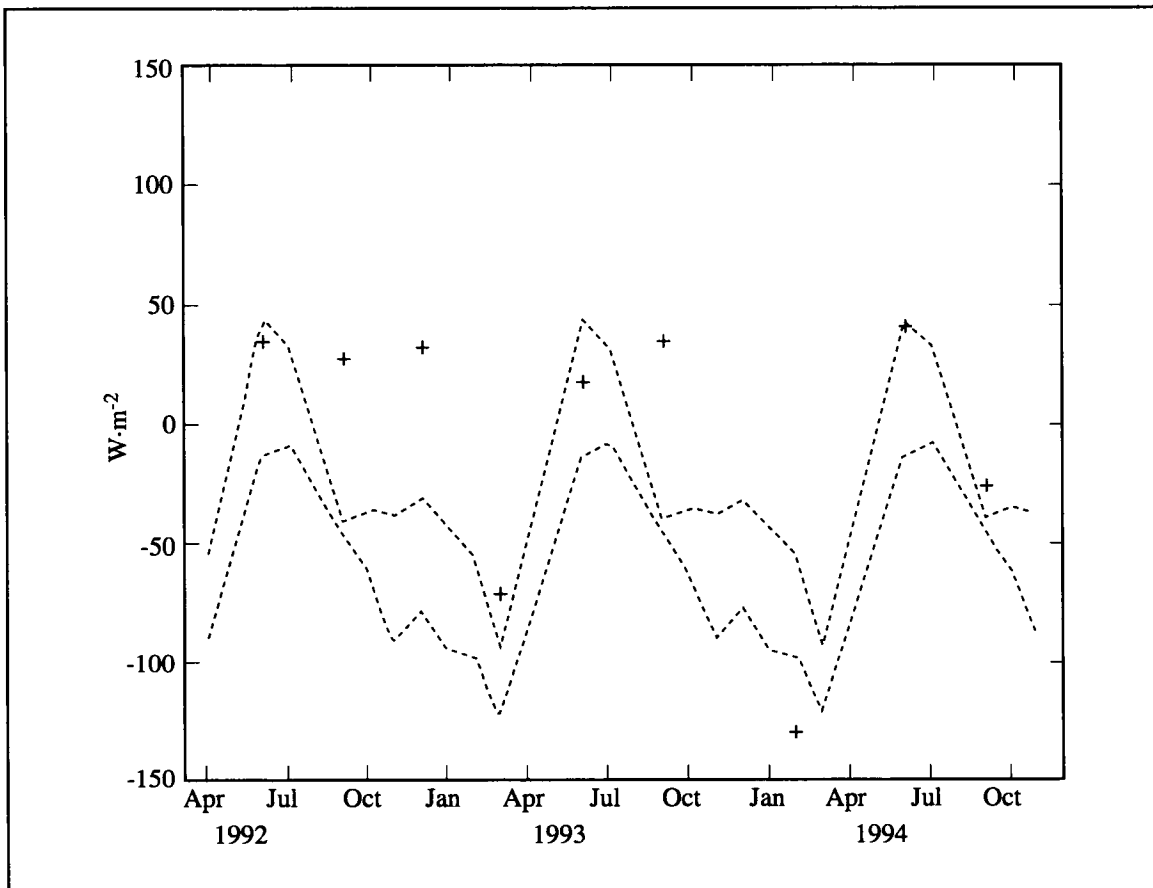


Figure 3.2-6. Heat flux divergence due to currents ($Q_V=Q_N-Q_T$) determined as a residual in the heat budget equation (crosses). The climatological envelope was determined by Etter (1996) using the envelope for Q_N shown in Figure 3.2-2 and the climatology for Q_T shown in Figure 3.2-5.

from Texas rivers may be important to the freshwater budget near the rivers' mouths but their combined discharge is only a fraction of that of the Mississippi and Atchafalaya. Combined daily discharge rates for the Mississippi (reduced to 53%) and Atchafalaya rivers (obtained from U.S. Army Corps of Engineers) and for rivers in Texas (Aransas, Brazos, Colorado, Guadalupe, Lavaca, Mission, Neches, Nueces, Sabine, San Antonio, San Bernard, and Trinity rivers, obtained from U.S. Geological Survey) were converted to the units of cm per month (Figure 3.2-9) by dividing the monthly mean discharge rates by the shelf area.

E. The rate of evaporation (E) was derived from the NCEP estimates of turbulent flux of latent heat (Q_E) using the relationship $E = Q_E/L$, where L is the latent heat of evaporation. In Figure 3.2-10, the seasonal NCEP evaporation estimates are plotted along with the seasonal climatological values of E .

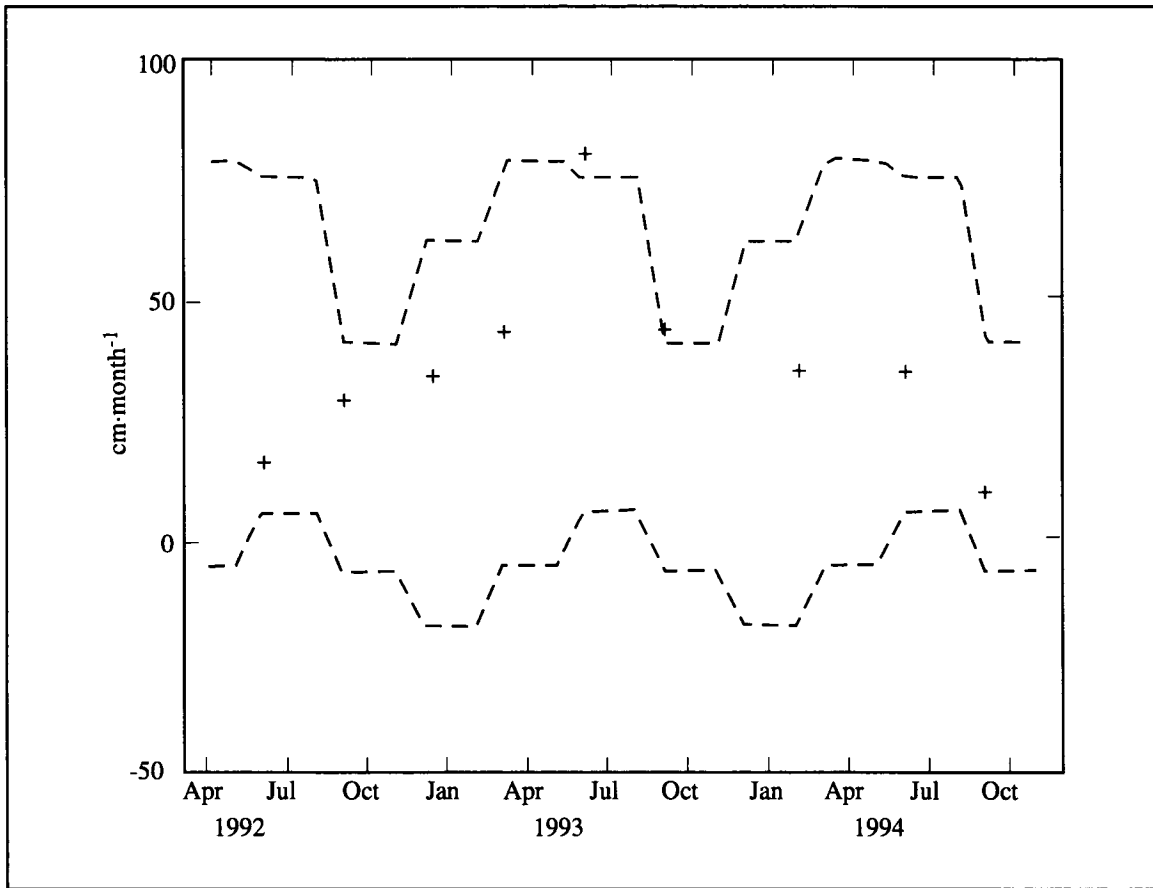


Figure 3.2-7. Freshwater flux divergence (F_w) as determined using the LATEX A hydrography data (crosses). Dashed lines indicate spread in seasonal, multi-annual climatological values derived by Etter (1996).

W. W is the rate of change in the freshwater volume, or the freshwater storage. W was calculated using salinity profile data collected during the LATEX A hydrography surveys. The rate of freshwater storage W was then calculated as the difference in V_f between successive cruises. The freshwater fraction (f) was first defined as

$$f = \frac{S_b - S}{S_b},$$

with

$$S = \frac{1}{D} \int_0^D s \, dz,$$

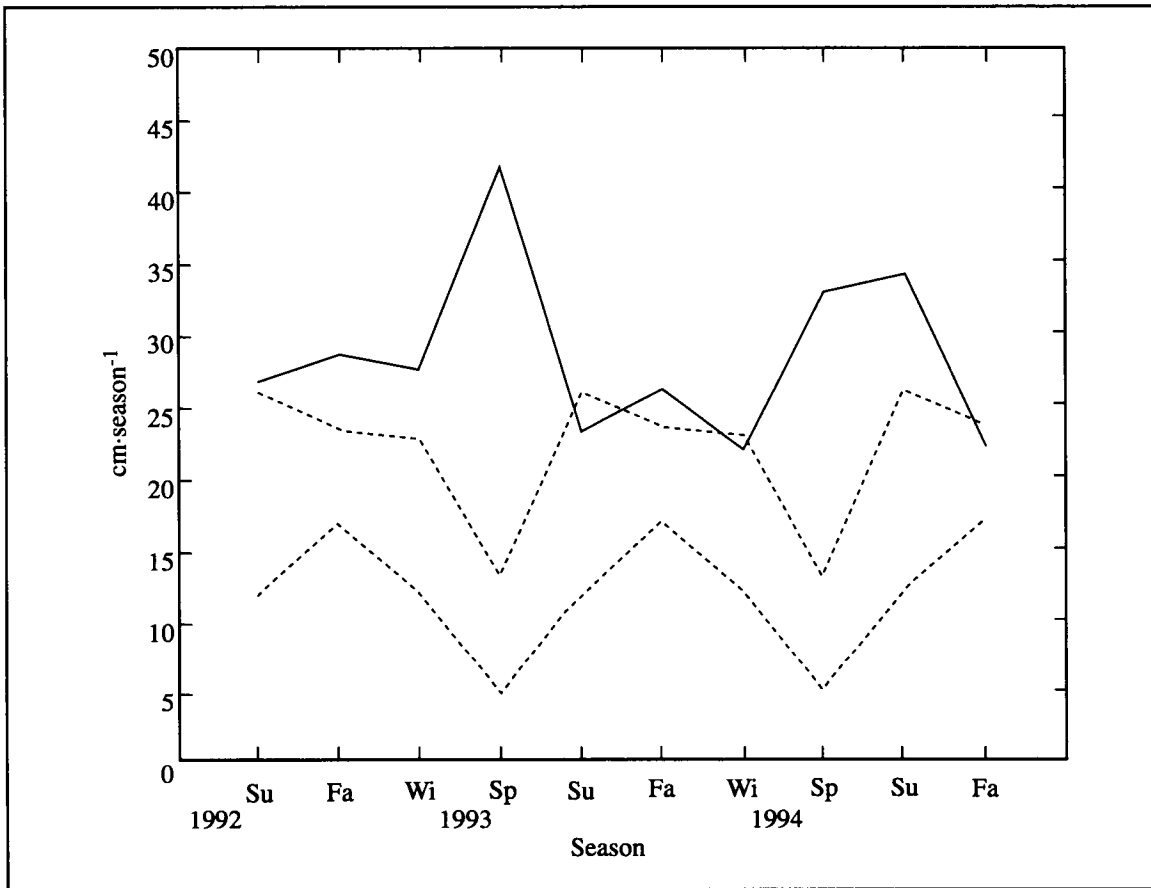


Figure 3.2-8. Seasonal march of precipitation (P) derived from the GPI data set (solid line). Dashed lines indicate spread in seasonal, multi-annual climatological values derived by Etter (1996).

and

- f = freshwater fraction,
- s = salinity at depth z [psu],
- z = depth in water column [m],
- S = column-integrated salinity [psu],
- S_b = baseline (or reference) salinity [psu], and
- D = depth of integration (bottom or 200 m, whichever is less) [m].

Next, the reduced freshwater thickness, or the equivalent water depth per unit area [m], (V_f), is defined as

$$V_f = f \times D.$$

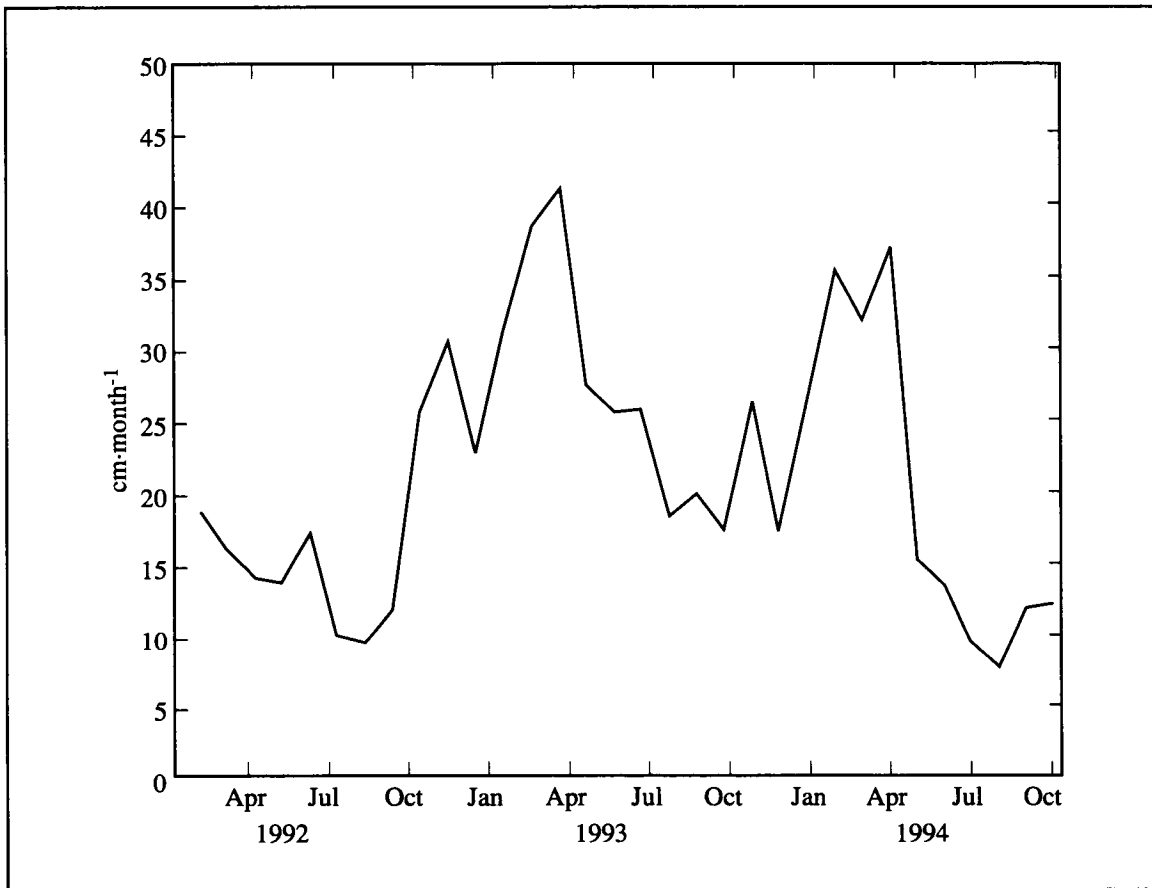


Figure 3.2-9. Combined monthly river input (R) from the Mississippi River (reduced to 53%), Atchafalaya River, and rivers in Texas.

Values of V_f were computed for each station of each cruise using the reference salinity of 37. In Figure 3.2-11, the temporal progression of the ten V_f values is compared with the baseline census, which is based on the Ulm (1983) salinity census. Values of V_f are larger than the baseline all three years. The salinity values Ulm used are known to be consistently high, which may account for the baseline curve being lower than that of the LATEX A data. In addition, river discharges were greater than the mean in 1993 and most of 1994, and oceanic precipitation estimates were greater than their baseline values in the spring of 1993 and 1994. Considering these factors, the values of V_f shown for 1992-1994 are reasonable. In Figure 3.2-12, W values are compared with the monthly climatological baseline derived from Ulm's salinity census. The temporal progression illustrates good agreement between W and the baseline, including the value based on a 5-month cruise interval (February 1994). Positive values of W indicate periods when the water column is freshening.

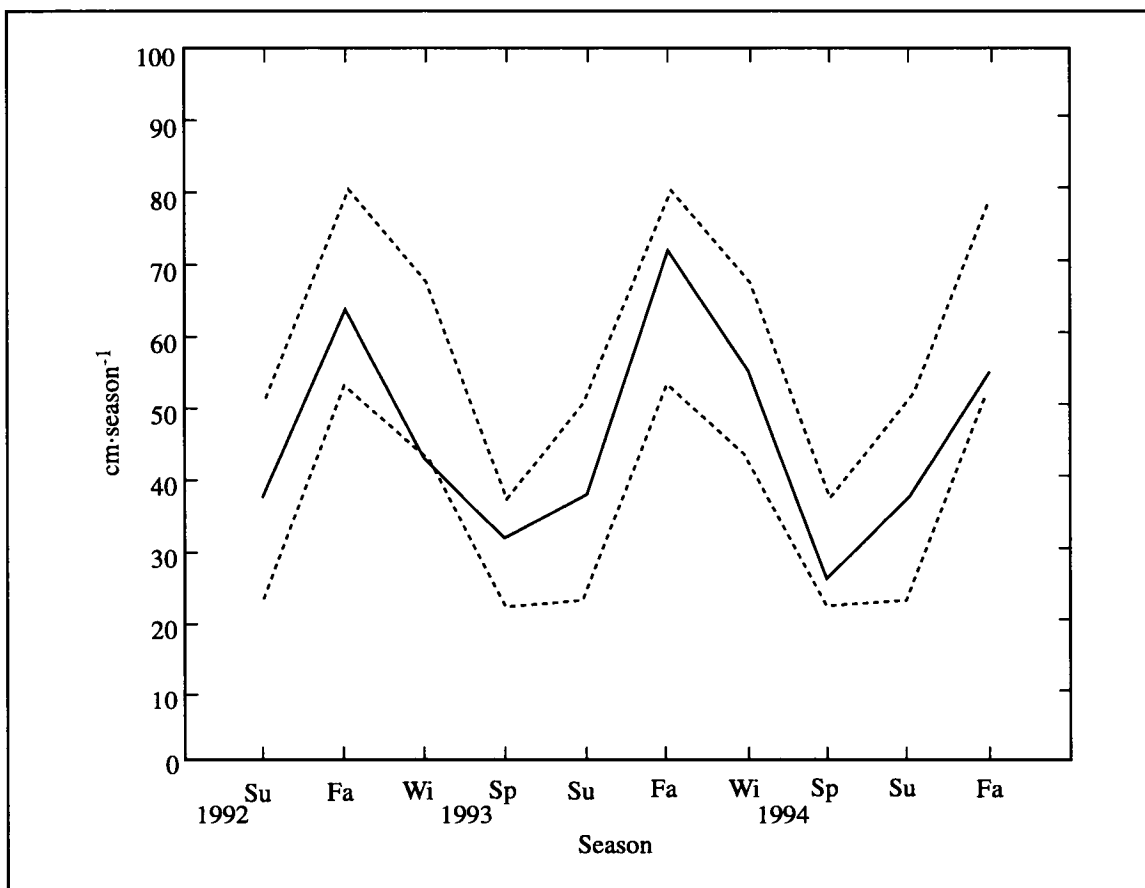


Figure 3.2-10. Seasonal march of the evaporation rate (E) as determined from the NCEP data set (solid line). Dashed lines indicate spread in seasonal, multi-annual climatological values derived by Etter (1996).

Discussion

The budget analysis for the Texas-Louisiana shelf was restricted by the spatial coverage of the ten hydrographic cruises. Instantaneous fields were computed for each of the ten cruises and differenced. Of the nine difference fields, only five covered the entire shelf.

Although previous climatological studies have provided useful baselines for regional investigations, comparisons have not been made with synoptic field data or with numerical model products. Moreover, these baselines have not been updated in more than a decade. The results of this study have expanded the baselines for the Texas-Louisiana shelf by updating the mean monthly heat budget parameters and by completing an analysis of the mean freshwater budget.

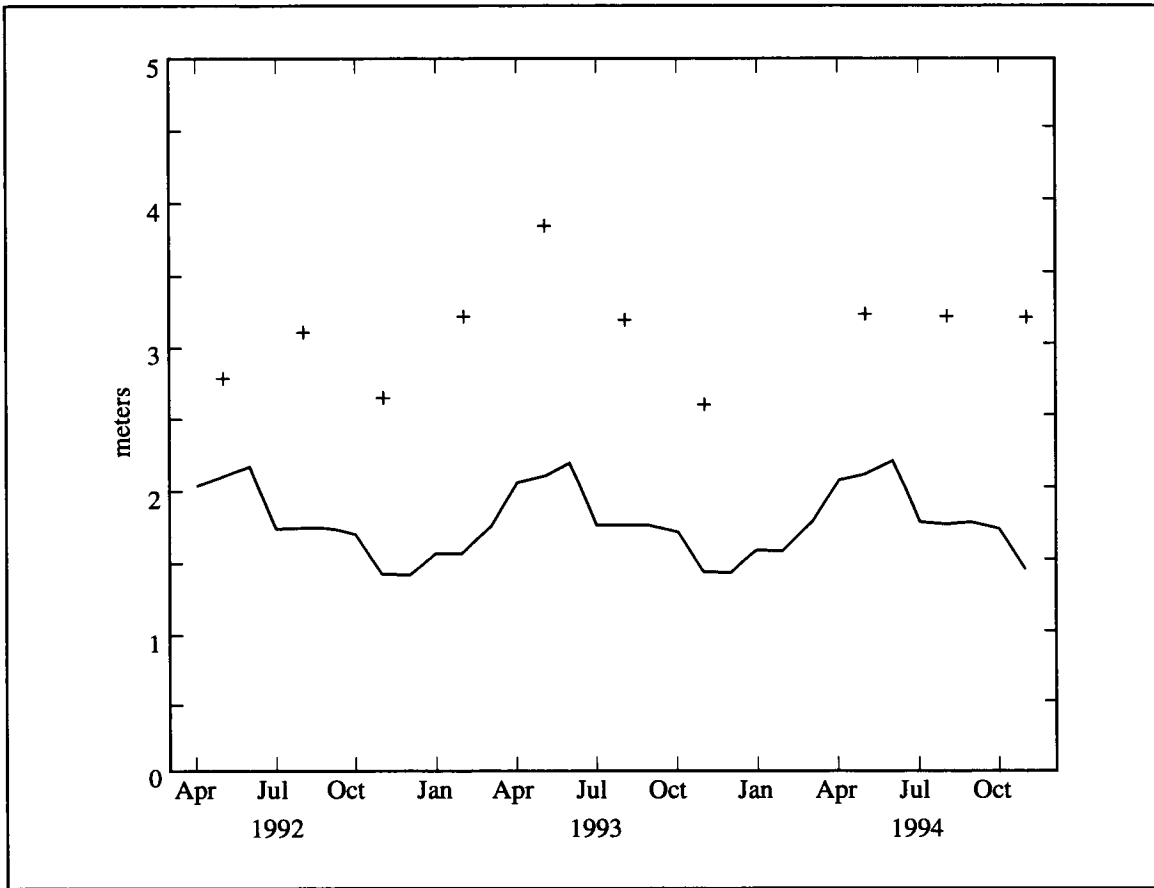


Figure 3.2-11. Reduced freshwater thickness (V_f) as determined using LATEX A hydrographic data (crosses) compared with the baseline climatology computed using Ulm's (1983) salinity census (solid line).

Comparisons of the computed heat budget parameters with the baseline climatologies generally showed good agreement. The eight values of the rate of oceanic heat storage (Q_T) agreed well with the climatic baseline. These results suggest that, in the long term, rate of change for heat storage follows a predictable pattern, particularly when using shelfwide averages that tend to dampen the effects of transient phenomena. The uneven distribution of computed values could not confirm the baseline Q_T maxima in April or the minima in November-December.

The heat flux divergence due to currents (Q_v) (Figure 3.2-6) showed a large interannual variability in each fall that is likely the result of accumulated errors. Five of the eight residual Q_v values fell within the climatic envelope while the three remaining values suggested more heat flux divergence ($Q_v > 0$) than indicated by the climatology alone. These departures

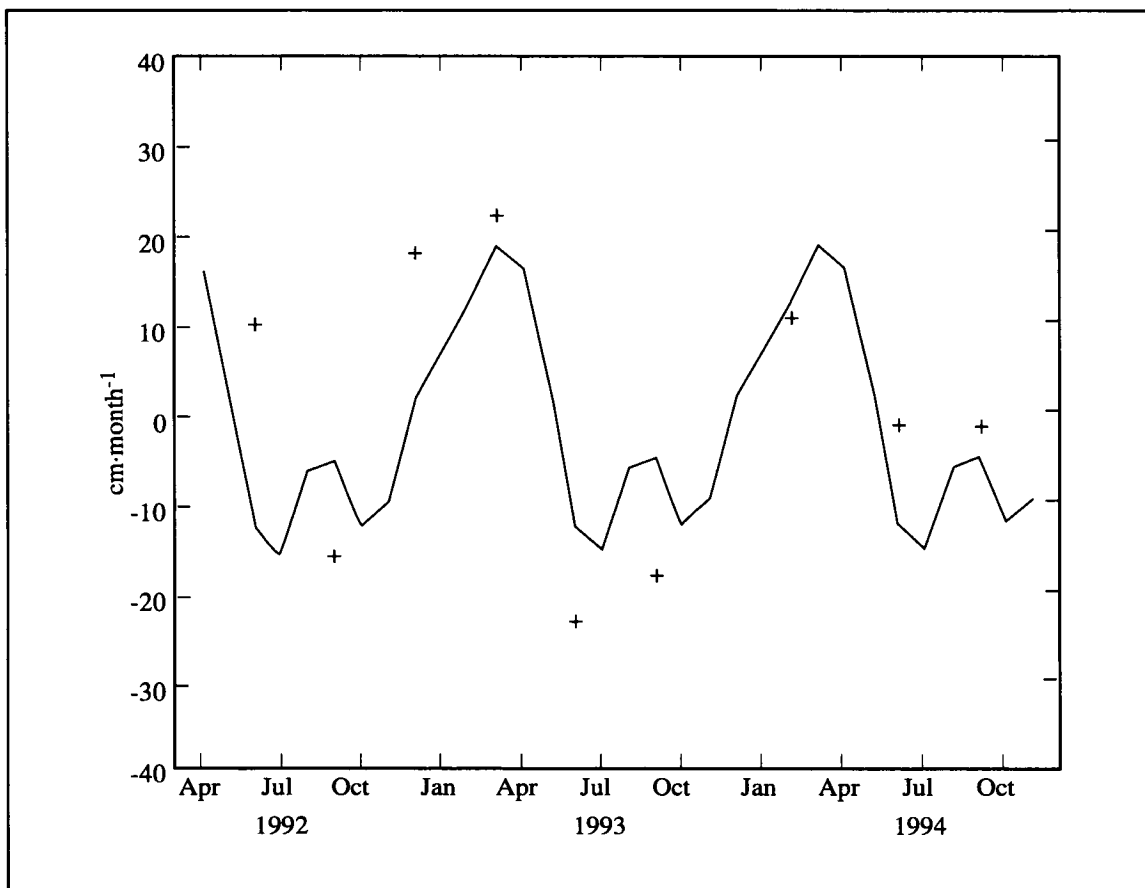


Figure 3.2-12. Rate of freshwater storage (W) as determined using the LATEX A data (crosses) and from the monthly baseline climatology (solid line).

of Q_v from the baseline can be attributed in part to departures of the NCEP Q_A values (Figure 3.2-4) from the climatology in December 1992, and in part to departures of the computed Q_T values (Figure 3.2-5) from the climatology in December 1992 and September 1993.

In general, the component parameters of the freshwater budget agreed well with the corresponding climatic baselines. The eight values of the rate of freshwater storage (W) were consistent with the climatic baseline. Values of the precipitation (P) departed from the baseline, but these departures were verified using coastal station data. Precipitation rates over the shelf can be estimated using 70-75% of the adjacent coastal precipitation rates, if direct measurements are unavailable. The temporal distribution of the rate of freshwater storage (Figure 3.2-12) generally followed the pattern of the monthly climatology, although

there was notable interannual variability. This was not unexpected in view of the interannual variability of the river discharge. The values of freshwater flux divergence (F_w) (Figure 3.2-7) fell within or very close to the climatological envelope; the temporal pattern closely followed that of W .

River discharge rates (R) were compared with the rate of freshwater storage (W) and with the rate of precipitation-minus-evaporation ($P-E$) in Etter (1996). The rate of freshwater storage tended to decrease with increasing river discharge when full-shelf (east + west) cruises were considered. When considering only the eastern shelf cruises, the rate of freshwater storage tended (with one exception) to increase with increasing river discharge. Thus, factors other than river discharge must be introduced to explain changes in the W fields for the western shelf. This suggests that much of the fresh water discharged from the Mississippi and Atchafalaya Rivers either is exported offshelf before reaching the western shelf or was in narrow, nearshore boundary layers inside the 10-m bathymetric contour and not sampled. Evidence from particle distributions (Section 5.1) supports the former.

There was a tendency for the rate of freshwater storage to increase as precipitation exceeded evaporation. However, this effect was more persistent in the case of the eastern-shelf cruises, where a pronounced linear relationship between the two existed.

4 SHELFWIDE CIRCULATION AND TRANSPORTS

4.1 Introduction: The Cochrane-Kelly schema for shelf-scale circulation

Cochrane and Kelly (1986) produced monthly mean fields of geopotential anomaly of the sea surface relative to 70 db for the Texas-Louisiana continental shelf. Their mean fields are based on data taken during monthly M/V GUS III cruises in 1963, 1964, and 1965. They compared the circulation inferred from their geopotential anomaly patterns to direct current observations and found good agreement. Their results, represented in Figure 4.1-1, portray for most of the year a circulation pattern on the inner shelf that is downcoast (directed from the Mississippi River toward Brownsville) with a low in geopotential anomaly over the central shelf and some evidence for eastward flow at the shelf edge.

The pattern of flow over the inner shelf is attributed principally to wind forcing; the dominant over-water winds have a downcoast component resulting in a downcoast flow. (See Csanady (1981) for a discussion of quasi-steady, wind-forced nearshore flow.) During much of the year, discharge from the Mississippi and Atchafalaya rivers adds fresher water to the nearshore edge of this circulation, presumably enhancing the downcoast flow. This pattern is interrupted in early summer (June) when winds over this shelf generally begin to change from downcoast to upcoast in direction. This results in a distinctly different pattern of geopotential anomaly in July and August with a high located over the shelf near the Texas-Louisiana border. The summer upcoast currents are perhaps more clearly inferred in Cochrane and Kelly's pattern of high surface salinity (not shown here) being driven upcoast by the nearshore circulation than by their geopotential anomaly patterns. With the reversal in late summer to downcoast wind directions, the cyclonic pattern is rapidly reestablished and commonly persists from September through May.

The preceding description of the shelf-scale circulation over the Texas-Louisiana shelf will be referred to here as the CK schema. The principal elements are:

- During nonsummer (approximately September through June) winds with a generally downcoast component drive downcoast currents over the inner shelf. Due to the concave orientation of the coast, a convergence of alongcoast winds occurs over the lower (south Texas coast) resulting in a convergence of currents over the inner shelf and an offshore, cross-shelf flow that contributes the southwest limb of a cyclonic circulation gyre with upcoast flow near the shelf break. This gyre is closed by shoreward, cross-shelf flow over the Louisiana shelf west of the Mississippi River mouth.
- During spring the prevailing winds over the inner shelf develop an upcoast component, beginning over the Mexican shelf and moving upcoast. Consequently, in spring the area of coastal current convergence migrates, under the influence of the wind, upcoast. This

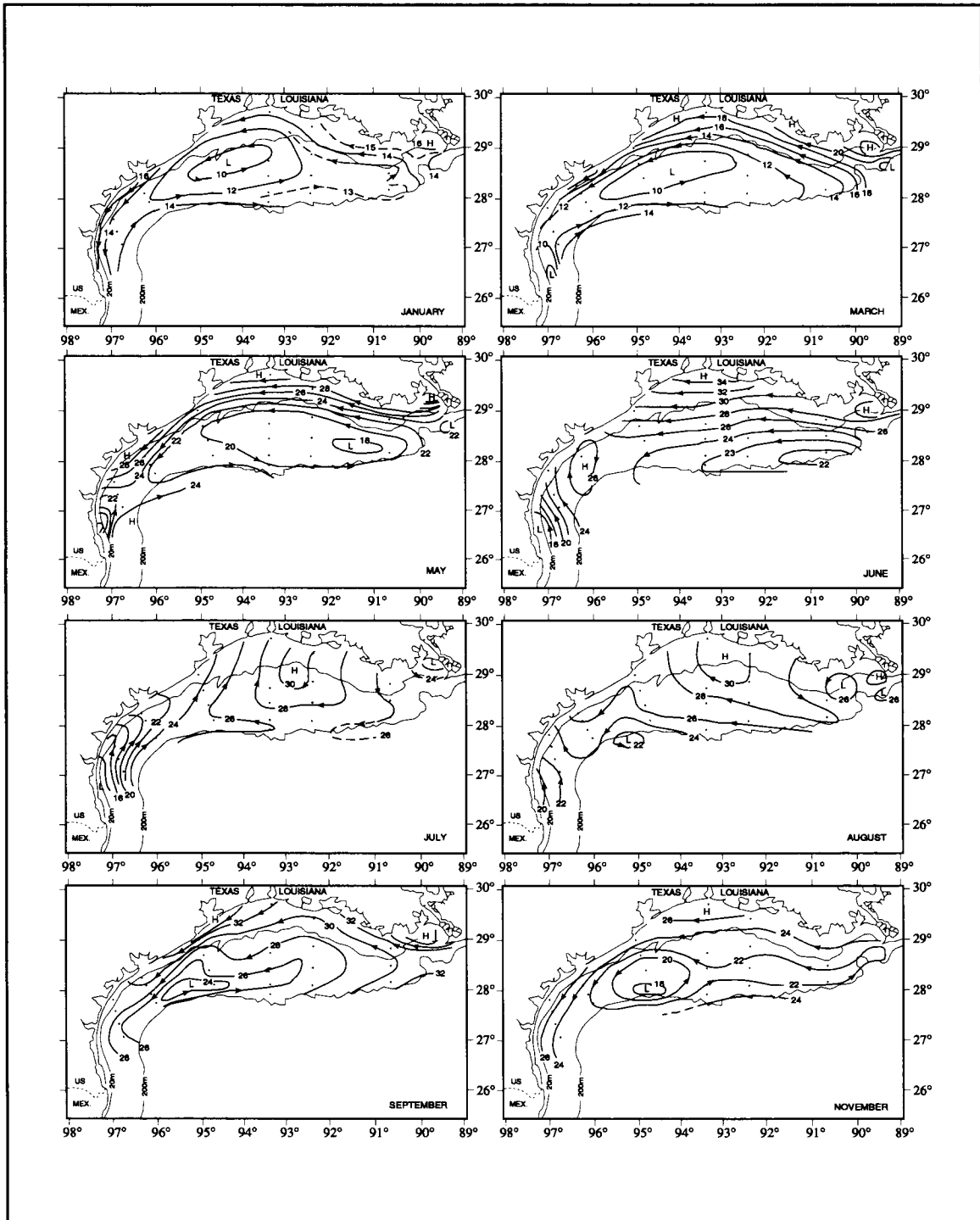


Figure 4.1-1. Monthly mean fields of surface geopotential anomaly (dyn cm) relative to 70 db from Cochrane and Kelly (1986) representing their proposed pattern of annual variability of the shelfwide circulation.

phenomena reaches Louisiana by July. Thus, the prevailing currents over the inner shelf are upcoast during summer.

- Downcoast winds generally are reestablished in August-September, at which time the nonsummer circulation gyre is reestablished.
- Shelf break currents are thought to be directed upcoast all year.
- Low-salinity surface water from the Mississippi-Atchafalaya rivers is advected down the shelf near the coast by the downcoast currents over the inner shelf in nonsummer. On average, the low salinity is enhanced during the period of maximum Mississippi-Atchafalaya discharge in spring.
- During summer brackish surface water is held over the Louisiana shelf by upcoast currents and results in a pool of low-salinity water distributed broadly across the shelf.
- The low-salinity surface waters distributed along the coast during nonsummer should contribute buoyancy forcing to enhanced shear flow downcoast, although this is not specifically stated as part of the CK schema.

4.2 Seasonal mean hydrographic fields as related to circulation, with estimates of interannual variability

Introduction

We constructed new mean fields of hydrographic variables for the Texas-Louisiana shelf and used them to examine the CK circulation schema. This material also was used to examine interannual variability and, to some extent, its causal mechanisms. Results are described in Li et al. (1997). Here we present a short version of that paper, but include additional figures.

This study began with an examination of available hydrographic data, including that from LATEX A. We identified 77 cruises having good quality data; 44 of which covered all or a significant portion of the Texas-Louisiana shelf. We focused on three periods: May representing spring, July-August representing summer, and November representing fall. We used ten May cruises (six with full-shelf coverage) yielding a total of 745 full-depth stations, nine July-August cruises (seven with full-shelf coverage) comprising 822 stations, and six November cruises (four with full-shelf coverage) with a total of 615 stations. The cruise identifiers and dates are listed in Table 4.2-1. Some cruises extended slightly into succeeding or preceding months.

Table 4.2-1. Hydrographic cruises on the Texas-Louisiana continental shelf from which data were used.

Cruise	Dates	# of stations
<i>May (spring)</i>		
GUS III - 4	26 Apr - 5 May 1963	41
GUS III - 5	13-22 May 1963	37
GUS III - 17	12-26 May 1964	41
OBDORSK - 64	26 May - 6 Jun 1964	29
GUS III - 29	19 May - 2 Jun 1965	41
Longhorn - 76	28 May - 7 Jun 1976	29
Longhorn - 77	1-20 May 1977	28
LATEX - H01	1-8 May 1992	114
LATEX - H05	26 Apr - 10 May 1993	215
LATEX - H08	23 Apr - 7 May 1994	170
Total		745
<i>July - August (summer)</i>		
GUS III - 7	10-17 Jul 1963	40
GUS III - 8	16-31 Aug 1963	41
GUS III - 19	9-19 Jul 1964	41
GUS III - 20	20 Aug - 2 Sep 1964	41
GUS III - 32	11-24 Aug 1965	41
90-G-10*	11-25 Jul 1990	108
LATEX - H02	1-8 Aug 1992	124
LATEX - H06	26 Jul - 7 Aug 1993	215
LATEX - H09	26 Jul - 7 Aug 1994	171
Total		822
<i>November (fall)</i>		
61-H-19*	11-13 Nov 1961	11
GUS III - 11	20 Nov - 2 Dec 1963	41
GUS III - 23	10-27 Nov 1964	41
LATEX - H03	5-13 Nov 1992	114
LATEX - H07	6-22 Nov 1993	238
LATEX - H10	1-14 Nov 1994	170
Total		615

* "G" is for the *R/V Gyre*; "H" is for the *R/V Hidalgo*. Ships used for LATEX cruises are identified in Table 1.1-2.

Methodology

Figure 4.2-1 shows the locations of hydrographic stations from the ten May cruises, nine July-August cruises, and six November cruises. Based on examination of the spatial scales of hydrographic variability (Section 4.3.1), these station distributions should be adequate to describe the larger scale distributions over the entire shelf.

Some of the variability characterized here as interannual may in fact be intraseasonal because cruises were carried out at different times during May (spring), July-August (summer), and November (fall) in different years. Also, wind variability during a given month is probably comparable to interannual variability, and this can influence the variability of the advection of properties. To reduce aliasing interannual with intraseasonal variability, we have averaged two 1963 and two 1964 May cruises to give one spring cruise for each of those years. Two July-August cruises in both 1963 and 1964 were treated in the same manner. This gave us eight May cruises, seven July-August cruises, and six November cruises.

Aliasing also may result because of measurement bias or scatter relative to the common accuracy or precision. We are not aware of such problems for the data used with the exception of that from GUS III. For those cruises, it is known that the salinities are biased toward high values and have lower precision than might be expected had a shipboard salinometer been used, which was not the case. Before beginning the analysis, we screened the GUS III salts and found two or three outliers per cruise with values greater than 37. They were replaced with values interpolated either between closely neighboring stations or between values located above and below. Because of the large natural variability, it is virtually impossible to determine less extreme outliers in the GUS III salinities for values in shallow water over the inner shelf. We plotted temperature versus salinity for all stations at the outer continental shelf used in this study both for GUS III and for LATEX cruises. The results (discussed in Li et al. 1997) showed the scatter and maximum offset for GUS III to be smaller by an order of magnitude than the maximum standard deviations observed for salinity from year to year. Thus, we do not think the problems with GUS III salinities contribute marked error to our results.

To obtain values of surface (3-m) geopotential anomaly relative to 70 db at stations shallower than 70 m, we first calculated geopotential anomaly relative to 70 db for offshore stations deeper than 70 m. Then, we used extrapolated specific volume anomaly values along the bottom to obtain geopotential anomaly to the deepest sample depth of successively shallower stations, as described and discussed in Li et al. (1997) and Appendix H.1.

For this analysis, we chose a grid scale of 15 minutes (approximately 27 km), comparable to the decorrelation scale for these variables (Li et al. 1996; Section 4.3.1). The grid was located to include points at whole degrees of latitude and longitude. The GMT (Generic

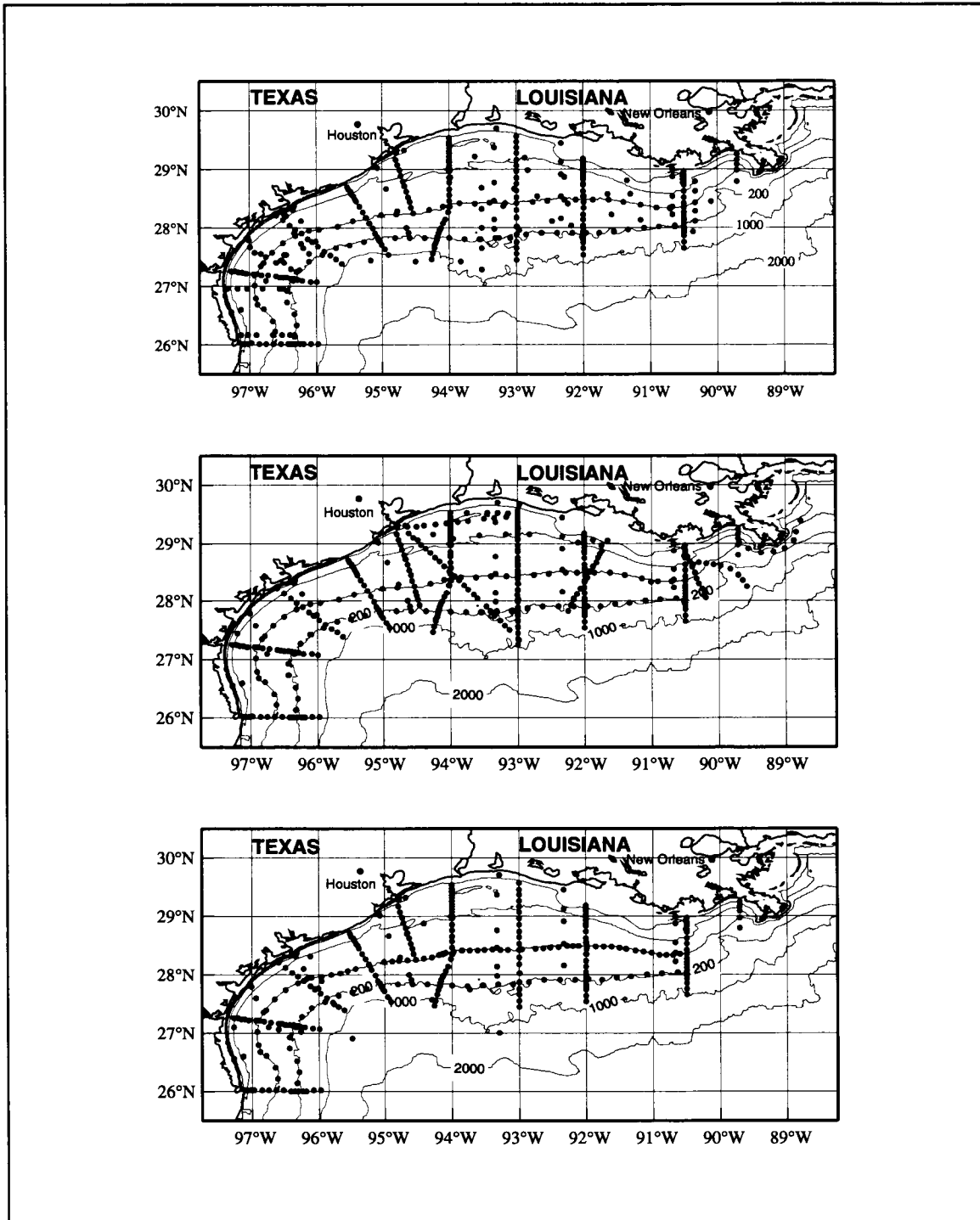


Figure 4.2-1. Locations of (upper) 745 hydrographic stations from ten May cruises, (middle) 822 hydrographic stations from nine July-August cruises, and (lower) 615 stations from six November cruises.

Mapping Tools) software package (Wessel and Smith 1991) was used to produce gridded values and contoured fields of surface (3-m) salinity (S), surface (3-m) temperature (T), and surface (3-m) geopotential anomaly relative to 70 db (GA) for each individual cruise. The objective analysis method used in GMT is based on an extension of the minimum curvature method of gridding described by Smith and Wessel (1990). We used a spline tension factor (0.25) recommended by the authors, which seemed to produce reasonable results compared to other values tried. The analysis method of the GMT package does not produce error fields.

From the gridded fields of each of the three properties for each individual cruise, we produced mean fields by averaging at grid points the values for the individual cruises. If we had produced mean fields by performing an objective analysis using all measurements of the variable in question, the resulting fields would have been biased toward the LATEX cruises because of the large number of LATEX stations compared to the total number of stations. The approach used gives equal weight to all cruises covering significant fractions of the shelf. The gridded mean fields for May, for July-August, and for November were contoured using the GMT package.

At each grid point of each field for the individual cruises we also calculated differences between the means and individual values. These differences were used to produce gridded, contoured fields of standard deviations for each variable representing the May, July-August, and November periods. We elected to show those mean fields produced from averages only at grid points covered by at least four individual cruises (see Li et al. 1997 for discussion). The standard deviation fields shown are based on the same data sets. This somewhat conservative approach results in mean fields that extend offshore only to about the 200-m isobath. However, most grid points are represented by more than four cruises, and in the peripheral regions the standard deviation estimates are more meaningful than they would be if the fields extended over the area covered by fewer than four cruises.

Estimated means and interannual variability of water properties and associated circulation for spring, summer, and fall

When interpreting these mean fields it should be remembered that we computed the geopotential anomaly field for each cruise and then averaged them to obtain mean geopotential anomaly fields—in contrast to computing the mean geopotential anomaly fields from mean temperature and salinity fields. Thus, the mean geopotential anomaly field does not necessarily correspond to the mean temperature and salinity fields.

Spring fields. The average May fields of surface salinity, geopotential anomaly, and surface temperature together with their standard deviations are shown in Figures 4.2-2, 4.2-3, and 4.2-4 respectively. Those for bottom salinity, temperature and potential density are shown

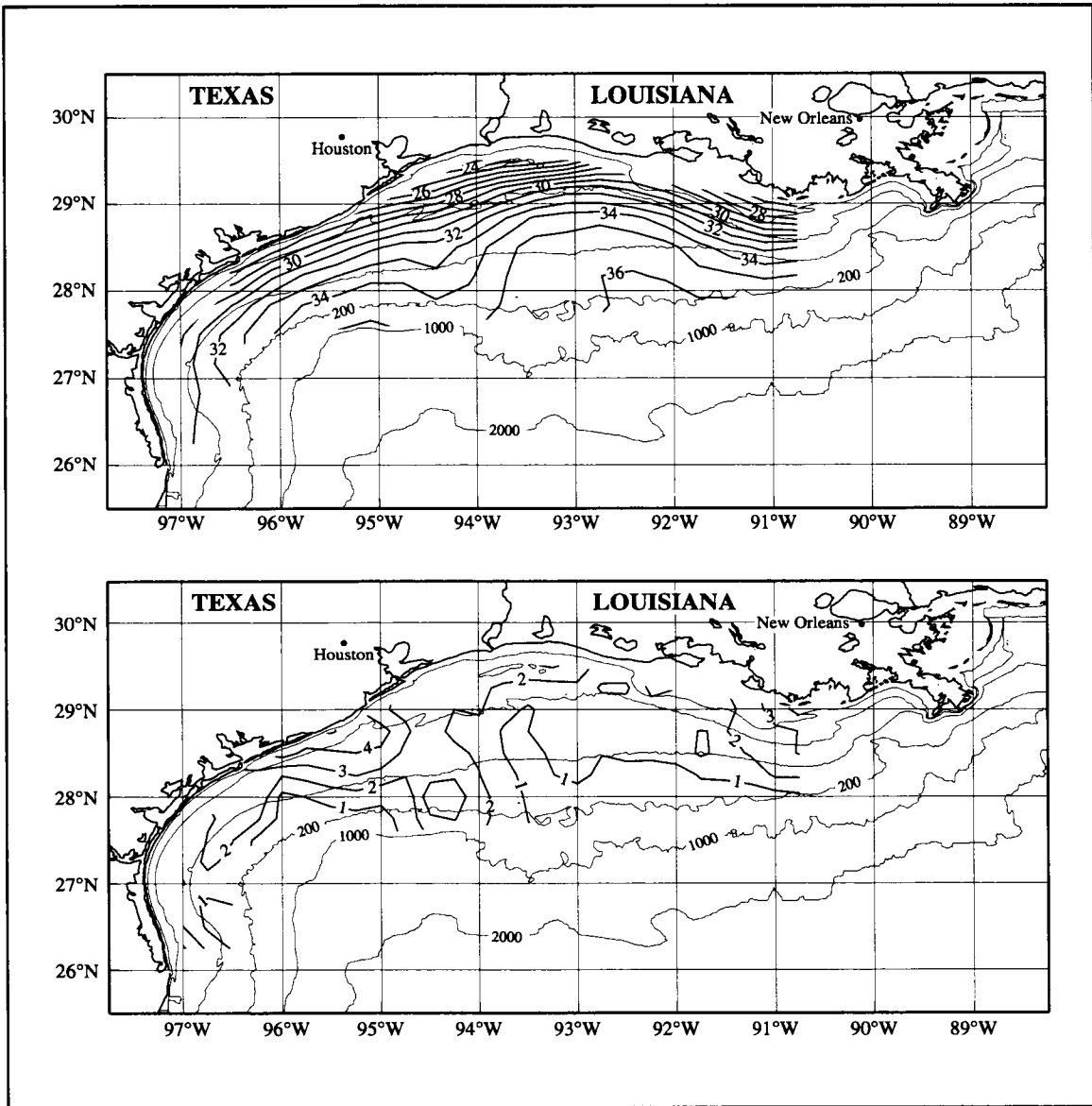


Figure 4.2-2. Average spring sea surface salinity (upper) and its standard deviation (lower) for eight May cruises.

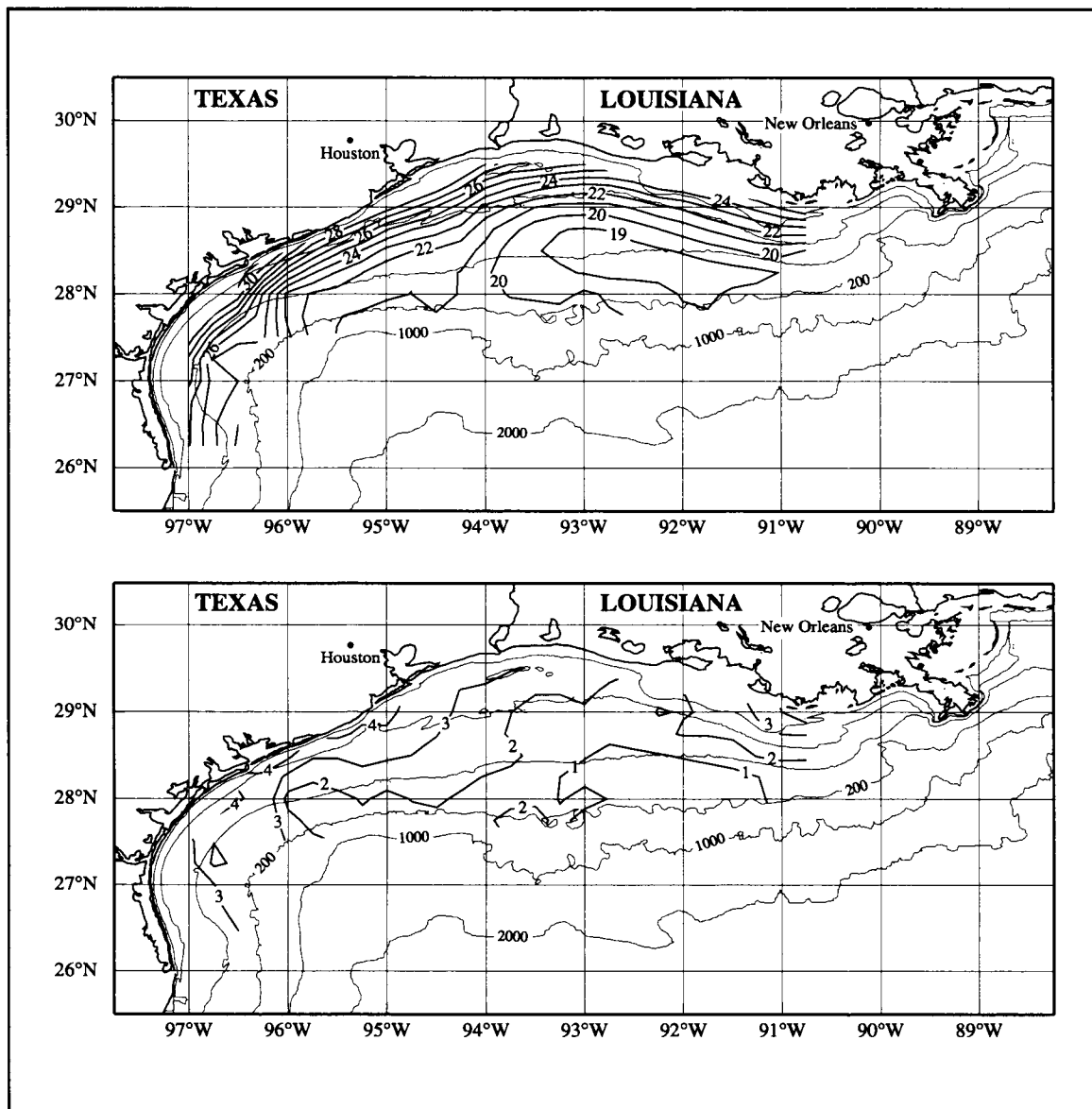


Figure 4.2-3. Average spring geopotential anomaly of sea surface relative to 70 db (upper) and its standard deviation (lower) for eight May cruises. Contours in dyn cm.

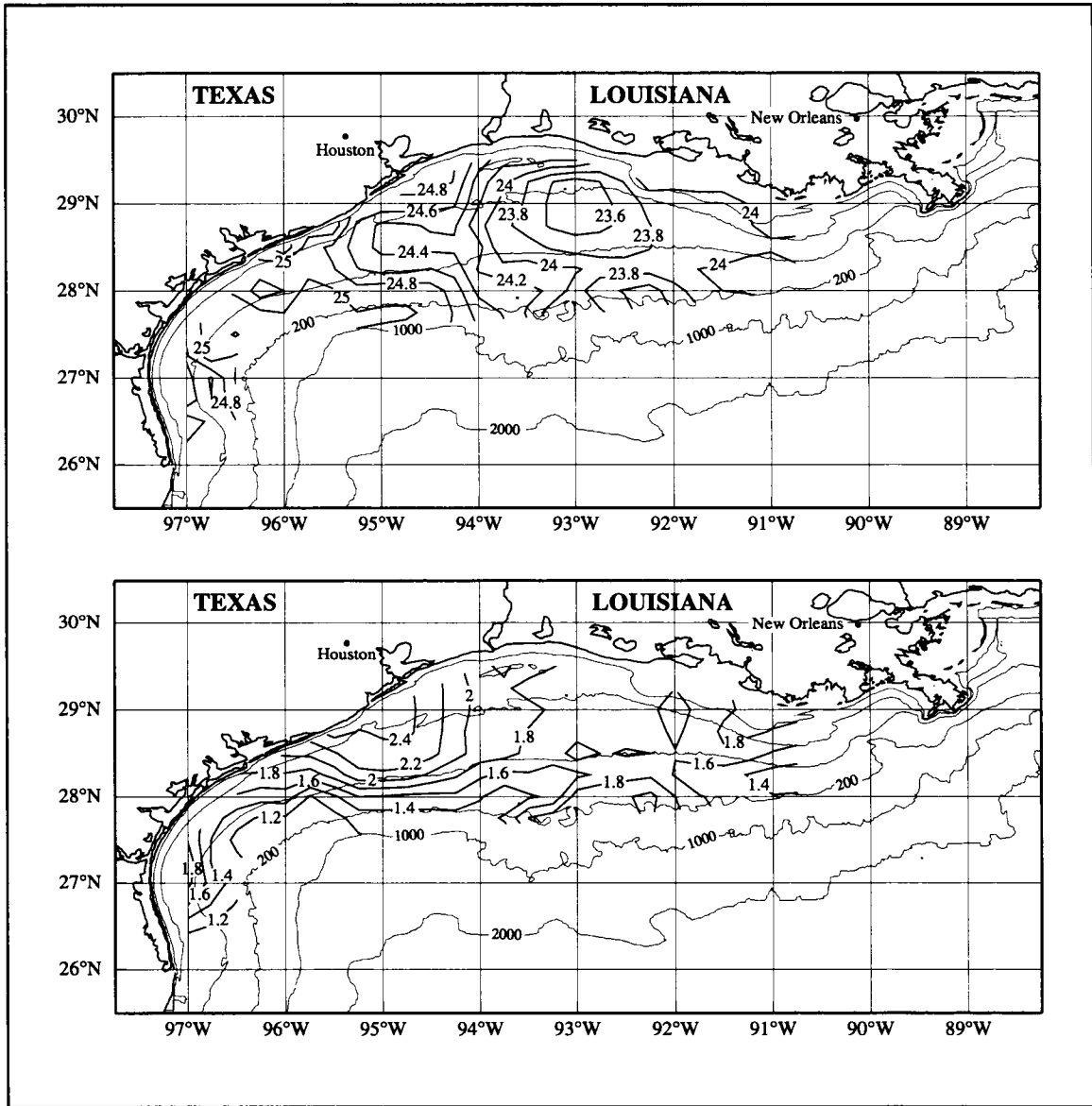


Figure 4.2-4. Average spring sea surface temperature (upper) and its standard deviation (lower) for eight May cruises. Contours in °C.

in Figures 4.2-5, 4.2-6 and 4.2-7. Figure 4.2-2 shows the average May distribution of sea surface salinity over the shelf. Features to be noted include the following:

- a. The principal salinity gradients are cross-shelf, with salinity increasing offshore due to the distribution of freshwater discharge along the coastal boundary.
- b. Near the coast, salinity values generally increase downcoast showing the diminishing effect of the Mississippi-Atchafalaya discharge with distance from the outflow.
- c. The largest cross-shelf gradients are over the inner shelf with the exception of the Texas shelf south of 28°N.
- d. The saltiest surface water is found over the outer shelf near 92°-93°W, corresponding to the center of the cyclonic feature in geopotential anomaly (Figure 4.2-3) and contributing to large cross-shelf gradients inshore of that feature. The source of this high salinity surface water must be the offshore Gulf. Thus, if it is a usual feature of this season it must be maintained by onshelf advection that is common in this season.

As expected, the standard deviation field for surface salinity has smallest values (less than 1 to 2) in the areas of smallest gradients: in the center of the high salinity surface water feature and off south Texas. This shows the small year-to-year variability in the high salinity tongue, and thus in the onshelf advection needed to maintain this feature. The largest values are found near shore—particularly near the mouth of the Mississippi and Atchafalaya rivers east of 91°W and along the central Texas coast from 95° to 96°W. Undoubtedly this pattern results from the large May-to-May variability in river discharge and downcoast movement of fresh waters, which may take about a month to reach the central Texas coast. Overall, the range of the mean surface salinity pattern is 12, whereas extreme values of standard deviations rarely reach 4.

The average May pattern of geopotential anomaly shown in Figure 4.2-3 has three principal features:

- a. Larger values and the highest gradients are located near the coast, suggesting a downcoast geostrophic coastal current. This is consistent with the plume of low salinity over the inner shelf.
- b. A partially closed cyclone exists over the eastern shelf, centered near 28.5°N, 92.5°W, with geopotential anomaly increasing offshore from the center. However, for the shelf west of 94°W no evidence of closed cyclonic circulation is seen.

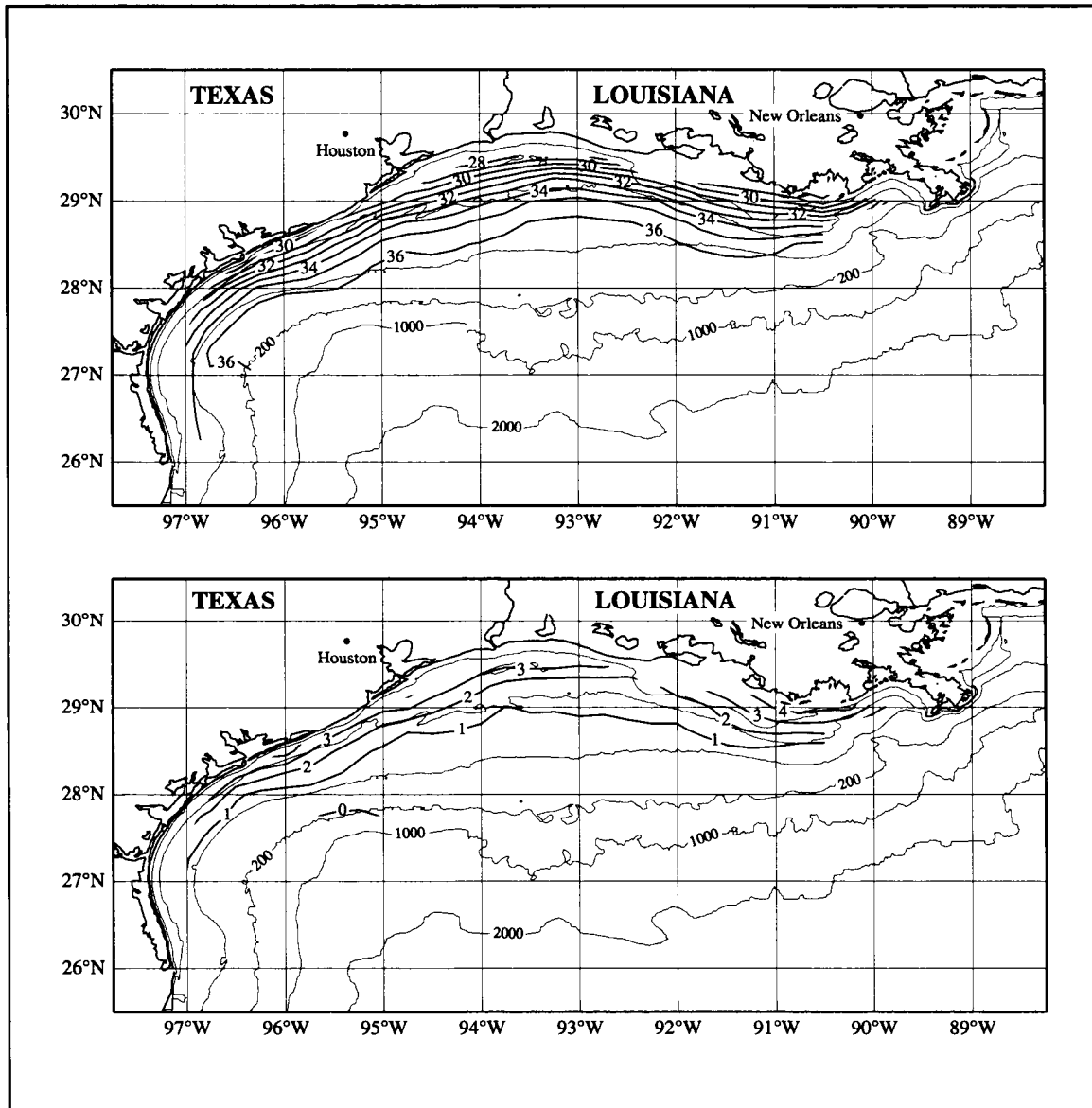


Figure 4.2-5. Average spring bottom salinity (upper) and its standard deviation (lower) for eight May cruises.

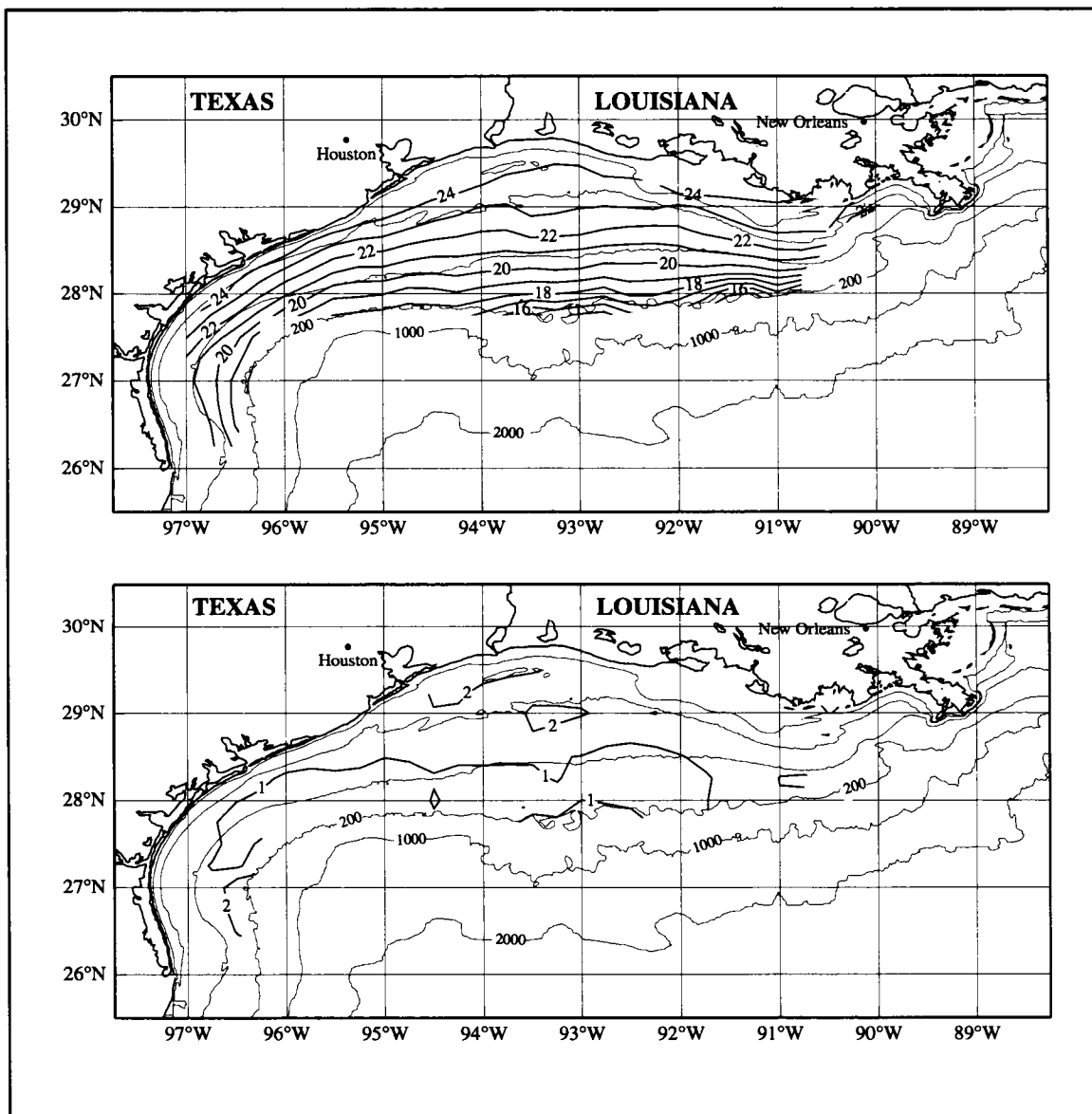


Figure 4.2-6. Average spring bottom temperature (upper) and its standard deviation (lower) for eight May cruises. Contours in °C.

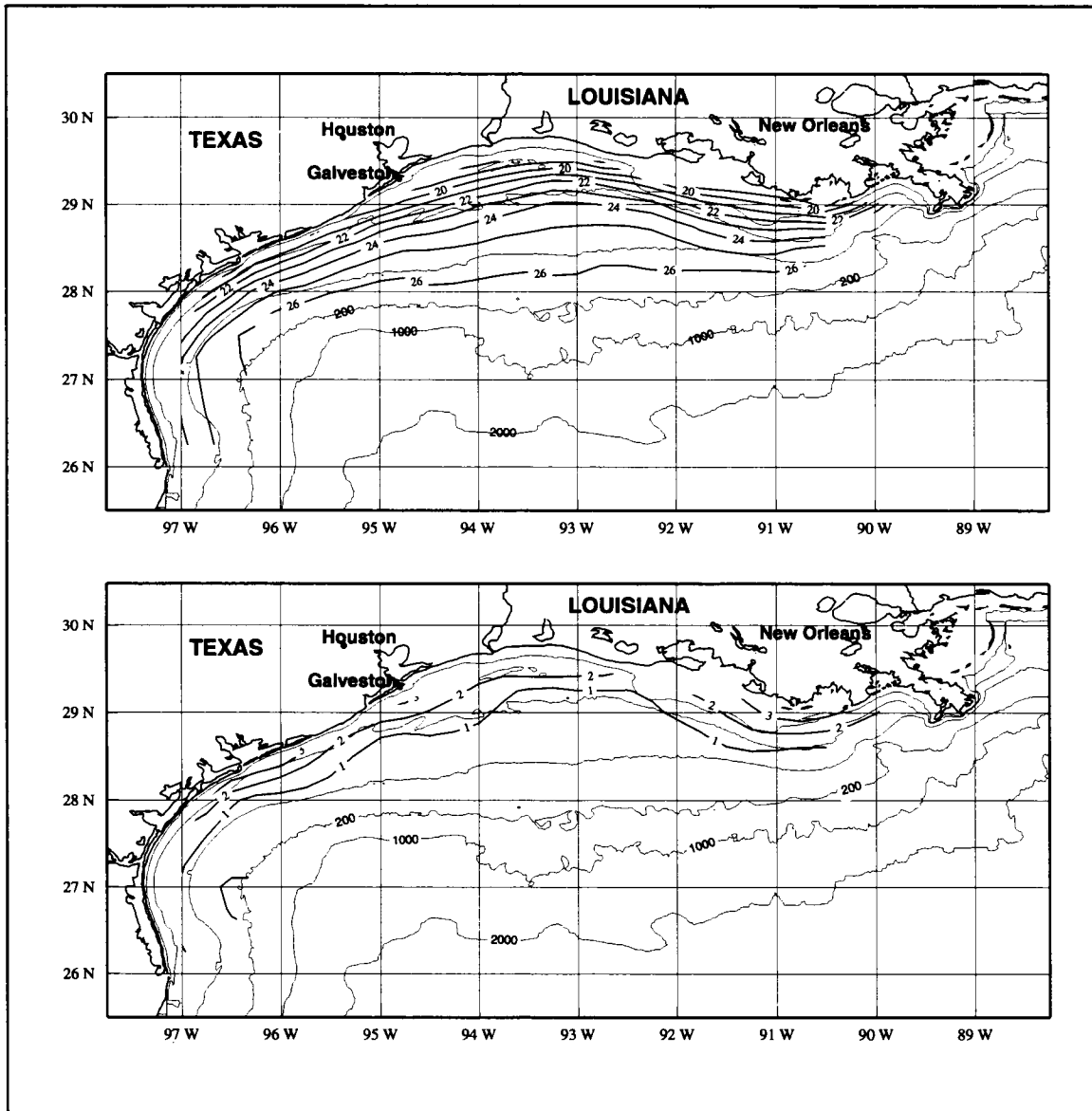


Figure 4.2-7. Average spring bottom potential density anomaly (upper) and its standard deviation (lower) for eight May cruises. Contours in $\text{kg}\cdot\text{m}^{-3}$.

- c. Highest values are found along the south Texas coast. This high is consistent with both the low salinity (Figure 4.2-2) and warm temperatures (Figure 4.2-4) seen over mid-shelf along the lower coast; surface isohalines generally curve seaward across the shelf.

The average alongshelf component of surface wind stress is directed downcoast from September through May. This is expected to force onshore surface Ekman flow and result in downcoast geostrophic flow over the inner shelf. Such is the case for our May mean pattern of geopotential anomaly. This downcoast flow carries with it the fresher waters of the Mississippi-Atchafalaya discharge. These fresh waters result in increased buoyancy nearshore and consequent increase in geopotential anomaly, or enhanced downcoast geostrophic flow.

Comparing Figure 4.2-3 with the May mean geopotential anomaly pattern of CK shown in Figure 4.1-1, one sees general agreement over the inner shelf and evidence for a cyclonic circulation over the eastern shelf but only downcoast shear west of 94°W. Differences may be expected because, although we have included the data used by CK in the production of our mean fields, we have added greatly to their data base.

The average May field of geopotential anomaly has a dynamic range of more than 10 dyn cm. The associated standard deviations (Figure 4.2-3) are less than 3 dyn cm over most of the shelf. Exceptions are found nearshore off the mouth of the Atchafalaya River and near Corpus Christi along the south central Texas coast where extreme values of standard deviation are greater than 4 dyn cm. The highs in the latter region are associated with the large year-to-year variation in salinity (Figure 4.2-2). Values of standard deviation are only 1 to 2 dyn cm in the region of the cyclonic circulation over the eastern shelf, implying that such circulation existed during most May periods sampled (see Figure 4.2-22).

Figure 4.2-4 shows the mean May distribution of surface temperature. Compared with the mean patterns for surface salinity and geopotential anomaly, gradients are weak and cross-shelf gradients are virtually absent in the temperature field. Two features are seen:

- a. Cooler water is located over the mid and outer shelf from about 91° to 94°W. Such a pattern is common in the surface temperature distributions for individual cruises and is consistent with the low in geopotential anomaly.
- b. Temperatures over the southwestern shelf are quite uniform with a range of less than 0.5°C and are warmer by about 1°C than over the eastern central shelf.

The standard deviation of surface temperature for individual cruises relative to the May mean (Figure 4.2-4) is between 1.5°C to somewhat greater than 2°C in most locations. This is comparable to or larger than the range of values in the mean field. We have examined

individual May fields of temperature difference relative to the May mean. These fields for individual cruises generally show negative values for cruises carried out before 10 May and positive values if after that date. This trend of anomalies and the large temperature standard deviation field can be explained by the rapid warming of the surface layers during spring due to increasing insolation and air temperature. Thus, we think that the mean field, though having a small range, is reasonable.

The mean bottom temperature for May (Figure 4.2-6) shows essentially along-isobath isotherms. The exception is just inshore of the 200-m isobath between 91° and 93°W where temperatures are as much as 3°C colder than along the western shelf edge. The inshore bottom temperatures in May are 4° to 5°C less than during July-August (Figure 4.2-12) by which time significant surface heating has occurred.

The standard deviations of individual cruise values from the mean bottom temperature range between 0.5° and 2.0°C over most of the shelf—values which are small compared to the range of the mean. Along the outer south Texas coast, however, standard deviations exceed 2°C. We attribute this to the frequent occurrence of anticyclones and cyclones seaward of the 200-m isobath in this region (Vukovich and Waddell 1991).

Summer fields. Fields of average surface salinity, geopotential anomaly, surface temperature, bottom salinity, bottom temperature, and bottom potential density for July-August with their standard deviations are shown in Figures 4.2-8 through 4.2-13. The average surface salinity distribution for July-August (Figure 4.2-8) shows a very simple pattern:

- a. The lowest values are found along the Louisiana coast east of 92°W, and from that area the salinity gradient is directed nearly radially outward.
- b. Salinities less than 30 are found across most of the shelf east of 91.5°W.
- c. Nearly uniform salinity values occur over the shelf off central and south Texas.

The average bottom salinity (Figure 4.2-11) has lowest values (< 32) inside the 10-m isobath from about 91° to 93°W. However, the gradient over the eastern half-shelf is essentially southward with values greater than 36 at the shelf edge and over the entire shelf west of about 95°W.

The standard deviation field for surface salinity (Figure 4.2-8) shows largest values (> 4) nearshore, east of 91.5°W, indicating large year-to-year variability in fresh water source for the summer season. In addition, the effect of wind on containing or enhancing the spread of surface discharge may contribute to the variability in this region. Short time-scale variability of the Mississippi plume, and thus surface salinity distributions, due to wind changes was

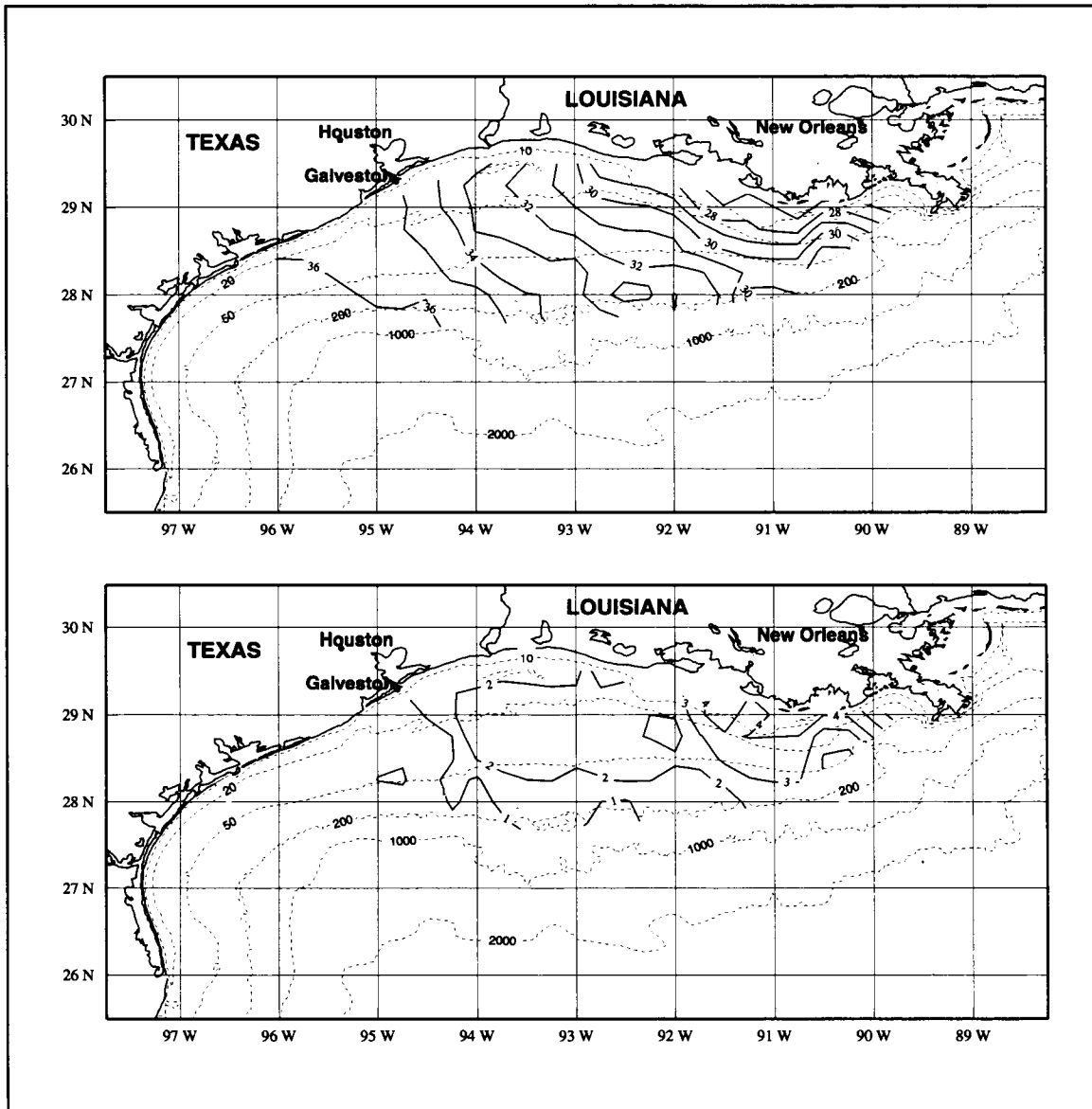


Figure 4.2-8. Average summer sea surface salinity (upper) and its standard deviation (lower) for seven July-August cruises.

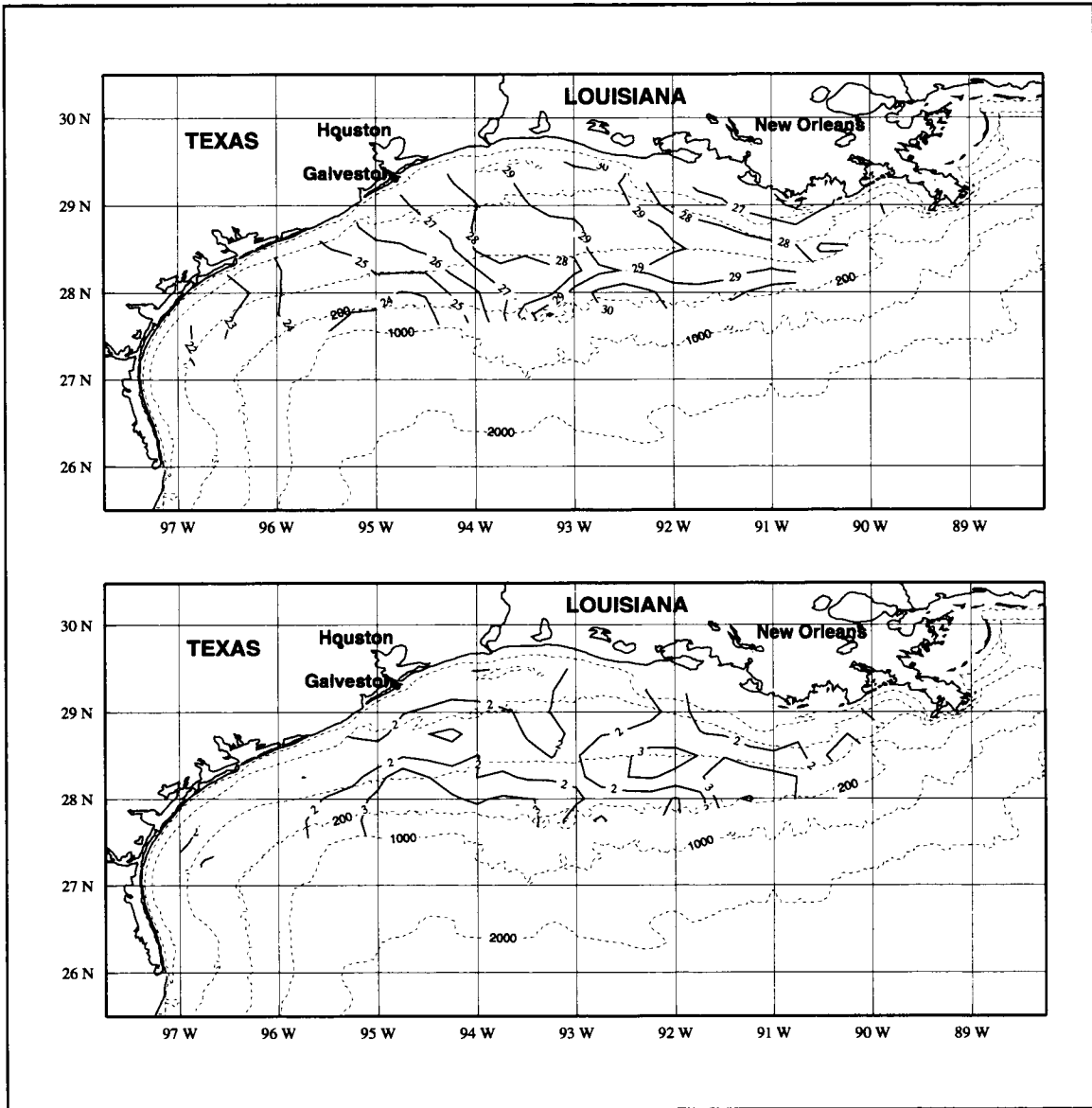


Figure 4.2-9. Average summer geopotential anomaly of sea surface relative to 70 db (upper) and its standard deviation (lower) for seven July-August cruises. Contours in dyn cm.

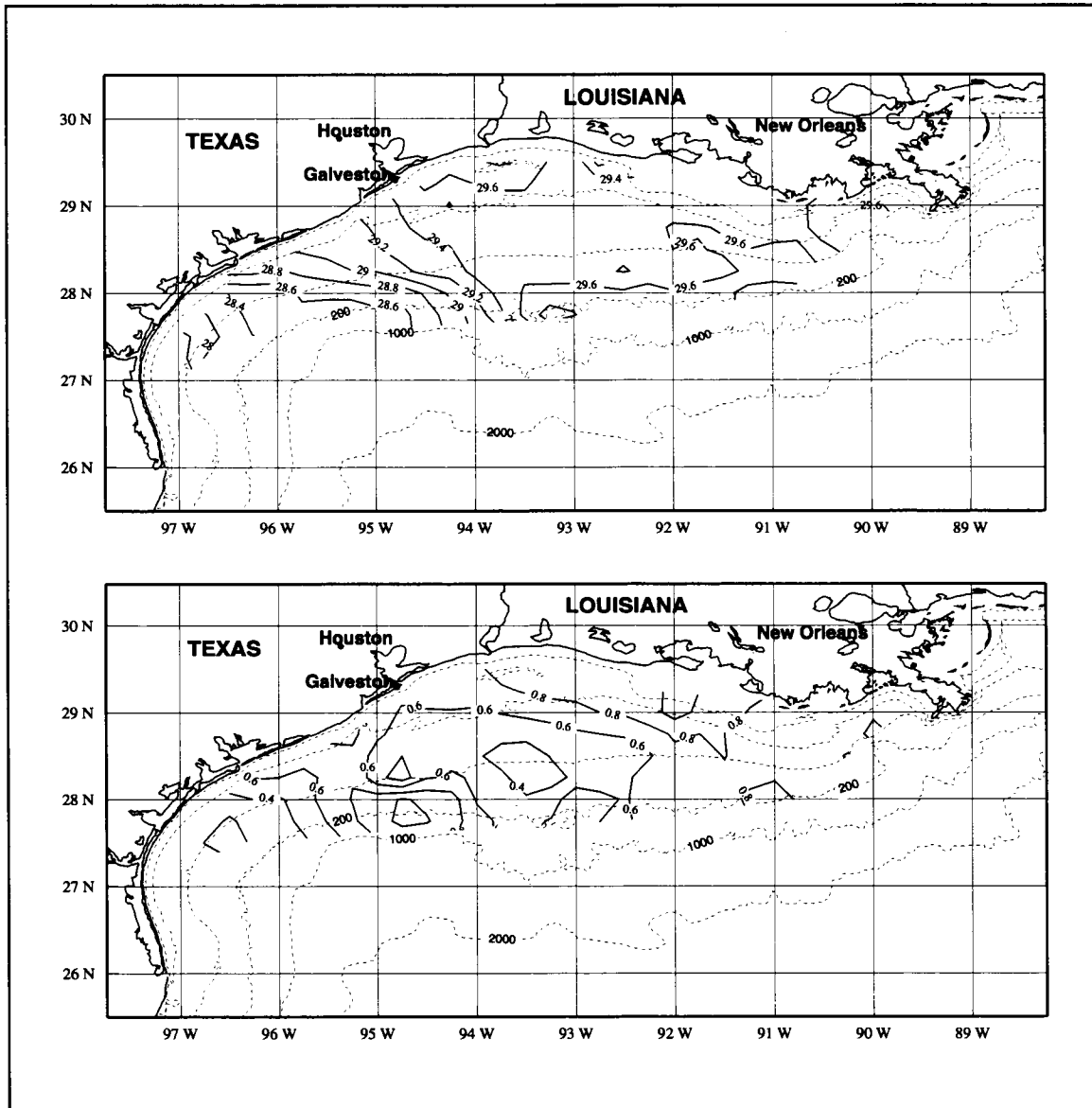


Figure 4.2-10. Average summer sea surface temperature (upper) and its standard deviation (lower) for seven July-August cruises. Contours in °C.

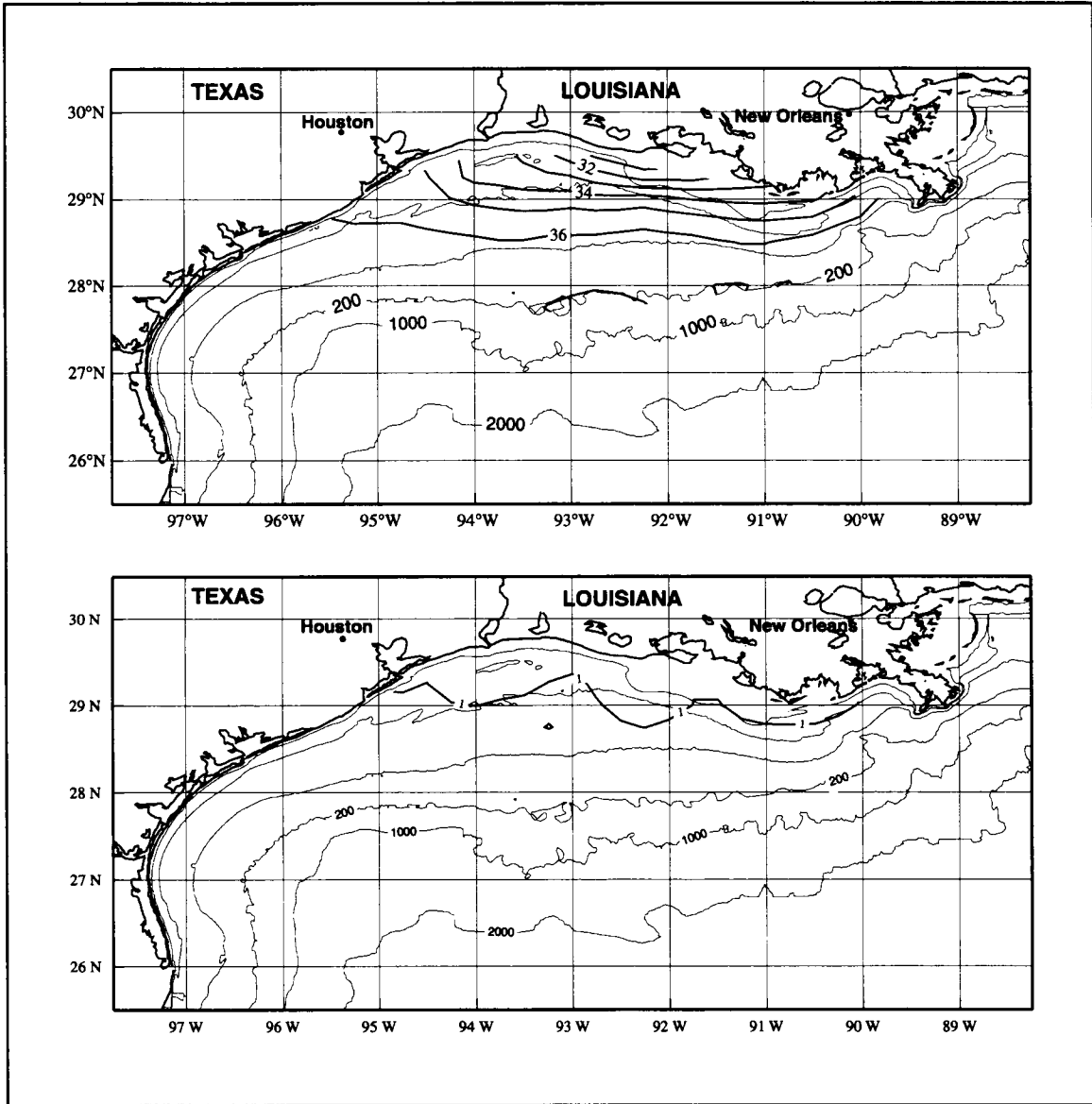


Figure 4.2-11. Average summer bottom salinity (upper) and its standard deviation (lower) for seven July-August cruises.

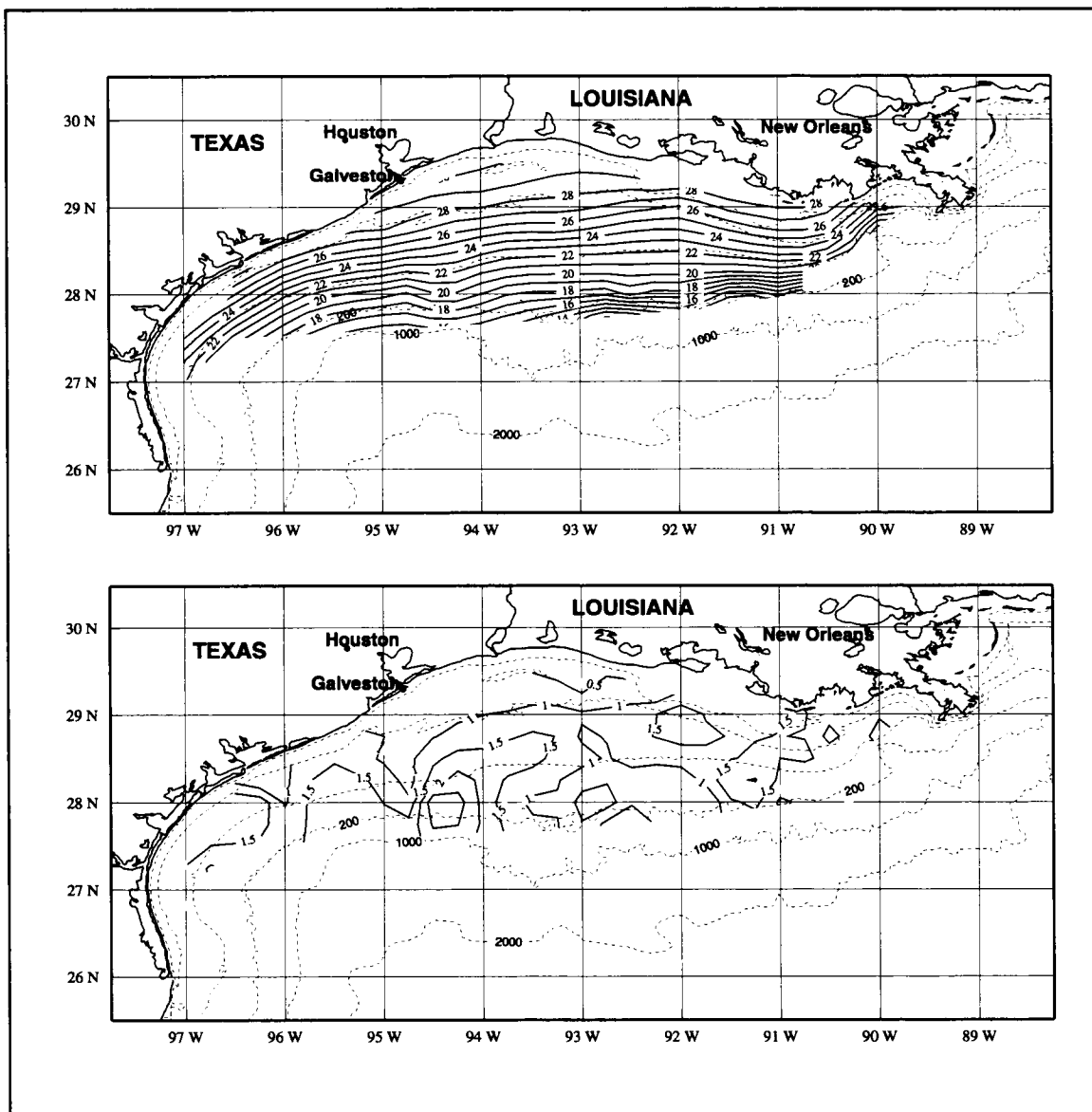


Figure 4.2-12. Average summer bottom temperature (upper) and its standard deviation (lower) for seven July-August cruises. Contours in °C.

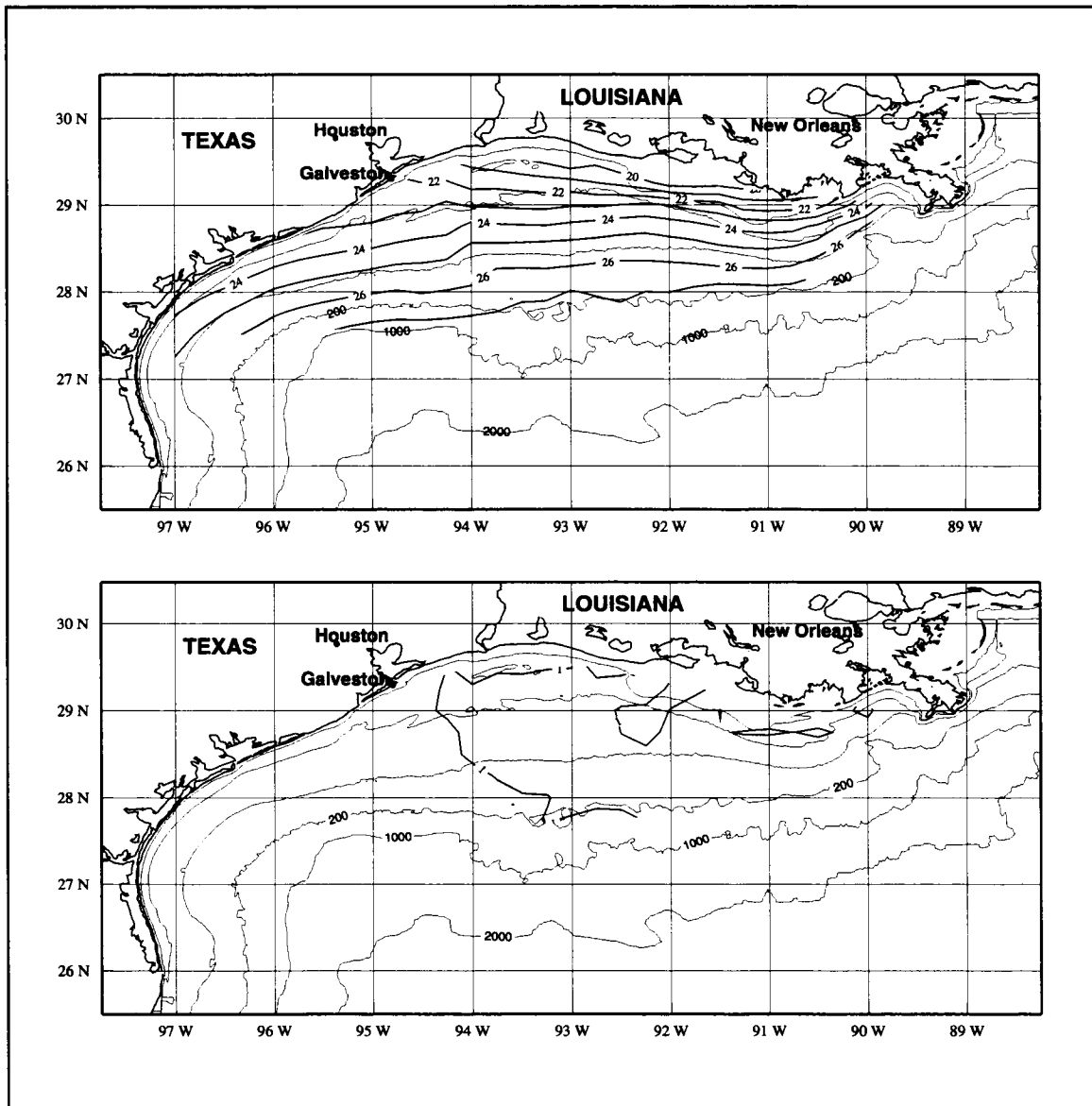


Figure 4.2-13. Average summer bottom potential density (upper) and its standard deviation (lower) for seven July-August cruises. Contours in $\text{kg}\cdot\text{m}^{-3}$.

discussed by Rouse (1996). Values over the shelf decrease downcoast to less than 1 west of 94.5°W . Thus, the lower shelf is little affected by freshwater sources in summer. Indications are that much high salinity water is regularly being carried upcoast by the circulation. The salinity field is perhaps the best indicator of the summer pattern of upcoast flow.

The July-August mean surface geopotential anomaly relative to 70 db (Figure 4.2-9) is dominated by a high located NW-SE across the shelf at 92° - 94°W . There is a general negative gradient downcoast and slightly lower values inshore near the Mississippi delta. In summer, a pattern of upcoast flow over the inner shelf is expected in response to forcing by wind stress which has an average upcoast component during July and August. This geopotential anomaly pattern may be interpreted as indicative of an upcoast flow over the south Texas coast. This is consistent with uniform, relatively salty water over the south Texas shelf (Figure 4.2-8) caused by upcoast advection. The standard deviations for geopotential anomaly (Figure 4.2-9) are rather uniform near 2 dyn cm over most of the shelf. Depending on how well the geopotential anomaly field represents the circulation, Figure 4.2-9 indicates possible downcoast flow along the inner Louisiana shelf resulting in some nearshore convergence along the upper Texas coast. In general we believe that the summer patterns of geopotential anomaly constructed by extrapolation into shallower water may be unrepresentative of the relative flow fields, because bottom isopycnals do not follow isobaths in summer (Figure 4.2-13) as well as in other seasons, and thus significant pycnobathic currents not represented in these fields may exist. Moreover, the LATEX direct current measurements indicate general upcoast currents over the inner shelf during summer (Section 4.4 and Appendix H.2).

The average summer surface temperatures (Figure 4.2-10) are highest east of 94°W , and generally decrease downcoast. This pattern is consistent with upcoast flow of cooler surface water along the south Texas coast. Such surface waters could result from near coastal upwelling (Cochrane et al. 1995; Appendix B.3). The range of the mean pattern is approximately 2°C . The standard deviation for this field ranges from 0.2° to 0.9°C , with an average of about 0.6°C .

In the mean July-August distribution (Figure 4.2-12), bottom isotherms generally follow isobaths. Exceptions are seen just inshore of the 200-m isobath along the shelf edge from about 91°W to 93°W ; there the bottom water at 200 m is colder by as much as 3°C than along the western shelf edge. (Note that the standard deviation values in that region range only from 1° to 1.5°C .) A possible explanation is that eastward flow at the shelf edge causes a bottom Ekman layer that induces onshelf movement and thus upwelling. Hsueh and O'Brien (1971) describe the dynamics of this situation with a model; however, we have not found other data to substantiate that this is the general case in summer for this region.

Fall fields. If monthly flow patterns over the inner shelf are primarily wind driven and correspond in alongshelf direction with the alongshelf wind component, November and

May patterns in hydrographic variables should be quite similar. Significant differences could be expected, however, due to differences in other external forcing mechanisms. As shown in Section 2.3, May is at the end of the period of maximum average discharge for the Mississippi-Atchafalaya river system; average discharge is at its minimum during October and November. Moreover, May is in the period of extreme warming by air-sea heat exchange; November is a time of extreme cooling, often including severe outbreaks of cold, dry continental air over the shelf (Sections 2.1.3 and 2.2).

In Figures 4.2-14 through 4.2-19 are shown the November mean fields for surface salinity, geopotential anomaly, surface temperature, bottom salinity, bottom temperature, and bottom potential density with their associated standard deviation fields. Compared with the May mean surface salinity field (Figure 4.2-2), November surface salinities over the inner shelf are much larger and the cross-shelf gradients smaller. This is expected because of the difference in river discharge—May follows the month of highest average Mississippi-Atchafalaya river discharge, but November follows the period of lowest average discharge. Even over the outer shelf, November mean values exceed those in May. The November isohalines more nearly follow isobaths than in May, though in the November field, as for May, the saltiest water present does extend further onto the shelf between 92° and 95° W than elsewhere.

The standard deviations of the six November surface salinity fields about the mean have a rather simple pattern. Values are near unity along the outer shelf and increase to somewhat above 2 toward shore. Values slightly in excess of 3 are found just south of 28° N and near 93.5° W. Unlike the pattern for May (Figure 4.2-2), no large interannual variability is seen near the Mississippi Delta during November.

The November mean field of geopotential anomaly (Figure 4.2-15) shows high values inshore, indicative of downcoast flow over the inner half of the shelf. Such downcoast flow is expected to be forced by the downcoast average alongshelf wind stress component for November (as discussed in conjunction with the spring fields), and is in agreement with downcoast flow in the May mean (Figure 4.2-3). We note that the cross-shelf gradients of geopotential anomaly 3 m relative to 70 db are stronger in May than in November. This is consistent with the expected enhanced downcoast buoyancy driving provided by more nearshore river waters in spring. However, LATEX A current measurements from 10 m depth over the inner shelf do not support stronger downcoast currents in May than in November, at least at 10 m depths. This disagreement may result in part because the river water effect on buoyancy driving might be confined largely above 10 m and partly because the downcoast barotropic component of flow may be larger in fall.

The mean May geopotential anomaly field (Figure 4.2-3) shows a partially closed low over the outer-to-mid shelf at 91° - 93.5° W. Over the outer shelf in November, there appear only

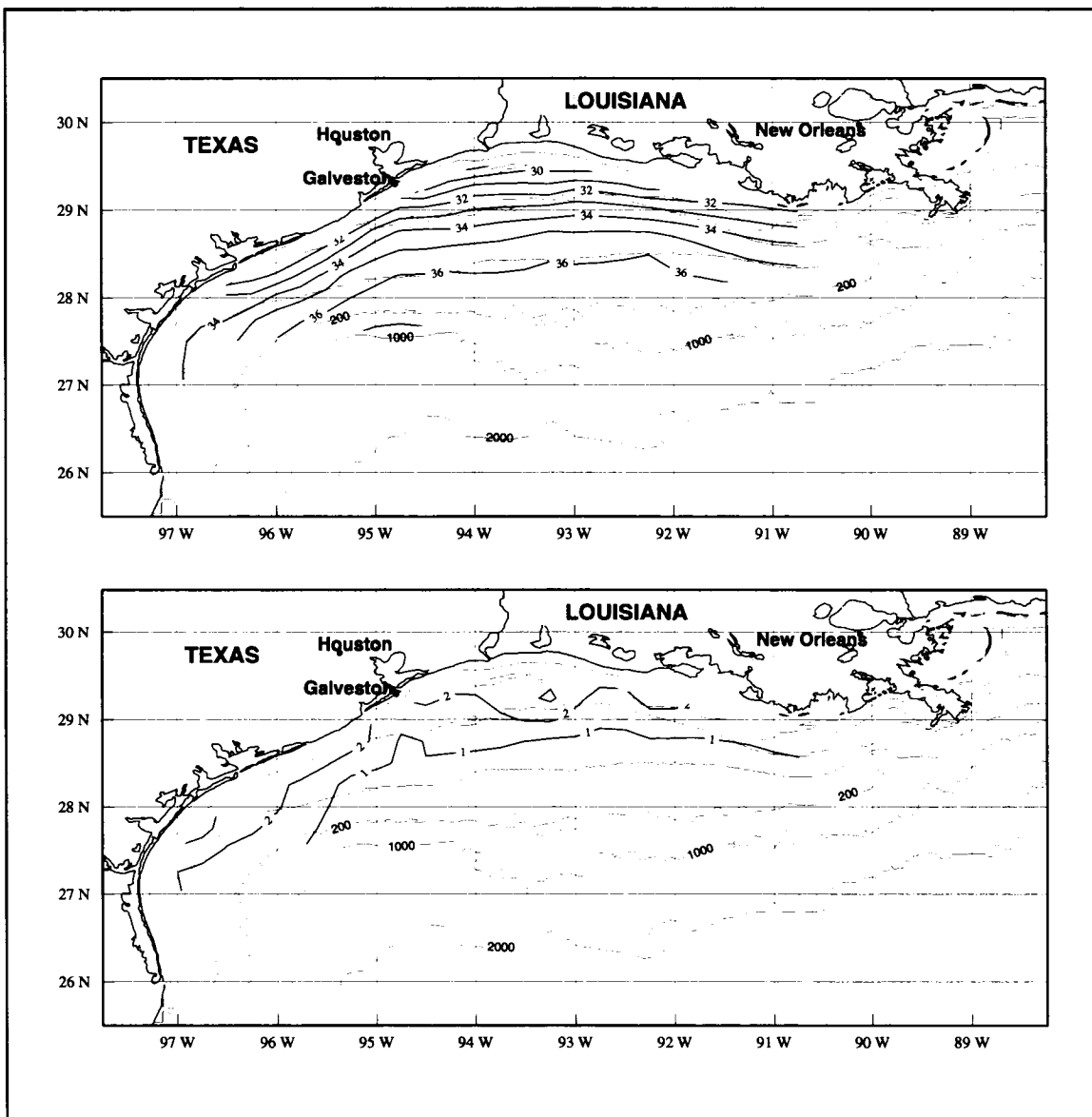


Figure 4.2-14. Average fall sea surface salinity (upper) and its standard deviation (lower) for six November cruises.

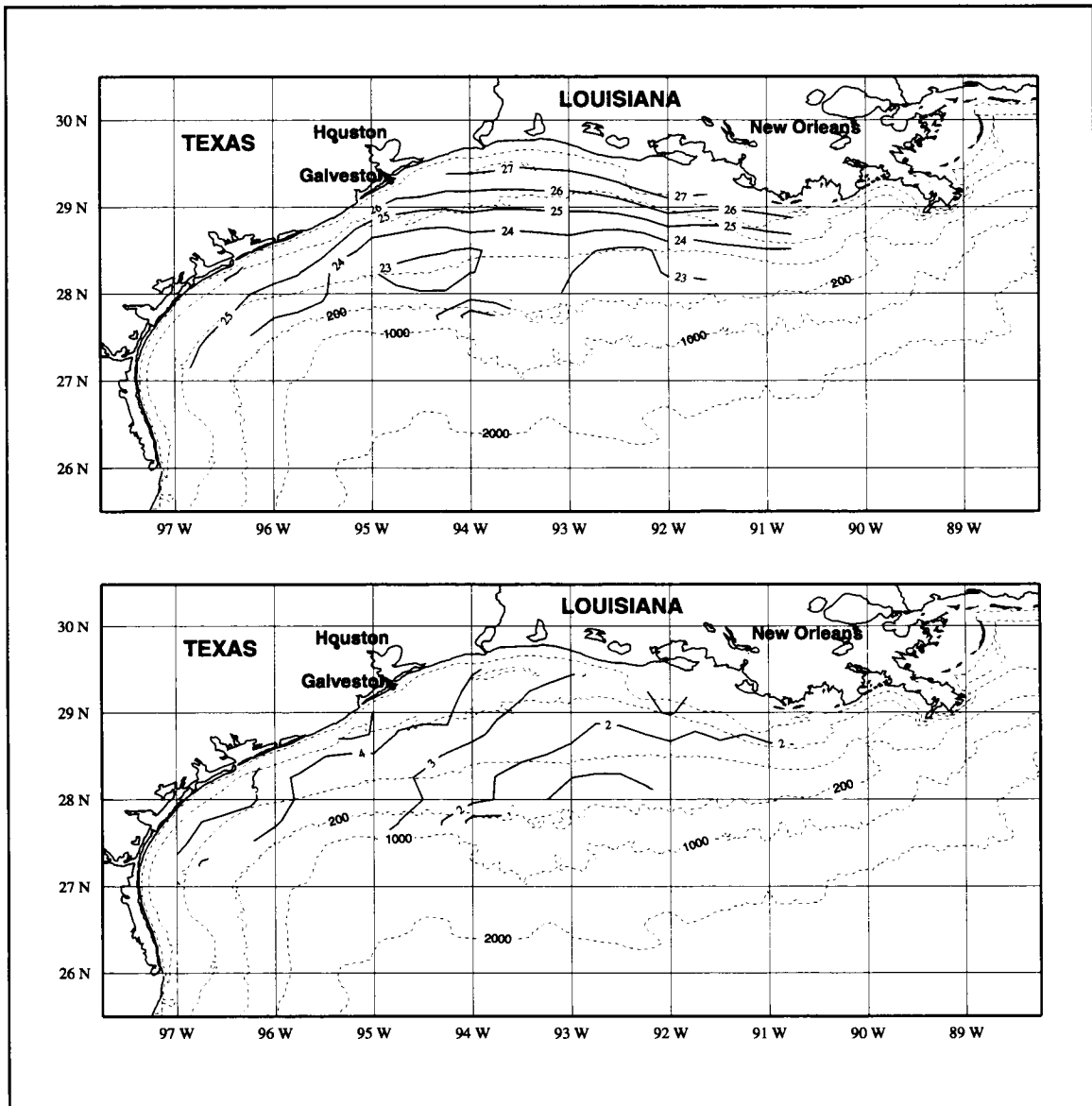


Figure 4.2-15. Average fall geopotential anomaly of sea surface relative to 70 db (upper) and its standard deviation (lower) for six November cruises. Contours in dyn cm.

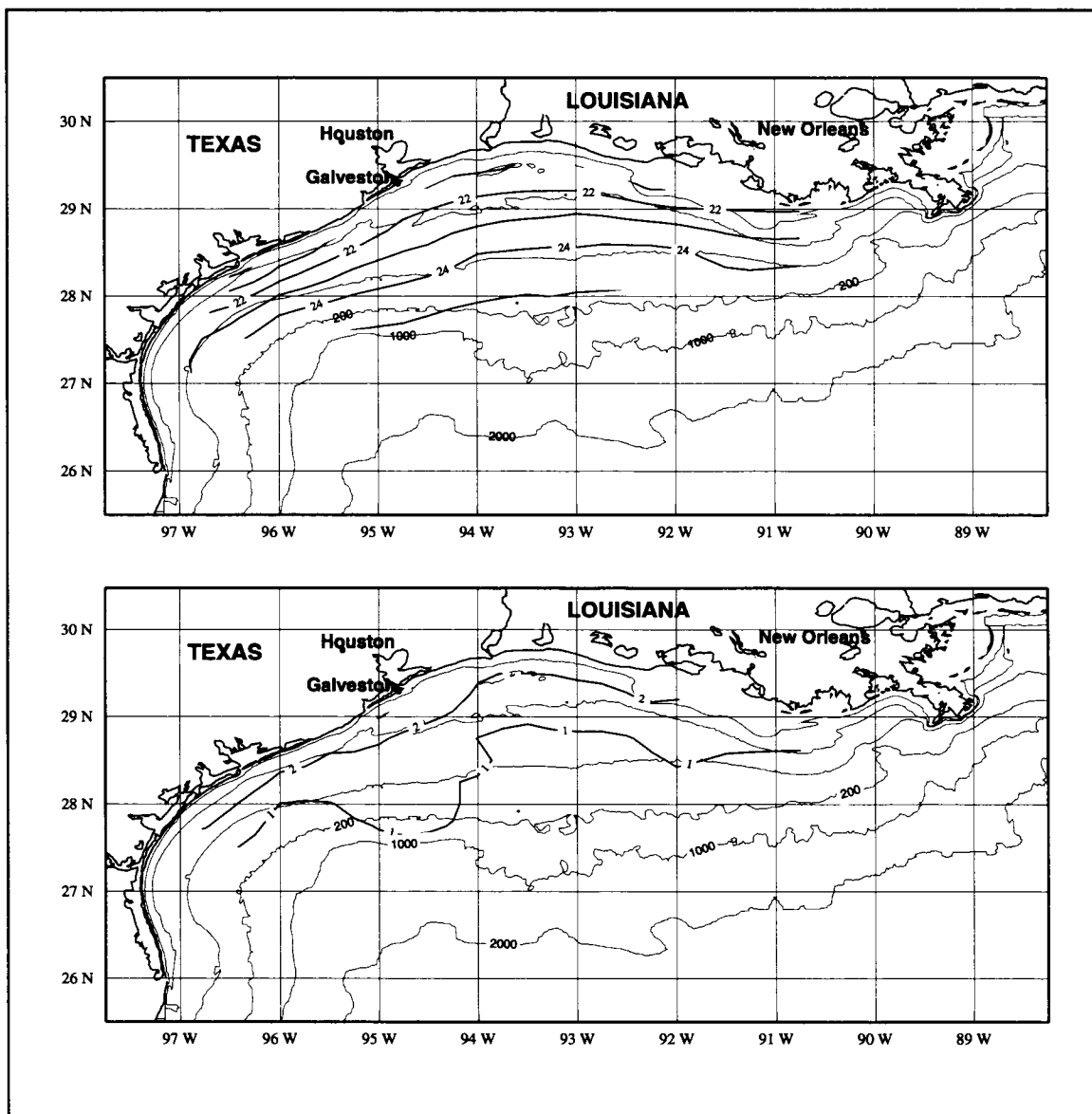


Figure 4.2-16. Average fall sea surface temperature (upper) and its standard deviation (lower) for six November cruises. Contours in °C.

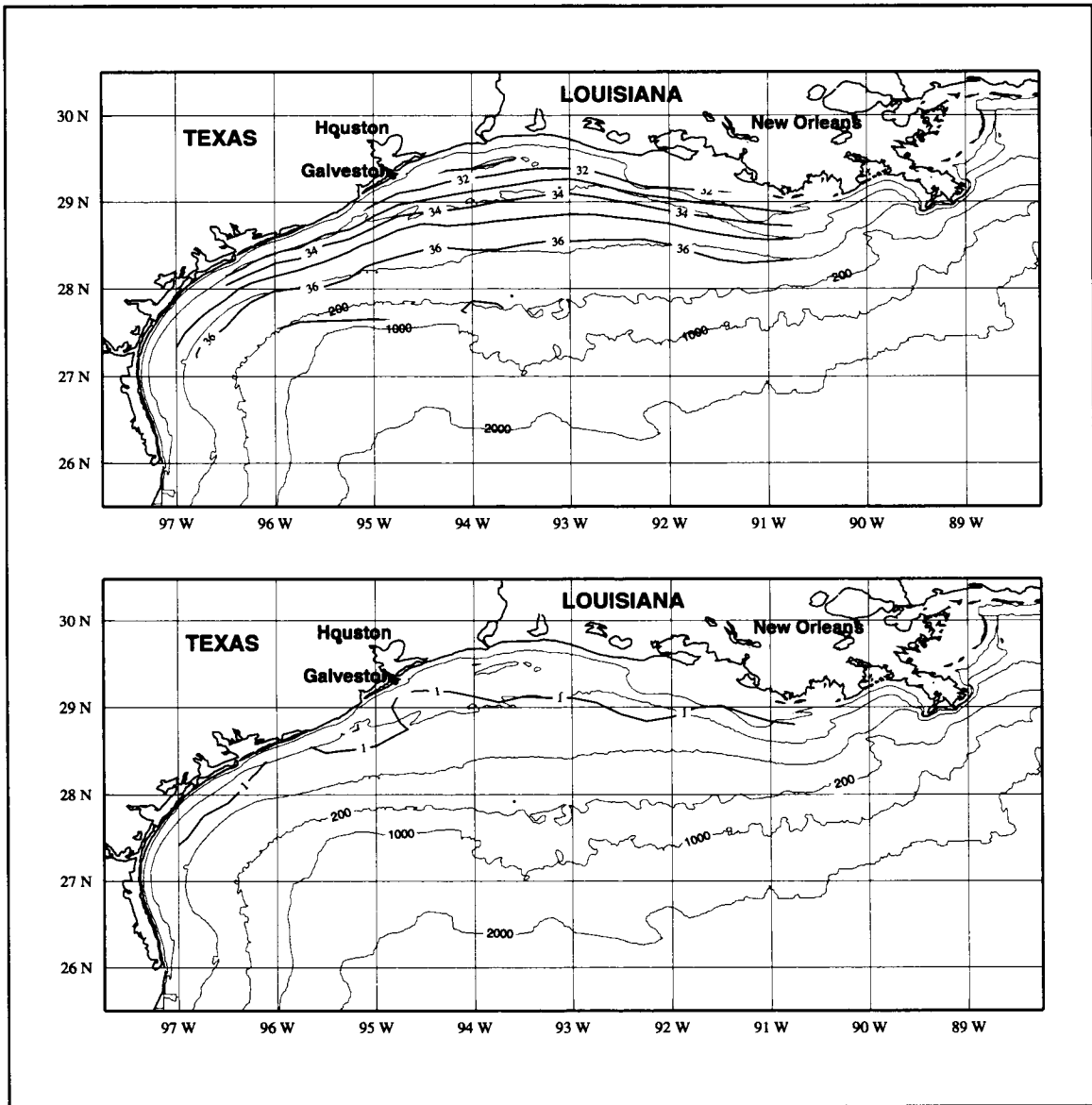


Figure 4.2-17. Average fall bottom salinity (upper) and its standard deviation (lower) for six November cruises.

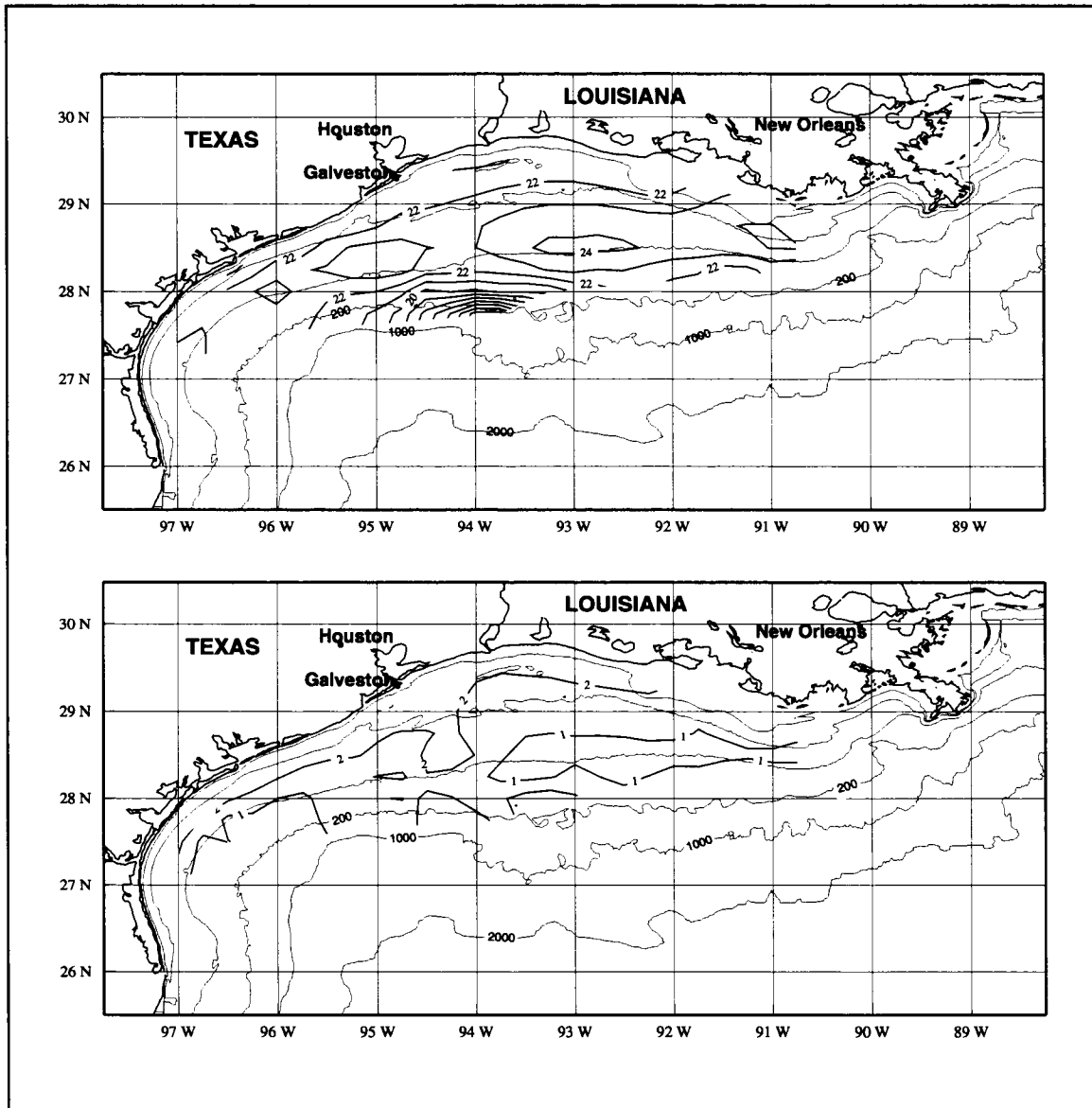


Figure 4.2-18. Average fall bottom temperature (upper) and its standard deviation (lower) for six November cruises. Contours in °C.

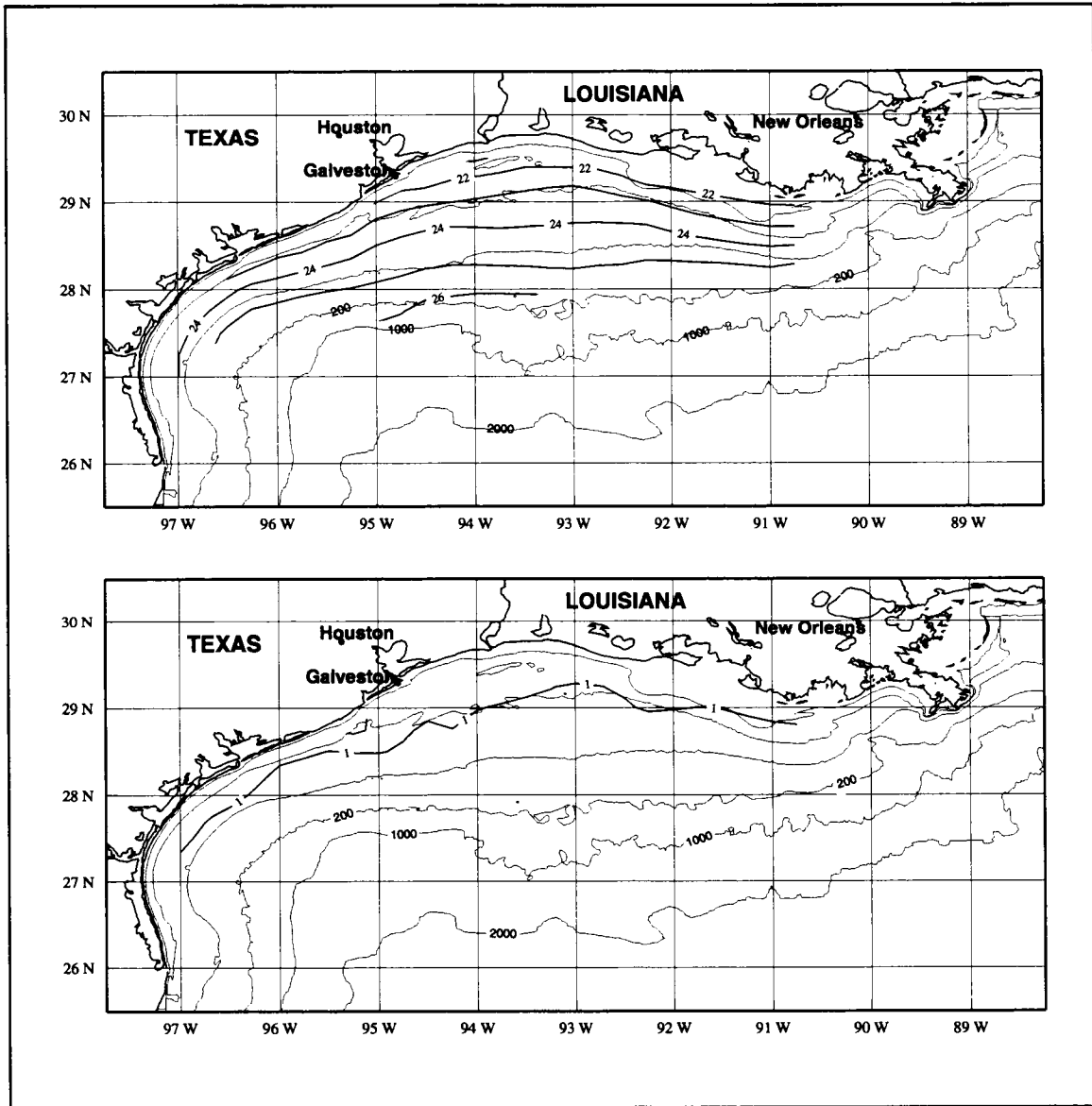


Figure 4.2-19. Average fall bottom potential density (upper) and its standard deviation (lower) for six November cruises. Contours in $\text{kg}\cdot\text{m}^{-3}$.

a small, weak closed low and a second semi-enclosed low. If the 23-dyn cm contours in Figure 4.2-15 were combined, the pattern would be one of a larger low extending east-southeast to west-northwest over the outer- to mid-shelf from about 92° to 95°W. The November mean field of CK based on only the GUS III data (Figure 4.1-1) shows a closed low over the outer shelf, with minimum values between 94° and 96°W. Our November mean does not substantiate this.

The standard deviation of individual geopotential anomaly fields relative to the November mean (Figure 4.2-15) is similar in shape and magnitude to that for May (Figure 4.2-3). Relative to May, greater values (> 5 dyn cm) are found in November along the south Texas coast and lower values near the Mississippi Delta. The smaller Mississippi-Atchafalaya discharge in November should give less interannual variability near the delta than during May. Cold air outbreaks in the fall are often associated with brief periods of upcoast wind over the lower Texas coast, and thus upcoast nearshore flow, which could account for the relatively large year-to-year variability in that area during November.

The November surface temperature field (Figure 4.2-16) shows values increasing offshore everywhere. Similar to the surface salinity field, slightly higher values are found further inshore over the eastern shelf than further downcoast. This surface temperature pattern with a range of 4°C is in stark contrast to the May mean (Figure 4.2-4) with its alongshelf gradients and small total range of values. The November distribution can be explained by the fact that outbreaks of cold air begin to cool the waters of this shelf as early as September, and by November the effects are clearly seen as a cross-shelf surface temperature pattern. The effects of such cooling are seen even in the mean November bottom temperature field (Figure 4.2-18), where temperatures in the inner shelf are less than 22°C (similar to surface values) and the maximum values are found over mid-shelf where cooling had not yet influenced bottom waters. Nowlin and Parker (1974) made a case study of the effects on this shelf of one such cold-air outbreak; they showed nearshore, 10-m temperatures to decrease by 5°C, and noticeable temperature changes to 100 m and offshore to 275 km due to the passage of only one front.

The year-to-year variability in November surface temperatures as estimated from the standard deviation of individual cruise patterns relative to the mean is slightly greater than 2°C near shore. This decreases to values less than 1°C over the shelf-slope break (Figure 4.2-16).

To examine whether the average distribution for a specific season is likely to be representative of an individual distribution sampled in that season, we prepared season histograms of differences between values of salinity, temperature, and geopotential anomaly for each of the individual cruises used and our seasonal mean fields at each grid point in the individual (1/4 x 1/4 degree) fields. These histograms (Figure 4.2-20) show highly tuned Gaussian distributions centered on zero differences—convincing evidence that a randomly selected

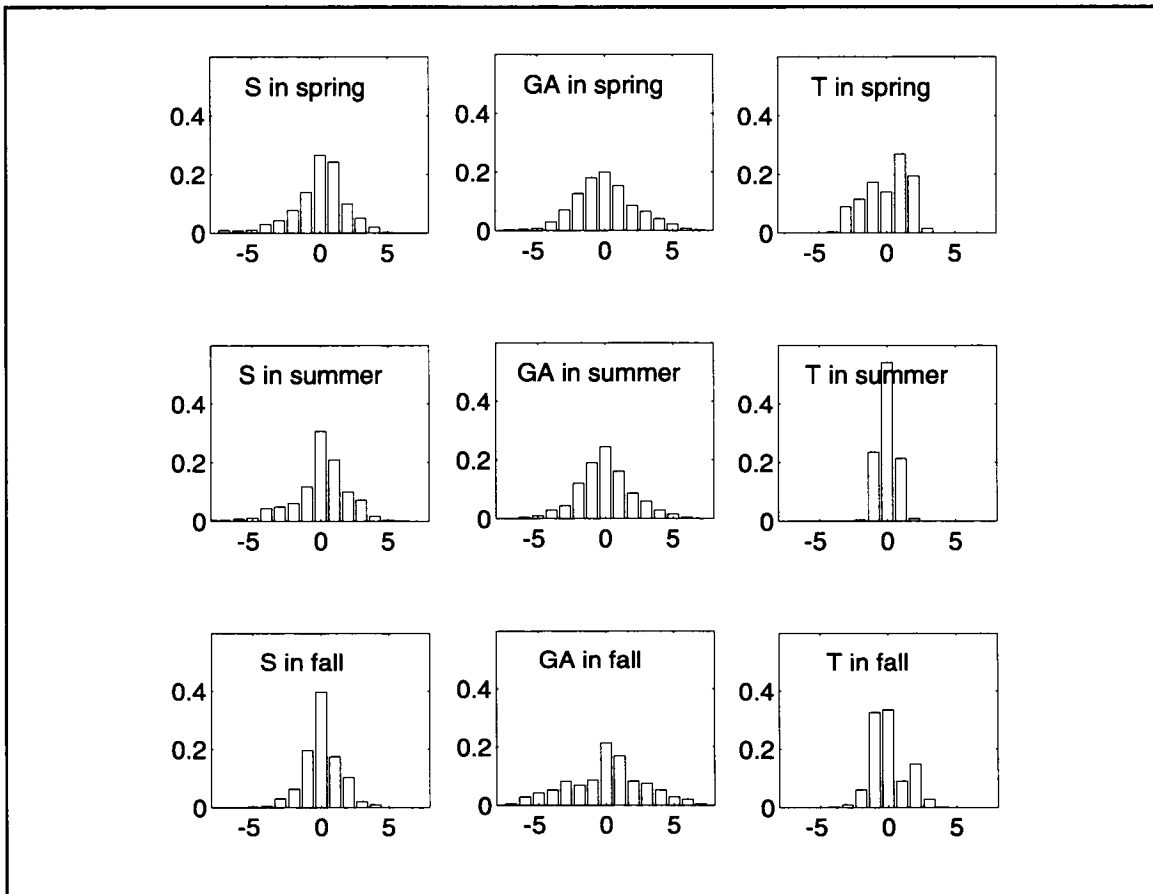


Figure 4.2-20. Histograms of residual fields, i.e., differences between gridded values of surface salinity, surface temperature ($^{\circ}\text{C}$), and geopotential anomaly (dyn cm) for individual cruise fields and those for mean fields. Comparisons include values from all individual cruise fields used to produce each seasonal mean.

individual field will be similar to the mean for the season of the individual field. Further evidence of this is provided by comparing the individual fields with the appropriate seasonal means. Figures 4.2-21 and 4.2-22 show station locations and contours for each individual field of salinity for the summer season and of geopotential anomaly for the spring season as sample illustrations.

In summary, for the Texas-Louisiana continental shelf we have prepared and examined mean fields, with standard deviations, of surface and bottom temperature and salinity and of geopotential anomaly representing spring, summer, and fall. The mean fields verify a bimodal cycle of geopotential anomaly and circulation patterns, although the patterns differ

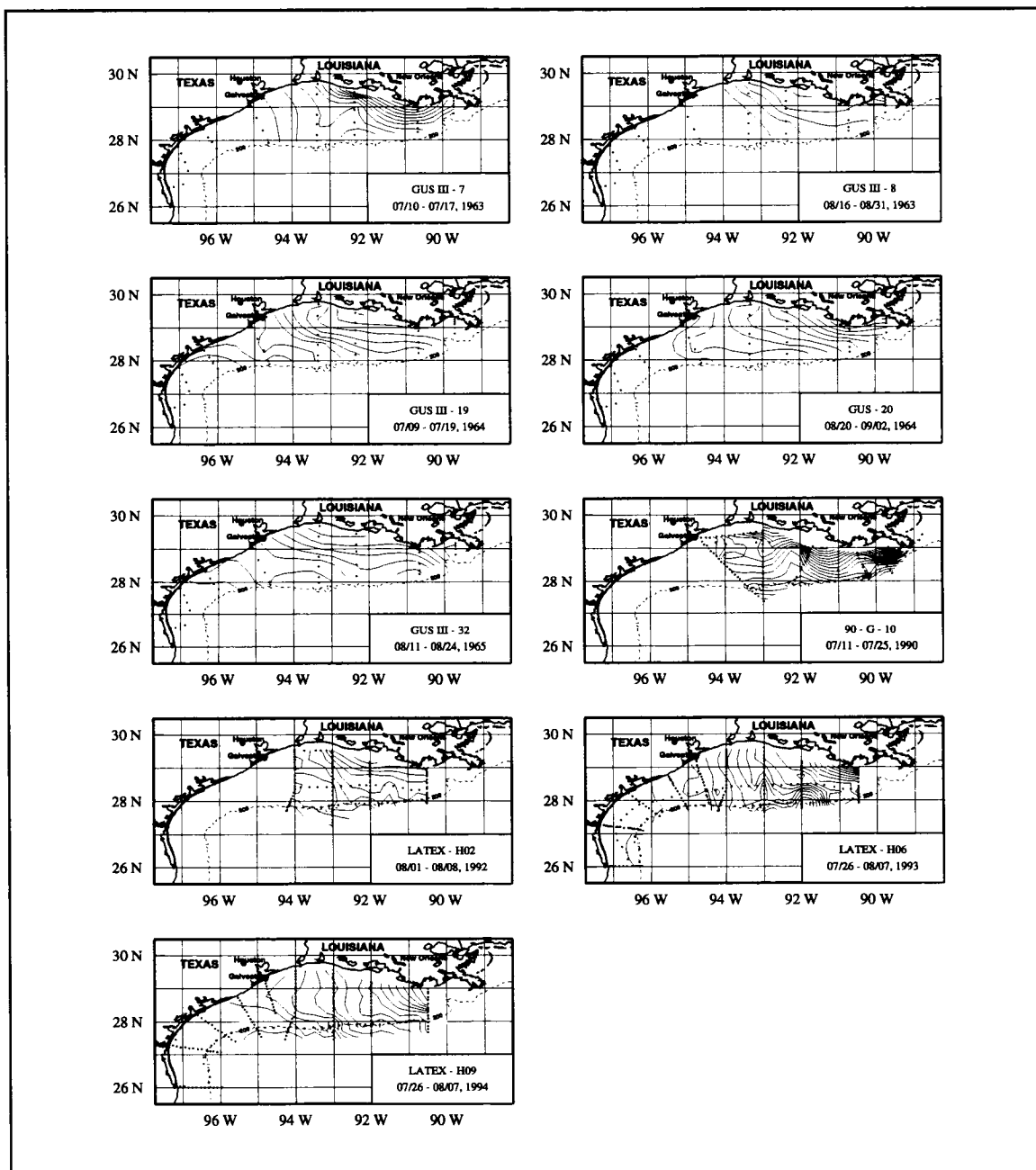


Figure 4.2-21. Surface salinity for the nine individual July and August cruises used to construct the summer mean fields. (Contour interval is 1; outer contour is 36, except for 90-G-10 for which outer contour is 35.) Also shown are positions of hydrographic stations for each cruise.

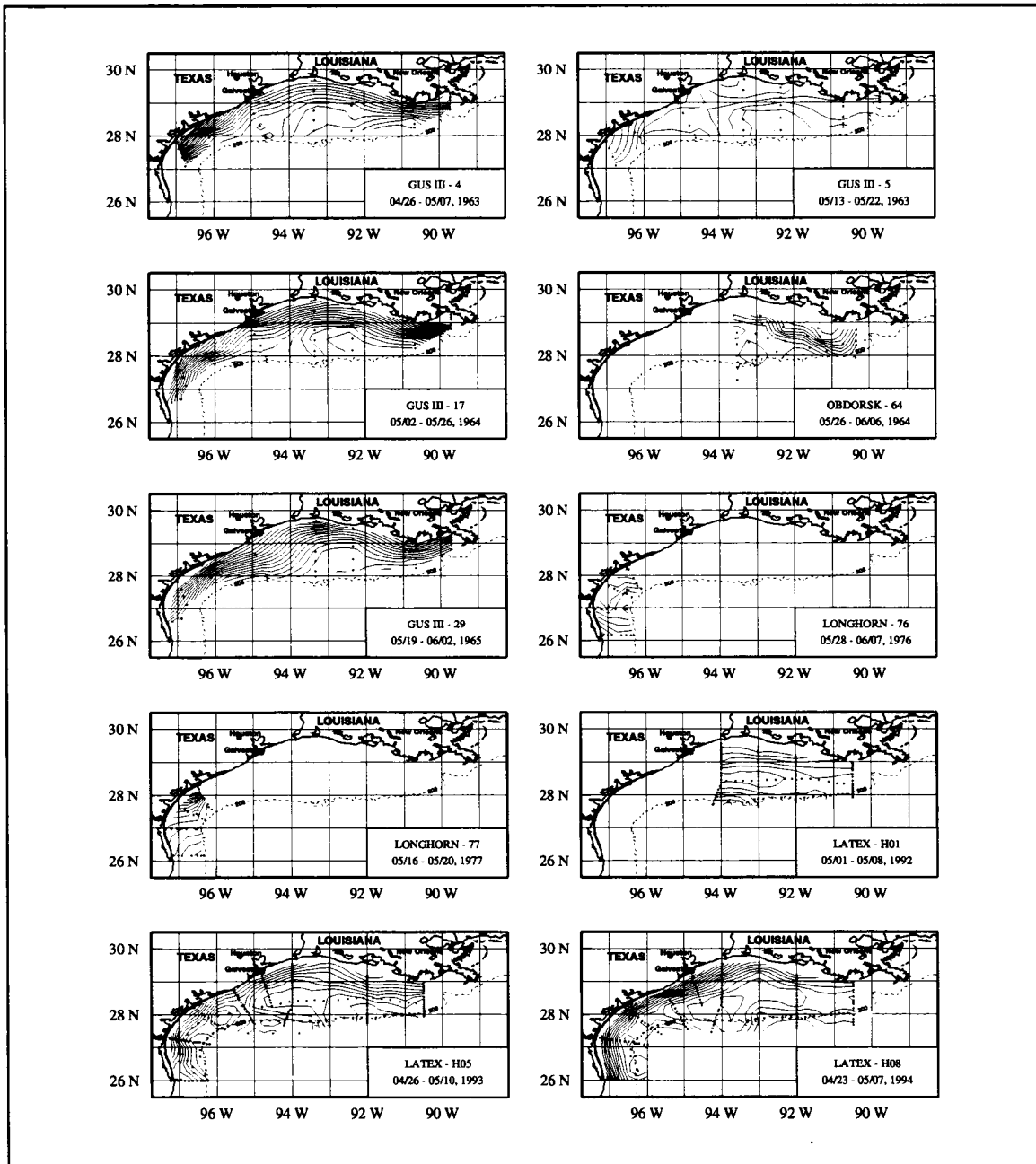


Figure 4.2-22. Geopotential anomaly relative to 70 db for the ten individual May cruises used to construct the spring mean fields. (Contour interval is 1 dyn cm.) Also shown are positions of hydrographic stations for each cruise.

somewhat from those inferred by CK using a subset of these data. Unlike the schema of CK, our mean fields indicate only weak upcoast flow over the outer eastern shelf in spring and only very weak upcoast flow over the outer shelf from 94°-95°W in fall. Based on the standard deviations, we have quantified the interannual spatial variations in geopotential anomaly, salinity, and temperature. These are the first mean fields of temperature and salinity distributions. Though we believe our mean fields are a significant improvement over previous descriptions of the shelfwide circulation and property distributions, it should be remembered that the estimates of variability are based on small samples.

The mean hydrographic patterns for the inner Texas-Louisiana shelf imply downcoast flow during both spring and fall. Differences in shelf-scale distributions of salinity and temperature as well as year-to-year variability are as might be expected considering the forcing mechanisms of air-sea heat exchange, Mississippi-Atchafalaya river discharge, and wind patterns over the inner shelf. A model study by Oey (1995) examines the relative effects of wind stress, river discharge, and interactions of offshore circulation eddies on the Texas-Louisiana shelf. His results for the inner shelf support the patterns seen here and in CK.

Interannual variability and effects of forcing mechanisms

Principal external physical forcing mechanisms for the circulation and property distributions over the Texas-Louisiana continental shelf are assumed to be:

- Wind stress,
- Mississippi-Atchafalaya river discharge,
- Meso-scale eddies in the offshore circulation near the shelf-slope break, and
- Surface heat exchange.

This forcing and the resulting circulation results in the redistribution of properties by internal mechanisms of

- horizontal advection that redistributes heat and salt cross-shelf as well as upcoast and downcoast, and
- upwelling-downwelling that can affect properties at all levels in the water column.

Examples of anomalous fields. The fields of standard deviations presented above estimate the interannual variability of our data sample. To illustrate the magnitude of the year-to-year variability that does occur, we present in this subsection examples of property distributions that differ greatly from the mean distributions. These examples were selected to illustrate the effects of various forcing mechanisms on interannual variability. This material is taken from Li et al. (1997).

We note that seasonal changes due to surface heat exchange dominate the variability of surface temperature. This is clearly seen by considering the differences between spring, summer, and fall surface temperatures in relation to standard deviations between different realizations in a given season (Figures 4.2-4, 4.2-10, and 4.2-16). Differences in mean fields between consecutive seasons, say spring to summer, are of order 5°C ; standard deviations of individual realizations in a season around the mean for that season range from order 0.5° to 2°C . Therefore, we give only minor attention to the interannual effects of surface heat exchange, and give here three examples focused principally on the effects of the three other main external forcing mechanisms.

As background, the river discharge from the Mississippi and Atchafalaya rivers and from the major Texas and Louisiana rivers to the west were reviewed in Section 2.3. The magnitude of the mean discharge of the latter lesser rivers is much lower than the Mississippi-Atchafalaya discharge. Generally the effects of lesser rivers is confined to estuarine and close inshore effects, but in times of anomalously large discharge, fresh water from these lesser rivers may affect significant areas of the shelf (e.g., in October 1994; see Appendix C).

Example 1: Low river discharge and upcoast winds in spring. A quite anomalous individual field of geopotential anomaly relative to the May mean was observed in 1963 on cruise 5 of GUS III. The individual field and residuals after subtracting the May mean are shown in Figure 4.2-23. In May 1963, the expected open cyclonic circulation was over the shelf, centered between 92° and 93°W . However, the 1963 geopotential anomaly pattern differs markedly from the mean (Figure 4.2-3) in two respects:

- a. The gradients of geopotential anomaly inshore from the cyclone are very much weaker than in the mean field. Near Galveston, residuals reach negative values of -6 dyn cm, which greatly exceed in absolute value the corresponding field of standard deviation (Figure 4.2-3) of individual cruise values about the mean. This may be attributed to the extremely low Mississippi and Atchafalaya river discharge during 1963 (Figure 2.3-1). For January and February, the average daily discharge was approximately 50% of the 64-year mean. Then, following a period in late March and early April when the rivers were in flood and discharge above average, the average discharge for April and May was some 30% less than the long-term average. The resulting surface salinity distribution for Cruise 5 (Figure 4.2-24) shows saltier water nearshore along the upper coast than is seen in the May mean (Figure 4.2-2).

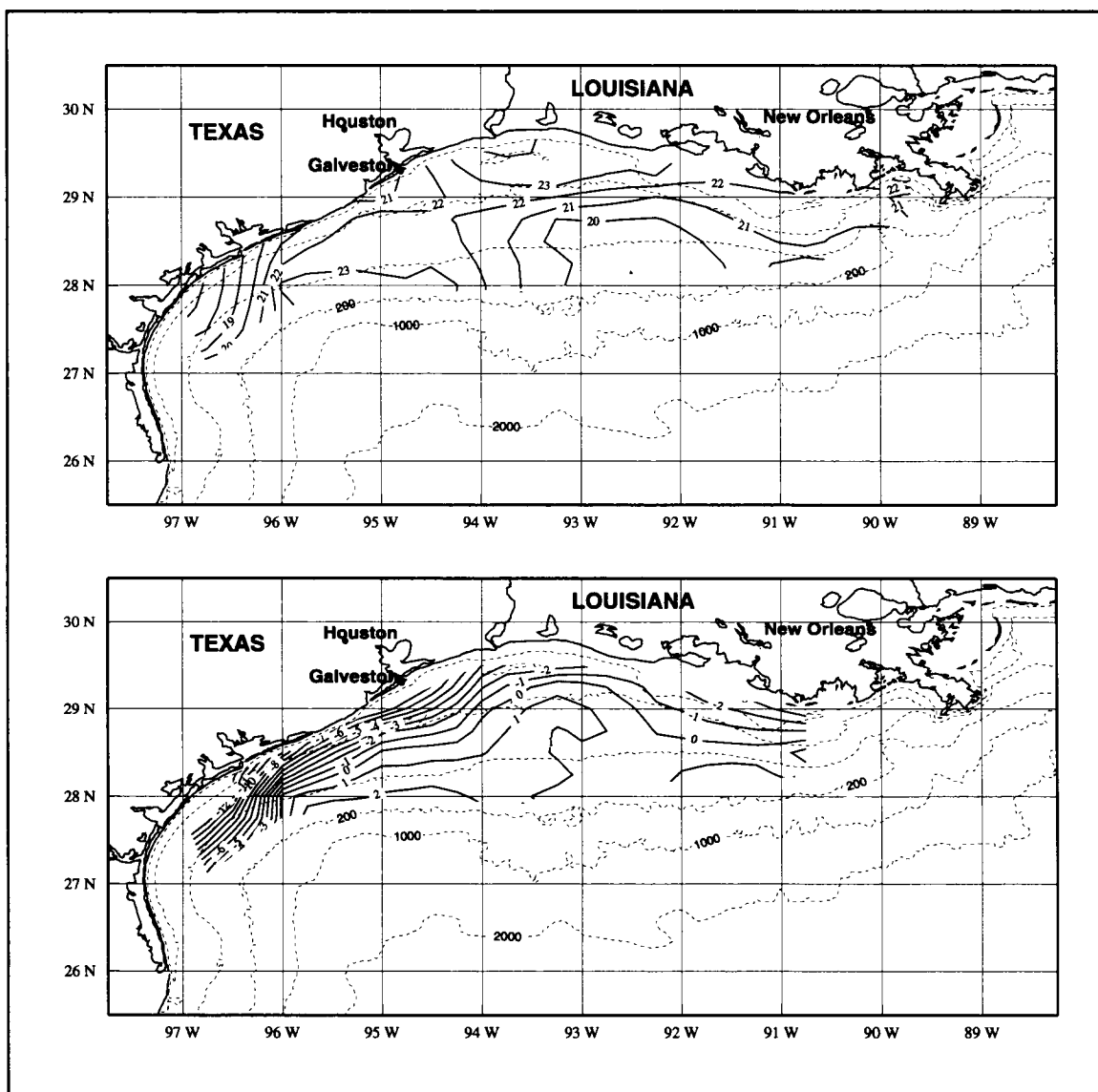


Figure 4.2-23. Geopotential anomaly of sea surface relative to 70 db (upper) for GUS III cruise 5 (13-22 May 1963) and corresponding residual field (lower) after subtracting the May mean geopotential anomaly field. Contours in dyn cm.

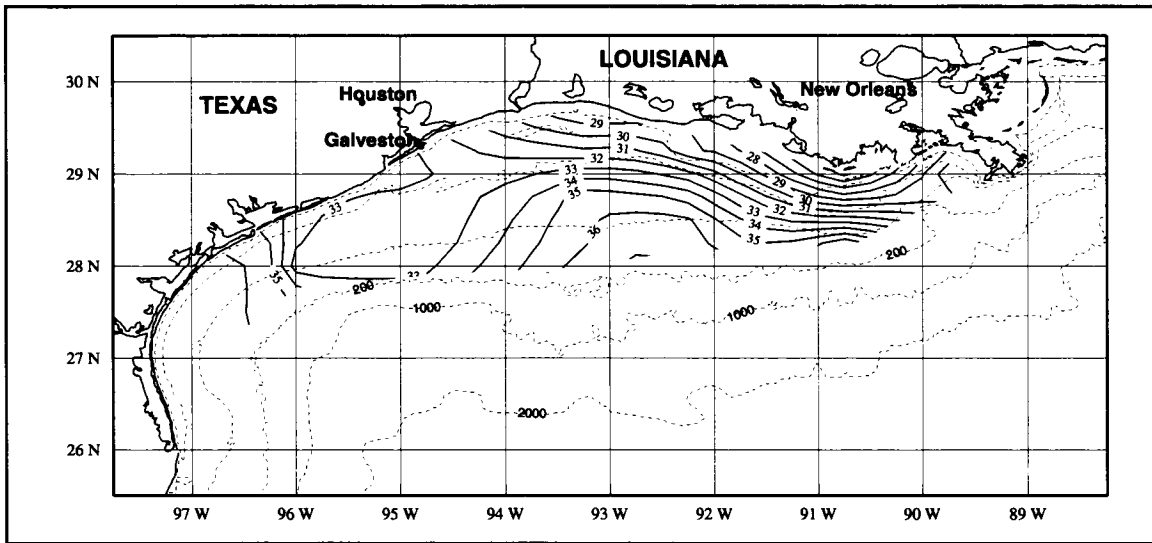


Figure 4.2-24. Sea surface salinity for GUS III cruise 5 (13-22 May 1963).

- b. The 1963 values near shore along the south Texas coast are so low relative to the mean (order of -10 dyn cm) that the cross-shelf gradient in that region is offshore (the reverse of the mean pattern). This would imply upcoast geostrophic shear flow over the south Texas coast in May 1963—the reverse of that expected for May. The very high surface salinities (>36) over the south Texas shelf for May 1963 (Figure 4.2-24), with salinity decreasing upcoast, are consistent with upcoast flow of relatively salty water compared to the May mean. (Bottom salinities for cruise 5, not shown, are greater than 36 over most of the shelf west of 94.5°W .)

The expected long-term trend in alongshelf wind component is typified by the 30-year mean record from the airport at Victoria, Texas, shown in Figure 4.2-25. During most of the year the alongshelf winds are downcoast, driving downcoast flow over the inner shelf. However, starting in the spring, events of upcoast winds are seen. They occur more and more frequently until sometime in June an upcoast component is sustained, with associated upcoast flow over the inner shelf characteristic of summer (July-August). Then, near the end of August the wind field rather suddenly turns downcoast and re-establishes downcoast currents. Thus there is considerable year to year variation in the time of the spring reversal, but the reversal at the end of the summer occurs at about the same time each year examined.

GUS III cruise 5 took place 13-22 May 1963. We examined the daily synoptic weather maps prepared by the NOAA Environmental Data Service for trends in alongshelf winds during May 1963. The winds offshore south and central Texas had an upcoast component

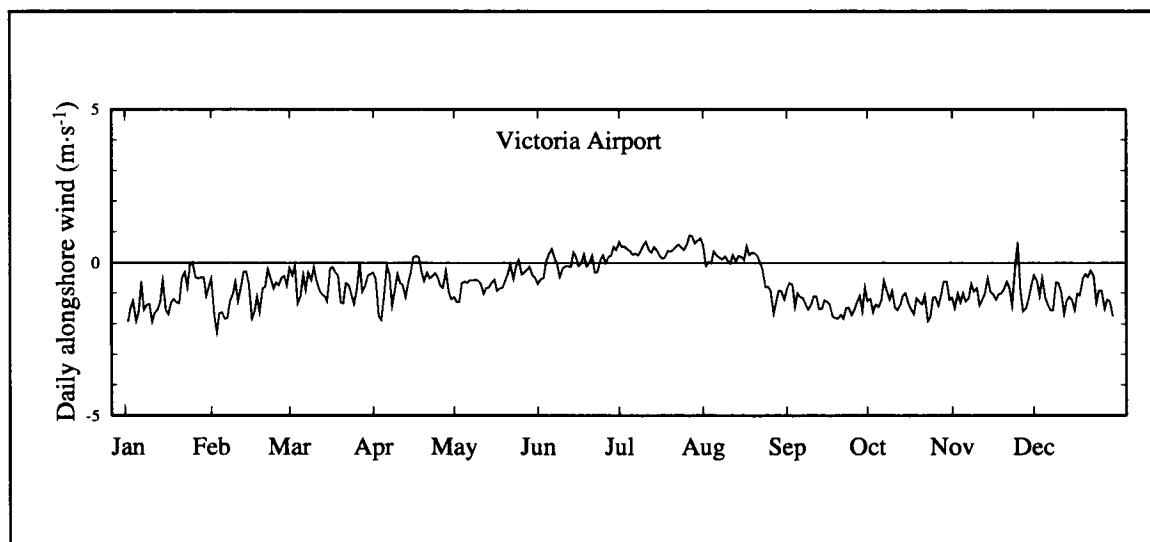


Figure 4.2-25. 30-year average daily alongshelf wind component (positive when directed upcoast) at Victoria airport, located on the coastal plain of central Texas.

from May 9 through 18. Upcoast wind components are seen also in the daily winds (not shown) from Victoria and Port Arthur, Texas, airports for the period 9-18 May. This short period of reversal in wind forcing appears to have been sufficient to cause the anomalous circulation pattern and property distributions seen over the lower Texas coast on cruise 5.

Example 2: High river discharge and offshore eddy effects in spring. Surface salinity for LATEX cruise H05 (26 April-10 May, 1993) is shown in Figure 4.2-26 (upper panel). Inner shelf values over the lower Texas coast agree well with the May mean (Figure 4.2-2). Over the central and eastern shelf, however, inner shelf values are less than the mean by as much as 4 in salinity. This was caused by anomalously large Mississippi-Atchafalaya discharge (Figure 2.3-1), which resulted in a pool of relatively fresh water near the delta.

The residuals of sea surface temperatures for LATEX cruise H05 after removal of the May mean field are also shown in Figure 4.2-26 (lower panel). The field is everywhere colder than the mean with residuals approximately double the standard deviation for May (Figure 4.2-4). We believe this illustrates two effects. First, this cruise was made from late April to early May, a time during which the shelf waters are experiencing considerable warming. So waters during this early May cruise should be colder than the mean. Second, and perhaps more important, the shelf had been receiving river discharge much above normal since November of 1992, the previous year. These same waters that had freshened the shelf prior to this cruise were cold and likely contributed to the anomalously cold situation observed.

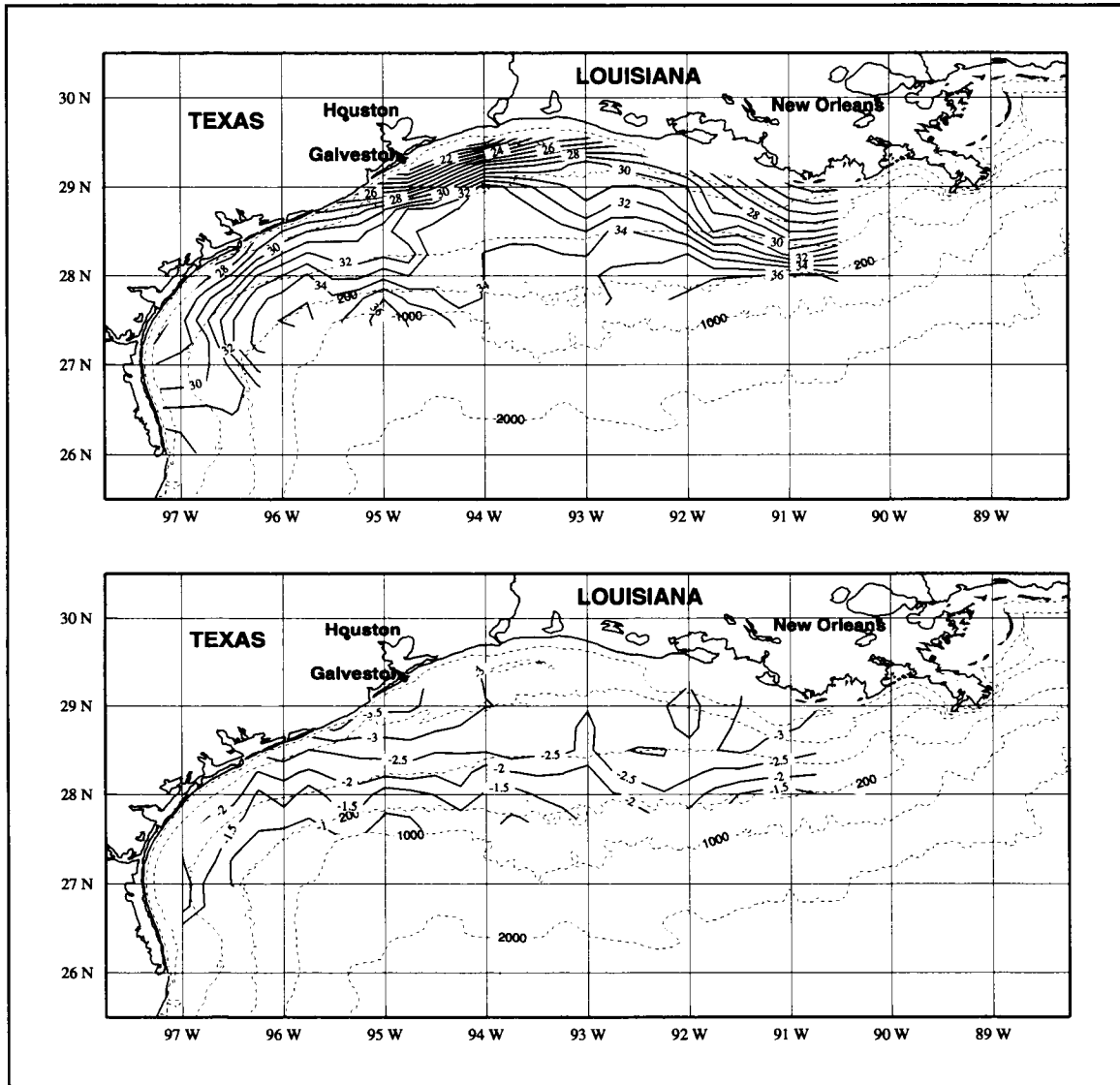


Figure 4.2-26. Sea surface salinity (upper) and residuals of sea surface temperature ($^{\circ}\text{C}$) (lower) relative to May mean for LATEX cruise H05 (26 April-10 May 1993).

The salinity pattern for cruise H05 also has two cross-isobath extensions of fresher water from inner toward outer shelf near 95°W and south of 27°N. The outer shelf property distributions during cruise H05 were greatly affected by the presence of eddies impinging on the shelf-slope break. Figure H.1-7 shows the surface geopotential anomaly relative to 400 db for cruise H05. A reference level of 400 db rather than 70 db was selected because it better illustrates the eddies.

Present during cruise H05 were an anticyclonic Loop Current eddy (Eddy Vazquez), centered off the shelf near 95°W, and an associated cyclonic eddy, centered to the west of Eddy Vazquez. The resulting flow pattern was of onshelf flow at 95.5°-96°W and offshelf flow at 94°-95°W and south of 26.5°N. This situation is discussed in more detail in Section 2.5. The occurrence of anticyclonic and cyclonic rings impinging on the slope and shelf break is expected to result in exchanges of water across the outer shelf edge as shown by Kelly (1988), Lewis et al. (1989), and in Appendices D and M.

Example 3: Downcoast wind in summer. The individual cruise chosen as another illustration of anomalous wind forcing is again a GUS III cruise, number 32 from 11-24 August 1965. The geopotential anomaly pattern is shown in Figure 4.2-27. Compared with the July-August mean (Figure 4.2-9), the implied flow pattern is strongly downcoast. However, the surface salinity pattern (Figure 4.2-27) is similar to the July-August mean (Figure 4.2-8) but shows two significant differences: (1) salty water extends less far upcoast during 1965 (compare positions of the 36 isohaline), and (2) isohalines in the mean field extend generally offshore to the shelf edge but are deflected more eastward with distance across the shelf in 1965. We believe that the first difference is due to a short period of downcoast flow which was in effect during cruise 32. The forcing for this flow was confirmed by examining winds from Port Arthur and Victoria airports; two strong downcoast wind events occurred between July 28 and August 17. A major part of the cross-shelf gradient in geopotential anomaly was found over the outer shelf, not necessarily forced by alongshelf winds. Combined with the configuration of isohalines and isotherms (not shown), this leads us to suspect that the circulation at the time of GUS cruise 32 was strongly influenced by offshore forcing—perhaps by a large cyclonic eddy.

Variability versus forcing indices. Having examined individual cruises to characterize and compare the variability in circulation and property distributions due to the principal external forcing mechanisms, we sought some simple way to relate cause and effect. For individual cruises, we prepared residuals of surface salinity and geopotential anomaly from the appropriate mean fields. These were averaged over three regions of the Texas-Louisiana continental shelf separated at 92°W and 94°W. Because the standard deviations in temperature were not large and interannual temperature variability is small relative to seasonal signals, we did not include temperature in this part of the study.

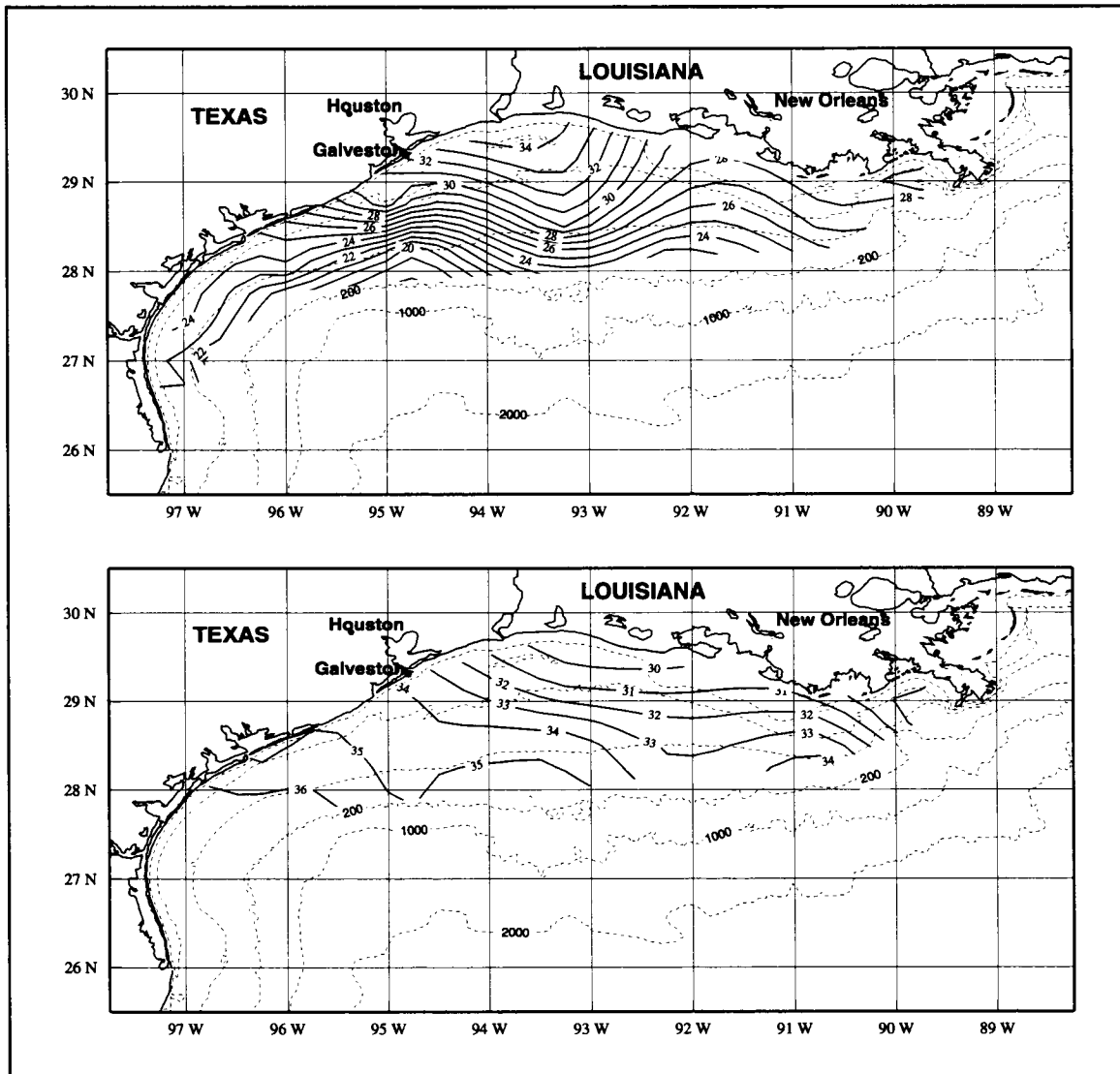


Figure 4.2-27. Geopotential anomaly (dyn cm) of sea surface relative to 70 db (upper) and sea surface salinity (lower) for GUS III cruise 32 (11-24 August 1965).

We plotted the residuals for individual cruises as a function of time of the cruises (not shown). The tendency was for residuals of salinity and of geopotential anomaly for the three areas of the shelf to vary in the same manner. This is evidence for alongshelf coherence in the year-to-year variations.

The residuals of geopotential anomaly are plotted against salinity residuals for spring, summer, and fall in the lower panels of Figures 4.2-28, 4.2-29, and 4.2-30, respectively. A linear fit of the data from each season gave significant (see next paragraph) correlations with the sign as expected—increased (decreased) salinity was associated with decreased (increased) geopotential anomaly. Only very few data points depart from this pattern. It should be noted that the fitted linear trends essentially passed through zero (a slight departure is seen for the fall season). The fact that this trend goes through zero for both variables might be just an artifact of the statistics. We believe, however, this demonstrates that the variability of geopotential anomaly is governed primarily by variability of salinity and confirms our earlier perception that interannual variability of temperature plays a very minor role in spite of its large, but very regular, seasonal variation.

The correlations between surface salinity residuals and residuals of geopotential anomaly, residuals of river discharge, and alongshelf wind index (shown in Figures 4.2-28 through 4.2-30) were all significantly different from zero at the 90% confidence level. All except salinity residual versus river discharge for May ($r^2 = 0.16$) differed from zero at the 95% confidence level. We calculated the multiple correlation of surface salinity anomaly with both wind index and river discharge anomaly. Values of r^2 were 0.23, 0.60, and 0.31 respectively for May, July-August, and November. Because of relatively high (spurious?) correlation between wind index and river discharge anomaly, the multiple correlations were not greatly increased relative to the best individual correlations.

We also prepared residuals of the Mississippi-Atchafalaya river discharge, relative to the long-term mean, for April-May, June-August, and October-November in years when we have data from individual cruises. The residuals of river discharge were averaged for these periods. The averages begin one month before the periods corresponding to residuals in salinity and geopotential anomalies, because it takes some time to distribute the Mississippi-Atchafalaya discharge along this shelf.

As seen in the middle panels of Figures 4.2-28 through 4.2-30, there is an expected negative correlation between the surface salinity anomalies and the anomaly of Mississippi-Atchafalaya river discharge for the corresponding period. By inspection, this correlation appears stronger for the eastern and central parts than for the western part of the shelf. The negative correlation seems best for summer. This might result because there is less wind influence in that season so that the effect of river discharge variability shows more clearly. Because of the negative correlation of salinity with geopotential anomaly, high river discharge is also accompanied by positive residuals of geopotential anomaly.

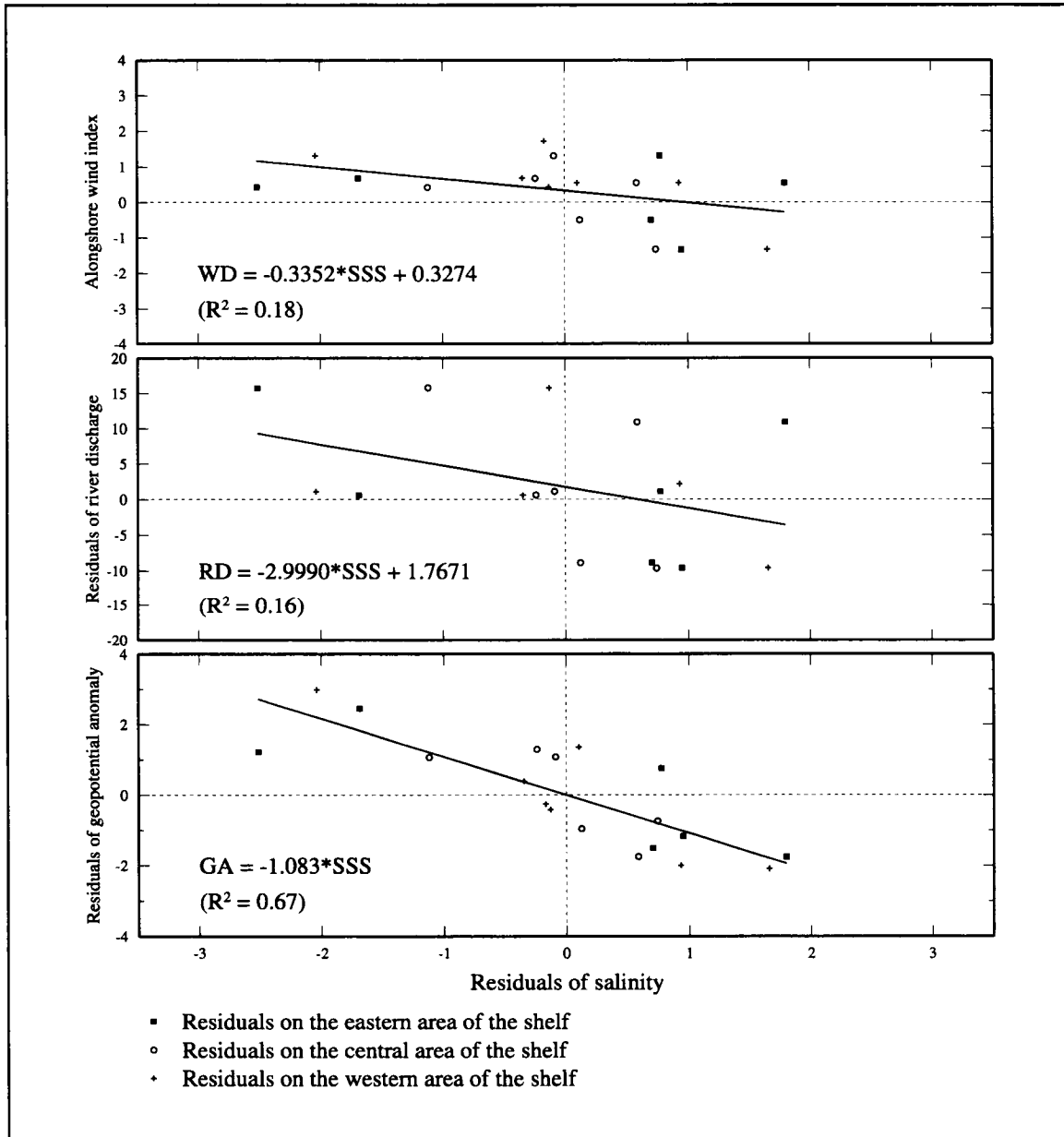


Figure 4.2-28. Residuals of sea surface salinity in May versus: (upper) alongshelf wind index at Port Arthur; (middle) residuals of daily river discharge ($10^3 \text{ m}^3 \cdot \text{s}^{-1}$) from the Mississippi and Atchafalaya Rivers in April and May; and (lower) residuals of geopotential anomaly (dyn cm) of sea surface relative to 70 db in May.

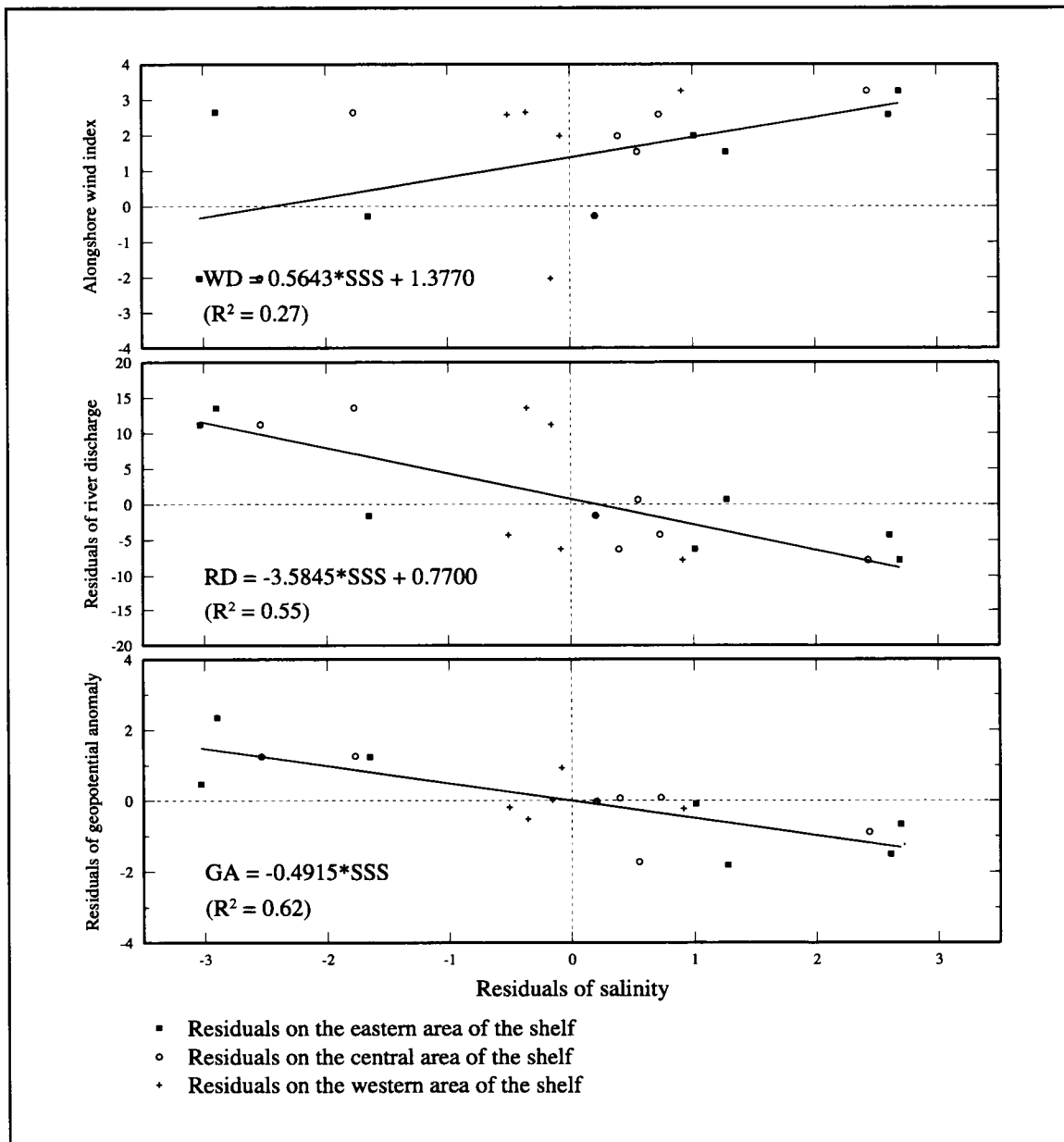


Figure 4.2-29. Residuals of sea surface salinity in July-August versus: (upper) alongshelf wind index at Port Arthur; (middle) residuals of daily river discharge ($10^3 \text{ m}^3 \cdot \text{s}^{-1}$) from the Mississippi and Atchafalaya Rivers in June-August; and (lower) residuals of geopotential anomaly (dyn cm) of sea surface relative to 70 db in July-August.

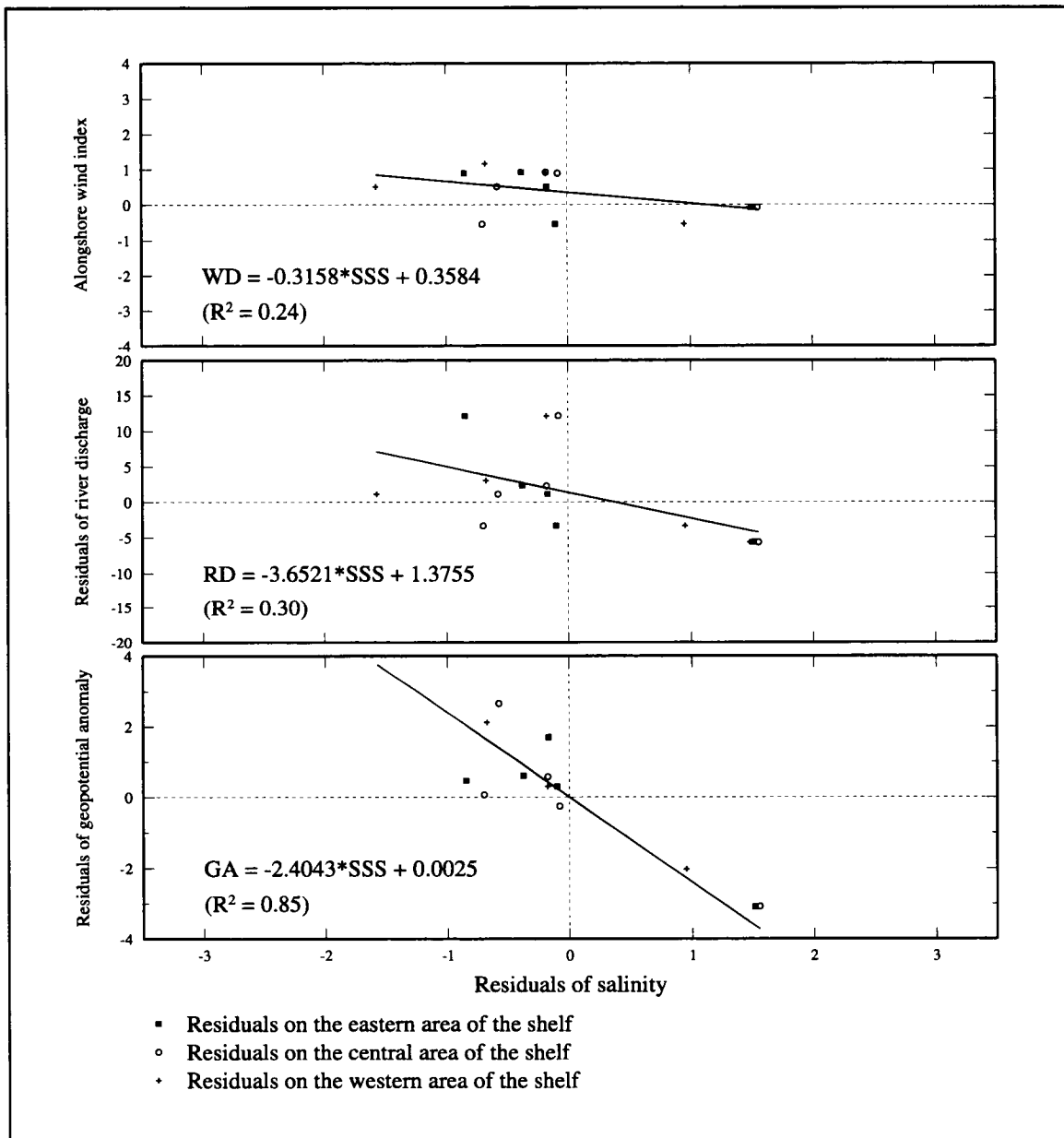


Figure 4.2-30. Residuals of sea surface salinity in November versus: (upper) alongshelf wind index at Port Arthur; (middle) residuals of daily river discharge ($10^3 \text{ m}^3 \cdot \text{s}^{-1}$) from the Mississippi and Atchafalaya Rivers in October and November; and (lower) residuals of geopotential anomaly (dyn cm) of sea surface relative to 70 db in November.

To examine the relationship between anomalies in alongshelf wind component and those in surface salinity and circulation, we defined an alongshelf wind index:

$$I = \frac{W_T - \overline{W}_T}{\overline{W}_T},$$

where W_T is the mean alongshelf wind component over the time period T , and \overline{W}_T is the 30-year mean of the daily alongshelf wind averaged over the period T . W_T is taken as positive in the direction of \overline{W}_T , i.e., it is positive upcoast for summer and positive downcoast otherwise. Thus:

$I > 0$ (< 0) indicates that the mean alongshelf wind during the period T is greater (less) than the 30-year mean alongshelf wind during the same period of the year.

$I < -1$ indicates that the mean direction of alongshelf wind over time period T is opposite to that of the 30-year mean alongshelf wind over the same period.

To apply this index, we used measured winds at the Port Arthur airport, located near the border between Texas and Louisiana, and selected T for each cruise as the period beginning 5 days before and extending through the cruise duration. Decreased (increased) salinity is expected for the case of increased downcoast (upcoast) wind component, forcing increased downcoast (upcoast) nearshore ocean currents. The linear fits (with low, though significant, correlation) support the expected relationship between wind index and salinity residuals.

Consider the spring and fall cases. For W_T greater than average (\overline{W}_T) the downcoast winds are anomalously large ($I > 0$) and we expect more low salinity water advected downcoast perhaps leading to negative salinity residuals. For W_T less than \overline{W}_T we expect the opposite relationship.

For the summer case, W_T and \overline{W}_T are positive upcoast. If W_T is greater than \overline{W}_T , we have anomalously large upcoast winds ($I > 0$) and expect enhanced upcoast advection of salty water leading to positive salinity residuals.

In attributing effects of circulation and property distributions to causal mechanisms, note that the time period over which the mechanism acted relative to the period in which the effect was observed is critical. For example, changes in river discharge may take considerable time (order of a month) to affect the entire shelf. On the other hand, effects forced by alongshelf winds are quite rapid (hours), and wind shifts can be frequent and of short duration. Also, for pre-LATEX cruises, we lack information on the presence or absence of offshore eddies. This has inhibited our examination of the effects of eddy-shelf interaction on the circulation.

It may be expected that the effects of river discharge and wind are not independent. For example, increased river discharge during periods of downcoast flow may further freshen the inshore regime and enhance the downcoast flow component (increase inshore geopotential anomaly). We have not considered such feedback mechanisms.

We have attempted with some success to develop simple indices to relate effects on salinity and geopotential anomaly by changes in alongshelf wind or river discharge. No index for offshore eddy effects was found.

4.3 Temporal and spatial scales of variability

To characterize the spatial variability in hydrographic variables and the circulation regime over this shelf, we undertook an examination of the energetic scales of spatial variability based on the observed temperature and salinity fields of the first seven LATEX cruises and acoustic Doppler current profiles from selected cruises. Two manuscripts resulted from that work (Li et al. 1996; Chen et al. 1998). The principal results are described here; details are left to the manuscripts.

We also undertook examination of the time series records of current, temperature, and salinity gathered from the LATEX A moorings to determine the temporal scales of variability over this shelf and to quantify the variability in distinct temporal bands. The principal results are summarized here.

In addition to characterizing the basic physical variability, the results of this work should be useful in follow-on measurement programs and for modeling studies of the circulation and property distributions on the Texas-Louisiana shelf with respect to the sampling scales required for adequate resolution. Knowledge of the spatial decorrelation scales is also a necessary ingredient for statistically-based objective analysis schemes.

4.3.1 Spatial scales from hydrography

We first used potential temperature (referred to here as θ , or just temperature) at 3 m, salinity (S) at 3 m, and geopotential anomaly at that depth relative to 70 db (referred to as GA) to characterize the spatial scales of hydrographic property distributions and circulation. A 3-m depth was selected because CTD values at that depth usually were available, whereas surface values often were not. Hereinafter we will refer to these 3-m values as surface values. To obtain geopotential anomaly values at stations in less than 70-m depth, specific volume anomaly was interpolated along the bottom from cross-shelf stations as described in Appendix H.1.

Spatial scales are presented for surface θ and S and for GA. In addition, for cross-shelf scales we compared these results with those obtained for cross-shelf distributions of θ and S

at $z/D = 1/2$ and 1, where z is the depth of the interpolated (or observed) value and D is water depth. We compared values of alongshelf scales obtained from surface θ and S with scales obtained from θ and S at 30- and 60-m depths along the 200-m isobath.

Spatial reference fields. To analyze for the shorter scales of energetic spatial variability, it is necessary to remove the longer spatial trends, here called reference fields. We sought to define spatial reference fields that were representative of the shelf-scale pattern of baroclinic circulation (property distributions) at the time of the observations.

We first formulated mean May fields of the hydrographic variables of interest based on historical and LATEX data (described in Section 4.2). Then we performed cross-shelf and alongshelf fits to those fields for use as spatial reference fields. Those fields were then removed from May LATEX A hydrographic fields to obtain the smaller-scale anomaly fields. Scales of the anomaly fields were estimated. Those scales seemed reasonable.

However, the shelf-scale background circulation is believed to vary dramatically with season (Cochrane and Kelly 1986; Section 4.4 and Appendix H), and interannual variations can be expected as well (Section 4.2). Thus, the mean May fields cannot be used as references for data collected at other times of the year. We sought a method of removing a reasonable reference field based on the synoptic cruise data to be analyzed. For this purpose, we investigated fitting the data both with polynomials and with Fourier representations. Polynomial fitting was selected because it requires no a priori scale length by which to parameterize scales corresponding to different orders, and it is the conventional method used in spatial or temporal trend removal. To determine the order of polynomial required to represent the reference fields, we first examined fits to the May mean field.

Based on these results, we obtained reference fields by fitting polynomials to individual May cruise data, removed those reference values to obtain the residual anomaly fields, and estimated the horizontal scales of the anomaly fields. The resulting scales were compared with those obtained by removing the mean field as the reference. Quadratics were found to provide satisfactory fits to cross-shelf reference fields or alongshelf reference fields over half the shelf length (Li et al. 1996).

As an example spatial reference field for surface salinity we show the dot-dash curve in Figure 4.3.1-1 upper. This is for a cross-shelf section along transect 4 (94°W) for the mean May surface distribution (Figure 4.2-2). The synoptic field of surface salinity along this same cross-shelf transect for data from May 1992 is shown by the solid curve in Figure 4.3.1-1 upper. Further examples of the reference fields are given in Li et al. (1996). The shelf-scale reference field is seen to have large variability relative to the residual, or anomaly, field obtained by subtracting the mean field from the synoptic field.

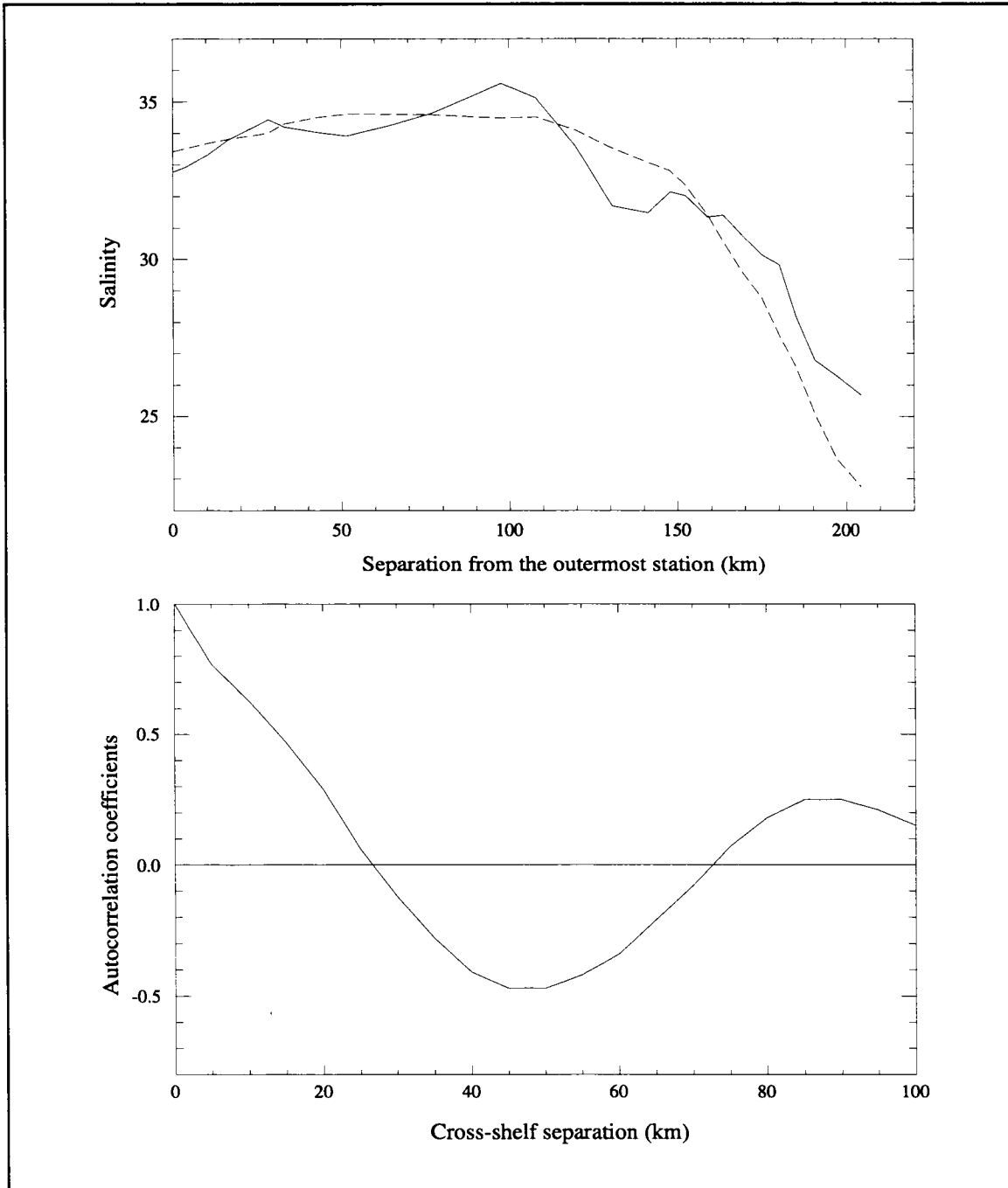


Figure 4.3.1-1. (Upper) (—) Surface (3 m) salinity observed at each station on transect 4 (94°W) during LATEX cruise H01 (May 1992); (---) surface salinity from mean May field (Figure 4.2.3-1) interpolated to H01 station positions. (Lower) Autocorrelation function for difference between H01 and May mean surface salinities as function of cross-shelf separation.

Spatial scales of anomaly fields. An example of the autocorrelations used to estimate spatial scales is given in Figure 4.3.1-1 lower for the residual field presented in the preceding paragraph. In this case, the first zero-crossing of the correlation function is approximately 27 km. Additional examples are given in Li et al. (1996).

For each individual cruise and transect examined, we removed the reference, or background, field obtained by fitting the cruise data along a cross-shelf transect or a semi-alongshelf transect with a quadratic. The resulting differences, or anomaly fields, were used to examine the energetic spatial scales smaller than the background shelf-scale patterns of circulation and property distribution. Alongshelf scales were determined along transects 9 and 10, located nearly along the 200-m and 50-m isobaths, respectively (Figure 1.2-3). Cross-shelf scales were determined along transects 2, 4, and 7, representing, respectively, the eastern shelf, the wider central shelf, and the more narrow southwestern shelf. Data from the first seven LATEX cruises were analyzed.

The resulting scales are presented in Table 4.3.1-1. These are based on the first zero-crossing of the correlation coefficients versus separation. Other studies (Denman and Freeland 1985; Rienecker et al. 1987) have shown that correlations versus spatial separation of scalar properties on the sea surface can be represented (fitted) reasonably well in terms of a function involving two spatial scales. One of these corresponds to the zero-crossing scale referred to in our analysis. The other is a scale characterizing the decay of the correlation for large separations. In many of these analyses, as applied to near coastal oceanographic data, it has been found that the two scales are quite comparable. As a test case for our data, we fitted the average correlation for GA along section 4 based on the first seven LATEX cruises using the parametric form

$$C(r) = [1 - (r/a)^2]e^{-0.5(r/b)^2}, \quad (4.3.1-1)$$

where r is separation, a is the zero-crossing scale and b is the Gaussian decay scale. The values of a and b giving the best fit (Figure 4.3.1-2) are 22.5 and 23.2 km, respectively. Based on this finding of nearly equal values of a and b , we feel justified in employing the first zero-crossing of the correlation function as a reasonable measure of the scale characterizing the anomaly variables discussed herein.

Table 4.3.1-1 shows considerable variability in the spatial scale estimates for a specific variable and transect because we chose to report the actual zero-crossings for the correlation functions rather than the zero-crossing of a fit to the functions. We include in Table 4.3.1-1 the mean scales for each variable and transect obtained by averaging the autocorrelation functions for all realizations (cruises).

The separation distance of interpolation chosen for calculating the correlation functions was 5 km for cross-shelf transects and 20 km for alongshelf transects. Li et al. (1996)

Table 4.3.1-1. Spatial scales (km) of surface anomaly fields of salinity, geopotential anomaly, and temperature along selected transects.

Cruise	Transect						
	2	4	7	10E	10W	9E	9W
# of cruises	7	7	3	7	3	7	3
<i>Salinity</i>							
H01	20	17		30		23	
H02	18	20		37		19	
H03	27	28		38		41	
H04	15	24		35		30	
H05	18	30	14	31	56	37	30
H06	16	32	13	26	29	32	30
H07	11	19	15	26	40	22	39
Mean*	18	22	14	31	38	30	32
<i>Geopotential Anomaly</i>							
H01	23	24		64		38	
H02	7	21		38		36	
H03	24	18		28		50	
H04	24	23		44		36	
H05	15	28	10	37	36	33	21
H06	22	20	17	36	40	37	38
H07	18	17	14	20	54	38	42
Mean*	20	21	14	35	40	38	34
<i>Temperature</i>							
H01	18	15		18		36	
H02	14	14		32		38	
H03	23	16		46		50	
H04	22	21		27		23	
H05	11	28	10	30	34	45	32
H06	16	9	9	26	33	43	25
H07	23	22	8	26	23	35	54
Mean*	17	18	9	30	31	37	36

* Obtained by averaging autocorrelation coefficients.

addressed the question of whether different results are obtained if data separated by smaller distances are used. The same spatial scales were found when using data with spatial resolution of 1-10 km cross-shelf and 10-20 km alongshelf to obtain the anomaly fields. Thus, the hydrographic sampling plan used in LATEX A should be adequate to estimate the scales of significant meso-scale variability.

Table 4.3.1-2 shows the cross-shelf anomaly scales of potential temperature and salinity for depths of 3 m, 0.5D, and D (where D is water depth). For any cross-shelf transect, the average values of scales for temperature or salinity for the first seven LATEX cruises are basically the same at surface, mid-depth, and bottom. These cross-shelf scales are nearly

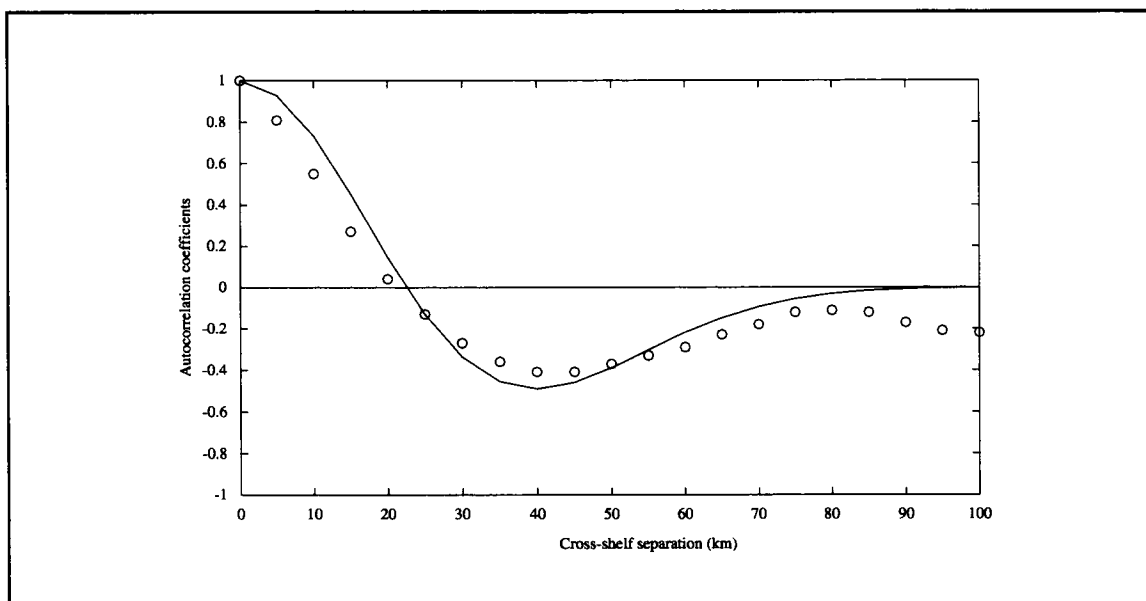


Figure 4.3.1-2. Average correlation of geopotential anomaly (open circles) along transect 4 (94°W) for the first seven LATEX cruises. Parametric fit (solid line) to the averaged values using the form shown in equation (4.3.1-1). Note that the zero-crossing scale ($a=22.5$ km) and the Gaussian decay scale ($b=23.3$ km) are essentially equal.

equal over the eastern and central shelf transects, but smaller for the southwestern transect 7. It has been suggested by C. Winant (personal communication) that the cross-shelf scales may be related to the width of the shelf.

Table 4.3.1-3 gives the alongshelf spatial scales for anomaly fields of potential temperature and salinity at depths of 3, 30, and 60 m along the eastern part of transect 9, located along the shelf break. The averaged scales for the seven cruises have no significant difference at different depths for either temperature or salinity, though the scales for temperature are slightly larger.

Having described the cross-shelf and alongshelf spatial scales for the anomaly fields, we present estimates for variances of the observed and anomaly fields. Table 4.3.1-4 shows the seven-cruise mean variance estimates for observed surface temperature, salinity, and geopotential anomaly relative to 70 db, as well as their anomaly fields obtained by removing quadratic fits from the observed fields. The results show that the mean variances for the observed surface temperature, salinity, and GA distributions are far greater cross-shelf than alongshelf. For the anomaly fields, the variances of salinity and temperature seem comparable

Table 4.3.1-2. Spatial scales (km) of anomaly fields of salinity and potential temperature along selected transects at depths of 3 m (sfc), 0.5D (mid), and D (btm), where D is water depth.

Cruise	Transect 2			Transect 4			Transect 7		
	sfc	mid	btm	sfc	mid	btm	sfc	mid	btm
# of cruises	7	7	7	7	7	7	3	3	3
<i>Salinity</i>									
H01	20	22	15	17	19	18			
H02	18	11	15	20	22	13			
H03	27	27	14	28	28	26			
H04	15	25	21	24	27	26			
H05	18	14	19	30	30	25	14	12	11
H06	16	14	18	32	34	15	13	19	15
H07	11	15	17	19	19	13	15	11	8
Mean*	18	18	18	22	24	19	14	11	12
<i>Potential Temperature</i>									
H01	18	13	29	15	10	23			
H02	14	19	19	14	17	15			
H03	23	18	17	16	15	19			
H04	22	14	28	21	17	19			
H05	11	20	19	28	19	20	10	14	14
H06	16	13	18	9	28	19	9	12	16
H07	23	19	10	22	10	32	8	12	10
Mean*	17	17	19	18	17	18	9	13	12

* Obtained by averaging autocorrelation coefficients.

Table 4.3.1-3. Spatial scales (km) for anomaly fields of salinity and potential temperature at 3, 30, and 60 m depths on the eastern part of transect 9 (along the 200-m isobath).

Cruise	<i>Salinity</i>			<i>Potential Temperature</i>		
	at 3 m	at 30 m	at 60 m	at 3 m	at 30 m	at 60 m
# of cruises	7	7	7	7	7	7
H01	23	43	26	36	17	38
H02	19	17	35	38	33	21
H03	41	42	29	50	33	38
H04	30	27	16	23	18	29
H05	38	36	37	45	16	56
H06	32	39	18	43	32	43
H07	22	37	54	35	57	53
Mean*	30	33	31	37	32	38

* Obtained by averaging autocorrelation coefficients.

Table 4.3.1-4. Mean variance estimates for the observed data and the anomaly fields of surface salinity, surface geopotential anomaly relative to 70 db, and surface potential temperature for selected transects based on data from the first seven LATEX cruises.

	Transect						
	2	4	7	10 E	10 W	9 E	9W
# of cruises	7	7	3	7	3	7	3
<i>Variance estimation for salinity</i>							
<i>C0—Variance of the raw salinity</i>							
<i>C1—Variance of the residual salinity</i>							
Mean C0	13.5	8.74	4.05	3.06	2.34	2.11	0.92
Mean C1	1.23	0.9	0.3	0.59	0.74	0.57	0.31
Mean C1/C0	9%	10%	7%	19%	31%	27%	34%
<i>Variance estimation for geopotential anomaly</i>							
<i>C0—Variance of the raw geopotential anomaly</i>							
<i>C1—Variance of the residual geopotential anomaly</i>							
Mean C0	7.42	2.86	9.72	3.28	6.25	2.95	2.20
Mean C1	0.77	0.51	0.61	1.35	2.63	1.43	1.25
Mean C1/C0	10%	18%	6%	41%	42%	48%	57%
<i>Variance estimation for surface potential temperature</i>							
<i>C0—Variance of the raw potential temperature</i>							
<i>C1—Variance of the residual potential temperature</i>							
Mean C0	2.41	2.19	1.22	0.29	0.74	0.26	0.42
Mean C1	0.16	0.09	0.12	0.07	0.22	0.14	0.14
Mean C1/C0	7%	4%	10%	23%	29%	54%	33%

cross-shelf and alongshelf, whereas that of GA is greater along the shelf than across it. It should be noted that the variances of the surface temperature, for both observed and anomaly fields, are much less than those of surface salinity and GA both cross-shelf and alongshelf. The ratios of mean variances of anomaly fields to those of the observed cross-shelf fields range from 4% to 18%, with an average around 10%. By contrast, the ratios range from 19% to 54% alongshelf, with an average around 35%. The mean ratios are larger for alongshelf than for cross-shelf distributions.

Summary of results. The data used to remove shelf-scale background fields and estimate scales of the residual or anomaly fields obtained by subtracting the background fields from synoptic data were obtained from the first seven LATEX A cruises. The hydrographic stations had 5- to 10-km cross-shelf and 20-km alongshelf separations. Computing anomaly fields and estimating their spatial scales based on data from 1-km cross-shelf and 10-km alongshelf

separations yields essentially the same results. The resulting analyses led to a general characterization of scales over the Texas-Louisiana shelf.

The cross-shelf scales of geopotential anomaly, surface salinity, and surface temperature over the western shelf are shorter (order 15 km) than those in the eastern and central shelf regions (order 20 km). Alongshelf scales (order 35 km) are essentially the same over the western and eastern regions of the shelf, over the mid-shelf (50-m isobath), along the shelf break (200-m isobath), and at different water depths along the 200-m isobath. It is shown that the spacing of observations along the LATEX hydrographic transects is adequate to resolve the mean anomaly scales, ranging from about 12 to 38 km for the different transects.

The results were subjected to several statistical tests. It is shown that for a given transect (cross-shelf or alongshelf), there are no significant differences between the anomaly scales obtained for the three variables, for estimates at three levels (surface, mid-depth, and bottom), or for the four seasons. Moreover, the standard deviation of sample estimates of scale, when normalized by the transect average, are not significantly different among transects. There is, however, a significant relationship between the transect-average anomaly scale and the length of the transect (across or alongshelf)—shorter transects having smaller anomaly scales.

Preliminary analysis of the horizontal scales associated with the detrended ADCP data seems to support the analysis based on the geopotential anomaly using CTD data, with cross-shelf scales of order 22 km on average and alongshelf scales of order 35 km. Also, like the scales determined from the hydrographic residual fields, there was not a significant variation between summer and fall.

Implications

From Table 4.3.1-4 it is clear that variances of the shelf-scale (reference) fields of observed salinity and temperature and calculated geopotential anomaly are greater across than along shelf. The spatial variance of the cross-shelf anomaly fields is around 10% of the cross-shelf reference fields; that of the alongshelf anomaly is about 35% of that in the alongshelf reference fields. Therefore, most of the spatial variance of the baroclinic circulation and property distributions is in the shelf-scale, which is the principal focus of the LATEX shelf study. Nevertheless, considerable variance is found at mesoscales in the anomaly fields.

The range of anomaly scales over the Texas-Louisiana shelf seems consistent with values of the baroclinic radius of deformation on this shelf, i.e., 10-25 km as estimated by Nowlin et al. (1991) but perhaps up to 35 km at the shelf-slope break. This radius of deformation is a natural scale of variability. It is expected that a spectrum of processes will excite variability at these scales. Direct forcing of the shelf circulation and thermal structure by the atmosphere at subinertial frequency (weather band and seasonal) tends to be at very large scales (order 400 km) and probably explains a large fraction of the variance of the shelfwide scales of

properties (Hsu 1988; Mitchum and Clarke 1986). Mechanisms by which some variance of properties may occur at small scales, of order 10 to 50 km, follow. Interaction of flow with rough bottom topography tends to cause a cascade of variance towards small scales (Rhines and Bretherton 1974); this might occur near the outer region of the Texas-Louisiana shelf (depths greater than 100 m), where canyons and coral reefs produce rugged relief. Another mechanism is the cascade of baroclinic geostrophic turbulence toward the radius of deformation (Rhines 1975, 1977); this is known to occur in deep oceanic realms, but might be suppressed in the shelf domain. The impact of the large freshwater discharge from the Mississippi and Atchafalaya Rivers produces small cross-shelf scales associated with the coastal front (Murray and Donley 1995), but the associated alongshore scales can be very large. Finally, another possible mechanism for generation of small scales (both cross- and alongshelf) is backward scattering of coastal trapped waves due to alongshelf changes in bathymetry (Wilkin and Chapman 1990). The most likely mechanism for producing the anomaly scales found in this study is that of Rhines and Bretherton (1974).

4.3.2 Temporal scales from current meters

The temporal variability of horizontal current velocity, temperature, and salinity was studied using data from the 27 LATEX moorings that had records longer than one year. (The records from moorings 44, 45, 46, and 47 were too short to use). Three components were calculated from the 40-hour, low-pass time series at each instrument location: record-length mean, annual signal, and residual signal. This section discusses the temporal variability for each of these components for current velocity, temperature, and salinity. Monthly average current fields are presented in Appendix H.2; some basic statistics associated with the moorings are given in Appendix I; and tidal and inertial signals are discussed in Appendix F.

The topmost instruments at each mooring are referred to here as being at a nominal 10-m depth. Actual depths are identified in Table 1.2-1. Figure 4.3.2-1 defines which moorings are associated with the various lines used in this discussion; most of these lines correspond to hydrographic transects for cross-referencing. Line 4 is used to represent patterns in the cross-shelf lines. For the analysis of the velocity components, the alongshelf velocity corresponds to the direction parallel to the orientation of the bathymetry averaged over mesoscale distances about each mooring and the cross-shelf velocity corresponds to the direction perpendicular to such bathymetry (Table 4.3.2-1). Positive alongshelf velocities are directed upcoast (Brownsville to the Mississippi Delta); positive cross-shelf velocities are directed onshore.

Record-length mean of temperature, salinity, and current velocity

The record-length means of 40-hr, low-pass data were computed at each current meter location. Due to gaps in the records, the number of days with samples varied by instrument location and parameter. Record length means and variances are given in Table 4.3.2-2.

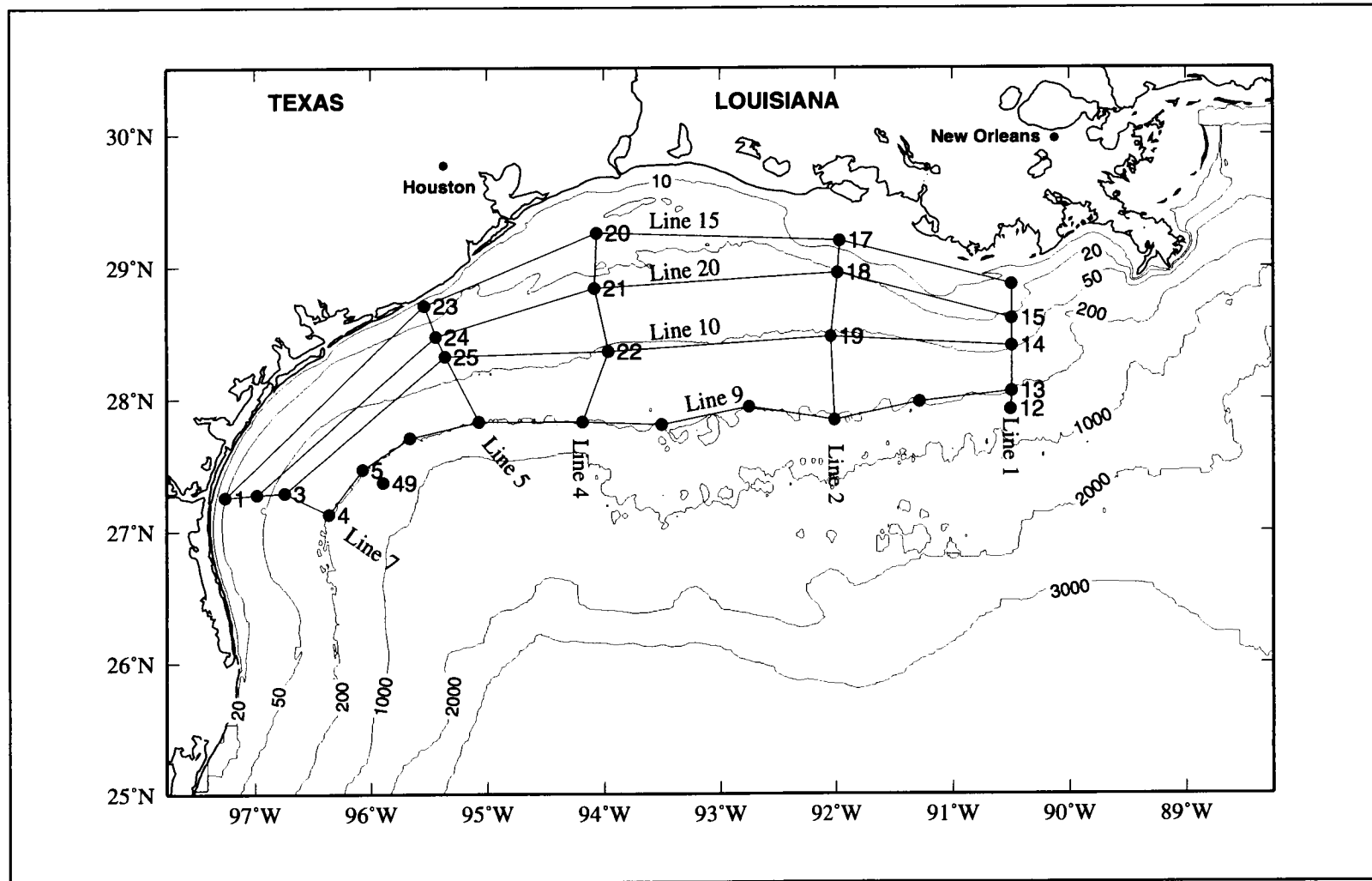


Figure 4.3.2-1. Illustration of moorings included on each line. Circles are mooring locations. Moorings on lines 1, 2, 4, 7, 9, and 10 were located near the corresponding hydrographic lines (Figure 1.2-3).

Table 4.3.2-1. Along- and cross-shelf orientations of LATEX A current measurement moorings relative to the local bathymetry. Angles are given relative to degrees true north.

Mooring no.	Alongshelf angle (°true N)	Cross-shelf angle (°true N)
1	11	281
2	24	294
3	29	299
4	29	299
5	47	317
6	74	344
7	83	353
8	93	3
9	86	356
10	93	3
11	85	355
12	72	342
13	70	340
14	53	323
15	57	327
16	65	335
17	108	18
18	110	20
19	93	3
20	81	351
21	81	351
22	81	351
23	65	335
24	68	338
25	74	344
44	50	320
45	43	313
46	53	323
47	38	308
48	86	356
49	44	314

Table 4.3.2-2. Recordlength means and variances of temperature, salinity, and along- and cross-shelf velocity from 40-hr low-pass current meter data.

Mooring	Temperature		Salinity		Alongshelf velocity		Cross-shelf velocity	
	Mean (°C)	Variance (°C) ²	Mean	Variance	Mean (cm·s ⁻¹)	Variance (cm ² ·s ⁻²)	Mean (cm·s ⁻¹)	Variance (cm ² ·s ⁻²)
(a) Top Current Meters								
1	22.3	22.1	32.7	8.4	-4.8	321.5	0.2	13.9
2	23.8	17.5	34.2	3.0	-7.5	391.6	-1.0	44.0
3	25.0	14.4	34.9	2.7	-0.2	206.3	-0.2	62.4
4	25.7	10.1	35.6	0.6	2.0	339.0	2.2	82.0
5	25.0	10.0	35.4	0.9	8.2	326.9	2.5	105.5
6	25.4	10.1	35.4	1.0	8.6	323.8	0.2	92.9
7	25.4	9.5	35.4	0.8	12.6	426.1	0.6	67.0
8	25.7	9.7	35.5	1.0	7.6	212.9	-0.2	73.8
9	25.8	9.3	35.5	0.7	4.5	146.9	-0.9	80.0
10	25.5	9.7	35.5	0.9	4.3	111.9	1.8	71.2
11	24.6	9.6	35.6	0.9	1.5	98.8	-0.4	47.6
12	25.2	7.4	35.8	0.3	1.5	351.1	-0.6	119.3
13	25.3	9.6	35.6	1.0	3.1	232.9	0.3	69.4
14	24.4	13.8	34.2	2.8	1.0	127.3	-0.4	67.7
15	24.1	14.4	33.8	4.6	-1.5	185.1	1.7	56.1
16	22.9	18.1	31.6	5.4	-3.3	89.9	0.9	20.7
17	22.4	35.5	24.8	21.2	-7.0	234.1	-0.8	37.8
18	23.4	20.4	31.6	5.7	-0.9	222.8	0.1	27.2
19	26.1	11.9	34.1	7.7	-4.6	248.4	3.4	121.9
20	22.7	35.0	27.4	22.4	-11.5	440.9	1.7	111.9
21	23.9	21.5	33.8	2.8	-3.4	120.9	-0.1	25.6
22	24.8	17.0	34.1	3.0	-2.6	225.3	5.0	98.8
23	23.4	27.9	30.8	12.0	-8.6	457.6	0.0	12.7
24	23.8	24.3	32.9	6.3	-9.4	400.5	-1.7	42.2
25	23.8	15.7	33.9	4.7	-4.9	163.6	-1.0	36.4
48	24.7	9.3	35.2	1.3	2.0	123.4	0.8	57.0
49	25.8	7.5	35.8	0.5	9.3	572.6	2.5	148.1
(b) Middle Current Meters								
3	23.2	12.9	35.8	0.1	-1.5	137.7	-0.3	25.6
4	19.1	2.5	36.4	0.0	-1.7	178.7	0.7	32.0
5	19.3	2.0	36.3	0.0	1.6	203.1	1.0	33.1
6	19.3	1.8	36.3	0.0	1.9	229.7	0.9	15.1
7	19.3	0.9	36.4	0.0	0.5	151.0	0.5	13.5
8	19.2	0.7	36.3	0.0	-1.0	153.4	-0.6	18.9
9	19.1	0.7	36.4	0.0	-0.1	50.3	1.3	12.1
10	19.0	0.8	36.4	0.0	1.0	68.8	1.1	10.9
11	19.3	0.6	36.4	0.0	0.7	99.1	0.8	17.2
12	19.1	1.1	36.5	0.0	-2.4	191.0	2.0	25.5
13	18.8	0.6	36.5	0.0	0.3	164.5	0.5	10.0
14	23.3	7.2	35.5	0.2	2.5	105.1	-1.8	41.4
19	23.5	9.4	34.9	1.8	-0.2	56.2	0.3	21.5
22	24.0	11.7	35.3	1.1	0.7	66.2	1.4	27.9
25	22.5	15.1	33.6	3.5	-3.3	168.9	-0.9	29.7
48	18.9	0.5	36.5	0.0	-1.3	55.1	0.2	11.2
49	19.6	1.4	36.5	0.0	5.5	311.1	1.0	66.3

Table 4.3.2-2. Recordlength means and variances of temperature, salinity, and along- and cross-shelf velocity from 40-hr low-pass current meter data. (continued)

Mooring	Temperature		Salinity		Alongshelf velocity		Cross-shelf velocity	
	Mean (°C)	Variance (°C) ²	Mean	Variance	Mean (cm·s ⁻¹)	Variance (cm ² ·s ⁻²)	Mean (cm·s ⁻¹)	Variance (cm ² ·s ⁻²)
(c) Bottom Current Meters								
1	20.6	19.6	none	none	-2.9	106.5	-0.8	16.5
2	23.3	9.8	35.2	0.7	-2.1	156.1	-1.7	33.8
3	22.1	7.3	35.5	3.4	-2.3	70.0	-1.4	14.3
4	15.0	2.3	35.9	0.1	-2.6	101.1	-0.1	7.2
5	15.0	1.0	35.9	0.1	-0.9	39.5	0.3	2.5
6	15.0	0.7	36.0	0.0	-2.0	44.0	0.7	2.0
7	15.0	0.5	36.0	0.0	-0.3	59.6	0.1	2.1
8	15.0	0.6	36.0	0.1	-0.6	7.0	0.5	1.6
9	14.8	0.6	35.9	0.0	-1.0	9.6	0.1	3.1
10	15.1	0.6	36.0	0.0	0.1	4.9	0.1	1.4
11	15.2	0.8	36.0	0.0	-2.0	26.7	-1.2	4.4
12	8.2	0.3	35.2	0.0	-1.4	4.8	-0.5	0.5
13	14.8	1.0	35.9	0.1	-3.4	69.9	-0.2	6.9
14	22.1	4.4	35.6	0.4	0.5	46.8	-0.7	13.4
15	22.8	6.2	35.7	0.3	-1.7	36.1	0.3	9.7
16	21.4	7.2	none	none	-1.6	15.7	0.5	15.4
17	19.9	13.4	none	none	-2.7	52.6	2.4	45.3
18	22.6	9.1	34.0	1.5	0.0	44.4	0.3	24.1
19	21.2	3.0	35.9	0.1	0.0	17.4	-0.2	4.6
20	22.4	22.6	none	none	-1.0	77.9	-0.4	29.6
21	23.7	14.1	34.7	0.8	-0.6	51.7	-0.7	15.1
22	21.5	4.9	36.0	0.2	-1.3	34.5	-0.4	10.1
23	22.1	20.3	none	none	-3.7	168.4	-0.8	47.9
24	22.8	18.8	34.9	0.4	-2.8	109.0	-1.0	30.2
25	22.8	10.3	35.3	0.6	-1.9	164.9	-1.3	26.6
48	14.8	0.8	35.8	0.1	0.5	13.9	0.4	5.0
49	8.4	0.4	35.2	0.0	-2.2	10.6	-1.7	11.4

The isotherms of mean temperature generally parallel the isobaths (Figure 4.3.2-2). At 10-m depths, the gradient is from cooler waters inshore to warmer waters offshore. Between 91° and 92°W, a band of cooler water reaches from the 50-m isobath to the shelf edge. The coolest mean temperatures at the shelf edge are found in this region. There is no such band at mid-depth or bottom meters. Vertical sections across and along the shelf show the isotherms are generally horizontal (Figure 4.3.2-3). Temperatures decrease with depth, with the coolest waters (< 15°C) being at the bottom at the shelf edge.

The mean isohalines approximately parallel the isobaths (Figure 4.3.2-4). Throughout the water column, freshest waters are found nearest the coast, particularly off Louisiana, and saltiest are at the shelf edge. Mean 10-m salinity shows very fresh water (≤ 30) inshore of the 20-m isobath along the Louisiana and east Texas coast (Figure 4.3.2-4a). The 34 isohaline

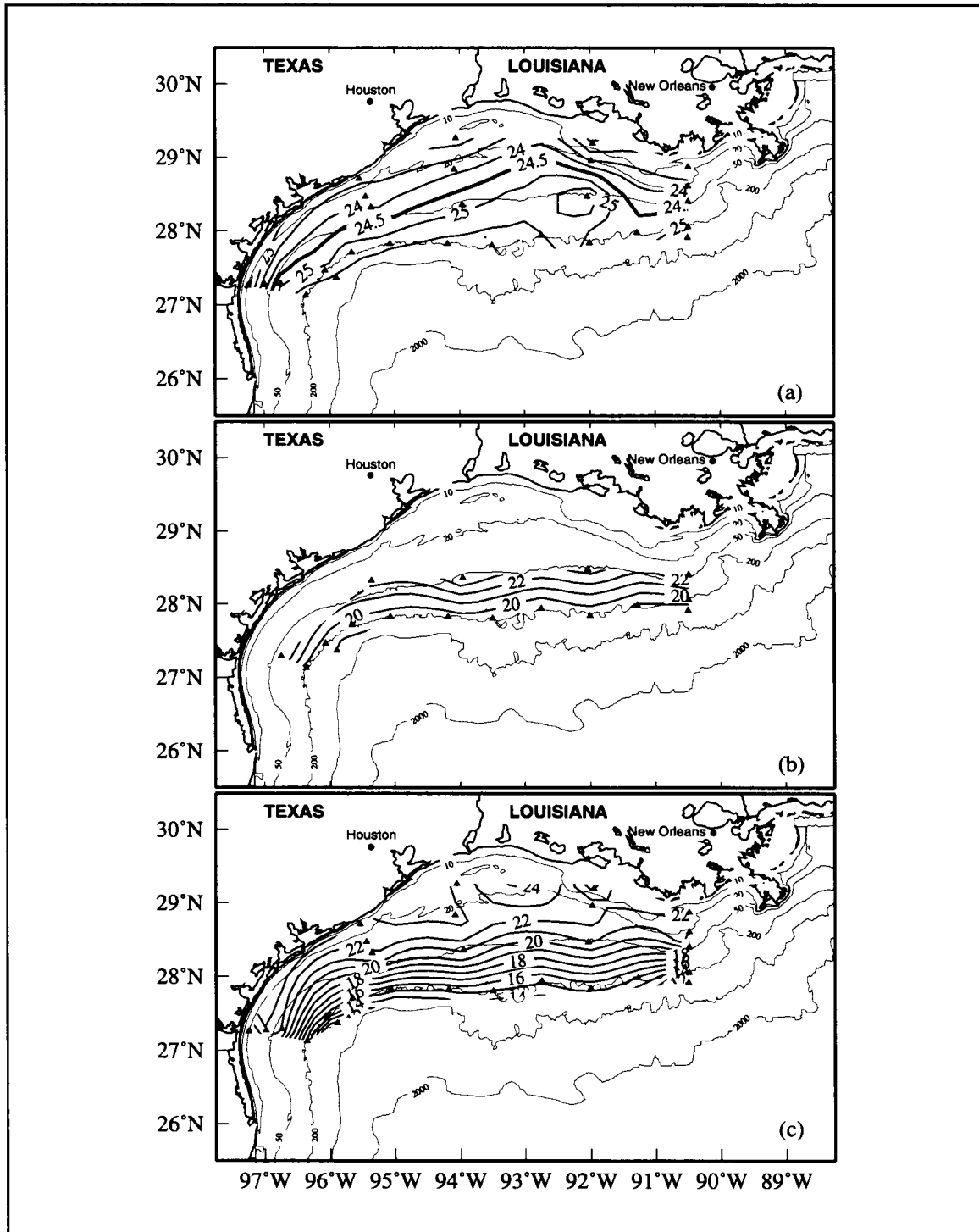


Figure 4.3.2-2. Recordlength mean temperature ($^{\circ}\text{C}$) of (a) top, (b) middle, and (c) bottom current meters. Solid triangles show mooring locations.

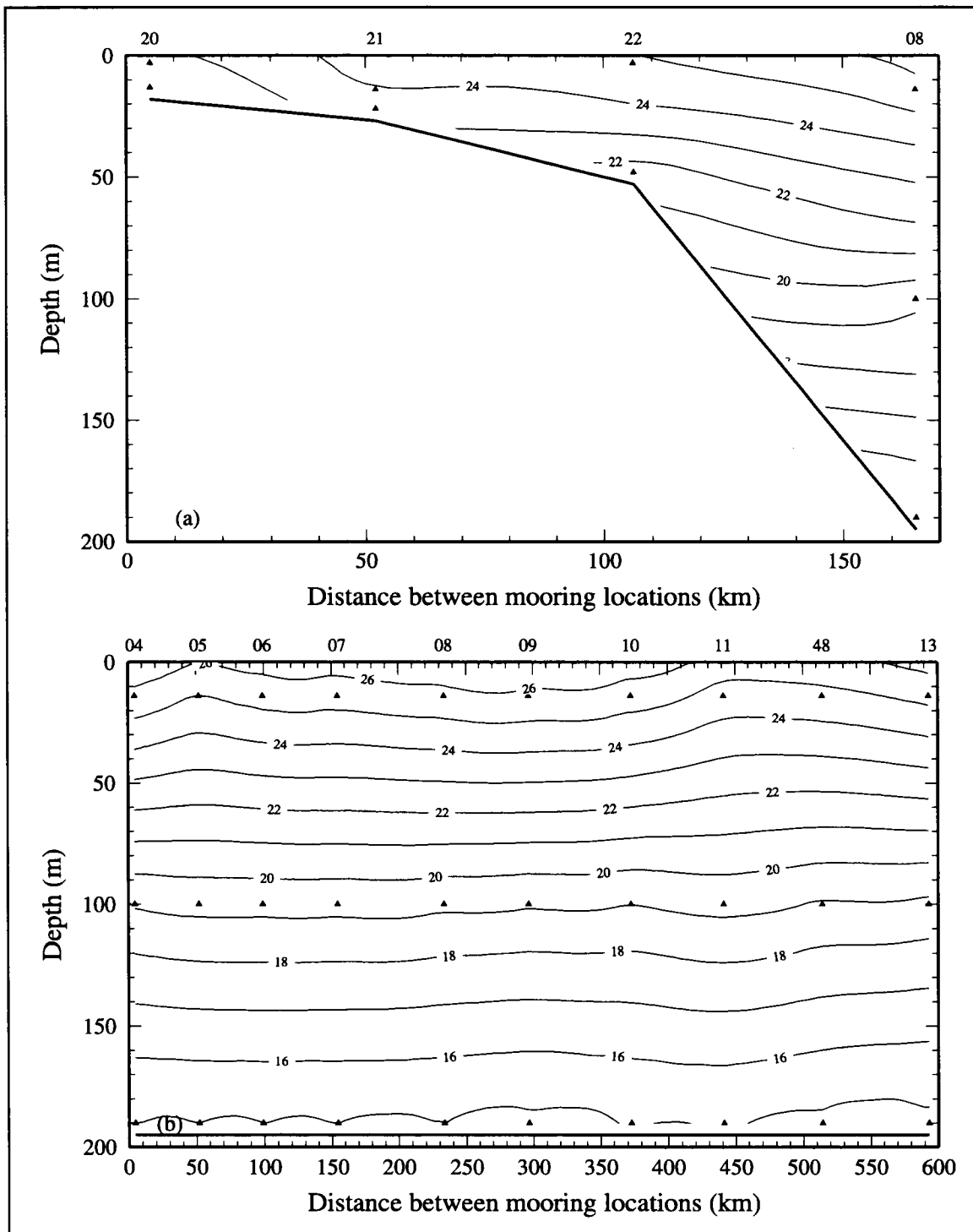


Figure 4.3.2-3. Recordlength means of temperature ($^{\circ}\text{C}$) from moorings on (a) line 4 and (b) line 9. Solid triangles show the instrument locations.

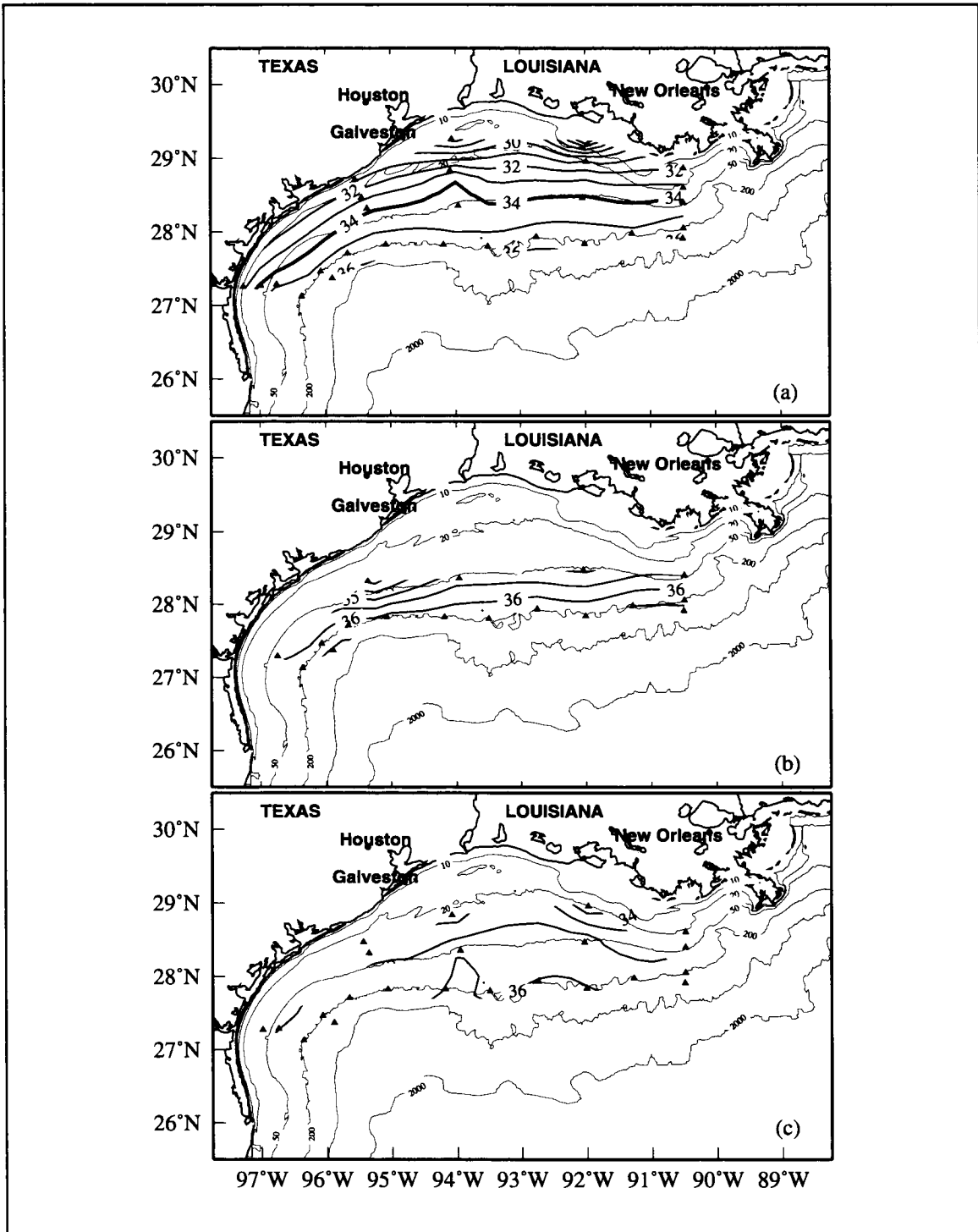


Figure 4.3.2-4. Recordlength mean salinity of (a) top, (b) middle, and (c) bottom current meters. Solid triangles show mooring locations.

approximately follows the 50-m isobath; fresher water occurs inshore and saltier water offshore of this isobath. We will see that the shelf consists of two regimes separated at the 50-m isobath. Vertical sections show that salinity increases with depth in the upper 100 m (Figure 4.3.2-5), although near the sea floor at the shelf edge there is a slight decrease in salinity. Mean isohalines exhibit a strong horizontal gradient inshore of the 50-m isobath (Figure 4.3.2-5a), but are approximately horizontal at the shelf edge (Figure 4.3.2-5b).

The two-regime structure of the shelf also is seen in the pattern of mean 10-m, alongshelf velocity components (Figure 4.3.2-6a). The $0 \text{ cm}\cdot\text{s}^{-1}$ isotach roughly follows the 50-m isobath. Inshore the mean flow is downcoast; offshore the mean flow is upcoast. The mean flow is strongly upcoast ($\geq 10 \text{ cm}\cdot\text{s}^{-1}$) at the shelf edge over the western half of the shelf. This is the region where anticyclonic eddies and associated cyclonic eddies were present for much of the LATEX field period (see Sections 2.5.1, 4.4.1, and 4.4.2 and Appendix H). On the inner shelf the strongest downcoast flows of $\geq 10 \text{ cm}\cdot\text{s}^{-1}$ are located near 95.5°W where the shelf narrows and the bathymetry changes from east-west to north-south. The mean flows at mid-depth are greatest at the western shelf edge where they are about $5 \text{ cm}\cdot\text{s}^{-1}$ (Figure 4.3.2-6b). The bottom mean flows are $\pm 3.5 \text{ cm}\cdot\text{s}^{-1}$ with the higher values at the western and far eastern shelf edges and at mooring 23 on the inner shelf bend (Figure 4.3.2-6c).

Vertical sections show the mean alongshelf currents in the upper 100 m generally follow the basic pattern of downcoast flow over the inner shelf and upcoast flow over the outer shelf (Figure 4.3.2-7a). Below 100 m, the mean current is a weak downcoast flow. At the shelf edge the mean alongshelf currents flow upcoast in the upper 100 m and weakly downcoast below (Figure 4.3.2-7b). The upcoast currents at the shelf edge were greatest at moorings 5 to 9; this may show the influence of the anticyclonic eddies present in this region for about 20 of the 32 months measured.

The pattern of the mean cross-shelf velocity component shows small currents ($\pm 2 \text{ cm}\cdot\text{s}^{-1}$) generally everywhere over the shelf (Figure 4.3.2-8). Over the inner shelf, the mean 10-m cross-shelf flows are onshore except at the bend of the western shelf where they are offshore. At the shelf edge, cross-shelf flows are $\pm 1 \text{ cm}\cdot\text{s}^{-1}$ except at moorings 4 and 5 on the western shelf where they exceed $2 \text{ cm}\cdot\text{s}^{-1}$ (Figure 4.3.2-9).

Annual signals of current velocity

Each time series record was processed with a 3-hour low-pass, cosine-Lanczos filter to produce hourly data sets for all instrument types. A maximum entropy routine filled gaps of two weeks or less, and a 40-hour low-pass, cosine-Lanczos filter removed tidal and inertial signals. A 30-day low-pass filter was applied to the velocity time series to reduce high frequency variability in the records that might alias the annual signal.

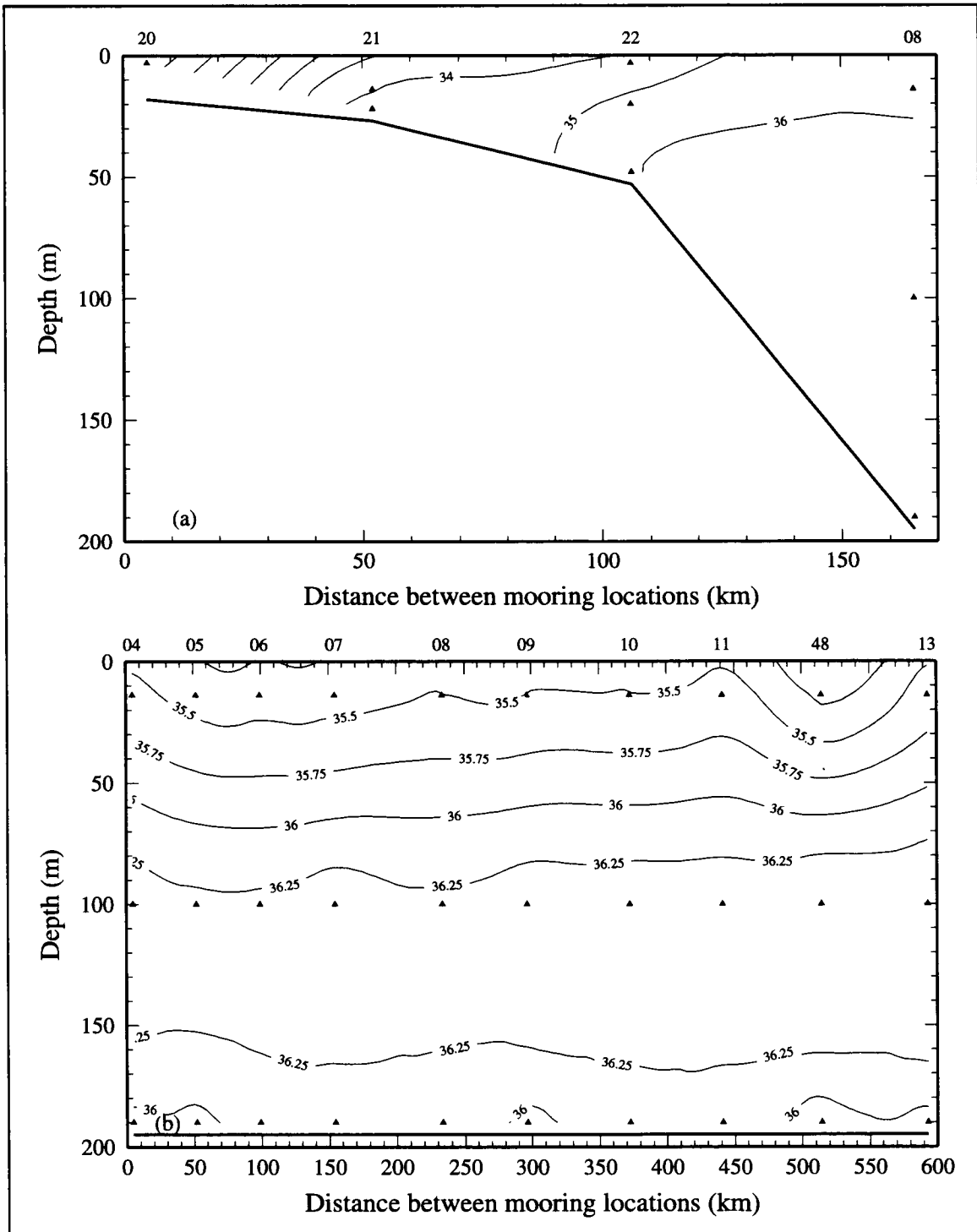


Figure 4.3.2-5. Recordlength means of salinity from moorings on (a) line 4 and (b) line 9. Solid triangle show the instrument locations.

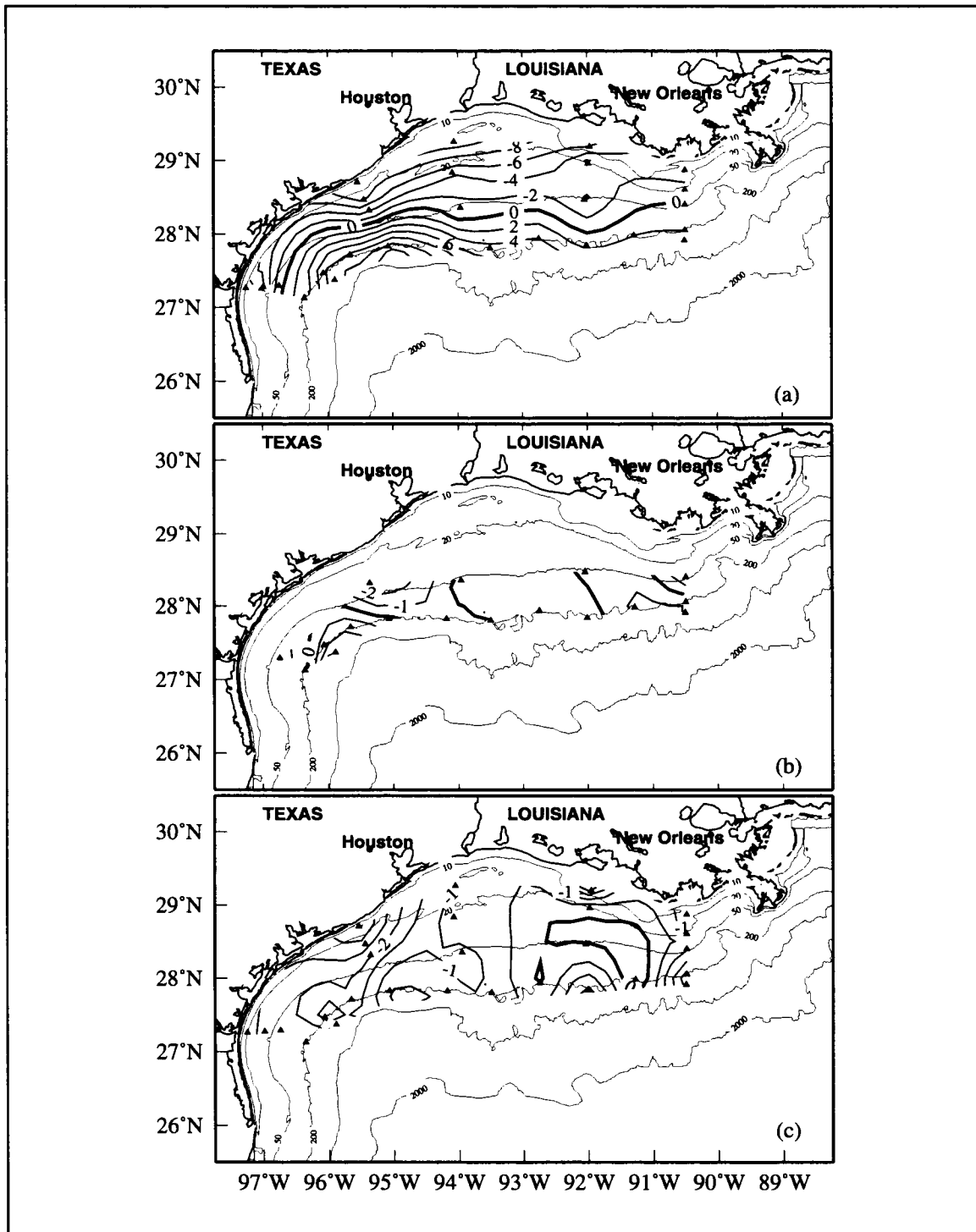


Figure 4.3.2-6. Recordlength mean alongshelf velocity component ($\text{cm}\cdot\text{s}^{-1}$) of (a) top, (b) middle, and (c) bottom current meters. Solid triangles show mooring locations.

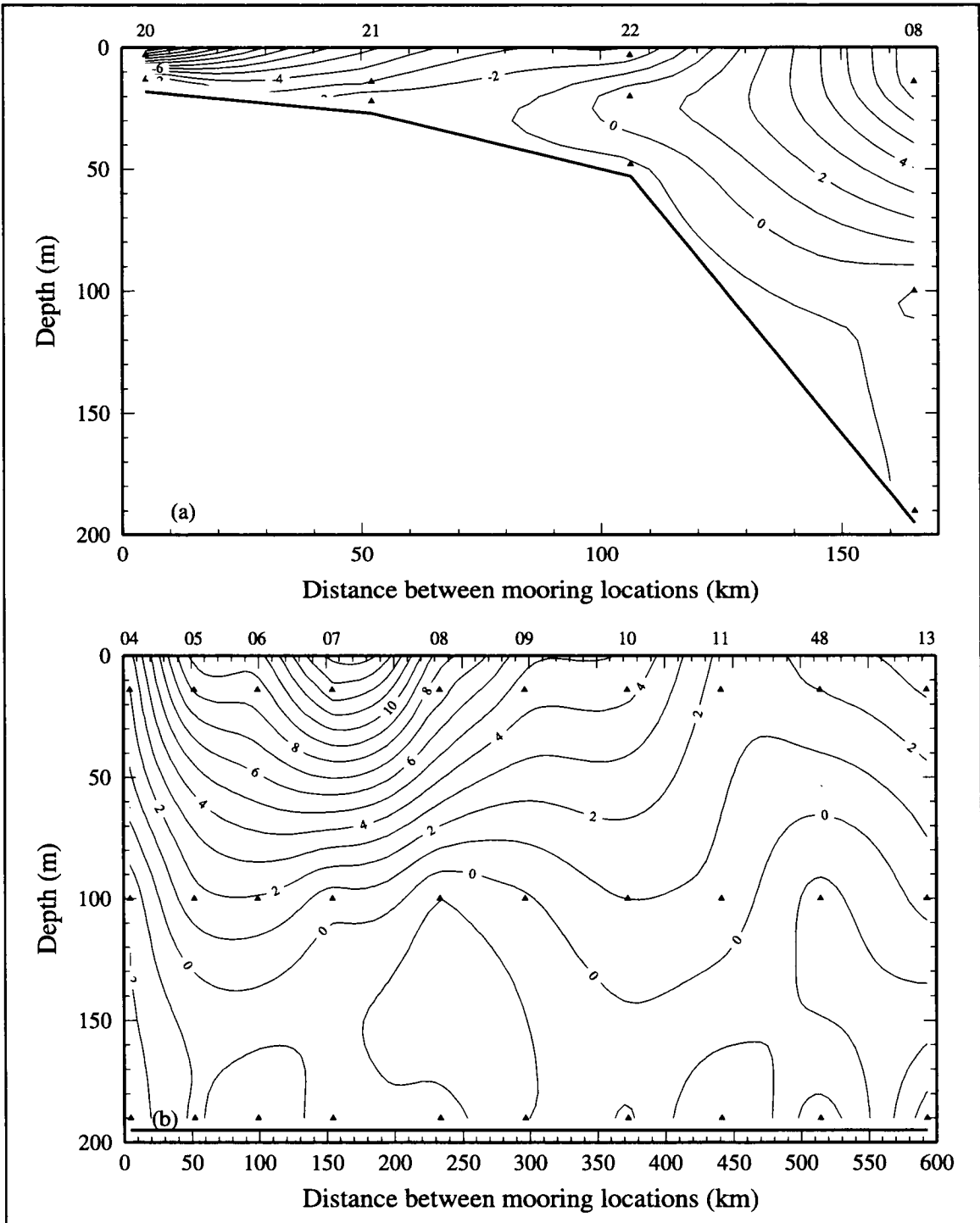


Figure 4.3.2-7. Recordlength means of alongshelf velocity component (cm·s⁻¹) from moorings on (a) line 4 and (b) line 9. Solid triangles show instrument locations.

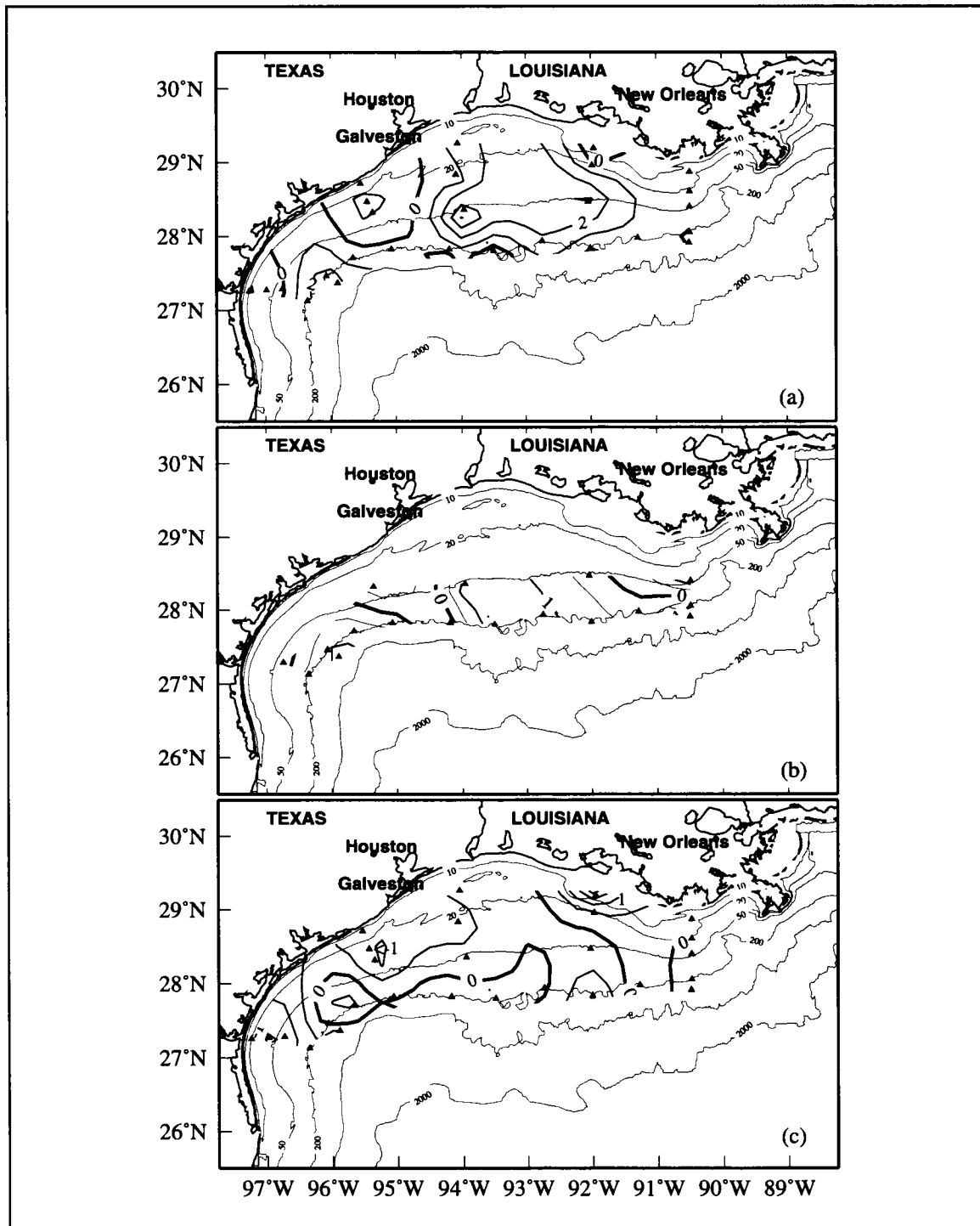


Figure 4.3.2-8. Recordlength mean cross-shelf velocity component ($\text{cm}\cdot\text{s}^{-1}$) of (a) top, (b) middle, and (c) bottom current meters. Solid triangles show mooring locations.

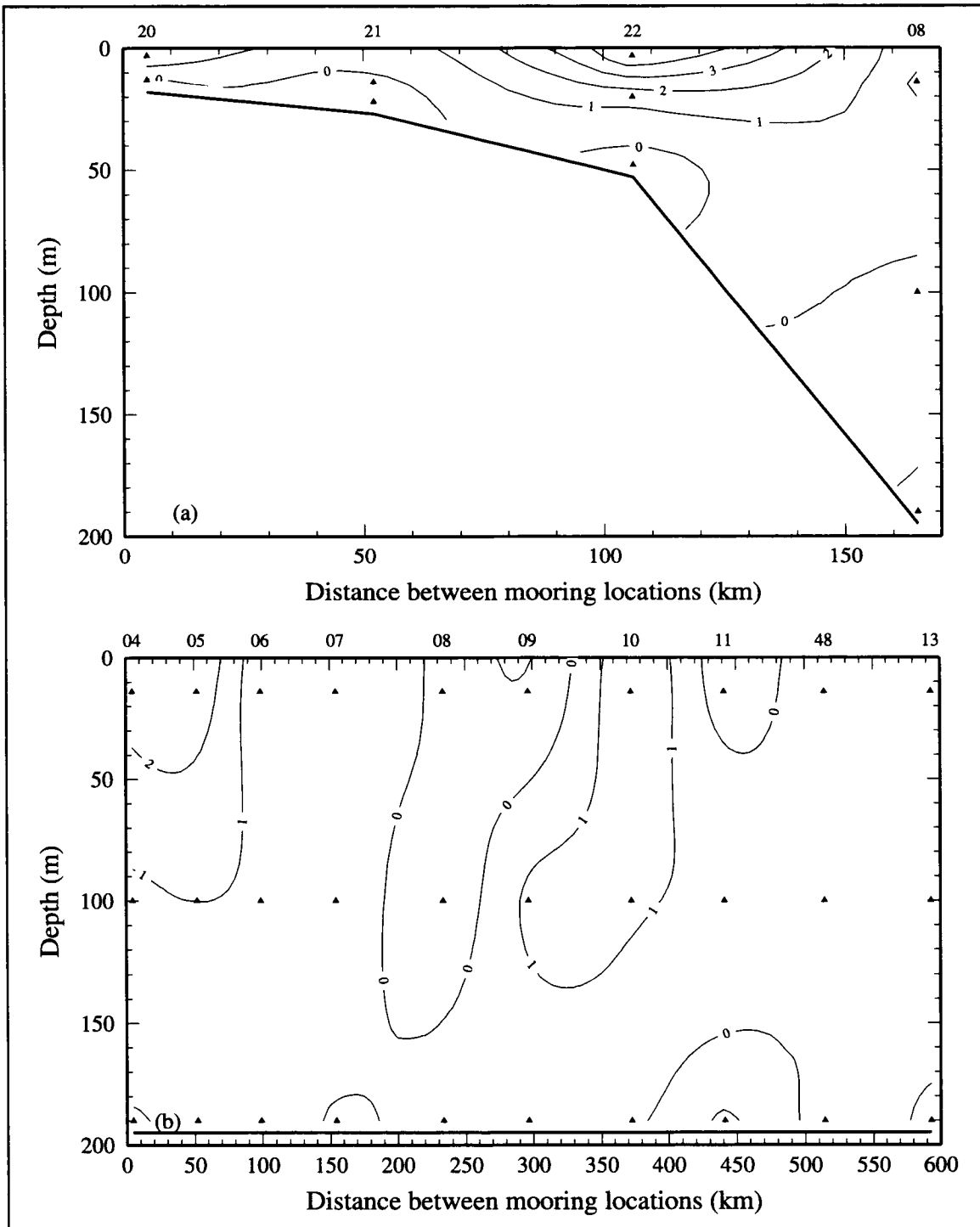


Figure 4.3.2-9. Recordlength means of cross-shelf velocity component ($\text{cm}\cdot\text{s}^{-1}$) from moorings on (a) line 4 and (b) line 9. Solid triangles show instrument locations.

Amplitudes of the annual signal were determined from these smoothed time series. The annual signal was defined as the fundamental plus its first four harmonics. Periods and frequencies are given in Table 4.3.2-3. To compute the annual signal for each meter location, the method of cyclic descent was applied to the time series (Bloomfield 1976; DiMarco 1998). This method removes the mean and fits selected frequencies iteratively by least squares.

Table 4.3.2-3. Periods and frequencies of the fundamental and first four harmonics of the annual signal.

Annual signal component	Period (days)	Frequency (cpd)
Fundamental	365.25	0.01720242
First harmonic	182.625	0.03440485
Second harmonic	121.75	0.05160727
Third harmonic	91.3125	0.06880970
Fourth harmonic	73.05	0.08601212

Alongshelf velocity. Figure 4.3.2-10 shows the annual signal of the 10-m, alongshelf velocity in groupings of alongshelf lines (see Figure 4.3.2-1 for moorings on the various lines). Within each line grouping, moorings are listed and marked in order from west to east. The annual signals on the inner shelf (lines 15, 20, and 10) show upcoast (positive) flow starting in May and ending in September, with maxima about July, and generally downcoast (negative) flow throughout the remainder of the year. This is consistent with the Cochrane and Kelly (1986) average monthly circulation pattern over the inner shelf and with circulation patterns derived by different methods from current and hydrographic data (Section 4.4 and Appendix H; Li et al. 1997). This pattern of the annual signal suggests the currents on the inner shelf are driven by the annual cycle of the winds (Section 2.1.2). The pattern is strongest at the moorings on line 20 (near 20-m water depths).

At the shelf edge, there is summer upcoast flow. In nonsummer months, there are periods of both downcoast and upcoast flow. Thus, the annual signal over the outer shelf is less well resolved than over the inner shelf. The complexity in the pattern at the shelf edge suggests that processes other than just wind influence the annual signal of alongshelf currents there.

Figure 4.3.2-11 shows the annual signal of bottom alongshelf current in alongshelf lines. The amplitudes are smaller than those at 10 m. The pattern over the inner shelf again shows upcoast flow during the summer and generally downcoast flow the remainder of the year. Thus the annual signal of velocity of the entire water column over the inner shelf is driven

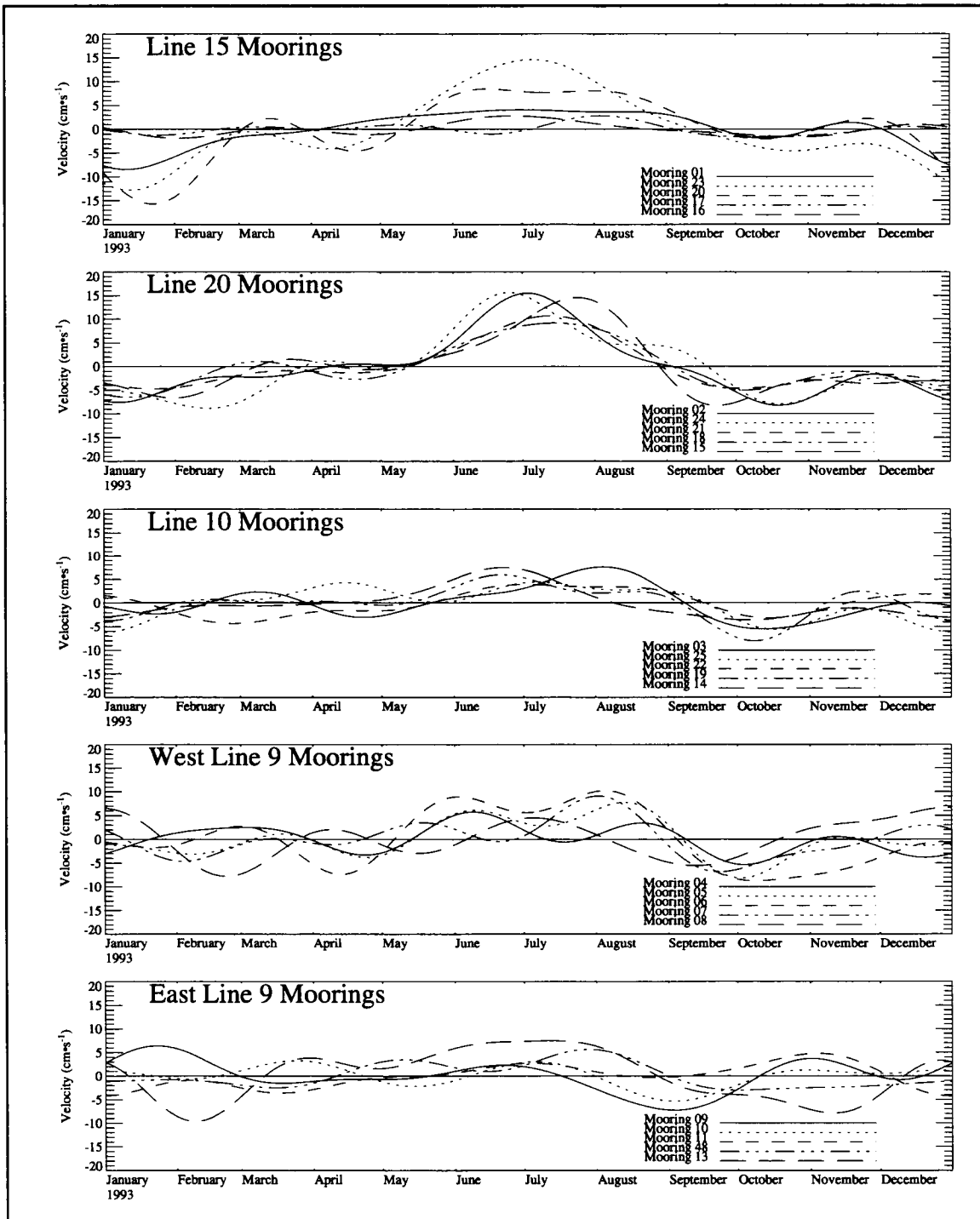


Figure 4.3.2-10. Annual signal of 10-m, alongshelf current velocity in groupings of alongshelf lines.

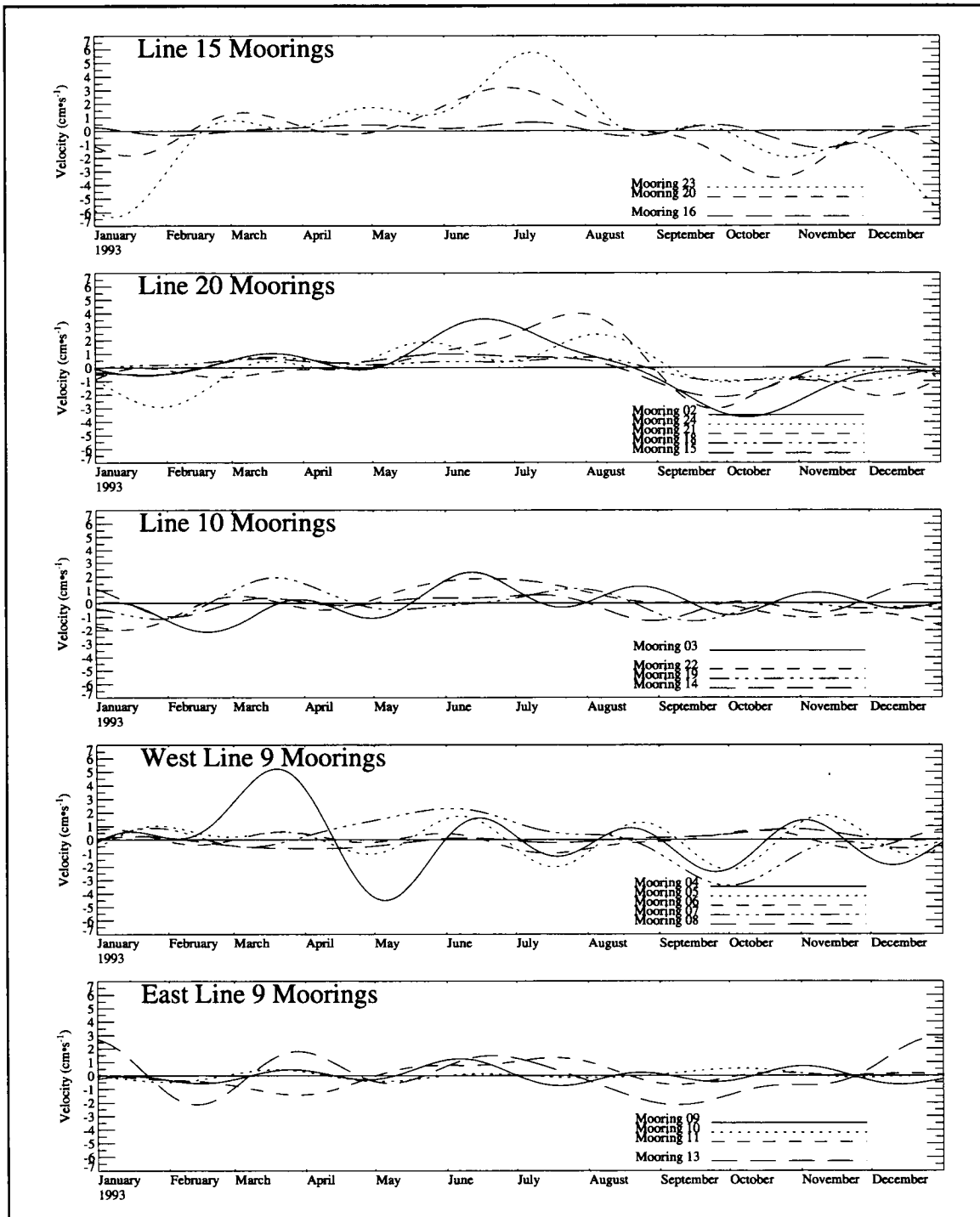


Figure 4.3.2-11. Annual signal of bottom, alongshelf current velocity in groupings of alongshelf lines.

mainly by the annual cycle of the winds. At the shelf edge, where the bottom is near the 200-m depth, the bottom alongshelf flow is very small (less than $\pm 3 \text{ cm}\cdot\text{s}^{-1}$), except at mooring 4 in the southwest, and no clear pattern emerges.

The percent of the total variance contributed by each of the five frequency components of the annual signal illustrates its relative importance. On average, the fundamental accounts for 44% of the total variance of 10-m, alongshelf velocity (Table 4.3.2-4). It represents about 60% of the variance inshore of the 50-m isobath, 47% along the 50-m isobath, and 34% at the shelf edge. Generally, the farther offshore the mooring, the less the fundamental contributes to the total variance. This is significant because the harmonics can include variance at the specified frequencies contributed by mesoscale phenomena, such as Loop Current eddies or associated cyclones adjacent to the shelf edge. At the bottom, the fundamental contributes 35-55% on the inner shelf, but only 25% at the shelf edge. The individual harmonics at the shelf edge account for between 12% and 24% of the annual signal.

Table 4.3.2-4. Average percent contribution of each period to the total variance of the annual signal for temperature, salinity, and along and cross-shelf velocities at the top (10-m depth) current meters.

Period (years)	Temperature (%)	Salinity (%)	Alongshelf (%)	Cross-shelf (%)
1.00	97.7	59.7	44.2	32.3
0.50	1.1	22.9	22.6	19.2
0.33	0.7	9.6	17.3	18.2
0.25	0.3	5.0	9.4	18.1
0.20	0.2	2.8	6.5	12.1

Taking the square root of the sum of the squares of the five components yields an amplitude that is a measure of the variability of the annual signal. Figure 4.3.2-12a shows the amplitudes of the annual signal of the 10-m, alongshelf velocity components. Amplitudes are more uniform and lower over the central shelf than over the eastern or western shelf regions. High values ($> 7 \text{ cm}\cdot\text{s}^{-1}$) occur at the east and west shelf edges and decrease radially to the northwest. The higher variability there is likely due to contributions of Loop Current eddy energy. The greatest variability occurs over the western inner shelf at the bend in the Texas coast at about 95.5°W . There the maximum amplitude is $10.5 \text{ cm}\cdot\text{s}^{-1}$. In this region, the fundamental contributes 70 to 80% of the total variance, compared to the 30-60% typical of other inner shelf regions. Thus, the maximum at the bend of the western inner shelf is likely due to a narrowing and strengthening in the upcoast/downcoast currents that vary annually.

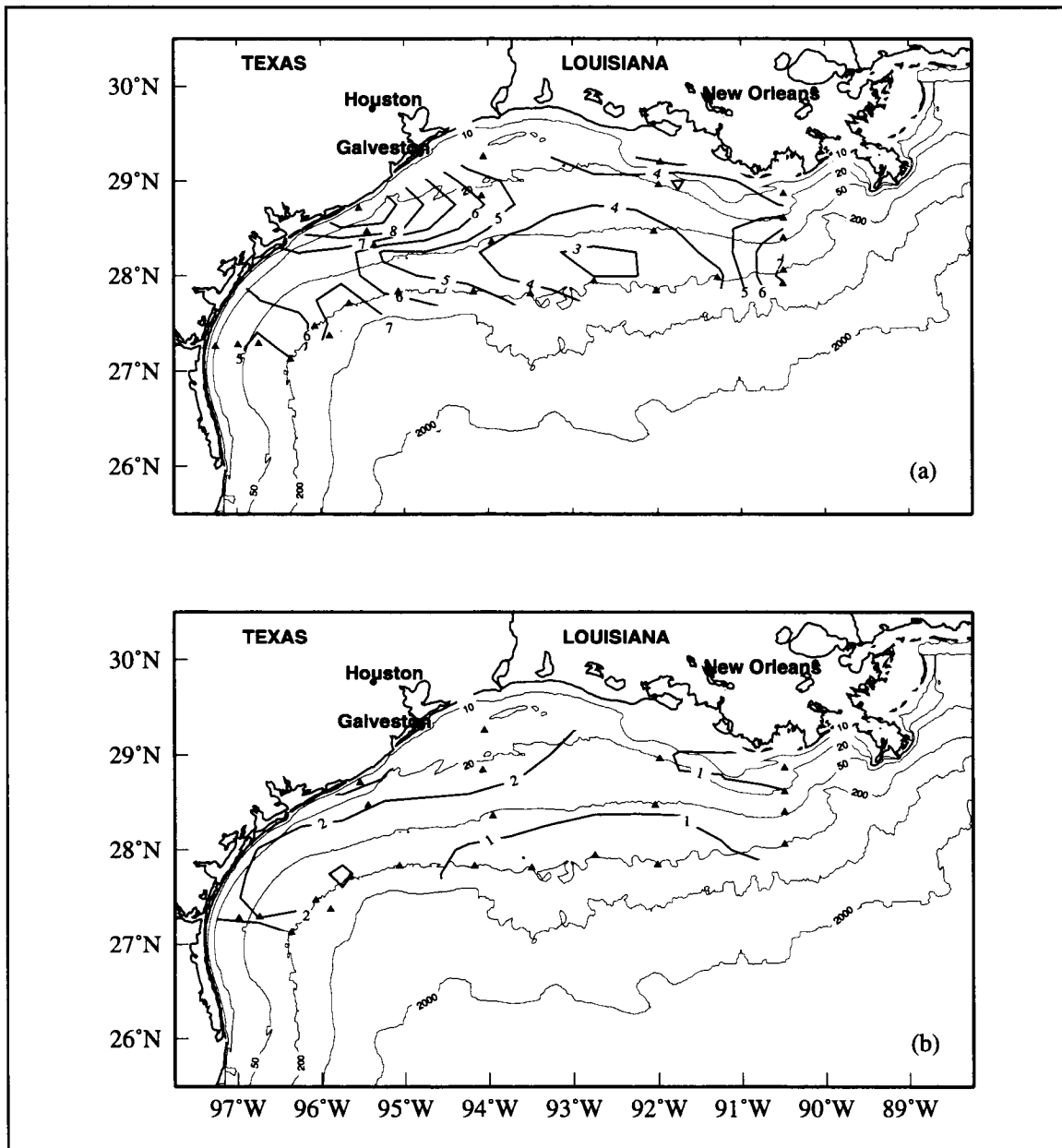


Figure 4.3.2-12. Amplitude of the annual signal of alongshelf velocity ($\text{cm}\cdot\text{s}^{-1}$) from (a) 10-m and (b) bottom current measurements. Triangles are mooring locations.

The amplitudes of the annual signal of bottom, alongshelf velocity components are small, even over the inner shelf in shallow water (Figure 4.3.2-12b). The greatest amplitudes are over the inner western shelf at the coastline bend. There are no highs at the eastern or western shelf edges as were seen in the 10-m amplitudes.

Vertical sections of the amplitude of the sum of squares of the annual signal of alongshelf velocity are shown for line 4 and line 9 (Figure 4.3.2-13). The vertical gradient of the amplitude is greatest nearshore and smallest at the shelf edge. On line 4, the minimum amplitude ($< 2 \text{ cm}\cdot\text{s}^{-1}$) occurs near the sea floor at the 50-m isobath. Along the 200-m isobath, the minimum amplitudes occur at about 100 m in the central shelf region (moorings 8 to 11) and deeper for moorings at the east and west ends of the line (Figure 4.3.2-13b). Along the shelf edge, eastern moorings 48 and 13 and western moorings 4 to 7 have large vertical and horizontal gradients compared to those at the central shelf edge. This pattern indicates that Loop Current eddies contribute variability to the annual signal.

Cross-shelf velocity. The cross-shelf velocity time series were smoothed and processed in the same manner as the alongshelf velocity time series. Figure 4.3.2-14 shows a cycle of the annual signal of 10-m cross-shelf velocity grouped in alongshelf lines. Within each line grouping, moorings are ordered from west to east. Extrema in the annual signal of the cross-shelf current are smaller than those of the alongshelf, in the range $\pm 6 \text{ cm}\cdot\text{s}^{-1}$, except for moorings at the 500-m isobath (not shown) where values of $\pm 10 \text{ cm}\cdot\text{s}^{-1}$ can be found. The patterns of annual signal vary widely from mooring to mooring and show the relatively large contribution of the harmonics to the annual signal. The fundamental contributes less than 40% of the total variance to the cross-shelf velocity annual signal, while the harmonics each contribute comparable amounts (Table 4.3.2-4). This leads to greater variability in time, and results in less discernible patterns for cross-shelf velocity. Figure 4.3.2-15 shows the annual signal for bottom cross-shelf velocity grouped in alongshelf lines. These signals are on the order of $\pm 1 \text{ cm}\cdot\text{s}^{-1}$, and no clear pattern emerges.

Inspection of the annual signal of velocity reveals that mooring data fall into three basic cases relating along- and cross-shelf velocity components. The first consists of a pattern of offshore flow when the alongshelf flow is upcoast and onshore flow when the alongshelf flow is downcoast (e.g., mooring 15 top in Figures 4.3.2-10 and 4.3.2-14). This is prevalent at moorings at the eastern end of the study region and on the central outer shelf. The second consists of a pattern of onshore flow with upcoast alongshelf flow and offshore flow with downcoast alongshelf flow (e.g., mooring 2 top in Figures 4.3.2-10 and 4.3.2-14). It is found mainly at moorings located over the western shelf and on the central inner shelf. The third case is when the mooring data exhibit no clear pattern.

We visually identified the pattern that currents tended to exhibit in July when alongshelf flows are generally upcoast. Figure 4.3.2-16 shows the resulting relationship between the

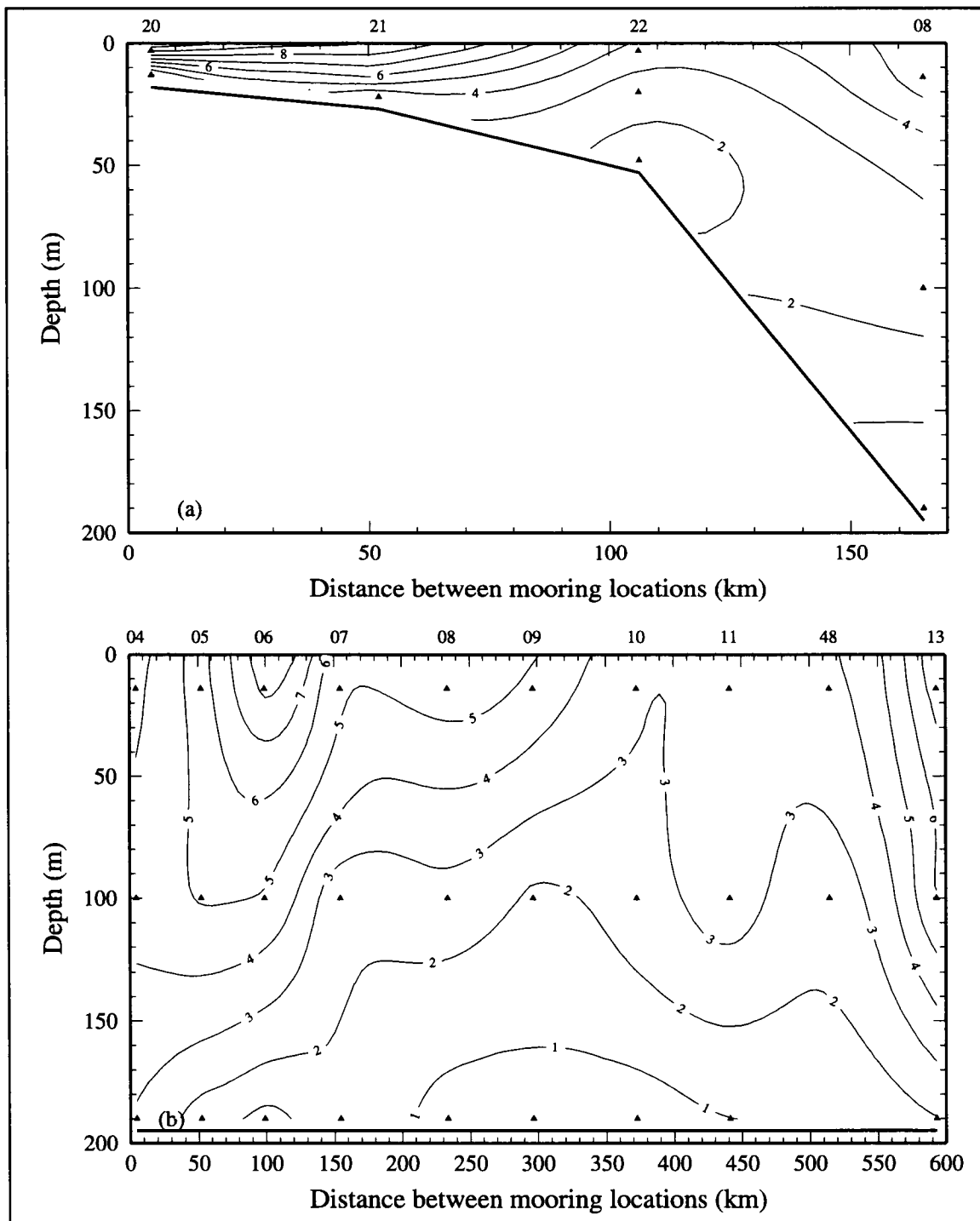


Figure 4.3.2-13. Amplitude of the annual signal of alongshelf velocity ($\text{cm}\cdot\text{s}^{-1}$) from moorings on (a) line 4 and (b) line 9. Triangles show instrument locations.

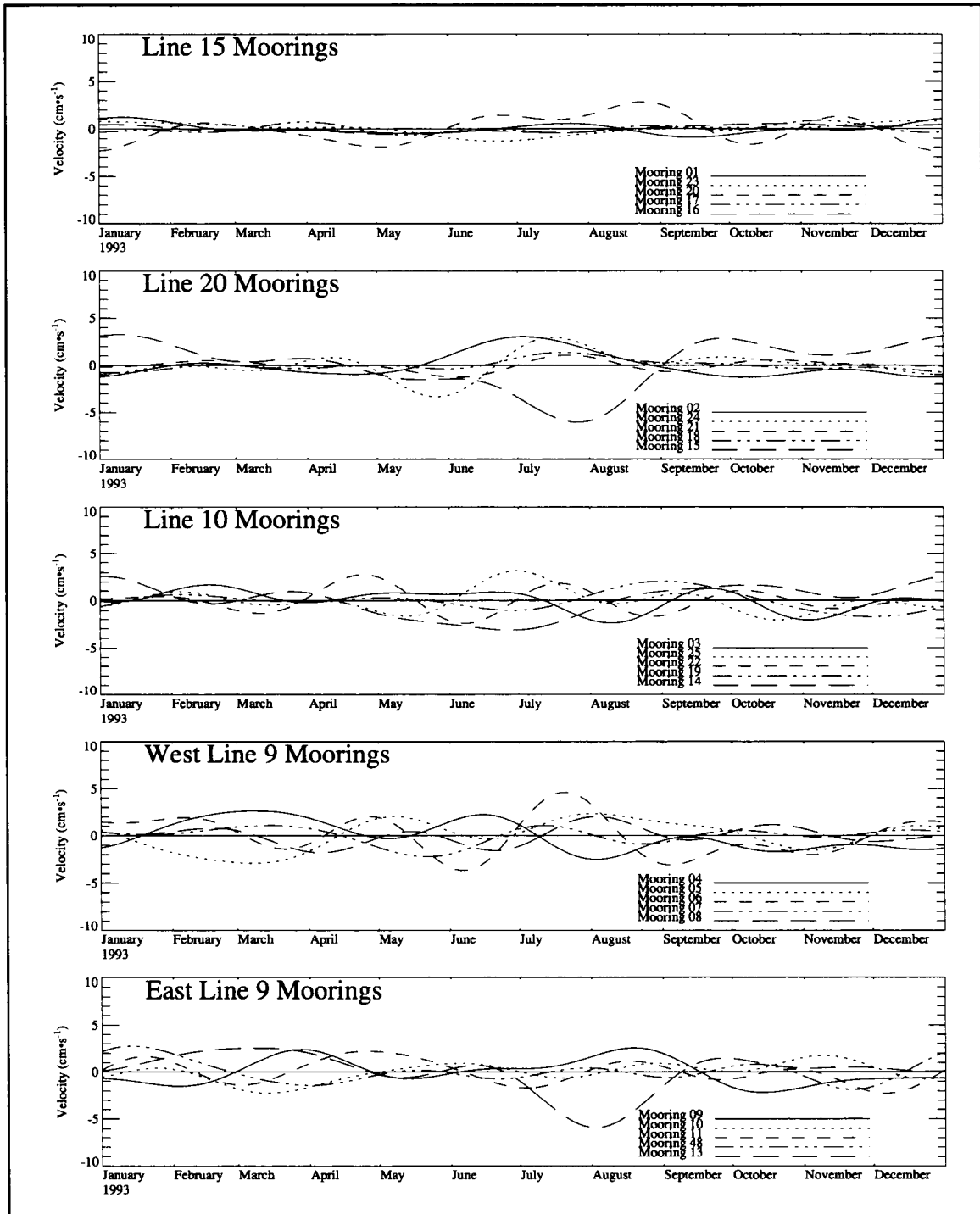


Figure 4.3.2-14. Annual signal of 10-m, cross-shelf current velocity in groupings of alongshelf lines.

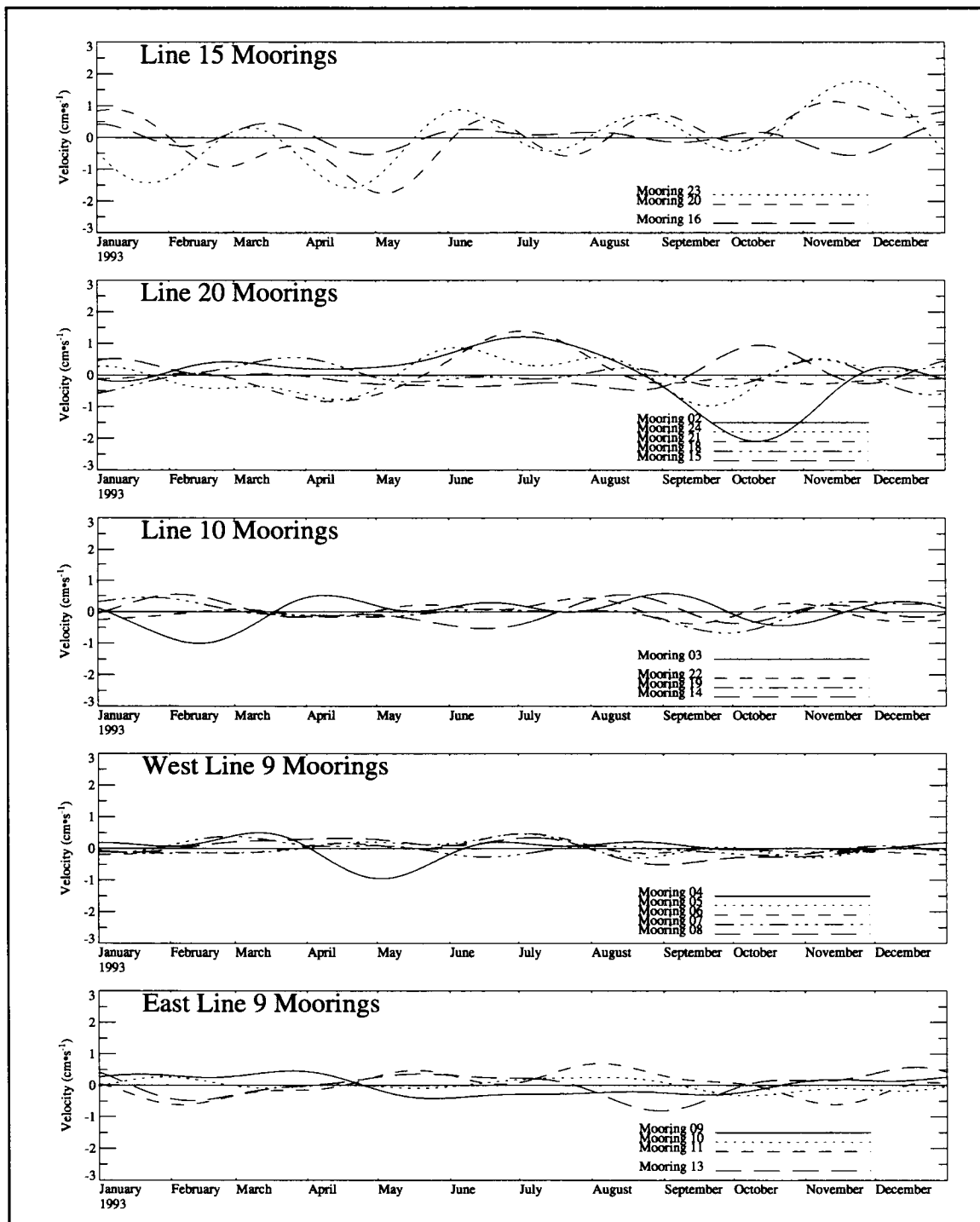


Figure 4.3.2-15. Annual signal of bottom, cross-shelf current velocity in groupings of alongshelf lines.

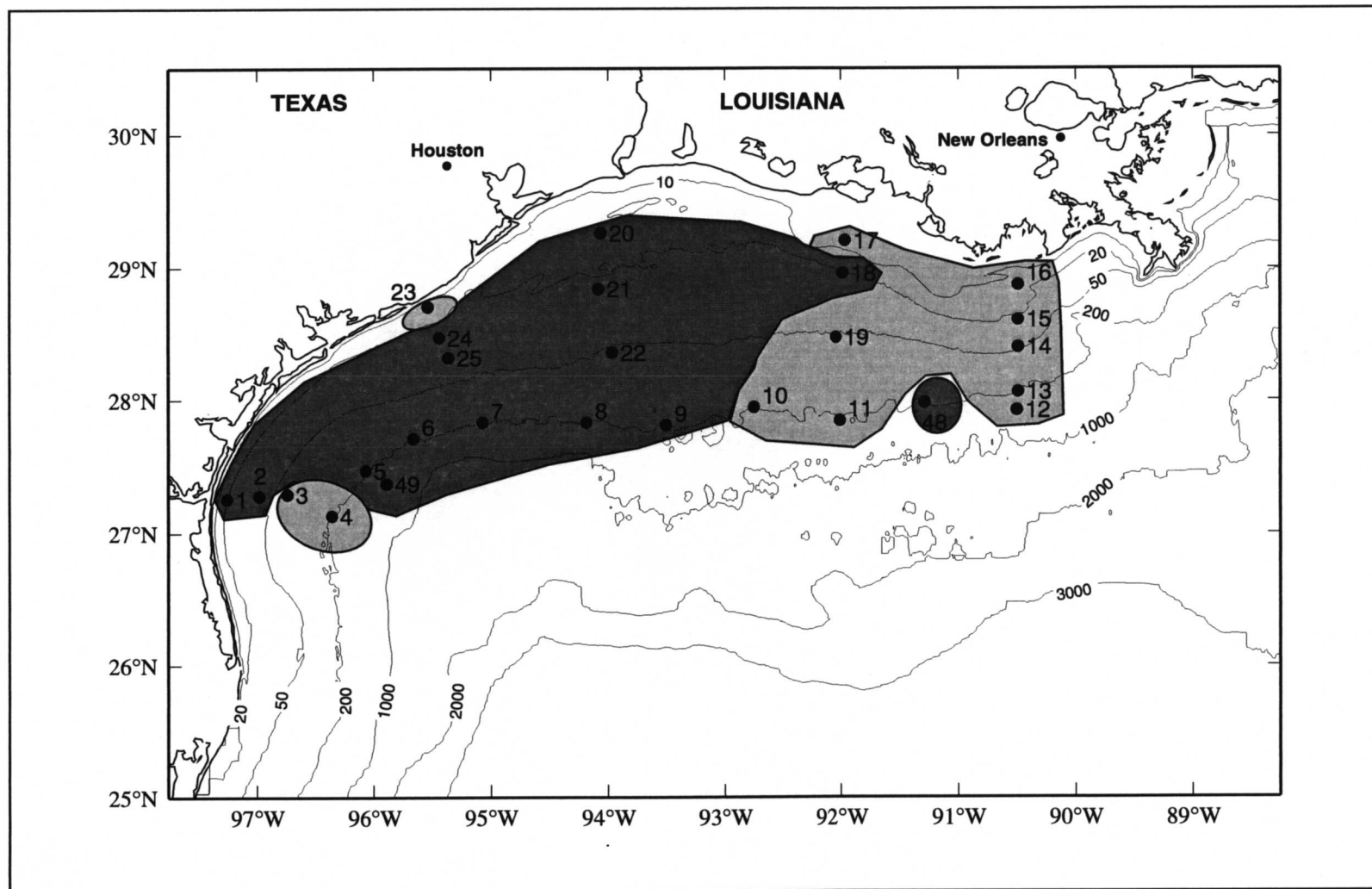


Figure 4.3.2-16. Tendency toward positive (darker) or negative (lighter) correlation between the annual signal of 10-m, alongshelf velocity and the annual signal of top, middle, or bottom depth cross-shelf velocity.

10-m annual signal of along- and cross-shelf velocity. The cross-shelf velocity at moorings east of 93°W tends to be offshore with upcoast flow. The cross-shelf velocity west of 93°W tends to be onshore with upcoast flow.

Using the time series of the annual signal, cross-correlations were computed for 10-m alongshelf velocity with 10-m and middle or bottom cross-shelf velocity. Table 4.3.2-5 shows the results. A positive correlation corresponds to onshore cross-shelf flow with upcoast alongshelf flow or offshore cross-shelf with downcoast alongshelf. A negative correlation corresponds to offshore cross-shelf with upcoast alongshelf flow or onshore cross-shelf with downcoast alongshelf flow. The cross-correlations suggest correlations are positive over the western shelf and negative over the eastern shelf. Thus, the pattern of the annual signal of shelf circulation tends to be anticyclonic during summer and cyclonic during nonsummer.

Figure 4.3.2-17 shows the amplitude of the sum of the squares of the annual signal for the cross-shelf velocity component. These amplitudes are smaller than those of the alongshelf velocity component. The amplitudes of the 10-m cross-shelf annual signal increases slightly offshore (Figure 4.3.2-17a). There is little variability over the central shelf. The regions of greatest variability are found at the southwestern and eastern ends of the study area, particularly at the shelf edge. There, the isopleths radiate northwest onto the shelf from the highs at moorings 12 and 49, respectively. This indicates a contribution of Loop Current eddy energy to the variability in the annual signal of cross-shelf velocity. The amplitude of the bottom, cross-shelf velocity is less than $1.3 \text{ cm}\cdot\text{s}^{-1}$ everywhere (Figure 4.3.2-17b). The amplitudes are smallest offshore in the deeper water.

The vertical structure of the amplitude of the cross-shelf velocity component shows highest amplitudes near the surface and decreasing with depth (Figure 4.3.2-18a). At the shelf edge, amplitudes are highest at the western and far-eastern ends and lowest in the central shelf edge region (Figure 4.3.2-18b). Again, this pattern is evidence of the influence of Loop Current eddies at the western and far eastern shelf edges.

Residual signals of current velocity

To produce the residual signals, the record-length mean, annual signal, and a linear trend were removed from each 40-hour low-pass current meter record. The residual signals of current velocity then were processed with a Fast Fourier Transform to examine the energy in the weather and the mesoscale bands. The weather band had frequencies (periods) of 0.50 to 0.10 cpd (2 to 10 days). Its high frequency limit was determined by the low-pass filtering; its low frequency limit was selected because the frequency of frontal passages during the LATEX period was on the order of 10 days in nonsummer (Section 2.1.3). The high frequency limit for the mesoscale band was 0.10 cpd (10 days) and the low frequency

Table 4.3.2-5. Cross-correlation of the annual signal of 10-m, alongshelf velocity with the annual signal of cross-shelf velocity at the top and bottom or middle depths.

Mooring	Top alongshelf to top cross-shelf		Top alongshelf to middle or bottom cross-shelf		Cross-shelf depth (m)
	Zero lag coefficient	Significance level (%)	Zero lag coefficient	Significance level (%)	
1	-0.576	95	-0.094	<50	19
2	0.928	95	0.773	95	30
3	-0.330	70	0.274	60	61
4	0.406	80	0.544	90	100
5	0.336	60	0.403	70	100
6	0.136	<50	0.280	60	100
7	-0.218	50	-0.288	60	100
8	-0.327	70	-0.137	<50	100
9	-0.733	95	-0.379	80	100
10	-0.441	80	-0.008	<50	100
11	0.025	<50	0.492	95	100
12	-0.252	60	0.320	60	100
13	-0.561	95	-0.120	<50	100
14	-0.946	95	-0.547	90	42
15	-0.954	95	-0.622	95	24
16	-0.560	95	0.497	95	17
17	-0.276	60	-0.661	95	5
18	0.779	95	0.231	60	21
19	-0.268	50	-0.462	80	44
20	0.597	95	-0.289	60	13
21	0.021	<50	0.782	95	21
22	-0.120	<50	0.121	<50	48
23	-0.943	95	0.247	70	13
24	0.170	<50	0.415	70	27
25	0.493	90	0.527	95	38
48	-0.029	<50	0.734	95	100
49	0.617	95	0.525	90	100

limit was 0.01 cpd (100 days). The lower limit was selected because gaps in the records would not allow longer periods to be resolved at all moorings. The mesoscale band is expected to contain energy from Loop Current and cyclonic eddies.

Figure 4.3.2-19a presents the distribution of the weather band kinetic energy (WBKE) at 10 m. The distribution shows WBKE increasing from the shelf edge to the inner shelf. The highest value ($80 \text{ cm}^2 \cdot \text{s}^{-2}$) occurs just offshore of Atchafalaya Bay at mooring 17. The broad central shelf has generally lower WBKE values than those of the eastern or western shelf regions. The eastern and central shelf edge WBKE values are lower than those at the western shelf edge.

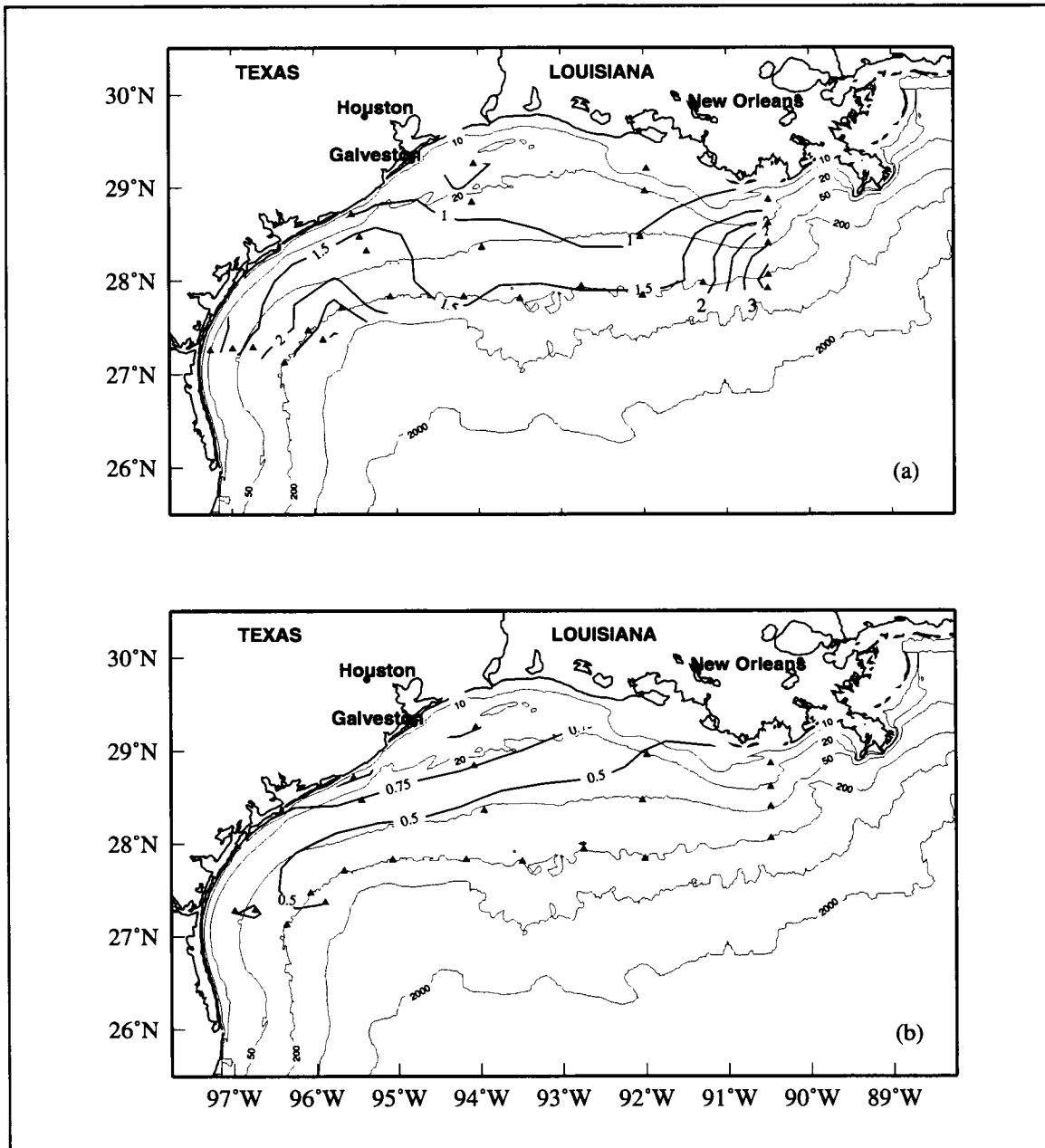


Figure 4.3.2-17. Amplitude of the annual signal of cross-shelf velocity ($\text{cm}\cdot\text{s}^{-1}$) from (a) 10-m and (b) bottom current measurements. Triangles are mooring locations.

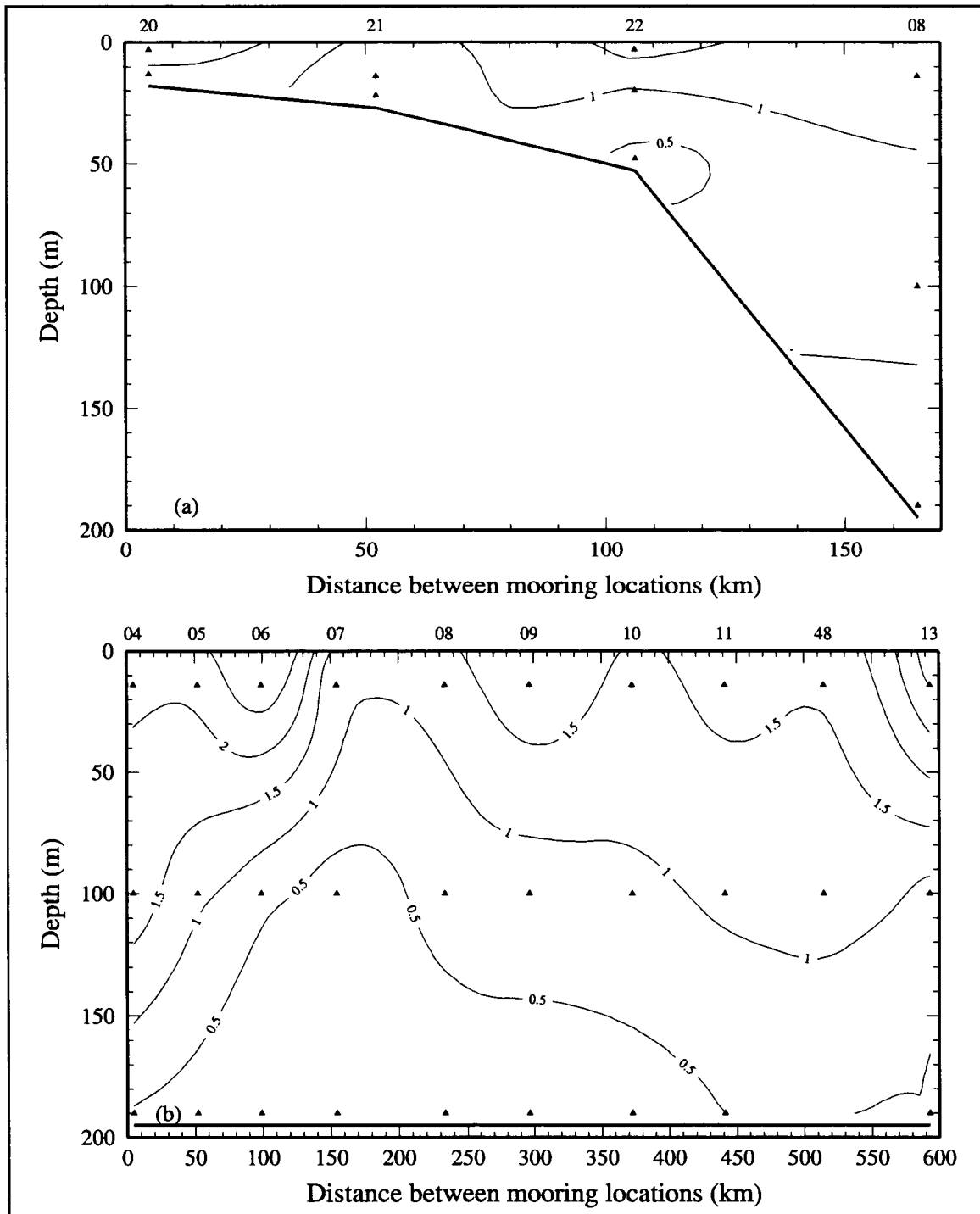


Figure 4.3.2-18. Amplitude of the annual signal of cross-shelf velocity ($\text{cm}\cdot\text{s}^{-1}$) from moorings on (a) line 4 and (b) line 9. Triangles show instrument locations.

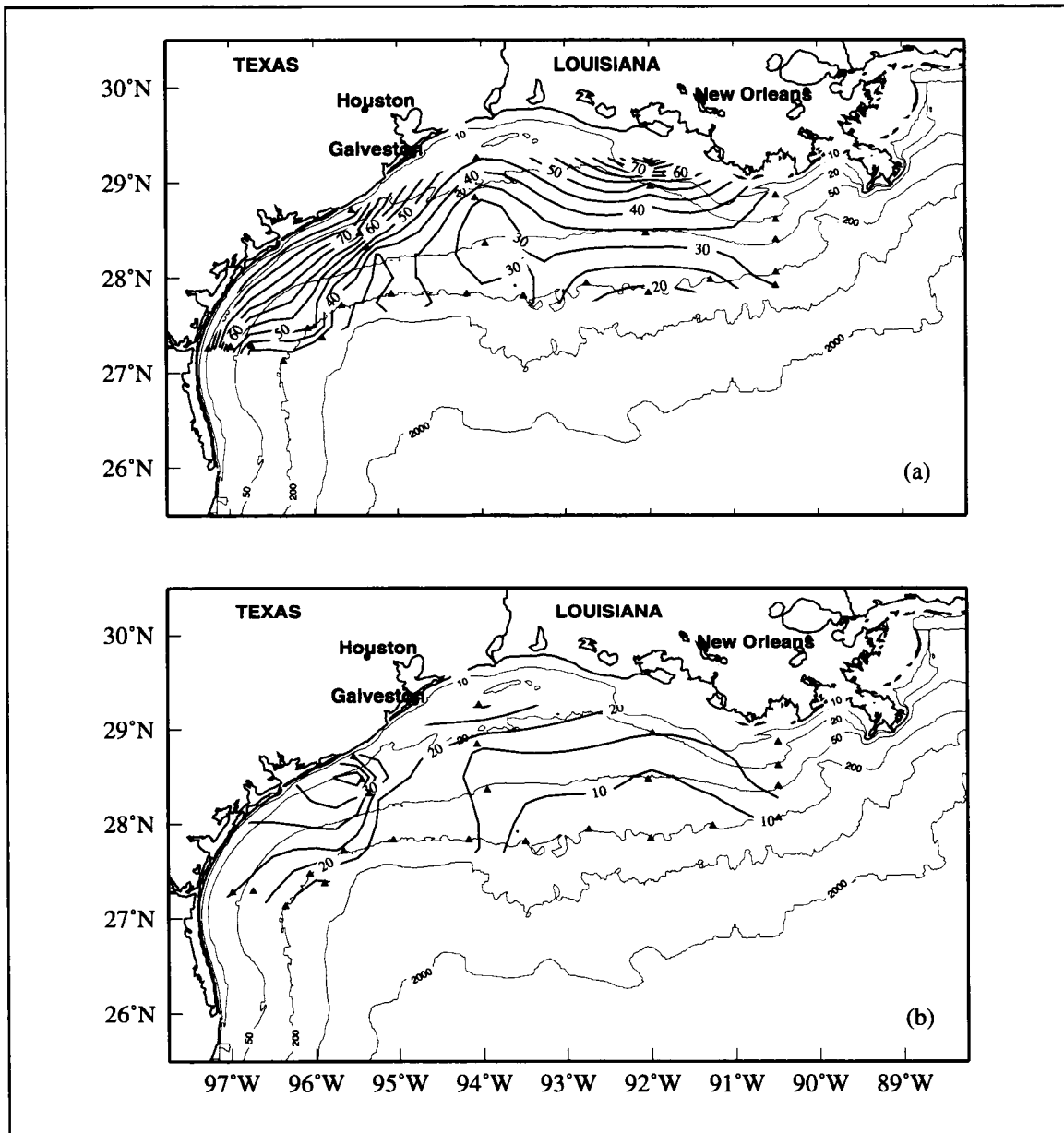


Figure 4.3.2-19. Weatherband kinetic energy ($\text{cm}^2 \cdot \text{s}^{-2}$) with period between 2 and 10 days from (a) 10-m and (b) combination middle/bottom mooring measurements. Triangles are mooring locations.

A composite of the bottom WBKE inshore of the 50-m isobath with the mid-depth WBKE at or offshore of the 50-m isobath is given in Figure 4.3.2-19b. The WBKE at depth is lower in magnitude than the 10-m WBKE; however, the pattern is similar, with values generally increasing onshore. The WBKE on the outer shelf is lower on the eastern and central shelf regions than over the western shelf. The inner western shelf has the largest gradient.

Figure 4.3.2-20 shows the distributions of the mesoscale band kinetic energy (MBKE) over the Texas-Louisiana shelf. MBKE values decrease from the shelf edge inshore. 10-m values and gradients over the western shelf are greater than over the central and eastern shelf regions (Figure 4.3.2-20a). Two maxima are seen over the western shelf: one at the shelf edge and the other nearshore on line 7. The far eastern shelf edge has a relative high in MBKE.

A composite of the bottom MBKE inshore of the 50-m isobath with the mid-depth MBKE at or offshore of the 50-m isobath is given in Figure 4.3.2-20b. Highs in MBKE occur at the western and far eastern shelf edges. These are separated by a region of relatively low MBKE over the central shelf edge. MBKE values at the bottom instruments at the shelf edge (not shown) also have maxima at the western and eastern shelf edge.

The ratio of WBKE to MBKE was determined to compare the energies in the two bands. Figure 4.3.2-21a shows the ratios at 10-m. These values generally parallel the isobaths. A value of 1.0, indicating WBKE and MBKE are of comparable magnitude, occurs between the 20- and 50-m isobaths. Inshore, the values are higher, indicating that the weather band dominates the residual energy distributions over the inner shelf. Offshore, the values are < 1 , indicating that the mesoscale band dominates over the outer shelf. Along line 7, however, the mesoscale band dominates across the entire shelf.

Figure 4.3.2-21b shows a composite of bottom ratios inshore of the 50-m isobath with the mid-depth ratios at or offshore of the 50-m isobath. The distributions approximately parallel the isobaths. Again, the ratio value of 1.0 roughly follows the 50-m isobath with larger values inshore and smaller values offshore. As with the 10-m ratios, this distribution indicates the WBKE dominates the residual energy distributions over the inner shelf and the MBKE dominates over the outer shelf. The ratios at the bottom of the outer shelf (not shown) are 1.0 or greater over the central shelf, where both WBKE and MBKE values are $< 3 \text{ cm}^2 \cdot \text{s}^{-2}$, and less than 1.0 at the eastern and western shelf edge and along line 7 of the far southwestern region.

The patterns of WBKE and MBKE show that the residual currents over the shelf are divided into two regimes separated at about the 50-m isobath. The inner shelf regime is driven mainly by the winds. The outer shelf regime is driven largely by mesoscale phenomena. The phase and squared-coherency diagrams in Section 4.5 show significant coherence in

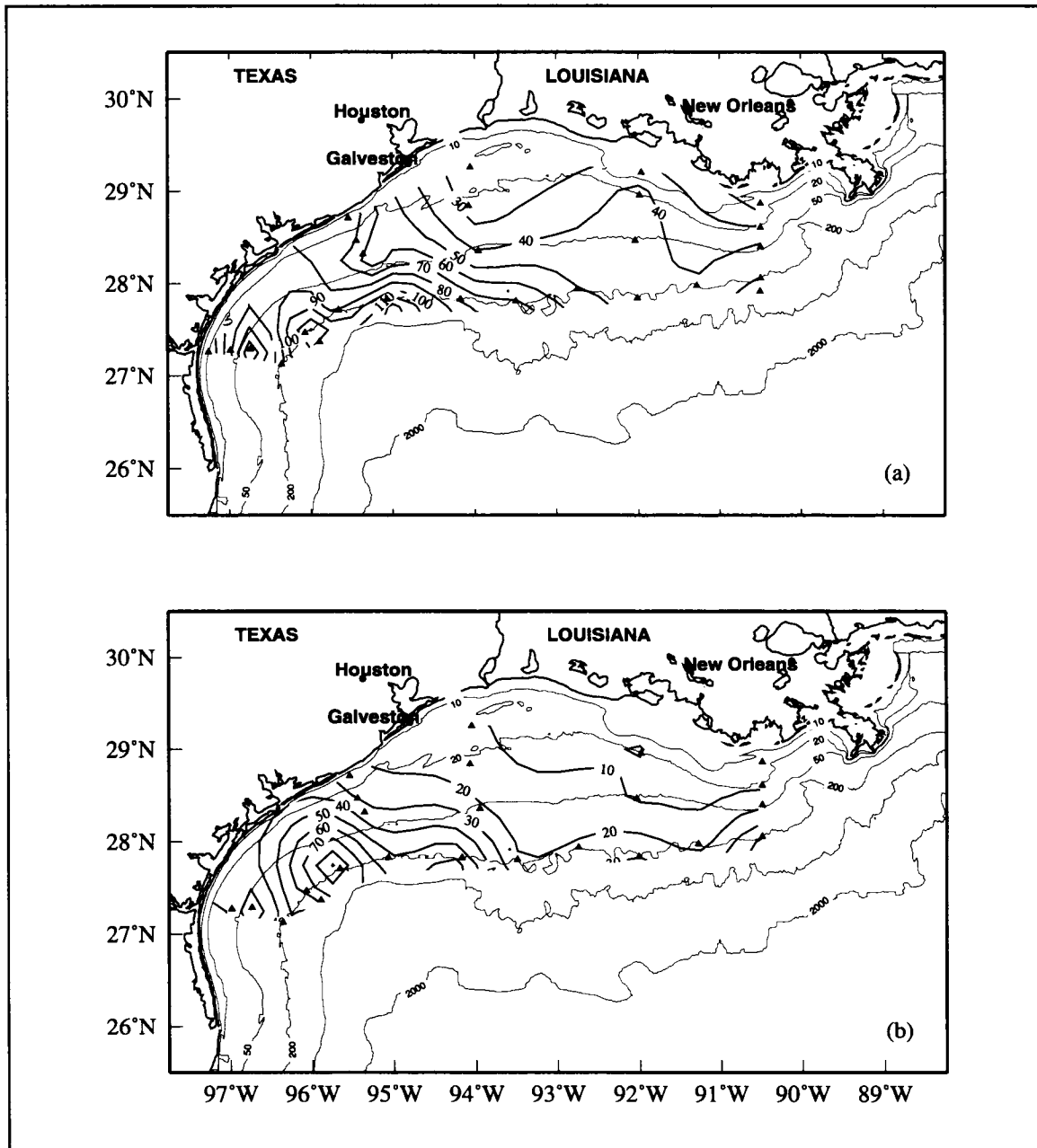


Figure 4.3.2-20. Mesoscale band kinetic energy ($\text{cm}^2 \cdot \text{s}^{-2}$) with period between 10 and 100 days from (a) 10-m and (b) combination middle/bottom mooring measurements. Triangles are mooring locations.

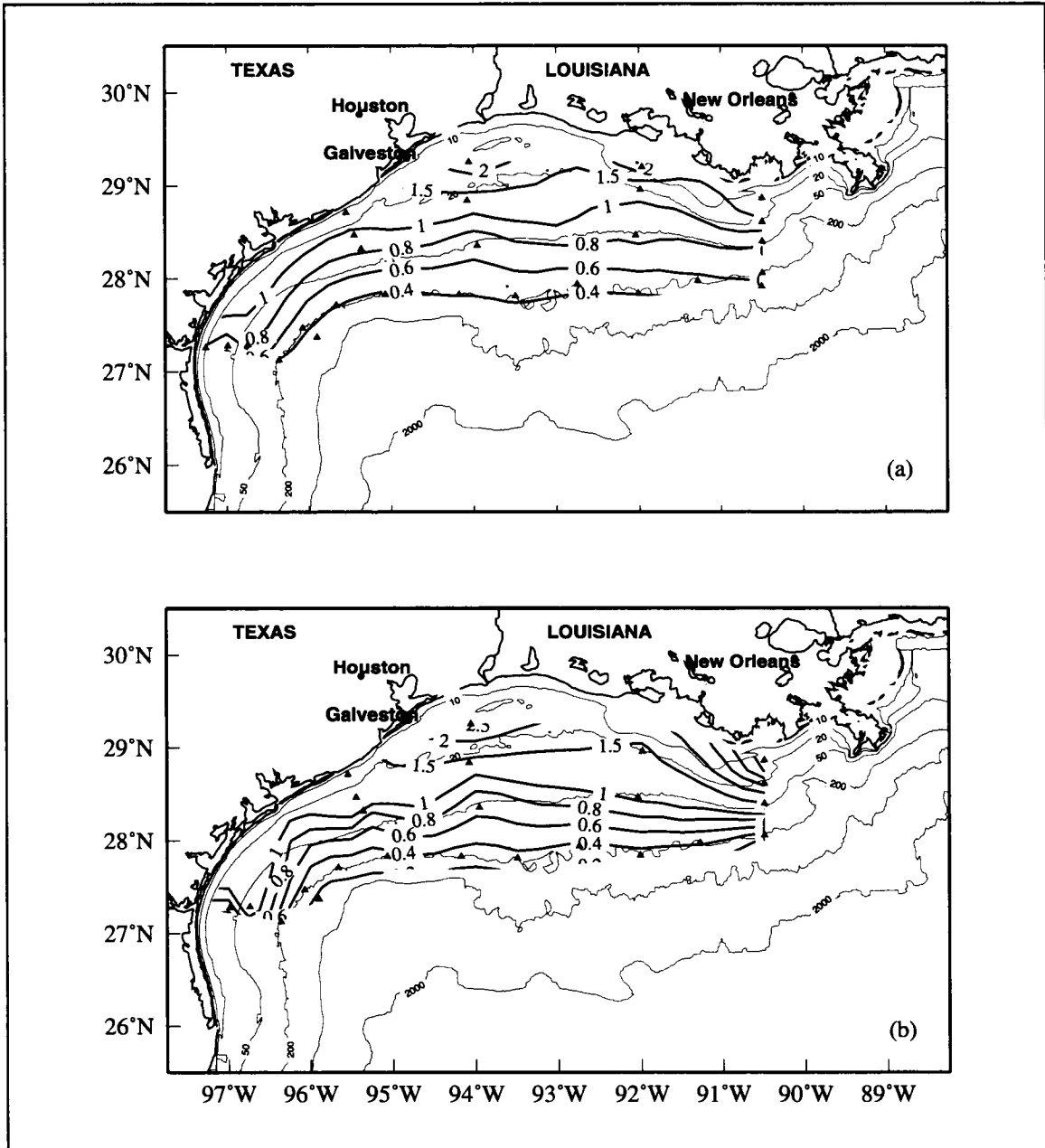


Figure 4.3.2-21. Ratio of weatherband to mesoscale band kinetic energy from (a) 10-m and (b) combination middle/bottom residual current measurements. Triangles are mooring locations.

the weather band between winds and currents over the inner shelf, but not over the outer shelf. Section 2.5.2 shows that the presence of mesoscale eddies significantly influences currents at the shelf edge. These sections support the conclusions given here.

Figure 4.3.2-22 shows the vertical distributions of WBKE and MBKE along the 200-m isobath. The WBKE decreases with depth throughout the water column (Figure 4.3.2-22a). Values are less than $40 \text{ cm}^2\cdot\text{s}^{-2}$, except over the western half of the shelf (moorings 4-9). There, the vertical gradient increases as total water depth decreases, indicating possible influence of Loop Current eddy energy in the weather band frequencies.

In contrast, the vertical distribution of MBKE along the 200-m isobath shows values $> 40 \text{ cm}^2\cdot\text{s}^{-2}$ extend to depth over the western shelf and into the upper waters of the eastern shelf (Figure 4.3.2-22b). Values over the western half shelf generally are higher throughout the water column than for the eastern half shelf. The vertical gradients are larger in the west than the east. This is evidence of the greater predominance of Loop Current eddies at the western shelf edge as compared to at the eastern shelf edge during the LATEX period. Some eddy presence at the eastern shelf edge is indicated by the sloping MBKE structure at moorings 48 and 13.

Temporal scales of residual currents

The temporal scales of the residual signals were determined first by calculating the autocorrelation function for each residual time series. Then, the number of days to the first zero crossing of the function was used as an estimate of the time scale of the dominant fluctuations of each series (Bryden and Pillsbury 1977). Because the records had gaps, the autocorrelations were found for each segment. Zero crossings for segments of 180 days or longer were averaged for each residual record and used in this analysis. Averaging was done by weighting the segments by length.

Figure 4.3.2-23 shows the distribution of the first zero crossing for the residual, 10-m velocity components. With the exception of the region between 95° and 96.5°W , the alongshelf component has time scales less than 10 days inshore of about the 50-m isobath and longer time scales offshore. This is as expected for wind-driven inner shelf flow and mesoscale influenced outer shelf flow. The exception is due to the influence of mesoscale eddies off the southwest shelf. The pattern of cross-shelf, residual current time scales is also influenced by the encroachment of eddies at the western shelf edge. However, the time scales of the cross-shelf, residual currents are generally within the weather band. That time scale has a maximum at about the 50-m isobath on line 1, and values decrease to the west, suggesting that the eastern cross-shelf residual velocity is influenced by the Mississippi-Atchafalaya river discharge.

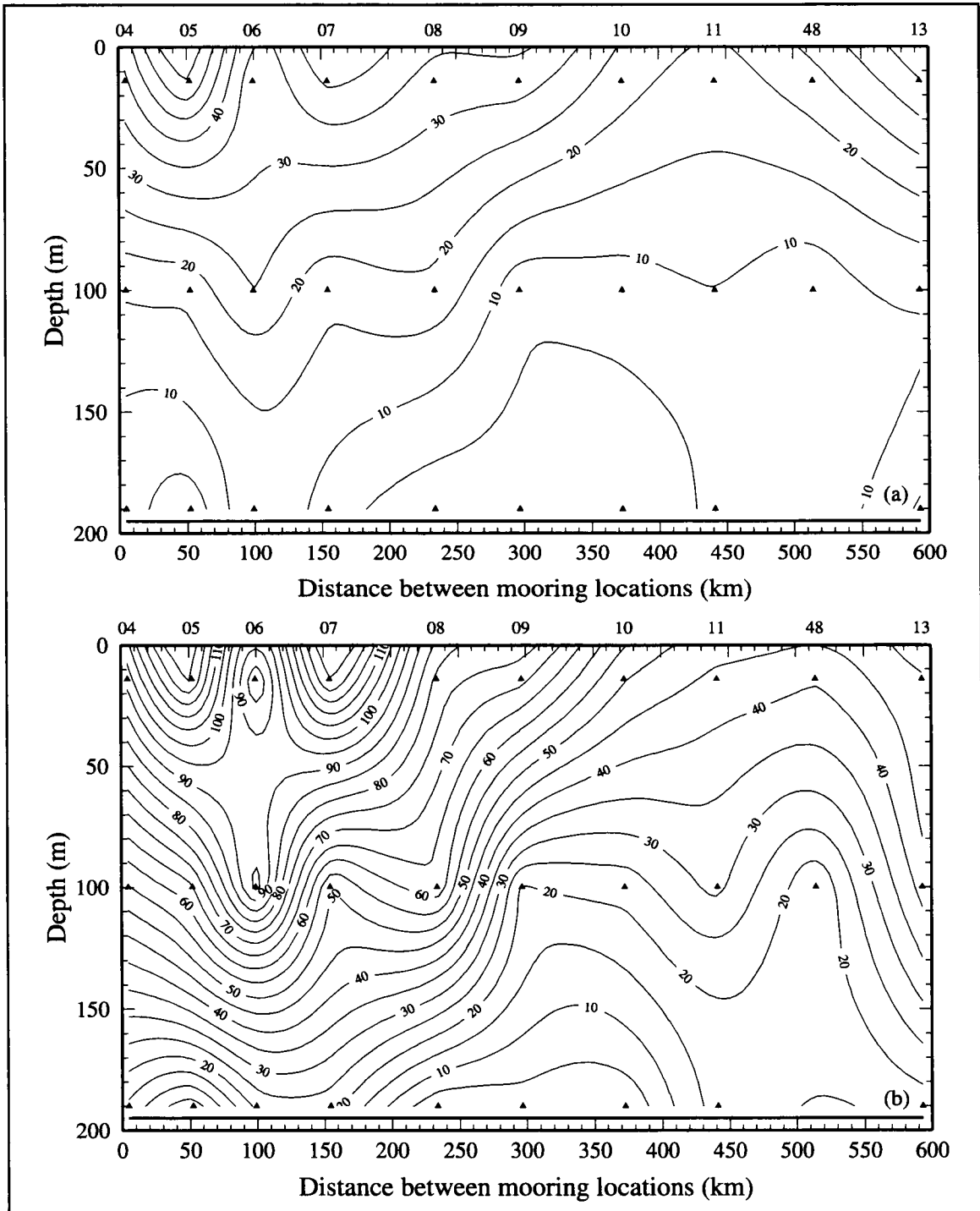


Figure 4.3.2-22. Kinetic energy ($\text{cm}^2 \cdot \text{s}^{-2}$) of the residual time series on line 9 in (a) the weatherband (period between 2 and 10 days) and (b) the mesoscale band (period between 10 and 100 days).

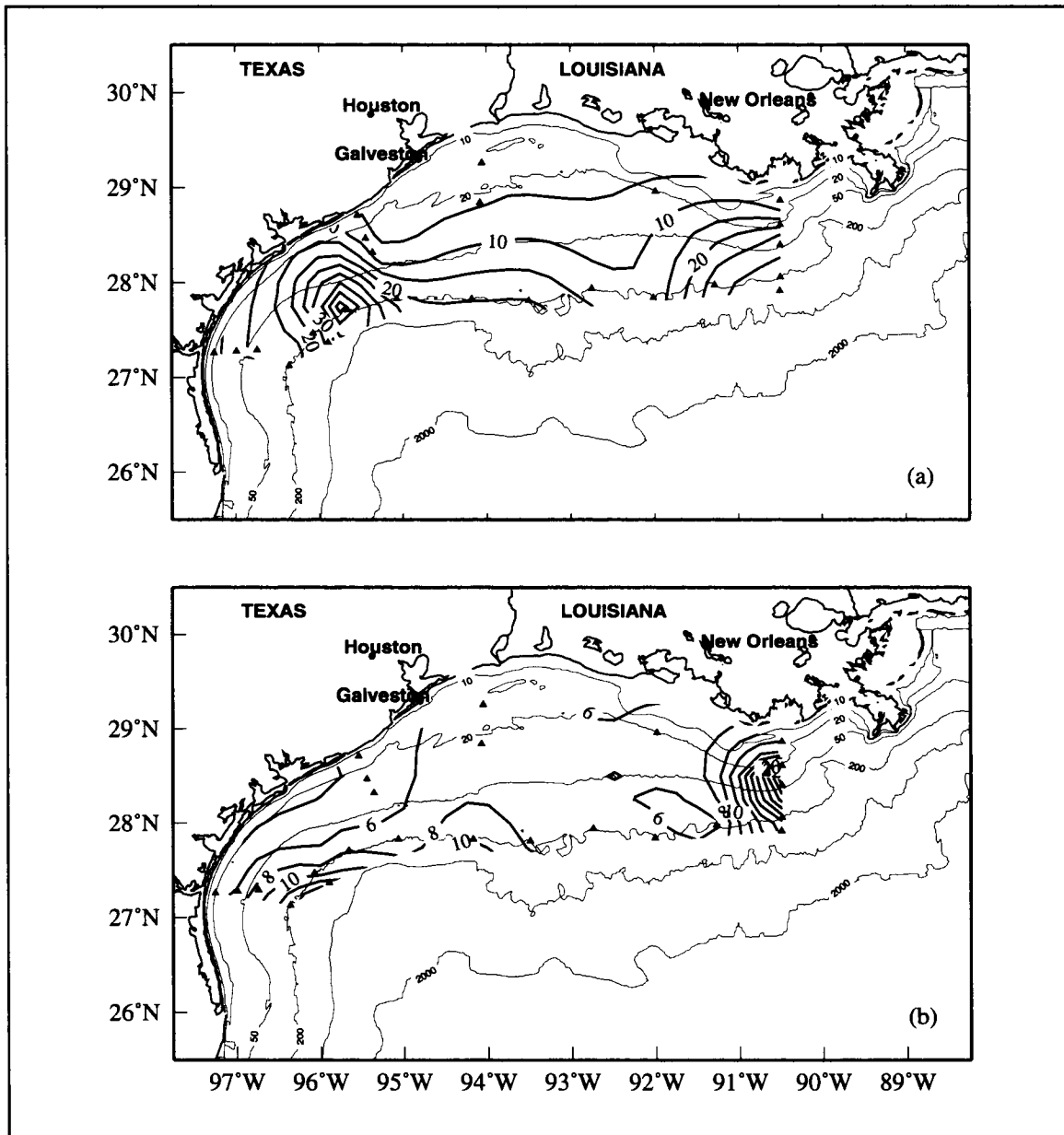


Figure 3.2.3-23. First zero crossing (days) of average autocorrelations for 10-m residual (a) alongshelf and (b) cross-shelf velocity ($\text{cm}\cdot\text{s}^{-1}$). Means were of length-weighted segments of 180 days or more.

Annual signal of salinity

The salinity time series were processed using the same procedure used for velocity except that the 30-day, low-pass filter was not applied. Figure 4.3.2-24 presents the annual signal of 10-m salinity in alongshelf groupings. The moorings within each line grouping are listed from west to east. At all but the innermost (line 15) moorings, a freshening occurs between April and September. It is greatest in the spring for the western shelf and in the summer for the eastern shelf. The fresh extrema occur in May on western lines 5 and 7, in June on line 4 over the west central shelf, and in July on lines 1 and 2 in the east. The western inner shelf moorings exhibit an increase in salinity during the summer, with maxima generally occurring in August. The innermost moorings of line 15 have salinity maxima in summer. These maxima are phase shifted, with the maximum at the east (mooring 16) occurring in early summer and in the west (moorings 1 and 23) in late summer. The shelf edge moorings have no pronounced maximum, but rather show a gradual increase in salinity after July. In general, the extrema at the shelf edge are smaller than those over the inner shelf.

As evidenced by these patterns, the annual signal of 10-m salinity responds to the cycles of currents and discharge from the Mississippi-Atchafalaya River. The river system discharges high volumes of fresh water onto the shelf during spring (Section 2.3). The currents carry this fresh water downcoast. This results in fresher water over both the east and west regions of the inner shelf, leading to the pattern of springtime freshening over the shelf. In summer, the currents are upcoast. This keeps the fresh water from the river system dammed over the eastern shelf. The upcoast summer currents also move saltier water from the south onto the western shelf. This results in the salinity maxima seen there in late summer. In fall, the downcoast current is reestablished and again carries fresh water to the inner western shelf, resulting in the secondary fall freshening.

We have insufficient data to analyze patterns of the annual signal of bottom or mid-depth salinity except at the shelf edge. Fluctuations of the annual salinity signal of the shelf edge moorings at the 100-m depth and the bottom do not exceed ± 0.4 , except at mooring 4. This mooring has a pronounced freshening in fall and a minor freshening in June and July.

Figure 4.3.2-25a shows the amplitude of the annual signal of salinity at 10-m and the bottom; amplitudes increase from the shelf edge to the inner shelf. Variability is greatest over the western inner shelf. The maximum occurs on the inner shelf at line 5, where the annual cycle of alongshelf current also is most variable. The fundamental frequency represents about 60% of the variance in the annual signal (Table 4.3.2-4). It represents about 70% of the variance at the shelf edge, 50% along the 50-m isobath, and 60% for moorings inshore of the 50-m isobath.

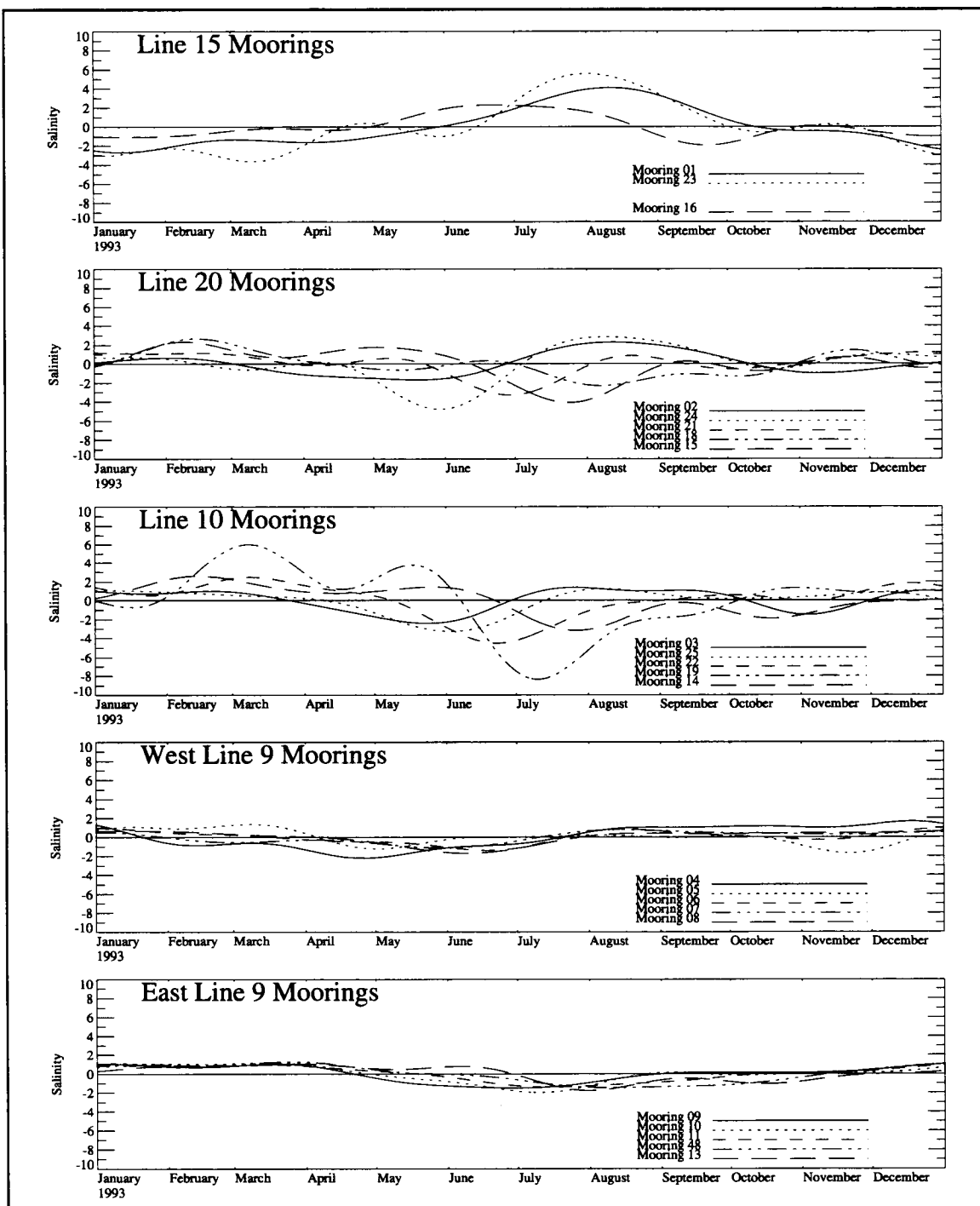


Figure 4.3.2-24. Annual signal of 10-m salinity in groupings of alongshelf lines.

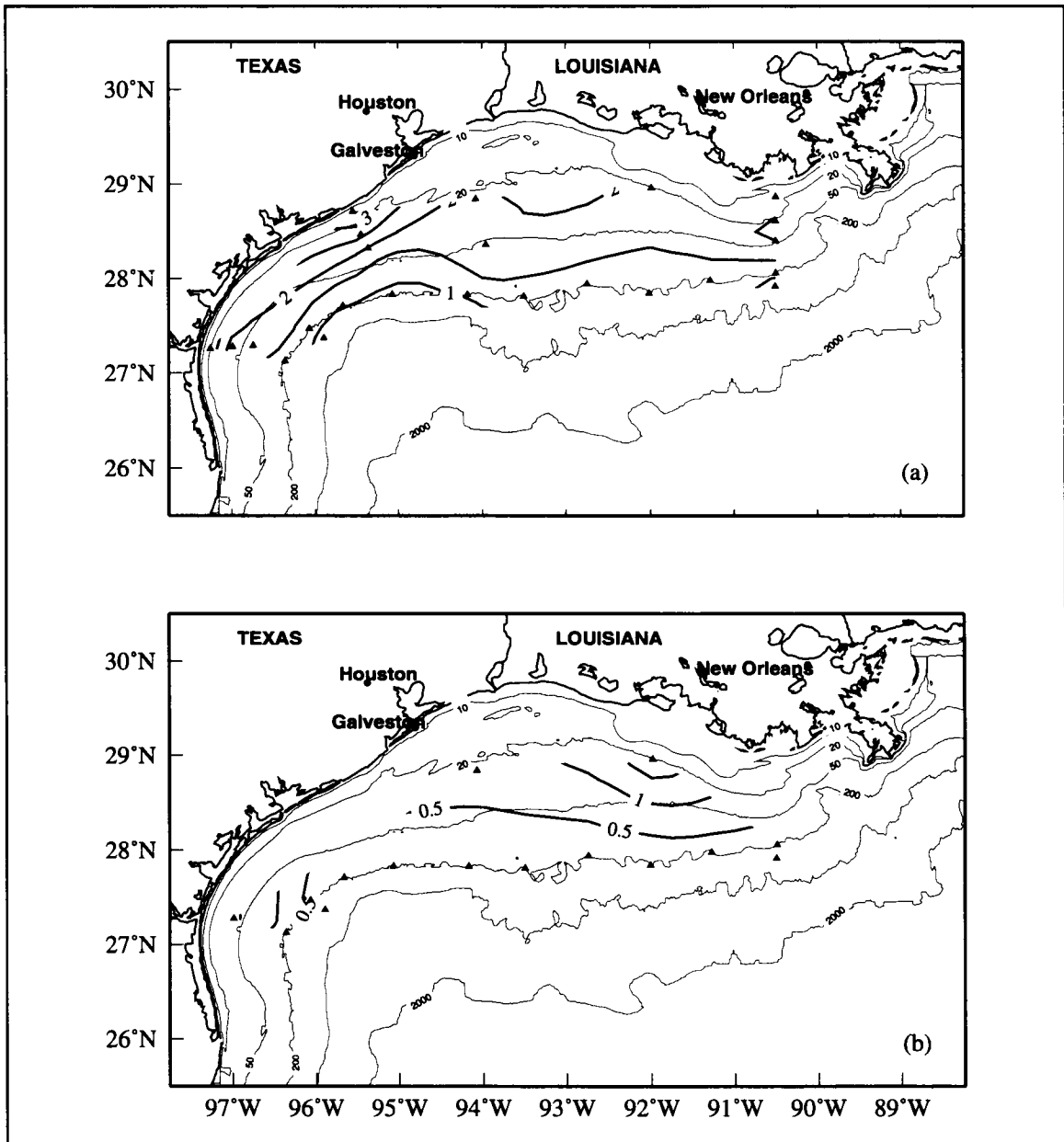


Figure 4.3.2-25. Amplitude of the annual signal of salinity from (a) 10-m and (b) bottom measurements.

The amplitude of the annual salinity signal at the bottom is shown in Figure 4.3.2-25b. At the shelf edge, these amplitudes are less than 0.25, except for mooring 4, which has an amplitude of nearly 1. Sparse data preclude identification of patterns over the inner shelf.

Figure 4.3.2-26 gives vertical sections of the salinity amplitude. In the cross-shelf direction along line 4, amplitudes decrease with depth. Variability is greater over the inner shelf, which is more affected by the river discharge, than over the outer shelf. Along the 200-m isobath, the variability decreases with depth for moorings 9-13 on the eastern shelf (Figure 4.3.2-26b). Over the western shelf, however, the variability at mooring 7 is less in the upper waters and greater at depth than is the variability at comparable depths at adjacent moorings. Moorings 4 and 5 exhibit an increase in variability below 150 m. The patterns in the western moorings likely reflect the contribution of the Loop Current eddies to the variability in the annual signal.

Residual signal of salinity

The record-length mean, the annual signal, and a linear trend were removed from the 40-hour low-pass salinity time series to produce the residual salinity time series. The standard deviation was computed at each mooring and mapped (Figure 4.3.2-27). The standard deviations at 10-m show the variability in residual salinity increases from the shelf edge to the innermost moorings. This reflects greater influence of the river discharge over the inner than outer shelf. From the limited data for bottom salinity, comparison of the standard deviations at the bottom and at 10-m show the variability of residual salinity decreases with depth. At the extreme western shelf edge, the variability is small, but is approximately twice that of the rest of the shelf edge, likely resulting from the Loop Current eddies and associated cyclones that influence that region.

The zero crossing for the autocorrelation function of residual salinity also was computed at each mooring. Time scales for residual salinity signals at 10-m are 20 to 50 days over most of the shelf. This suggests that salinity is relatively unresponsive to forcing in the weather band, as by frontal passages. The shelf edge generally has shorter time scales (20 days) than the inner shelf. The central inner shelf is more uniform, with time scales about 30 days, than the east or west inner shelf regions. There are insufficient data to identify patterns at depth.

Annual signal of temperature

The temperature time series were processed using the same procedure as for salinity. Figure 4.3.2-28 gives the annual signals of 10-m temperatures in alongshelf line groupings. The moorings are listed from west to east within each grouping. The 10-m temperature annual signals show gradual heating in spring and summer, peaking between mid-July and mid-September, then rapid cooling through the fall to a minimum between mid-January and

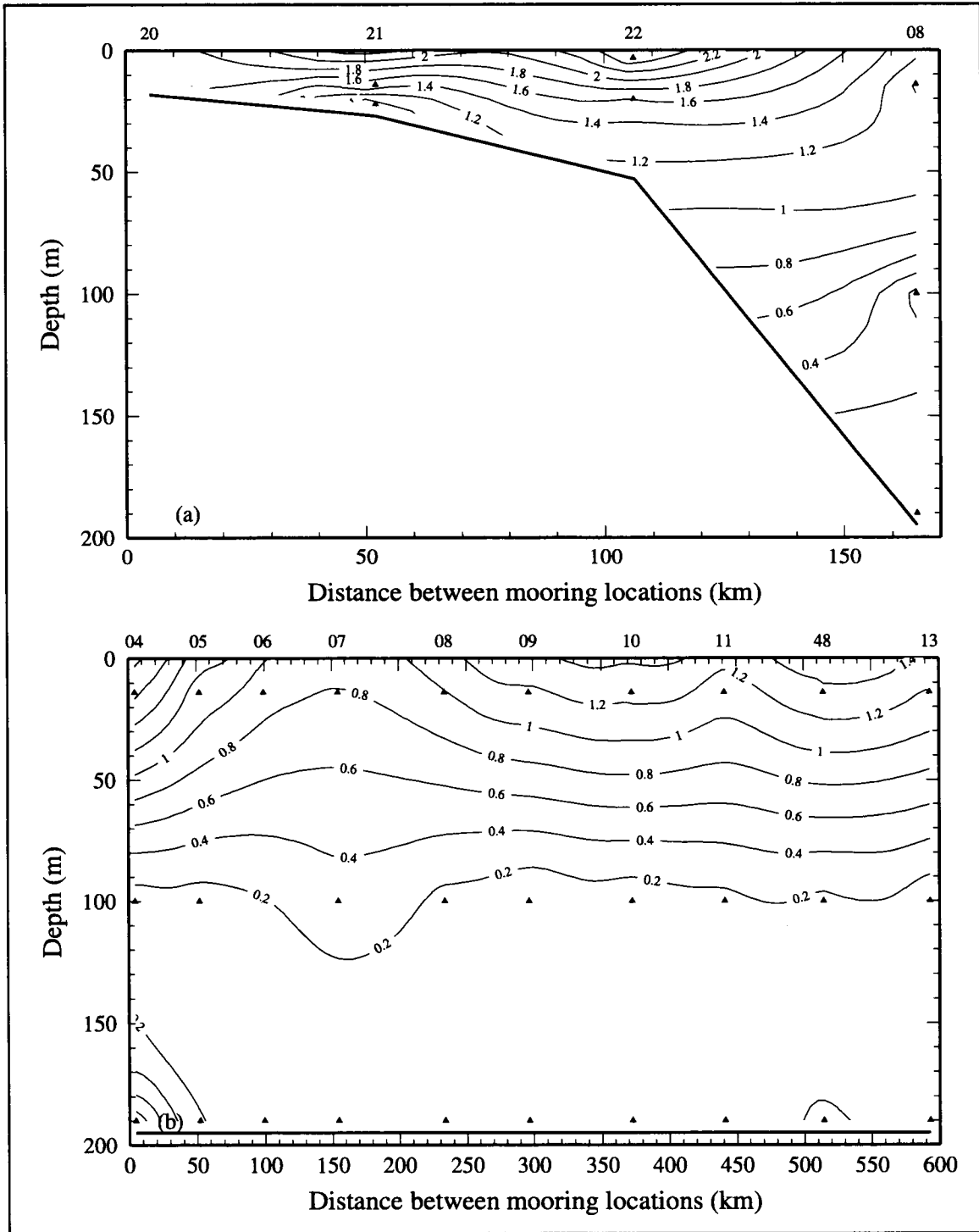


Figure 4.3.2-26. Amplitude of the annual signal of salinity from moorings on (a) line 4 and (b) line 9. Triangles show instrument locations.

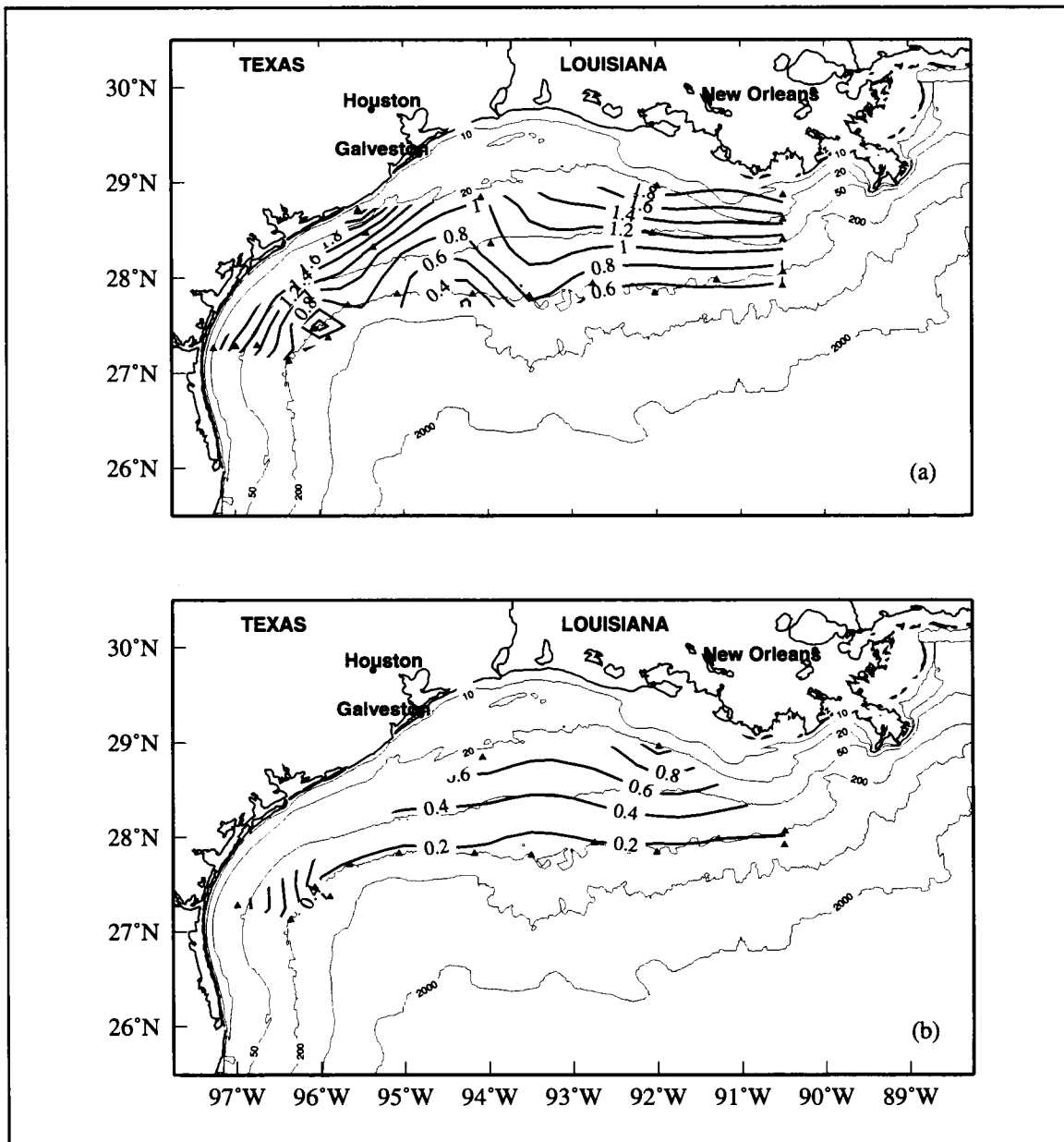


Figure 4.3.2-27. Standard deviation of residual salinity from (a) 10-m and (b) bottom measurements. Triangles show mooring locations.

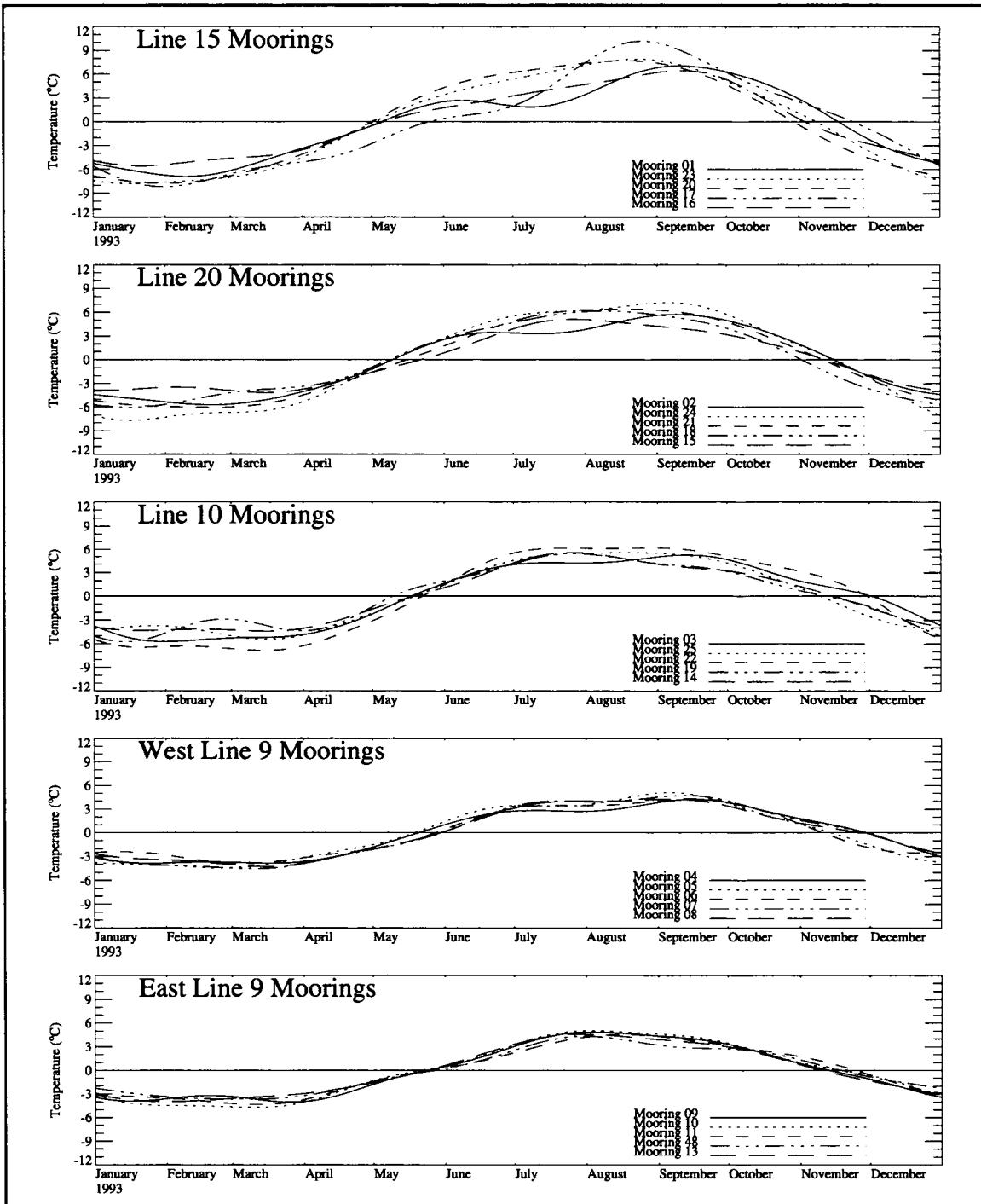


Figure 4.3.2-28. Annual signal of 10-m temperature (°C) in groupings of alongshelf lines.

mid-March. This pattern evidences the response of the annual temperature signal to the annual cycle of insolation (see Section 3.2). Warm peaks generally occur earlier in the east (line 1 moorings) than in the southwest (line 7 moorings). The warm period is longest at the innermost moorings and shortest at the shelf edge. There is more variability in the extrema over the inner shelf than at the shelf edge. Maxima for the innermost moorings range from 6°C to 10°C, while those for the shelf edge moorings are a more uniform 4-5°C. At all moorings, the fundamental for the 10-m temperature contains nearly all of the variance in the annual signal (97.7% on average, Table 4.3.2-4).

Considerably more variability is contributed to the annual signal of bottom temperature (Figure 4.3.2-29) by the harmonics than for the signals at 10 m. Mooring 23 (in depths of less than 10 m) has multiple pronounced extrema. Over the rest of the inner shelf, the pattern shows a warming and cooling pattern similar to that of the 10-m temperature, but extrema generally are sharper and shifted one to two months later. Maxima occur mainly from September to October and minima from February to March. The pattern over the shelf edge fluctuates around zero by $\pm 1.0^\circ\text{C}$, except at mooring 4, which has larger amplitudes and variability. There are no distinct temperature extrema at the shelf edge bottom, although periods of warmer values occur from September to January and April to June, and periods of cooler values occur from January to April and June to September.

Figure 4.3.2-30 shows amplitudes of the annual signal of temperature. At 10 m, the amplitudes increase from the shelf edge to the inner shelf. The maximum variability occurs on the inner shelf of line 5. The annual signal minimum is at the eastern shelf edge. The eastern inner shelf also has less overall variability than the central or western inner shelf regions. The broad central shelf has fairly uniform amplitudes of about 6°C.

The fundamental represents approximately 70% of the variance of bottom temperature. Amplitude contours for bottom temperature (Figure 4.3.2-30b) roughly parallel isobaths. The gradients are strongest at the western end of the shelf and weakest in the central shelf. The eastern shelf is less variable along a given isobath than in the western or central shelf. The amplitudes over the inner shelf range from 3 to 6°C. Except at mooring 4, the amplitude of bottom temperature at the shelf edge is less than 1°C, which is of the order of the error associated with this estimate; thus, partitioning variability between the fundamental and harmonics is not meaningful.

Figure 4.3.2-31 shows amplitudes for temperature in vertical section for line 4 and line 9. On line 4, the annual variability of temperature is smaller at the shelf edge than over the inner shelf. On line 9, the amplitude isolines are roughly horizontal, with greatest amplitudes near-surface and smallest amplitudes at the bottom. Variability below 100 m is small with amplitudes typically less than 1°C except at mooring 4 with an amplitude of 1.4°C at the bottom.

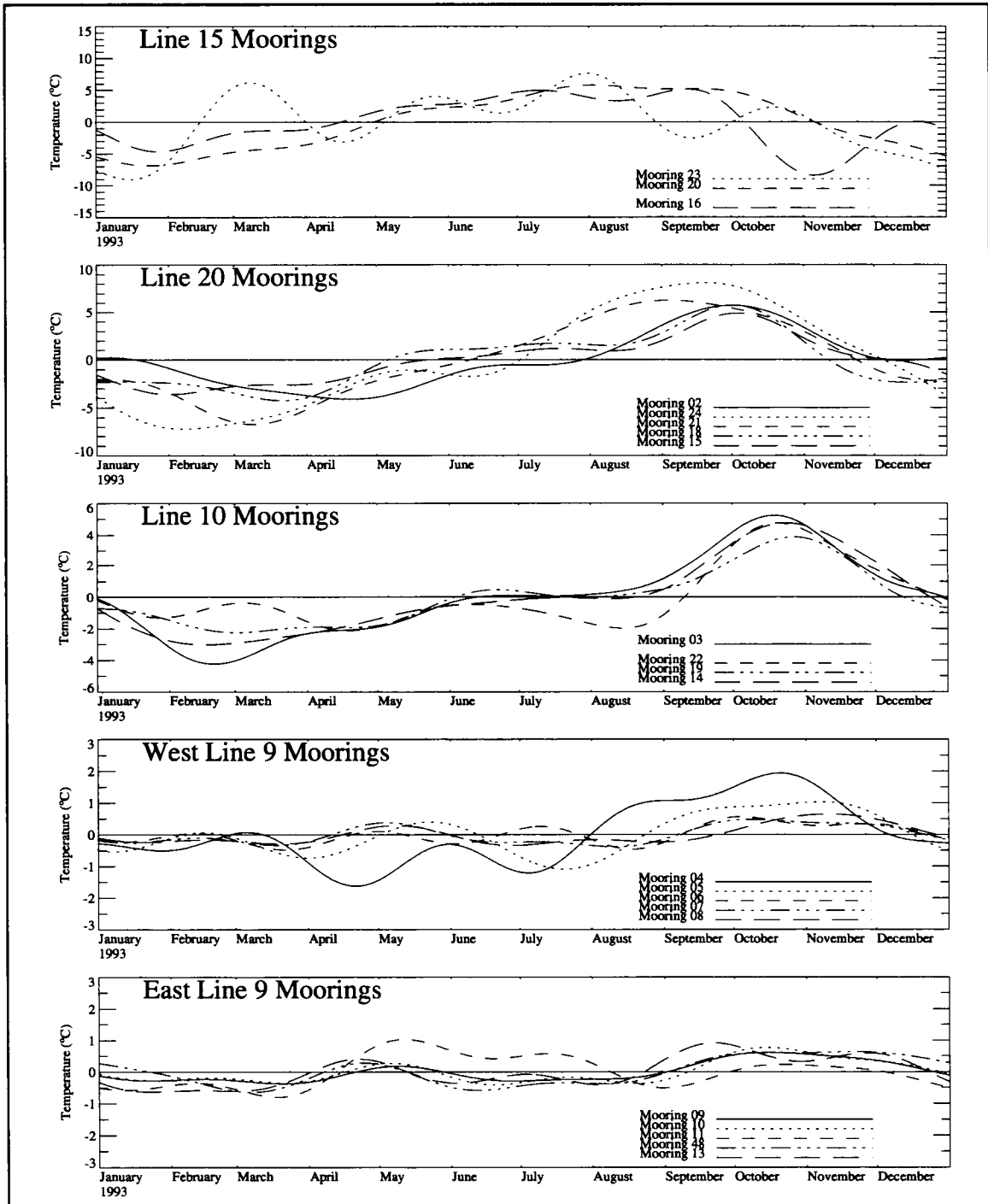


Figure 4.3.2-29. Annual signal of bottom temperature (°C) in groupings of alongshelf lines (scales are variable).

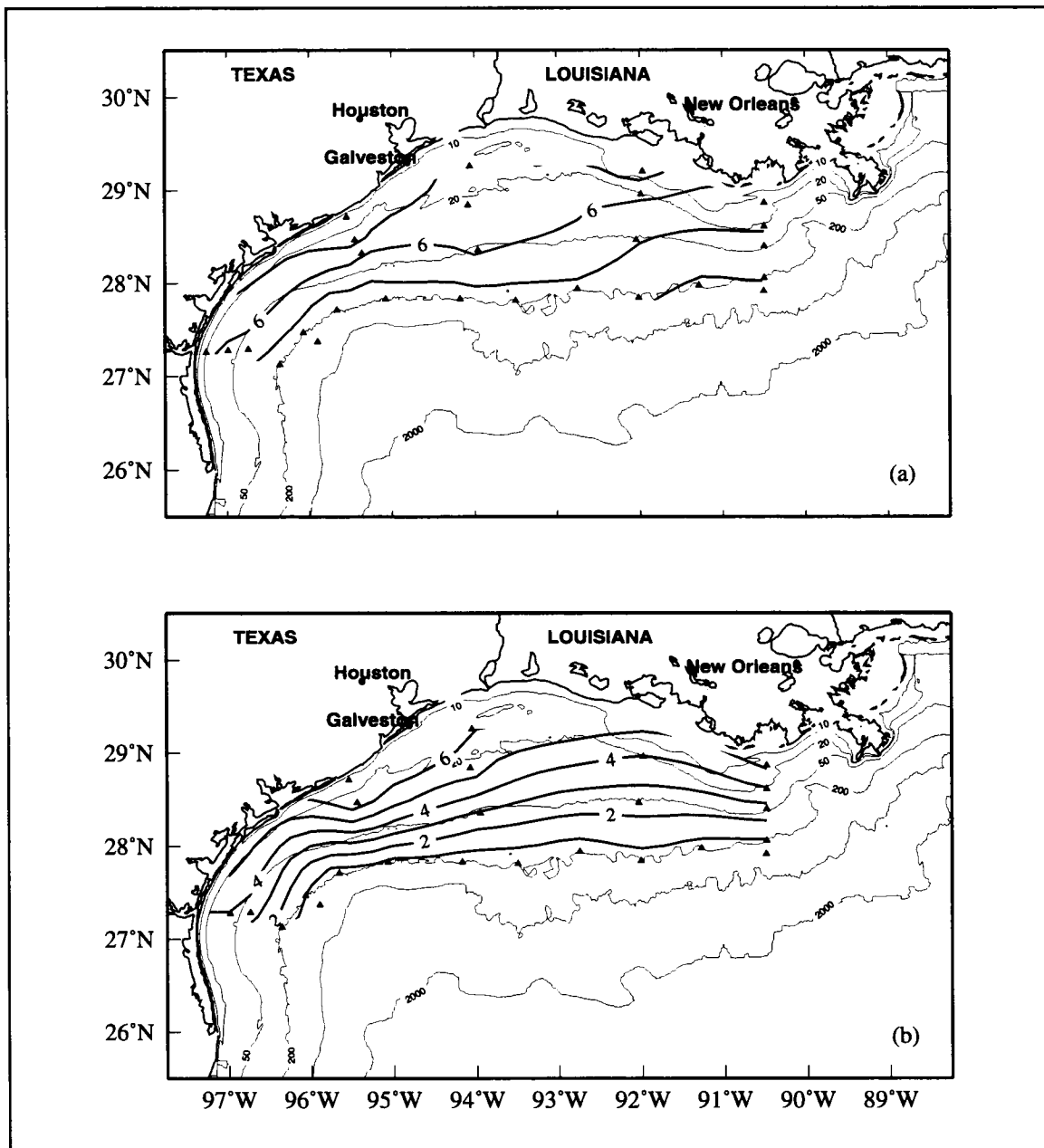


Figure 4.3.2-30. Amplitude of the annual signal of temperature ($^{\circ}\text{C}$) from (a) 10-m and (b) bottom measurements.

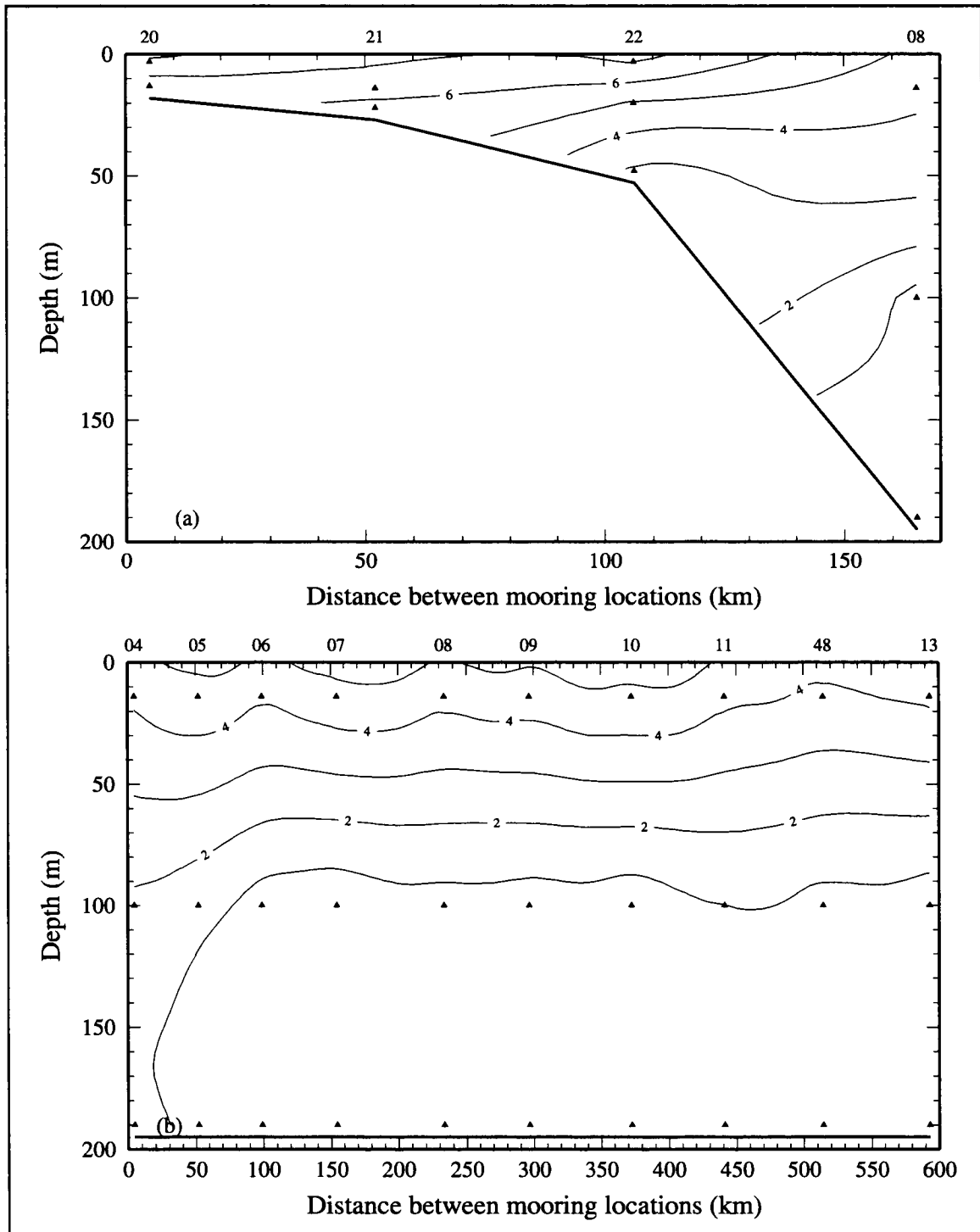


Figure 4.3.2-31. Amplitude of the annual signal of temperature ($^{\circ}\text{C}$) from moorings on (a) line 4 and (b) line 9. Triangles show instrument locations.

Residual signal of temperature

The residual temperatures were computed by removing the record-length mean, the annual signal, and a linear trend from the 40-hour low-pass time series. The standard deviations for each residual time series were computed and mapped (Figure 4.3.2-32). The standard deviations of the 10-m residual temperature are smallest at the shelf edge and increase inshore. The largest variability is off Atchafalaya Bay. Variability there is also large in the bottom residual temperatures. The standard deviations of bottom residual temperature also decrease shoreward (Figure 4.3.2-32b). Over the inner western shelf, there is more variability in the bottom residual than in the 10-m temperature.

The zero crossings for the autocorrelation functions of residual temperature were computed. Time scales for the 10-m residual temperature are typically 20 to 60 days across the whole shelf. This is greater than the weather band scale of 2 to 10 days, suggesting that 10-m temperature does not respond to forcing at weather band frequencies. The range of typical scales at the bottom also is 20 to 60 days. The longest time scales for temperature, both at 10 m and the bottom, are located at the western shelf edge, with 10-m scales exceeding 70 days. These longer scales indicate Loop Current eddies at work on western shelf edge.

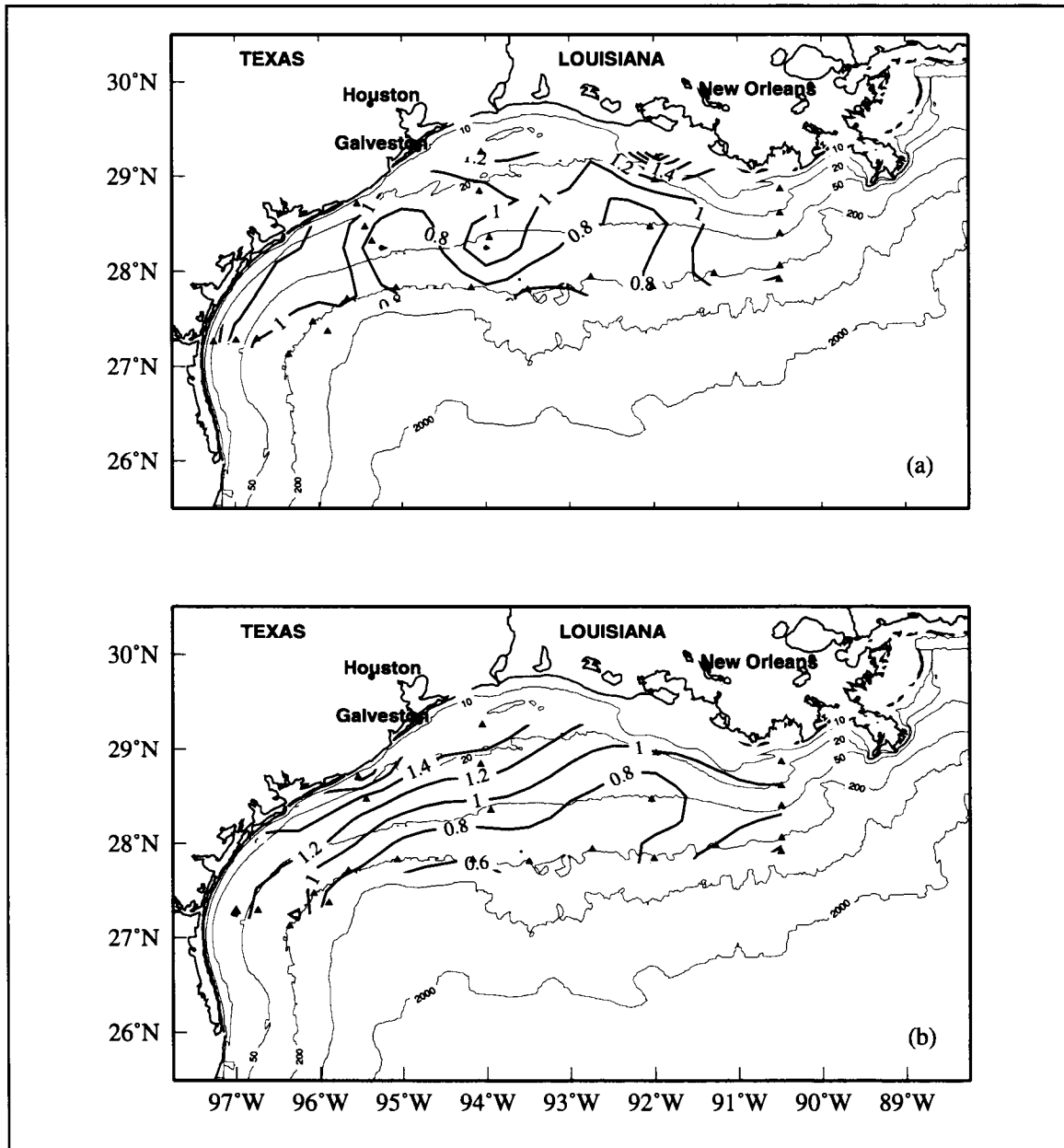


Figure 4.3.2-32. Standard deviation of residual temperature ($^{\circ}\text{C}$) from (a) 10-m and (b) bottom measurements. Triangles show mooring locations.

4.4 Shelf-scale currents observed during LATEX

We examined the current fields over the Texas-Louisiana shelf during the 32-month LATEX field period, April 1992—November 1994. In Section 4.4.1 we show monthly mean velocity streamfunctions during that period constructed from the direct observations. Together with monthly mean transport streamfunctions, these were computed by Cho (1996) and have been reported by Cho et al. (1998). Additional realizations of the current fields as observed during LATEX are found in Appendix H: fields of geopotential anomaly for twelve periods of hydrographic surveys, and monthly mean currents obtained by objectively gridding the current meter observations.

In Section 4.4.2, the patterns of monthly velocity streamfunctions are examined using EOFs. The amplitude variation of energetic modes is compared with wind stress variation.

The vertical structure of measured currents is briefly described in Section 4.4.3. Although there were only two or three current meters on each LATEX A mooring, and thus the vertical resolution of horizontal velocity is not good, the agreement between vertical shear measured by the moored arrays and that measured by shipboard ADCP seems remarkably good (Appendix J.2).

4.4.1 Monthly mean streamfunctions from direct observations

Using the monthly means of the LATEX A 40-hr low-pass current data at 6-hr intervals from the 10-m instruments, streamfunction fields were computed by Cho (1996). He used two methods that showed good agreement; here we describe the method he preferred. Then we discuss the velocity streamfunctions constructed using the overall 32-month mean, monthly means, and the summer and nonsummer means of the observed currents.

Cho's preferred method is a least-square regression analysis to find the coefficients of a streamfunction expansion expressed in terms of a series of trigonometric basis functions (Vastano and Reid 1985). This method has been applied to generate optimal mesoscale flow fields in the Oyashio Frontal Zone (Vastano and Reid 1985) and in the California Current off Point Sur (Njoku et al. 1985). A root mean square (rms) error of the fit can be computed by this method. The streamfunction is taken as,

$$\psi(\xi, \eta) = \sum_n \sum_m (A_{n,m} \cos m\alpha\xi + B_{n,m} \sin m\alpha\xi) \sin n\beta\eta, \quad (4.4.1-1)$$

where $\alpha = \pi/L_\xi$, $\beta = \pi/2L_\eta$, ξ and η represent the alongshelf and cross-shelf axes, L_ξ and L_η represent alongshelf and cross-shelf ranges of the domain, and $A_{n,m}$ and $B_{n,m}$ are coefficients to be determined. The streamfunction, ψ , is zero at the coastal boundary

($\eta = 0$) by the last sine term of this equation, thus enforcing the condition of no flow across the coastal boundary. The coefficients $A_{n,m}$ and $B_{n,m}$ are obtained by minimizing the following error measure:

$$\sigma^2 = \frac{1}{j_{\max}} \sum_j [(\tilde{u} - u_j)^2 + (\tilde{v} - v_j)^2], \quad (4.4.1-2)$$

where

$$\tilde{u} = -\frac{\partial \psi}{\partial \eta} = -\sum_n \sum_m (A_{n,m} \cos m\alpha\xi + B_{n,m} \sin m\alpha\xi) n\beta \cos n\beta\eta \quad (4.4.1-3)$$

and

$$\tilde{v} = \frac{\partial \psi}{\partial \xi} = \sum_n \sum_m (-A_{n,m} \sin m\alpha\xi + B_{n,m} \cos m\alpha\xi) m\alpha \sin n\beta\eta. \quad (4.4.1-4)$$

This formulation assumes nondivergent flow which is visually inconsistent with fields of measured 10-m currents. However, the monthly average fields should be largely nondivergent. A complementary, divergent flow pattern could be extracted from the data in the same manner to quantify convergence.

An orthogonal, boundary-fitted, curvilinear coordinate is employed for the streamfunction generation. The low-frequency circulation and transport in a coastal region is expected to be strongly constrained by the bathymetry (Csanady 1982). This specification of a coordinate system has the advantages that the no-flow condition along the coastal boundary is easily specified and the offshore (seaward) boundary can be aligned along an isobath. For generating the boundary-fitted grid for the LATEX shelf, the methodology developed by Mellor (1993) was used. The two-dimensional transformation between rectangular (x, y) and orthogonal coordinates (ξ, η) is accomplished by using the orthogonality conditions. Figure 4.4.1-1 shows the grid generated by this method. The inshore and offshore boundaries were fitted to smoothed representations of the coast and the 1000-m isobath. The observed velocity is transformed into the orthogonal system and then the streamfunction of equation (4.4.1-1) is obtained by the minimizing equation (4.4.1-2). A linear set of equations for the coefficients is solved using standard lower/upper triangular (LU) decomposition techniques. The rms error of the fitting is computed using equation (4.4.1-2).

Streamfunctions were generated using different combinations of harmonics in the alongshelf (m) and cross-shelf (n) directions. Increasing the number of harmonics reduced the rms error of fitting. However, increasing the number of harmonics resulted in noisy patterns of

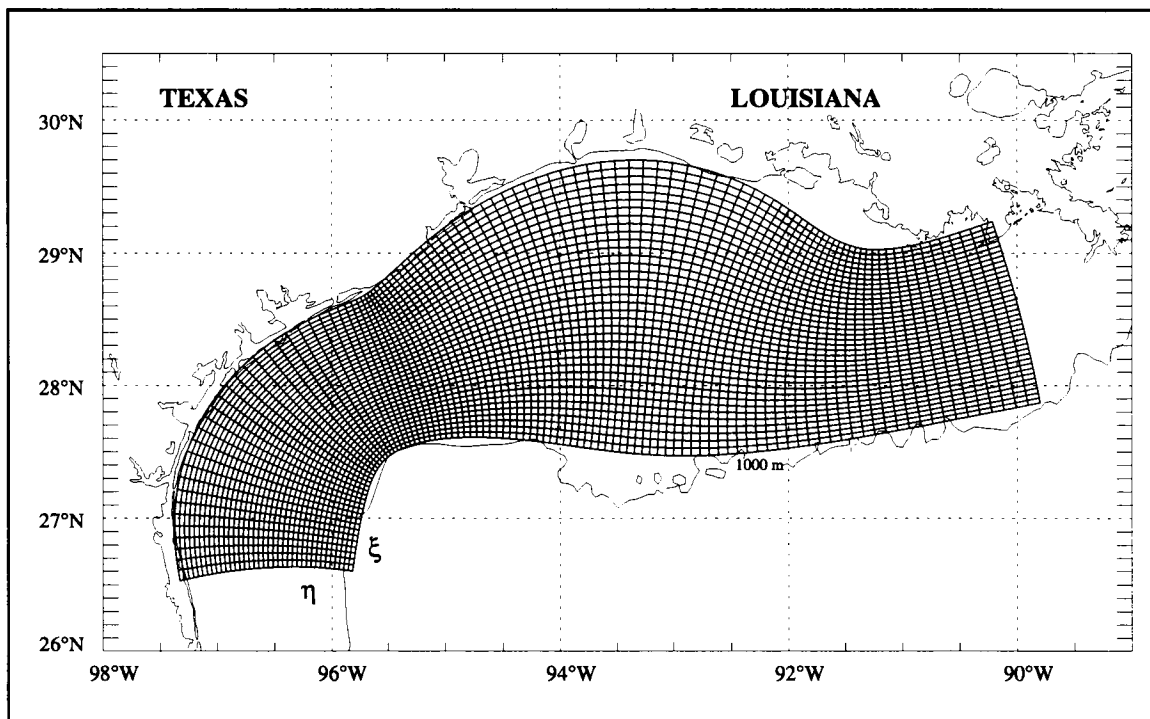


Figure 4.4.1-1. The orthogonal, boundary-fitted curvilinear coordinate system used for calculating streamfunction.

streamfunction, i.e., patterns inconsistent with the resolution of the data. A reasonably smooth streamfunction pattern demands the use of lower harmonics at the expense of higher rms error. The number of degrees of freedom of the observation field was at most 31. For the $m = 7$ and $n = 4$ case, the system was close to being undetermined and the noisiness of the streamfunction field was to be expected. In many cases of the monthly mean observation fields, the degrees of freedom of the field were decreased by the lack of current meter data. Although the number of harmonics that produces a reasonably smooth streamfunction pattern is not the same for different monthly mean velocity fields, for simplicity, $m = 3$ and $n = 2$ were used throughout this study.

The velocity streamfunction generated from the 32-month recordlength mean currents is shown in the top panel of Figure 4.4.1-2. The root mean square (rms) residual error is $2.37 \text{ cm}\cdot\text{s}^{-1}$ for the streamfunction field. This can be compared with the rms speed of $6.32 \text{ cm}\cdot\text{s}^{-1}$ for the observation field. The ratio of the two rms values is 0.38, or 0.14 in relative error variance. The rms error accounts for discrepancies in both speed and direction. The relatively small residual value indicates that the field is represented adequately. The residual rms error is possibly due to a horizontally divergent component in the observed

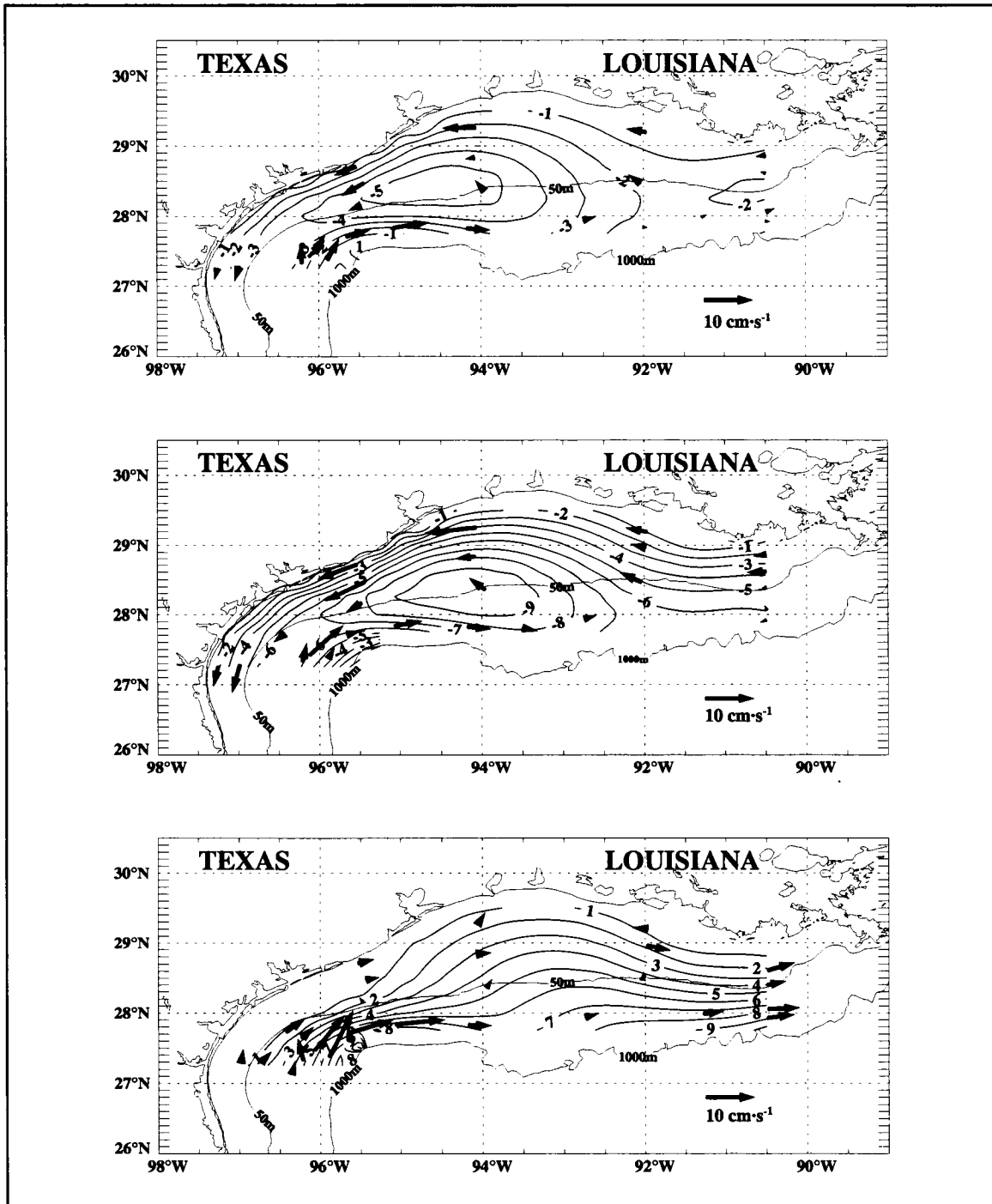


Figure 4.4.1-2. Shelfwide 10-m velocity streamfunction fields from recordlength means (upper panel), nonsummer means (middle panel), and summer means (lower panel). Unit of streamfunction is $10^7 \text{ cm}^2 \cdot \text{s}^{-1}$.

flow. The rms errors of fit and the corresponding rms speeds for each monthly streamfunction representation are shown in Table 4.4.1-1. The values of rms error generally depend on the rms speeds. For more details, refer to Cho (1996) or Cho et al. (1998).

The streamfunction fields for January 1993 and 1994 (Figure 4.4.1-3) showed strong downcoast flows over the inner shelf. Over the southwestern shelf edge, strong flow related to Eddy Vazquez (Eddy V) was directed upcoast in 1993 (Appendix D). The pattern for 1994 showed more closure over the outer shelf than for 1993, and the strongest upcoast currents at the shelf edge were from 93° to 95°W.

The streamfunctions for February (Figure 4.4.1-4) were similar to those for January, especially over the inner shelf. The amplitude of downcoast flow over the inner shelf in 1993 was weaker than in 1994. Apparently, Eddy V had moved eastward since January based on the location of maximum shelf-edge currents. March patterns (Figure 4.4.1-5) also showed downcoast nearshore flow, but somewhat decreased relative to February, especially in 1993. There was indication of considerable cross-shelf flow over the eastern outer shelf.

The April patterns (Figure 4.4.1-6) differed from year to year, especially in strength of the downcoast flow over the inner shelf, which was very strong in 1994 relative to 1992 and 1993. This is a good illustration of the year-to-year variability of the circulation over this shelf.

May streamfunctions (Figure 4.4.1-7) still evidenced downcoast flow over the inner shelf. At the shelf edge in the west, there is eddy driven upcoast flow in 1992 and 1993. Onshelf flow across the 50-m isobath is prominent east of 94°W.

Table 4.4.1-1. The root mean square (rms) speed of monthly current and rms error of the velocity streamfunction fit.

	1992		1993		1994	
	rms speed	rms error	rms speed	rms error	rms speed	rms error
January			19.78	9.52	14.70	7.03
February			13.35	5.92	12.73	8.17
March			8.66	4.06	9.18	7.68
April	9.11	6.69	8.23	4.45	12.07	5.48
May	10.59	4.49	11.99	6.39	9.64	5.67
June	13.04	6.77	12.34	6.60	10.14	5.32
July	17.89	12.87	15.10	8.03	11.87	7.99
August	13.51	8.35	18.55	8.26	6.23	4.64
September	8.98	5.25	11.23	3.94	10.16	6.27
October	12.27	4.65	12.53	4.24	14.46	6.18
November	10.59	3.94	16.43	4.62	13.89	5.51
December	14.84	5.98	12.15	6.64		

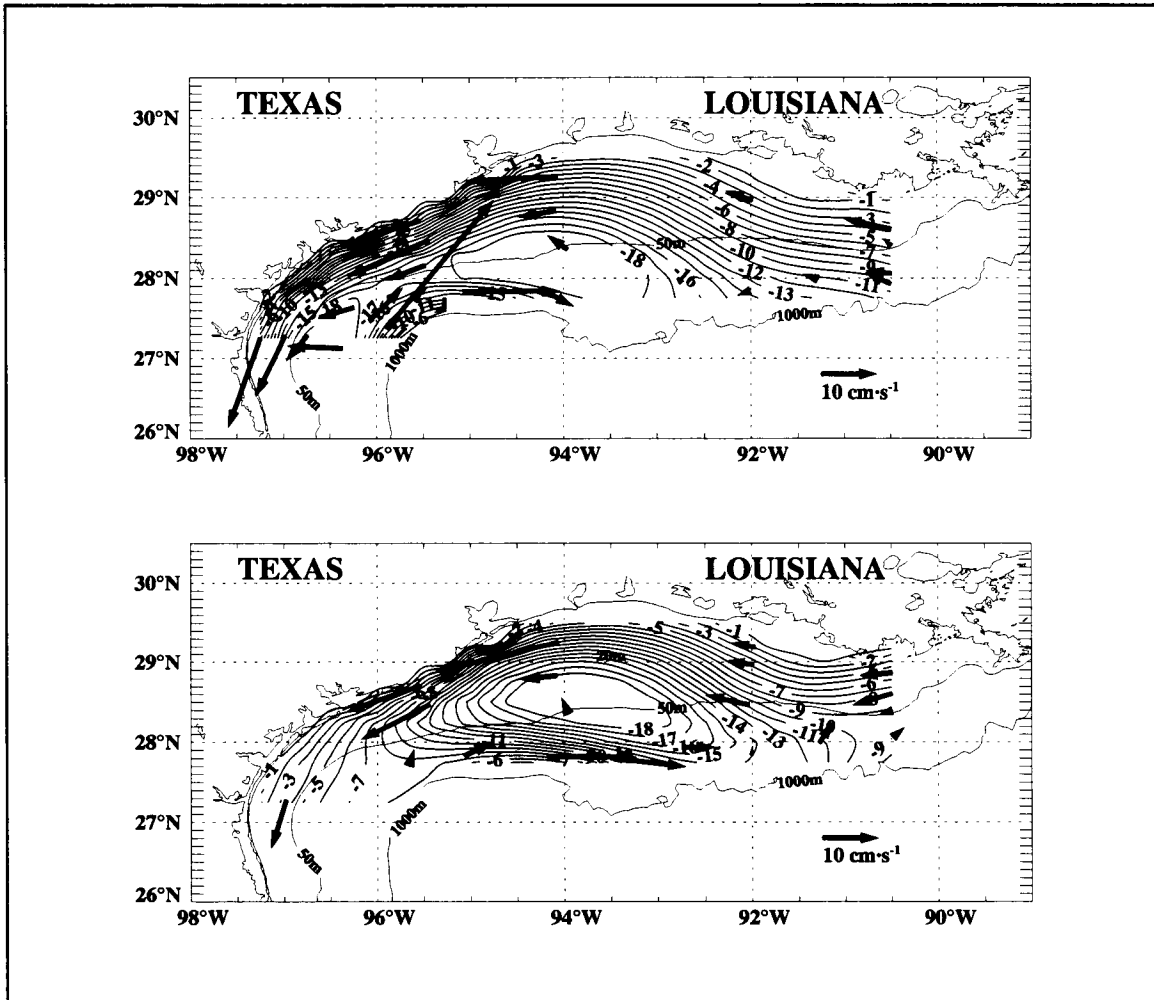


Figure 4.4.1-3. Shelfwide monthly mean 10-m velocity streamfunction field for January of 1993 (upper panel) and 1994 (lower panel). Arrows represent monthly mean 10-m current vectors. The unit of streamfunction is $10^7 \text{ cm}^2 \cdot \text{s}^{-1}$.

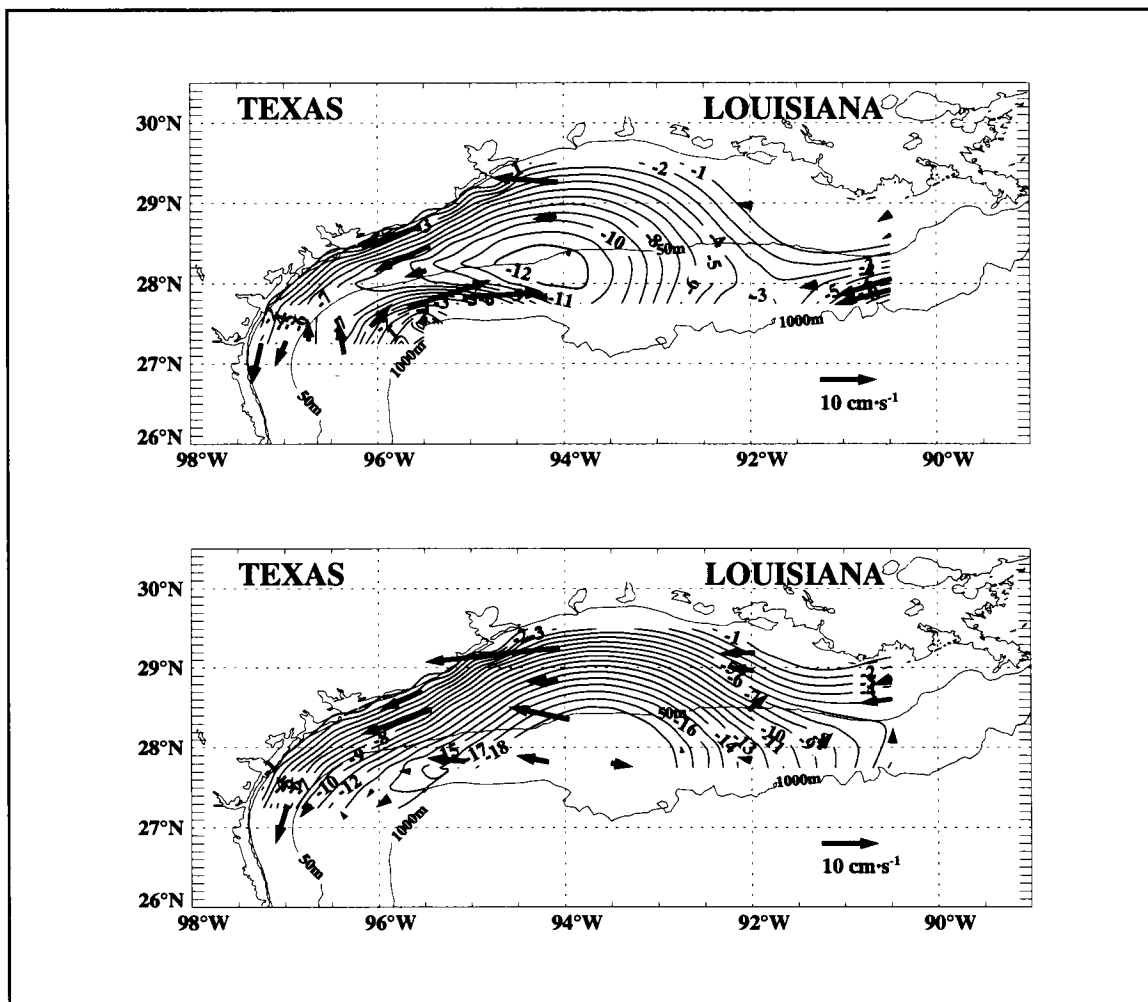


Figure 4.4.1-4. Shelfwide monthly mean 10-m velocity streamfunction field for February of 1993 (upper panel) and 1994 (lower panel). Arrows represent monthly mean 10-m current vectors. The unit of streamfunction is $10^7 \text{ cm}^2 \cdot \text{s}^{-1}$.

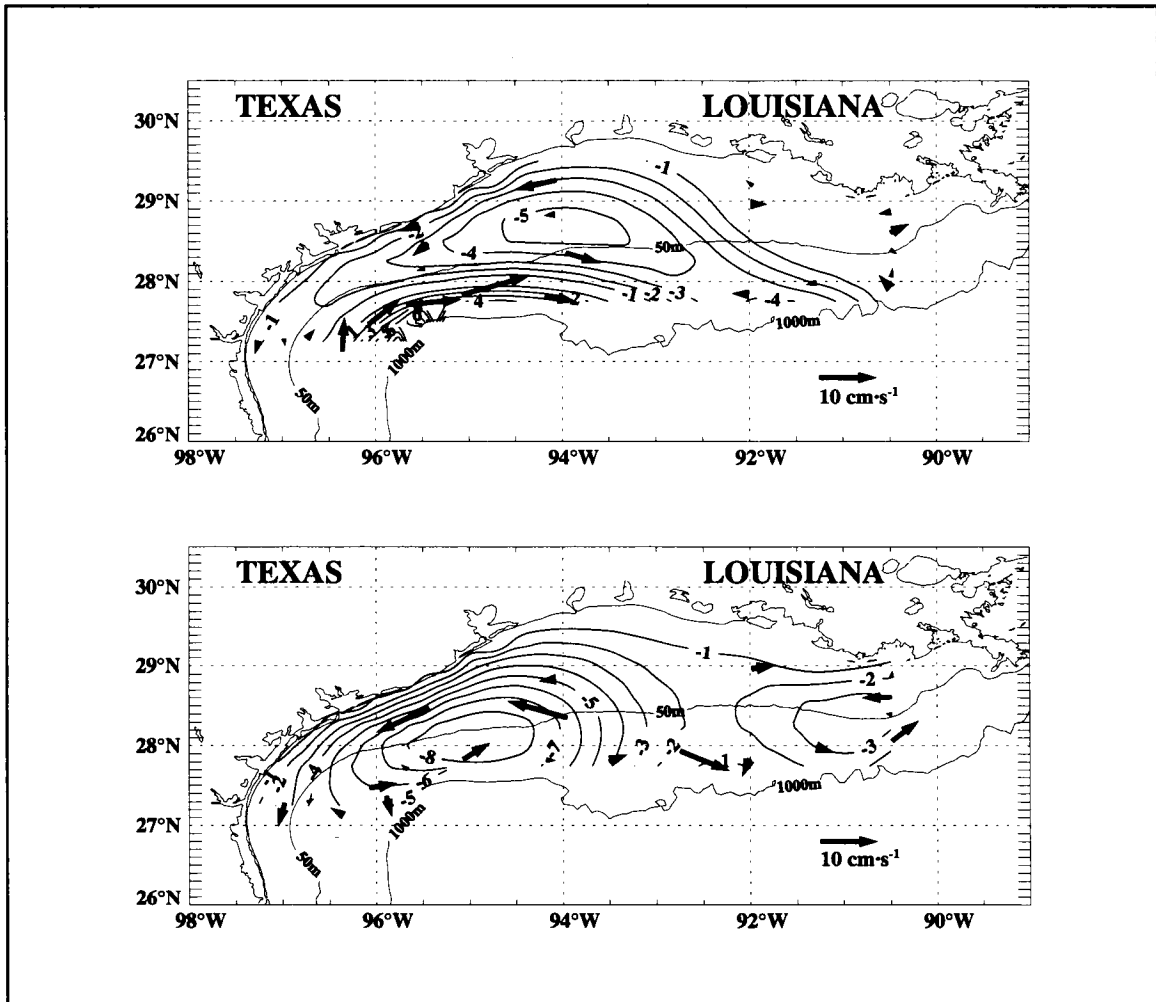


Figure 4.4.1-5. Shelfwide monthly mean 10-m velocity streamfunction field for March of 1993 (upper panel) and 1994 (lower panel). Arrows represent monthly mean 10-m current vectors. The unit of streamfunction is $10^7 \text{ cm}^2 \cdot \text{s}^{-1}$.

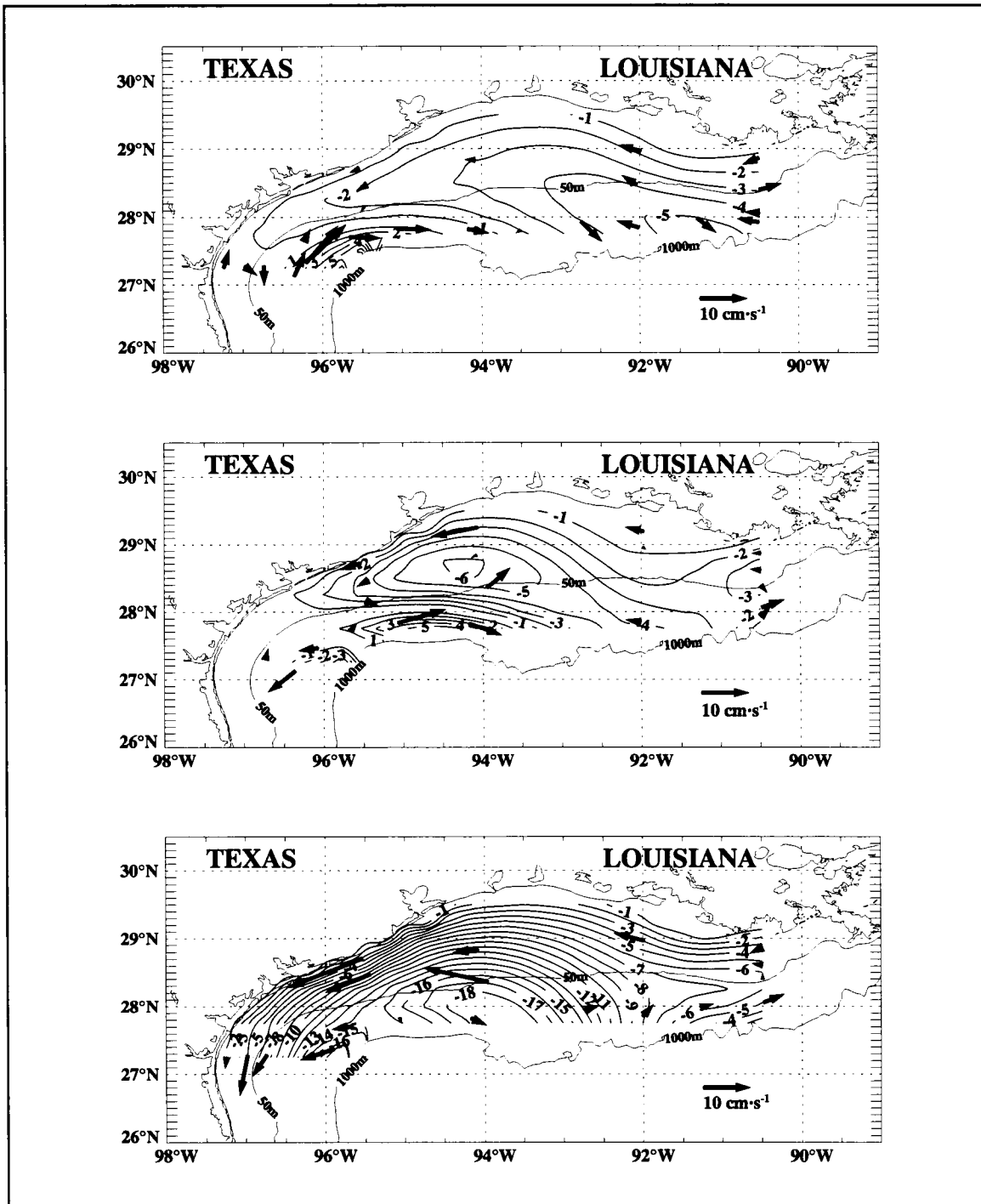


Figure 4.4.1-6. Shelfwide monthly mean 10-m velocity streamfunction field for April of 1992 (upper panel), 1993 (middle panel), and 1994 (lower panel). Arrows represent monthly mean 10-m current vectors. The unit of streamfunction is $10^7 \text{ cm}^2 \cdot \text{s}^{-1}$.

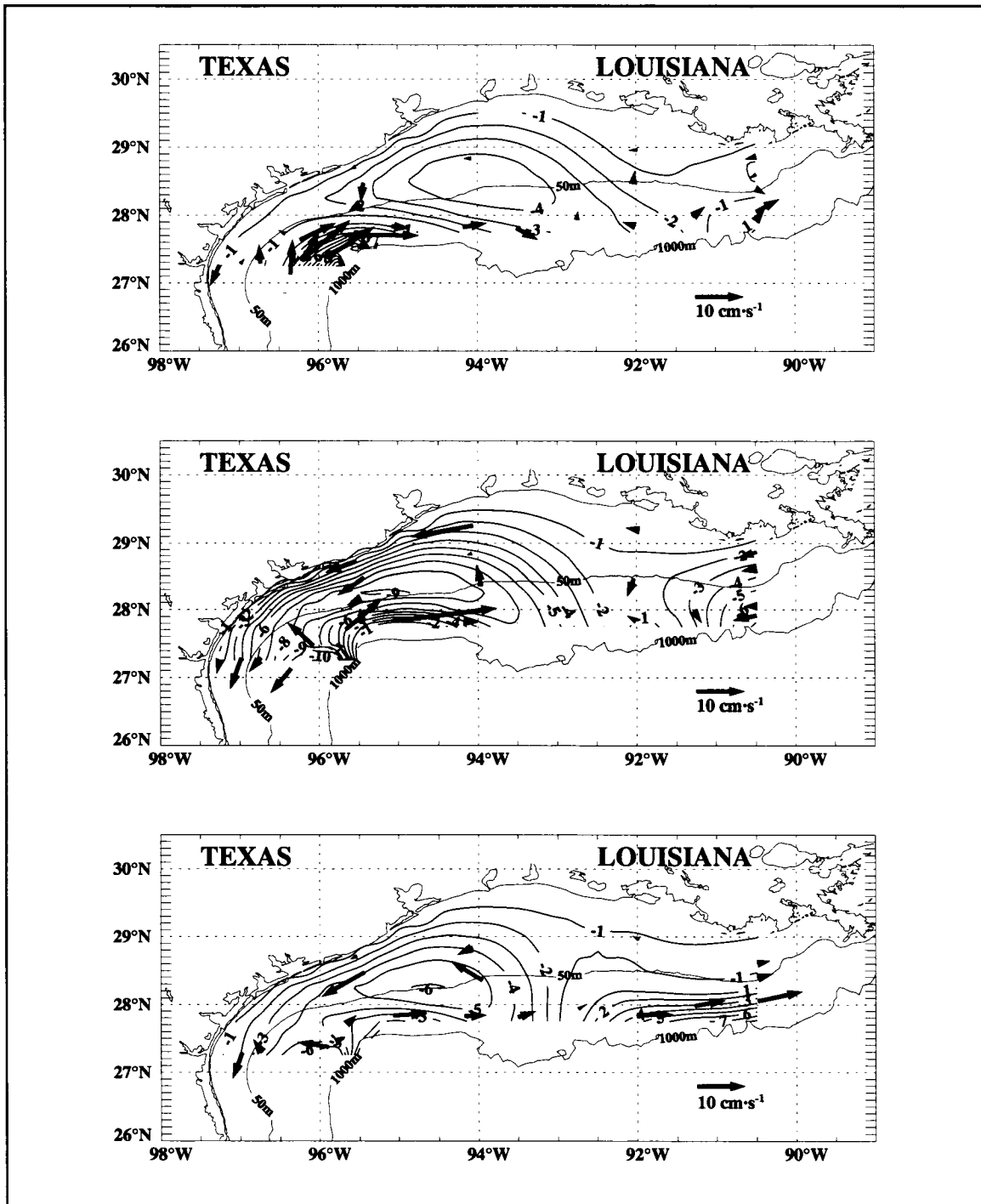


Figure 4.4.1-7. Shelfwide monthly mean 10-m velocity streamfunction field for May of 1992 (upper panel), 1993 (middle panel), and 1994 (lower panel). Arrows represent monthly mean 10-m current vectors. The unit of streamfunction is $10^7 \text{ cm}^2 \cdot \text{s}^{-1}$.

The June patterns for 1992 and 1994 (Figure 4.4.1-8) showed strong upcoast flow over both inner and outer shelf. The transition from the nonsummer to summer pattern of alongshelf wind component, and of resulting alongshelf currents, had been completed in time to affect the June average during these two years. In June 1993, the currents over the inner shelf were very weak but, in the average, had not turned upcoast. In July, upcoast flow was the dominant feature in all three years (Figure 4.4.1-9). In 1992, however, there was an anticyclonic cell over the southwestern shelf, which could be due to the method of the streamfunction generation. In 1994, some downcoast flow existed over the eastern inner shelf.

The return to a pattern of downcoast flow over the inner shelf usually occurs near the end of August because of the transition to a downcoast alongshelf wind component. We see in Figure 4.4.1-10 large differences between the three August mean fields. In 1993 there was a typical summer pattern of upcoast flow. The pattern for 1994 appeared more like a nonsummer situation. The 1992 pattern was intermediate between the other two; downcoast flow was found over the inner western shelf. There was onshore, cross-shelf flow between 93° and 96° W.

By September, the transition to downcoast flow over the inner shelf was complete in 1992 and 1994 (Figure 4.4.1-11). In 1993, an anticyclonic cell appeared over the western inner shelf. This is considered to be caused by an instability of the method used to generate the streamfunction—the number of observations was too small in spite of using only small numbers of harmonics. The other method used to generate streamfunctions did not show this anticyclonic cell for this month, and the inner shelf currents were downcoast as expected after the transition to nonsummer regime.

The October streamfunction patterns (Figure 4.4.1-12) evidenced quite strong downcoast currents over the inner shelf in all three years, but specially in 1994. In 1992, there was a closed cyclonic gyre over the mid-shelf between 92° and 95° W, with downcoast currents at the shelf edge. Again in November downcoast flow prevailed over the inner shelf in all three years (Figure 4.4.1-13). Strong cross-shelf currents over the outer shelf between 92° and 96° W are portrayed in 1994. In 1993, there was an unusual wave pattern to the streamlines. This did not appear in the alternative method of obtaining streamfunctions, and so is judged to be an artifact of the method. The December velocity streamfunctions (Figure 4.4.1-14) also showed downcoast flow over the inner shelf in 1992 and 1993. In 1992, a closed cyclonic cell appeared over the central part of the shelf. In 1993, the shelf break current was variable.

In conclusion, based on the monthly velocity streamfunctions for the shelfwide low-frequency circulation, there is a distinct difference between the nonsummer and summer periods. The streamfunction patterns for the nonsummer mean (September-May) and the summer mean (June-August), based on all current data (from April 1992 through November 1994), are

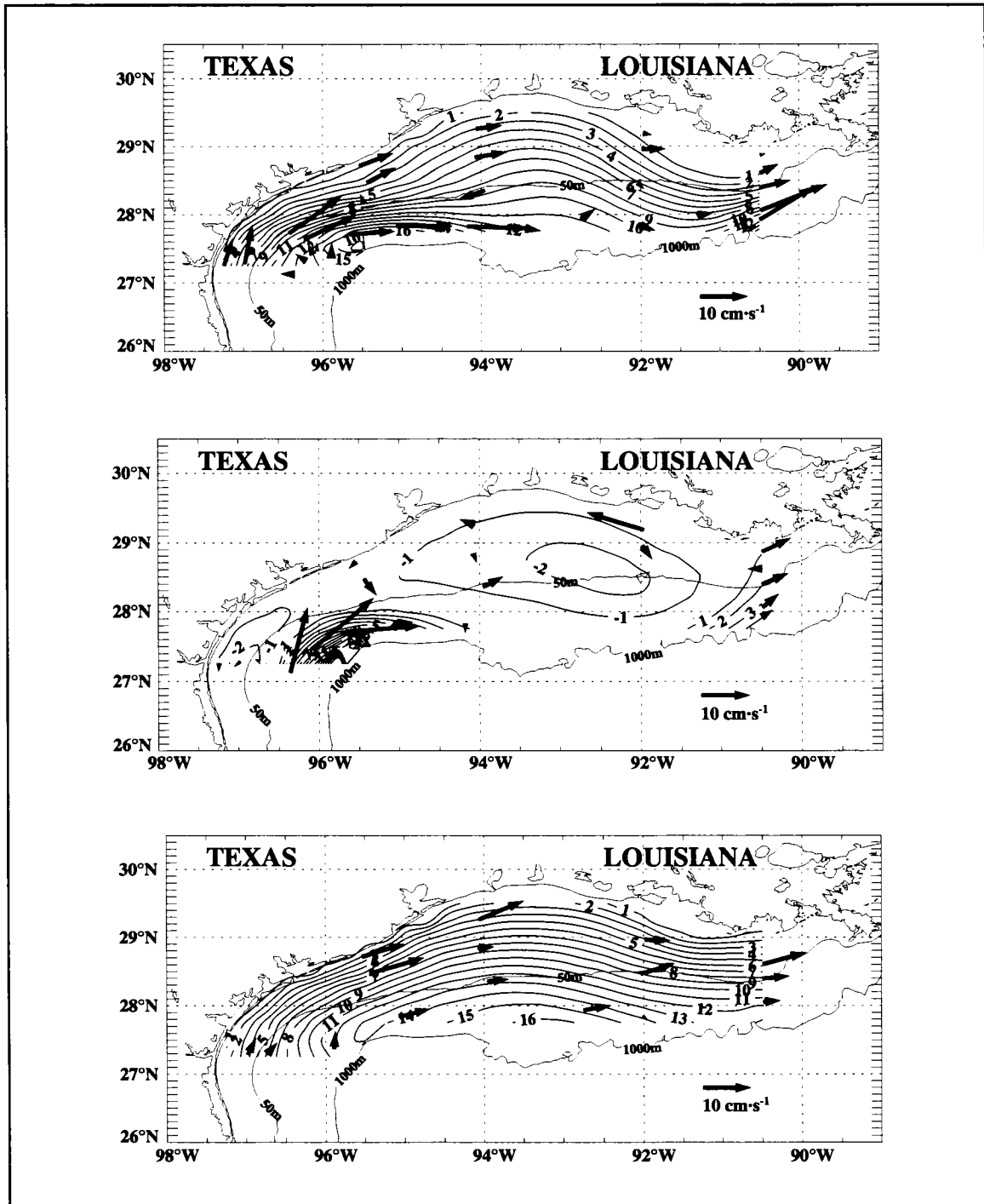


Figure 4.4.1-8. Shelfwide monthly mean 10-m velocity streamfunction field for June of 1992 (upper panel), 1993 (middle panel), and 1994 (lower panel). Arrows represent monthly mean 10-m current vectors. The unit of streamfunction is $10^7 \text{ cm}^2 \cdot \text{s}^{-1}$.

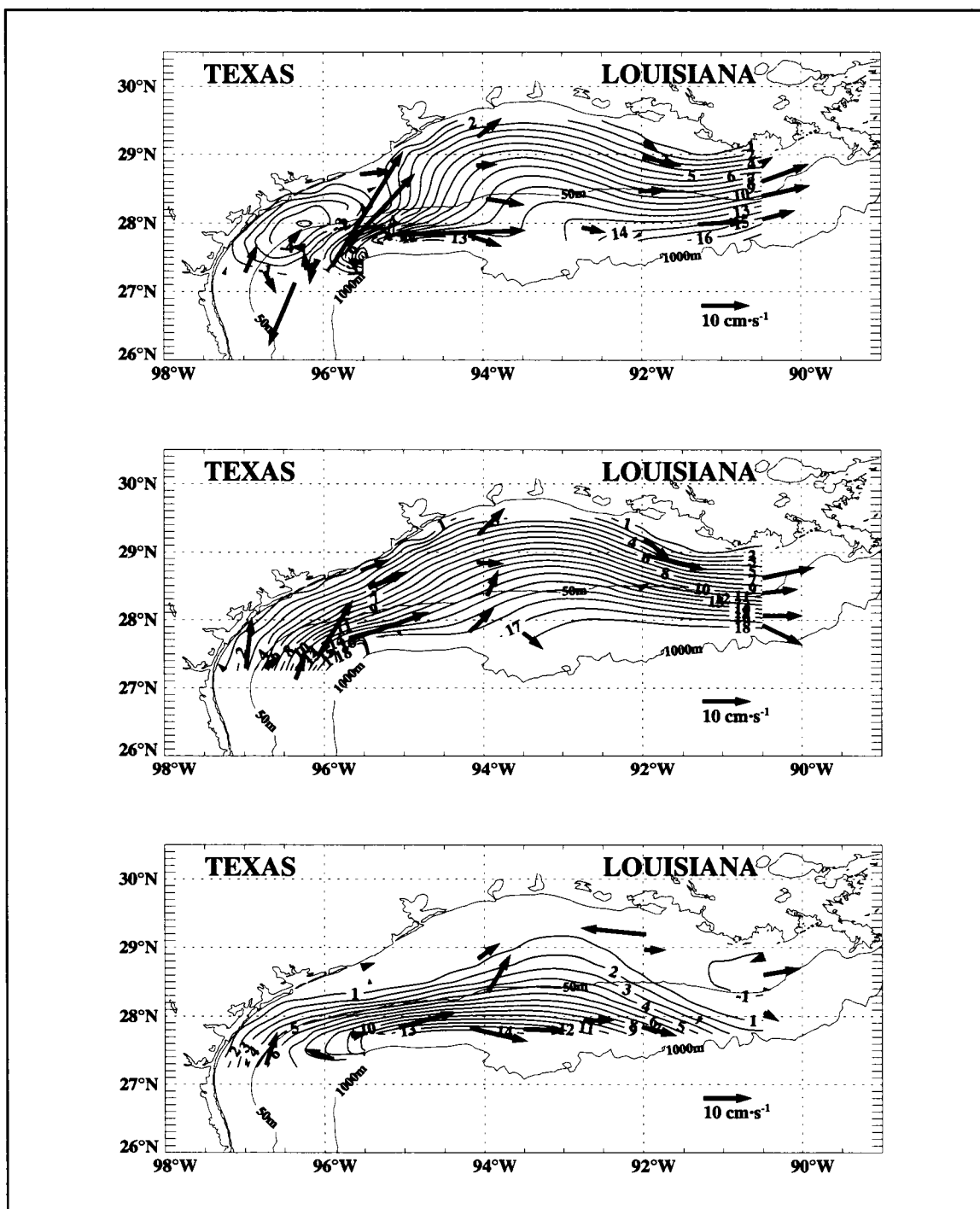


Figure 4.4.1-9. Shelfwide monthly mean 10-m velocity streamfunction field for July of 1992 (upper panel), 1993 (middle panel), and 1994 (lower panel). Arrows represent monthly mean 10-m current vectors. The unit of streamfunction is $10^7 \text{ cm}^2 \cdot \text{s}^{-1}$.

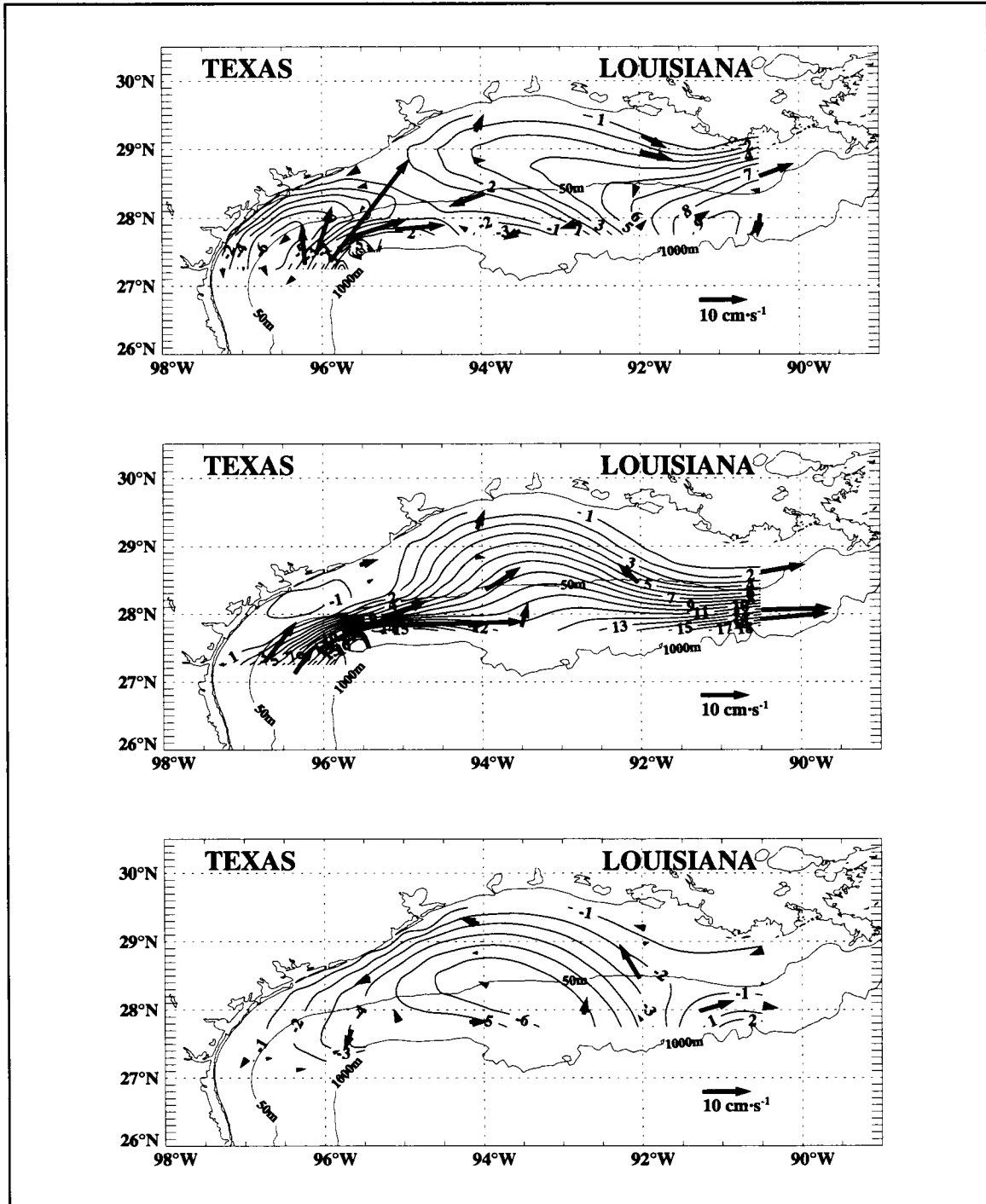


Figure 4.4.1-10. Shelfwide monthly mean 10-m velocity streamfunction field for August of 1992 (upper panel), 1993 (middle panel), and 1994 (lower panel). Arrows represent monthly mean 10-m current vectors. The unit of streamfunction is $10^7 \text{ cm}^2 \cdot \text{s}^{-1}$.

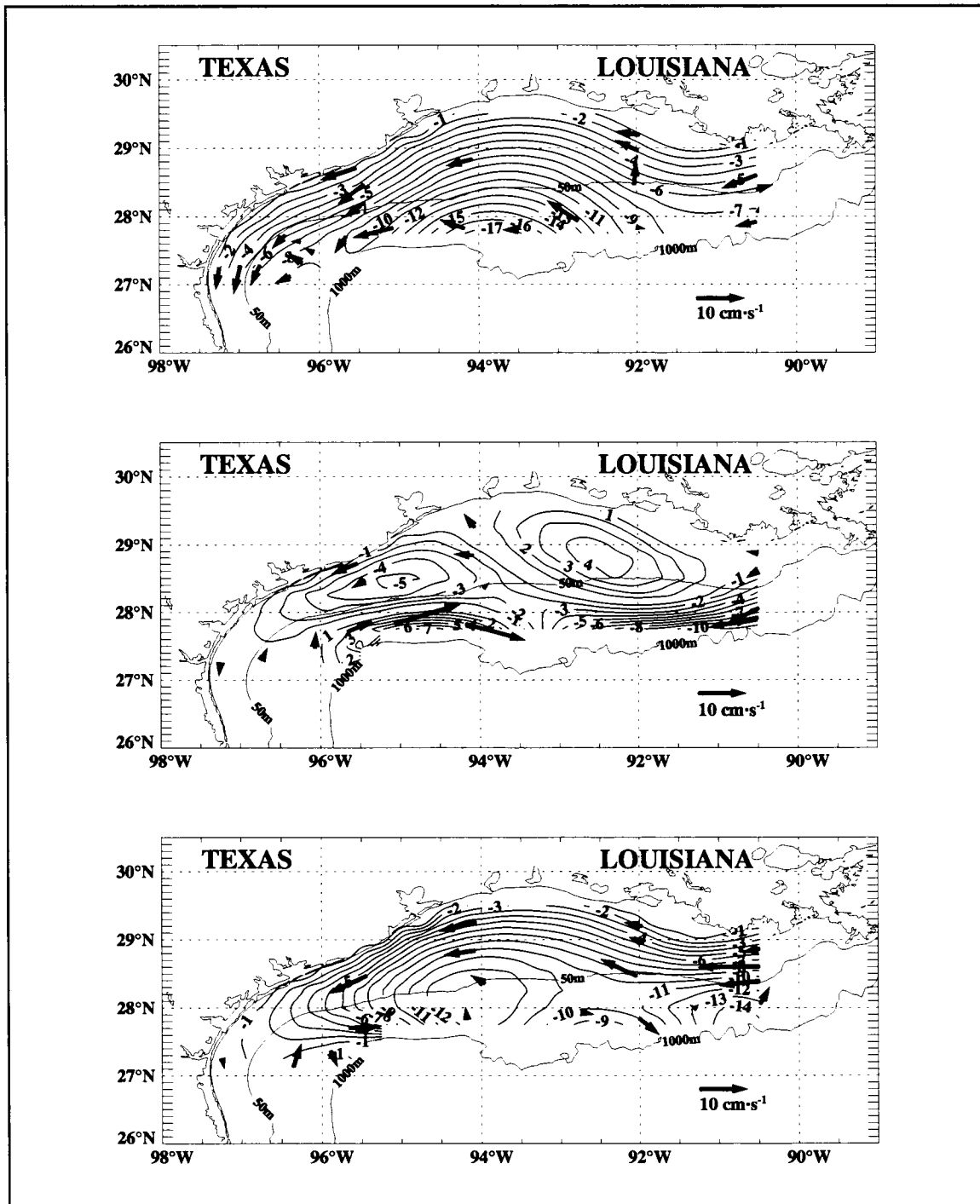


Figure 4.4.1-11. Shelfwide monthly mean 10-m velocity streamfunction field for September of 1992 (upper panel), 1993 (middle panel), and 1994 (lower panel). Arrows represent monthly mean 10-m current vectors. The unit of streamfunction is $10^7 \text{ cm}^2 \cdot \text{s}^{-1}$.

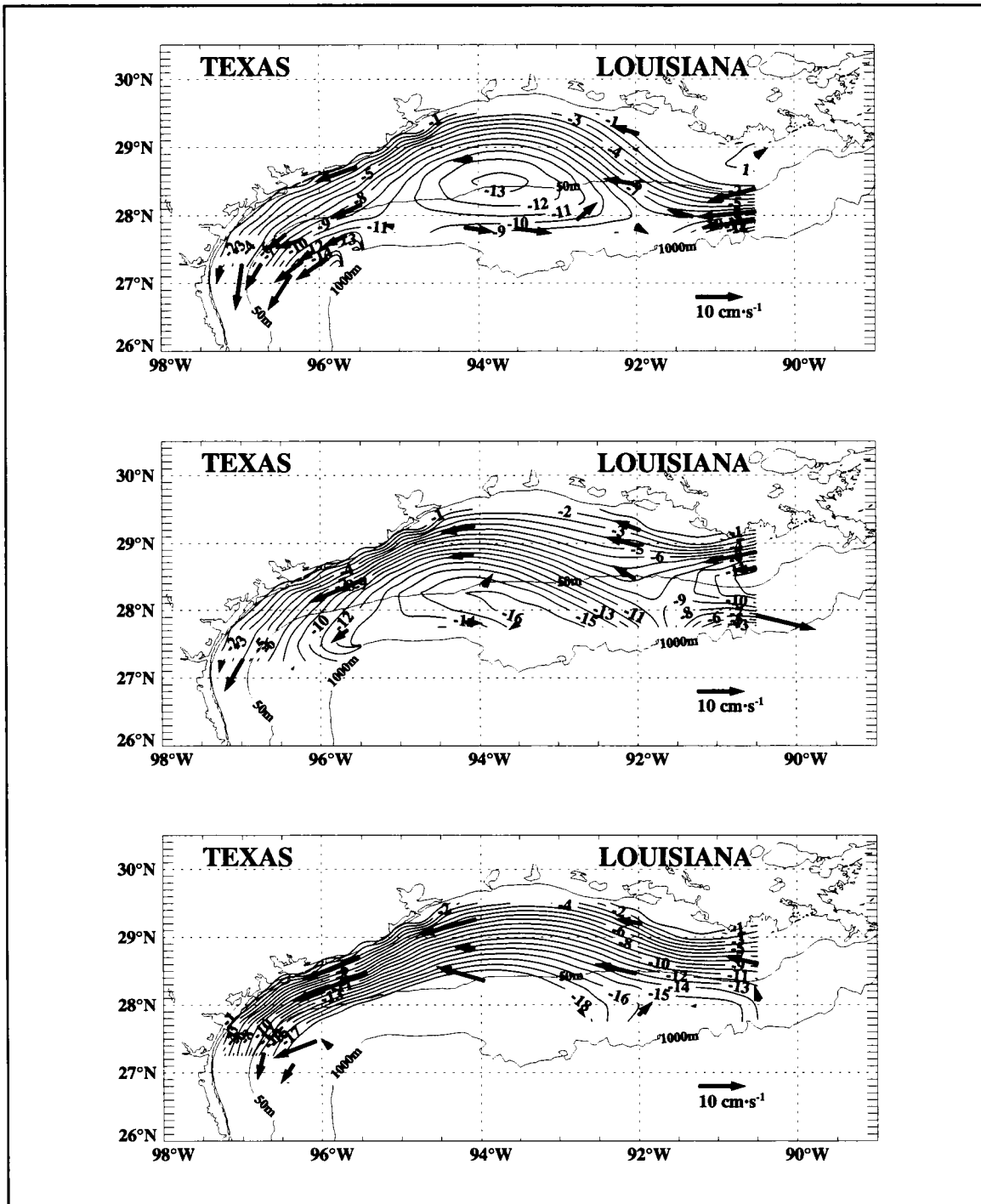


Figure 4.4.1-12. Shelfwide monthly mean 10-m velocity streamfunction field for October of 1992 (upper panel), 1993 (middle panel), and 1994 (lower panel). Arrows represent monthly mean 10-m current vectors. The unit of streamfunction is $10^7 \text{ cm}^2 \cdot \text{s}^{-1}$.

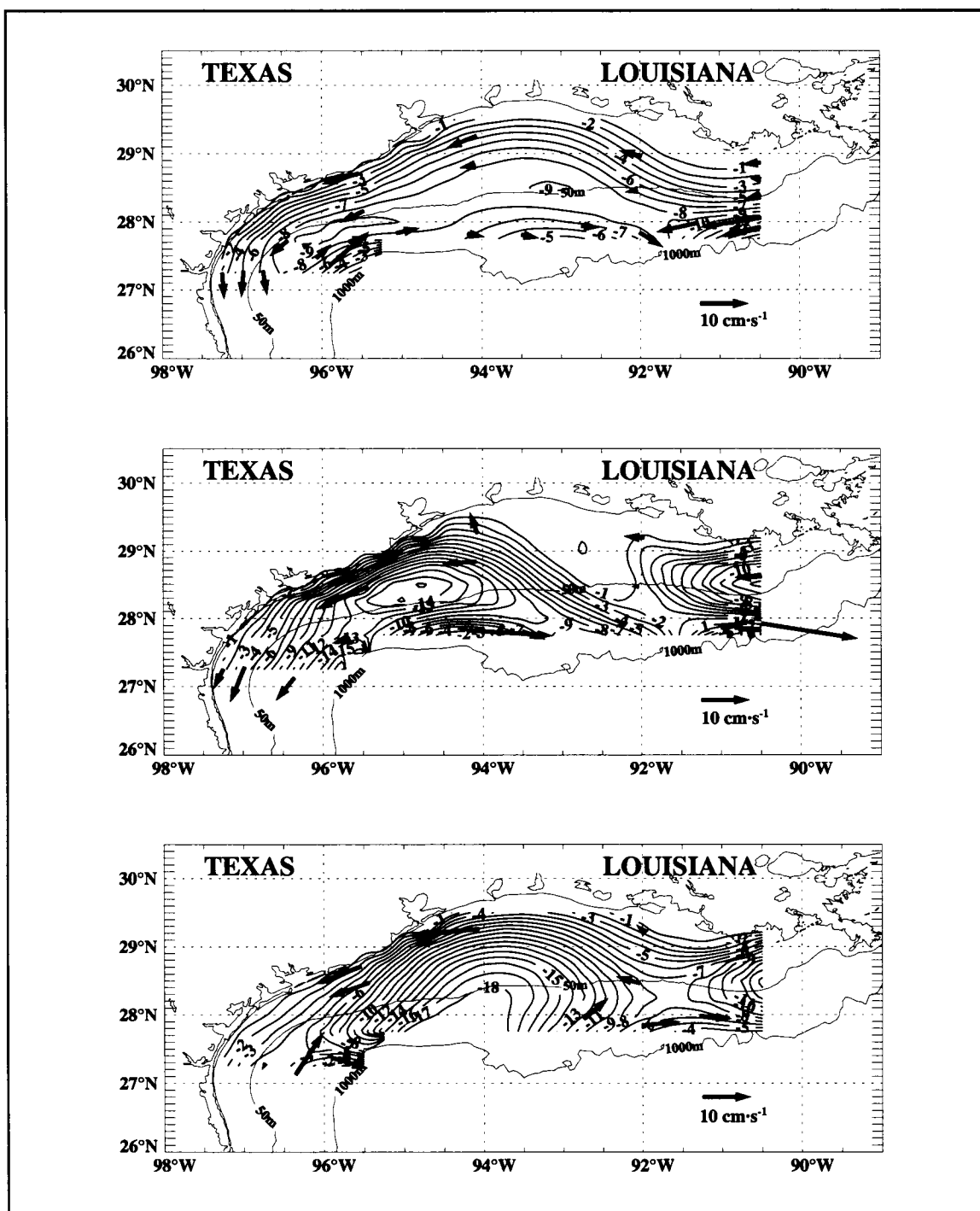


Figure 4.4.1-13. Shelfwide monthly mean 10-m velocity streamfunction field for November of 1992 (upper panel), 1993 (middle panel), and 1994 (lower panel). Arrows represent monthly mean 10-m current vectors. The unit of streamfunction is $10^7 \text{ cm}^2 \cdot \text{s}^{-1}$.

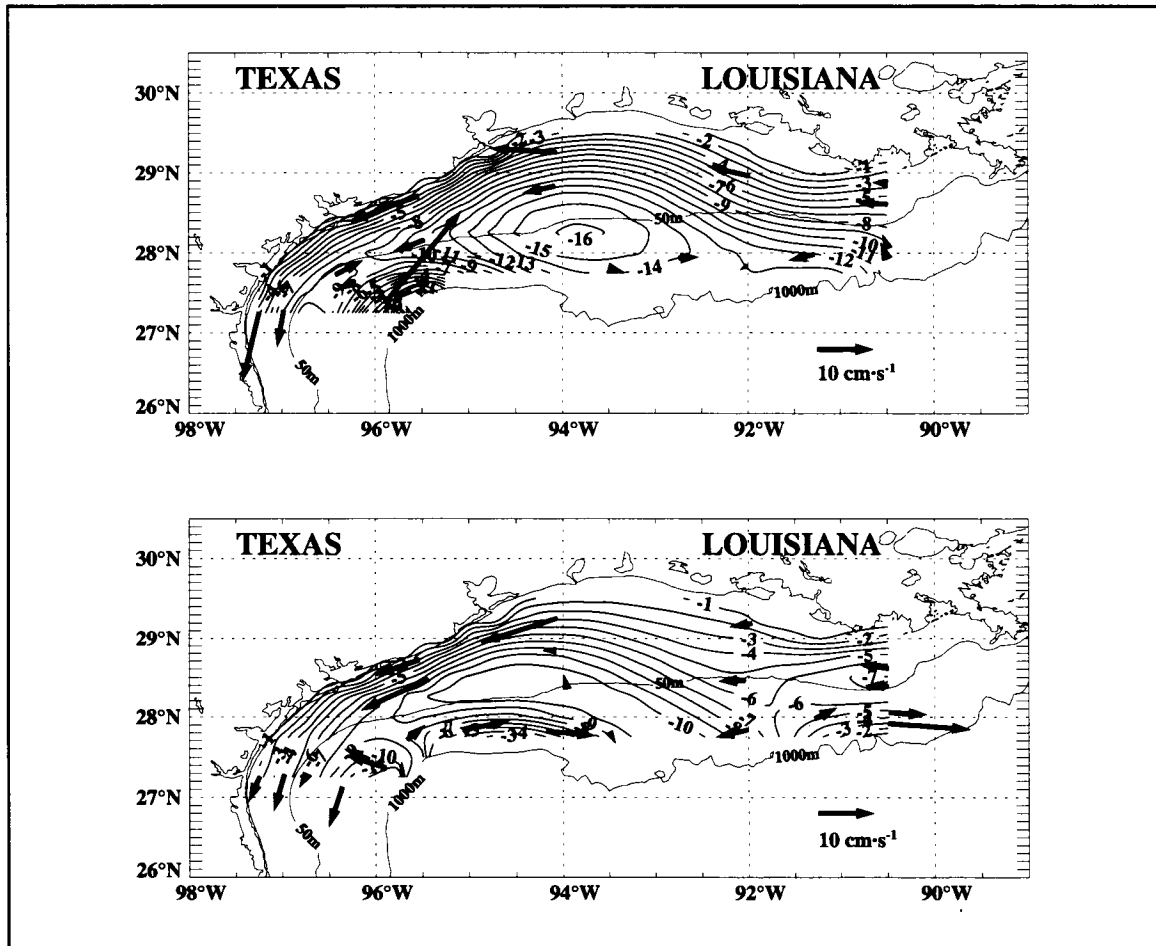


Figure 4.4.1-14. Shelfwide monthly mean 10-m velocity streamfunction field for December of 1992 (upper panel) and 1993 (lower panel). Arrows represent monthly mean 10-m current vectors. The unit of streamfunction is $10^7 \text{ cm}^2 \cdot \text{s}^{-1}$.

shown in Figure 4.4.1-2. The rms speeds are $8.25 \text{ cm} \cdot \text{s}^{-1}$ for the nonsummer mean and $8.86 \text{ cm} \cdot \text{s}^{-1}$ for the summer mean. The corresponding rms errors of the streamfunction fits are $3.61 \text{ cm} \cdot \text{s}^{-1}$ and $4.50 \text{ cm} \cdot \text{s}^{-1}$. The nonsummer average pictures an elongated cyclonic gyre centered mid-shelf near 94°W , although the cyclonic circulation over the shelf is pictured as strongly closed in only 7 of 23 monthly fields. Cross-shelf flow is seen to the east and west of the gyre's center. The summer pattern is of upcoast flow over the entire shelf.

4.4.2 Patterns of variability of velocity streamfunctions

We used EOFs to describe the shelfwide patterns of variability of the streamfunctions described in Section 4.4.1 (Cho 1996; Cho et al. 1998). Mathematically, EOFs are the eigenvectors determined from a data covariance matrix. The analysis is very efficient in finding the principal patterns (modes) with dominant variance (North 1984; Preisendorfer 1988). EOF analysis has been widely used to find the dominant pattern of covariability in ocean current meter data (Kundu et al. 1975; Kundu and Allen 1976; Winant et al. 1987). The eigenvalues obtained in the analysis are time-average energy (variance) of the various modes. The sum of the eigenvalues is equal to the total energy. EOF analysis is efficient in finding the dominant pattern of variability because usually the dominant variance can be represented by only a few modes (those having the largest eigenvalues). Amplitudes of the various modes can be computed. Thus, if a time series of fields are decomposed into EOFs, a time series of amplitudes is generated.

In addition to the EOF analysis, the variability ellipses of current on each meter were obtained by principal-axis decomposition of the two-dimensional distribution of current fluctuation. The eigenvalues determine the major and minor axes of the ellipse, and the eigenvector determines the orientation of these axes. Some results are presented in Section 4.4.3 to illustrate seasonal and depth dependence of variability.

The first three sample EOFs found for the monthly streamfunction variability explain 89.2, 3.4, and 2.2% of the variance, respectively. The North et al. (1982) “rule of thumb” for EOF sample variability shows that the first (very dominant) mode is robust, but the second and higher modes can be subject to significant mixing of modal patterns for different 32-month realizations. What this means is that one cannot expect other possible realizations of 32 months prior to or after the sample period to have the same EOF patterns for modes 2 and higher. However, for the LATEX sample period of observations, one can still employ these modes as appropriate structure functions to represent that particular data set.

The structures of the first two modes are shown in Figure 4.4.2-1 and the amplitude time series in Figure 4.4.2-2. The first EOF has a very simple structure, showing alongshelf flow over the entire shelf. The amplitude time series of the first EOF generally shows downcoast flow (positive values) during nonsummer and upcoast flow (negative values) in summer. This is the pattern expected over the inner shelf for primary driving by alongshelf wind stress.

Hourly fields of 10-m level wind velocity components (LATEX winds; Section 2.1.2) were used to construct hourly alongshelf components of wind stress at six locations nearly equally spaced along the 20-m isobath between 90.5°W and 26°N. From this information, monthly averages of the alongshelf stress components were evaluated, and then an average of these

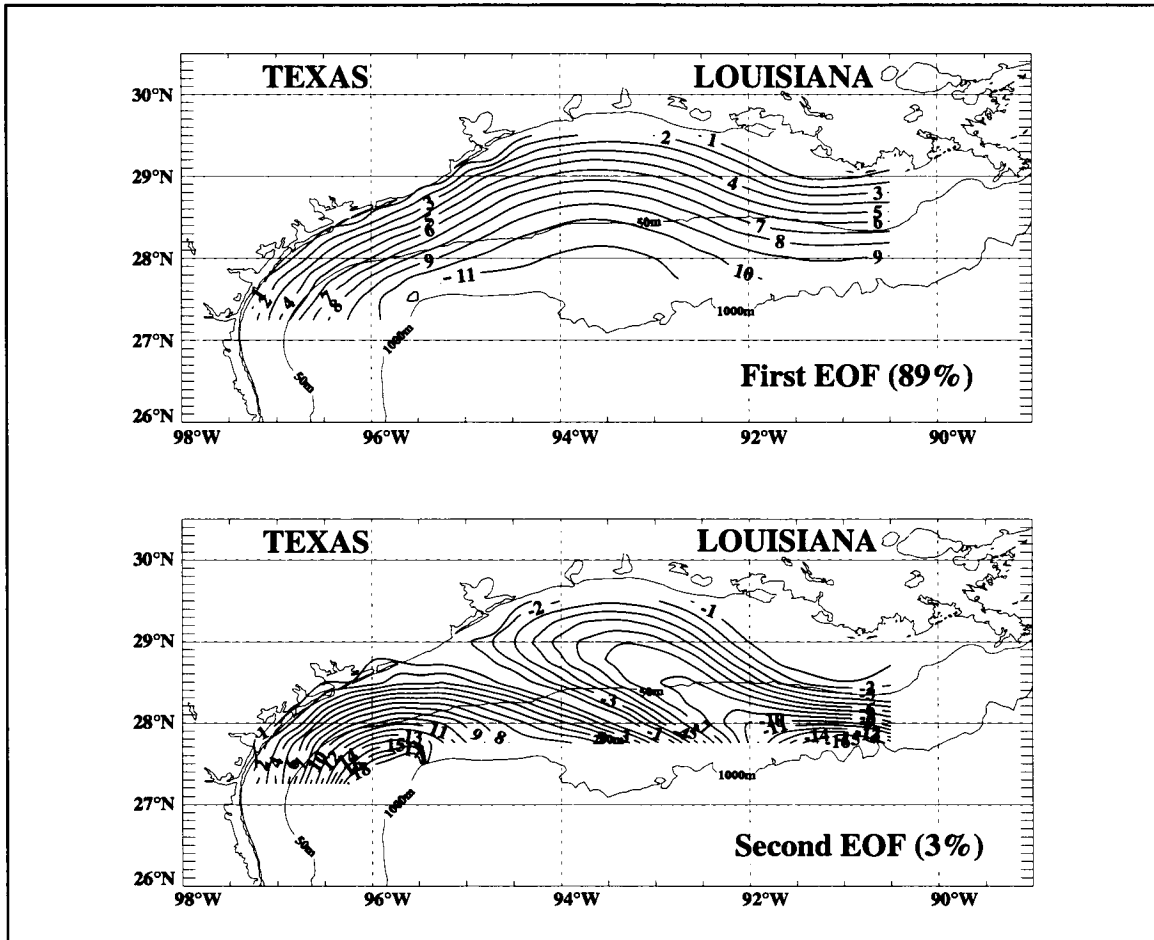


Figure 4.4.2-1. Structure of the first two EOFs calculated from the 32 monthly mean 10-m velocity streamfunction fields. The percent of variance in each mode is indicated. The unit of streamfunction is $10^7 \text{ cm}^2 \cdot \text{s}^{-1}$.

six values were obtained for each of the 32 months of the current measurements. The resulting sequence, shown in Figure 4.4.2-3, characterizes the wind forcing on the inner shelf; it shows downcoast forcing during the nonsummer regimes and upcoast forcing during the summer regimes.

One notes striking similarity between the monthly alongshelf wind stress of Figure 4.4.2-3 and the amplitude of the first EOF mode shown in Figure 4.4.2-2. The two sequences have a squared correlation of 0.83, providing strong evidence that wind stress is the primary forcing for the first EOF pattern of circulation on the Texas-Louisiana shelf. A strong correlation of near-coastal current with alongshelf wind stress was found by CK. The present

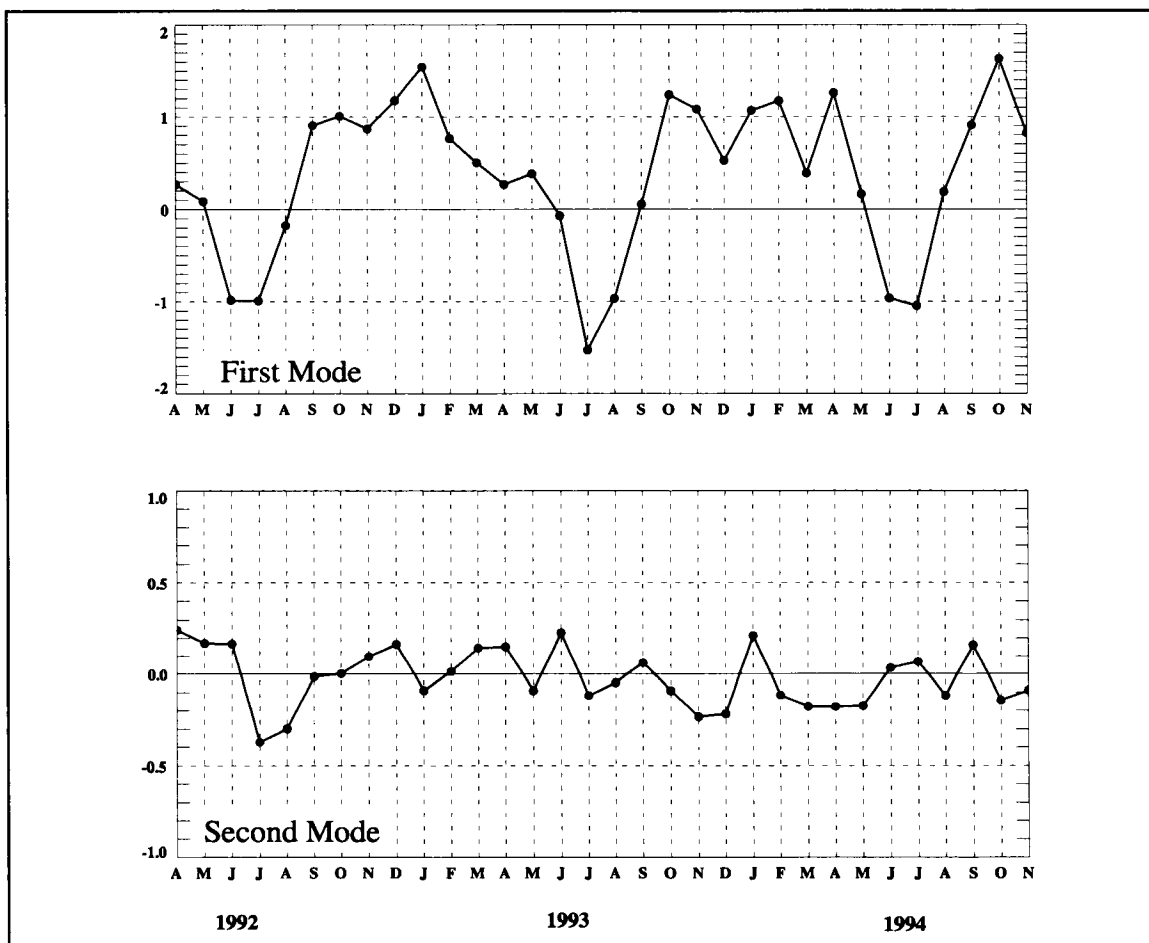


Figure 4.4.2-2. The amplitude ($10^7 \text{ cm}^2 \cdot \text{s}^{-1}$) time series of the first two EOFs for the monthly mean 10-m velocity streamfunctions.

results imply that the wind influence is essentially shelf wide, since the unidirectional current structure of the first EOF extends to the shelf break.

The second EOF shows a pattern of two half-cell structures with opposite senses of circulation; these result in on- and offshore flows over the shelf. It is hypothesized that the second and higher EOFs are forced by and therefore characterize the Loop Current eddy processes at the shelf break, particularly in the southwestern part of the study area. In contrast to the amplitude time series for the first EOF, those of the second EOF do not seem to have a seasonal pattern, and there is no significant correlation between the monthly wind stress signal of Figure 4.4.2-3 and the monthly amplitudes for the second EOF given in

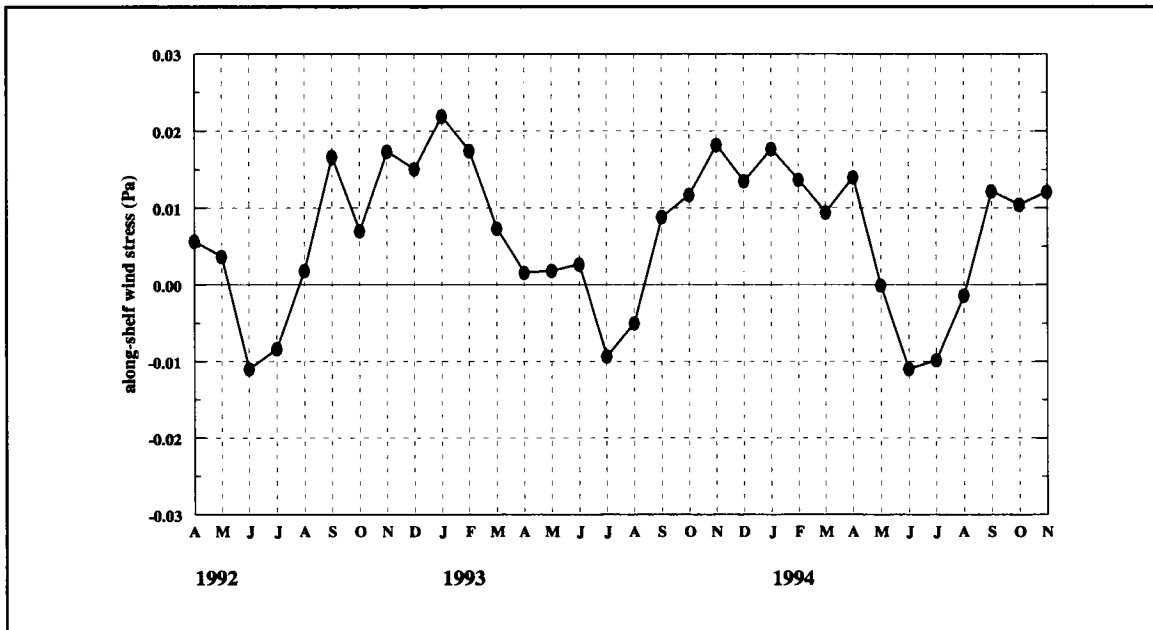


Figure 4.4.2-3. Sequence of monthly mean alongshelf wind stress characterizing the Texas-Louisiana inner shelf for the period April 1992 through November 1994 (downcoast is positive). Values were calculated from hourly analyzed wind components produced by Wang using the LATEX wind fields (Wang 1996; Wang et al. 1998a) at six nearly equally spaced points along the 20-m isobath from 90.5°W to 26°N (Figure 4.6-2), averaged for the six points, then averaged over each month.

Figure 4.4.2-2. This provides further evidence that the monthly variations of wind forcing produce monthly variations of circulation having dominantly a first EOF pattern. Furthermore the fraction of the total variance of the monthly mean circulation that is wind-driven and of first EOF pattern is about 0.89 times 0.83 or nearly 74%.

4.4.3 Vertical structure of seasonal currents

Previous studies of the vertical structure of measured horizontal currents from the Texas-Louisiana shelf are quite limited. Smith (1979) described the structure in 33 m depth off Aransas Pass, Texas, based on current measurements at four levels. He showed a decrease in current speed and counterclockwise turning of the current vector with increasing depth, suggesting a spiral pattern. Kelly et al. (1985) evaluated the vertical structure of currents at the Bryan Mound site using six current meters between the surface and bottom in 22 m of water. They found that variability depended upon the wind direction; for wind with an upcoast component, the cross-shelf component of mean current was directed offshore in the upper meters and onshore at other depths, indicating an upwelling condition. Chen (1995) analyzed the vertical structure along the 50- and 200-m isobaths using ADCP velocity profiles recorded during February, July, and November 1993. He showed that the first three EOFs account for more than 90% of the total energy along those isobaths. The first EOFs had quasi-barotropic structures; the second EOFs had first baroclinic structures.

In this section, we describe the vertical mean patterns of alongshelf and cross-shelf current components and vectors at individual moorings along the 20-, 50- and 200-m isobaths based on the LATEX A current measurements. It was shown in Sections 4.2, 4.4.1, and 4.4.2 that the dominant characteristic of the shelfwide, low-frequency circulation is the contrast between the nonsummer and summer periods. Therefore, following Cho (1996), the mean vertical structures were investigated for these two seasons. Forty-hour, low-pass currents sampled at 6-hr intervals were used; data gaps of less than two weeks were filled by the maximum entropy method (Press et al. 1986).

Along the 20-m isobath

Figure 4.4.3-1 shows the mean vertical structure of currents at moorings along the 20-m isobath averaged for nonsummer and summer periods. The moorings are arranged from upcoast (mooring 15) to downcoast (mooring 1). Each mooring had two current meters: near 10 m depth and near the bottom. See Table 1.2-1 for water depths and instrument configuration for each mooring.

From the mean vector plots, the flow is seen to have a 180° phase change between the summer and nonsummer. The cross-shelf component of mean flow is very small compared to the alongshelf component, indicating that the current is strongly polarized in the alongshelf direction at the 20-m isobath. In addition, some cyclonic shear with depth is seen in nonsummer. Cyclonic shearing is consistent with bottom Ekman shearing; the bottom meters clearly show frictional decrease of amplitude in many moorings and presumably are located in bottom Ekman layers. The cyclonic shear with depth occurs in the EOF depth structure characterizing the variability from the recordlength mean (Cho 1996).

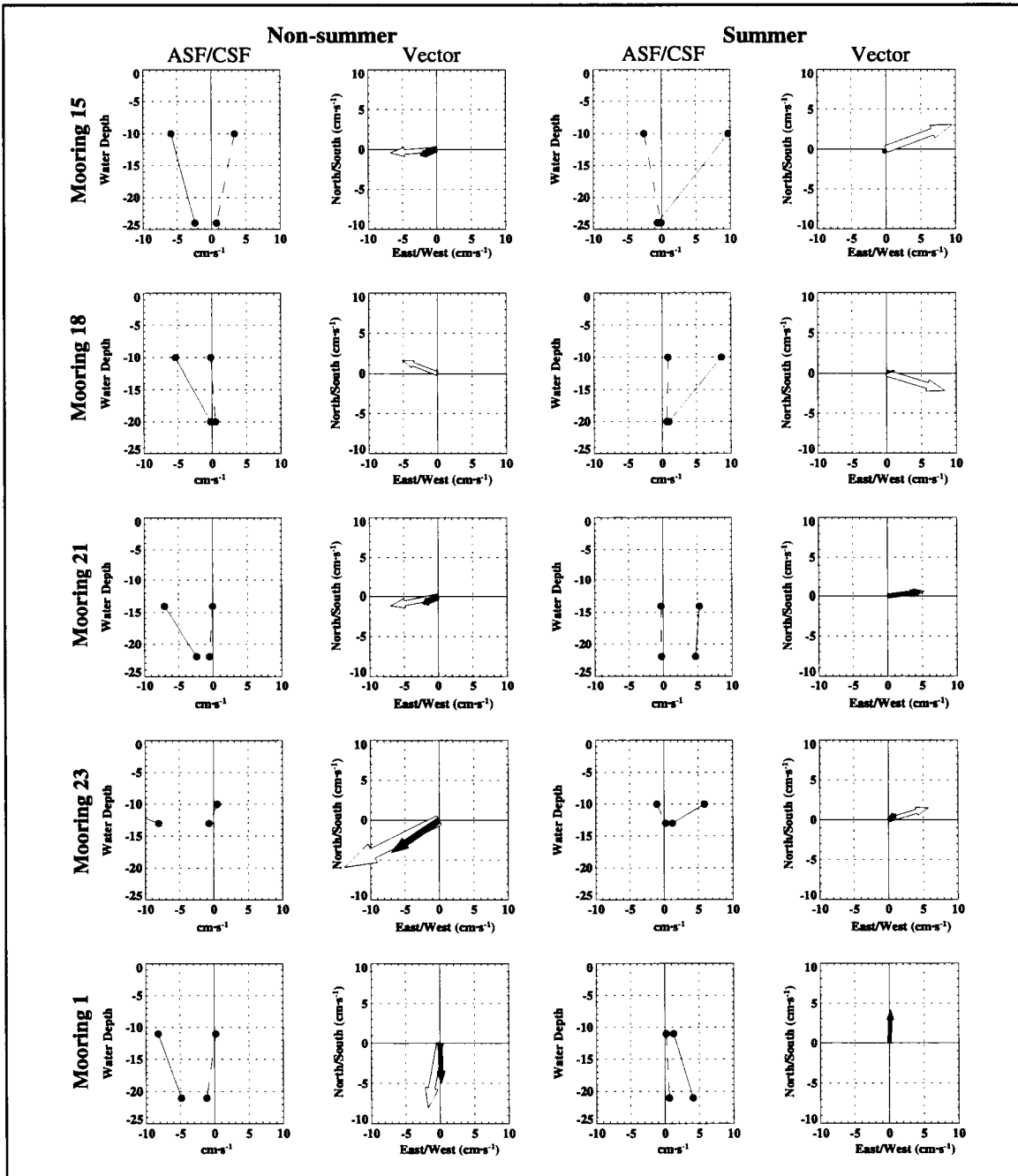


Figure 4.4.3-1. Alongshelf (solid) and cross-shelf (dashed) current components and vector plots (open arrows represent upper meters) averaged for nonsummer and summer periods at moorings along the 20-m isobath. Mooring numbers are indicated at the left. Positive speeds are upcoast or offshore.

Kelly et al. (1985) also found vertical shear on the inner shelf, showing the cross-shelf component of mean current was directed offshore at upper instruments and onshore at lower meters during upcoast winds in the summer. During nonsummer, the direction of cross-shelf flow at top and bottom are opposite to that in summer.

Figures 4.4.3-2 and 4.4.3-3 show vector means with variability ellipses for the top, middle, and bottom instruments for nonsummer and summer periods, respectively. Along the 20-m isobath, mean currents and their variability decrease with depth in both seasons. The alongshelf polarization is clear. (See Section 4.4.2 for method of evaluation of variability ellipses.)

Along the 50-m isobath

Figure 4.4.3-4 shows the vertical profile of mean currents at moorings along the 50-m isobath in nonsummer and summer. These moorings had current meters at 10 m, mid-depth, and near bottom. The cross-shelf components were relatively small except for the top meters on moorings 19 and 22, located between 92° and 94°W. This cross-shelf mean flow is also seen in Figures 4.4.3-2 and 4.4.3-3. In general, the mean flows at the 50-m isobath had principal components downcoast in nonsummer and upcoast in summer. However, the vertical structures of the mean currents show considerable variability from mooring to mooring and season to season, suggesting a more complex structure than for the 20-m isobath. There is evidence of onshore flow over the east shelf and of offshore flow over the west shelf in nonsummer, as should be expected with mean cyclonic circulation.

Along the 200-m isobath

The vertical structures of alongshelf and cross-shelf current components and their vector plots averaged for the nonsummer and summer are shown in Figure 4.4.3-5. At most of the moorings, but particularly in the west, the mean 10-m currents are strong and upcoast in both seasons. Amplitudes are larger for summer. This is seen also in Figures 4.4.3-2 and 4.4.3-3. For a number of these moorings there is large counterclockwise turning of mean vectors with depth, perhaps indicative of bottom Ekman layers associated with the interaction of anticyclonic eddies and the shelf edge.

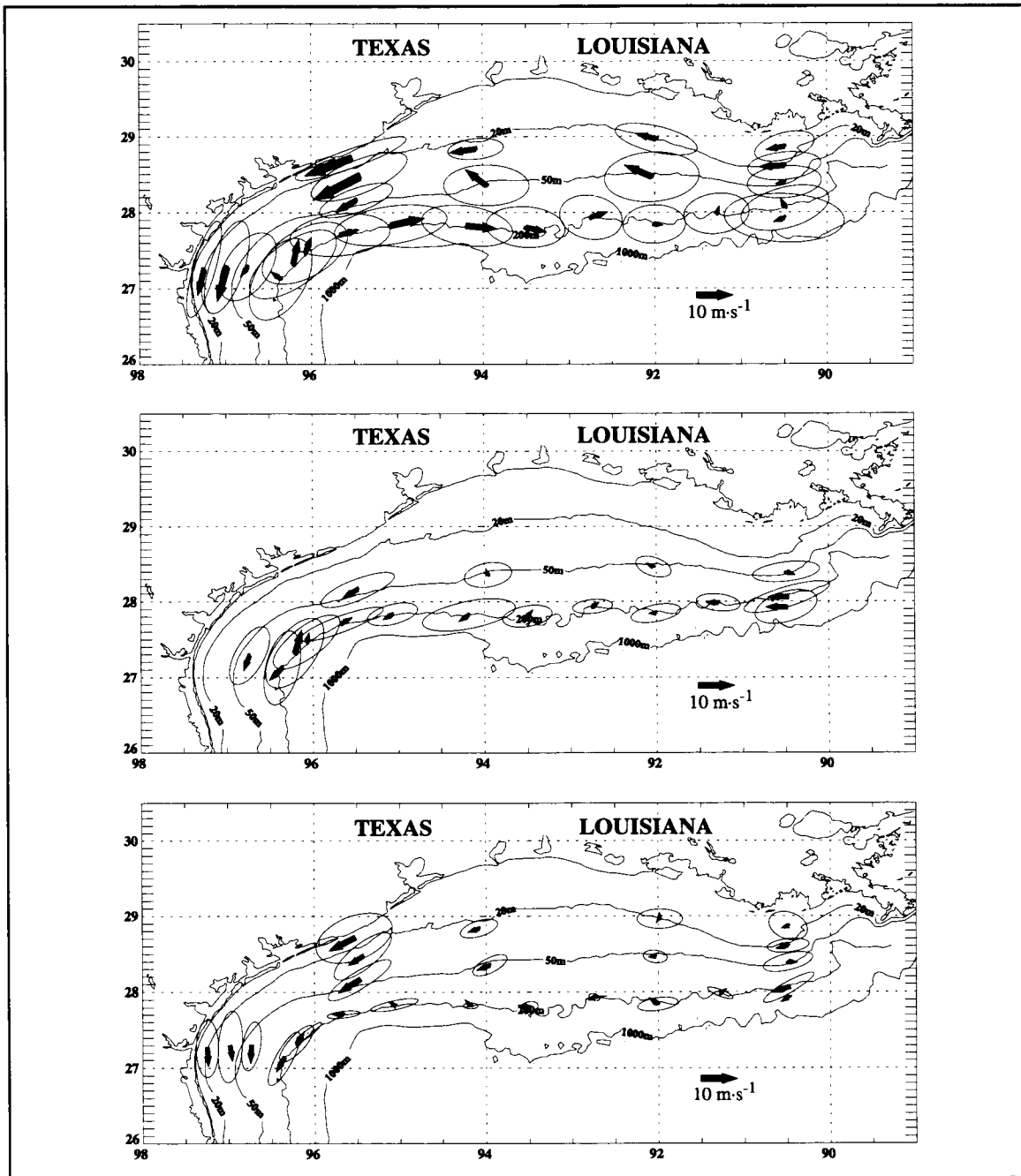


Figure 4.4.3-2. Nonsummer mean vectors and their principal variability ellipses at the 10-m, mid-depth, and near-bottom instruments of the LATEX A moorings.

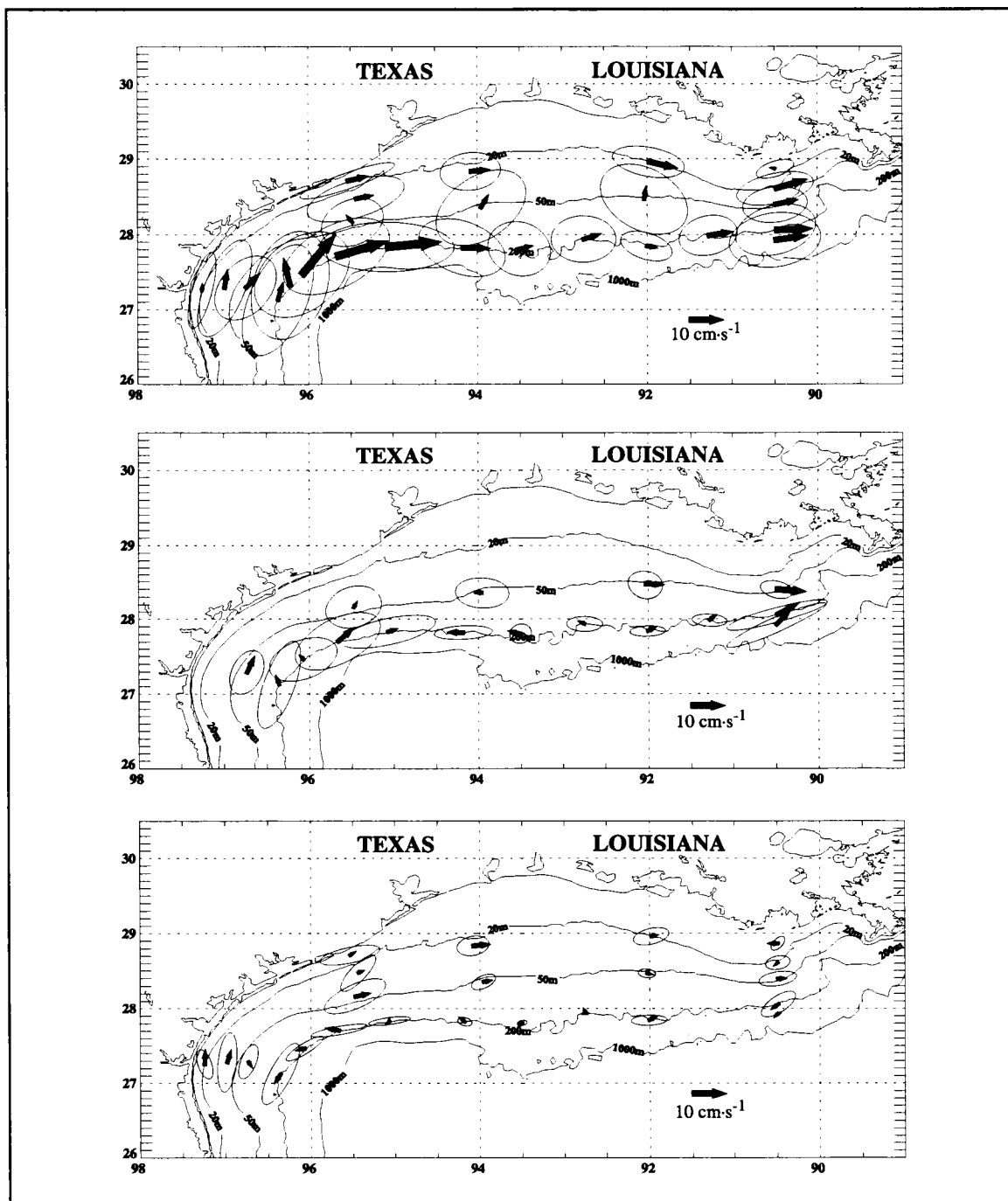


Figure 4.4.3-3. Summer mean vectors and their principal variability ellipses at the 10-m, mid-depth, and near-bottom instruments of the LATEX A moorings.

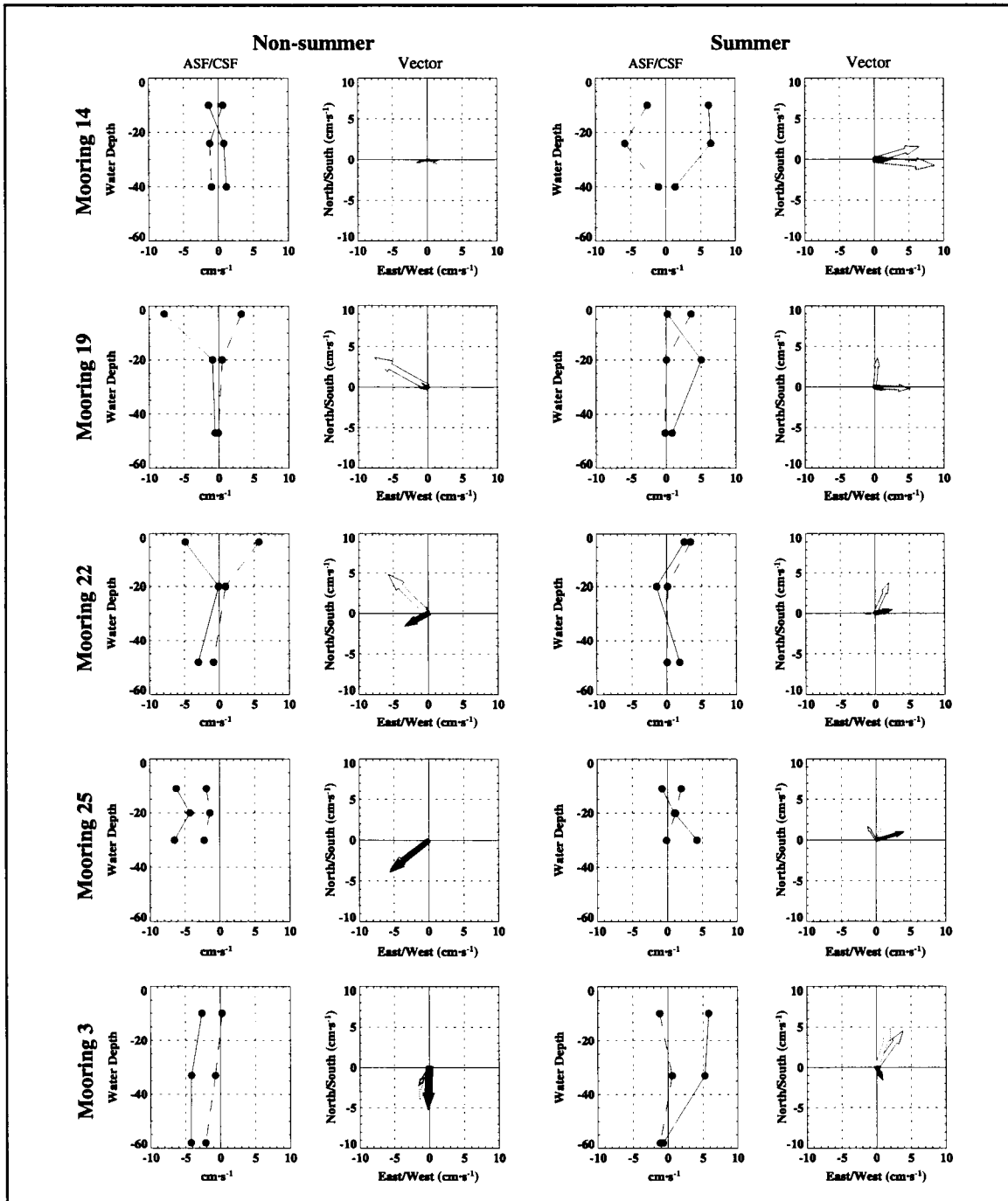


Figure 4.4.3-4. Alongshelf (solid) and cross-shelf (dashed) current components and vector plots (open arrows represent upper meters and dashed arrows represent mid-depth meters) averaged for nonsummer and summer periods at moorings along the 50-m isobath. Mooring numbers are indicated at the left. Positive speeds are upcoast or offshore.

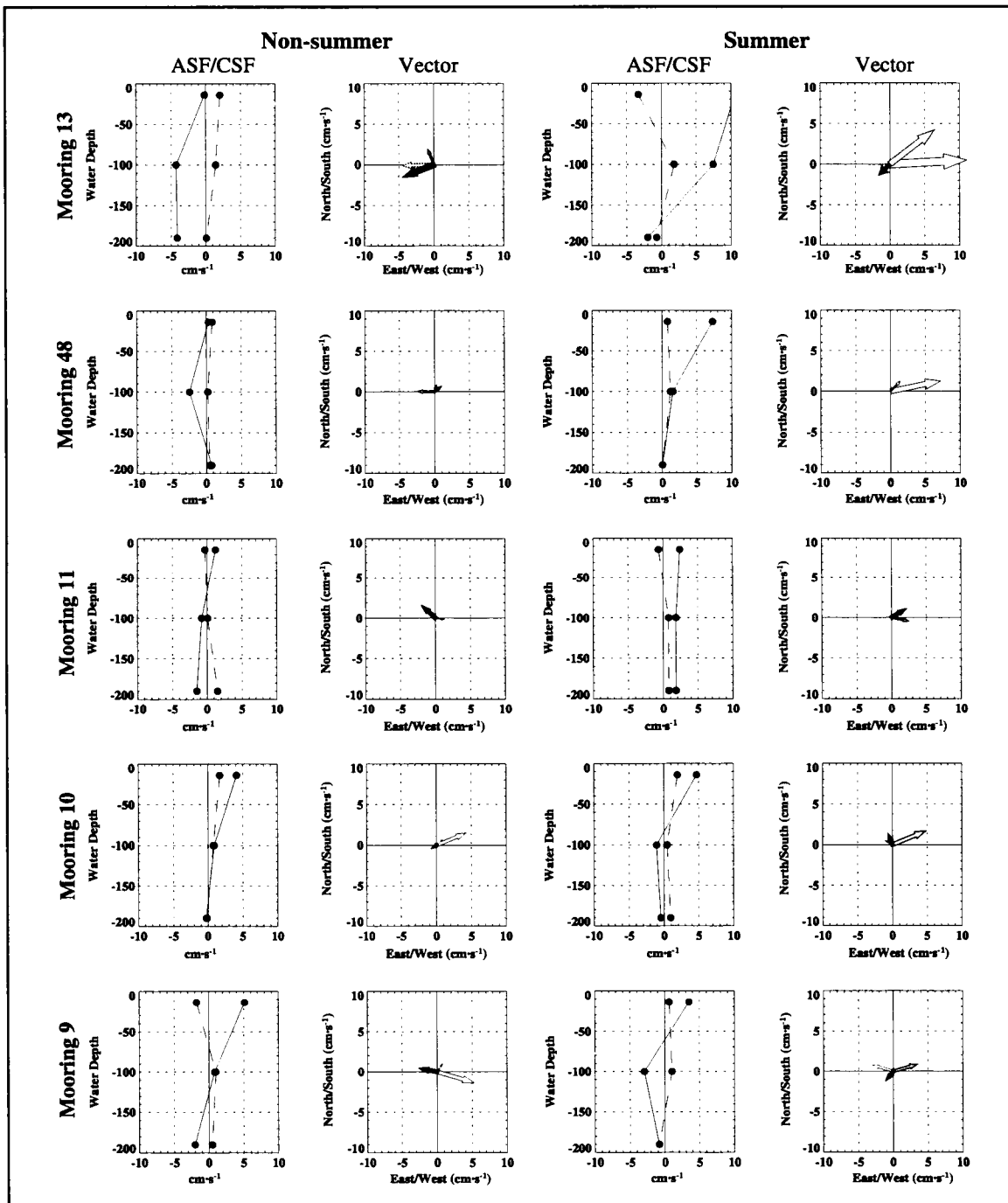


Figure 4.4.3-5. Alongshelf (solid) and cross-shelf (dashed) current components and vector plots (open arrows represent upper meters and dashed arrows represent mid-depth meters) averaged for nonsummer and summer periods at moorings along the 200-m isobath. Mooring numbers are indicated at the left. Positive speeds are upcoast or offshore.

4.5 Coherence of winds and currents

Introduction

In this section we describe the coherency between 10-m currents and gridded surface winds. The construction of hourly surface (10-m) winds on a 0.5° by 0.5° grid over the Texas-Louisiana shelf and adjacent region for the period April 1992 through November 1994 was described in Section 2.1.1. We first compare observed winds with gridded analyzed winds at grid locations close to observational locations. Comparing the gridded and observed winds at these locations gave us confidence for analyzing the wind-current coherency at current meter locations where observed wind data does not exist. Then, we describe the wind-current coherency and phase relations for selected alongshelf and cross-shelf mooring lines.

Hourly winds and hourly 3-hr low-pass filtered current meter data were used in this study. DiMarco et al. (1997) discuss the filters and methods used with the current meter data. For this study, gaps in the observed winds and the current meter records of less than 24 hours were filled using linear interpolation. Coherency, phase, and transfer functions were estimated using codes based on the spectrum analysis software package of the MATLAB Signal Processing Toolbox (Little and Shore 1992).

Comparison of observed with gridded, analyzed winds

Figure 4.5-1 shows the alongshelf and cross-shelf components of gridded and observed winds at five locations from 1 April 1992 through 1 June 1992: BUSL1, 42020, 42019, L50, and L53 (see Figure 2.1.1-1 for station locations). The gridded winds at each location appear smoother than the observed winds, especially during times of abrupt wind speed change. The spatial scales of the winds varied seasonally from 100-200 km in the fall and winter to 500-800 km in the summer (W. Wang private communication). Thus, wind fields in summer were spatially coherent over much of the Texas-Louisiana shelf, as seen in Figure 4.5-1. The time series from BUSL1, L50, L53, and 42019 are nearly identical, showing events occurring nearly simultaneously across the shelf. The coherency at these stations is evident in both high and low frequency variations. However, the time series at 42020, in the southwestern section of the study area, is less coherent with winds east of 93°W , particularly those at BUSL1 which is approximately 550 km away. This lack of coherency is especially evident at high frequencies. Note that, although there are no observed data at 42019 after 22 April 1992, the gridded time series is continued through 1 June 1992.

BUSL1 was chosen for a statistical comparison of gridded with observed winds because it had few gaps during the examination period, providing the longest record for analysis. Figure 4.5-2 shows the spectra at BUSL1 for the gridded and observed alongshelf and cross-shelf wind components offset by season. The spring season was defined as March,

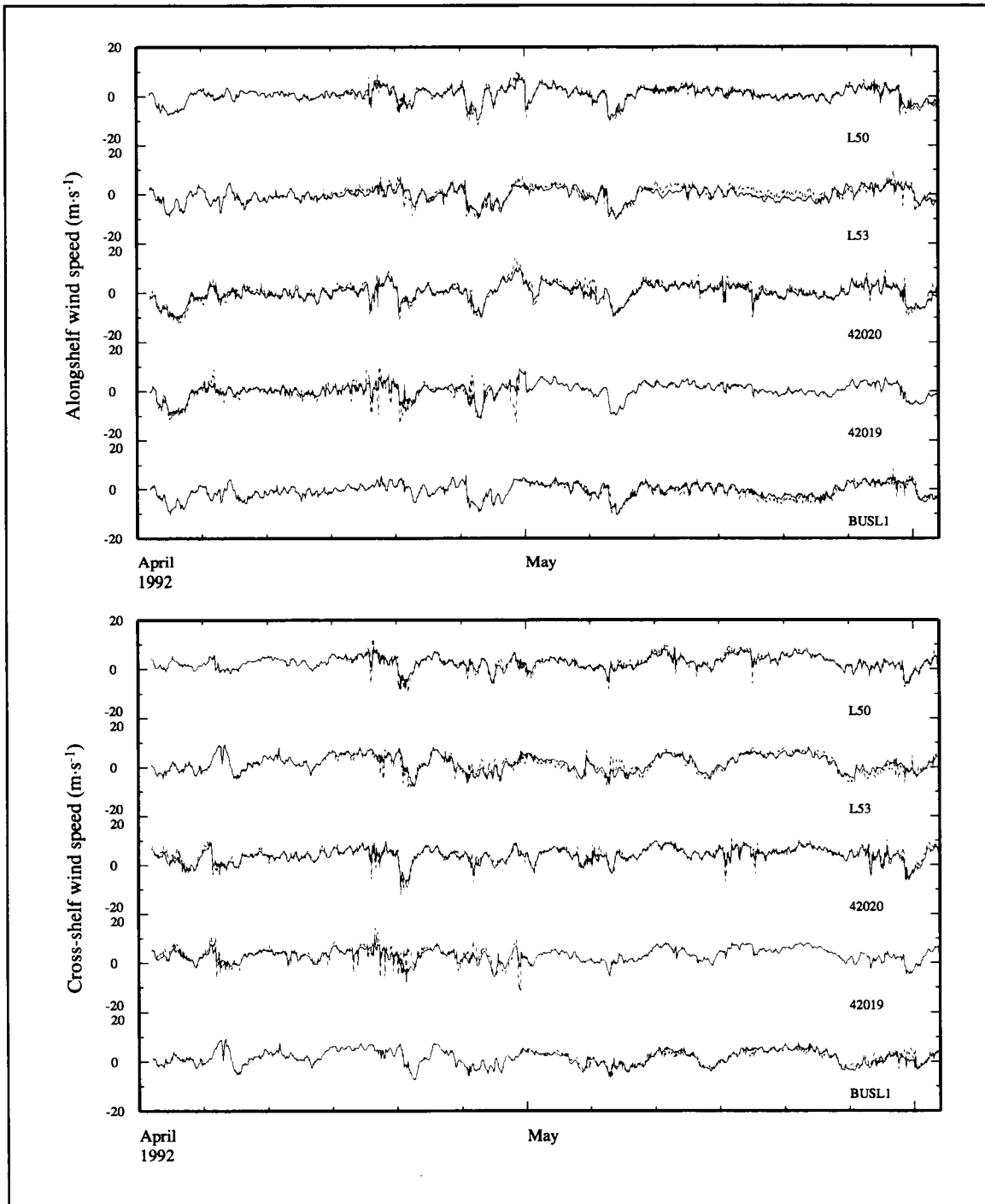


Figure 4.5-1. Gridded (solid) and observed (dashed) alongshelf (upper panel) and cross-shelf (lower panel) winds at L50, L53, 42020, 42019, and BUSL1 from 1 April 1992 to 1 June 1992.

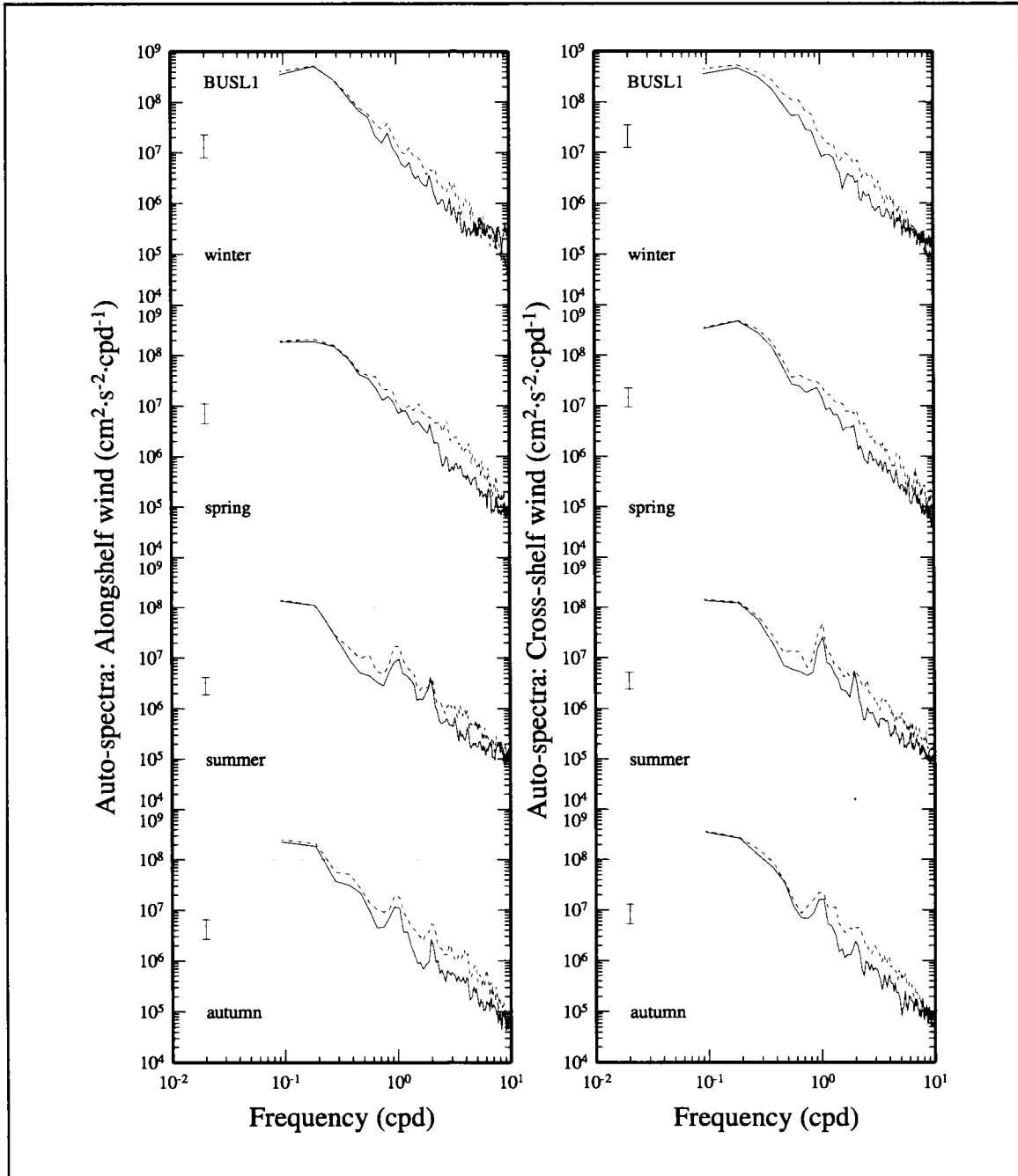


Figure 4.5-2. Autospectra of alongshelf (left) and cross-shelf (right) gridded (solid) and observed (dashed) winds at BUSL1.

April, and May; other seasons were defined accordingly. The conclusions drawn from analysis of these winds are representative of similar analyses at other observed wind locations:

- 1) Strong diurnal and semi-diurnal peaks appear in summer and remain, though less pronounced, through autumn. These peaks are not present in winter or spring.
- 2) The high-frequency energy falls off more rapidly for gridded winds, presumably due to the smoothing effects of gridding.
- 3) There is a large difference in total seasonal wind energy. Winter shows larger absolute energy in the weather band (2-10 days) than summer due to more frequent frontal passages. A dotted horizontal line is drawn at $10^8 \text{ cm}^2\cdot\text{s}^{-2}\cdot\text{cpd}^{-1}$ for comparison of the absolute energy in the weather band. In summer versus winter energy, there is half an order of magnitude difference at periods of nine days. Section 4.3.2 discusses the energy of ocean currents associated with the weather band, its spatial distribution, and the ratio of weather band energy to mesoscale (10-100 days) energy over the Texas-Louisiana shelf.

Energy between 2- and 10-day periods “fills in” the spectrum during winter; i.e., energy steadily increases from shorter to longer periods. During the summer, the spectrum falls off rapidly at longer periods after the diurnal peak and then increases at periods of four days and longer. The lack of energy in the weather band during summer is believed due to the infrequent occurrence of frontal passages in that season (see Section 2.1.3).

Figure 4.5-3 shows the phase and coherency squared of the gridded winds versus observed winds by season for both alongshelf and cross-shelf directions at BUSL1. In all four seasons we see that the coherency is, in general, above the 95% confidence interval for all periods. The least confidence is at high frequencies, again reflecting the smoothing effects of the wind extremes seen in the time series plots and spectra. In general, the phase is very close to zero, indicating that events in the observed time series occur simultaneously with events in the gridded time series. More variability in phase, however, is seen for high frequencies in winter than in summer.

Figure 4.5-4 is a representative sample plot of a transfer function for each season at BUSL1. As one would hope, the transfer functions are essentially one for the cross-component and same-component functions. This result was also seen for other seasons at this location and for all seasons at other locations.

Based on this and similar statistical comparisons at other observational locations, we are confident that the time series of gridded wind provide good representations of the winds; they are very good for periods greater than 6 hours. Therefore we used the gridded winds at grid points nearest current meter locations to study wind-current coherence.

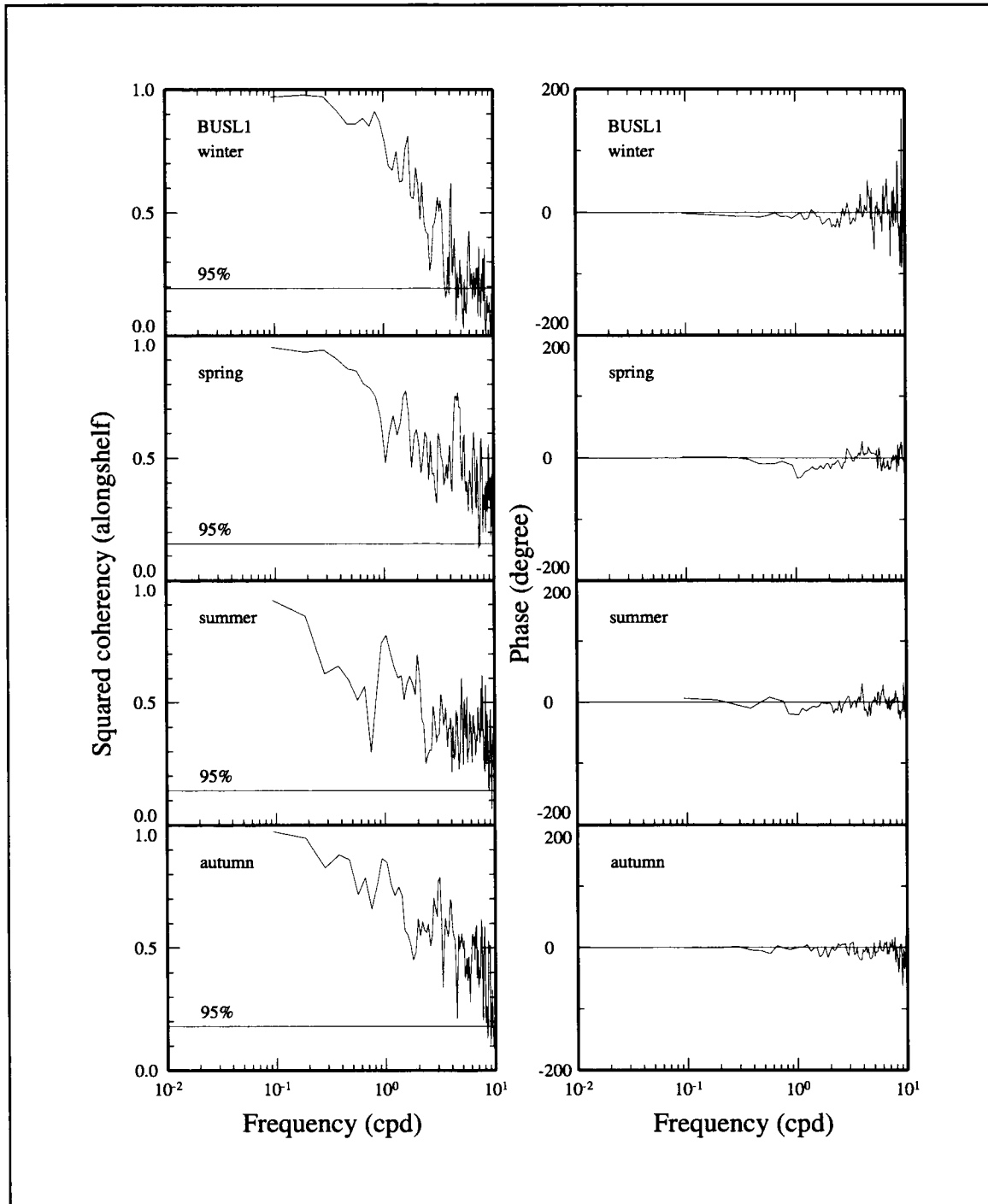


Figure 4.5-3a. Squared coherency (left) and phase (right) for alongshelf components of gridded and observed winds by season at BUSL1.

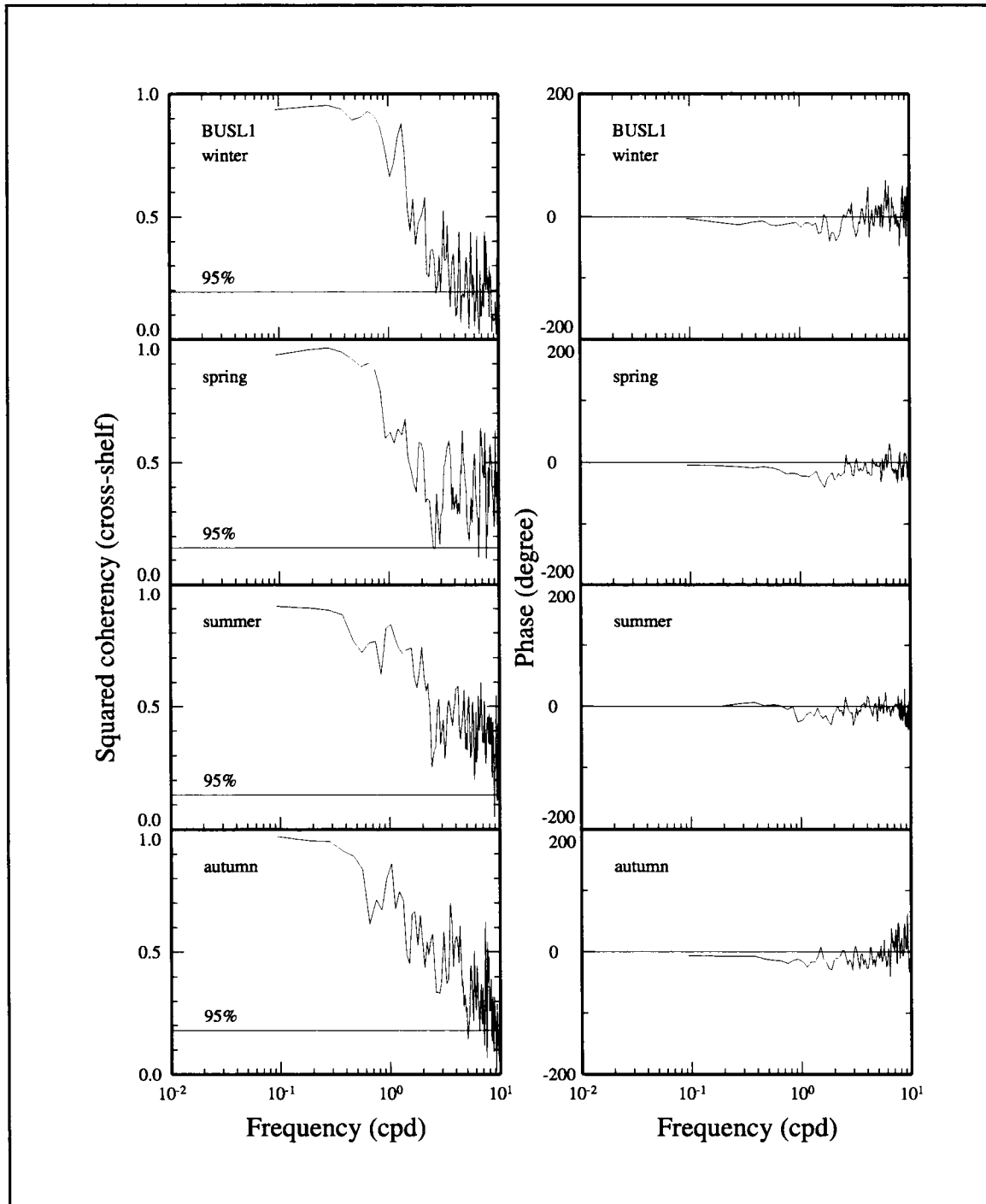


Figure 4.5-3b. Squared coherency (left) and phase (right) for cross-shelf components of gridded and observed winds by season at BUSL1.

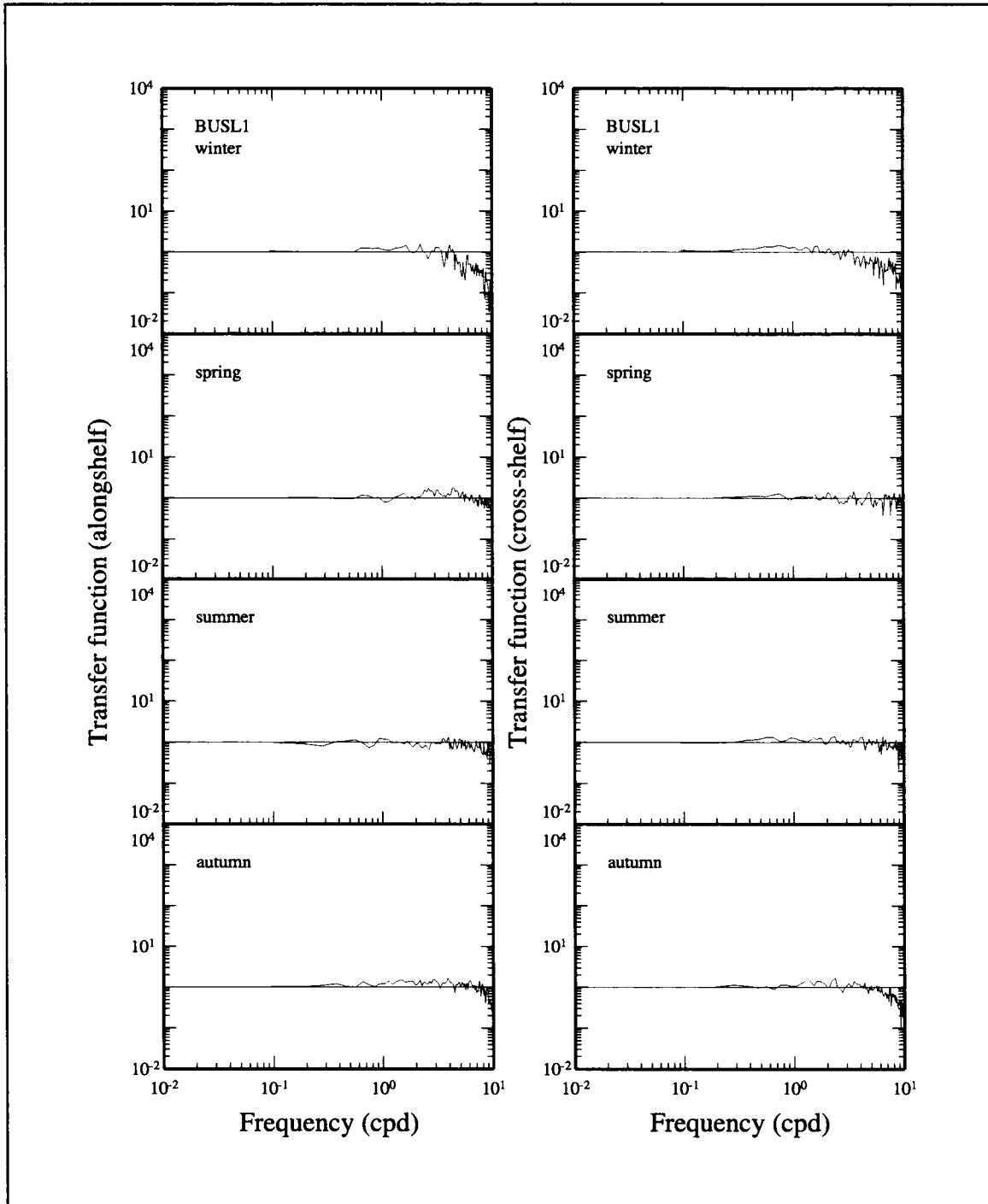


Figure 4.5-4. Transfer functions of alongshelf (left) and cross-shelf (right) components of gridded and observed winds by season at BUSL1.

Current-wind coherence

The time series of current and gridded wind were grouped into seasons. Then spectra, coherence, and phase were estimated over each resulting seasonal time series. Seasons were defined as described above.

Figure 4.5-5 shows the auto-spectra of currents and winds for each season at mooring 23. Again we see a spectral peak centered around diurnal periods in the summer currents. We believe these peaks are due to diurnal thermal cycling caused by the heating and cooling of the upper ocean when the shelf waters are highly stratified. The upper ocean then responds strongly to diurnal wind variation. In other seasons, the spectral peaks around diurnal periods are due in part to frontal passages that force inertial oscillations. For more discussion of thermally induced diurnal cycling, see Appendix F.2. The horizontal line drawn at $10^8 \text{ cm}^2 \cdot \text{s}^{-2} \cdot \text{cpd}^{-1}$ again serves to illustrate the relative energy in the weather band in different seasons. Winter shows the largest energy in the weather band for both wind and current meter data. Weather band energy is significantly reduced during summer.

We illustrate the difference in wind-current coherence as a function of distance from shore, or depth, by examining coherence at moorings 23, 24, 25, and 7. These moorings are located, respectively, at increasing distances from the coast and in increasing water depths (~ 10 to 200 m), near 95°W . To obtain a clear interpretation of the cross-shelf differences in wind-current coherency, we focus attention on separate energy bands: weather band (2-10 day periods) and diurnal band (periods of approximately 1 day).

Analysis of the alongshelf coherence and phase at mooring 23 indicates significant coherence for periods longer than two days (Figure 4.5-6). The phase of the coherence shows that the current response to the wind forcing can be thought of, after smoothing, as an approximate exponential curve sloping downward to the left from about 90° at 2-day periods to 20° and less at 10-day periods. This suggests a current response of less than 1 day for all components in the weather band. The cross-shelf wind and current components at mooring 23 (not shown) do not show significant coherence in the weather band except during spring. The positive phase at these periods during the spring indicates a 1-2 day response of cross-shelf currents to cross-shelf winds.

Farther from shore at mooring 24 (Figure 4.5-7), we see significant coherency between alongshelf components at periods longer than five days that persists throughout the year and spans all seasons. During summer, however, the coherence between three and eight days falls off. The alongshore wind-current phase relationship is similar to that seen at mooring 23. Figure 4.5-8 indicates that at mooring 25 there is significant coherence between the alongshelf winds and currents in the weather band only during the winter and spring seasons. (Note that at mooring 25 data were available from three summer seasons, but only

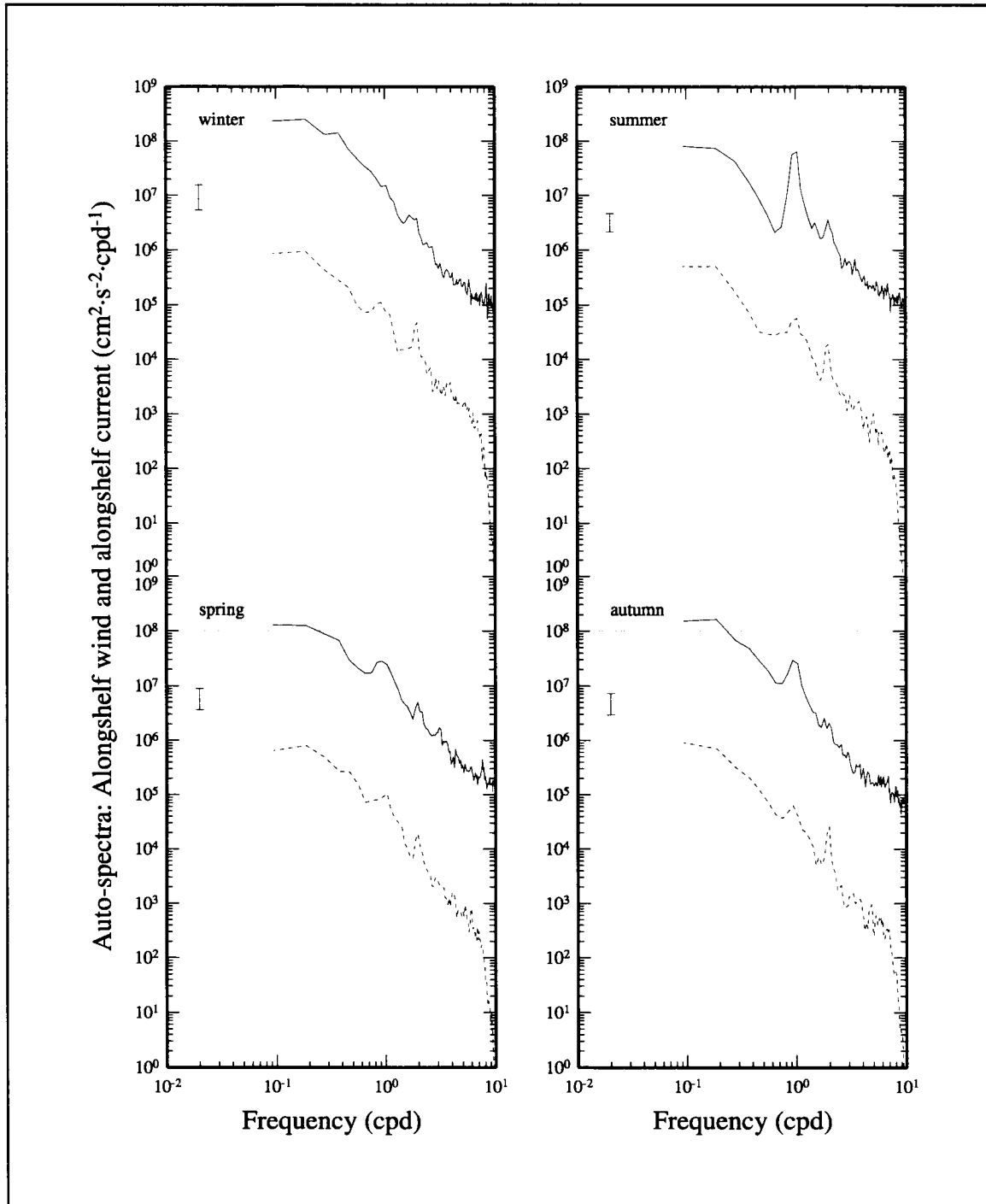


Figure 4.5-5a. Autospectra of alongshelf components of current (dashed) and gridded wind (solid) at mooring 23 by season.

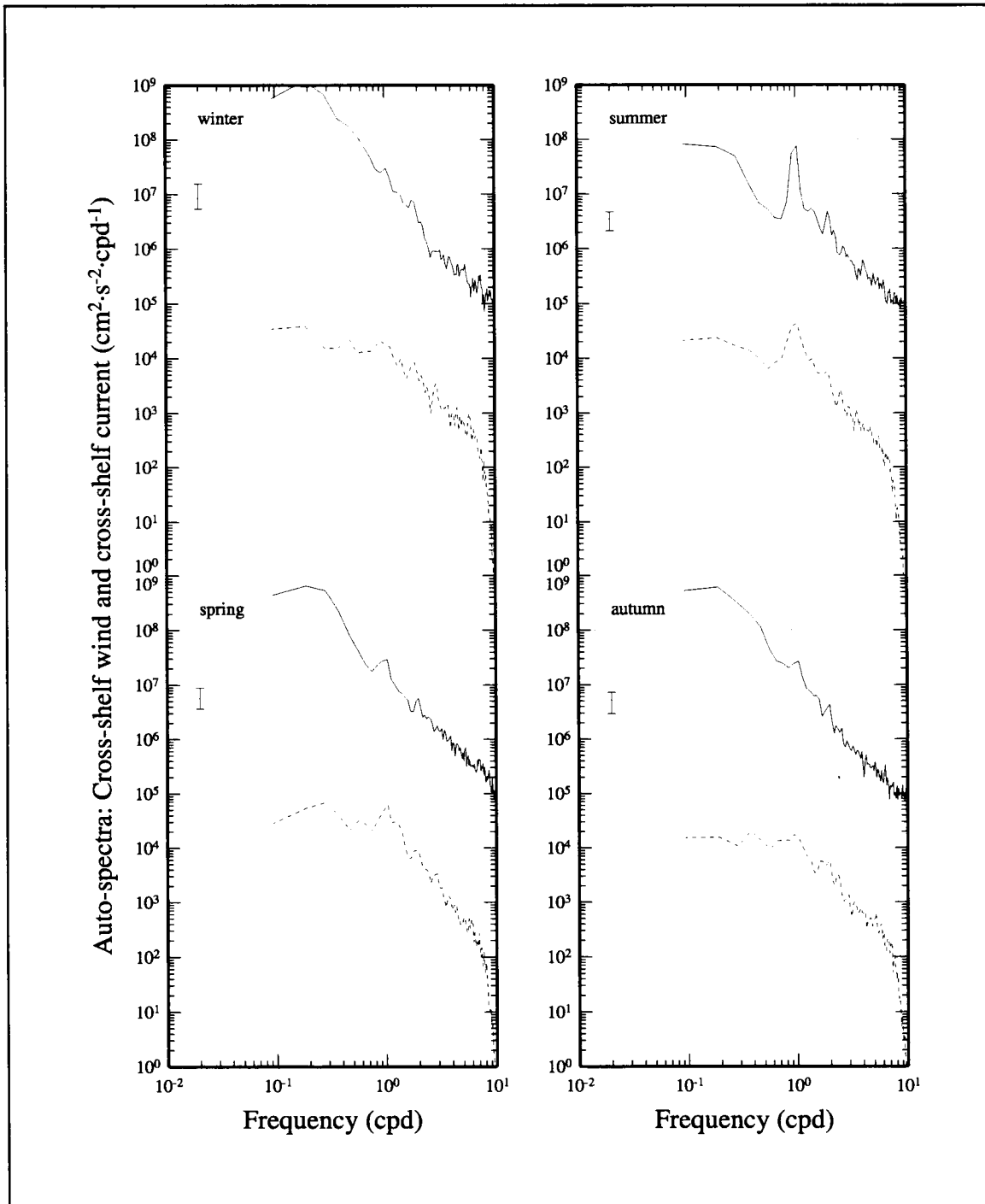


Figure 4.5-5b. Autospectra of cross-shelf components of current (dashed) and gridded wind (solid) at mooring 23 by season.

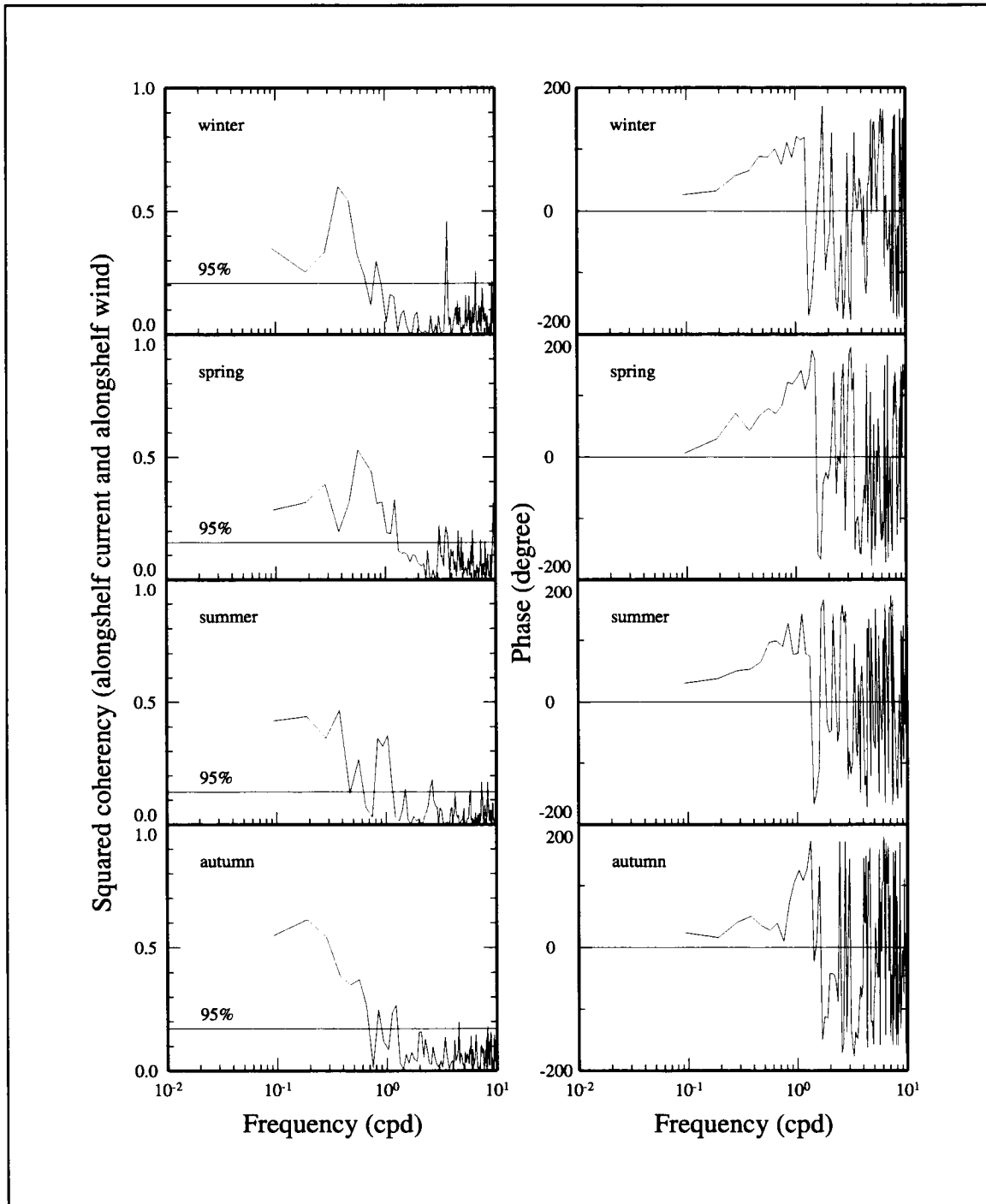


Figure 4.5-6. Squared coherency (left) and phase (right) between alongshelf current and alongshelf gridded wind by season at mooring 23. Positive phase indicates winds leading currents.

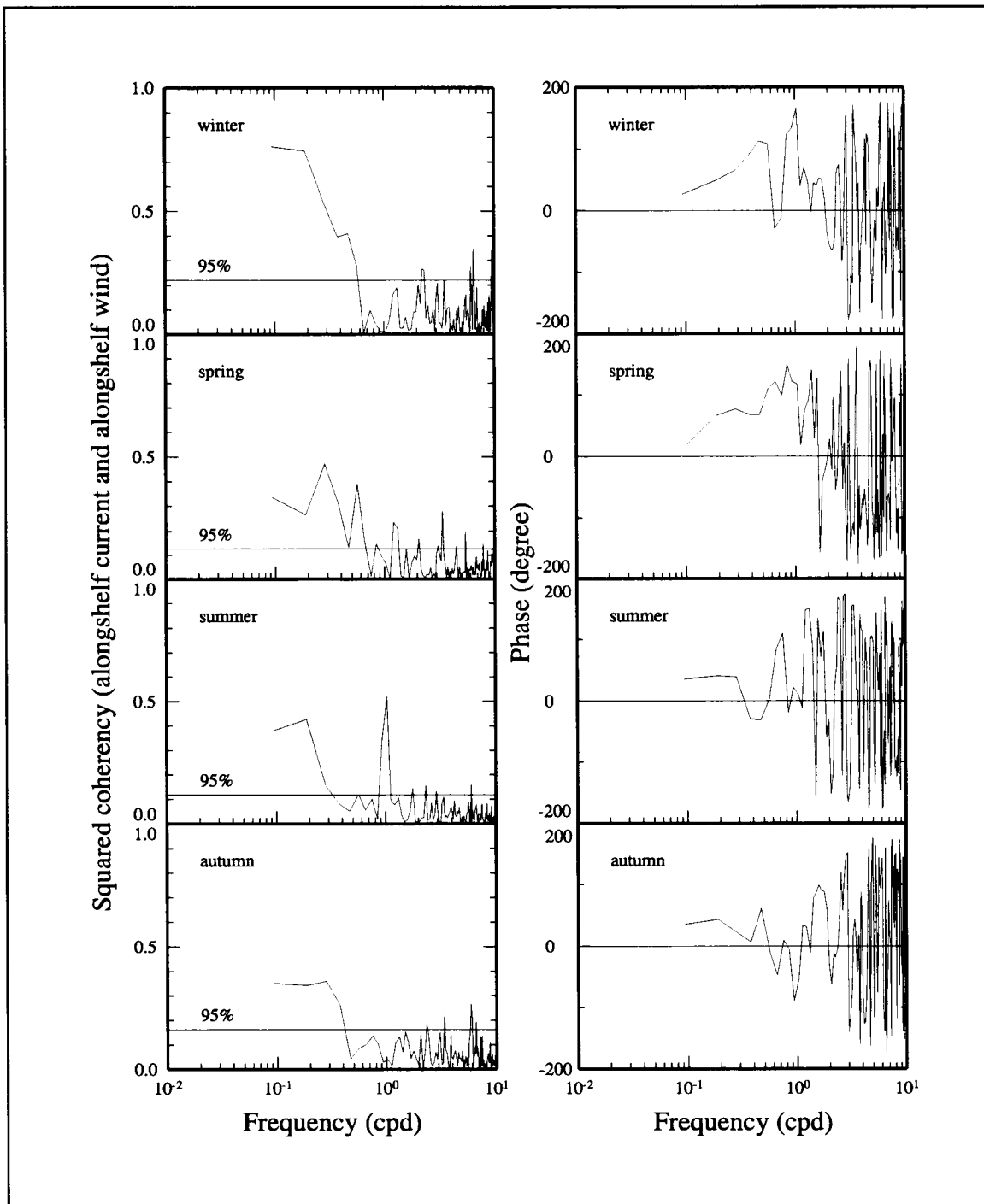


Figure 4.5-7. Squared coherency (left) and phase (right) between alongshelf current and alongshelf gridded wind by season at mooring 24. Positive phase indicates winds leading currents.

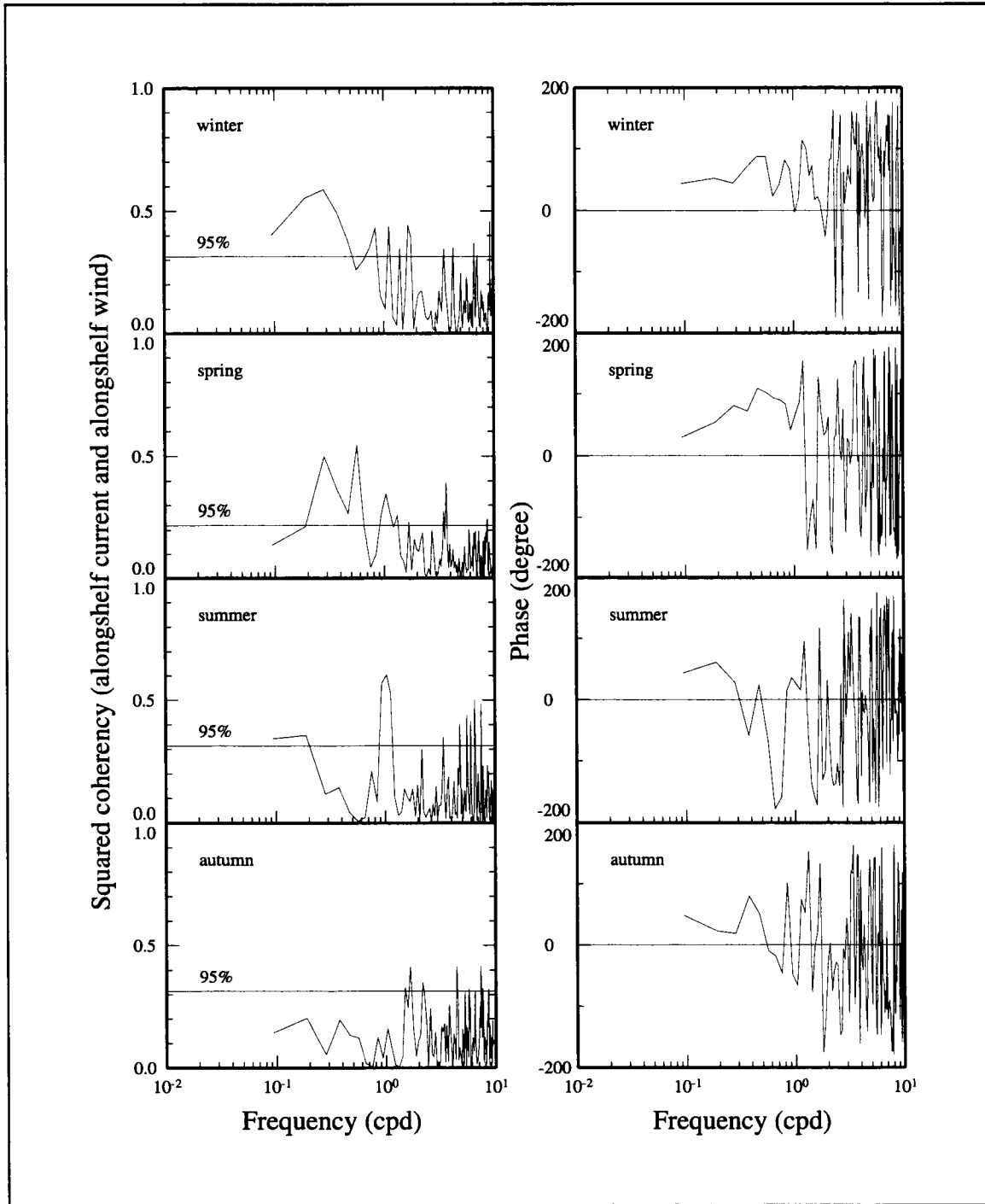


Figure 4.5-8. Squared coherency (left) and phase (right) between alongshelf current and alongshelf gridded wind by season at mooring 25. Positive phase indicates winds leading currents.

for one realization for other seasons.) The phase again is similar to the phase seen at moorings 23 and 24 during winter and spring. For the cross-shelf components (not shown) we see very little coherence between wind and current. At the shelf edge mooring 7 (Figure 4.5-9), there is no significant coherence for either cross- or alongshelf wind and current components during any season in the weather band.

At diurnal periods there is strong coherence and positive phase (winds leading currents) during the summer months across the shelf at moorings 23, 24, 25, and 7 for both the alongshelf and cross-shelf components. Very little coherence is seen at these locations during other seasons. This supports our view that thermally induced diurnal current cycling is also coupled to the winds and occurs most prominently in summer when the water column is highly stratified.

To illustrate the difference in wind-current coherence over the inner shelf, we present in Figures 4.5-10 through 4.5-13 the squared coherency and phase for the alongshelf components of the upper current meter and gridded winds for the coastal moorings 1, 20, 17, and 16. Moorings 1, 23, 20, 17, and 16 are located near the 10-m isobath increasing distance upcoast from approximately 27.3°N to 90.5°W.

In the weather band, there generally is less coherency in the eastern moorings (16, 17, and 20) than in the western (1 and 23). However, during winter there is significant coherency across the shelf. At diurnal periods, moorings 1, 23, and 20 show significant coherency during spring, summer, and sometimes fall with a phase of 9-12 hr. At moorings 17 and 16, there is no significant coherency during any season for diurnal periods. This pattern continues for the next set of inner shelf moorings (2, 24, 21, 18, and 15) with alongshelf winds being more coherent with alongshelf currents in the west than in the east. Over the outer shelf (50 m and deeper), there is little coherence between winds and currents.

Analysis of cross-shelf currents versus cross-shelf winds and cross-shelf currents versus alongshelf winds gave no evidence of significant coherency in the weather band during any season. For cross-shelf winds versus alongshelf currents, we saw significant coherence at mooring 23 and moorings east of 23 at 2-5 day periods during spring, fall, and winter. At mooring 20 there is significant coherence in the 4-10 day band during summer. As is the case for coherence between alongshelf wind and current, the coherence between cross-shelf wind and current is significant in the diurnal band during the non-winter months, particularly summer, over much of the shelf. However, mooring 16 does not show significant coherence at the diurnal bands during winter.

In summary, current/wind coherency over the Texas-Louisiana shelf in the weather and diurnal bands is greatest near shore and at downcoast mooring locations for alongshelf current and wind components. There is more coherency in nonsummer months, when there

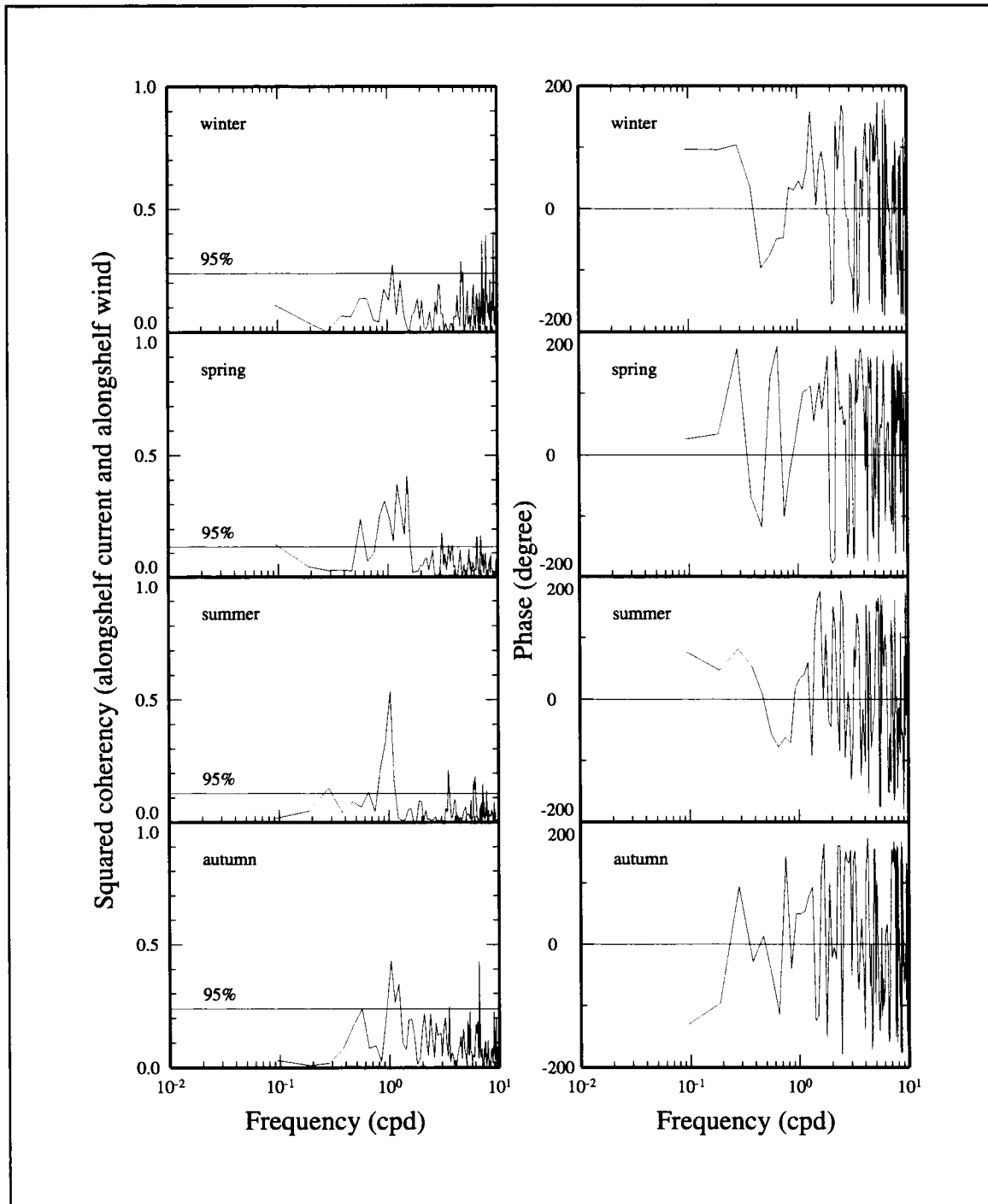


Figure 4.5-9. Squared coherency (left) and phase (right) between alongshelf current and alongshelf gridded wind by season at mooring 07. Positive phase indicates winds leading currents.

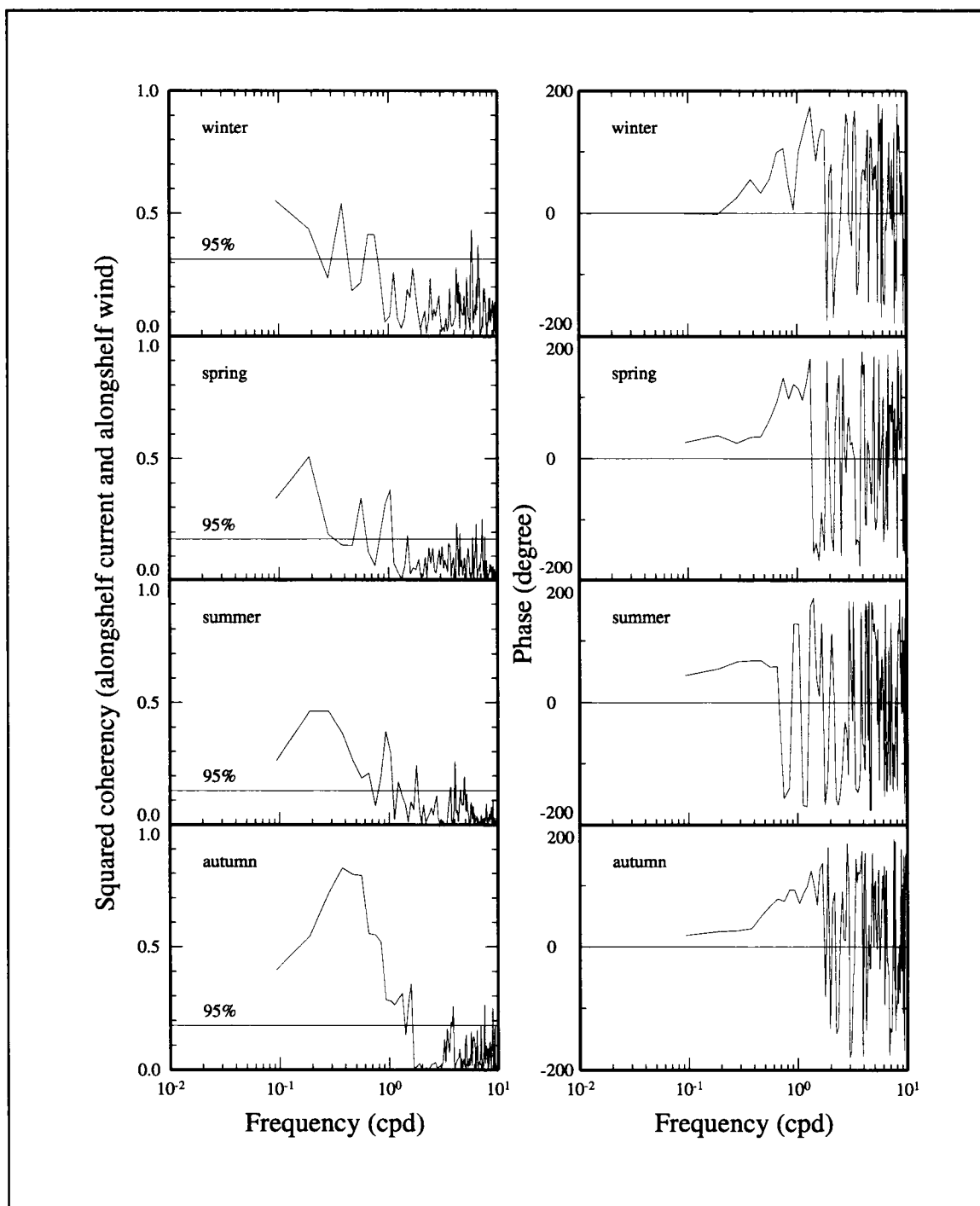


Figure 4.5-10. Squared coherency (left) and phase (right) between alongshelf current and alongshelf gridded wind by season at mooring 01. Positive phase indicates winds leading currents.

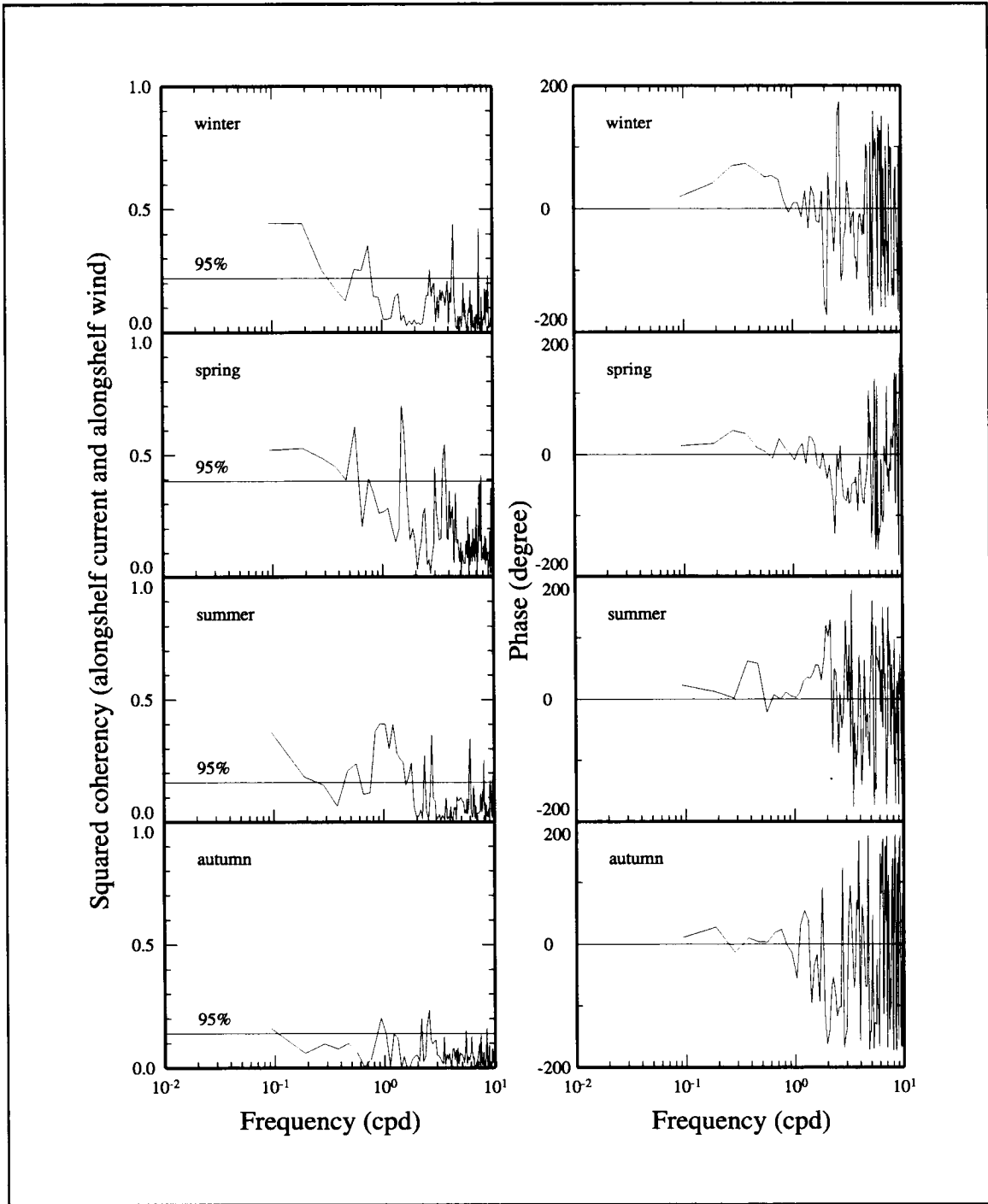


Figure 4.5-11. Squared coherency (left) and phase (right) between alongshelf current and alongshelf gridded wind by season at mooring 20. Positive phase indicates winds leading currents.

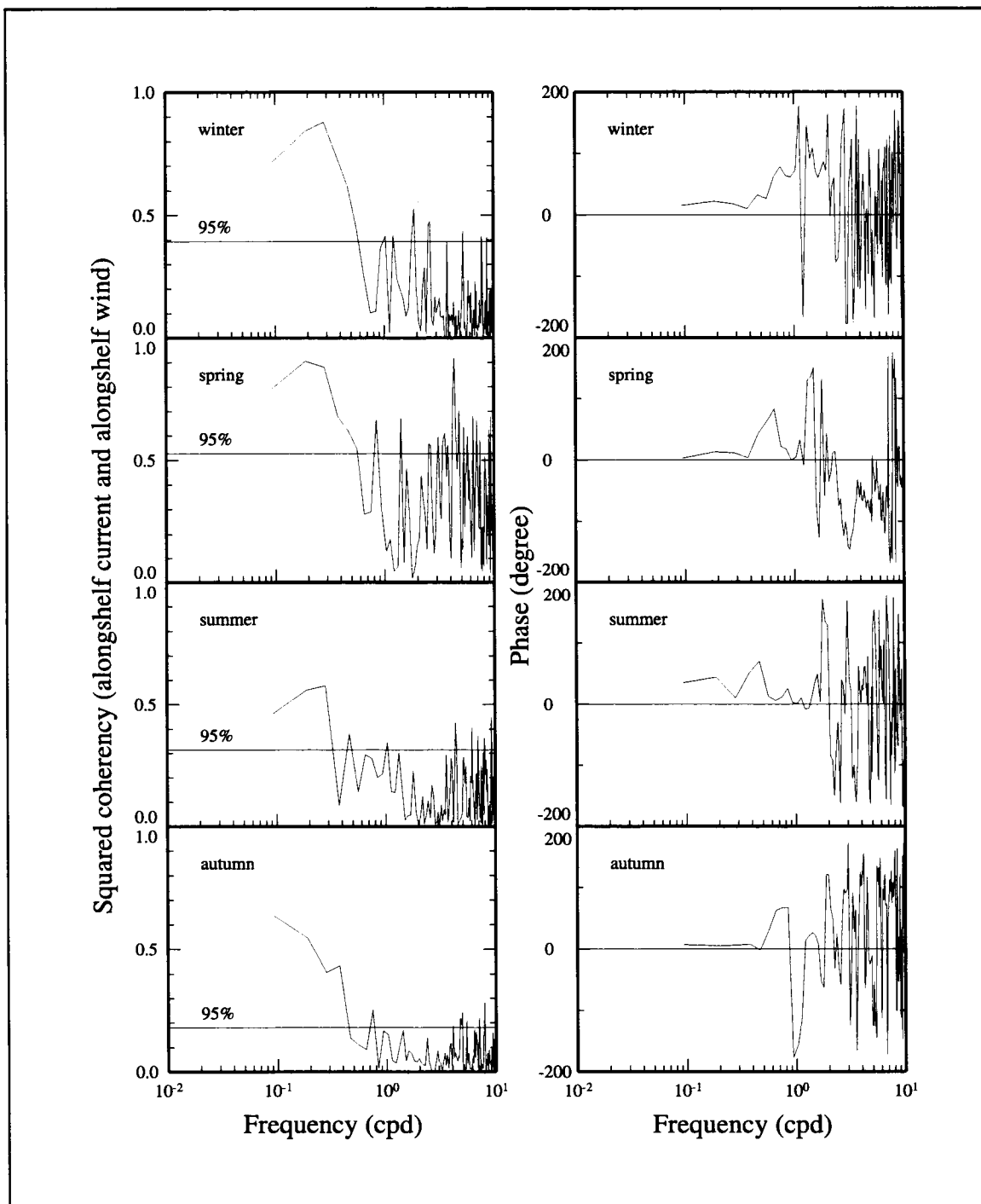


Figure 4.5-12. Squared coherency (left) and phase (right) between alongshelf current and alongshelf gridded wind by season at mooring 17. Positive phase indicates winds leading currents.

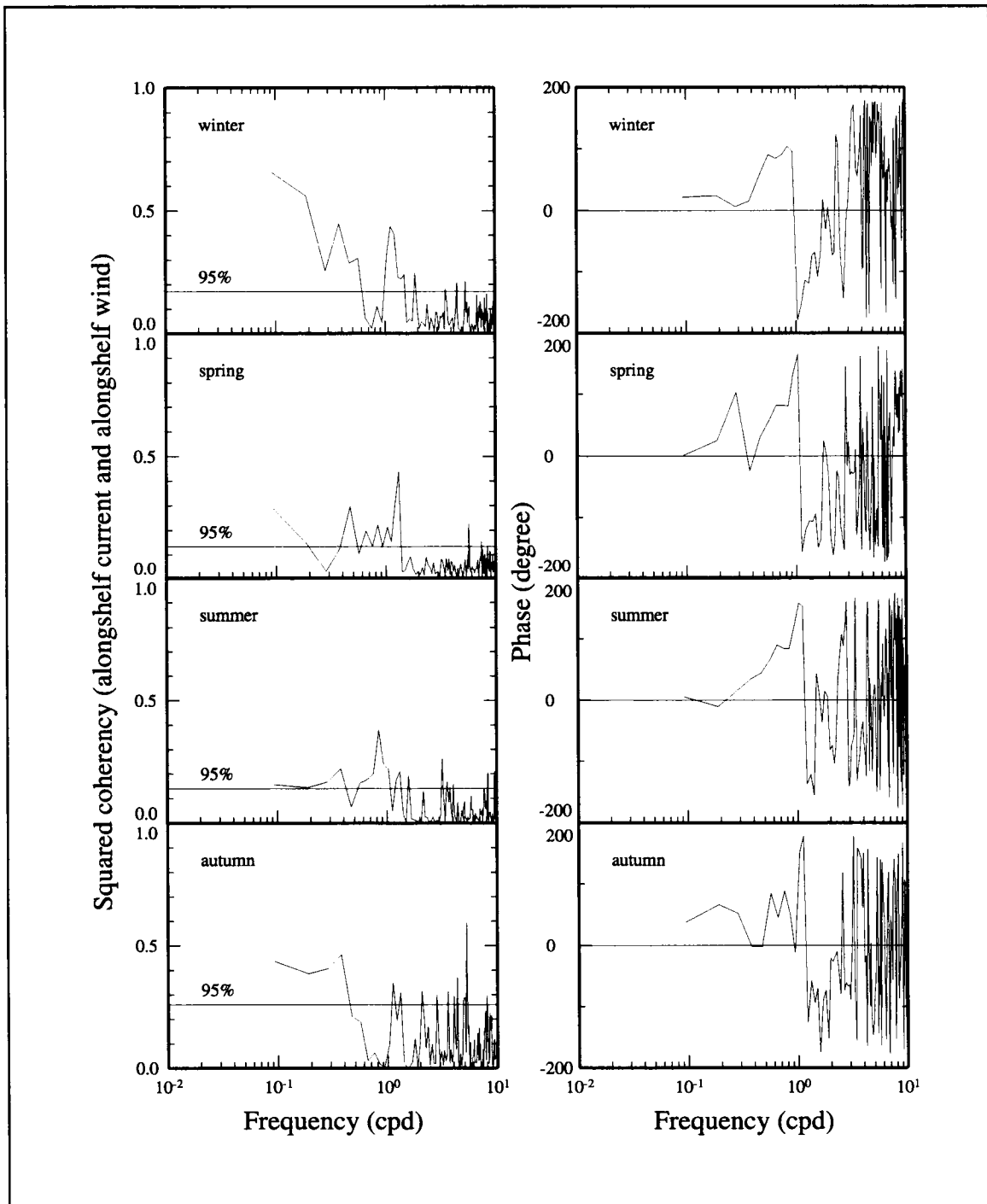


Figure 4.5-13. Squared coherency (left) and phase (right) between alongshelf current and alongshelf gridded wind by season at mooring 16. Positive phase indicates winds leading currents.

are more frequent frontal passages. The alongshelf current versus cross-shelf wind coherence is significant in the weather band during the nonsummer months when frontal passage frequencies are greatest. In the diurnal band significant coherence occurs in non-winter months and is coincident with strong stratification and thermally induced cycling.

4.6 General shelfwide circulation based on LATEX results

Introduction

As discussed in Section 4.2, the principal external forcing mechanisms for the general circulation over the Texas-Louisiana continental shelf are wind stress, buoyancy effects due to river discharge, and effects of the offshore circulation, i.e., the anticyclonic and cyclonic current rings found over the continental slope. Their effects and the relative importance of these mechanisms have been described on the basis of a model for the circulation over this shelf by Oey (1995).

Section 2 describes the wind and river discharge acting on this shelf and offshore eddies that were adjacent to the shelf during April 1992 through November 1994, the LATEX field period. Sections 3.1, 4.2, 4.3, 4.4, and Appendix H describe the general patterns of hydrography and circulation as measured during LATEX. Section 4.2 describes the seasonal patterns of general, shelfwide circulation based on a set of LATEX and historical data, and gives indications of interannual variability and its relation to the principal forcing functions.

Our intention in this section is to give an overview regarding the shelfwide circulation and its forcing mechanisms based on observations and analyses carried out during LATEX. The findings will be summarized at the end of this section. It will be seen that our results differ in several aspects from the CK schema of low-frequency, shelfwide circulation (described in Section 4.1) and that important new findings have been added.

In the upper panel of Figure 4.6-1 we show an example of the daily alongshelf component of wind from Victoria, Texas, a site located near the central part of the Texas-Louisiana coast. This was produced by averaging the 30-year record of winds at that location. The alongshelf component is generally downcoast except during a period in summer when it is upcoast. The early summer transition from downcoast to upcoast is characterized by numerous episodic reversals and generally occurs in June. Typically (based on 30-year records from coastal stations that we have examined) winds are upcoast during July and August and shift abruptly downcoast at the end of August. On average, they then remain downcoast from September through May. Also shown in the lower panel of Figure 4.6-1 is the annual cycle of daily winds during the period April 1992 through November 1994 averaged from six locations distributed along the 20-m isobath (see Figure 4.6-2 for locations). The pattern of alongshelf wind shift for this period is remarkably similar to the climatology of the upper panel although

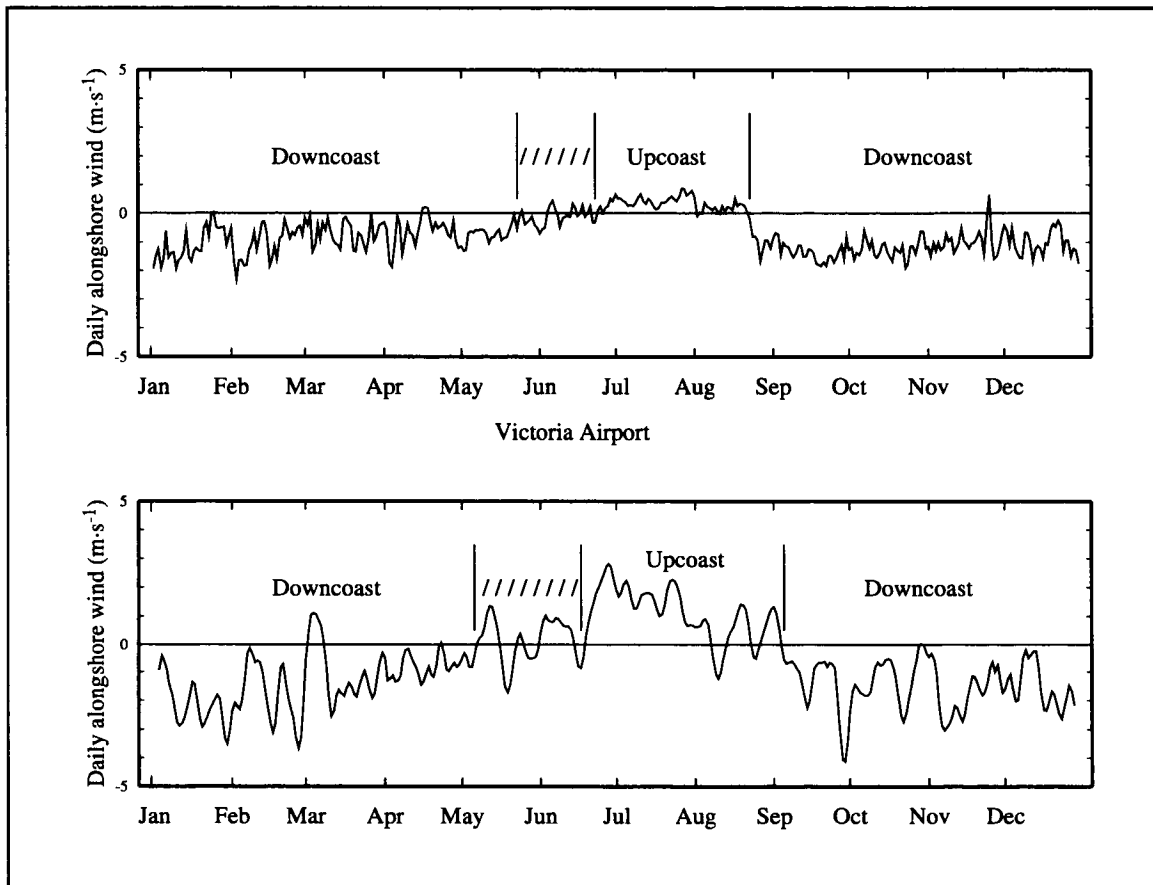


Figure 4.6-1. (Upper panel) 30-year average daily alongshelf wind component observed at Victoria, TX. Periods of dominant downcoast (tangent to general coast line in direction from Mississippi to Rio Grande rivers) and upcoast directions are indicated. (Lower panel) Daily average alongshelf wind during the period April 1992 through November 1994 estimated by the average from six locations along the 20-m isobath (see Figure 4.6-2 for locations). Positive values correspond to wind components directed upcoast (in sense from Mexico to the Mississippi Delta).

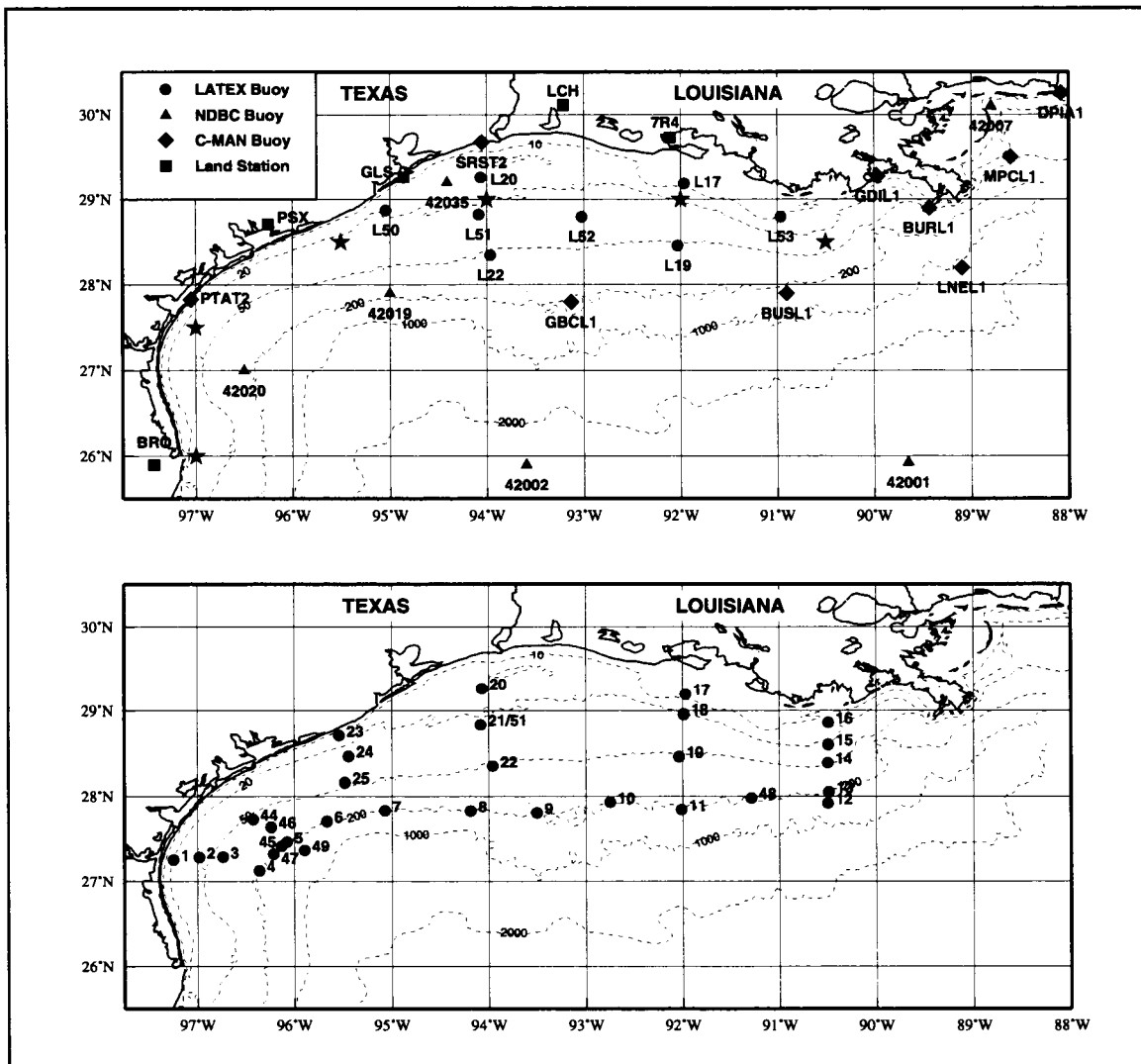


Figure 4.6-2. Locations of meteorological stations (upper panel) from which wind observations were available including gridded winds determined at locations shown by stars and of moorings (lower panel) from which current observations were available from April 1992 through November 1994.

the reversals are shifted in time, as discussed later in this section. We will present examples to illustrate that the average times of the reversals vary as a function of position along this coast. It should be noted that there are numerous short periods during which the alongshelf direction of the wind stress is reversed for several days relative to its average direction, and we have found that the response of the coastal flow to such reversals is quite rapid (less than 24 hours).

In response to this temporal pattern of alongshelf wind stress, CK proposed that ocean currents over the inner shelf should be downcoast from September through May, transition to upcoast in June, and remain upcoast during July and August. This pattern was substantiated by their study based on hydrographic data collected in 1963-1965 aboard the R/V GUS III and limited current observations. Based on direct current measurements made as part of the LATEX study, we have substantiated this wind effect and subsequent flow pattern over the inner Texas-Louisiana shelf.

CK acknowledge the effects of river discharge on the salinity distributions, especially over the inner shelf. We describe the spreading of Mississippi-Atchafalaya river discharge in relation to the circulation and wind regime. Buoyancy effects (changes in vertical stability and geopotential anomaly) of river discharge on the shelf circulation also are illustrated; increase in river discharge enhances the downcoast shear flow over the inner shelf in the presence of downcoast winds favorable for the alongshelf distribution of the fresher water. Li et al. (1996; Section 4.2) demonstrate that interannual highs in geopotential anomaly over this shelf result principally from anomalously low salinity.

The effects of offshore rings are to be seen in our hydrographic fields and our monthly current meter fields and their averages. These are illustrated in Sections 2.5, 4.2, and 4.4 and Appendix H. We further illustrate such effects using currents measured at the shelf edge and a series of maps of sea surface height anomaly covering the region of the outer shelf and continental slope.

Monthly to seasonal variability of shelfwide circulation and hydrography

Monthly averaged horizontal currents at 10 m and at mid-depth or bottom. In Figure 4.6-2 are shown the locations of moored current meters from which fields of horizontal currents were constructed and the locations of meteorological observations from which fields of surface wind and wind stress were constructed for the period April 1992 through November 1994 (see Section 2.1.1 for details). For each month of the observation period at each observing site, vector averages of the currents at each observation depth were produced, provided there were at least ten days of data. For moorings inside the 50-m isobath, two current meters were deployed on each mooring, located near 10 m beneath the sea surface and near the bottom. Moorings in water depths of 50 m or more had three current meters—

the third located at mid-depth. Monthly averaged current vectors for the 10-m and bottom or mid-depth (where available) instruments are shown in Figure 4.6-3 for 1992-1994. Thus the deeper of the vectors are from depths ranging from about 15 m inshore to about 200 m at the shelf break.

There is a general agreement in direction between the 10-m and deeper current vectors pictured in Figures 4.6-3, although there are some large differences. (Vertical structure is further described in Section 4.4.3; differences in direction are addressed further in Section 2.5.2.) The deeper current vectors generally are smaller, as might be expected, with notable exceptions over the eastern shelf edge—especially in late summer and fall of 1992, February 1993, and late spring and early summer of 1994.

Examining currents over the outer shelf (depths greater than 50 m), the largest monthly mean vectors occurred near the shelf edge, especially from about 94° to 96°W. These resulted from a series of anticyclonic rings, separated from the Loop Current in the eastern Gulf of Mexico, impinging on the slope and shelf edge in that location, and occasionally east of 93°W, during the period of the observations.

CK inferred upcoast flow at the shelf edge from their monthly averaged distributions of geopotential anomaly. The shelf edge array of LATEX A current meter moorings were spaced about 90 km apart along the 200-m isobath. It seems clear from Figure 4.6-3 that the monthly averaged currents along the outer shelf edge were not often in the same general direction (either upcoast or downcoast). The dominant areas of high-speed, upcoast flow are associated with anticyclonic rings which are found at different locations along the shelf edge at different times. This gives rise to large interannual variability; compare 1994 when rings were largely absent with the other two years. (When the 10-m current fields are gridded and averaged over longer periods; e.g., over all nonsummer months, a consistent upcoast flow at the shelf edge emerges.)

Monthly currents over the inner shelf (water depths less than 50 m) were downcoast in nonsummer months (September through May); they were upcoast in summer. By far the strongest monthly mean downcoast currents appear nearshore and along the central to south Texas coast.

The lack of an organized upcoast flow along the outer shelf edge is confirmed by five other analyses presented in this report. (1) The monthly velocity streamfunction fields and their principal EOFs (Sections 4.4.1 and 4.4.2) do not show regular upcoast flow over the outer shelf in nonsummer as do CK. (2) The analysis for annual, including seasonal, signals in the current records (Section 4.3.2) shows that bimodal patterns of monthly currents seen over the inner shelf are not present over the outer shelf. (3) Objectively gridded fields of monthly currents (Appendix H.2) merely show more clearly the patterns of Figure 4.6-3. (4) Twelve

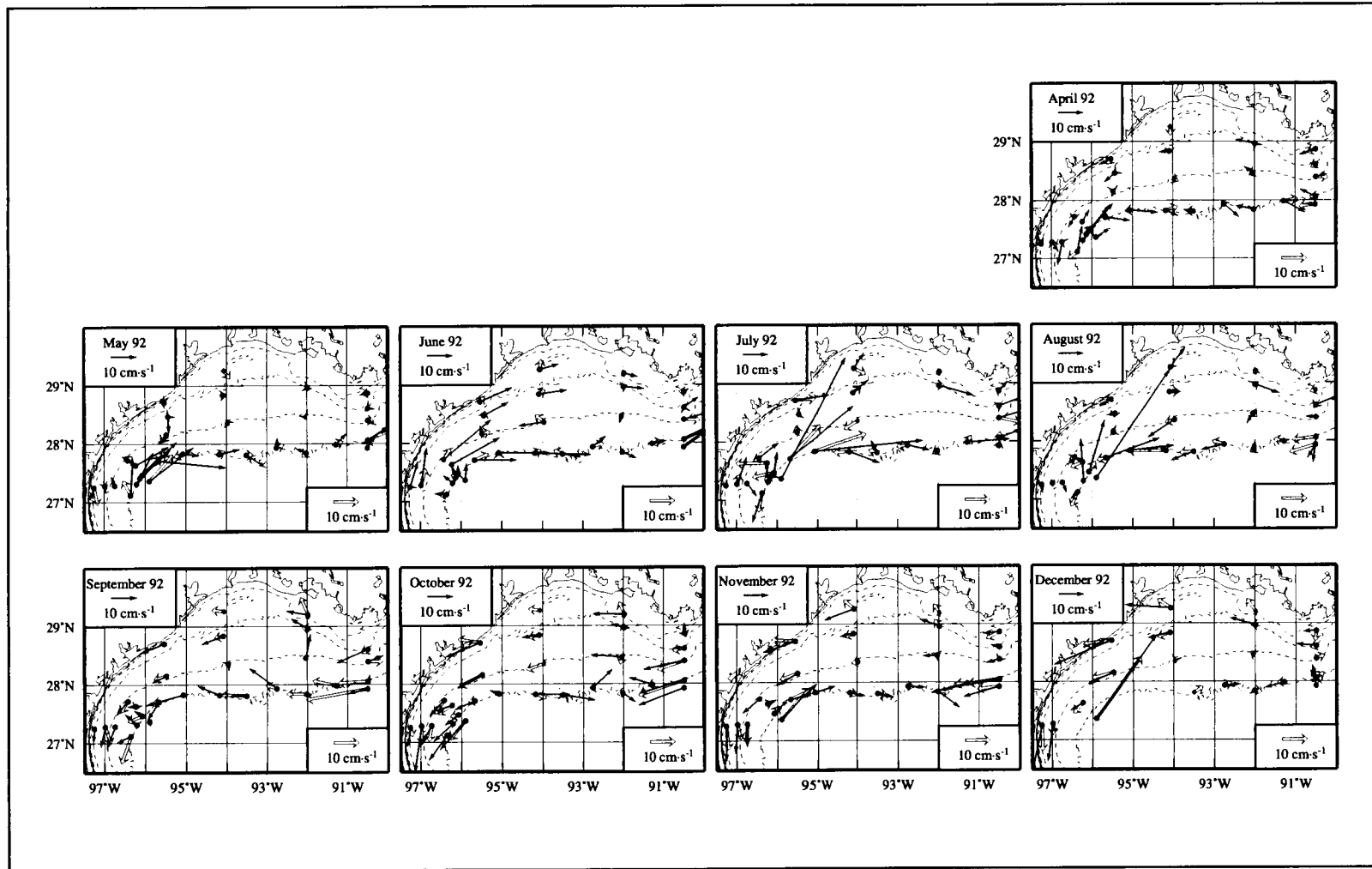


Figure 4.6-3a. Monthly averaged current vectors for 10-m instruments (thin arrows) and for mid-depth or near-bottom instruments (wide arrows) for 1992. Beginning inshore, isobaths are shown for 10, 20, 50, and 200 m.

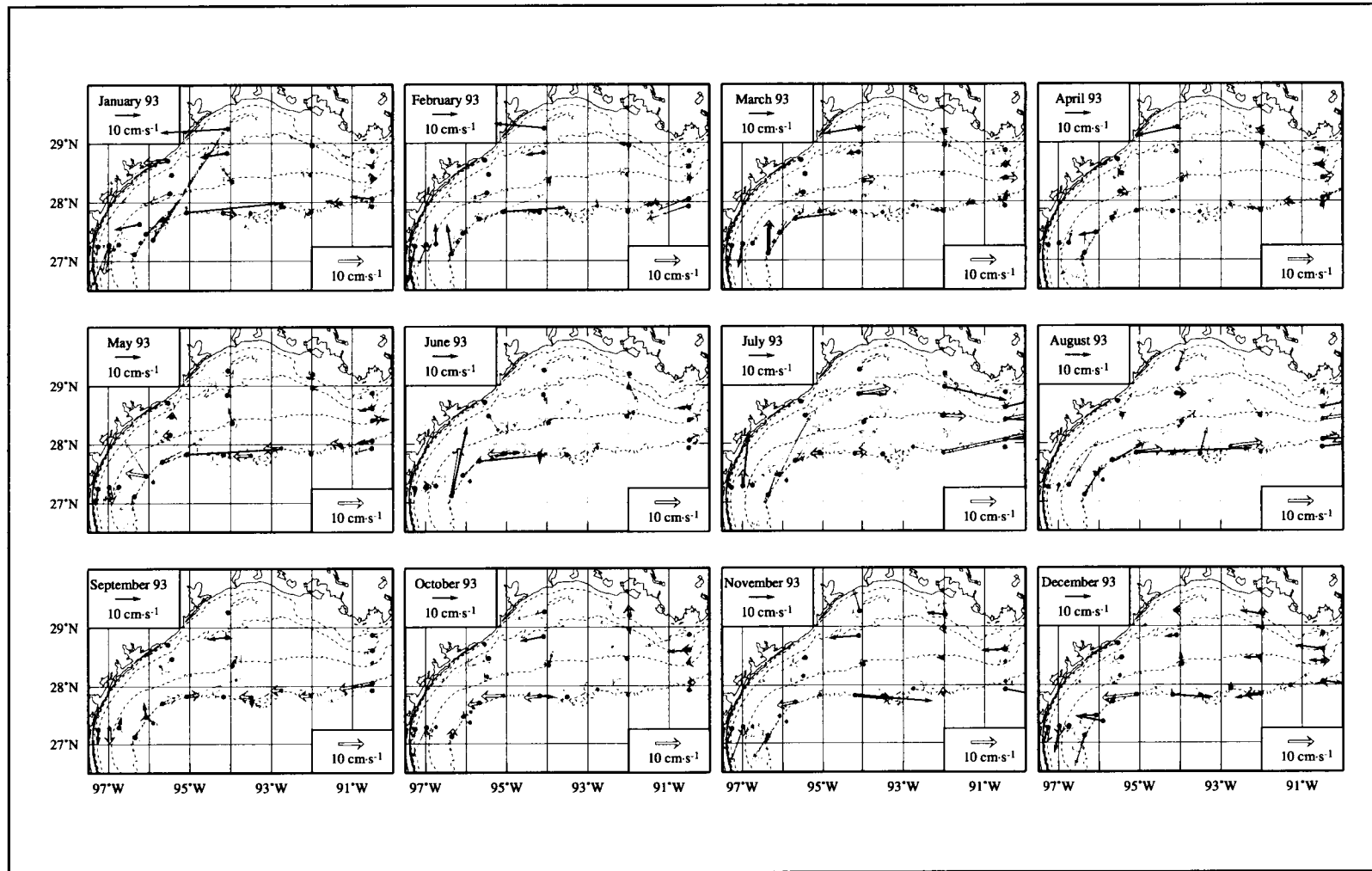


Figure 4.6-3b. Monthly averaged current vectors for 10-m instruments (thin arrows) and for mid-depth or near-bottom instruments (wide arrows) for 1993. Beginning inshore, isobaths are shown for 10, 20, 50, and 200 m.

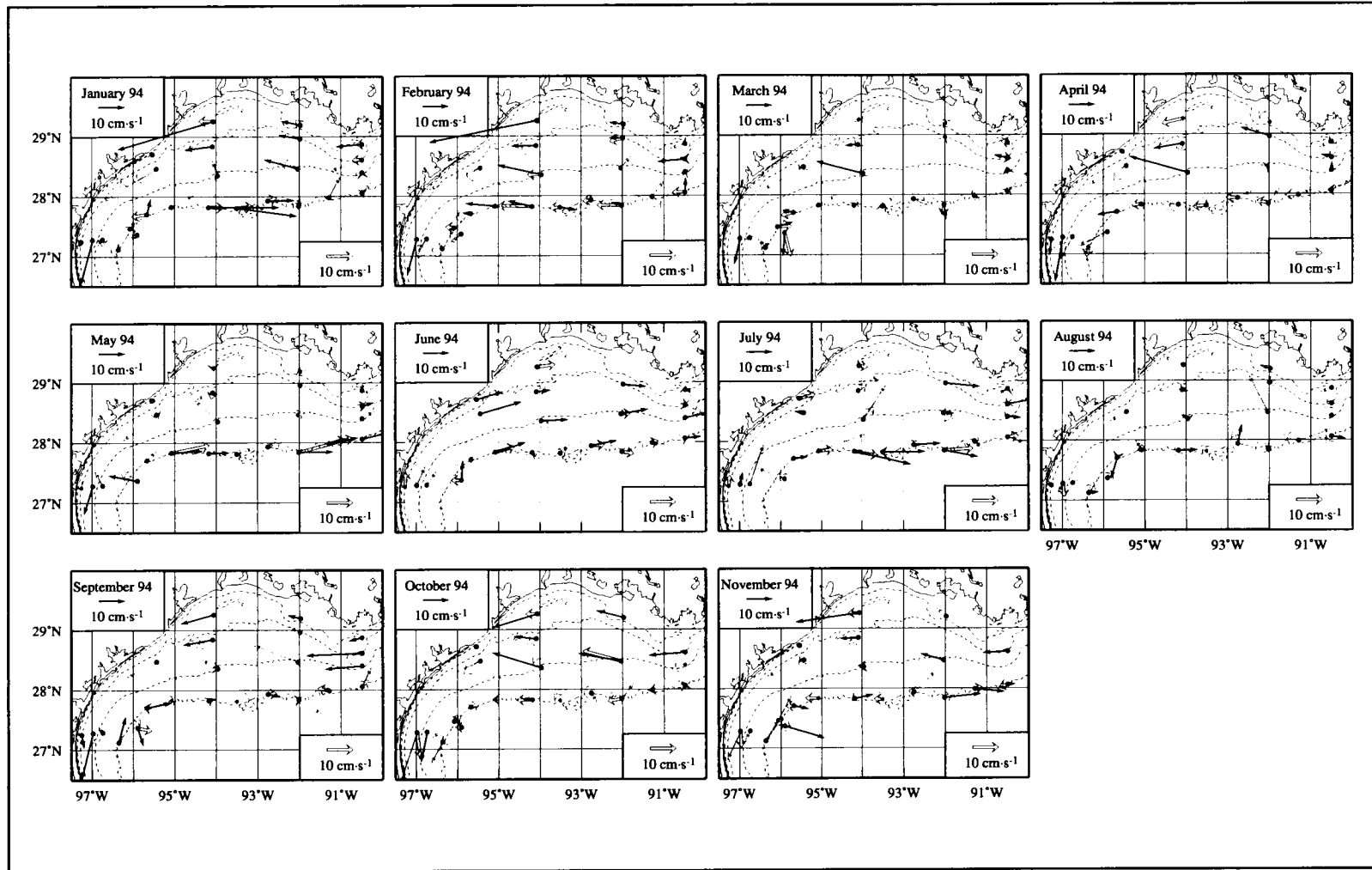


Figure 4.6-3c. Monthly averaged current vectors for 10-m instruments (thin arrows) and for mid-depth or near-bottom instruments (wide arrows) for 1994. Beginning inshore, isobaths are shown for 10, 20, 50, and 200 m.

fields of geopotential anomaly constructed from LATEX A, LATEX C, and GulfCet data (Appendix H.1) may be taken to infer clearly the predominant effects of offshore eddies on the shelf edge circulation and that such circulation is no regular function of season. (5) Examination of the influence of Loop Current eddies on the monthly average currents at the shelf edge (Section 2.5.2) clearly shows that the circulation there responds to the presence of eddies adjacent to the shelf edge.

An important feature to note in the monthly currents (Figure 4.6-3 and Appendix H.2) is the relatively large cross-isobath flow that occurs over the outer shelf. In some cases large cross-shelf flow extends shoreward past the 50-m isobath.

It is natural to inquire regarding the response of the deeper circulation relative to that at the 10-m level. Qualitative comparison of vertical structure of seasonal currents was presented in Section 4.4.3. We performed quantitative estimates of vertical current response for shorter periods. We used 3-hr low-passed records sampled hourly to calculate coherence and phase between the currents at 10 m and those at deeper levels for a representative set of current meter moorings. Moorings were chosen that had relatively long unbroken time series and that represented the inner (near 20-m depth), mid (near 50-m depth), and outer (near 200-m depth) regions of the western, central, and eastern shelf: moorings 2, 3, and 4 in the west; 21, 22, and 8 near 94°W, and 16, 14, and 13 along approximately 90.5°W. (See Figure 4.6-2 for mooring positions.)

We chose the longest continuous records from those moorings and subdivided them into 42-day segments to increase confidence in the results. The number of segments available ranged from 5 to 16. This allows examination of vertical current coherence for periods through the weather band. As shown in Section 2.1.3, frontal passages occur over the Texas-Louisiana shelf on average about every seven days during September-May but only every one to two months during June-August. The current records examined here included segments from all seasons.

Based on these calculations, 10-m currents at the inner shelf mooring 2 and mooring 3 just offshore from the 50-m isobath were coherent at the 95% significance level with deeper currents for periods greater than about 2 days (Table 4.6-1). This also was the case for alongshelf components at inner shelf moorings 21 and 16, but the cross-shelf components there showed little coherence. At moorings 22 and 14 located near the 50-m isobath the alongshelf components between 10-m and mid-depth currents were coherent for periods greater than 2.5 to 3 days; bottom and mid-depth currents were coherent for periods greater than 4 to 6 days. Along the 200-m isobath, 10-m currents were coherent with those at mid-depth for periods greater than 4 to 10 days, with one exception; bottom and mid-depth current components were not coherent.

Table 4.6-1. Period ranges for which currents on the same moorings were coherent at the 95% significance level.

	27.3°N	94°W	90.5°W
<i>Nearshore Moorings</i>	2	21	16
U B-T	> 2.3 d	> 1.7 d	>2 d
V B-T	> 2 d	> 8 d	2-7 d; > 19 d
<i>Mid-shelf Moorings</i>	3	22	14
U M-T	> 1.8 d	> 2.5 d	> 2.9 d
V M-T	> 1.8 d	> 12.5 d	> 3.1 d
U B-M	> 2 d	> 4 d	> 4.9 d
V B-M	> 2 d	no	> 4.2 d
U B-T	> 2 d		> 4.8 d
V B-T	> 2.2 d		> .6 d
<i>Shelf-edge Moorings</i>	4	8	13
U M-T	> 10 d	> 9 d	> 4 d
V M-T	> 11 d	> 4 d; phase not stable for > 15 d	no
U B-M	2-11 d	no	> 4.5 d
V B-M	2-11 d	no	no
U B-T	no	no	no
V B-T	no	no	no

We may conclude that over the inner shelf alongshelf currents are coherent throughout the water column for subinertial periods but cross-shelf currents are more coherent in depth downcoast than upcoast. Also, alongshelf currents at locations from the 50-m isobath to the shelf edge are coherent down to depths of about 100 m for periods of order 5-10 days and longer. Thus, we may take the surface (10-m) currents as representative of the response of the alongshelf flow over the inner shelf to subinertial forcing.

Seasonal patterns of geopotential anomaly and surface salinity. For hydrographic cruises with good quality data and covering major portions of the Texas-Louisiana shelf, Li et al. (1996; Section 4.2) constructed mean distributions of temperature, salinity, and geopotential anomaly relative to 70 db representing the spring, summer, and fall seasons. Figure 4.6-4 shows their distribution of surface salinity for November, May, and July-August.

The effect of upcoast flow is seen in the surface salinity pattern for summer. Salinities greater than 36 extend across the shelf as far upcoast as central Texas. As Li et al. (1996;

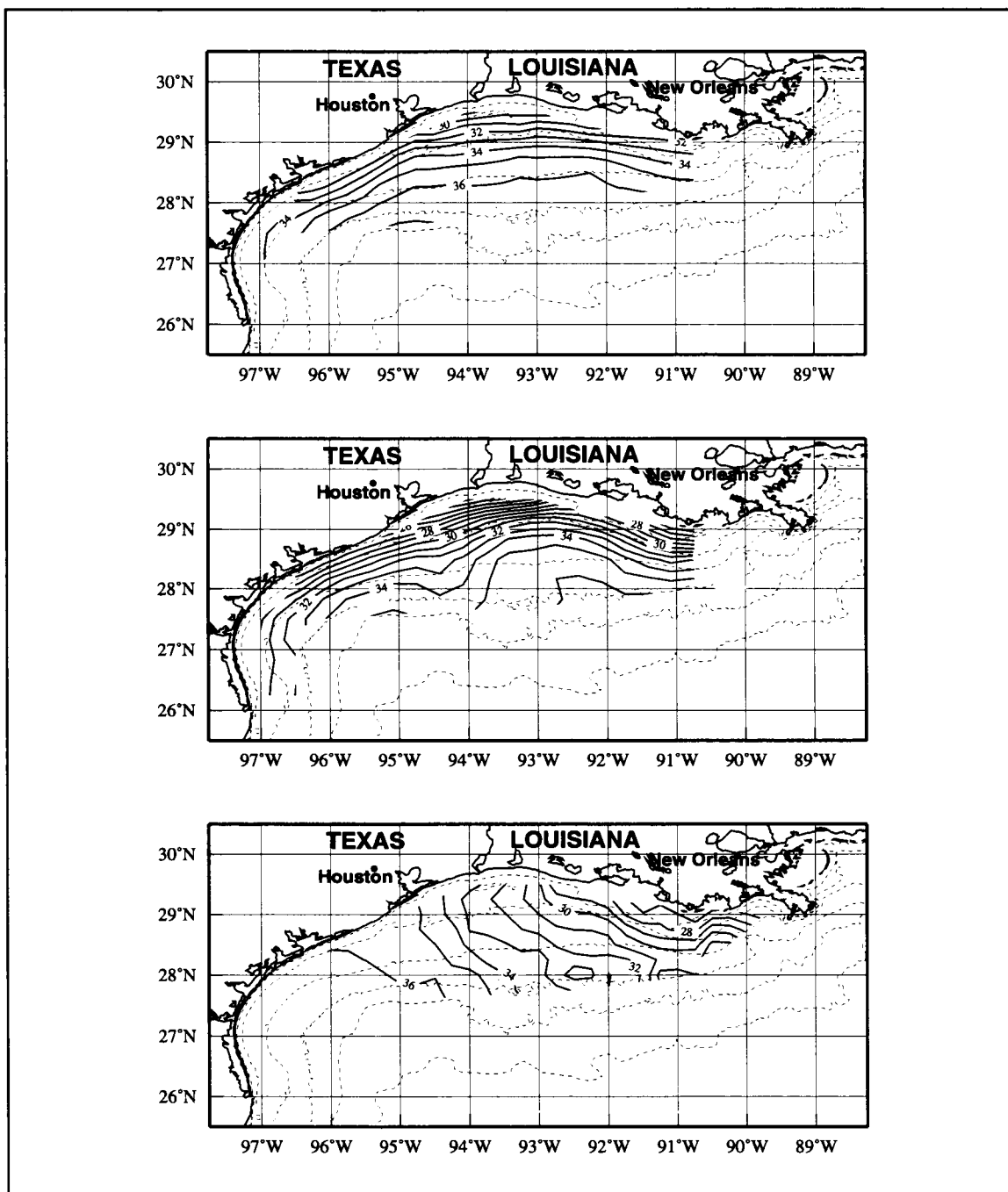


Figure 4.6-4. Average sea surface salinity in fall (upper) for six November cruises, in spring (middle) for ten May cruises, and in summer (lower) for nine July-August cruises.

Section 4.2) found, these high salinities extend through the water column. By contrast with summer, the average fall and spring distributions are consonant with downcoast flow transporting relatively fresh water influenced by the Mississippi and Atchafalaya rivers over the inner shelf.

In Figure 4.6-5 are shown average distributions of surface geopotential anomaly relative to 200 db based on data from the seven LATEX A nonsummer cruises and the three summer cruises. Also shown with the appropriate averages are the 10-m current vectors averaged over the months September-May (nonsummer) and June-August (summer) of the period April 1992 through November 1994.

The distribution of geopotential anomaly and average currents for the average nonsummer period (Figure 4.6-5 upper panel) clearly indicate downcoast flow over the inner shelf. The average currents inside the 50-m isobath are nearly along isobaths, with stronger currents offshore Texas than off Louisiana. Relatively good agreement is seen between circulation inferred from the geopotential anomaly field and measured currents. The effects of the frequent occurrence of anticyclonic rings off the shelf edge near 95°W are clearly seen. One wonders whether there would be the impression of open cyclonic flow over the eastern outer shelf, if such ring effects were absent.

The summer averaged 10-m currents from the LATEX A data (Figure 4.6-5 lower panel) show generally upcoast flow over the inner shelf. That is supported by the average geopotential anomaly distribution except over the central (93° to 95°W) inner shelf where there is considerable disagreement. The cross-isobath orientation of geopotential anomaly in that region doubtless results from large along-isobath variation in density. The along-isobath density variation results because high salinity water is being moved upcoast by the prevailing upcoast currents over the inner shelf during summer, resulting in an alongshelf salinity gradient. In that situation, the method (of Montgomery and Csanady) used here and by Li et al (1996) to construct geopotential anomaly fields over sloping bathymetry may not represent the geostrophic shear because they do not account for pycnoclinal currents (Sheng and Thompson 1996). Thus, we prefer to accept the direct measurements as more representative of the average. As mentioned before, the upcoast flow is substantiated by the distribution of salinity during the summer (Figure 4.6-4). We return to this matter later in this section.

As in nonsummer, the average summer currents over the outer shelf are influenced strongly by the presence of rings over the slope. When viewed in detail, the measured currents agree well with currents inferred from the geopotential anomaly for the outer shelf. The geopotential anomaly pattern shows a considerably more complicated pattern, with features of smaller scale than can be resolved by the spacing of the current meters. A continuous eastward flow at the outer shelf edge is not indicated in either season.

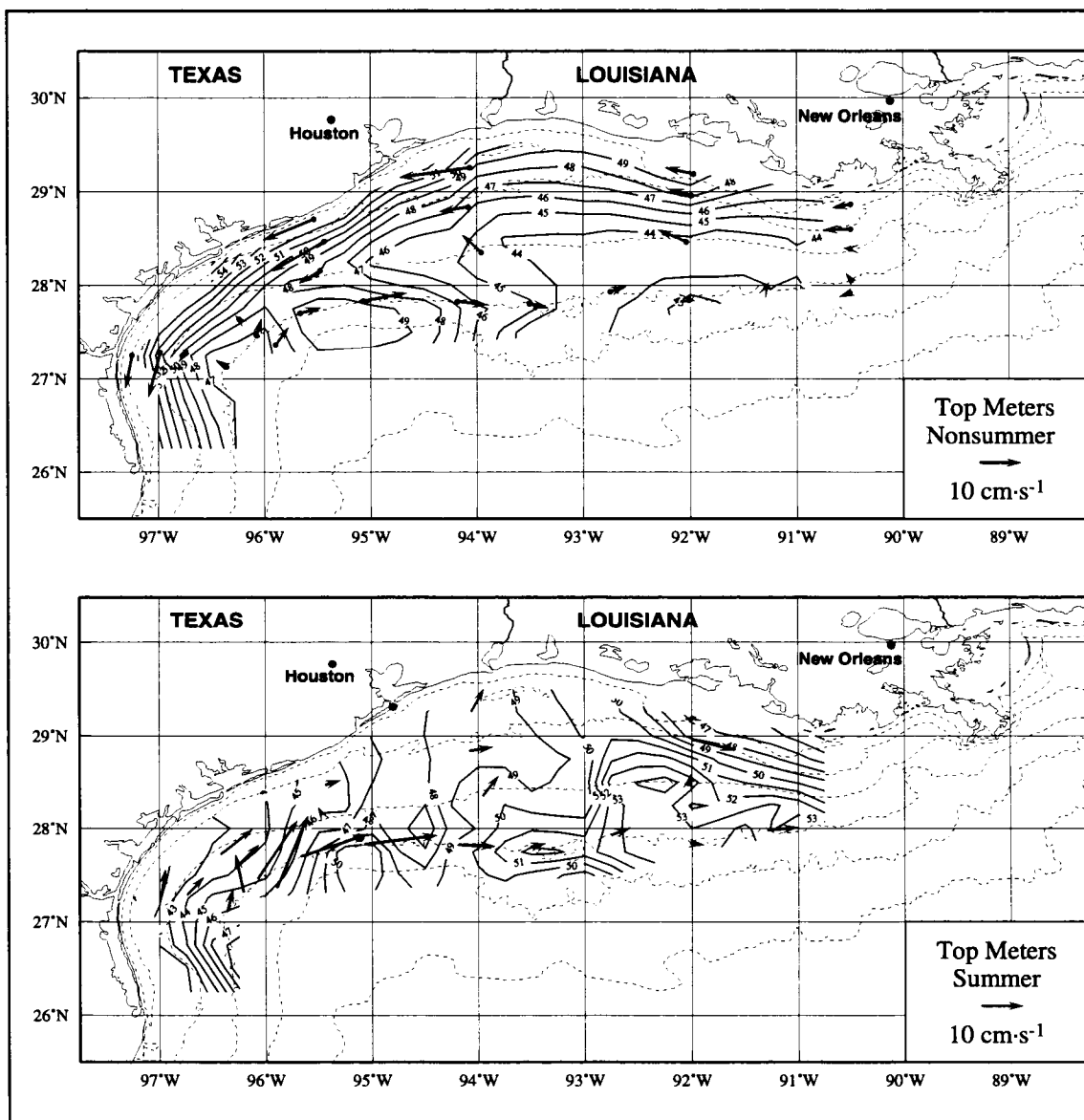


Figure 4.6-5. Average surface geopotential anomaly relative to 200 db based on the seven LATEX A nonsummer cruises (upper) and on the three summer cruises (lower). The 10-m current vectors averaged over the months September-May and June-August of the period April 1992 through November 1994 also are shown.

Wind forcing and response over the inner shelf

Monthly distributions of 10-m currents in relation to those of surface wind stress. The monthly averaged 10-m currents and surface wind stress (provided there were at least ten days of data) are shown in Figure 4.6-6 for 1992-1994 for all current meter moorings and for the meteorological buoys and platforms shown in Figure 4.6-2.

Monthly averaged wind stress vectors are seen to have downcoast components for all months other than June, July, and August. Nearshore winds have upcoast components for at least two months of that period: for June and July in 1992, for July and August in 1993, and for June and July in 1994. In June 1993 and August 1994 winds were essentially onshore. The direction of alongshelf flow over the inner shelf (depths less than 50 m) conformed to the direction of the alongshelf wind component; flow was downcoast in months other than June through August. For summer the flow was upcoast in months when the mean alongshelf wind was upcoast (particularly over the southern region of the shelf) and somewhat mixed in months when the mean wind was onshore.

As noted before there are large year-to-year differences in the current regime, particularly over the outer shelf. There is also year-to-year variation in the time of transition from downcoast to upcoast flow over the inner shelf.

Bimodal annual pattern of alongshelf wind forcing. Using the LATEX analyzed wind fields for this shelf (Section 2.1.1), we examined how the annual pattern of alongshelf wind component varied spatially along the shelf. The annual cycle of daily mean alongshelf wind stress component constructed from these analyzed fields are shown in Figure 4.6-7a for six locations along the 20-m isobath. The six locations are shown in Figure 4.6-2. For comparison, we show in Figure 4.6-7b annual cycles of daily mean alongshelf wind stress components constructed using long-term (30- to 46-yr) records from five airport stations distributed along the Texas and Louisiana coastal plain between Brownsville and Lake Charles.

Clearly seen in both series of annual cycles is a systematic difference in the length of the period and the strength of upcoast winds as a function of location along the coast. The time of the average transition from downcoast to upcoast wind stress component occurs earliest in the year along the south Texas coast and is progressively later as one moves upcoast toward the Mississippi Delta. However, the time of transition from summer to nonsummer regime appears to remain nearly fixed in time, near the end of August, independent of location. Finally, it should be noted that the strength of upcoast winds decreased dramatically with increasing distance upcoast from Mexico. There is little clear transition off Louisiana.

The patterns for the LATEX period (Figure 4.6-7a) appear to be typical of the longer-term climatology of Figure 4.6-7b. Averaging the alongshelf wind stress cycles in Figure 4.6-7a

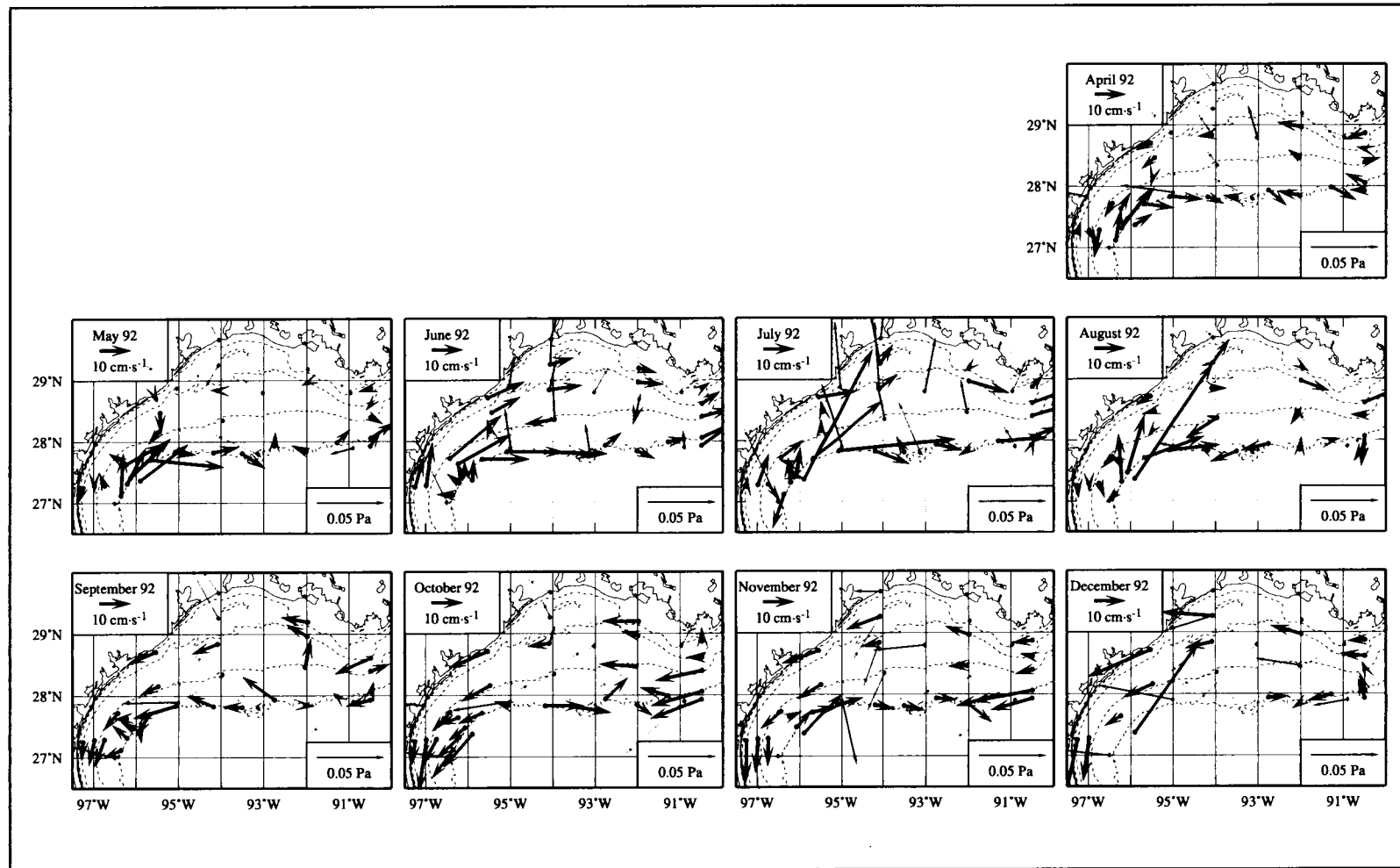


Figure 4.6-6a. Monthly averaged 10-m current vectors (heavy arrows) and surface wind stress vectors for 1992 at current meter moorings and offshore meteorological sites shown in Figure 4.6-2. Beginning inshore, isobaths are shown for 10, 20, 50, and 200 m.

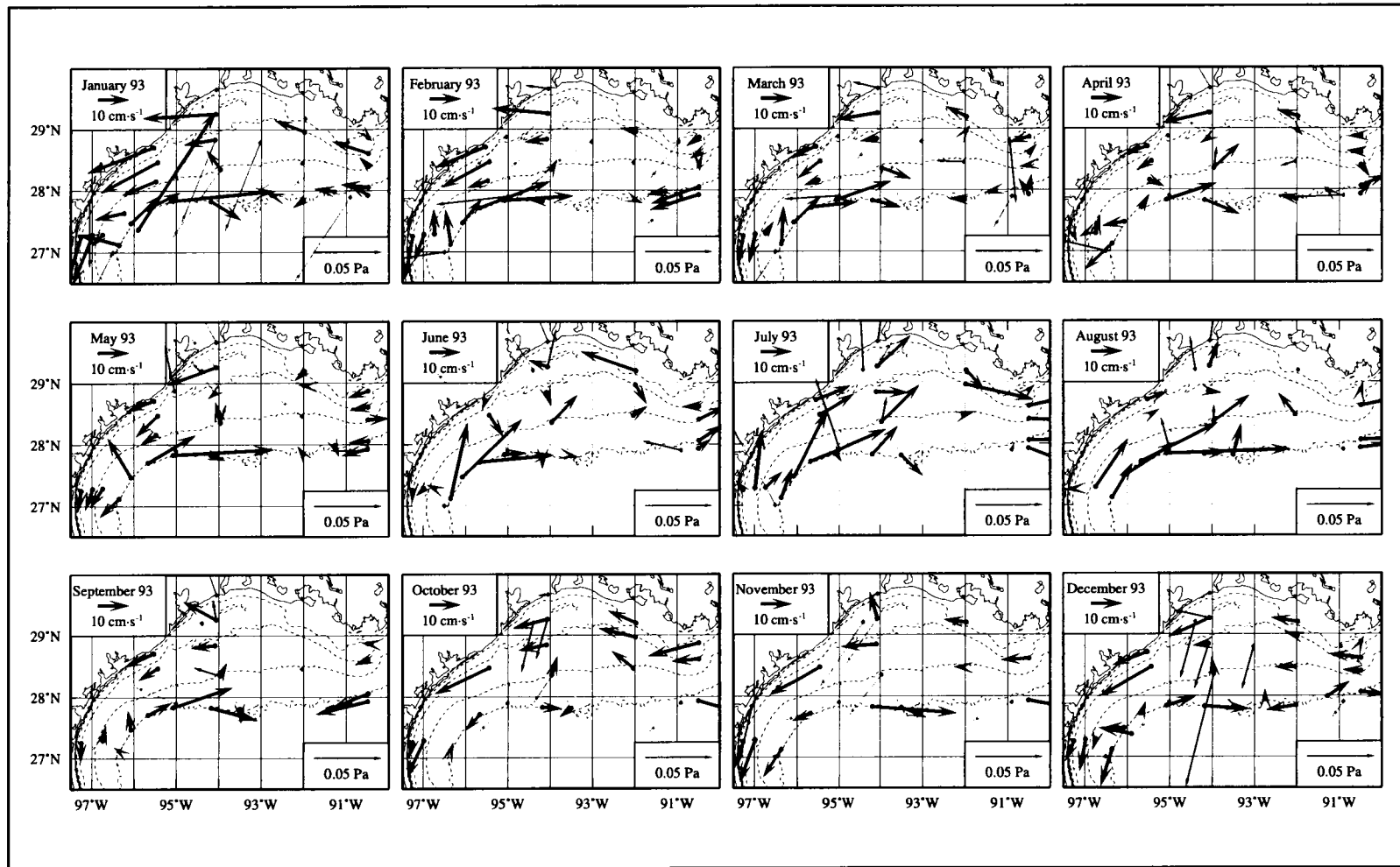


Figure 4.6-6b. Monthly averaged 10-m current vectors (heavy arrows) and surface wind stress vectors for 1993 at current meter moorings and offshore meteorological sites shown in Figure 4.6-2. Beginning inshore, isobaths are shown for 10, 20, 50, and 200 m.

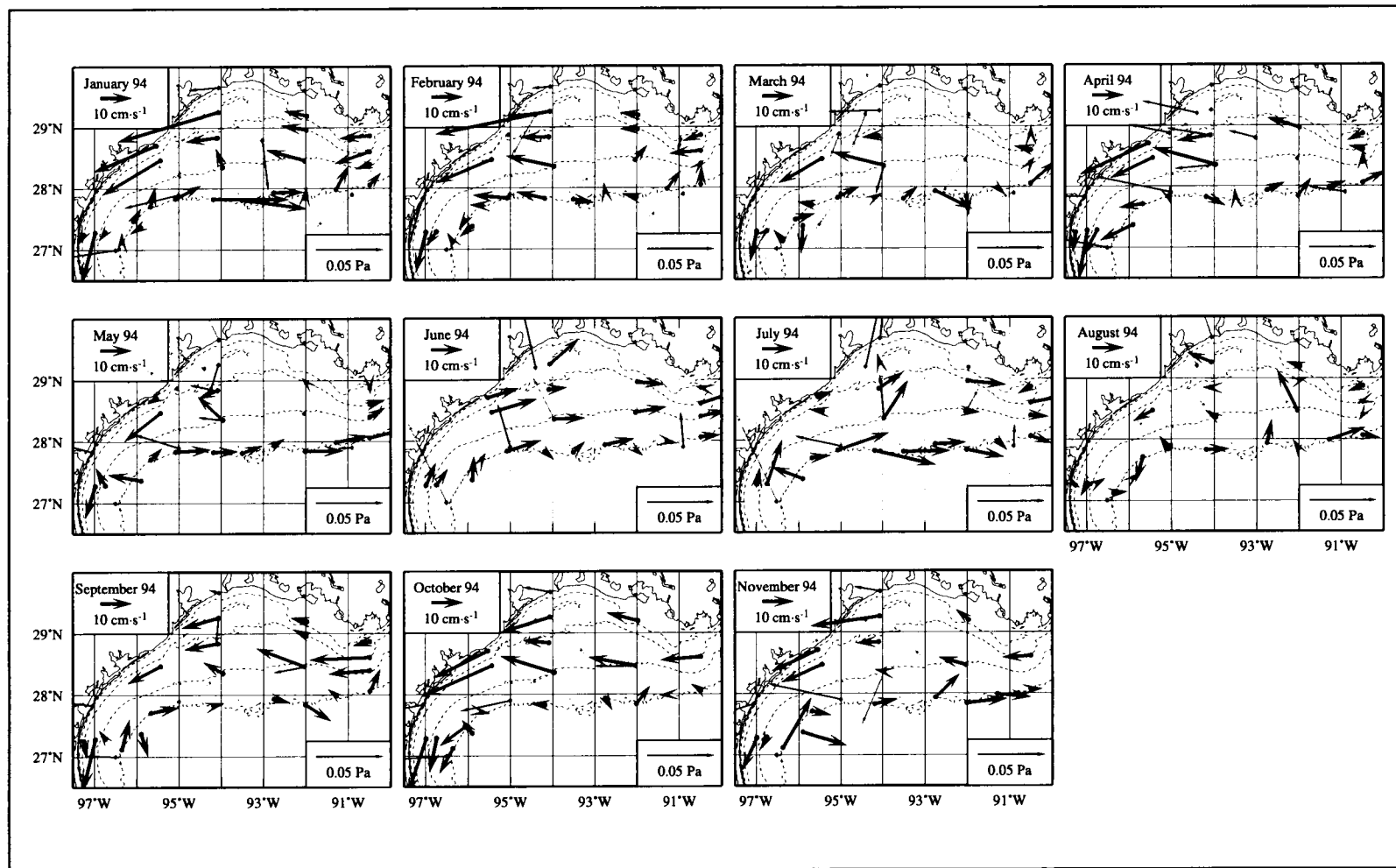


Figure 4.6-6c. Monthly averaged 10-m current vectors (heavy arrows) and surface wind stress vectors for 1994 at current meter moorings and offshore meteorological sites shown in Figure 4.6-2. Beginning inshore, isobaths are shown for 10, 20, 50, and 200 m.

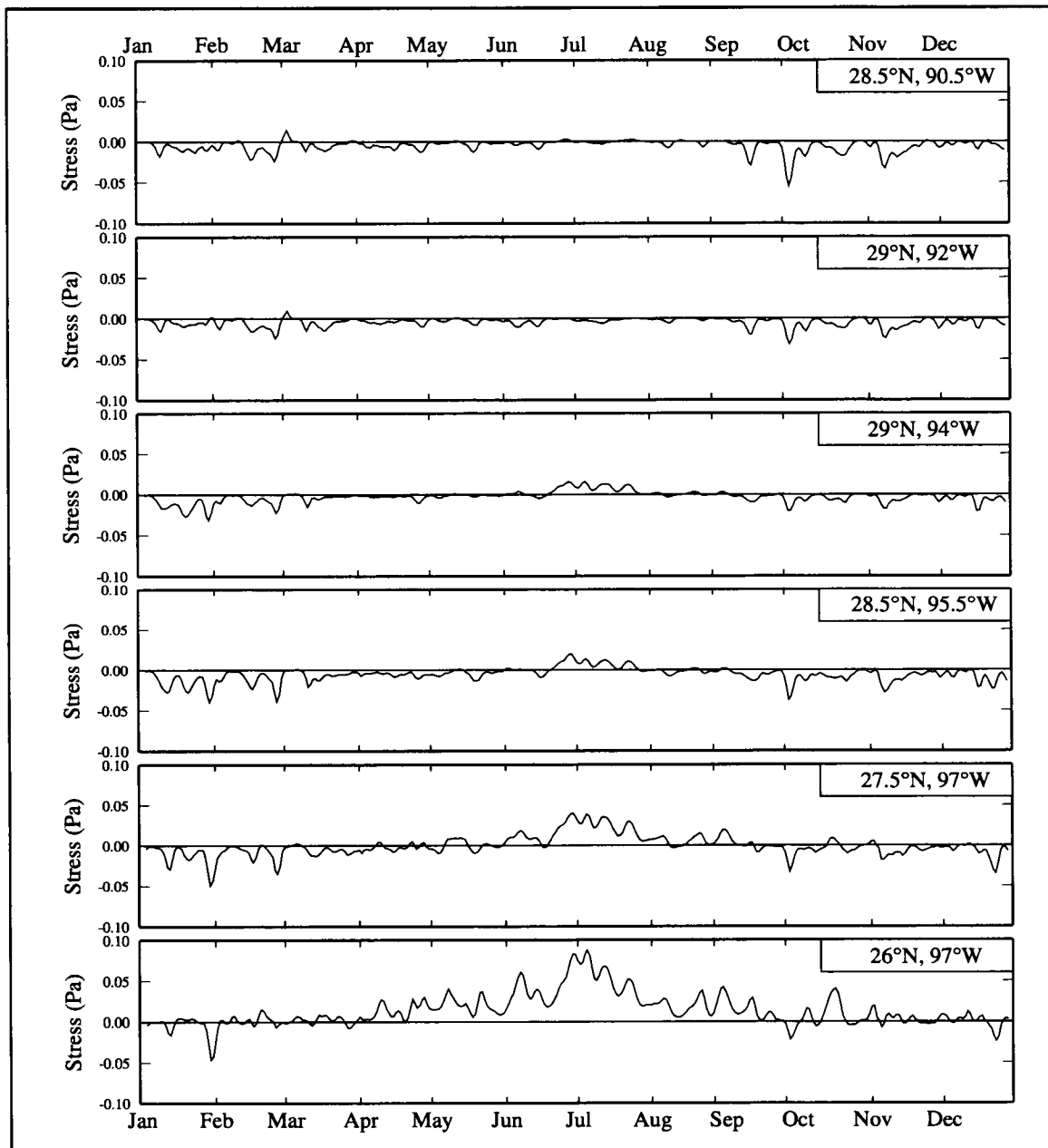


Figure 4.6-7a. The annual cycle of daily mean alongshelf wind stress components for six locations along the 20-m isobath. The six locations are shown in Figure 4.6-2. The wind components were taken from the hourly analyzed wind fields for the northwest Gulf of Mexico produced by Wang (1996) for the period April 1992 through November 1994.

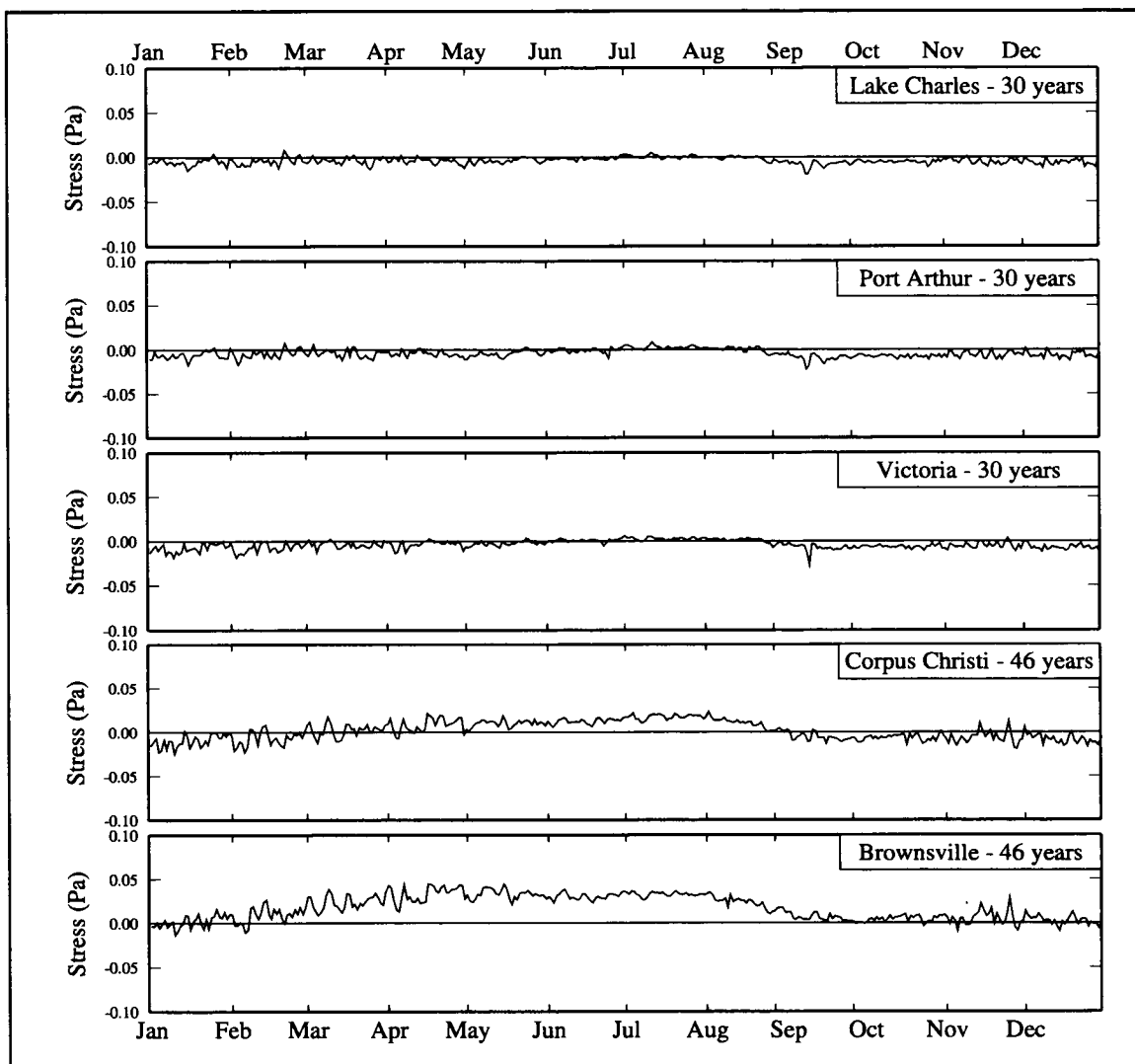


Figure 4.6-7b. The annual cycle of daily mean alongshelf wind stress components constructed from long-term (30-year) records from airport stations located, from north to south along the Texas and Louisiana coastal plains, at: Lake Charles, Port Arthur, Victoria, Corpus Christi, and Brownsville.

from the six offshore locations gives a spatially averaged cycle that closely resembles the long-term annual cycle for the central Texas coastal plain (Figure 4.6-1). Again the similarity is striking, but on average the late spring transition from downcoast to upcoast occurred earlier during the LATEX period than in the climatology.

For comparison with the winds in Figure 4.6-7a, Figure 4.6-8 shows average daily alongshelf components of 10-m current over the period April 1992 through November 1994 from five moorings located near the 20-m isobath (see Figure 4.6-2 for locations). Also shown is the series of daily values obtained by averaging the components at the six locations. The average current series was constructed by applying a five-point filter (weights 1/9, 2/9, 3/9, 2/9, 1/9) to the series shown at the five mooring locations.

To examine the average relationship between alongshelf wind and current components for the LATEX period, we constructed an annual series of daily averages for each (Figure 4.6-9). The wind series was constructed by applying to the series of daily wind components averaged at six stations along the 20-m isobath (shown in the lower panel of Figure 4.6-1) the same filter used to prepare the average of the current time series shown in the lower panel of Figure 4.6-8. That time series is repeated in Figure 4.6-9. Thus both series represent spatial averages along the 20-m isobath offshore Texas and Louisiana for the LATEX period. The two series are remarkably similar, with a maximum cross correlation of 0.89 at zero lag, indicating a close correspondence between the alongshelf wind and current components over the LATEX period.

Correlation between alongshelf wind and current. *Monthly transition of flow over inner shelf.* There is a clear relationship between the upcoast-downcoast transition in monthly mean wind fields and ocean currents over the inner shelf. As an example, we show the transition from nonsummer to summer and back for 1992. Current vectors for May, June, August, and September 1992 are shown in Figures 4.6-10 through 4.6-13. They were produced by objective analysis of monthly averaged current measurements from 31 LATEX current meters suspended approximately 10 m below the sea surface. The objective analysis method used to produce gridded fields of currents in this study is based on an extension of the minimum curvature method of gridding described by Smith and Wessel (1990), which is contained in the GMT software package (Wessell and Smith, 1991). The fields of current vectors shown were obtained by objective analysis from those averages at a 15-minute grid. We think that the analyzed fields are reasonable representations of the observed current fields.

Also shown in Figures 4.6-10 through 4.6-13 are the corresponding objectively-analyzed fields of monthly averaged surface wind stress (Wang, 1996; Wang et al., 1996). In May 1992, the average wind stress over the inner shelf had a downcoast component everywhere north of about 27.5°N. The flow over the inner shelf was likewise downcoast. Eastward

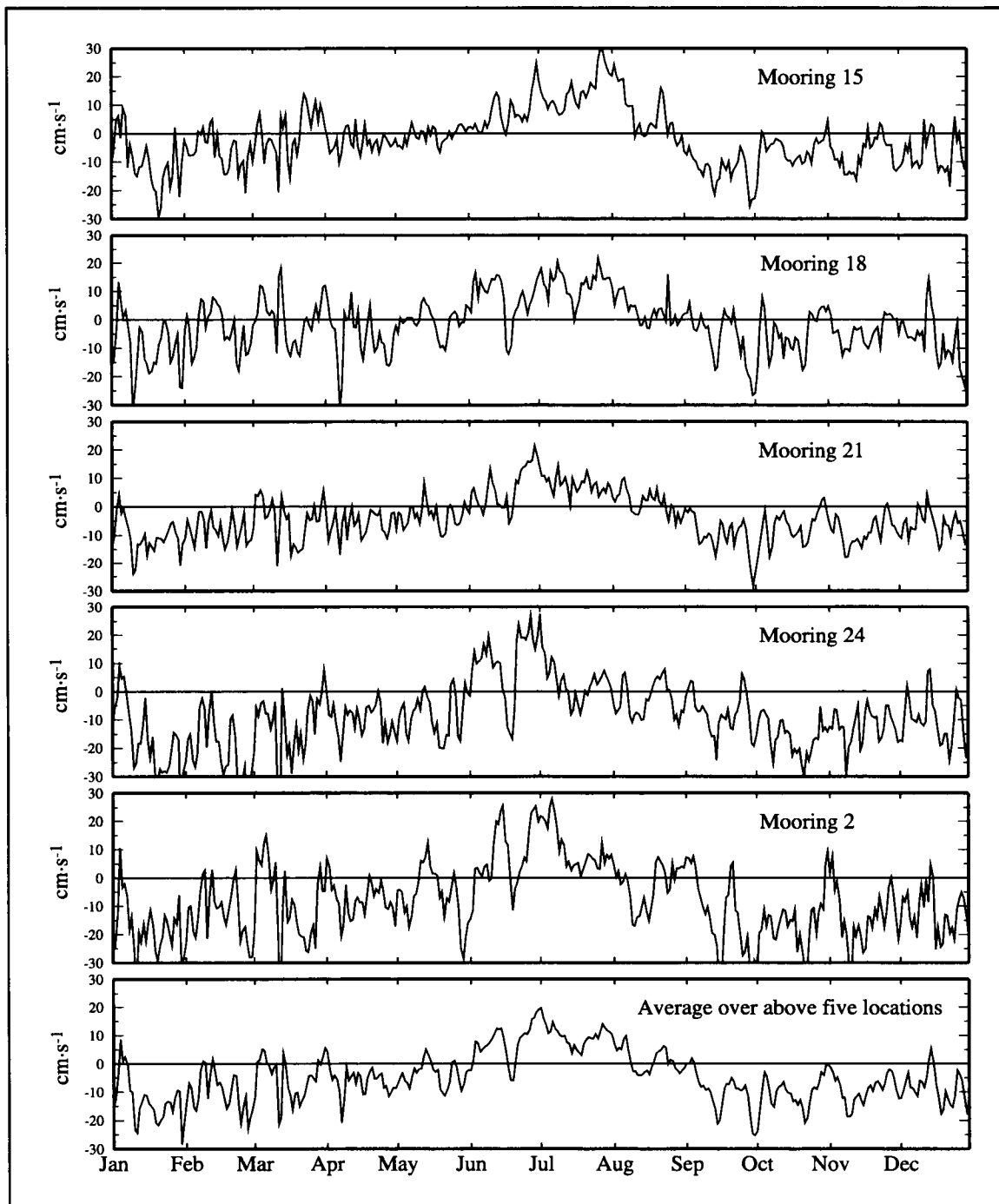


Figure 4.6-8. Average daily alongshelf component of 10-m current over the period April 1992 through November 1994 from five moorings located near the 20-m isobath (see Figure 4.6-2 for locations). Also shown is the series of daily values obtained by averaging the components at the five locations.

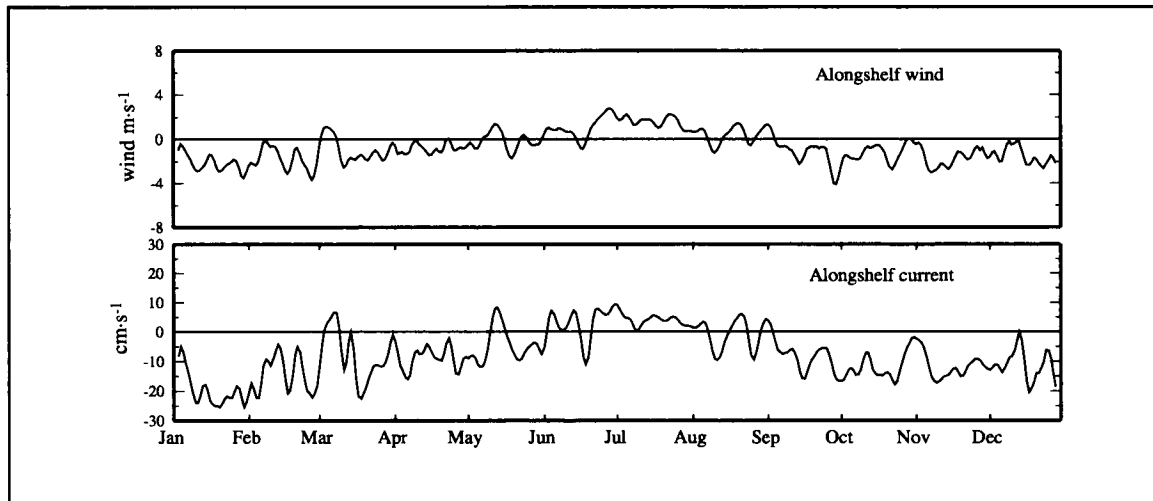


Figure 4.6-9. Daily alongshelf surface wind stress (upper) averaged over the six locations shown in Figure 4.6-2 and alongshelf current component (lower) at 10 m below the sea surface averaged for the five 20-m isobath moorings shown in Figure 4.6-8 during the period April 1992 through November 1994. Components are positive when directed upcoast, i.e., from Brownsville toward the Mississippi. Both series smoothed with five-point filter with weights 1/9, 2/9, 3/9, 2/9, 1/9.

flow over the outer shelf was strong between about 95° to 96° W due to the presence of an anticyclonic ring situated over the continental slope. Note the tendency for offshore cross-shelf flow northeast of the ring and onshore flow between 91° and 93° W.

In June, the monthly average wind stress (Figure 4.6-11) had an upcoast component over the entire inner shelf. The flow over the outer shelf was likewise generally upcoast, except near mid-shelf between 92° to 94° W. The situation in July 1992 (not shown) was essentially the same as for June, except that the effect of the ring off the shelf near 95° was more pronounced. During August the wind stress over the inner shelf shifted from upcoast to downcoast over the eastern and central shelf, though the average winds were very weak. The resulting monthly average current field (Figure 4.6-12) showed upcoast flow off Louisiana and downcoast flow off Texas. After the transition in alongshelf wind stress direction during August, wind stress over the inner shelf during September (Figure 4.6-13) was all downcoast, and the outer shelf flow likewise was downcoast.

Thus, the nonsummer circulation regime had been fully restored by September 1992. The anticyclonic ring seen in May remained over the continental slope and continued to influence

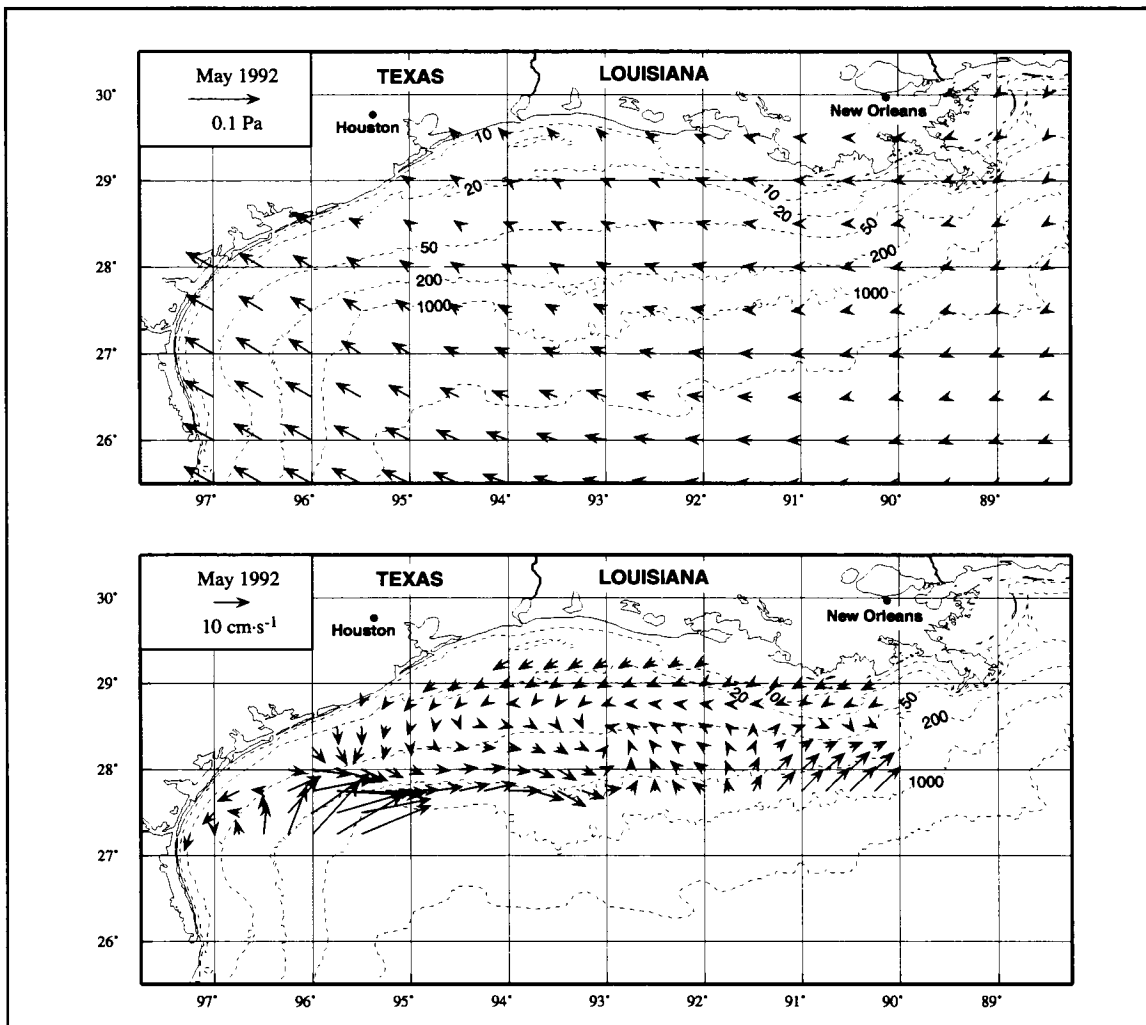


Figure 4.6-10. Objectively analyzed surface wind stress (upper) and 10-m currents (lower) from monthly averaged observations for May 1992.

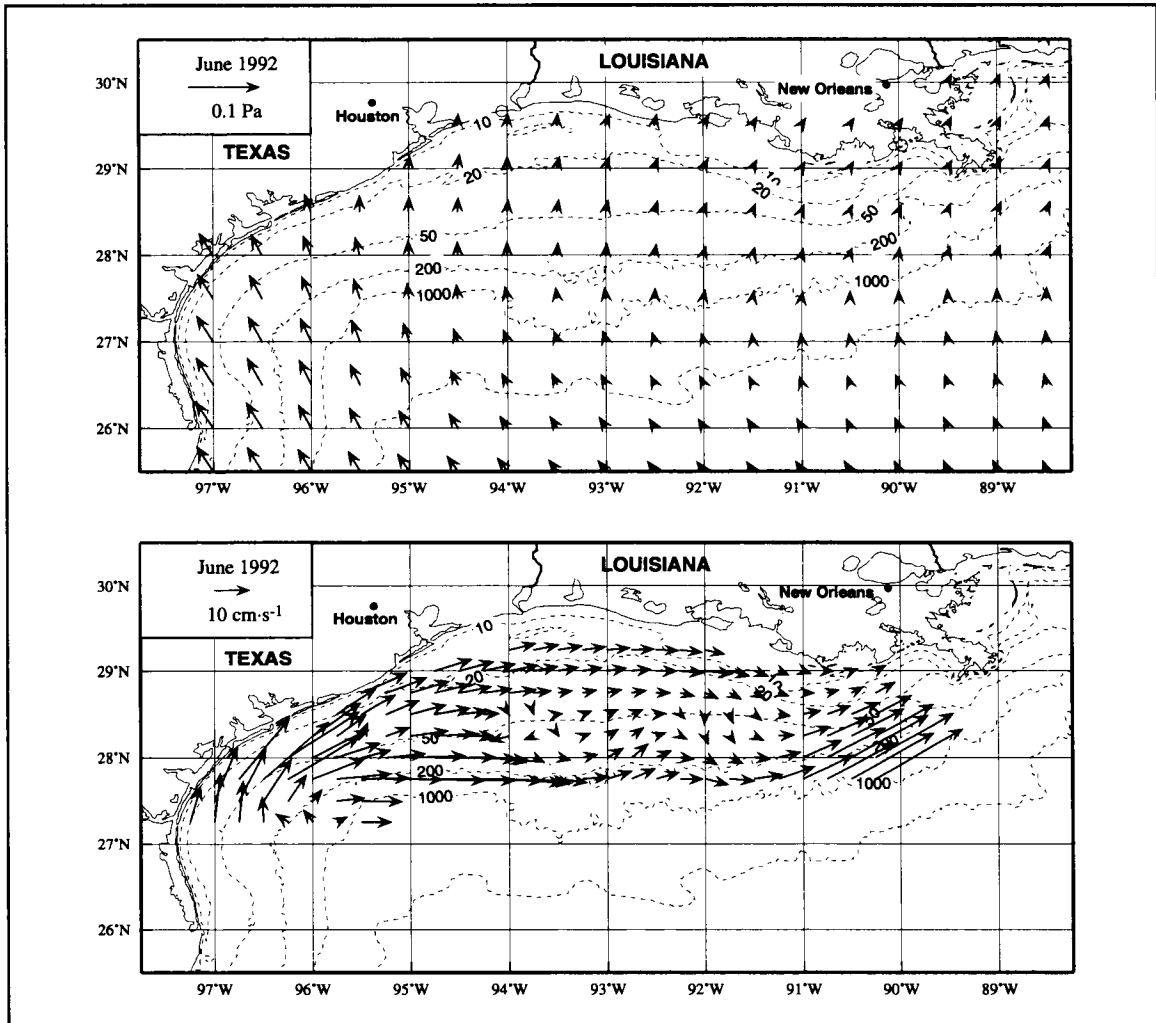


Figure 4.6-11. Objectively analyzed surface wind stress (upper) and 10-m currents (lower) from monthly averaged observations for June 1992.

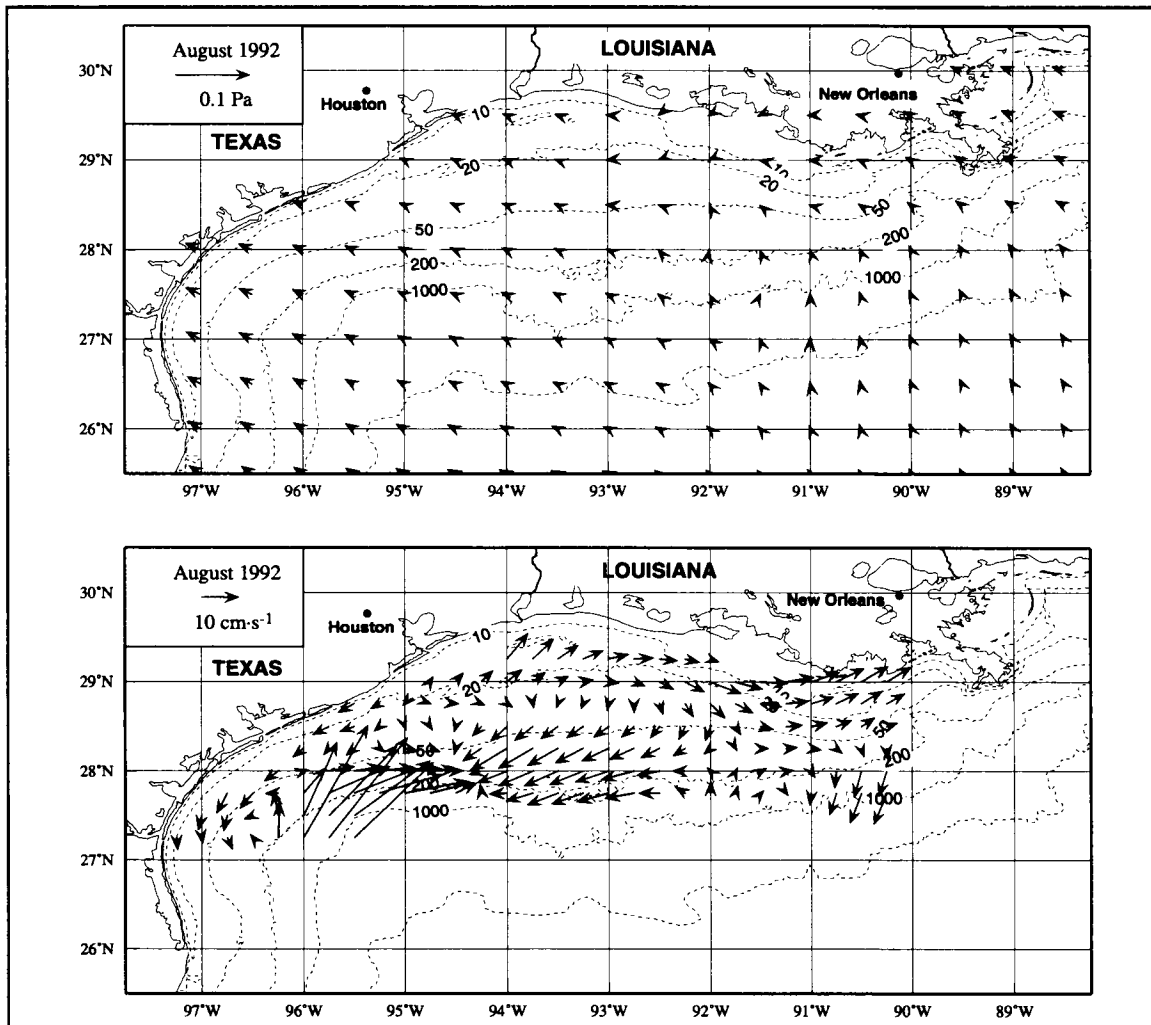


Figure 4.6-12. Objectively analyzed surface wind stress (upper) and 10-m currents (lower) from monthly averaged observations for August 1992.

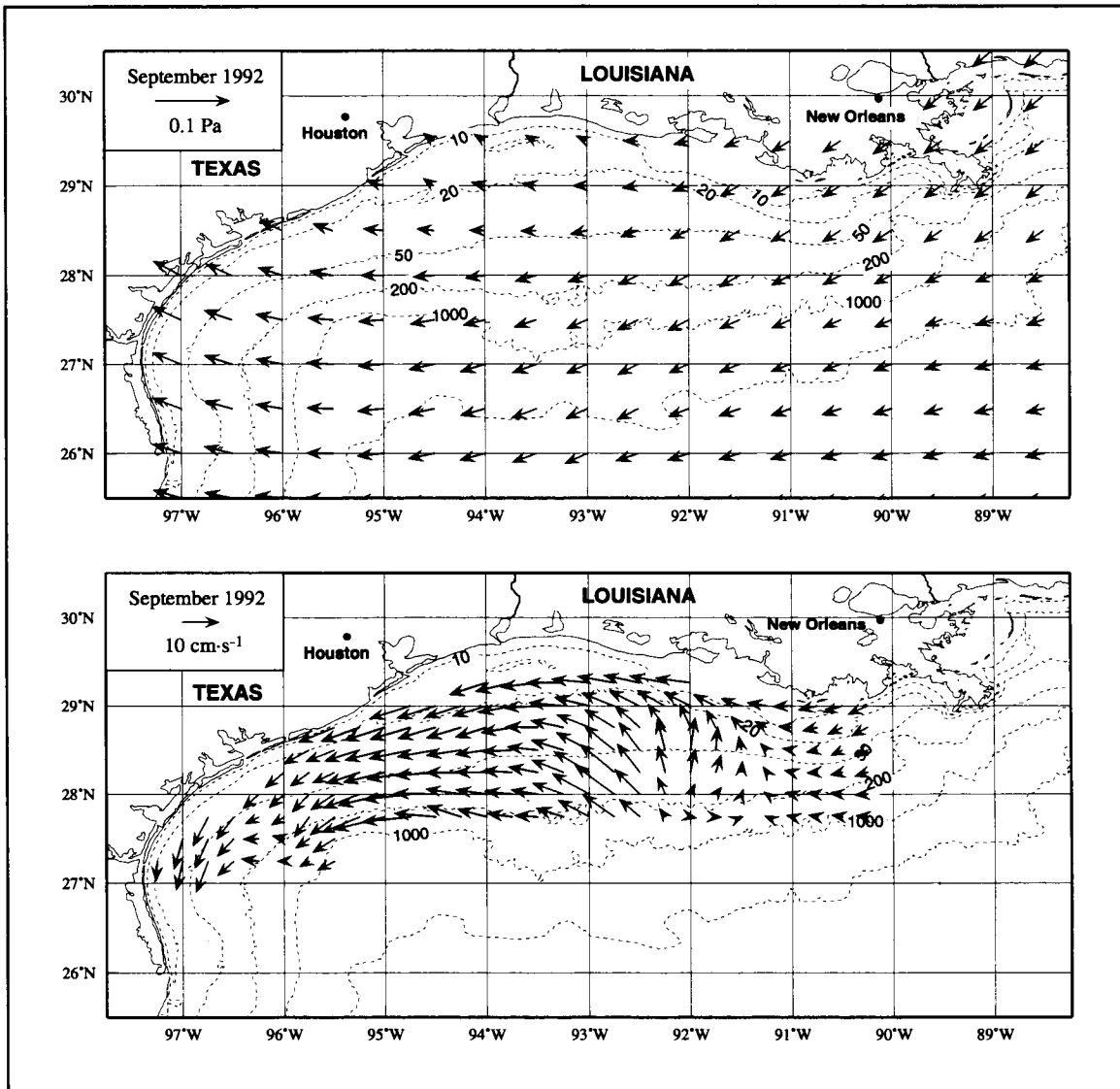


Figure 4.6-13. Objectively analyzed surface wind stress (upper) and 10-m currents (lower) from monthly averaged observations for September 1992.

the outer shelf circulation through August. In September, its effects are not evidenced in the monthly average current field.

It is noteworthy that the cross-shelf components of these monthly averaged flow fields are often quite large. Of the months shown, this is specially the case for May and September 1992.

Short response times. Many extreme meteorological events take place over the Texas-Louisiana shelf, including cold air outbreaks, cyclogenesis, and the passage of hurricanes. Strong wind forcing occurs with these events, which consequently causes strong current response over the shelf. Nine extreme events that occurred during the LATEX observation period were selected for the study of short-term response, including the Storm of the Century, Hurricane Andrew, and several cold fronts. A 10-day period including each event was selected for study.

For each period, the hourly alongshelf component of 10-m current measured at each mooring was plotted along with the alongshelf wind components measured at the closest meteorological buoy. Examination of these plots revealed close correspondence between wind and current in many cases. Examples for three moorings are shown in Figure 4.6-14 for the period 1-10 November 1992 (including a strong cold air outbreak). Alongshelf currents from moorings 1, 2, and 3 located across the south Texas shelf are plotted with alongshelf wind components from NDBC buoy 42020 (see Figure 4.6-2 for mooring and buoy locations). For direction changes the alongshelf wind seems to lead the alongshelf current components. Here that time lag is referred to as the response time of the currents to wind changes—measuring the approximate time after a reversal in alongshelf wind direction that the alongshelf, 10-m current over the inner shelf reverses direction.

The cross-correlations between alongshelf wind and alongshelf current components for all current meter moorings with nearby meteorological buoys were calculated for each of the nine 10-day events. Figure 4.6-15 shows the cross-correlations for moorings 1, 2, and 3 during the period of the cold air outbreak shown in Figure 4.6-14. Maximum values of correlations were 0.67 at moorings 1 and 2, and time lags associated with the maximum values at the two moorings were about 3 and 5 hours. At mooring 3, the maximum correlation value was 0.53 and time lag was about 2 hour. The 95% confidence level was about 3.3 for these cases. The maximum cross-correlation value and the corresponding time lag were determined for each current meter mooring for each of the nine 10-day events. At each mooring location the values were averaged over the nine event periods, and maximum correlation values were contoured (Figure 4.6-16). Taking the 95% significance level (conservatively identified with correlation values of 0.4) as the criteria for the areal extent over which alongshelf current direction responds significantly to short period, alongshelf wind change, the response region extends offshore to about the 200-m isobath near the

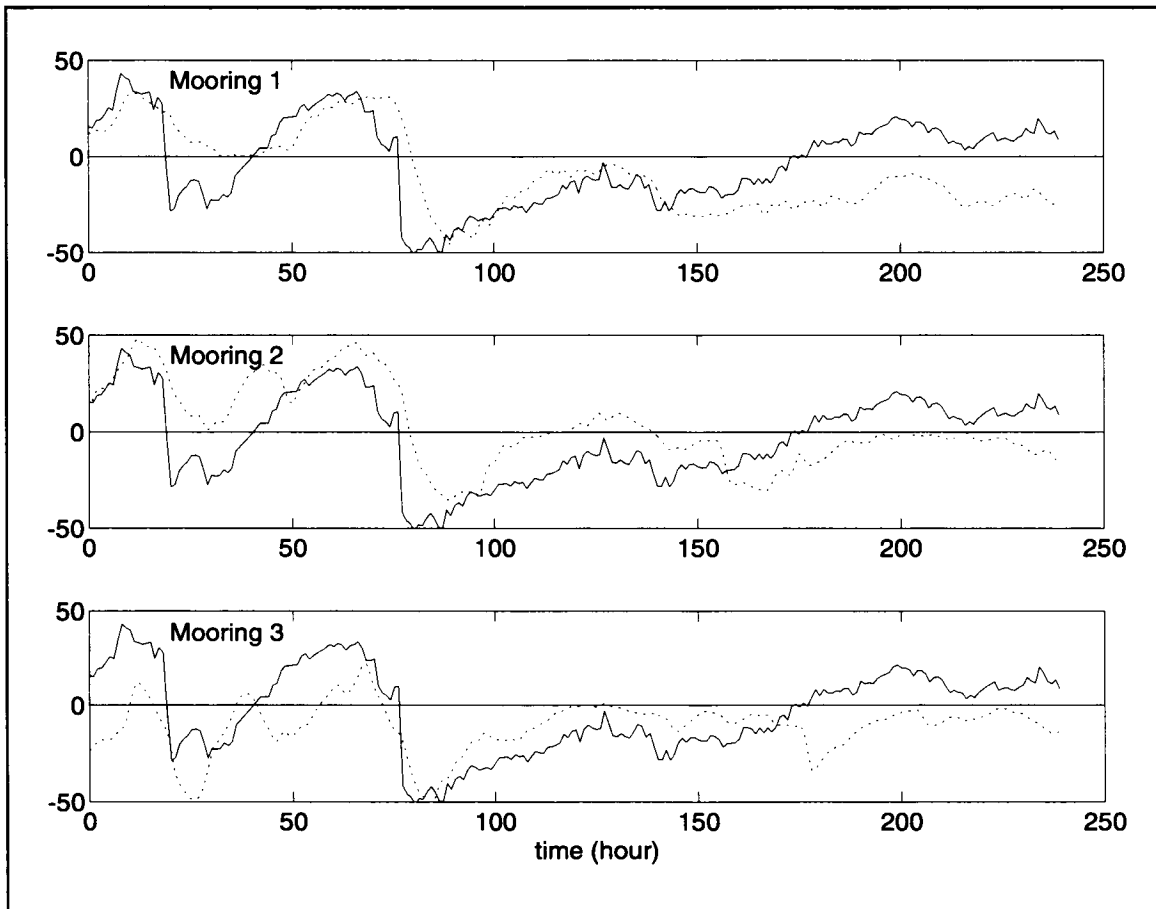


Figure 4.6-14. Alongshelf component of wind from NDBC buoy 42020 (solid lines) plotted with alongshelf components of 10-m currents (dashed lines) measured at moorings 1, 2, and 3 for the period 1-10 November 1992 (including a cold-air outbreak). Speeds in $\text{cm}\cdot\text{s}^{-1}$; upcoast (in sense from Mexico to the Mississippi River) is positive.

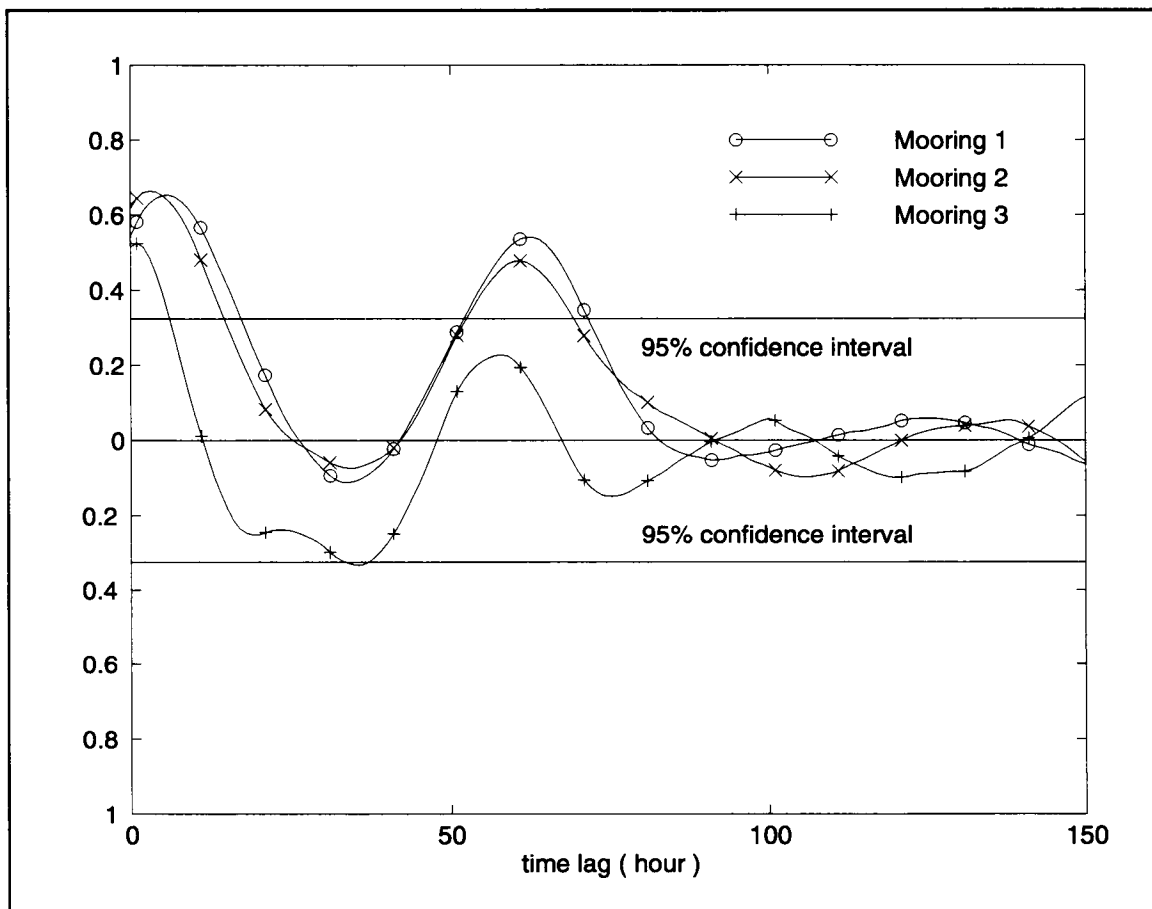


Figure 4.6-15. Cross-correlations of alongshelf wind and current for the cases shown in Figure 4.6-14.

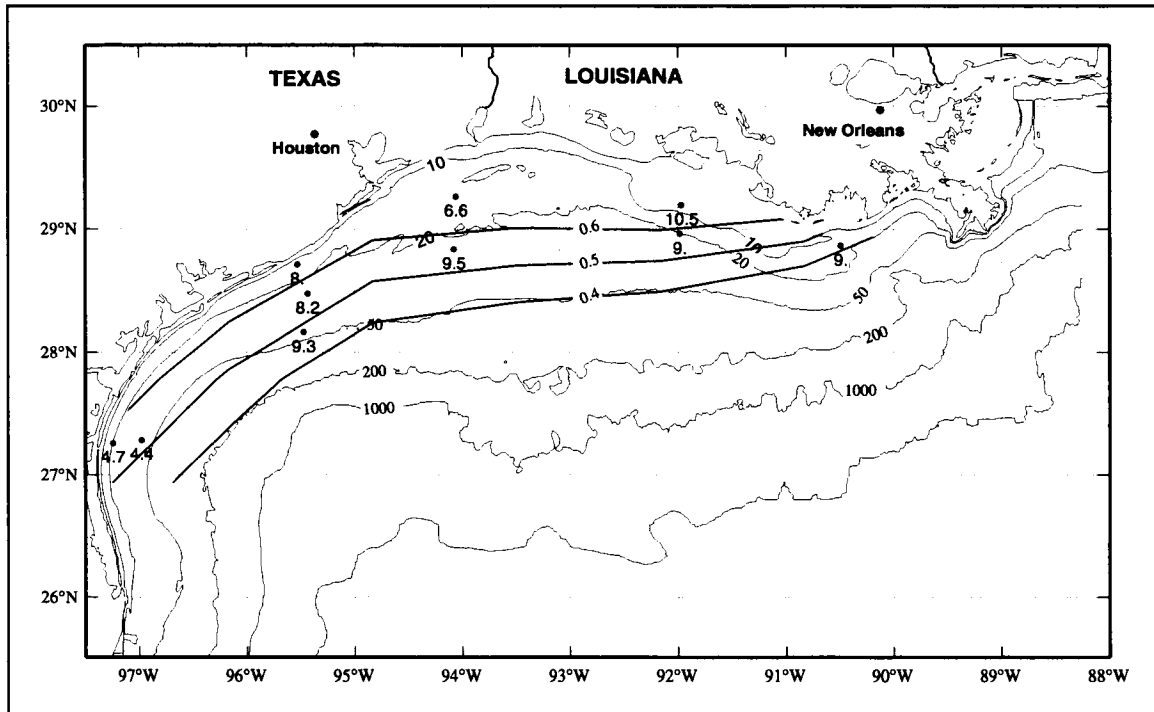


Figure 4.6-16. Maximum cross-correlations between alongshelf component of surface wind and alongshelf component of 10-m current contoured for values of correlations greater than or equal to 0.4. Based on estimates from nine 10-day periods each including an extreme meteorological event, e.g., cold-air outbreak or cyclogenesis, at each of the mooring locations shown in Figure 4.6-2. Values of lag (in hours) for the maximum cross-correlation are given by mooring positions.

Mexican border but is confined to shallower depths upcoast (the 50-m isobath over the central shelf and near the 20-m isobath off the Mississippi Delta).

Also given in Figure 4.6-16 are the lags (in hr) corresponding to the maximum averaged cross-correlation. These response times are shown only for the region of significant response; outside that region, the values fluctuated widely. The response time is only 4 to 5 hours off the south Texas coast. It generally increases upcoast, reaching values of about 10 hours off the Mississippi Delta.

Buoyancy effects of river discharge

Figure 2.3-1 shows annual cycles of daily discharge for the Mississippi and Atchafalaya rivers based on the 64-year average and for 1992, 1993, and 1994. The maximum in the long-term average occurs in April and the minimum in September-October. There is large interannual variability; discharge for the LATEX observing period generally was higher than average. Also shown is the cycle of daily average discharge from the sum of the thirteen principal rivers of Texas and Louisiana west of the Atchafalaya River based on 20 to 77 years of data for individual rivers. The sum of their discharge is so much smaller than that from the Mississippi-Atchafalaya that its effect is not often seen more than 30 km from shore; the Texas flood of October 1994 is clearly an exception—discussed in Appendix C.

The mean May surface salinities (Figure 4.6-4) are much lower than in November both near the source of the fresh water and also over the entire inner shelf. Remembering that river discharge is much larger before and during May than before and in November, and that the alongshelf wind components are downcoast in both seasons, we conclude that the distributions differ principally because of the river discharge difference. The buoyancy effect of the larger amount of fresh water over the inner shelf during May than during November leads to larger inshore values of geopotential anomaly during May, and thus enhanced downcoast geostrophic shear.

The surface salinity pattern for July-August is completely different from that for May though separated in time by only one month. Salinities greater than 36 extend halfway up the Texas coast in July-August; this is indicative of upcoast flow under the action of upcoast alongshelf wind stress component. As noted earlier, river discharge rates are about the same in July-August and in November. However, we see that the fresh water discharge of November is distributed along the inner shelf by downcoast flow, while the discharge is held near the mouth of the river system by the upcoast flow in summer.

Li et al. (1996; Section 4.2) prepared average distributions of surface salinity and surface geopotential anomaly relative to 70 db for May, July-August, and November based, respectively, on 10, 9, and 6 individual cruises. For each cruise examined, residuals of

geopotential anomaly and surface salinity relative to the seasonal mean were examined in relation to departures of river discharge from the long-term (64-year) average and an index of alongshelf wind component appropriate to the times of the cruises. As expected, positive residuals of river discharge were correlated with negative surface salinity residuals. The residuals of geopotential anomaly were found to be significantly negatively correlated with those of surface salinity, with an intercept of approximately zero. This confirms that freshwater discharge enhances the downcoast shear flow over the inner shelf through buoyancy forcing. Also, it indicates that salinity plays the dominant role relative to temperature in year-to-year variability of geopotential anomaly. Enhanced downcoast (upcoast) wind components resulted in negative (positive) surface salinity residuals. Most correlations were significant (different from zero) at the 95% confidence level.

While the geopotential anomaly and its cross-shelf gradient nearshore show striking differences between fall and spring that are well correlated with river discharge, the measured near-surface currents nearshore do not show a similar contrast between spring and fall. This could be due to a larger barotropic component of flow in spring (thus not reflected in the dynamic topography) or to pycnocathic effects not included in the geopotential anomaly.

Many of the LATEX A current meter records included time series of conductivity and temperature that have been used to produce time series of salinity at the mooring locations. We examined the relationships between changes in salinity at different locations along the inner shelf to estimate the time needed to transport fresh water from the Mississippi River mouth to the south Texas shelf in nonsummer and saline water from lower Texas shelf to the central Texas-Louisiana shelf in summer. We calculated the cross-correlation of salinity for the adjacent pairs of current meter moorings along 10-m isobath for nonsummer season and along 20-m isobath for summer season. Only 10-m records were considered because the low-salinity discharge would not normally be seen at deeper instruments. The periods chosen to represent nonsummer and summer are from October 1 to April 30 and from June 1 to August 31, respectively. To improve confidence in the cross-correlations we divided the periods of measurement common to each pair of records into several segments of 45 to 75 day length. Then cross-correlation estimates were obtained by averaging the cross-correlation over all common segments for each current meter pair.

We used the lags corresponding to the maximum values in the cross-correlation estimates to indicate the time required for salinity signals at 10 m to be detected from one mooring to another. In nonsummer, the maximum estimated correlation between the Mississippi-Atchafalaya river discharge rate and the salinity at mooring 16 (location shown in lower panel of Figure 4.6-2) occurs near 9 days, which means it takes about 9 days to advect fresh water from the Mississippi mouth to mooring 16. The corresponding advection speed is about $14 \text{ cm}\cdot\text{s}^{-1}$. From mooring 16 to mooring 20, the time needed for advection is around 40 days, giving a speed of about $10 \text{ cm}\cdot\text{s}^{-1}$. The lag of maximum correlation between moorings

20 and 1 is about 20 days, giving an average downcoast speed for the lower Texas coast near $20 \text{ cm}\cdot\text{s}^{-1}$. Based on these results the time needed to transport the relatively fresh water from the mouth of the Mississippi to mooring 1 is about two months. The nonsummer downcoast advection speeds seem greater on the lower coast than off Louisiana or eastern Texas; this is agreement with our observations of the monthly average current vectors.

In summer the currents flow upcoast, and, as we have seen, one would expect salinity increases to be propagated upcoast, especially along the Texas coast, which was observed. Probably because in summer the salinity difference between central and eastern inner shelf is not great, the cross-correlations did not yield consistent maxima.

Effects of offshore eddies on outer shelf circulation

The effects of anticyclonic Loop Current eddies and associated cyclonic eddies on the region adjacent to the shelf is to be seen in the figures of Appendix H. Discussion of these effects is presented throughout this report—notably in Sections 2.5, 4.2, 4.4.1, and 4.4.2, as well as earlier in this section. We offer the following points:

- Because of the sporadic occurrence of rings adjacent to the shelf, interannual and even intra-seasonal variability over the outer shelf is quite large.
- The mean eastward flow at the shelf edge (for monthly scales) results from series of ring currents and not from a seasonal current pattern.
- The occurrence of rings seems most frequent off the lower Texas shelf, less frequent off the Louisiana shelf, and infrequent off the upper Texas shelf. Perhaps this is due to bathymetric constraints—the slope is wider off the upper Texas shelf.
- Cross-isobath currents over the shelf edge (200-m isobath) due to eddies are frequent and of large speeds; the inner shelf (depths less than 50 m) is less affected, though for some periods, especially off south Texas, such effects can be pronounced.

Principal conclusions

Our principal conclusions regarding shelf-scale currents and forcing for the Texas-Louisiana shelf are summarized in the following statements.

- The mean currents based on the 32 months of LATEX data are downcoast over the inner shelf and upcoast over the outer shelf.

- The annual (yearly plus three harmonics) signal of currents over the inner shelf is of downcoast flow during nonsummer (September through May) and upcoast flow during summer; over the outer shelf there is no coherent pattern to the annual signal.
- The kinetic energy of currents in the mesoscale band (periods between 10 and 100 days) is greatest at the shelf edge ($50\text{-}100\text{ cm}^2\text{-s}^{-2}$ at 10 m depth) and decreases toward shore. Such currents are greatest at the shelf break between 94° and 96°W and result largely because of offshore eddies—particularly anticyclonic Loop Current eddies.
- The kinetic energy of currents in the weather band (periods between 2 and 10 days) is greatest near shore ($\sim 100\text{ cm}^2\text{-s}^{-2}$ at 10 m depth) and decreases offshore over the shelf. Currents are well correlated with wind stress in the weather band; they are most energetic in winter and spring and decrease to a minimum in summer with infrequent frontal passages.
- Forcing for circulation over the inner shelf is essentially by wind stress and buoyancy contrast.
- Currents over the inner shelf are largely forced by wind stress. The correlation between monthly averaged, alongshelf current and alongshelf wind stress is positive and highly significant, with the general pattern of downcoast forcing in nonsummer months and upcoast forcing in summer months. Examination of the principal EOF of monthly velocity streamfunction and the monthly alongshelf wind stress give evidence that wind-forced alongshelf currents over the outer shelf are in the same direction as those over the inner shelf though much weaker and may be masked by the effects of offshore eddies.
- The bimodal (summer versus nonsummer) pattern of alongshelf currents over the shelf is interrupted by energetic wind events that alter the direction of alongshelf wind stress—usually for periods of a few days. The region in which alongshelf current direction changes in a statistically significant manner to short period, alongshelf wind change extends offshore almost to the shelf break near the Mexican border but is confined to shallower depths upcoast (the 50-m isobath over the central shelf and near the 20-m isobath off the Mississippi Delta). Within this region current reversals follow wind stress reversals in less than 1 day; response times vary from about 4 hours off south Texas to almost 10 hours off Louisiana.
- The Mississippi-Atchafalaya river discharge is historically maximum in spring, however interannual variability is large. The fresh waters contribute to buoyancy forcing over the inner shelf, thus increasing the downcoast geostrophic shear. The total discharge by U.S. rivers west of the Atchafalaya is very small relative to Mississippi-Atchafalaya discharge

on average. However, in cases of extreme discharge, water from Texas rivers may occasionally enhance buoyancy forcing of downcoast flow.

- The flow near the shelf edge is greatly influenced by the presence of eddies adjacent to the shelf. The upcoast (eastward) flow at the shelf edge envisioned in the CK schema is the result of integrated effects of anticyclonic eddies impinging on the shelf edge.
- Although onshelf and offshelf flow may occur over the shelf break to maintain continuity of the pattern of alongshelf currents over the shelf, large cross-isobath currents due to offshore eddies are frequent and may dominate the property exchange across the shelf break.

5 ECOLOGICAL STUDIES

The focus of LATEX was on the hydrographic and circulation regimes. To understand hydrographic distributions and circulation over the shelf, it was imperative to observe the full shelf on each cruise and to repeat this sampling for interannual comparisons. The low-frequency cycle of hydrographic and circulation variability can be observed by sampling three times per year. Thus, to meet our objectives within the available budgets the number of hydrographic cruises was reduced from four to three per year.

There are insufficient data to determine whether the biological seasons of the shelf are the same as the hydrographic seasons. Because cruises were conducted in each of the four calendar seasons, the biological data are presented in that format. The variation in the ecological data from three realizations each in spring, summer, and fall suggests there may be at least three biological seasons over the LATEX shelf. These seasons are governed largely by the wind-driven current regime (upcoast in summer, downcoast in nonsummer), the discharge conditions of the Mississippi-Atchafalaya river system (high in spring, low in summer, moderate in fall and winter), and, for pigments, seasonal light conditions. With only one “winter” realization, we cannot conclude whether there is a fourth biological season or whether winter conditions are essentially a continuation of fall conditions.

Sampling during LATEX A hydrographic surveys included vertical profiling of light transmission and dissolved oxygen concentration and discrete measurements of dissolved oxygen, nutrients, suspended particle mass, and pigments at selected stations. These data can be synthesized with the physical measurements to describe basic elements of the ecology of the Texas-Louisiana shelf. In this section we offer four such syntheses.

Profiles of light transmission were converted to particle beam attenuation coefficients, which, correlated with direct measurements of suspended particle mass, have been used to describe particle distributions. In Section 5.1 we present descriptions by cruise of the particle distributions in the surface layer, entire water column, and bottom nepheloid layer, discuss seasonal and interannual variability, and give examples of effects on distributions by physical phenomena—current rings near the shelf edge and river discharge.

In Section 5.2 we describe the spatial and seasonal distributions of nitrate, phosphate, and silicate, and we discuss the influence of Loop Current eddies on these distributions. Using nitrate as an example, we present a quantitative estimate of the effect of Mississippi-Atchafalaya discharge on nutrient distributions over the Texas-Louisiana shelf.

Section 5.3 presents the distributions of dissolved oxygen observed during the ten LATEX A hydrographic cruises. Seasonal and spatial patterns are described with indications of

interannual variability due to the presence of fresh water and to phytoplankton abundance (inferred from chlorophyll-a). Observed occurrences of hypoxia are described; we examine the relationships of diminished bottom oxygen to vertical stability of the water column, to low surface salinity, and to enhanced bottom values of nitrate.

Finally, in Section 5.4 we describe the observed seasonal distributions of chlorophyll-a. Algal class distributions are inferred from the distributions of phytoplankton accessory pigments evaluated for five hydrographic cruises.

5.1 Suspended particle distributions

Introduction

The principal focus of this section is to describe suspended particle distributions on the Texas-Louisiana continental shelf during the LATEX A hydrographic cruises, from April 1992 through November 1994. In addition, some processes important in the transport of modern fine-grained sediments are identified.

Modern sediments are those that have been deposited since the Holocene marine transgression. Their distributions are assumed to be in equilibrium with processes currently acting on the shelf. On this shelf, modern sediments consist mostly of sand, silt, and clay-sized particles. Modern sand deposits are restricted to the coastal zone, where waves and alongshore currents are energetic enough to transport them along shelf. Modern silts and clays are observed offshore from the sands; in places, these fine-grained sediments extend to the shelf edge, defined here as the shelf-slope break near the 200-m isobath. The sedimentary record indicates that fine-grained sediments can cross the shelf most effectively at two places: the eastern study area and the south Texas shelf. Fine-grained modern sediments blanket the shelf in these areas (Curry 1960).

Suspended particle transport is determined by the shelf circulation. Most of the fine-grained sediments entering the Texas-Louisiana shelf today do so via the Mississippi and Atchafalaya river plumes. Alongshelf currents driven by alongshelf wind stress components are directed to the west and southwest during nonsummer, transporting fine-grained sediment along the inner shelf. Cochrane and Kelly (1986) speculated that wind convergence on the south Texas shelf drives shelf current convergence, resulting in the seaward transport of shelf water and sediment. More recently, Loop Current rings (Brooks 1984; Vidal et al. 1992) and smaller cyclones and anticyclones (Hamilton 1992) have been observed to influence the flow and hydrography (Cochrane and Kelly 1994) near the shelf edge. Evidence from other shelves suggests that these phenomena may be important for moving sediment from the shelf to the deep ocean (Washburn et al. 1993).

Recent studies of suspended sediments on the Texas-Louisiana shelf have focused on the bottom nepheloid layer (BNL). Shideler (1981) found that lithogenous, silt-sized particles dominated the suspended particles in the BNL of the south Texas shelf, and that nepheloid layers were thickest when the underlying substrate was silt and clay. Sahl et al. (1987) found that 29 to 90% of all particles suspended in the water column were contained in the BNL, and that this large variability may be related to energetic processes near the shelf edge.

In the Methods section, sampling and measurement methods are reviewed. Then we describe the variability of particle concentrations in surface waters, the mass of particles in the water column, and the percent of water column particles suspended in the bottom nepheloid layer for each cruise and season. Next, the impact of ring-shelf interaction processes on particle distributions is illustrated through an example. Then the impact of Mississippi-Atchafalaya river discharge is examined by comparing plume particle distributions during extremely high discharge and more normal conditions. Finally we present a synopsis of total suspended particulate loading observed during LATEX.

Methods

A SeaTech transmissometer (25-cm beam length, 660-nm wavelength) was interfaced with the Sea-Bird Model 911+ CTD used at each LATEX A hydrographic station. A transmissometer measures light attenuation, providing an indirect method of measuring particle mass in ocean waters. Particle mass is measured directly by filtering water samples. Most studies of suspended particulate matter (SPM; the mass of particles per volume of water) use both techniques; the direct measurements of particle mass provide data for converting light attenuation into particle mass.

A specially designed frame for the CTD system and additional sensors allowed water flow without undue perturbation past all instruments during descent. The transmissometer was factory calibrated several times during the field program. In addition, prior to each cast, air calibration data were collected to correct raw data. Particle beam attenuation coefficient (PBAC) was calculated from the corrected transmission data. Additional details are in Jochens et al. (1998).

Surface and bottom water samples were collected with 10-liter Niskin sampling bottles at many stations on each cruise. Water samples were processed for SPM by filtering a measured volume through a 47-mm polycarbonate Nucleopore filter with 0.4 μm pores. Filters were triple weighed prior to each cruise and were dried and triple weighed after each cruise. For each cruise several Nucleopore filters were subjected to the same weighing process as the SPM filters, but no seawater sample was passed through these filters. These blanks provided correction values that were applied to the final filter weights for each cruise. All SPM filters

were examined ashore using a dissecting microscope; filters found to be contaminated were eliminated from the data set.

The correlation between PBAC and SPM allows the optical data to serve as an estimator of SPM. Correlation is expected to be sensitive to the sedimentary environment. Depending on the source of the suspended particles, different particle environments exist in surface and bottom waters on the shelf. The primary source of suspended particles in water near the bottom is resuspension from the sea bed. The primary sources of suspended particles in surface waters are river and bay discharge, in situ production by organisms, and wind-borne dust. Of course, there is transfer of particles between the two environments, e.g., in shallow water when bottom sediments are suspended throughout the whole water column, or in deeper water when organic particles settle from the surface layer into bottom waters. However, because the particle populations are expected to differ, independent correlations between PBAC and SPM are used for surface and bottom waters.

The correlations for the surface and bottom data sets for all cruises except H06 are shown in Figure 5.1-1. Excellent correlations (significant at the 99% level) were obtained on cruises H01, H03, H04, H05, H07, H08, and H09, allowing separate equations to be used for calculating SPM from PBAC for surface and bottom waters. Correlations were likewise excellent for bottom waters on cruises H02 and H10. However, less significant correlations (at the 95% level) were found for surface data on cruises H02 and H10; this might be due partly to the small number of surface samples available and partly to the small range of PBAC values associated with the available surface samples. Combining the surface and bottom data sets for each of these cruises produced good correlations.

For cruise H06, microscopic examination of the SPM filters revealed considerable contamination of samples. Contaminated samples were dropped from the analysis; no usable correlation between SPM and PBAC could be obtained for the surface data. Merging surface and bottom data did not improve the correlation. Therefore, for this cruise, optical data are used to describe and estimate particle distributions; SPM was not estimated.

To apply the linear relations for calculating SPM from optical data, the water column was divided into shallow and deep portions. Stations in water depths greater than 200 m were not included because they were not considered part of the shelf province. Vertical transmissometer profiles were examined for the presence of bottom nepheloid layers (BNLs). The bottom correlation relation was applied to waters in the BNL, and the surface equation was applied to the rest of the water column. At stations where intermediate depth nepheloid layers were found above the BNL, the waters within the intermediate nepheloid layers were included in the BNL if there was no water of surface optical properties separating the layers. Generally, nepheloid layers are easily identified in the transmissometer data; Figure 5.1-2 shows an example. Exceptions to this were stations in shallow coastal waters where there

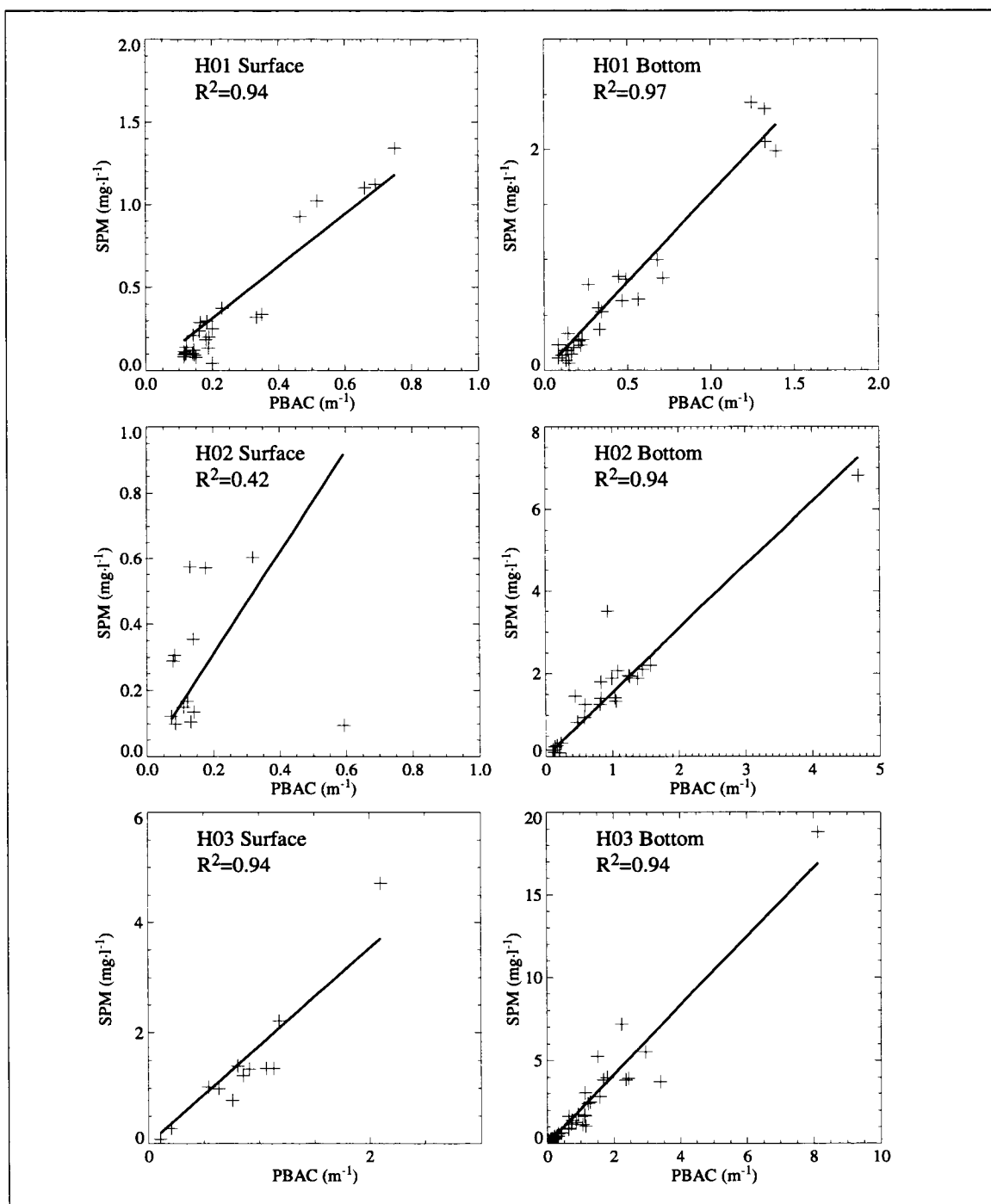


Figure 5.1-1. Linear correlations between PBAC and SPM for the LATEX A hydrographic cruises; crosses represent data points. Separate correlations were obtained for surface and bottom waters except for cruises H02 and H10, for which surface and bottom data were merged.

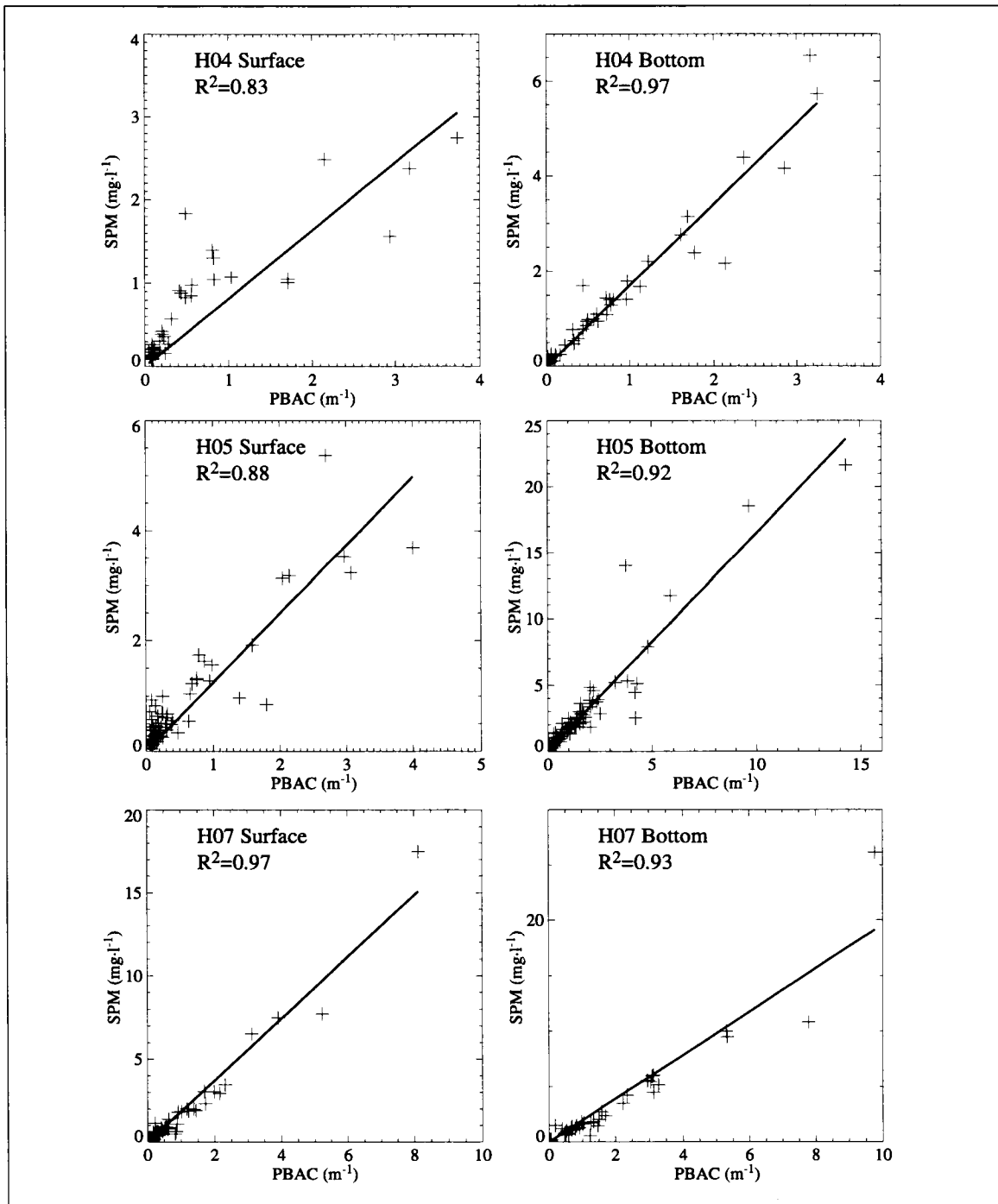


Figure 5.1-1. Linear correlations between PBAC and SPM for the LATEX A hydrographic cruises; crosses represent data points. Separate correlations were obtained for surface and bottom waters except for cruises H02 and H10, for which surface and bottom data were merged. (continued)

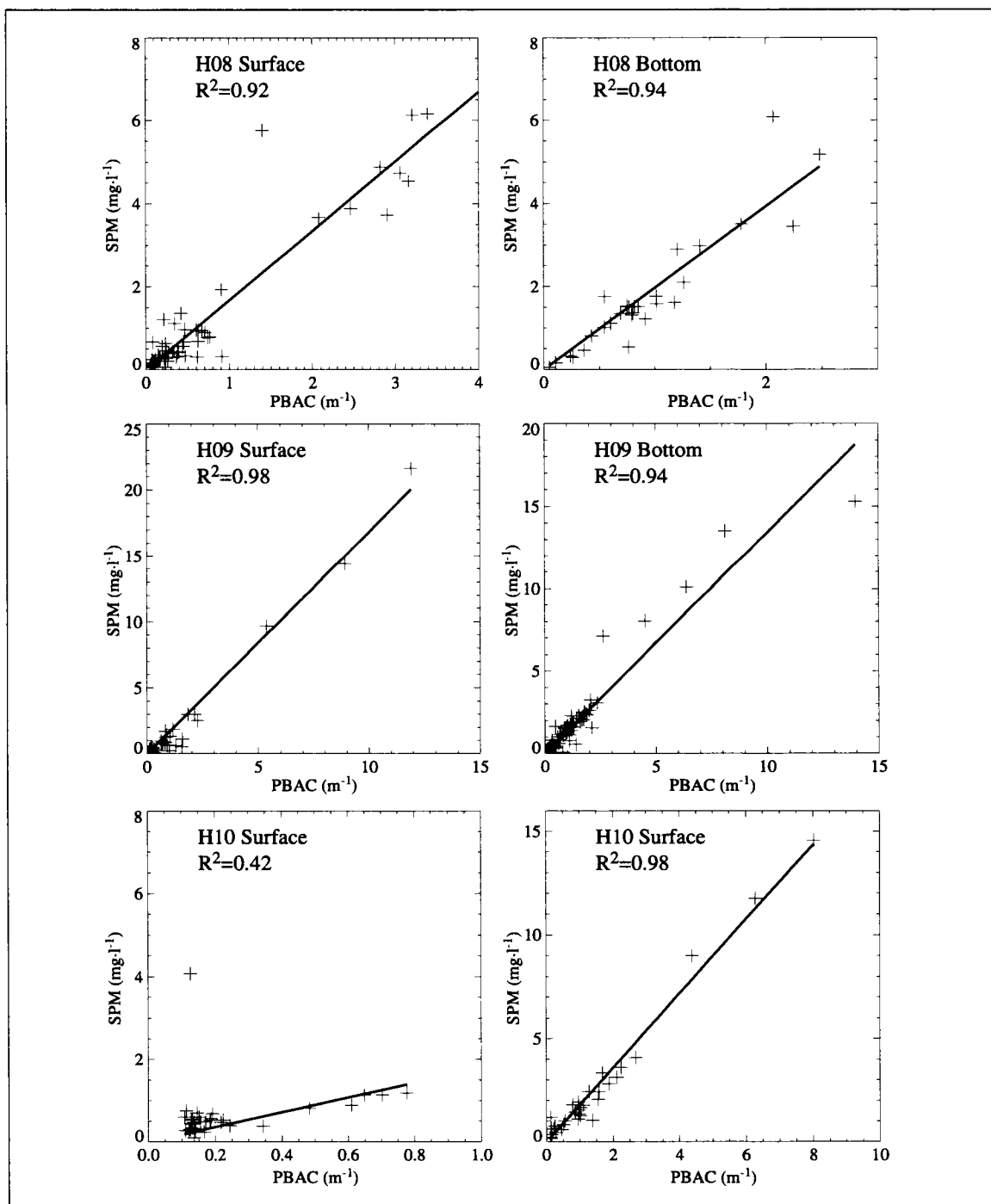


Figure 5.1-1. Linear correlations between PBAC and SPM for the LATEX A hydrographic cruises; crosses represent data points. Separate correlations were obtained for surface and bottom waters except for cruises H02 and H10, for which surface and bottom data were merged. (continued)

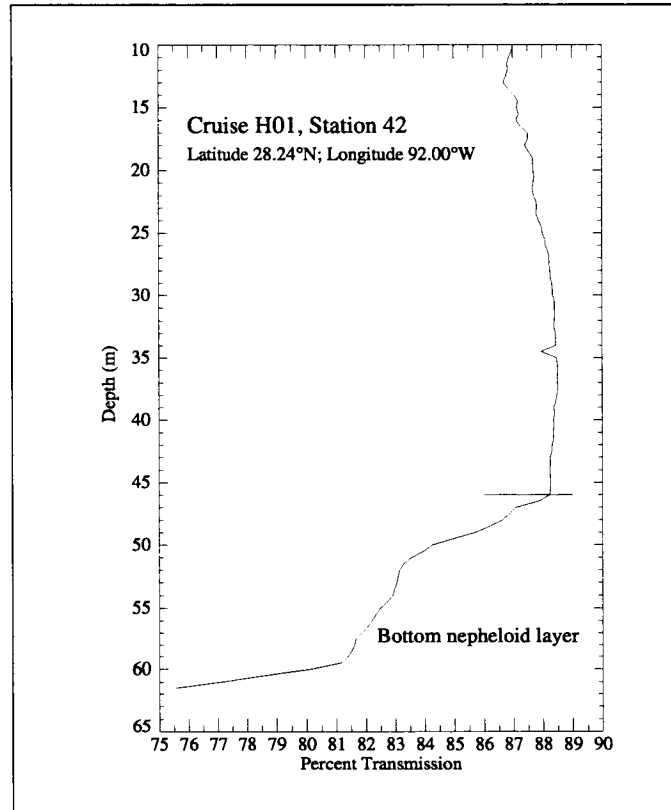


Figure 5.1-2. Depth profile of percent transmission for station 42 on cruise H01, taken along line 2 on 4 May 1992.

was no well defined BNL. In cases where station profiles of optical data still revealed differences between surface and bottom waters, the depth at which the optical properties changed was chosen to divide the water column. If there was no obvious difference between optical properties of surface and bottom waters, mid-depth was chosen to divide the water column. On cruises H02 and H10, the relation determined for the combined data was used throughout the water column.

Description of particle distributions by cruise

The Mississippi and Atchafalaya rivers supply most modern sediments to the Texas-Louisiana continental shelf, and these sediments undergo many deposition and resuspension cycles. When sediments first enter the Gulf, they are suspended in low-density river plumes. The sediment load creates a turbid surface layer, also called a surface nepheloid layer. Eventually sediments settle out of the river plumes and are deposited on the sea floor. As these particles

are acted on by shoaling waves and shelf currents, they are resuspended, transported, and eventually redeposited on the sea floor again. This cycle can occur many times. Particles usually travel close to the seafloor while in resuspension and transportation cycles, creating a turbid layer adjacent to the seafloor—the bottom nepheloid layer. This layer is quite important in particle transport because it contains relatively high concentrations of particles (order $1.8 \text{ mg}\cdot\text{l}^{-1}$ in the BNL, compared to order $0.8 \text{ mg}\cdot\text{l}^{-1}$ at the surface).

We present and discuss surface (3-m) distributions of suspended particulate matter calculated from PBAC or PBAC to identify distributions of particles contained in river plumes and coastal water. Distributions of total mass of SPM in the water column identify places and times (and sometimes processes) responsible for significant particle transport. We also present distributions of the percent of total SPM in the water column that is contained in the bottom nepheloid layer. This can be useful in differentiating between locations where bottom currents alone determine the flux of particles versus locations where significant particle transport occurs near surface or at mid-depth.

Cruises H01-H04 covered only the eastern half of the shelf; cruises H05-H10 surveyed the entire study area. For summer cruise H06, optical data could not be converted to particle mass. Distributions of particle beam attenuation coefficients (PBAC) are presented as proxies for near-surface SPM distributions. The descriptions are presented in order of spring (H01, H05, H08), summer (H02, H06, H09), fall (H03, H07, H10), and winter (H04).

Cruise H01 (30 April-9 May 1992). Cruise H01 sampled only the eastern study area in May 1992. Surface particle concentrations were highest at the coast and generally decreased across the shelf (Figure 5.1-3). The cruise occurred after the peak Mississippi-Atchafalaya river discharge for that year. Surface waters with salinities less than 30 were found over that part of the shelf with water depths less than 50 m (the inner shelf). Surface waters with particle concentrations greater than $1 \text{ mg}\cdot\text{l}^{-1}$ were also confined to the inner shelf. Surface transport of suspended particles was important on the eastern shelf; less than 50% of the particles in the water column were contained in the BNL over most of the study area—less than 25% at the shelf edge. Thus most of the relatively low mass of sediment in the whole water column ($< 25 \text{ g}\cdot\text{m}^{-2}$) was above the BNL.

Cruise H05 (25 April-11 May 1993). Surface particle concentrations were highest at the coast and generally decreased across the shelf (Figure 5.1-4). The 1993 spring high discharge of the Mississippi and Atchafalaya rivers was much greater than average and continued from March through May. During cruise H05, the Mississippi-Atchafalaya plume spread practically to the shelf edge east of 92°W . There, low salinity (< 30) surface waters extended out to the 50-m isobath, and surface waters with particle concentrations greater than $1 \text{ mg}\cdot\text{l}^{-1}$ extended nearly to the 200-m isobath. These waters formed a surface nepheloid

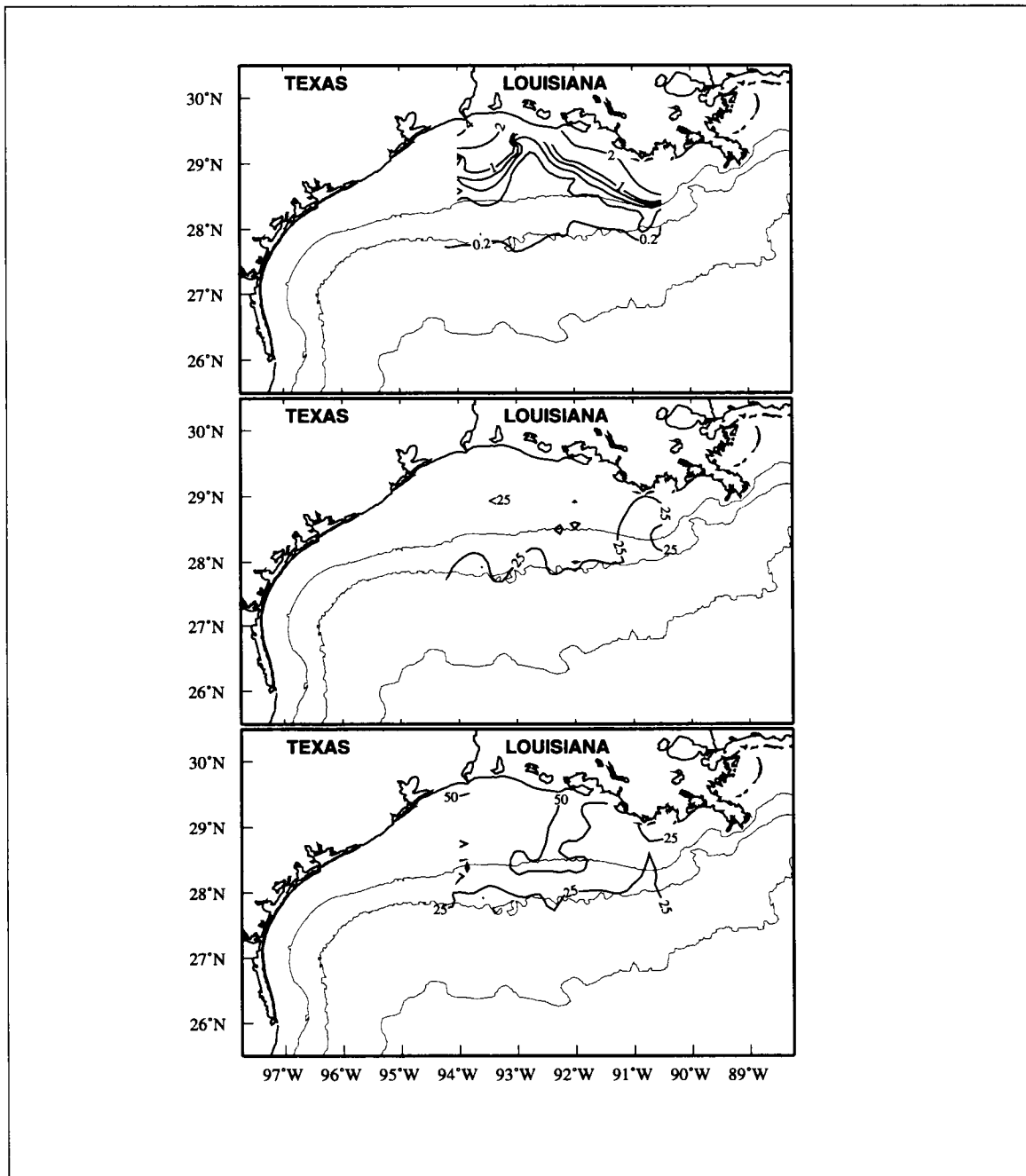


Figure 5.1-3. Particle distributions during cruise H01. (Upper panel) SPM ($\text{mg}\cdot\text{l}^{-1}$) as calculated from PBAC data. Contour interval is $0.2\text{ mg}\cdot\text{l}^{-1}$ up to 1.0. Contour interval is $1\text{ mg}\cdot\text{l}^{-1}$ above 1.0. (Middle panel) Mass of sediment in the water column under one square meter of sea surface. Contour interval is $25\text{ g}\cdot\text{m}^{-2}$. (Lower panel) Percent of total sediment mass in the water column that is contained in the BNL.

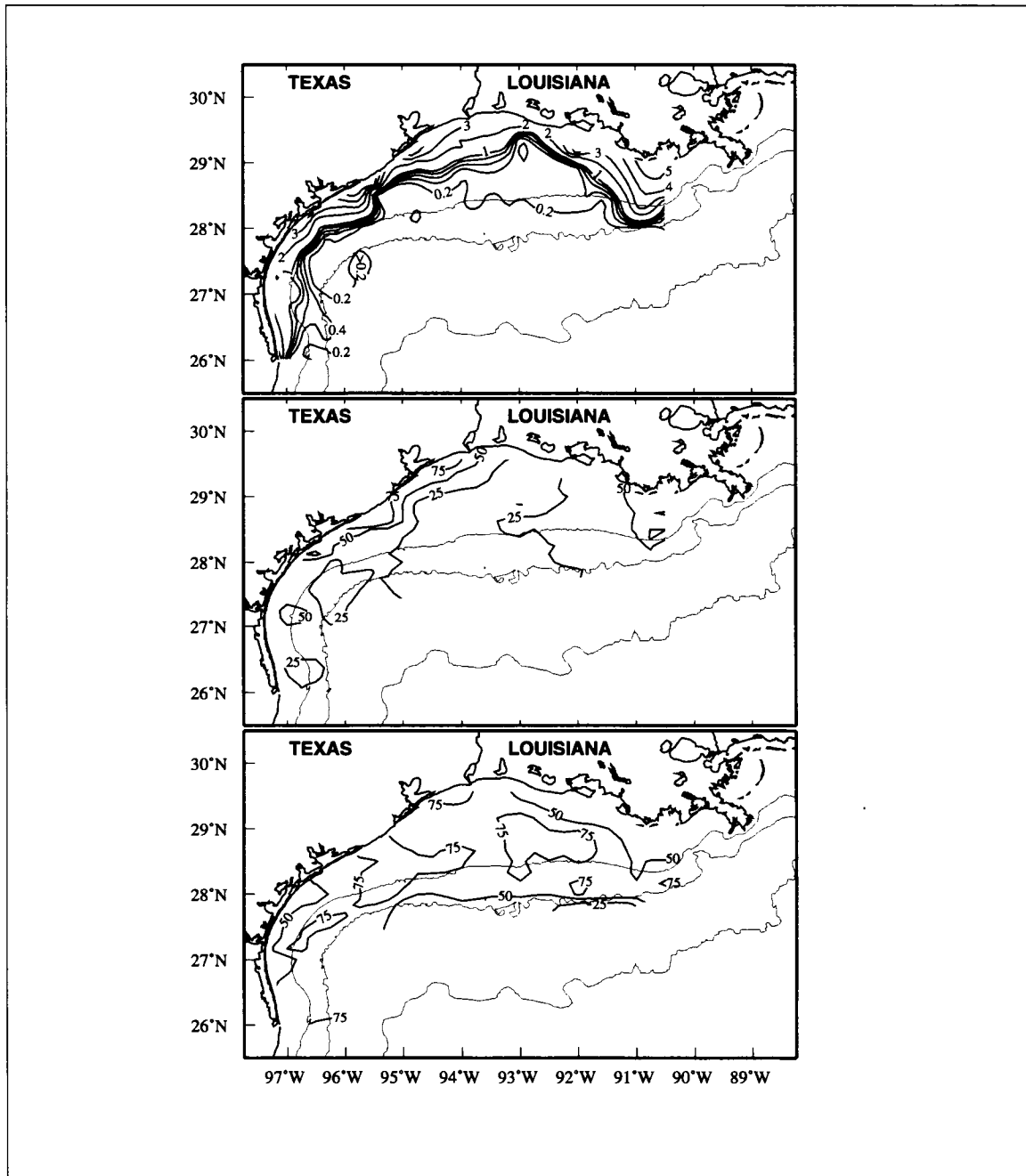


Figure 5.1-4. Particle distributions during cruise H05. (Upper panel) SPM ($\text{mg}\cdot\text{l}^{-1}$) as calculated from PBAC data. Contour interval is $0.2\text{ mg}\cdot\text{l}^{-1}$ up to 1.0. Contour interval is $1\text{ mg}\cdot\text{l}^{-1}$ above 1.0. (Middle panel) Mass of sediment in the water column under one square meter of sea surface. Contour interval is $25\text{ g}\cdot\text{m}^{-2}$. (Lower panel) Percent of total sediment mass in the water column that is contained in the BNL.

layer about 10 m thick. Surface transport of suspended particles was more important in that region, where less than 50% of the particles in the water column were in the BNL, than over most of the shelf .

West of the seaward extension of the Mississippi-Atchafalaya plume (92°W), surface waters with particle concentrations of greater than 1 mg·l⁻¹ were confined to the inner shelf except near the Texas-Mexico border. A plume of surface water with particle concentrations greater than 0.4 mg·l⁻¹ was transported from the inner shelf to the shelf edge near 26.5°N. Some of this turbid water flowed off the shelf under the influence of offshore eddies, as described below.

West of 92°W, the largest water column particle masses were observed on the inner shelf. Particle masses in excess of 50 g·m⁻² were found near the coast between 94° and 97°W. On the south Texas shelf, in the area where surface waters with high particle concentrations crossed the shelf and entered the off-shelf regime, masses in excess of 50 g·m⁻² were found at mid-shelf. On most of the shelf west of 92°W, greater than 50% of the particle mass was in the BNL, indicating bottom transport of suspended particles was important over that portion of the shelf.

Cruise H08 (24 April-7 May 1994). As in 1993, the spring river discharge in 1994 was well above the long-term average; it remained so from late January through most of May. Surface salinities indicate the river plume was confined to nearshore resulting in no surface nepheloid layer at the stations on the easternmost station line. There surface particle concentrations exceeding 1 mg·l⁻¹ were restricted to the inner shelf, the total mass of particles in the water column was low, and less than 50% of the particles were in the BNL (Figure 5.1-5). On the outer shelf where the surface plume was not present, more than 50% of the particles were transported in the BNL.

Very high surface particle concentrations (> 5 mg·l⁻¹) were found on the inner shelf between 91° and 95°W. In this same area and extending to 96°W, there was high particle mass in the water column (> 50 g·m⁻²). Over most of the shelf, more than 50% of the particle mass was in the BNL. Surface particle concentrations decreased to the southwest, as did SPM mass. On the south Texas shelf, surface waters with particle concentrations exceeding 0.4 mg·l⁻¹ extended across the shelf in approximately the same location as during cruise H05. However, during cruise H08 this cross-shelf particle transport was primarily a surface phenomenon—less than 50% of the low water column particle mass (< 25 g·m⁻²) was in the BNL.

Cruise H02 (31 July-9 August 1992). Cruise H02 sampled in the eastern study area only (Figure 5.1-6). Low salinity surface waters (< 30) were confined to the inner shelf east of 93°W. This salinity pattern is a reflection of the eastward transport of shelf waters in the summer. Surface waters with high SPM concentrations (> 1 mg·l⁻¹) were also confined to two localized regions: a very small area off Atchafalaya and Vermilion Bays and a larger

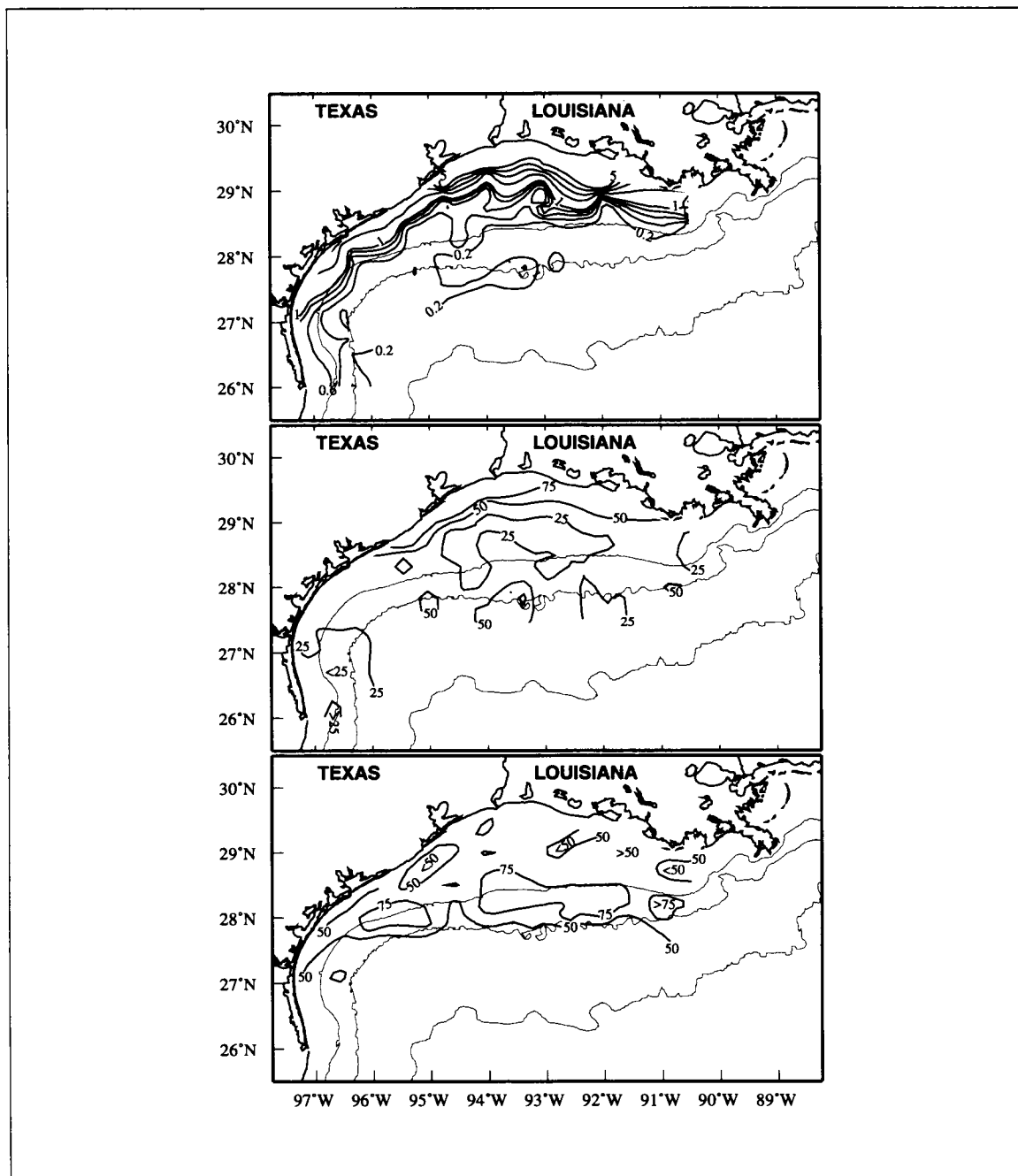


Figure 5.1-5. Particle distributions during cruise H08. (Upper panel) SPM ($\text{mg}\cdot\text{l}^{-1}$) as calculated from PBAC data. Contour interval is $0.2 \text{ mg}\cdot\text{l}^{-1}$ up to 1.0. Contour interval is $1 \text{ mg}\cdot\text{l}^{-1}$ above 1.0. (Middle panel) Mass of sediment in the water column under one square meter of sea surface. Contour interval is $25 \text{ g}\cdot\text{m}^{-2}$. (Lower panel) Percent of total sediment mass in the water column that is contained in the BNL.

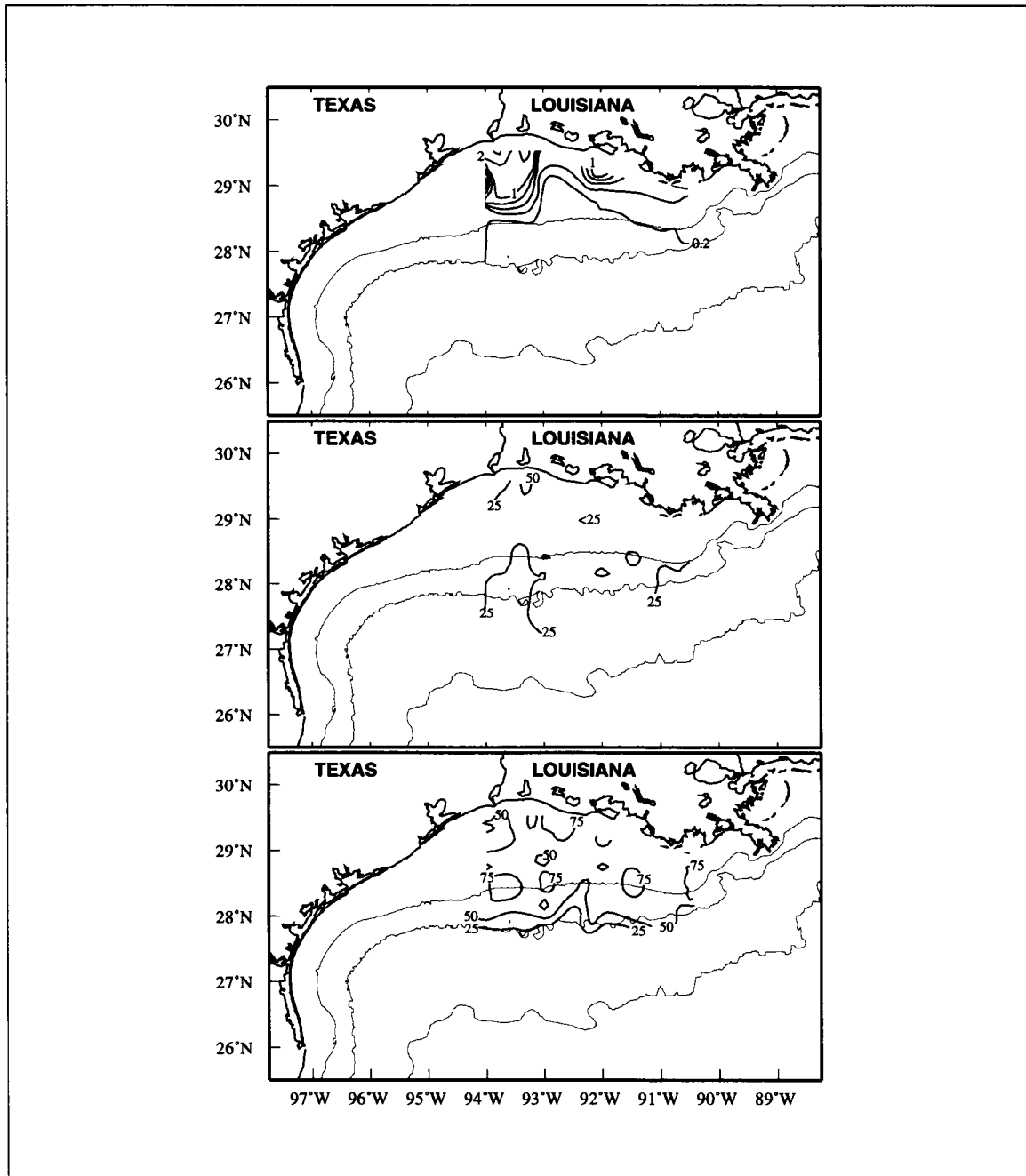


Figure 5.1-6. Particle distributions during cruise H02. (Upper panel) SPM ($\text{mg}\cdot\text{l}^{-1}$) as calculated from PBAC data. Contour interval is $0.2\text{ mg}\cdot\text{l}^{-1}$ up to 1.0. Contour interval is $1\text{ mg}\cdot\text{l}^{-1}$ above 1.0. (Middle panel) Mass of sediment in the water column under one square meter of sea surface. Contour interval is $25\text{ g}\cdot\text{m}^{-2}$. (Lower panel) Percent of total sediment mass in the water column that is contained in the BNL.

region off the Sabine River mouth. The mass of sediment in the water column during this cruise was generally low, less than $25 \text{ g}\cdot\text{m}^{-2}$ on most of the shelf. On most of the shelf, greater than 50% of the SPM in the water column was in the BNL.

As mentioned, the surface $\text{SPM} > 1 \text{ mg}\cdot\text{l}^{-1}$ is confined to two regions, one being off the mouth of the Sabine River. The Sabine River had a fourfold increase in average daily discharge between 1 August ($\sim 50 \text{ m}^3\cdot\text{s}^{-1}$) and 2 August ($\sim 200 \text{ m}^3\cdot\text{s}^{-1}$), with high discharge sustained through the cruise period; earlier, pulses of high flow occurred throughout June and into early July ($\geq 100 \text{ m}^3\cdot\text{s}^{-1}$). Stations in this area along line 4 were taken on 3 August local time; stations in this area along line 3 were taken on 8 August; also, there were five stations taken between the innermost stations on lines 3 and 4 on 8 August. Thus, the high SPM here may be attributable to this localized high river discharge. Note also that the only place with total water column mass $\geq 50 \text{ g}\cdot\text{m}^{-2}$ is within this area, and that this area is the one part of the inner shelf where most of the SPM is not in the BNL. This is evidence that the “smaller” rivers can significantly affect local particle distributions even though the Mississippi-Atchafalaya River discharge is generally dominant.

Cruise H06 (25 July-7 August 1993). Although the SPM data for H06 were insufficient to establish a correlation with PBAC that would allow quantitative estimates of SPM, the PBAC data derived from the transmissometer data can provide qualitative information, especially spatial distributions. The discharge of the Mississippi-Atchafalaya river system during the summer of 1993 was well above the historical mean. A region of low salinity water (< 30) extended along the nearshore over the eastern inner shelf. The largest surface PBAC values also are found along the eastern inner shelf (Figure 5.1-7 middle panel). Note that the pattern of cruise H09 (August 1994) shows largest PBAC values ($> 0.4 \text{ m}^{-1}$) occur where the surface particle concentrations are large (Figure 5.1-7 lower panel and Figure 5.1-8). This suggests that on cruise H06 high surface particle concentrations extended along the nearshore over the eastern inner shelf as well. On the western shelf, however, the surface PBAC values for H06 are very low, being generally $< 0.2 \text{ m}^{-1}$ everywhere. This contrasts with the values for cruise H09, which are high along the inner western shelf, and suggests the surface particle concentrations on the western shelf during H06 were unusually low.

Cruise H09 (26 July-7 August 1994). In July-August 1994, river discharge from the Mississippi and Atchafalaya rivers was low compared to spring. Waters from the spring flood were still on the shelf and had been transported to the east by summer currents. These low salinity surface waters extended across the shelf east of 93°W , where even seaward of the 200-m isobath surface salinities were less than 30. Turbid surface waters ($> 1 \text{ mg}\cdot\text{l}^{-1}$) extended over the inner shelf in this low salinity area (Figure 5.1-8). They formed a surface nepheloid layer about 10 m thick. The mass of particles in the water column of the area overlain by the plume was low to moderate ($< 25 \text{ g}\cdot\text{m}^{-2}$), and less than 50% of the particle mass was in the BNL.

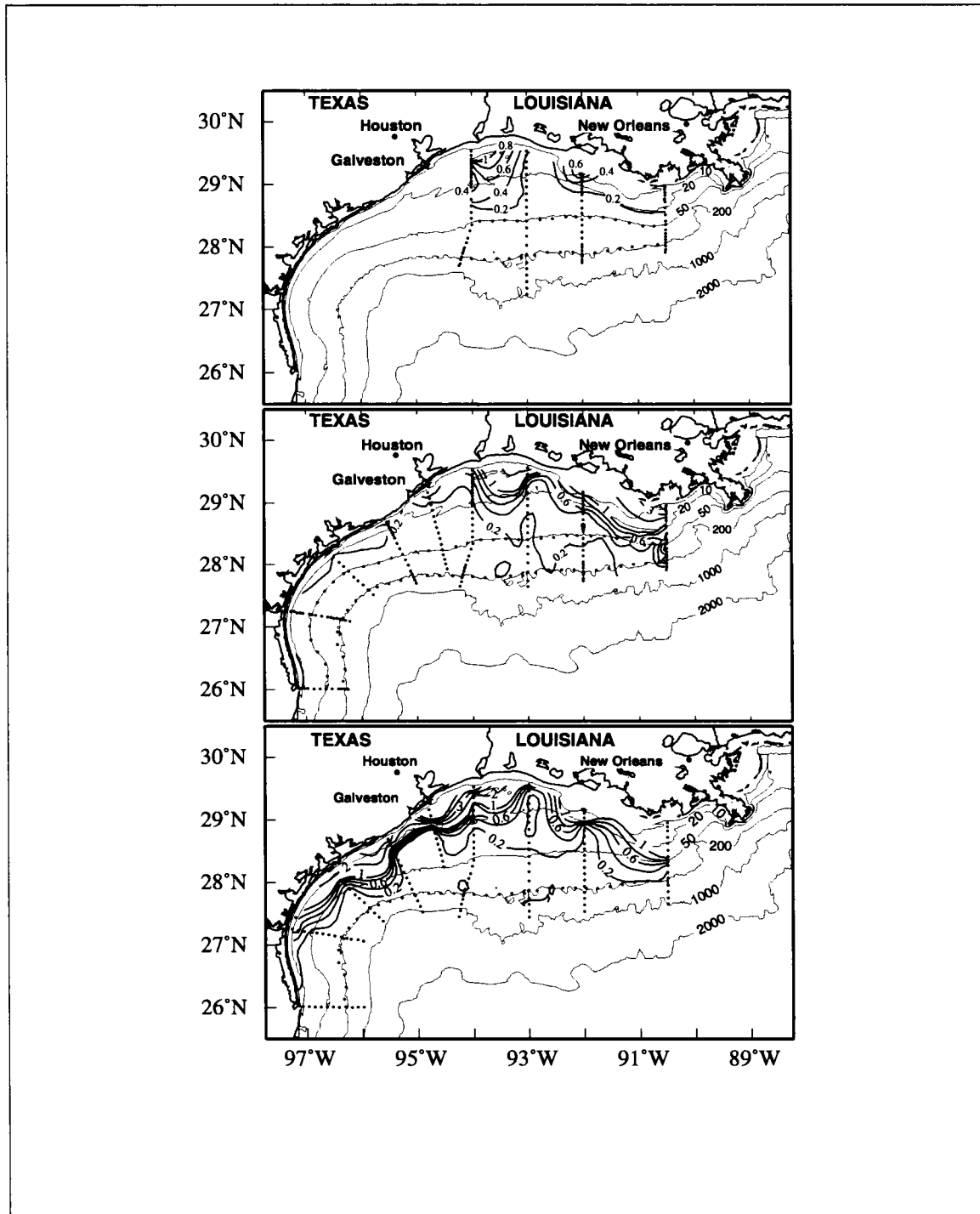


Figure 5.1-7. Summer particle beam attenuation coefficient (m^{-1}) distributions for cruises (upper panel) H02 in August 1992, (middle panel) H06 in August 1993, and (lower panel) H09 in August 1994.

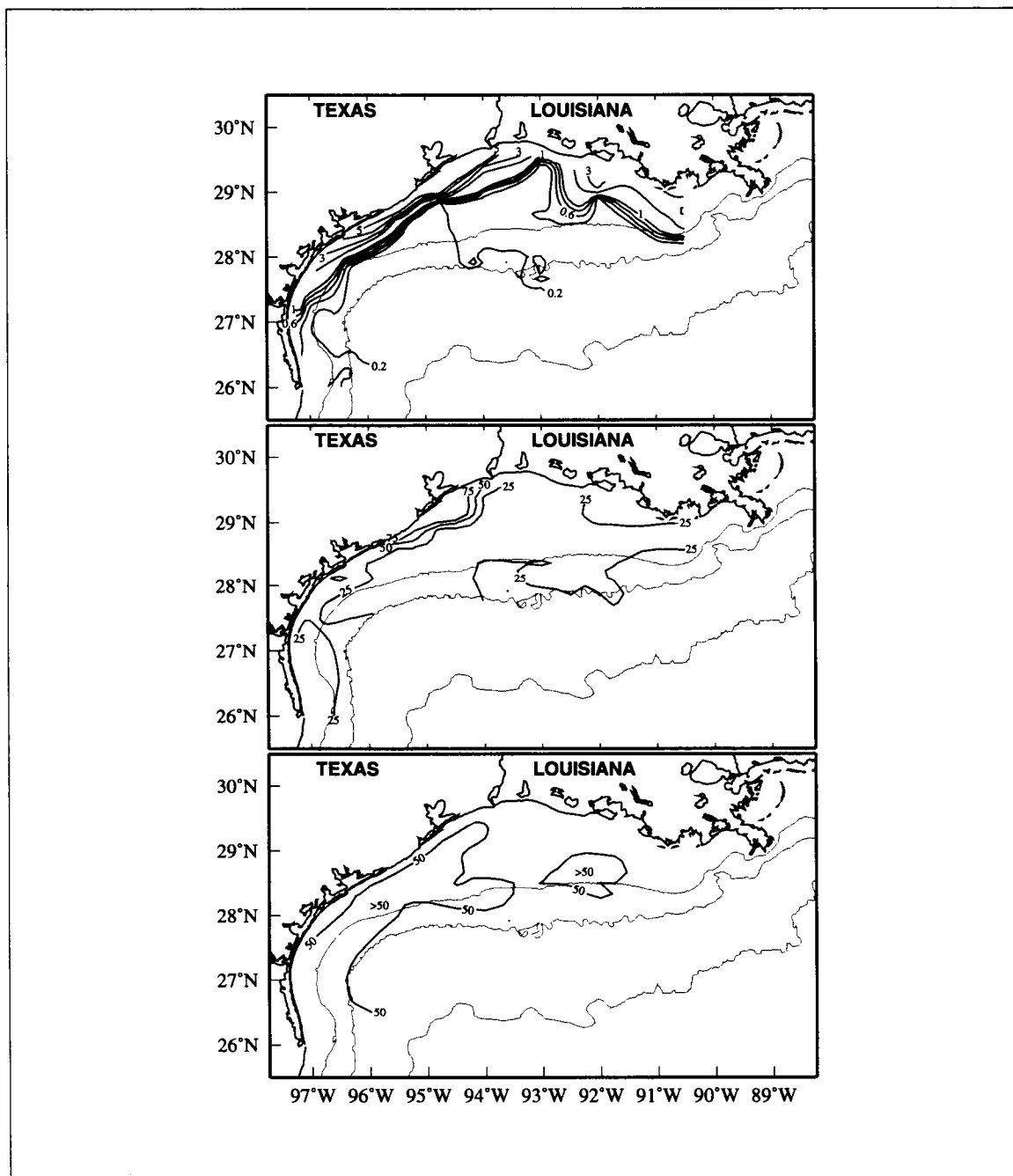


Figure 5.1-8. Particle distributions during cruise H09. (Upper panel) SPM ($\text{mg}\cdot\text{l}^{-1}$) as calculated from PBAC data. Contour interval is $0.2 \text{ mg}\cdot\text{l}^{-1}$ up to 1.0. Contour interval is $1 \text{ mg}\cdot\text{l}^{-1}$ above 1.0. (Middle panel) Mass of sediment in the water column under one square meter of sea surface. Contour interval is $25 \text{ g}\cdot\text{m}^{-2}$. (Lower panel) Percent of total sediment mass in the water column that is contained in the BNL.

West of 93°W, surface waters with particle concentrations exceeding 1 mg·l⁻¹ were found on the inner shelf as far south as 27.5°N. Near 26°N, surface particle concentrations were low (< 0.3 mg·l⁻¹). Highest surface particle concentrations (> 5 mg·l⁻¹) were observed nearshore between 94° and 96°W. This area corresponded to the area with the highest water column SPM (> 50 g·m⁻²). Over the rest of the shelf, the particle mass in the water column was less than 25 g·m⁻². Over much of the eastern shelf approximately < 50% of the suspended particles were in the BNL; over most of the western shelf the percentage was greater than 50%. We believe that upwelling was occurring along the south Texas coast during August. In addition, two cyclones and one anticyclone were off the western shelf edge during this period. Either of these types of phenomena could have contributed to the larger fraction of suspended particles in the BNL for the western than for the eastern shelf.

Cruise H03 (4-13 November 1992). Cruise H03 sampled only the eastern study area (Figure 5.1-9). Low salinity surface waters were confined to the inner shelf during this cruise. The inner shelf also had high surface SPM values exceeding 5 mg·l⁻¹. Mass of particles in the water column was moderately high on most of the eastern shelf, with values greater than 50 g·m⁻² nearshore on the inner shelf between 90.5° and 93.5°W. In that area, more than 50% of the SPM resided in the BNL. In the region with surface SPM values of 10 mg·l⁻¹, off Cameron, Louisiana, the total water column SPM exceeded 75 g·m⁻².

Cruise H07 (6-22 November 1993). Surface salinities over the eastern shelf were lower than 30, reflecting the downcoast transport of the low salinity waters. Surface particle concentrations exceeding 1 mg·l⁻¹ extended across the inner shelf (Figure 5.1-10), but a well developed surface nepheloid layer was not present at the easternmost station line. On the south Texas shelf, surface concentrations of 0.4 mg·l⁻¹ extended nearly to the shelf edge. Most of the shelf had moderate to high water column SPM (> 25 g·m⁻²). Highest water column SPM values (> 75 g·m⁻²) were observed nearshore between 90.5° and 92°W and also between 94° and 96°W. The percent of SPM in the BNL varied but generally was less than 75%, with large areas of the shelf having less than 50% of suspended particles in the BNL, suggesting surface transport of particles was important.

Cruise H10 (2-13 November 1994). Lowest salinities were found on the inner shelf off central and south Texas, possibly due to a large rainfall event and associated high river discharge from Texas rivers in mid-October 1994 (Appendix C). Surface waters with the highest particle concentrations were found on the inner shelf off western Louisiana and eastern Texas (> 5 mg·l⁻¹; Figure 5.1-11). On the eastern shelf, surface concentrations of greater than 1.0 mg·l⁻¹ extended over the inner shelf, but no surface nepheloid layer was present. Inner shelf surface waters with particle concentrations exceeding 1 mg·l⁻¹ extended west and south to 27.5°N. On the south Texas shelf, surface particle concentrations were low (< 0.4 mg·l⁻¹) compared to the rest of the inner shelf. Water column SPM was greater than 25 g·m⁻², except for the inner shelf west of 94.5°W. The percent of SPM in the BNL varied, large areas of the shelf having values less than 50%.

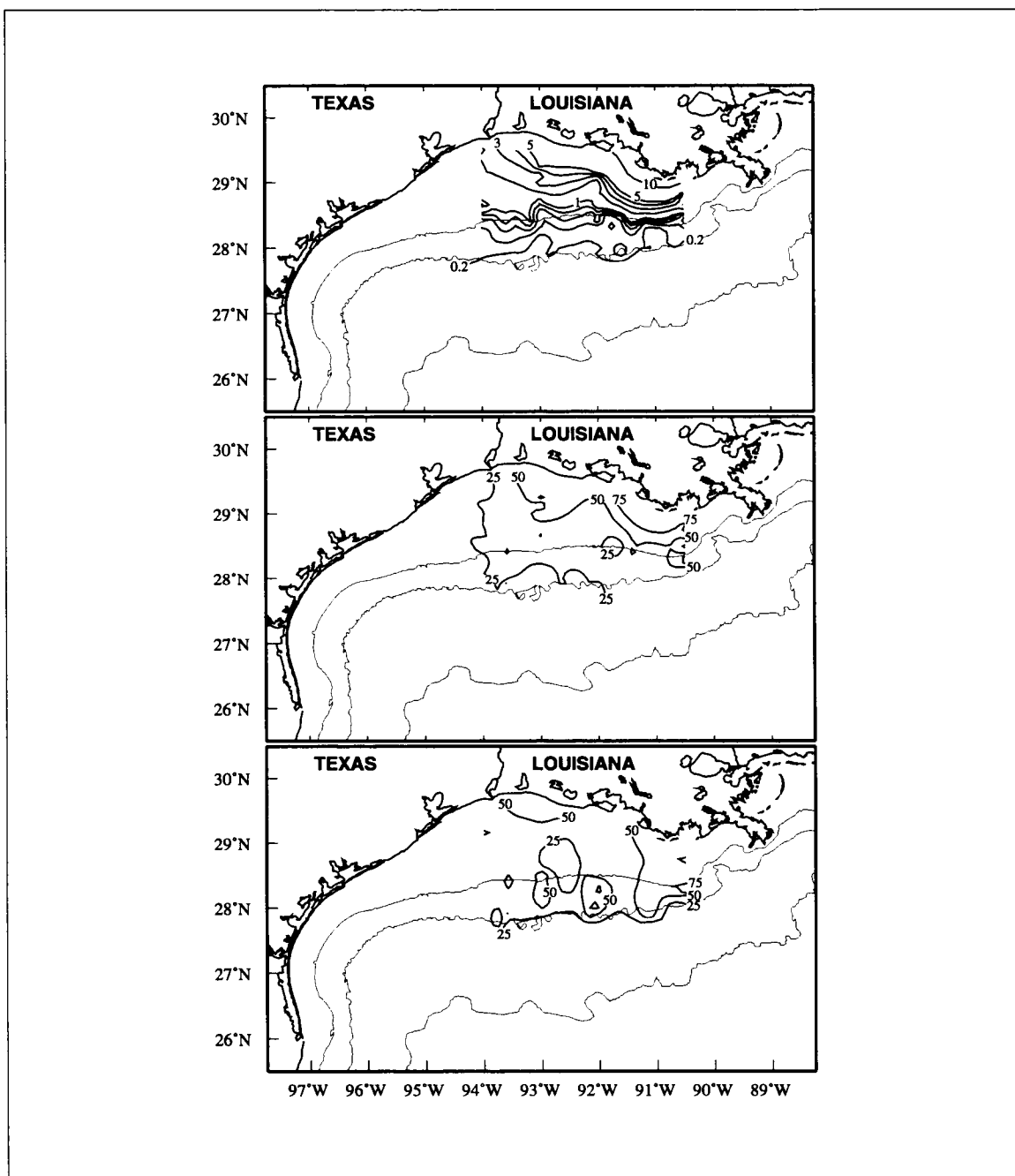


Figure 5.1-9. Particle distributions during cruise H03. (Upper panel) SPM ($\text{mg}\cdot\text{l}^{-1}$) as calculated from PBAC data. Contour interval is $0.2\text{ mg}\cdot\text{l}^{-1}$ up to 1.0 . Contour interval is $1\text{ mg}\cdot\text{l}^{-1}$ above 1.0 . (Middle panel) Mass of sediment in the water column under one square meter of sea surface. Contour interval is $25\text{ g}\cdot\text{m}^{-2}$. (Lower panel) Percent of total sediment mass in the water column that is contained in the BNL.

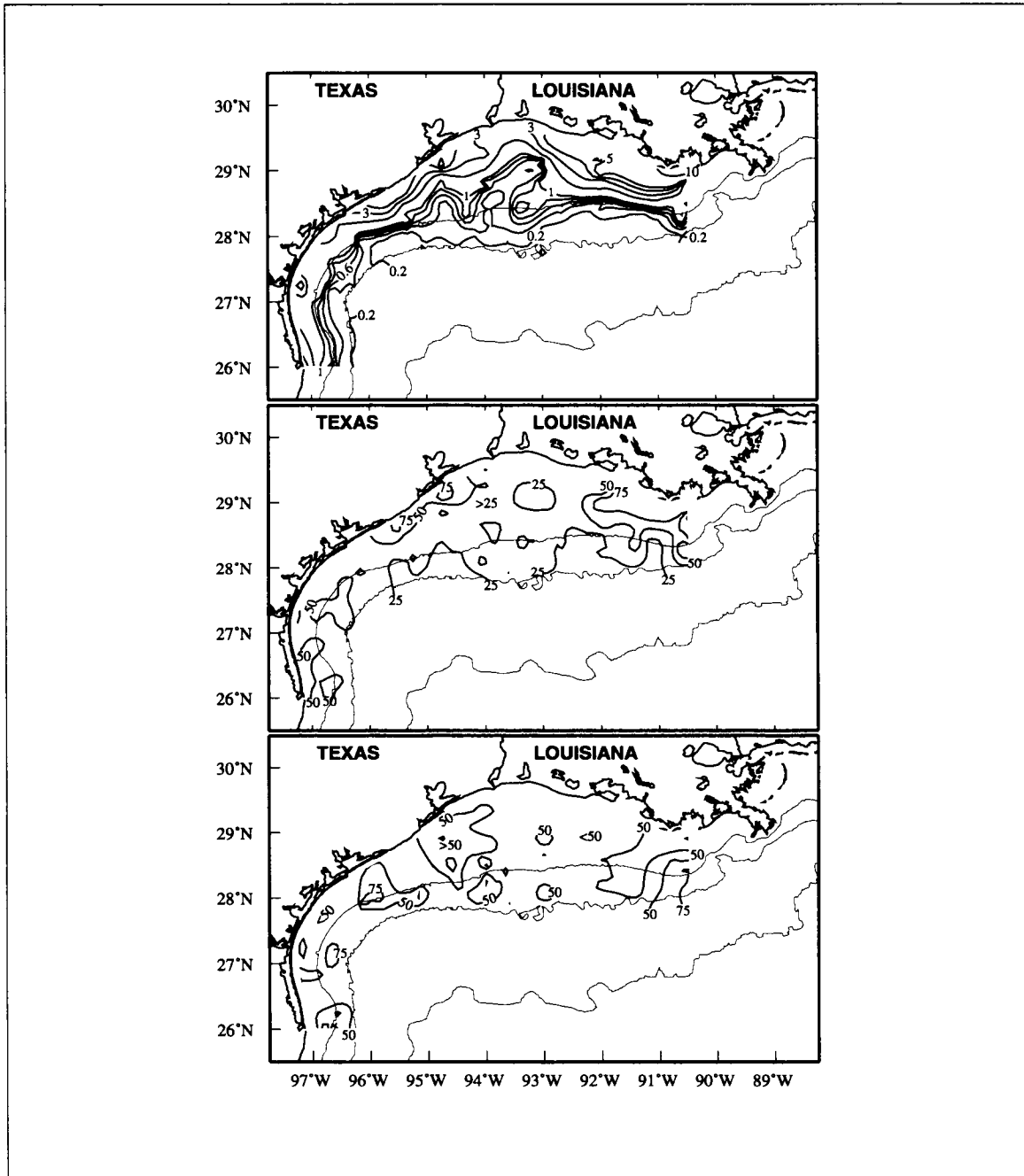


Figure 5.1-10. Particle distributions during cruise H07. (Upper panel) SPM ($\text{mg}\cdot\text{l}^{-1}$) as calculated from PBAC data. Contour interval is $0.2\text{ mg}\cdot\text{l}^{-1}$ up to 1.0. Contour interval is $1\text{ mg}\cdot\text{l}^{-1}$ above 1.0. (Middle panel) Mass of sediment in the water column under one square meter of sea surface. Contour interval is $25\text{ g}\cdot\text{m}^{-2}$. (Lower panel) Percent of total sediment mass in the water column that is contained in the BNL.

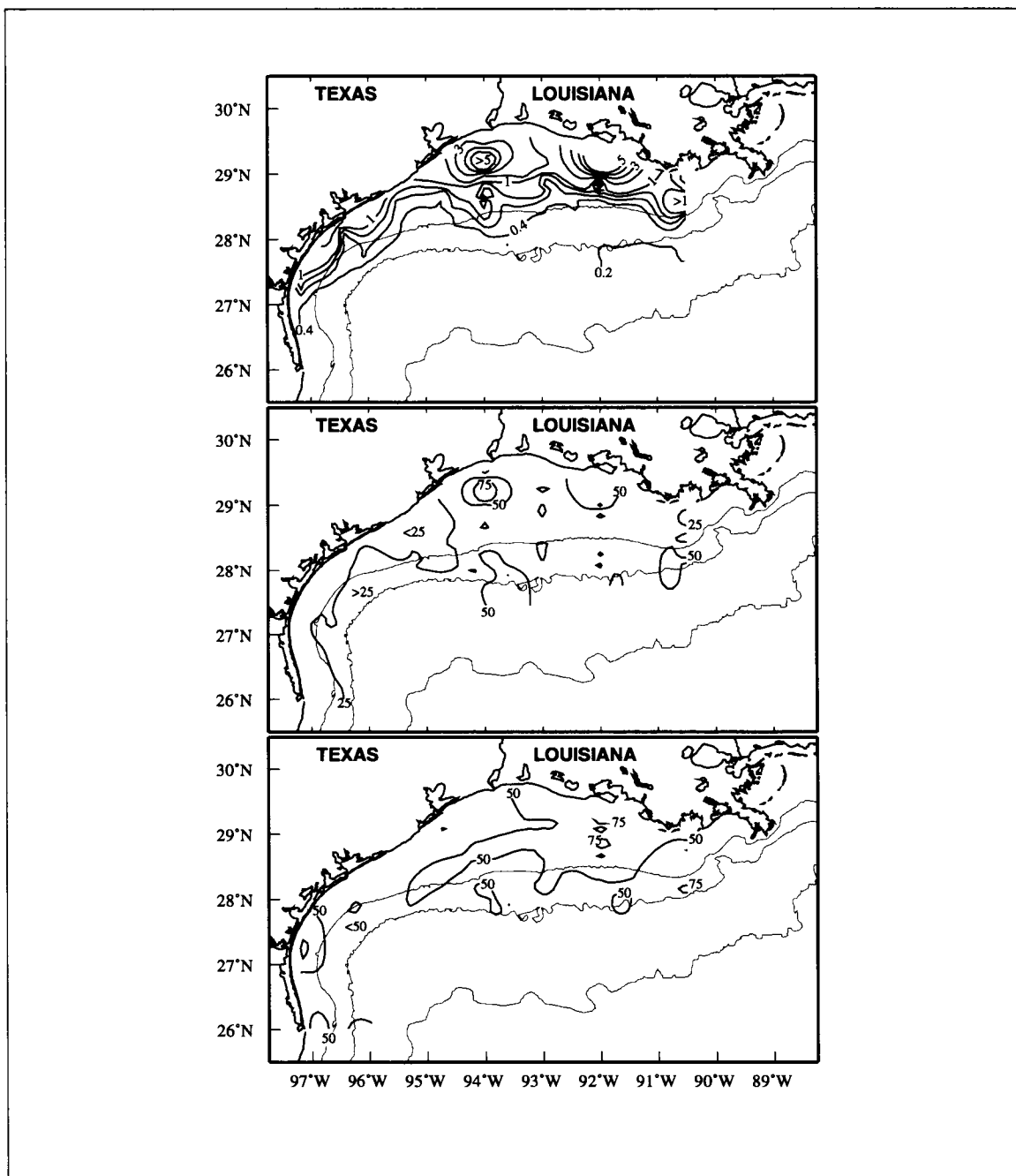


Figure 5.1-11. Particle distributions during cruise H10. (Upper panel) SPM ($\text{mg}\cdot\text{l}^{-1}$) as calculated from PBAC data. Contour interval is $0.2\text{ mg}\cdot\text{l}^{-1}$ up to 1.0 . Contour interval is $1\text{ mg}\cdot\text{l}^{-1}$ above 1.0 . (Middle panel) Mass of sediment in the water column under one square meter of sea surface. Contour interval is $25\text{ g}\cdot\text{m}^{-2}$. (Lower panel) Percent of total sediment mass in the water column that is contained in the BNL.

Cruise H04 (4-13 February 1993). Cruise H04 sampled only over the eastern shelf, and is the only winter hydrography cruise for the LATEX program (Figure 5.1-12). Although during this cruise low salinity surface waters on the easternmost line extended seaward of the 50-m isobath, surface waters with SPM exceeding $1 \text{ mg}\cdot\text{l}^{-1}$ were confined to the inner shelf. Distributions were similar to fall 1992 (cruise H03), except that surface and water column values were less for the winter cruise and a somewhat higher percentage SPM was found in the BNL.

Seasonal and interannual variability

Table 5.1-1 shows for each cruise estimates of SPM in the water column and the percent total water column SPM in the bottom nepheloid layer. For cruises with more than 50% of stations having water column SPM values greater than $25 \text{ g}\cdot\text{m}^{-2}$, columns 5 and 6 are shaded. Note that, with the exception of cruise H01, the spring and fall cruises appear to have the largest total SPM. There also is a marked difference in percent of total SPM found in the BNL on cruises H05, H08 and H02 (shaded in column 7) and on other cruises.

Spring distributions. Surface SPM patterns seen in 1992, 1993, and 1994 were similar. All three years evidenced spread of the surface nepheloid layer, associated with high surface SPM values, to about the 50-m isobath over the eastern shelf and downcoast alongshelf to the limit of the surveys. East of 92°W , the surface nepheloid layer extended to the 50-m isobath in 1992 and to the shelf edge in 1993. Along the south Texas coast, there is evidence for offshore, cross-shelf flow of surface particles in both years sampled (1993 and 1994). Both 1993 and 1994 had extensive nearshore areas with surface SPM values $> 5 \text{ mg}\cdot\text{l}^{-1}$, while 1992 did not.

Total sediment loads were least in 1992, with values mostly $< 25 \text{ g}\cdot\text{m}^{-2}$. High values ($\geq 50 \text{ g}\cdot\text{m}^{-2}$) were found clustered along the coast in the other years sampled. Additionally, in 1993, high total sediment loads were found to extend to the 50-m isobath east of 91.5°W . In 1994, the surface and total sediment load was confined to the shallow portion of the inner shelf, and total sediment loads seemed largest for the three years. Total sediment loads were least in 1992 when high values were not found clustered along the coast as in the other years sampled.

In both 1993 and 1994, the BNLs contained 50% or more of the total SPM over essentially all of the shelf except for the coastal boundary layer on the eastern shelf, where the surface nepheloid layer was prominent. Moreover, in both those years, there were large mid-shelf areas over which more than 75% of the total SPM was found in BNLs. By contrast, less than 50% of the total SPM was found in BNLs in 1992, except for over a small area seaward of Atchafalaya Bay.

Table 5.1-1. Summary of water column SPM and percentage of SPM in BNL for each cruise. Table entries are percent of stations.

cruise	season	total no. of stations	% of stations with water column SPM values ($\text{g}\cdot\text{m}^{-2}$)			SPM in BNL > 50%
			< 25	25 to 50	> 50	
H01	spring	102	73	27	0	25
H05	spring	164	46	38	16	81
H08	spring	121	47	37	16	67
H02	summer	108	80	19	1	67
H09	summer	122	66	28	6	37
H03	autumn	101	35	49	16	32
H07	autumn	186	23	50	27	43
H10	autumn	120	38	45	17	38
H04	winter	101	64	33	3	37

We attribute the large interannual difference between 1992 and the two following years to the difference in river discharge. Mississippi-Atchafalaya discharge was below long-term mean for late winter and spring of 1992, but it was much above the mean for essentially the same period in 1993 and 1994. The difference in the offshore extent of the surface nepheloid layer in 1993 and 1994 may be due in part to the different wind, and so current, regimes. In April 1994, the downcoast currents over the inner shelf were stronger than in 1993.

Summer distributions. It might be expected that the upcoast currents over the inner shelf during summer would block downcoast spread of nearshore surface nepheloid layers, or even transport sediments found along the south and central Texas shelf up the coast. Because of the limited spatial coverage of cruise H02 (Figure 5.1-6), it is not possible to confirm or deny this scenario, although the localized areas of high surface SPM in 1992 suggest there is little downcoast transport of sediments. However, for cruise H09 (Figure 5.1-8) the nearshore surface SPM concentrations are large all along the Texas-Louisiana shelf, even near Brownsville.

The patterns of high surface PBAC ($> 1 \text{ m}^{-1}$) over the eastern shelf are similar in all three years, with highest values nearshore between 90.5° and 92.5°W and off the Sabine River (Figure 5.1-7). The PBAC patterns over the western shelf, however, differ in the two years sampled (1993 and 1994). There are no high PBAC values for summer 1993 (cruise H06) over the western shelf, in contrast to summer 1994 (cruise H09) where values greater than 1 m^{-1} extend along the nearshore western shelf to 27.5°N . This suggests interannual variability in summer surface particle concentrations.

Total water column SPM are greatest for H09 west of the Louisiana border offshore from east Texas. Likewise, the highest total values for cruise H02 are found near the Texas-Louisiana border. These may be due more to localized effects than to general circulation.

During August of 1992 (H02), half or more of the total SPM in the water column was found in bottom nepheloid layers except for very near shore and at the shelf edge. That cruise covered only the eastern shelf. During cruise H09 (August 1994), however, the eastern shelf mostly showed less than half of the total SPM in BNLs, while the western shelf showed the opposite situation.

Based on comparison of these two summer distributions, one might assert that the activity in bottom nepheloid layers is quite variable from one summer to another. We also noted large differences in the patterns of SPM found in the coastal surface nepheloid layer between 1993 and 1994.

Fall distributions. Inner shelf surface values were as large or larger than for spring. The cross-shelf extent of high surface values was greater than for spring, except in the extreme east.

In fall, the winds re-establish the downcoast circulation on the inner shelf. As expected under this regime, the spread of nearshore high surface particle concentrations is downcoast in all three years. The differences between years are in the offshore extent of the high concentrations and the concentration levels. Generally, over the eastern shelf the high concentrations cover the whole inner shelf to the 50-m isobath. Over the western shelf, however, the high concentrations spread to the 50-m isobath in 1993, but only to the 20-m or less isobath in 1994. The maxima in concentration were approximately $10 \text{ mg}\cdot\text{l}^{-1}$ in 1992 and 1993, but only about $5 \text{ mg}\cdot\text{l}^{-1}$ in 1994. We attribute these interannual differences in surface SPM concentration patterns to the river discharge levels, which in 1992 were above average, in 1993 were well above average, and in 1994 were average.

The total water column SPM was relatively high where the surface SPM concentrations were at maximum. In 1992 and 1993, they generally were largest in the nearshore east of 92°W , while in 1994 the largest values were localized. The percent SPM in the BNL was mostly $< 50\%$ in all three years.

Winter distribution. Only one winter cruise (H04) was made, and that sampled only over the eastern shelf (Figure 5.1-12). At that time surface SPM values were relatively high nearshore east of 91°W . The surface nepheloid layer decreased in particle load offshore and to the west of the eastern line 1, but nevertheless showed values of $1 \text{ mg}\cdot\text{l}^{-1}$ almost to the 50-m isobath east of 92°W . Water column SPM over the eastern shelf followed the pattern

of higher values ($25 \text{ g}\cdot\text{m}^{-2}$ but generally $> 50 \text{ g}\cdot\text{m}^{-2}$) in the northeast and lower values ($< 25 \text{ g}\cdot\text{m}^{-2}$) in the southwest. Over much of the inner shelf, more than 50% of the total SPM was within bottom nepheloid layers; the largest percentages were found at mid-shelf locations.

The relatively large SPM found in the eastern nearshore region is attributed to the fact that the Mississippi-Atchafayala discharge increased to about twice its long-term daily mean in November 1992 and remained high through the period of this cruise. Thus, the resulting particle distributions should not be assumed typical of the winter season.

Effects of current rings near the shelf edge on particle distributions over the shelf—an example

In four (H05, H08, H09, and H07) of the five pictured full-shelf distributions of surface SPM, relatively high values are seen to extend to or past the shelf edge of south Texas below 27°N . This argues for the occurrence of offshore, cross-shelf transports in this region as a common circumstance. An examination of the H05 data set shows that the interaction of cyclones and anticyclones with shelf circulation may be an important mechanism for effecting offshelf transport of SPM.

Hydrographic data, including surface salinity and surface PBAC, as well as satellite AVHRR sea surface temperatures, show that inner shelf water was transported across and off the south Texas shelf in April-May 1993. This flow was driven by a Loop Current anticyclonic ring (the northern part of Eddy V) and a companion cyclone impinging on the shelf edge off south Texas (Jochens et al. 1994). These are shown, labeled V_n and WC, in Figure D-10 of Appendix D, which shows the AVHRR sea surface temperature distribution for 12 May 1993, one day after the end of cruise H05. Also shown in that figure are anomalies of sea surface height from satellite altimetry averaged over the period 9-19 May 1993. It is seen clearly in the sea surface temperature distribution that the southern limb of the cyclone directed shelf edge water off the shelf.

During much of the period of cruise H05 (25 April-11 May 1993), the alongshelf wind components were convergent south of Corpus Christi. This wind pattern may have helped drive currents offshore to near the southward limb of the cyclone. Near the shelf edge, offshelf flow was enhanced by the circulation of the cyclone. The distribution of PBAC at 3 m during cruise H05 (Figure 5.1-13) shows that surface waters with values greater than 0.3 m^{-1} were transported off the shelf near 26.5°N . Note that northeast of this turbid plume, along the 200-m isobath at about 95.5°N , is an area of PBAC values greater than 0.1 m^{-1} . This water may be the remnant of the turbid plume, after it had circulated around the cyclone. Here strong currents between the cyclone and Eddy V_n were directed onto the shelf. These transported the turbid surface water back onto the shelf edge. Eddy V_n also pulled water off

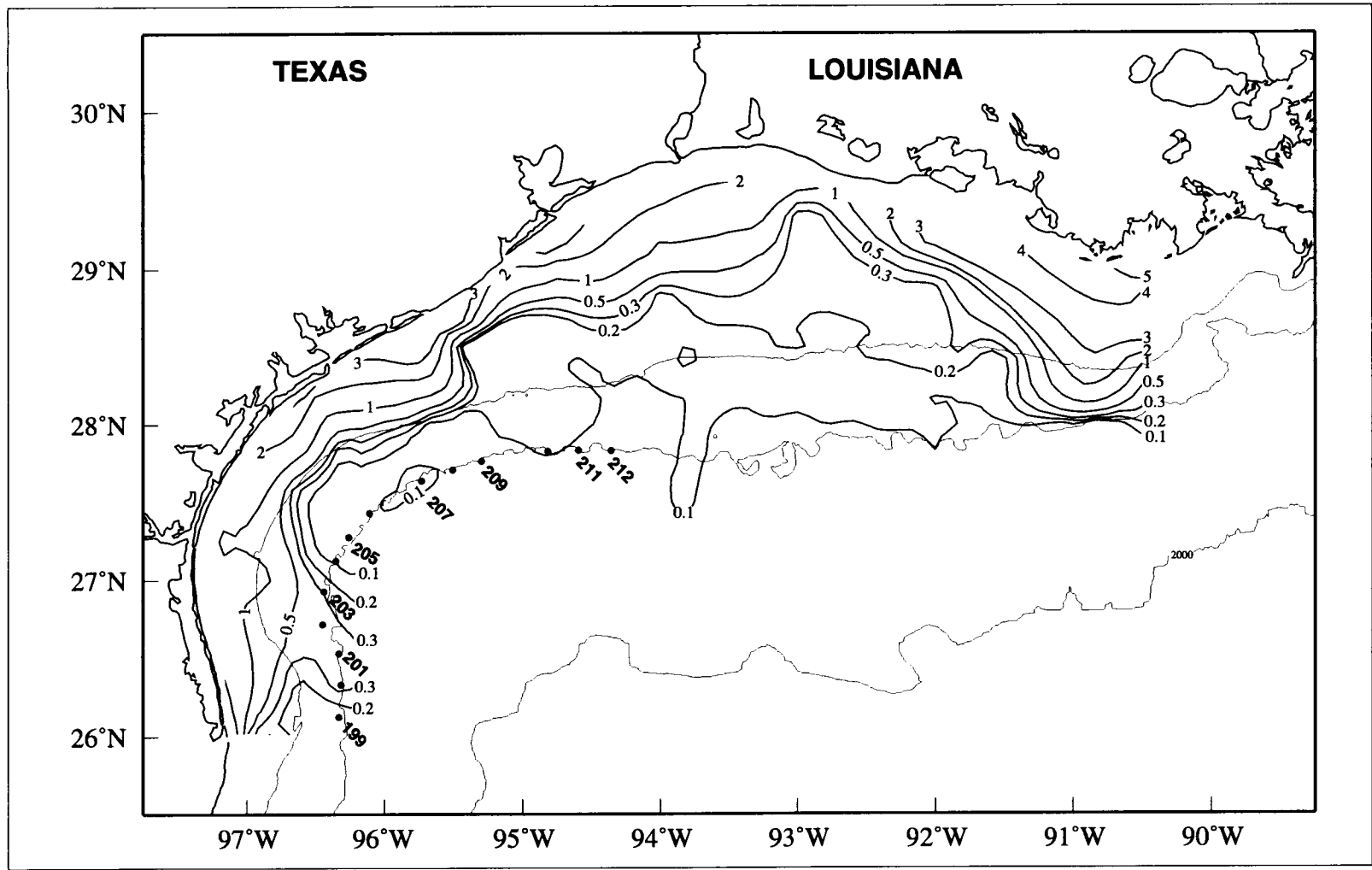


Figure 5.1-13. Particle beam attenuation coefficient (m^{-1}) at 3 m during cruise H05 (25 April-11 May 1993). The contour intervals vary. The locations of stations 199 through 212 are indicated.

the shelf, as evidenced by the finger of water with PBAC $> 0.1 \text{ m}^{-1}$ extending offshore at about 94°W .

The cyclone and Eddy V_n also were effective in transporting SPM off the shelf at mid-depths. Figure 5.1-14 shows a series of profiles of PBAC at cruise H05 stations along the 200-m isobath. High particle concentrations are indicated by high PBAC values. At the shelf edge, layers of high particle concentration often occur at mid-depth; these are intermediate nepheloid layers. Stations 207, 208, and 209 appear to have been in the region of onshore flow under the action of Eddy V_n . Eddy water is deep ocean water that generally has low particle concentrations, and no intermediate nepheloid layers were observed at those stations. On the northeastern side of Eddy V_n (stations 210, 211, and 212) where offshore flow occurred, intermediate nepheloid layers were present. These layers were not coincident with major fluorescence peaks, suggesting they were shelf sediments of mineral matter transported off the shelf.

Intermediate nepheloid layers were observed at stations 199 to 206, that were either in the limb of the cyclone where flow was offshore or in the southwestward, along-isobath flow in the case of station 206. For southwestward along-isobath flow, the resulting bottom Ekman layer would have offshore near-bottom currents, perhaps accounting for the BNL at station 206.

Mississippi-Atchafalaya plume during a year of unusually high discharge—an example

For each of the LATEX A hydrographic cruises, salinity and PBAC at 3 m along the easternmost station line 1 were correlated. Except for the November cruises (H03, H07, and H10), there is strong correlation (at the 99% level) between the two variables, with PBAC decreasing as salinity increases. The poorer correlations in November—which are still significant at 99% for H03, 95% for H07, and 65% for H10—were due to the relatively high salinities found all along line 1 at this time of the year.

Salinity on this part of the shelf is controlled principally by mixing of the Mississippi-Atchafalaya plume with ocean water. The correlation between salinity and PBAC in the eastern study area indicates that the offshore movement of the plume transports modern sediment across the shelf. Walker (1996) found that the variability in the location of the sediment plume of the Mississippi River to the east of our study area was a function of river discharge and wind forcing. Seasonal and interannual variability were functions of river discharge while day-to-day variability was a function of winds.

The period from May 1992 through August 1993 included both very low and very high river discharge. Thus, using surface PBAC data from the first six cruises, we can examine the variability in the plume due to variability in river discharge. The distribution of PBAC at 3 m for the eastern shelf is shown in Figure 5.1-15 for each of these cruises.

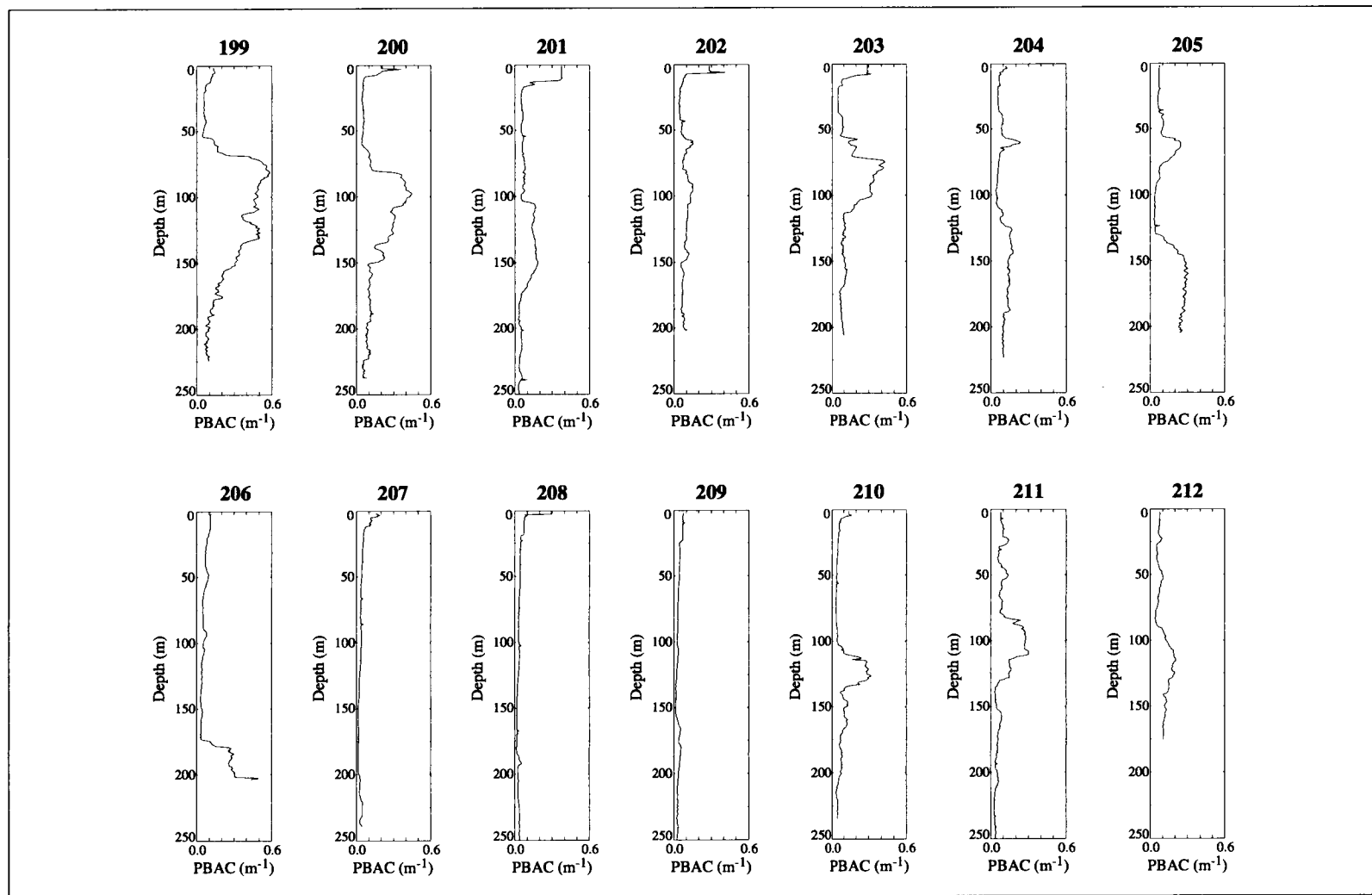


Figure 5.1-14. Vertical profiles of particle beam attenuation coefficient (m^{-1}) taken on 9 and 10 May 1993 on cruise H05. Station locations are shown in Figure 5.1-13.

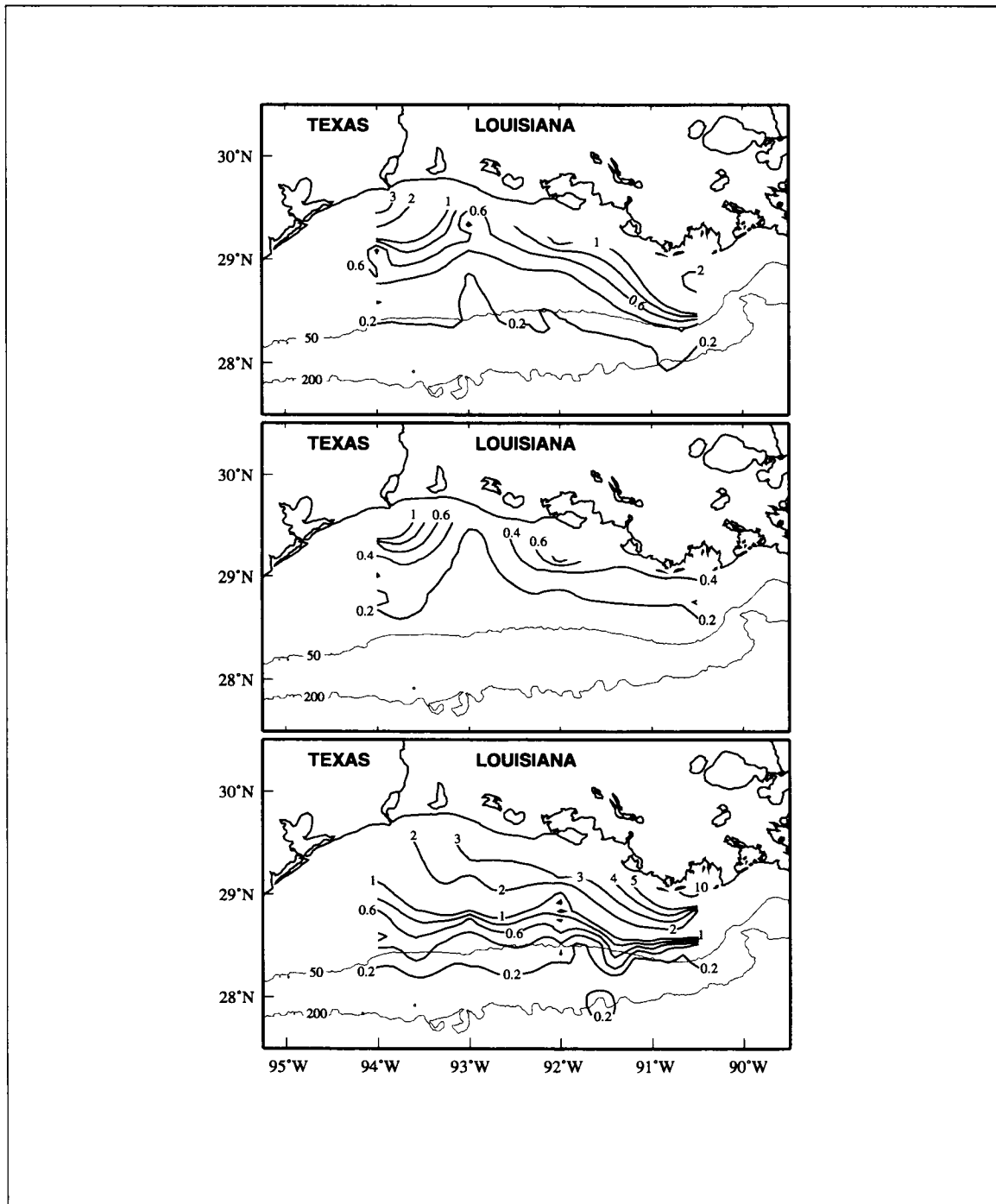


Figure 5.1-15a. Particle beam attenuation coefficient at 3 m depth for the eastern LATEX A study area in 1992 for the May cruise H01 (upper panel), August cruise H02 (middle panel), and November cruise H03 (lower panel). The contour interval is 0.2 m⁻¹ from 0.2 to 1.0 and is 1.0 for larger values.

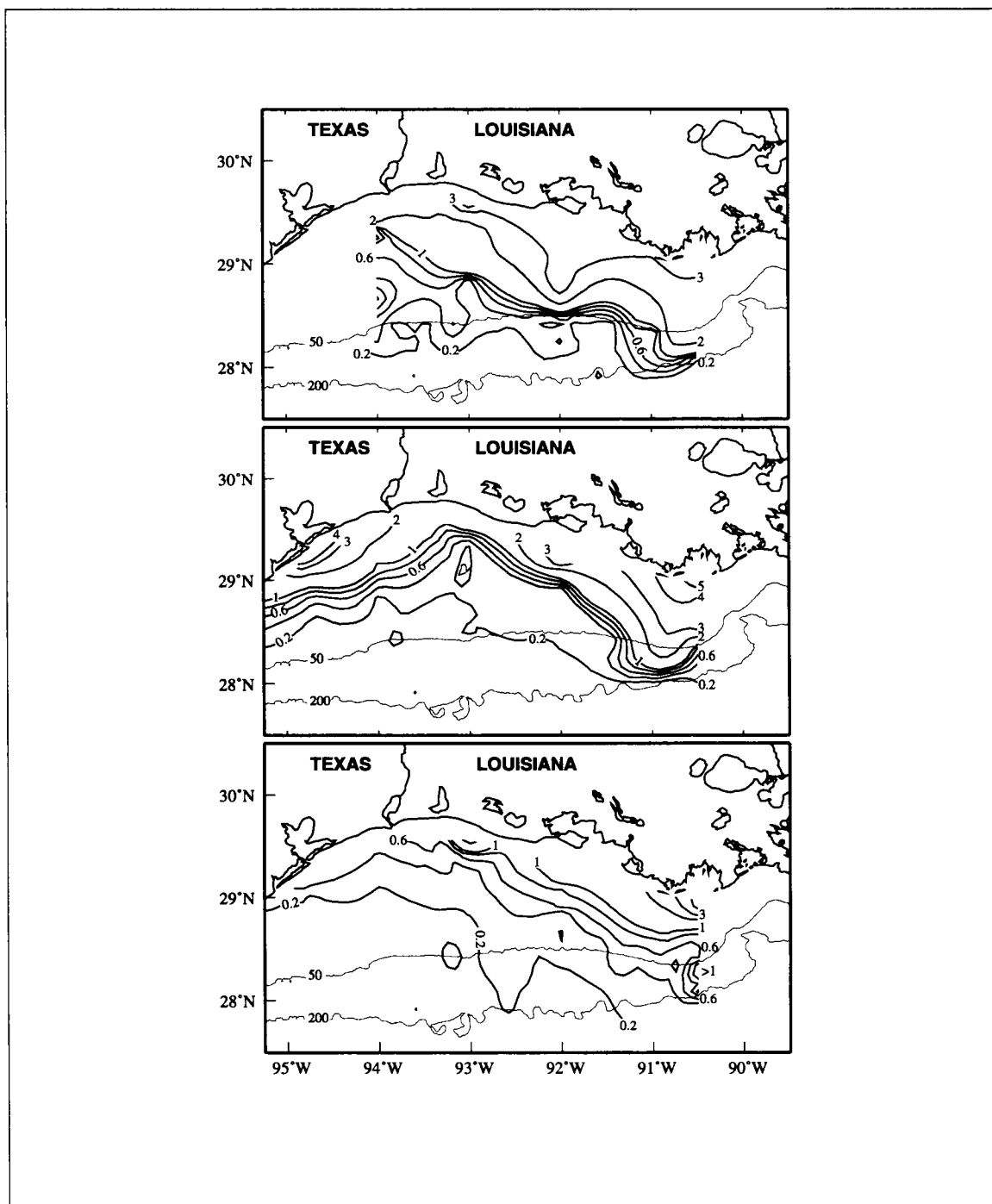


Figure 5.1-15b. Particle beam attenuation coefficient at 3 m depth for the eastern LATEX A study area in 1993 for the February cruise H04 (upper panel), May cruise H05 (middle panel), and August cruise H06 (lower panel). The contour interval is 0.2 m⁻¹ from 0.2 to 1.0 and is 1.0 for larger values.

The pattern of 1992 Mississippi-Atchafalaya river discharge was near the 64-year mean pattern with three exceptions: (1) spring discharge was low, and (2) discharge peaked to approximately twice the norm in August and again (3) in November through January. Cruise H01 was conducted in May after the peak of the spring discharge. The low discharge, westward transport of that discharge by shelf currents, and the settling of particles out of the water prior to the cruise resulted in a small plume. Surface waters with PBAC values exceeding 1 m^{-1} were confined to very near the coast. In August (cruise H02), PBAC values of surface waters again were quite low over most of the shelf due to the low river discharge and low energy waves typical of summer.

During the time of cruise H03 in November 1992, river discharge was at its annual low. However, the river discharge had been above average from mid-July to mid-October. Surface waters with PBAC values exceeding 1 m^{-1} were found outward past the 20-m isobath over the eastern shelf. Immediately after cruise H03, river discharge began to increase, and from that time through almost all of 1993 daily discharge exceeded the 64-year average. By February 1993 (H04), approximately three months of higher than average discharge had occurred. Although the river plume had expanded as a surface nepheloid layer to the shelf edge east of 91°W , surface SPM distributions were very similar to November otherwise. We attribute the relatively large plume for November and the only slightly expanded plume in February to the circulation regime. Downcoast alongshelf currents over the inner shelf were weaker than usual in fall 1992, so the higher than average July-October discharge was not removed from the eastern shelf. Further evidence for this is seen in the distributions shown in Figure 5.1-9. By contrast, downcoast alongshelf currents were relatively strong in winter of 1992-93, and we hypothesize that much of the flood water was moved rapidly downcoast in a coastal current. Comparing Figures 5.1-9 and 5.1-12, it is seen that the particle loading was greater over the eastern shelf during November 1992 than during February 1993.

By May 1993 (H05), there was considerably more SPM in the surface layer along line 1, extending to the shelf edge. The remainder of the eastern shelf showed no significant increase in surface SPM relative to February. Even in August 1993 (H06), there was a large amount of fresh water on the shelf. July-August river discharge exceeded the spring peak for the 64-year mean, and the impact of this discharge resulted in unusually large particle distributions for August. Surface waters with PBAC values exceeding 1 m^{-1} were found even to the shelf edge at line 1 and along the nearshore part of the inner shelf west of 93°W . By comparison, August was a time of lowest surface PBAC in the 1992 annual cycle; no surface values exceeded 1 m^{-1} along line 1, and values lower than 0.2 m^{-1} extended well shoreward of the 50-m isobath throughout the study area. In contrast, the August 1993 PBAC values of 0.2 m^{-1} extended to the shelf edge as far west as 92.5°W .

In summary, high surface values of particle beam attenuation coefficients, and by inference high surface SPM values, over the eastern shelf can be related to sustained high discharge

rates of the Mississippi-Atchafayala rivers. However, the spatial distributions of those surface nepheloid layers are broadly influenced by the circulation. In nonsummer, if the dominant downcoast flow over the inner shelf is diminished, there is more likelihood that the surface particle distributions will extend further seaward over the shelf than for large downcoast flow which sweeps the surface nepheloid layer away in a coastal boundary layer.

Average suspended particulate loading for the Texas-Louisiana shelf

The total water column values of SPM, the distributions for which are shown by cruise in Figures 5.1-3 - 5.1-6 and 5.1-8 - 5.1-12, were averaged to give a mean value for each cruise (Figure 5.1-16). Values for the eastern shelf (east of 94°W) and the entire shelf, when observations allowed, are plotted.

The pattern of average water column SPM that emerges presents a maximum in the fall season. This is true for the entire shelf, but is even more striking for the eastern half. Ignoring the one winter realization (cruise H04), each year shows a minimum in summer, maximum in fall, and an intermediate value in spring.

Interannual variability also is present, however. For each season, 1992 values were less than those for the corresponding season in 1993 and 1994. We attribute this to the fact that 1992 was a year of less than average Mississippi-Atchafayala river discharge, but in 1993 and 1994 the discharge was higher than average. Our examination of Mississippi-Atchafayala river discharge and average water column SPM over the shelf on a cruise-by-cruise basis did not reveal a unique relationship. The discharge was below the norm for two months preceding cruises H01 and H02, for which average SPM had the lowest values, and discharge was well above average for two months preceding cruises H07 and H08, for which average SPM values were quite large. However, for other cruises the correspondence was not so good.

We also examined the relationship between average water column SPM and the average amount of that load in the bottom nepheloid layer, shown in 5.1-17. The four cruises for which average water column SPM was low ($< 25 \text{ g}\cdot\text{m}^{-2}$ for the eastern shelf) were H01, H02, H04, and H09. Those are the same cruises for which average SPM in the BNL was low. Looking at Figure 5.1-16, there is an average difference of about $15 \text{ g}\cdot\text{m}^{-2}$ between the four low-valued cruises and the other cruises. The analogous difference of average SPM in the BNL between the four low-valued cruises and the other cruises is at least $10 \text{ g}\cdot\text{m}^{-2}$. Thus, the high average water column SPM may result when the bottom nepheloid layers are transporting more material. The causal factors for such enhanced BNL transport include large near-bottom currents (e.g., enhanced coastal current or bottom currents over outer shelf due to current eddies) or enhanced wind wave activity.

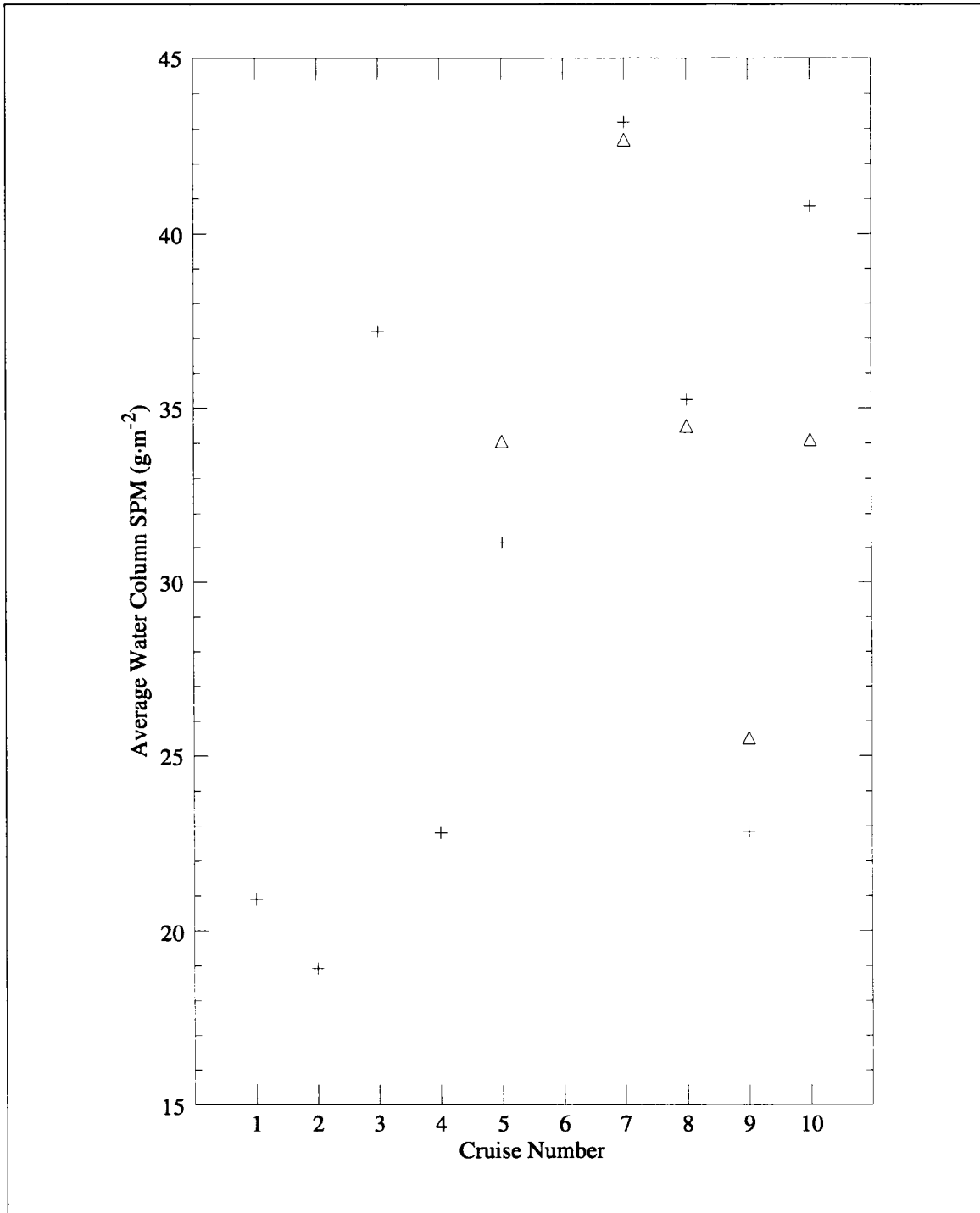


Figure 5.1-16. Average water column SPM (g·m⁻²). Pluses represent average values over the eastern shelf (east of 94°W). Triangles represent average values over the entire shelf for cruises with full shelf coverage.

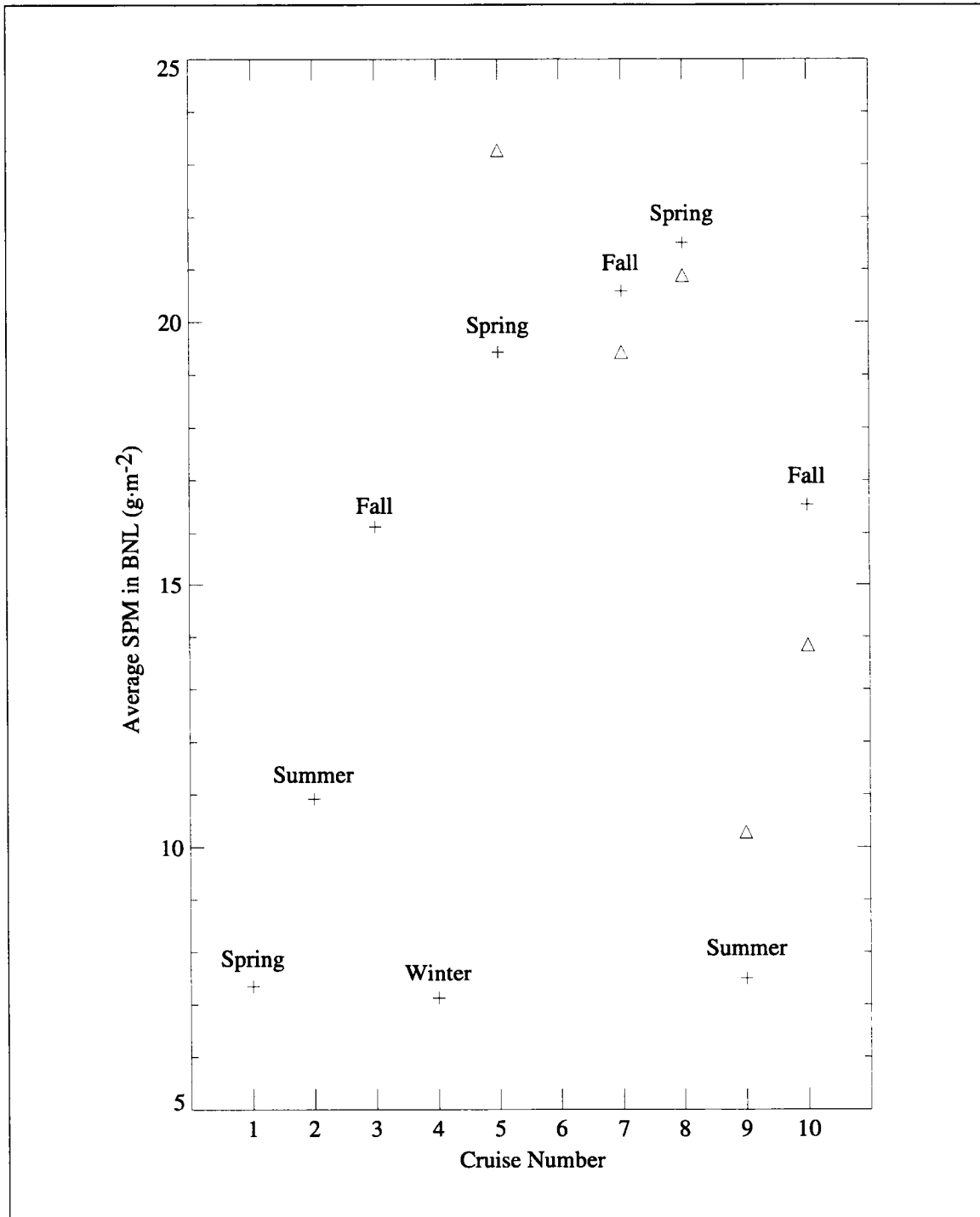


Figure 5.1-17. Average SPM in BNL ($\text{g}\cdot\text{m}^{-2}$). Pluses represent average values over the eastern shelf (east of 94°W). Triangles represent average values over the entire shelf for cruises with full shelf coverage.

5.2 Nutrient distributions

Introduction

Nutrient sources and distributions are especially important in the Gulf of Mexico. Overabundant nutrients contribute to oxygen depletion, fish kills, and noxious algal blooms, as well as diminished fisheries, recreation, and aesthetic values. More than 70% of the total nitrogen and phosphorus input to the Gulf enters via the Mississippi and Atchafalaya rivers. Most of the nutrient-laden water from those two rivers enters directly onto the Texas-Louisiana continental shelf. In this section, LATEX A nutrient data are discussed in terms of surface distributions, seasonal changes, and interannual variability. We begin this section with a brief summary of the processes that affect nutrient input and removal on the Texas-Louisiana shelf and a brief description of the LATEX A nutrient data. Next we report the spatial and seasonal patterns of nutrient distribution on the shelf. Finally, we discuss the dynamics of specific processes responsible for nutrient distribution.

It is generally accepted that concentrations of nutrients, such as nitrate, nitrite, phosphate, silicate, urea and ammonia, on the Texas-Louisiana shelf are controlled by both biological and physical processes; the LATEX A data confirm this. These processes result in low nutrient concentrations in the surface waters of the Gulf of Mexico (Barnard and Froelich 1981) and higher concentrations nearshore, especially near the mouth of major rivers (Ho and Barrett 1977). Past studies have shown that processes affecting nutrient concentrations on the shelf include river discharge, coastal currents and winds, intrusion of open Gulf waters, upwelling, biological activity, rainfall, and proximity to coastal marshes (Ho and Barrett 1977; Barrett et al. 1978; Brooks 1980; Flint and Rabalais 1981; Dagg 1988; Sahl et al. 1993). Other studies have suggested the probable importance of the sediments as an additional important source of remineralized nutrients to the near-bottom shelf waters (Kamykowski and Bird 1981). Figure 5.2-1 is a schematic diagram of nutrient input and removal processes on the Texas-Louisiana shelf.

While the general processes controlling shelf nutrient distributions are understood, the relative magnitude of the processes has not been well defined. The major processes controlling nutrient distributions on the Texas-Louisiana shelf are the large input of nutrients from the Mississippi and Atchafalaya rivers, biological consumption of nutrients, the annual cycle of wind-driven currents that transport nutrient-rich waters over the shelf, and the effects of current eddies near the shelf edge. These will be the focus of this section.

Nutrient data

Samples were collected for nutrient analysis at every station on all ten LATEX hydrographic cruises (Sections 1.1 and 1.2). Nitrate, nitrite, phosphate, silicate, ammonia, and urea were

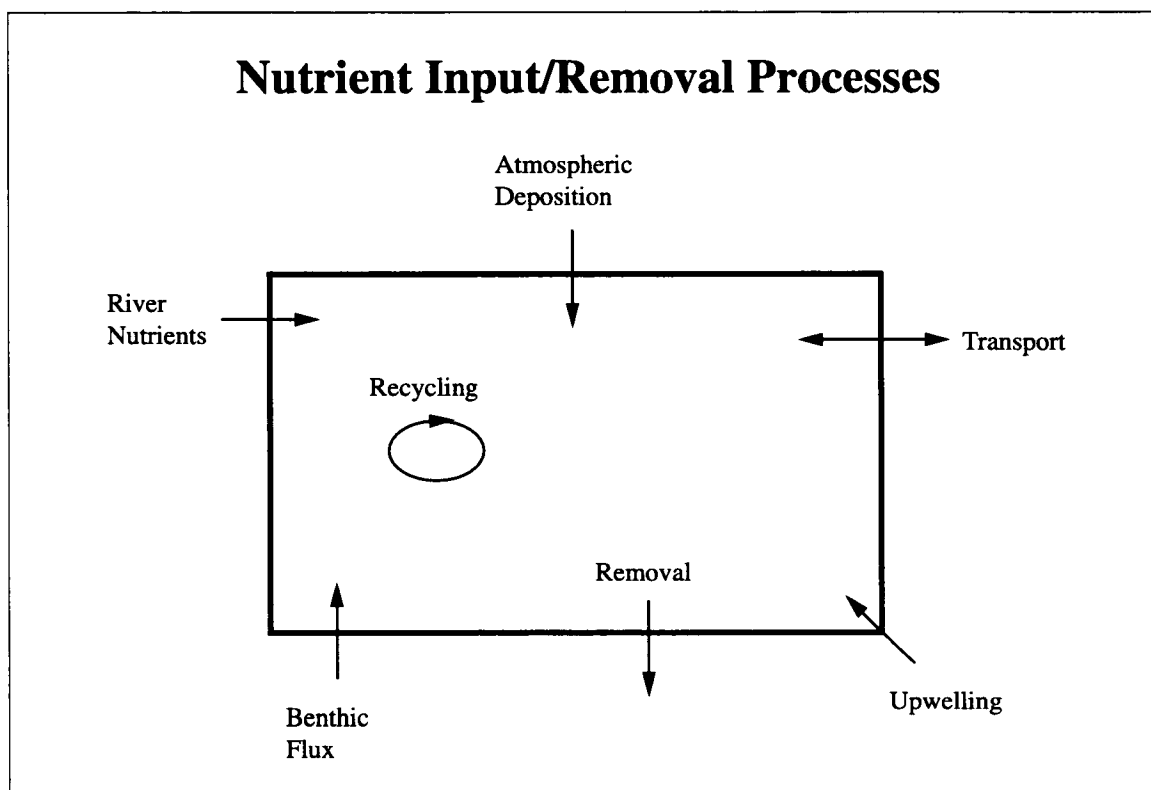


Figure 5.2-1. Box model diagram of processes affecting nutrient concentrations on the Texas-Louisiana continental shelf.

measured at every water depth sampled on these cruises. A detailed description of the methods used to assess nutrient concentrations can be found in the LATEX A Hydrography Data Report (Jochens et al. 1998). Over 13,000 samples were analyzed from 1637 stations on the LATEX cruises. Data for all nutrients are available in the LATEX A data base and have been archived at NODC. This section discusses the major nutrients on the shelf—nitrate, phosphate, and silicate.

To determine the data quality of nitrate versus salinity, silicate versus salinity, and nitrate versus phosphate, plots were constructed for each cruise. As expected, because of biological activity surface nutrient concentrations are non-conservative with salinity. Below 150 m, there is no light for photosynthesis, so nutrients are not consumed. The property-property plots revealed generally conservative nutrient behavior below 150 m, although nutrient increases in these deeper waters can result from microbial decomposition of organic material, mainly phytoplankton. Examples of deep water property-property plots from cruises H01, H05 and H10 are shown in Figure 5.2-2. All deep-water nitrate versus salinity relationships

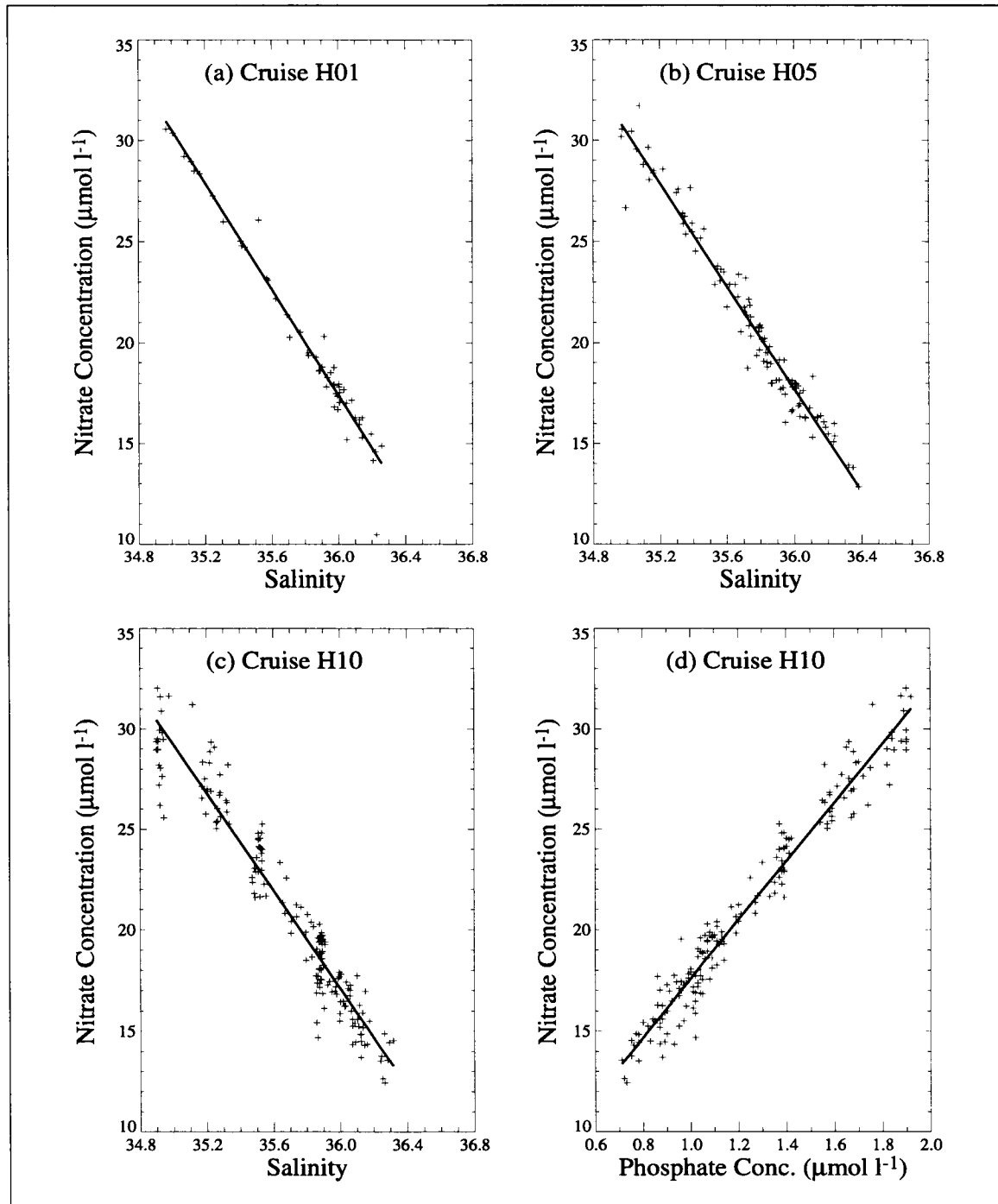


Figure 5.2-2. Nitrate concentration versus salinity in all water samples collected below 150 m depth for LATEX A cruises H01 (a), H05 (b), and H10 (c). (d) Nitrate versus phosphate concentrations in the same samples for cruise H10. The slope of this line is 14.6.

were linear. Nitrate versus phosphate plots also were linear, with an average slope of 14.6. That this ratio is close to the classical N/P (Redfield) ratio for marine organic material provides confidence that the nutrient data are of high quality. In surface waters, both nitrate versus phosphate and nitrate versus silicate diagrams (not shown) have positive nitrate-axis intercepts, indicating that when silicate or phosphate is depleted, nitrate remains. Thus, Texas-Louisiana shelf waters are not nitrate limited for primary productivity.

River nutrient data were obtained as concentrations from the Jefferson Parish Water Quality Laboratory, Jefferson Parish, Louisiana, and the U.S. Geological Survey. The data from the Water Quality Laboratory were weekly composite samples collected from the Mississippi River from October 1991 to December 1994. The data from the U.S. Geological Survey were limited in number and consisted of spatially integrated samples collected from the Mississippi River in Belle Chasse, Louisiana, from October 1991 to September 1994, and from the Atchafalaya River in Morgan City, Louisiana, from October 1991 to September 1993. River discharge data for the Mississippi and Atchafalaya rivers were received from the U.S. Army Corps of Engineers in New Orleans, Louisiana, and are shown in Section 2.3.

Space-time changes of nutrient inventories

To investigate the spatial and seasonal patterns of nutrient distributions, the Texas-Louisiana shelf was divided into 49 boxes with sides of 30 minutes in latitude and longitude (Figure 5.2-3), and average areas of 2724 km². The western shelf is covered by boxes 1-17; the eastern shelf by boxes 18-49. For each cruise, station nutrient data were interpolated vertically to produce average values in 5-m depth intervals. These 5-m interpolated values then were averaged to the center location of each of the boxes using an averaging technique that weighted measurements closest to the box center more than those farther away. Using the average concentration at the box center of each of the 5-m bins, a nutrient mass was calculated for every 5-m slab. The masses in the 5-m slabs of each box were summed over the upper 60 m (taken to represent the photic zone) and over the full depth. The mass totals of each nutrient for the upper 5-m, the upper 60-m, and the full depth then were calculated for the eastern shelf for all ten LATEX A cruises and for the western shelf for cruises H05 through H10.

Figures 5.2-4 through 5.2-6 show seasonal means of nitrate, phosphate, and silicate mass in megamoles (Mmol) plotted by box number for the upper 5-m bin of each box. Nutrient data measured during cruises H01, H05, and H08 were averaged for each box to determine the spring mean; data for H02, H06, and H09 were averaged for the summer mean; and data from H03, H07, and H10 were averaged for the fall mean. No mean was calculated for the one winter cruise, H04 in February 1993 (not shown). Boxes that are within the 50-m isobath are denoted in the figures with a circle enclosed by an open square on the figures. Note that

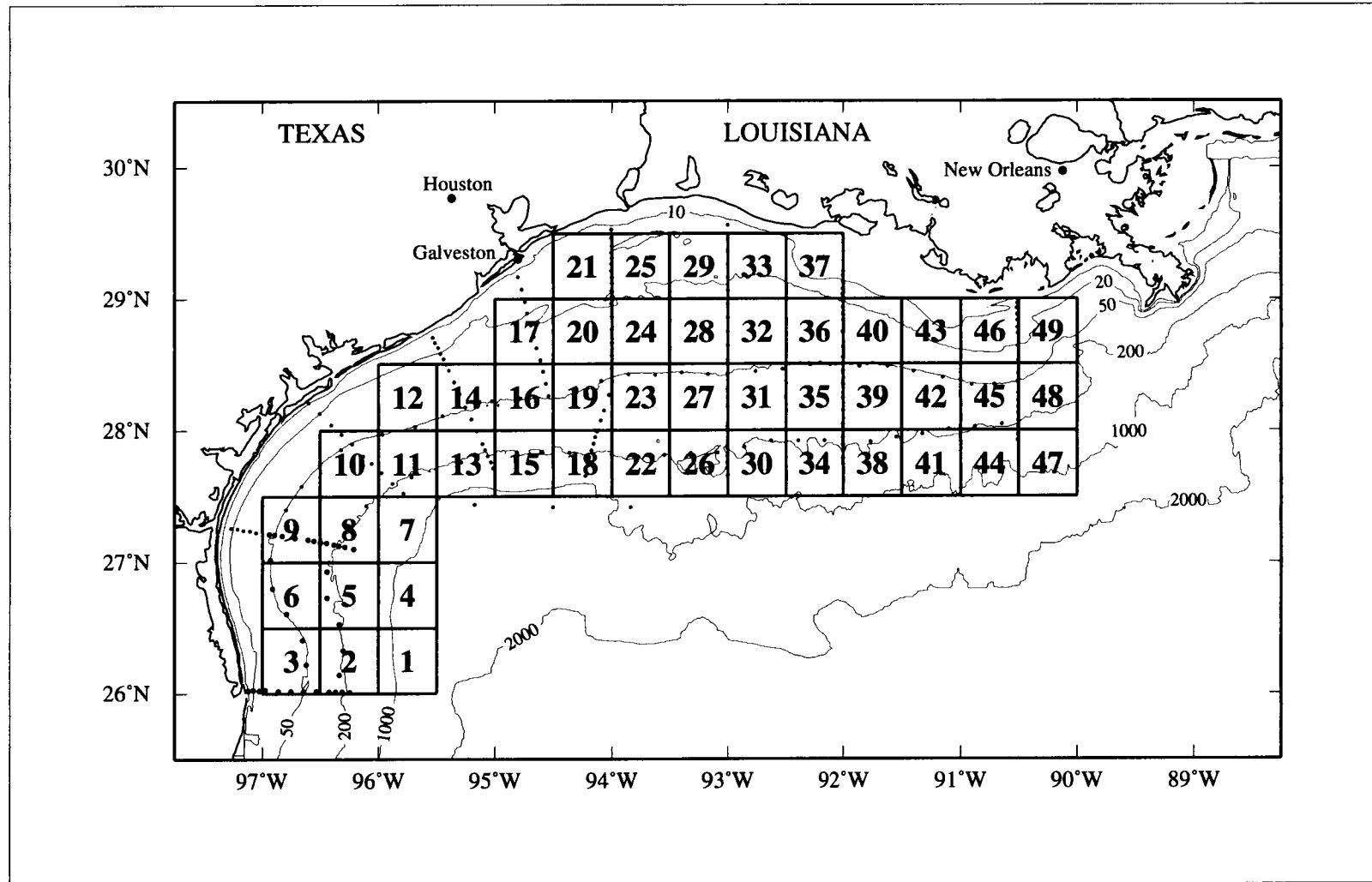


Figure 5.2-3. Texas-Louisiana shelf study area divided into boxes for nutrient data comparisons. Each box measures 30 minutes of longitude by 30 minutes of latitude and has an average area of 2728 km².

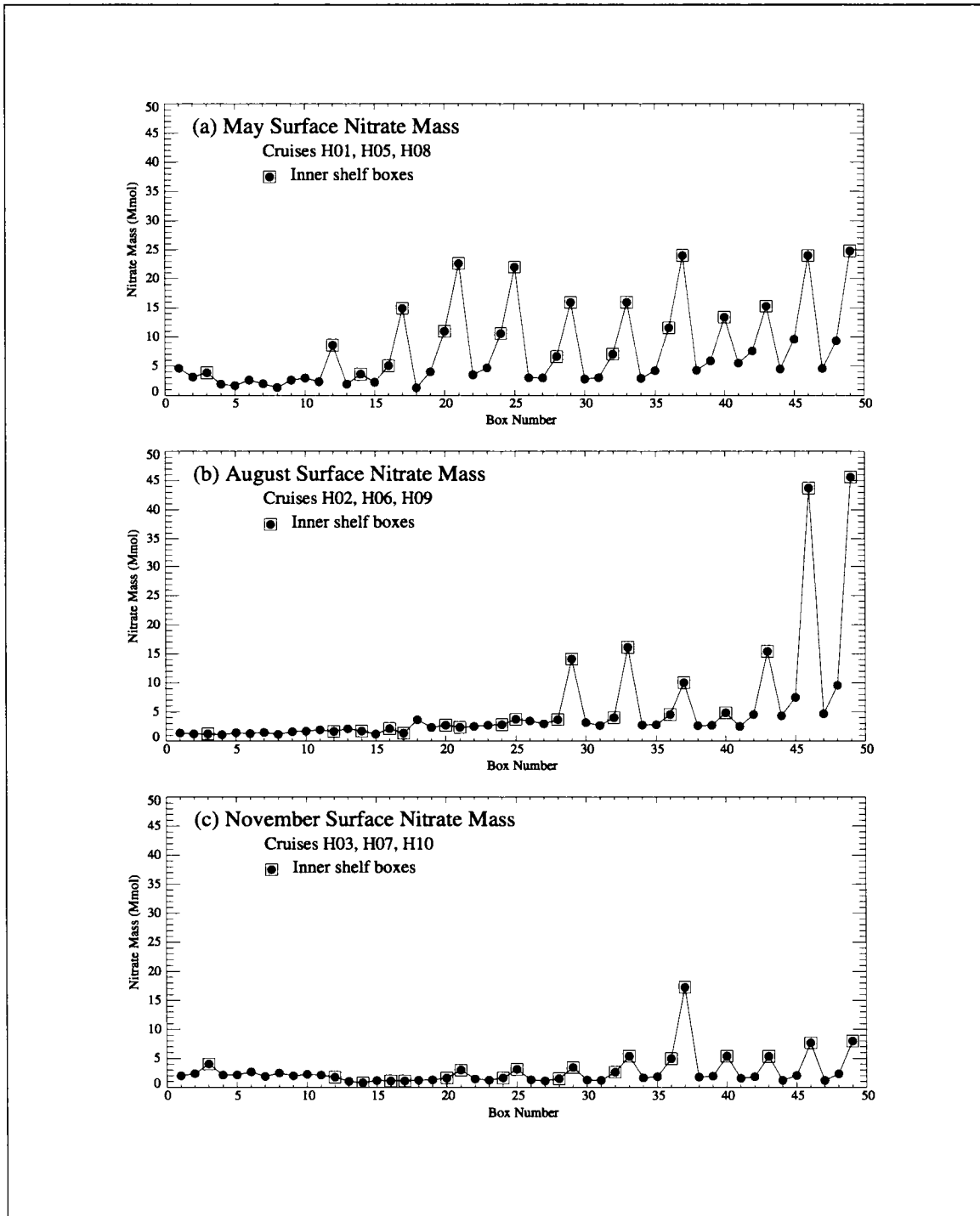


Figure 5.2-4. Seasonal average surface nitrate inventories plotted by box number (see Figure 5.2-3) for (a) spring, (b) summer, and (c) fall for all LATEX A hydrography cruises except H04. Boxes 18-49 are on the eastern shelf.

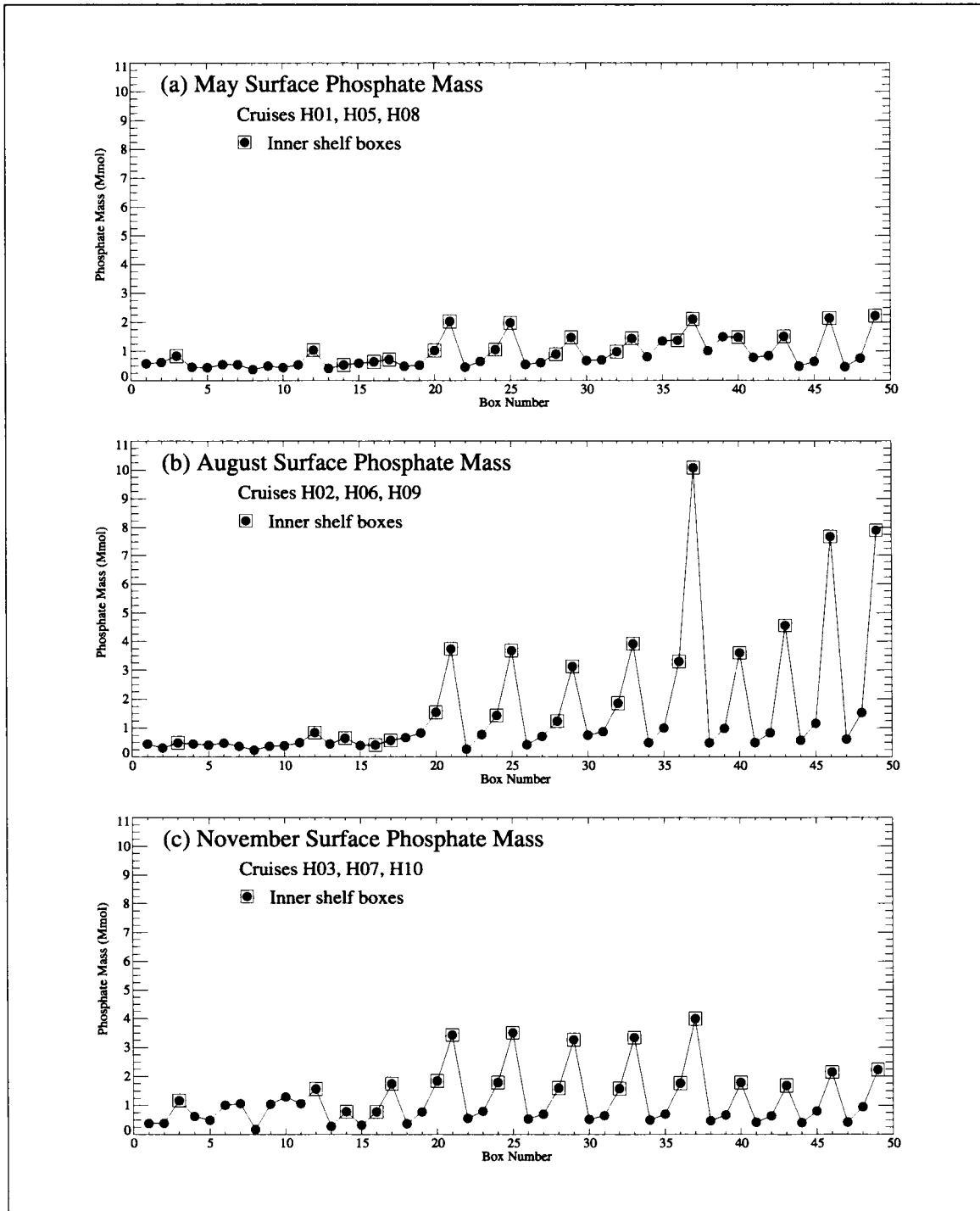


Figure 5.2-5. Seasonal average surface phosphate inventories plotted by box number (see Figure 5.2-3) for (a) spring, (b) summer, and (c) fall for all LATEX A hydrography cruises except H04. Boxes 18-49 are on the eastern shelf.

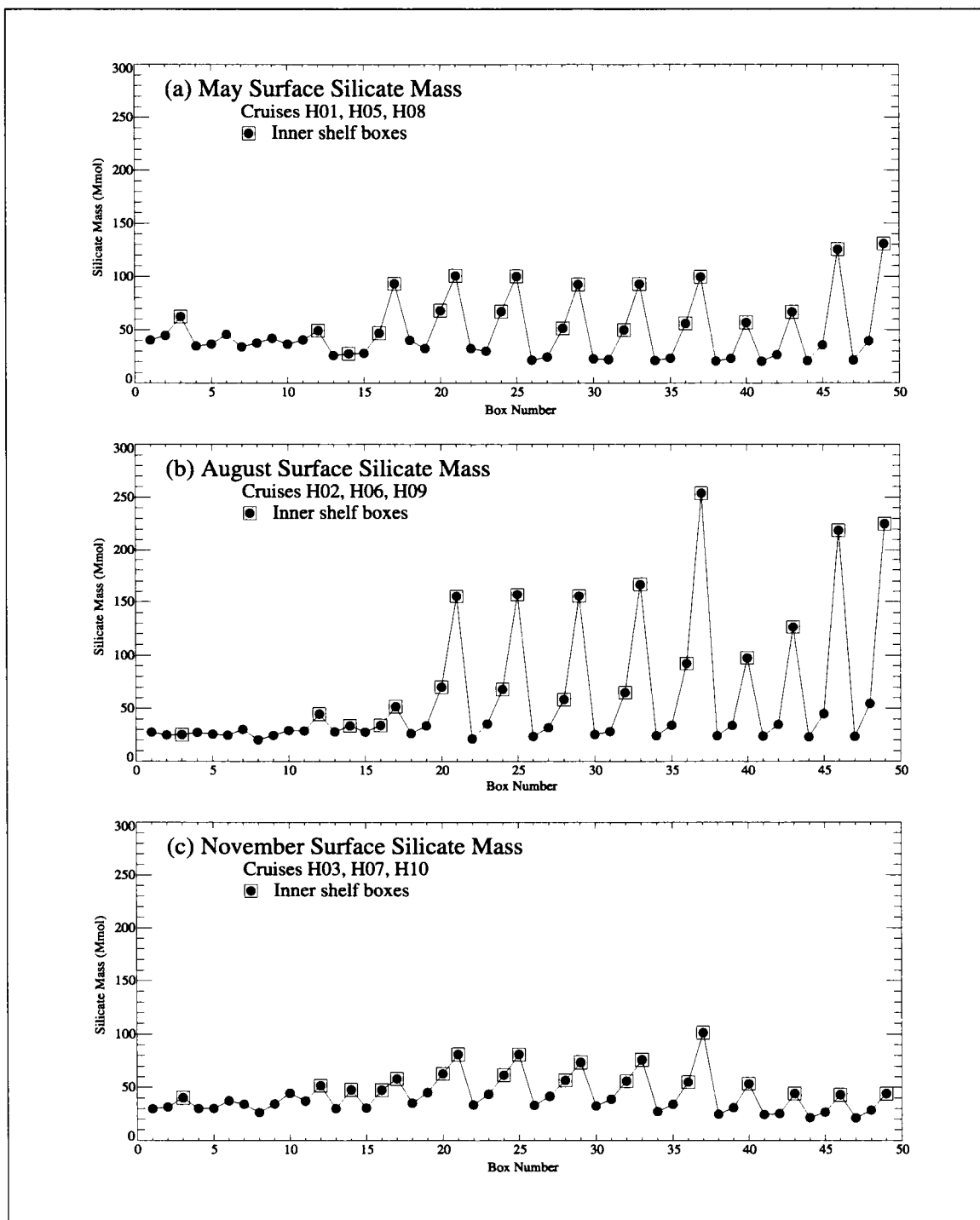


Figure 5.2-6. Seasonal average surface silicate inventories plotted by box number (Figure 5.2-3) for (a) spring, (b) summer, and (c) fall for all LATEX A hydrography cruises except H04. Boxes 18-49 are on the eastern shelf.

the box numbering scheme is such that groups of three to four boxes are oriented from offshore to onshore.

The overall spatial patterns of the three nutrients closely track each other (Figures 5.2-4, 5.2-5, and 5.2-6). Nutrient mass increases shoreward, with the mass over the outer shelf being relatively small everywhere. The inner eastern shelf has more nutrient mass than the inner western shelf. These patterns are consistent with the eastern coast location of the major riverine source of the nutrients.

In general, the nitrate mass peaks during the spring (Figure 5.2-4). Fall nitrate masses were highest just west of Atchafalaya Bay (boxes 32-37), with elevated levels also occurring west of the Mississippi River discharge (boxes 46 and 49). Over the western shelf, the nitrate mass in fall is slightly elevated compared to that of summer and is similar to that of spring. This likely is due to the different circulation patterns that occur between the summer and nonsummer seasons. In summer, the currents are upcoast; this prevents the nutrient-rich waters discharged by the Mississippi-Atchafalaya river system from moving downcoast to the western shelf. Additionally, the Texas river flows are low and estuarine discharge is minimal during summer, so the only source of significant quantities of nutrients to the western shelf would be local inputs from shelf-edge or coastal upwelling. In nonsummer, the currents are downcoast and sweep higher nutrient-content waters from the eastern shelf to the western shelf. The highest surface nitrate masses of any season were found in summer nearest the Mississippi River outflow (boxes 46 and 49). These high values occurred during the time when the summer wind/current patterns push the surface river water to the east.

In contrast with nitrate, the phosphate and silicate masses peak during summer with the highest masses occurring adjacent to the riverine nutrient sources just west of the Atchafalaya Bay (box 37) and nearest the Mississippi River discharge (boxes 46 and 49). These summer peaks suggest that phosphate and silicate may be strongly biologically controlled (see below). During fall, the surface silicate and phosphate masses are highest over the wide central shelf between 92°W and 94°W (boxes 18-37). As with nitrate, the phosphate and silicate masses over the western shelf are elevated in fall relative to summer. Spring is the season that exhibits the smallest overall phosphate mass and fall shows the smallest overall silicate mass.

Figures 5.2-7 through 5.2-9 show histograms of the inventories of nitrate, phosphate, and silicate mass in gigamoles (Gmol) for the eastern and western shelves for each cruise. The histograms represent the sum of the nutrient mass in the upper five meters of all boxes over each shelf regime (the surface inventory) and the sum of the nutrient mass in the upper 60 meters (the photic zone inventory).

For all three nutrients, there is a large difference in surface inventories for the western and eastern shelf regions, with eastern values being several times larger than western values.

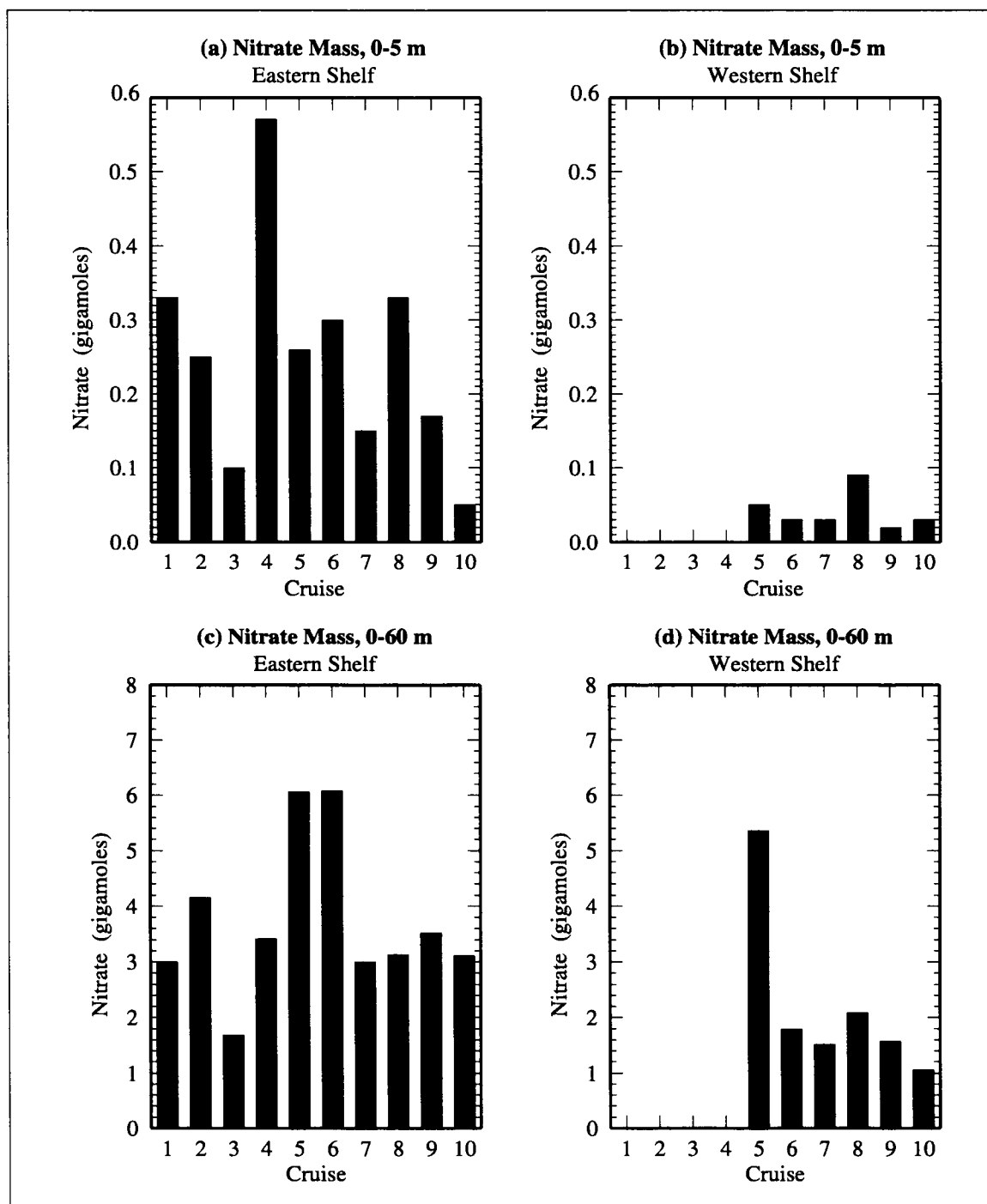


Figure 5.2-7. Surface inventories (Gmol) of nitrate on the (a) eastern shelf during all LATEX A cruises and (b) western shelf during the six full-shelf cruises. Nitrate inventories for the photic zone (0-60 m) are shown for the (c) eastern shelf and (d) western shelf.

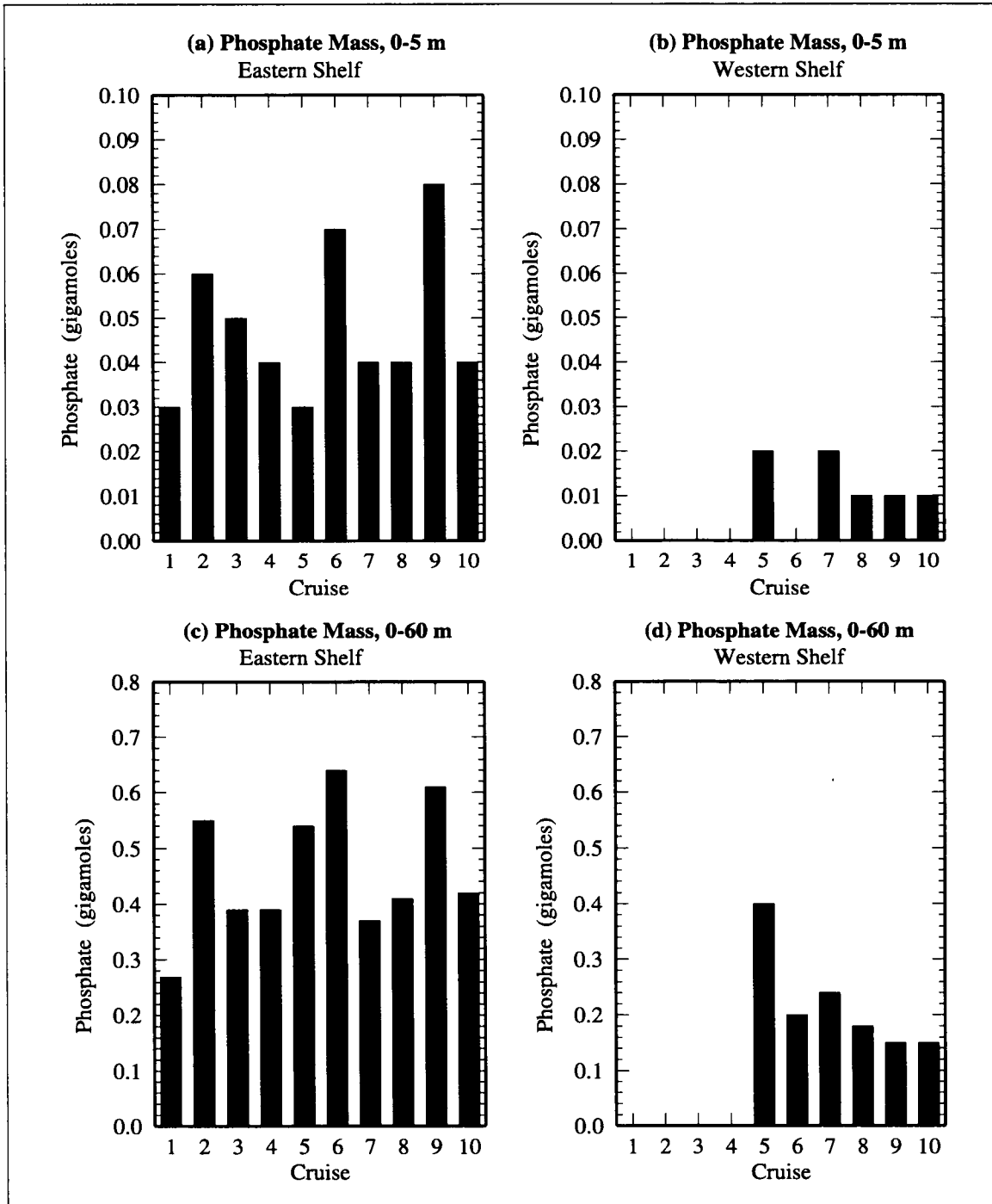


Figure 5.2-8. Surface inventories (Gmol) of phosphate on the (a) eastern shelf during all LATEX A cruises and (b) western shelf during the six full-shelf cruises. Phosphate inventories for the photic zone (0-60 m) are shown for the (c) eastern shelf and (d) western shelf.

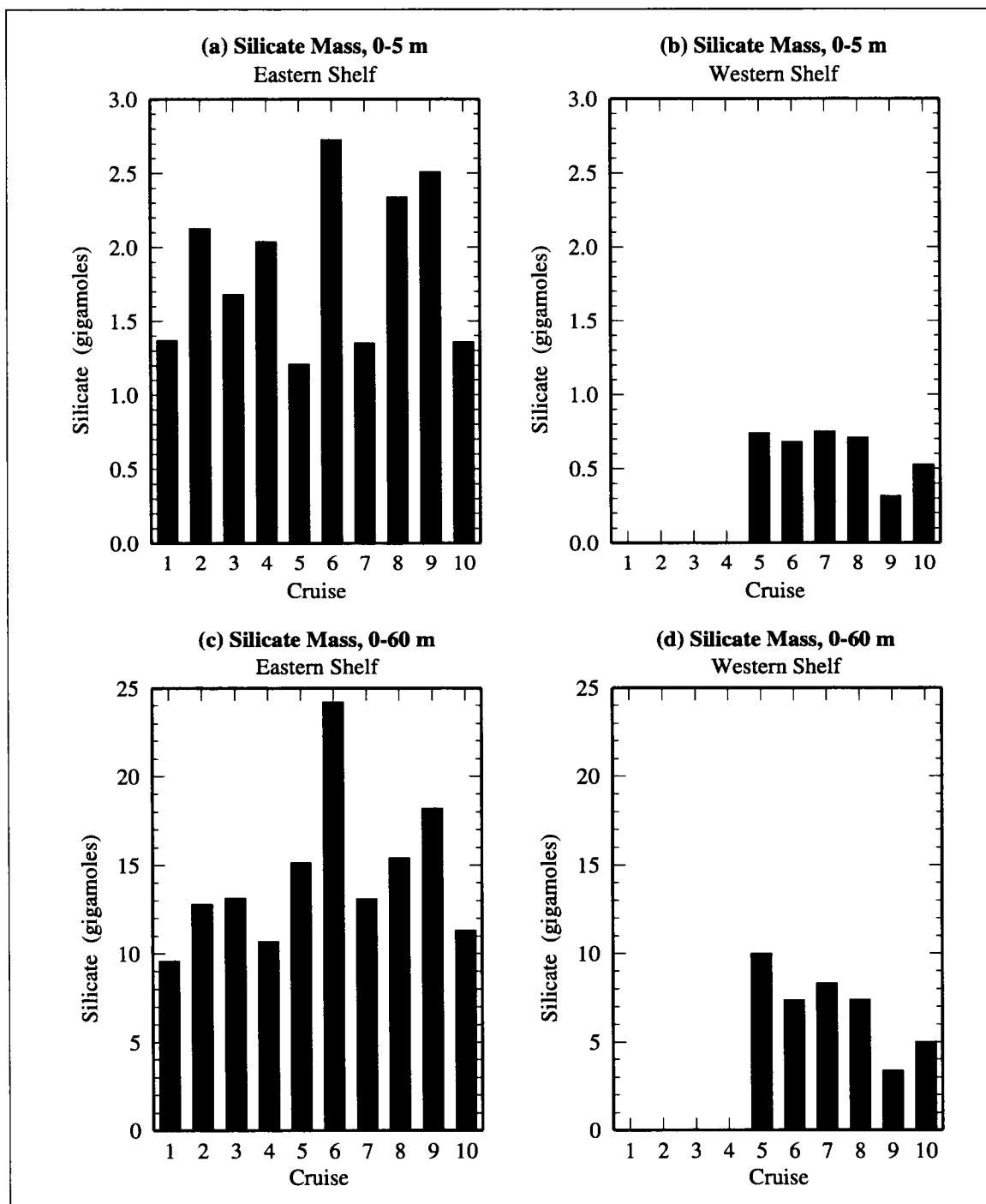


Figure 5.2-9. Surface inventories (Gmol) of silicate on the (a) eastern shelf during all LATEX A cruises and (b) western shelf during the six full-shelf cruises. Silicate inventories for the photic zone (0-60 m) are shown for the (c) eastern shelf and (d) western shelf.

When the 60-m photic zone is considered, this disparity in total mass becomes smaller. This reflects the greater impact of the high nutrient inputs from the Mississippi-Atchafalaya river discharge over the eastern shelf.

Seasonal variations were present in the surface nitrate inventories for spring, summer, and fall (Figure 5.2-7 a and b). In general, the peaks occurred during the spring cruises, when the river input of nutrients was highest. Levels in summer were lower than in spring, except for the eastern shelf in summer 1993. The spring 1993 (H05) surface nitrate inventories were high, but the summer inventories (H06) were higher. The high surface nitrate mass on the eastern shelf seen during H06 occurred during a record summer discharge of the Mississippi River. This discharge had little effect on the western shelf, which exhibited the pattern of peak mass in spring. Lowest surface nitrate inventories on the eastern shelf were measured during the period of low river input that coincided with the fall cruises. Lowest inventories on the western shelf, however, occurred in summer, when the upcoast wind and current regime prevented the nutrient-rich river waters from reaching the western shelf. The largest surface nitrate mass was during winter cruise H04. Because there was only one winter cruise, we will not try to interpret this high value with respect to the seasonal patterns of the other seasons except to note that the fall 1992 and winter 1993 Mississippi-Atchafalaya river discharges were higher than average.

Photic zone nitrate inventories are an order of magnitude greater than surface nitrate inventories (Figure 5.2-7 c and d). This in part reflects the phytoplankton activity in the surface that diminishes the nutrients and the decay at depth that replenishes them, as well as the substantial difference in volumes associated with the surface and photic zone inventories. The seasonal pattern of a spring peak is seen in the photic zone inventories for the western shelf, but not the eastern shelf. The pattern indicates highest masses on the eastern shelf occur during summer, rather than spring. Over both shelf regimes, the low in photic zone inventories occurs in fall.

The seasonal patterns for surface and photic zone inventories of phosphate and silicate over the eastern shelf are different from those of nitrate. The peak values generally occur during summer. The lowest values of phosphate mass occur in spring; for silicate, they occur in spring or fall. This suggests that phosphate and silicate inventories are not as dependent on the river discharge as nitrate, and may be strongly biologically controlled. Excess nitrate available for primary production during the spring and fall could lead to depletion of water column phosphorus that phytoplankton need for growth. Consumption of silicate by the preponderance of diatoms in eastern shelf surface waters (Bontempi 1995) would explain the lower surface silicate levels during spring and fall. Studies of primary production during the LATEX A hydrography cruises by Al-Abdulkader (1996) and Chen et al. (1996) showed that primary production rates, and accompanying nutrient consumption rates, are highest in the spring and fall and lowest during summer. Rabalais et al. (1996) noted that the same

seasonal variability was found in previous studies of the Louisiana shelf. Thus, nutrients on the Texas-Louisiana shelf are consumed at a more rapid rate in the spring and fall than during the summer, leading to the peaks in phosphate and silicate seen in the summer.

On the western shelf, low inventories of phosphate and silicate for each of the two years sampled occur during summer and the highs in spring. The inventories on the western shelf throughout 1993, a year of high discharge from the Mississippi-Atchafalaya river system, are greater than the same seasons in 1994, a year of high flow in the winter and spring and nearly average discharge in the summer and fall. On average, the surface inventories of phosphate and silicate on the eastern and western shelves account for approximately 10% of the inventories for the photic zone.

Nitrate distributions and the effect of the Mississippi-Atchafalaya discharge

We now will consider nitrate distributions and examine the effect of the Mississippi-Atchafalaya river discharge on these distributions. Figure 5.2-10 shows the distributions of the surface nitrate concentration ($\mu\text{mol}\cdot\text{l}^{-1}$) measured along the cruise track for each cruise during May (spring; Figure 5.2-10a), August (summer; Figure 5.2-10b), November (fall; Figure 5.2-10c), and February (winter; Figure 5.2-10d).

In general for all cruises, the highest surface nitrate values were found on the inner shelf, usually adjacent to Atchafalaya Bay (fall), Barataria Bay (summer), or the Sabine River (spring). Over the eastern shelf, a decreasing surface nitrate gradient extended from inshore to offshore except in summer and fall 1994 (H09 and H10). Of the six western shelf cruises, only the spring 1994 realization (H08), which was sampled in a spring with especially strong downcoast winds over the inner shelf, exhibited this gradient pattern. Concentrations on the eastern shelf were higher than those on the western shelf, except for the fall 1994 cruise H10, which was conducted after record October floods from the Texas rivers (Appendix C). Except for the single winter realization, the surface nitrate concentrations in spring were highest overall with low values over the shelf in fall and lowest values in the summer.

River input of nitrate is variable both seasonally and interannually. Discharge from the Mississippi-Atchafalaya river system dominates the riverine inputs, with Texas rivers contributing less than 5% of the fresh water discharged to the Texas-Louisiana shelf on average (Section 2.3). During the study period, the flow of the Mississippi-Atchafalaya river system varied widely. Total river discharge during 1992 was near the 64-year average; 1993 total discharge was the highest of the 64 years. Daily flows during 1993 and 1994 were well above the average in spring, but 1992 spring flows were below average. Flows in November and December were above average all three years. During summer 1993, river flows were significantly above average from July through November and attained record status during August.

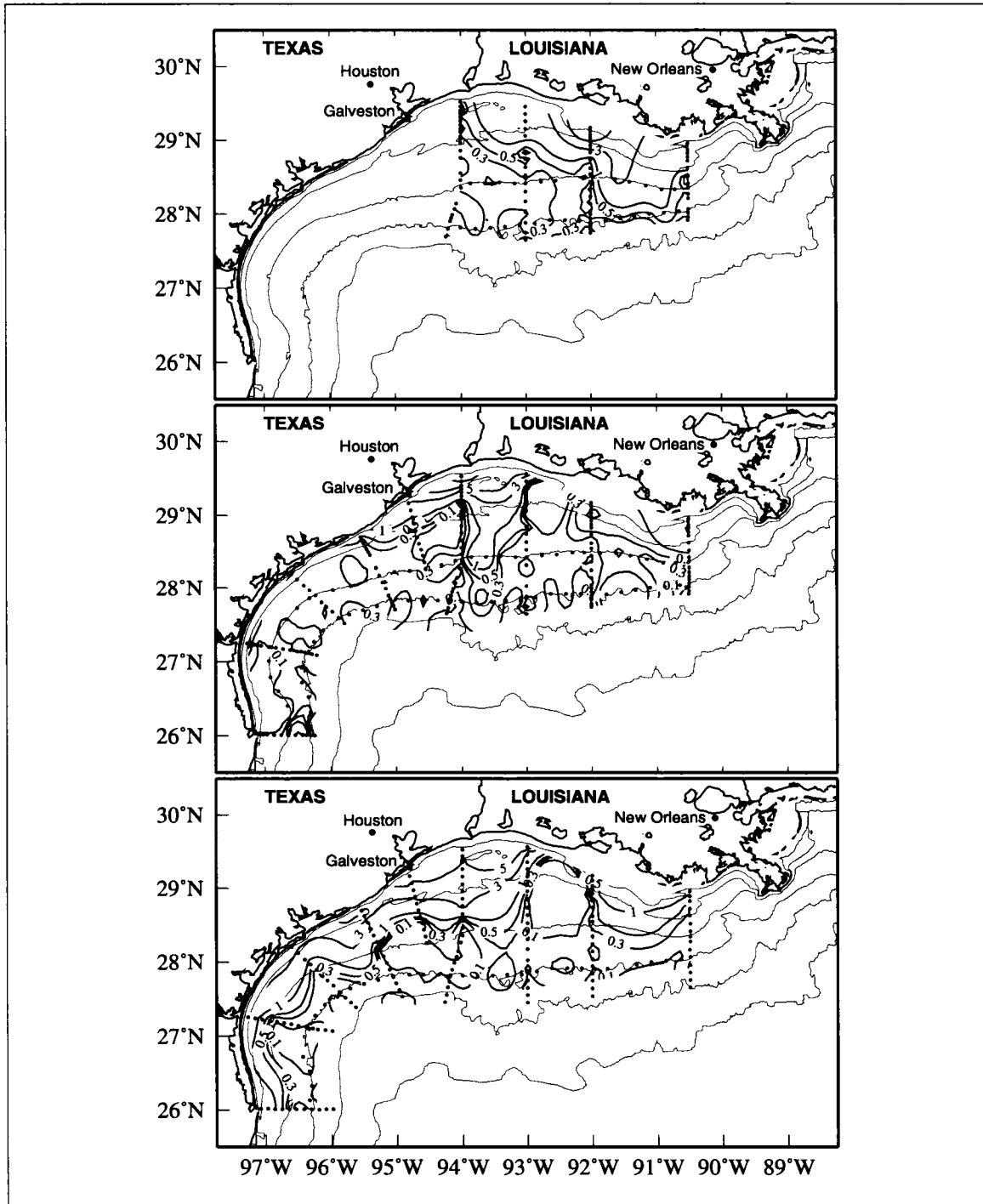


Figure 5.2-10a. Spring surface nitrate concentrations ($\mu\text{mol}\cdot\text{l}^{-1}$) for LATEX A hydrographic cruises H01 in May 1992 (top), H05 in May 1993 (middle), and H08 in May 1994 (bottom).

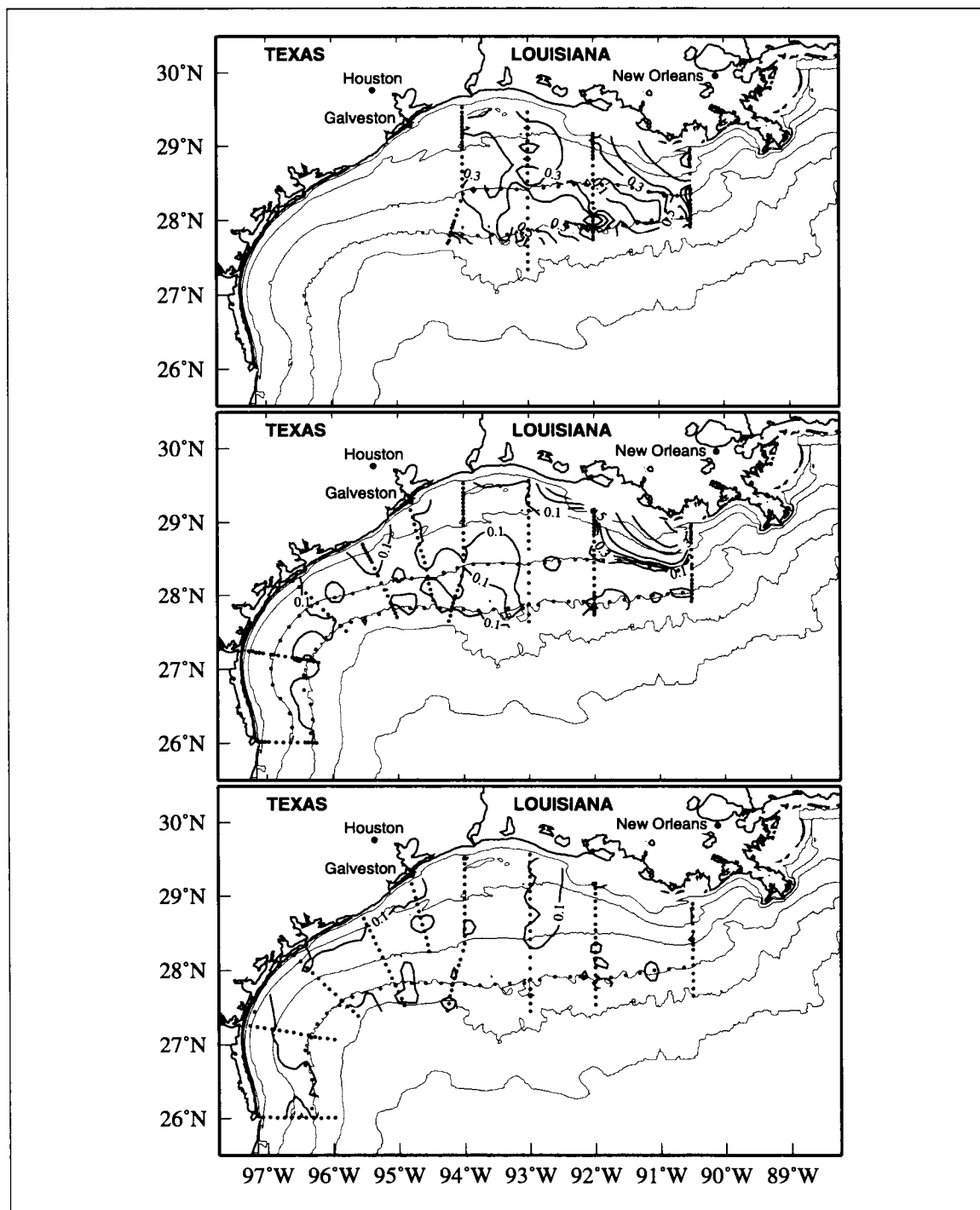


Figure 5.2-10b. Summer surface nitrate concentrations ($\mu\text{mol}\cdot\text{l}^{-1}$) for LATEX A hydrographic cruises H02 in August 1992 (top), H06 in August 1993 (middle), and H09 in August 1994 (bottom).

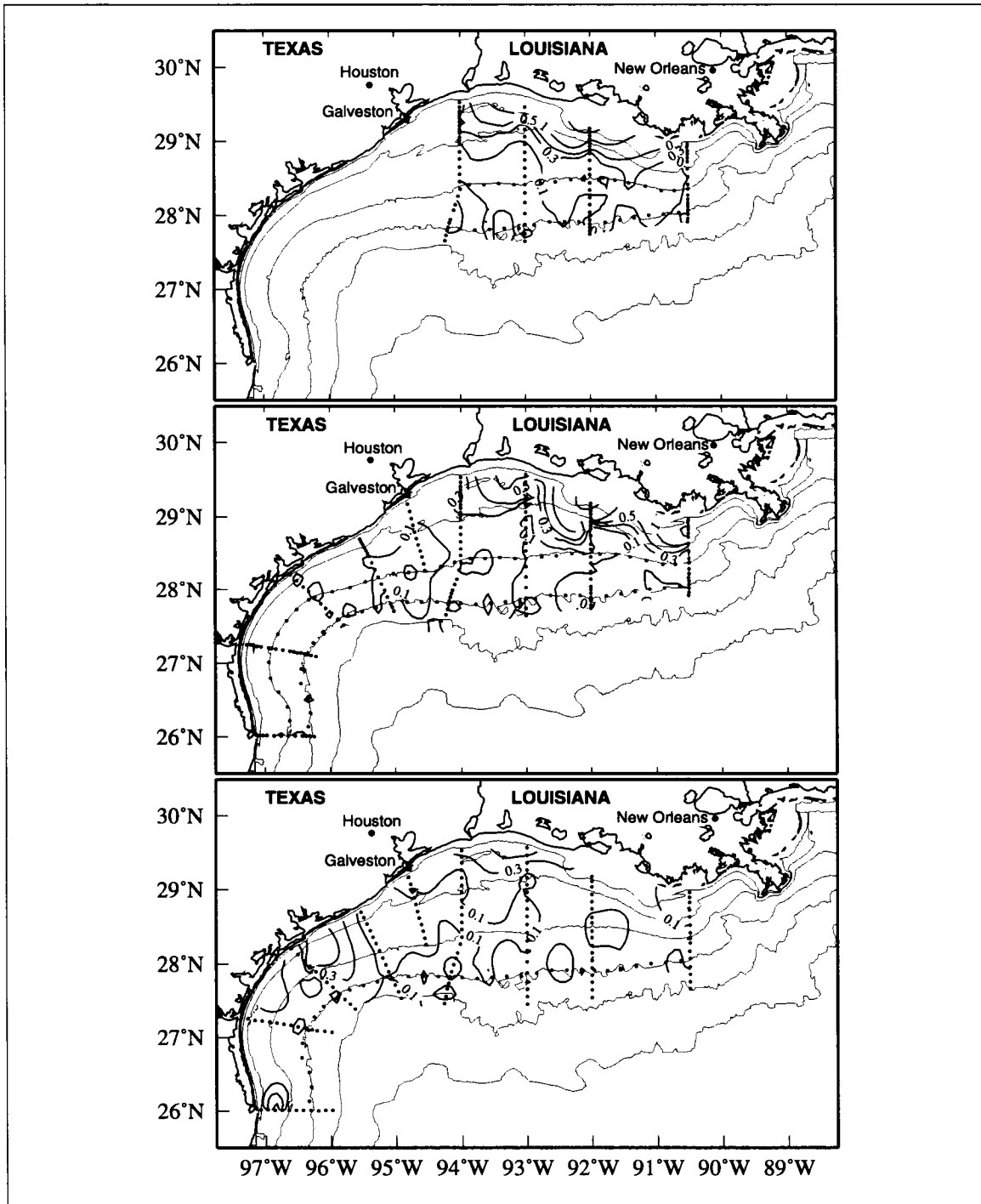


Figure 5.2-10c. Fall surface nitrate concentrations ($\mu\text{mol}\cdot\text{l}^{-1}$) for LATEX A hydrographic cruises H03 in November 1992 (top), H07 in November 1993 (middle), and H10 in November 1994 (bottom).

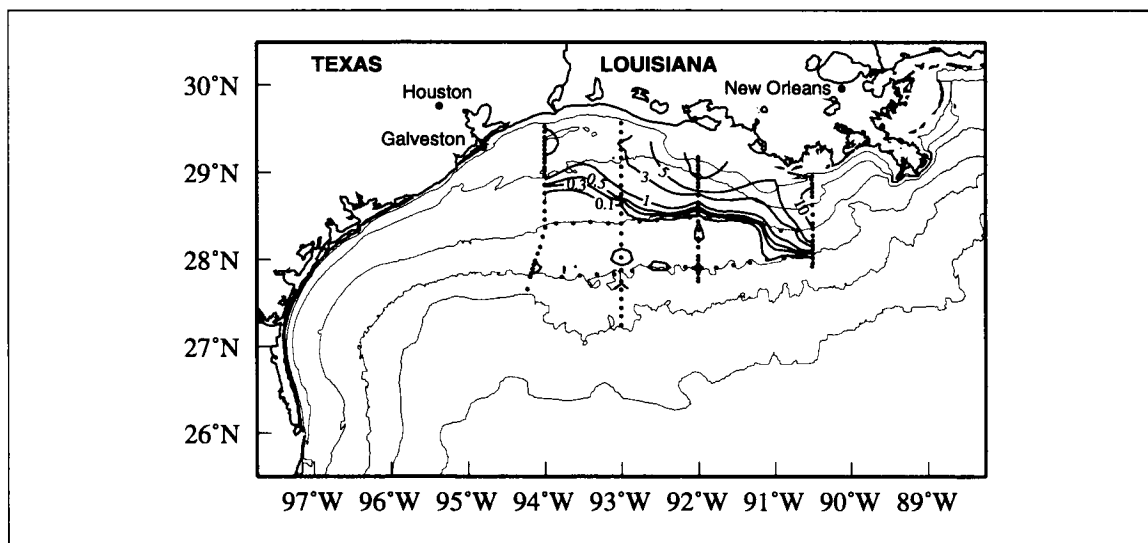


Figure 5.2-10d. Winter surface nitrate concentrations ($\mu\text{mol}\cdot\text{l}^{-1}$) for LATEX A hydrographic cruise H04 in February 1993.

Figure 5.2-11 (top) shows the daily and monthly average of the Mississippi-Atchafalaya river system discharge during January 1992 through December 1994. Approximately half of the Mississippi River output flows westward to the Louisiana shelf (Dinnel and Wiseman 1986). The Atchafalaya River discharge also flows onto the Louisiana shelf. Spring peaks in river discharge are clearly seen in both river records, as well as secondary peaks occurring in late fall/early winter and late summer.

The nitrate concentrations of the rivers were combined with the river discharge data to compute the nitrate flux associated with the Mississippi-Atchafalaya discharge. Figure 5.2-11 (bottom) shows the nitrate flux due to the Atchafalaya River, half the Mississippi River output, and the sum of the two discharges. Missing nitrate flux values for the Atchafalaya River were filled using linear interpolation. Points at the end of this record were extrapolated based on the Mississippi River nitrate flux and discharge.

Again we see strong seasonal variation in nitrate flux, with peaks in the flux occurring in spring. There is, however, significant interannual variability in the nitrate flux during the peak periods of river discharge. In particular, the spring river discharges of 1993 and 1994 are approximately equal, yet the nitrate flux is 50% larger in 1993 than in 1994. The nitrate flux of spring 1992, a low river flow year, is of the same order as the nitrate flux of 1994, a year of high river discharge. Secondary peaks in late fall/early winter and late summer are seen in the nitrate flux and are coherent with the peaks seen in the river discharge.

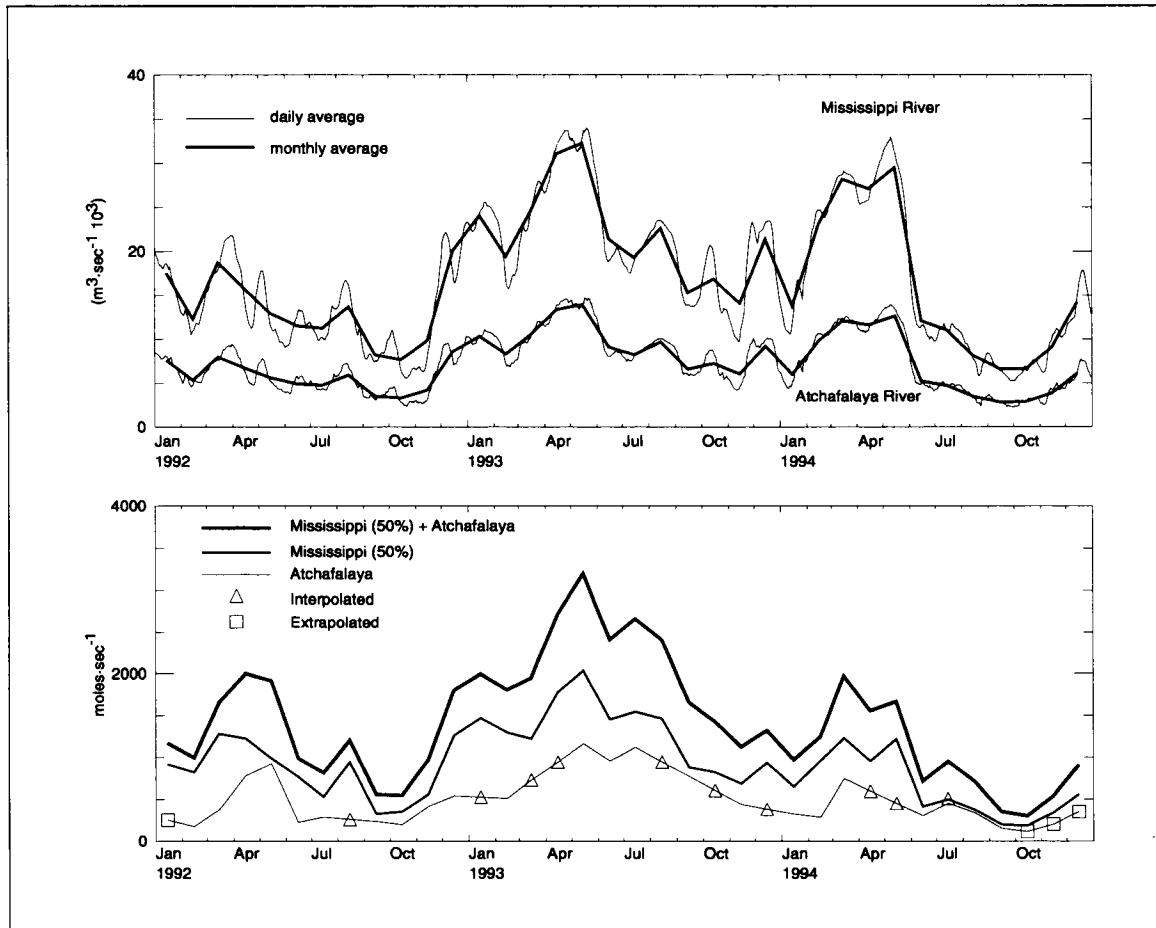


Figure 5.2-11. Daily and monthly (bold) average Mississippi and Atchafalaya River discharge (top) and nitrate flux from Atchafalaya River, 50% of Mississippi River, and their sum (bottom) during January 1992 through December 1994.

To determine the relationship between riverine input of nitrate and surface nitrate on the shelf, we compared an average river nitrate flux with the surface nitrate mass on the shelf. First, we computed the average river nitrate flux for the two-months preceding each cruise to incorporate the lag between the river's input to the shelf and the distribution of nitrate over the shelf area. Then, we plotted the two-month average nitrate flux versus the surface nitrate masses for the east and west shelves by cruise. Figures 5.2-12 and 5.2-13 show the results for the east and west shelves. Note that the range of the east shelf surface nitrate ordinate is an order of magnitude larger than that of the west shelf ordinate range.

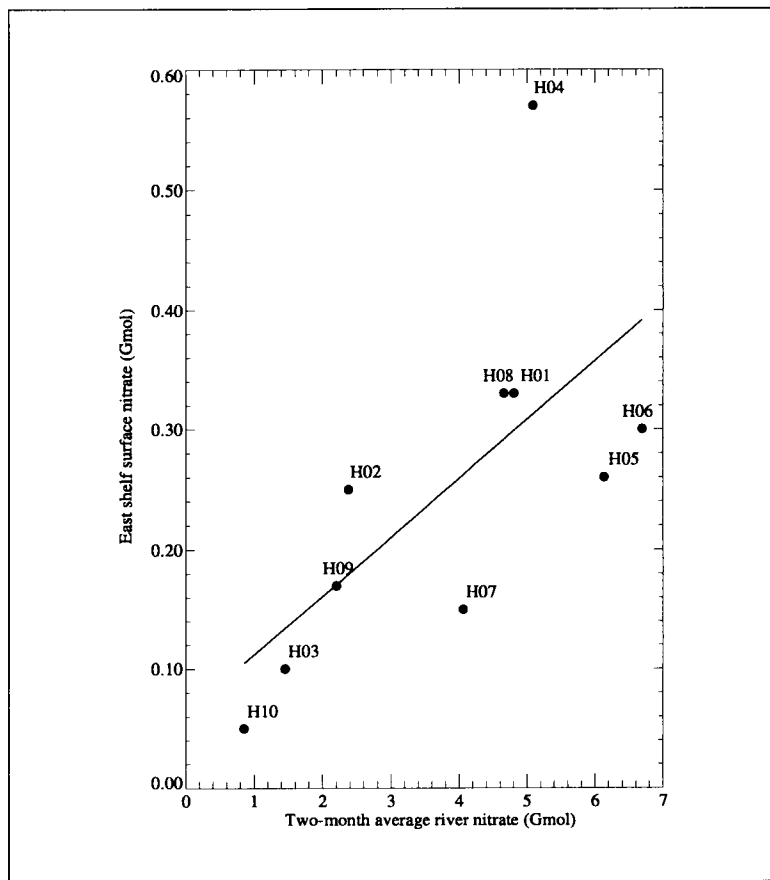


Figure 5.2-12. East shelf surface nitrate (Gmol) versus two-month average river nitrate (Gmol) for each LATEX A hydrographic cruise. Linear fit shown is $y = 0.06269 + 0.04914 * x$; r^2 is 0.44244 with a significance level of 97.5%.

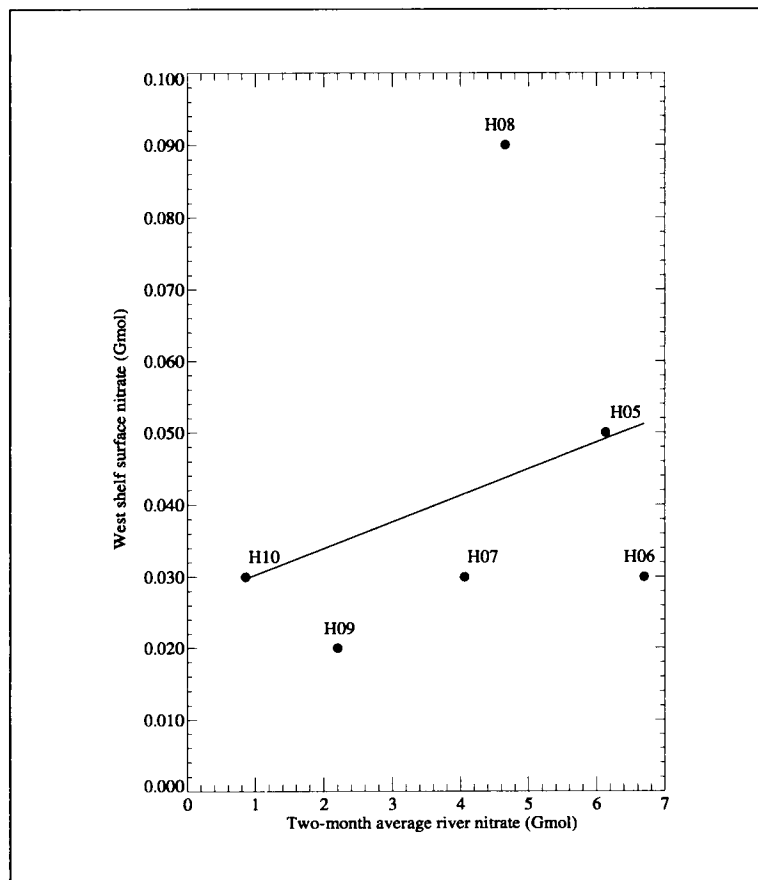


Figure 5.2-13. West shelf surface nitrate (Gmol) versus two-month average river nitrate (Gmol) for LATEX A full-shelf hydrographic cruises. Linear fit shown is $y = 0.026596 + 0.0036763 * x$; r^2 is 0.10423 with a significance level between 60% and 75%.

On the eastern shelf, there is significant correlation between the river nitrate input and the surface nitrate mass, with an r^2 value of 0.44 at the 97.5% significance level (Figure 5.2-12). On the western shelf, however, the correlation is poorer, with an r^2 of 0.10 at less than the 75% significance level (Figure 5.2-13). These results indicate that the flux of nitrate, and by extension of other nutrients, from the Mississippi-Atchafalaya river system has substantial influence on the surface nutrient masses on the eastern shelf.

Influence of Loop Current eddies on nutrient distributions

During cruise H05, Loop Current Eddy V_n encroached on the western shelf edge (Section 2.5.1 and Appendix D). This provided an opportunity to examine the effect of a Loop Current eddy on the nutrient distributions at the shelf edge. To understand how eddy interaction affects the nutrient distribution on the shelf, we examined vertical profiles of nutrients from several stations and vertical contour sections along the 200-m isobath. For the vertical nutrient profiles, we selected three hydrographic stations from H05 that represent the different water masses involved in the eddy encroachment. All three stations are along the 200-m isobath. Station 81 represents the far field water mass that was remotely located relative to the eddy. Station 209 was located in the northern periphery of the anticyclonically rotating eddy. Station 205 was in the west side of a cyclonic eddy located just west of the anticyclonic eddy.

Nutrients are used by the phytoplankton in the photic zone and are replenished by decay in the deeper waters. Thus, deeper waters generally are nutrient-rich compared to upper waters. Figure 5.2-14 shows the vertical profiles of nitrate, phosphate, and silicate at the three stations. All three profiles show increasing nutrient concentration with depth. However, because the circulation in the cyclonic eddy raises nutrient-rich deep waters higher in the water column, the nutrient concentrations at a given depth below the mixed layer are higher in waters of the cyclone than in those of the far field. In contrast, the nutrient concentrations at a given depth in the anticyclone are less than those in the far field waters because the circulation of the anticyclone pushes the nutrient-poor surface waters down into the water column.

The contrast between the cyclonic, anticyclonic, and far field nutrient distributions can be seen in the vertical sections of nutrients along the 200-m isobath (Figures 5.2-15 through 5.2-17). The presence of the eddy is clearly seen in the nitrate, phosphate, and silicate concentration contours between stations 206 and 212. The contours bow downward, indicating reduced nutrient concentrations in the area occupied by the northern periphery of the Loop Current eddy. Between stations 202 and 205, the contours show increased nutrient concentrations at depth due to the presence of the western cyclone. Sahl et al. (1997) describe further the nutrient exchange processes attributed to Eddy V_n .

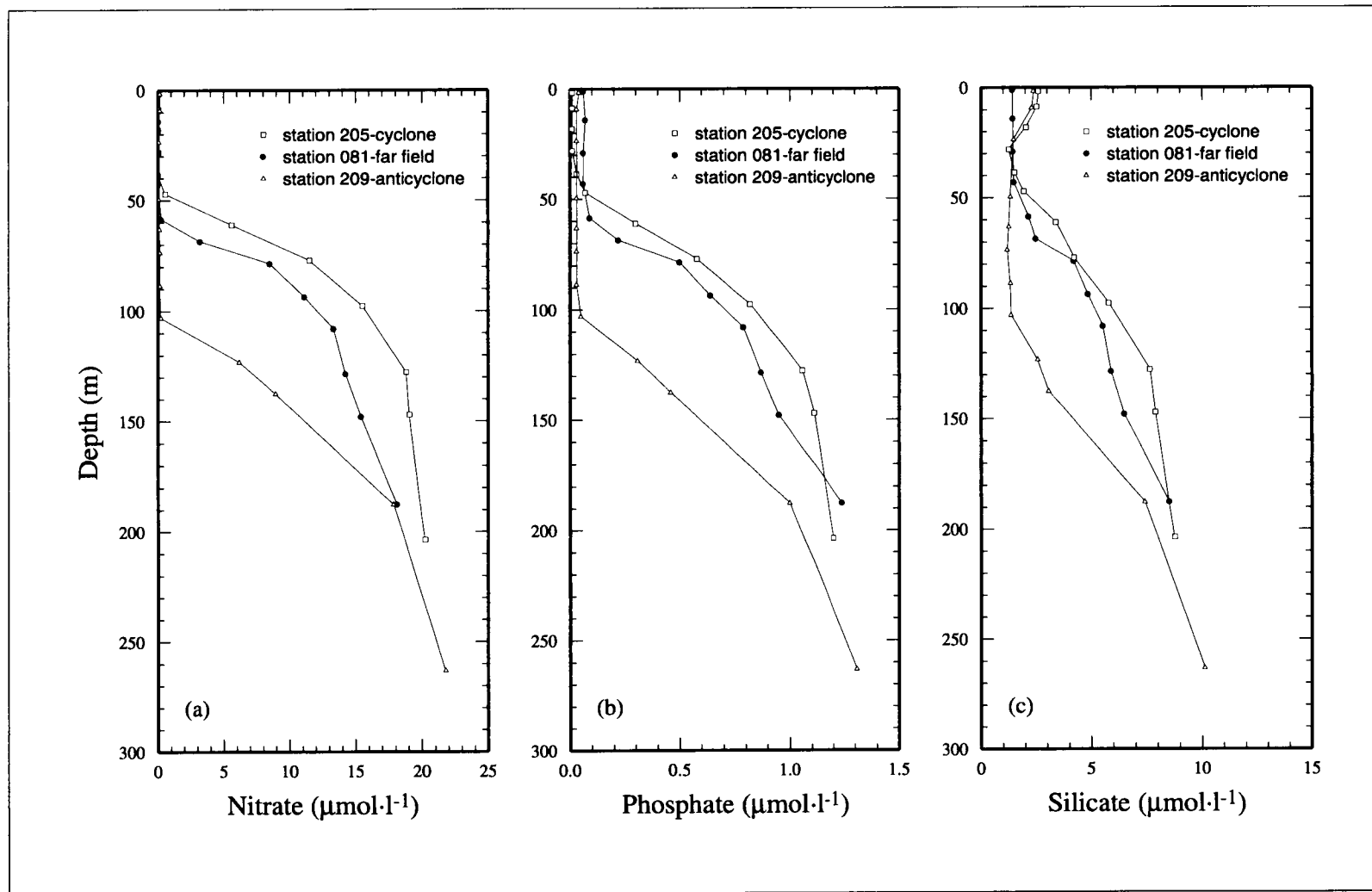


Figure 5.2-14. Depth profiles of (a) nitrate, (b) phosphate, and (c) silicate at hydrographic stations 81 (farfield), 205 (cyclone), and 209 (anticyclone) during hydrographic cruise H05.

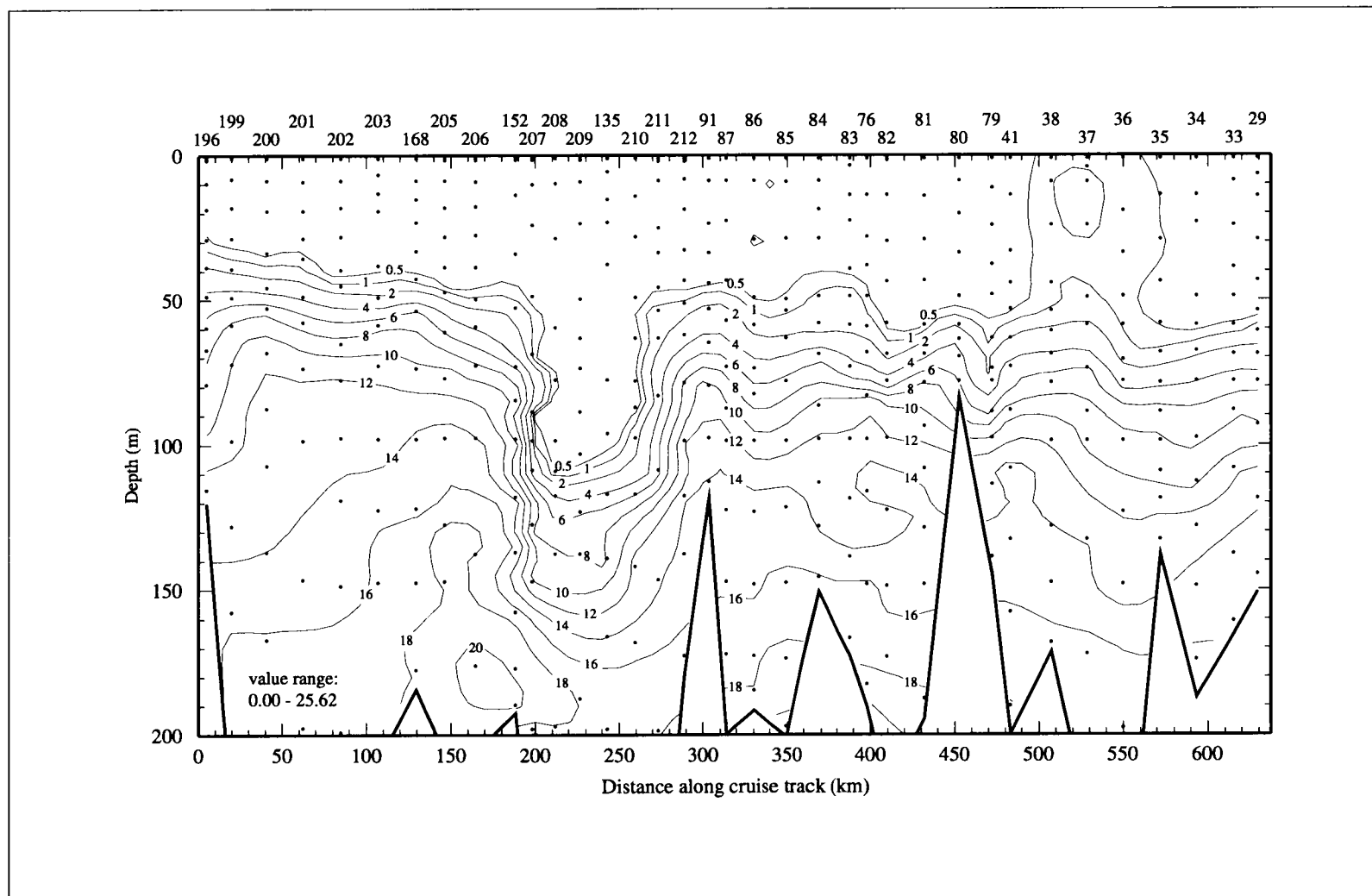


Figure 5.2-15. Vertical contours of bottle nitrate ($\mu\text{mol}\cdot\text{l}^{-1}$) along 200-m isobath during hydrographic cruise H05. Dots indicate sample locations.

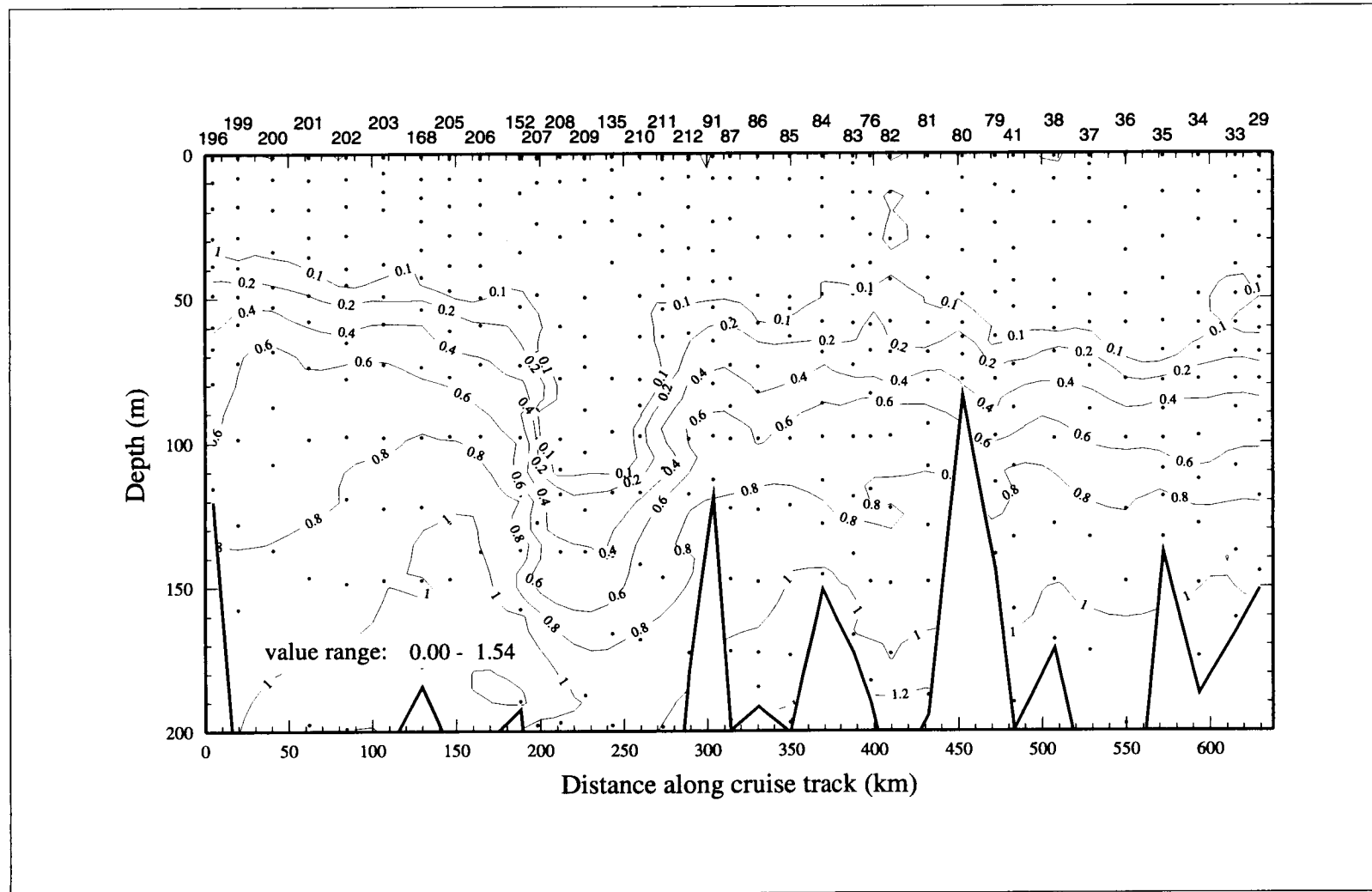


Figure 5.2-16. Vertical contours of bottle phosphate ($\mu\text{mol}\cdot\text{l}^{-1}$) along 200-m isobath during hydrographic cruise H05. Dots indicate sample locations.

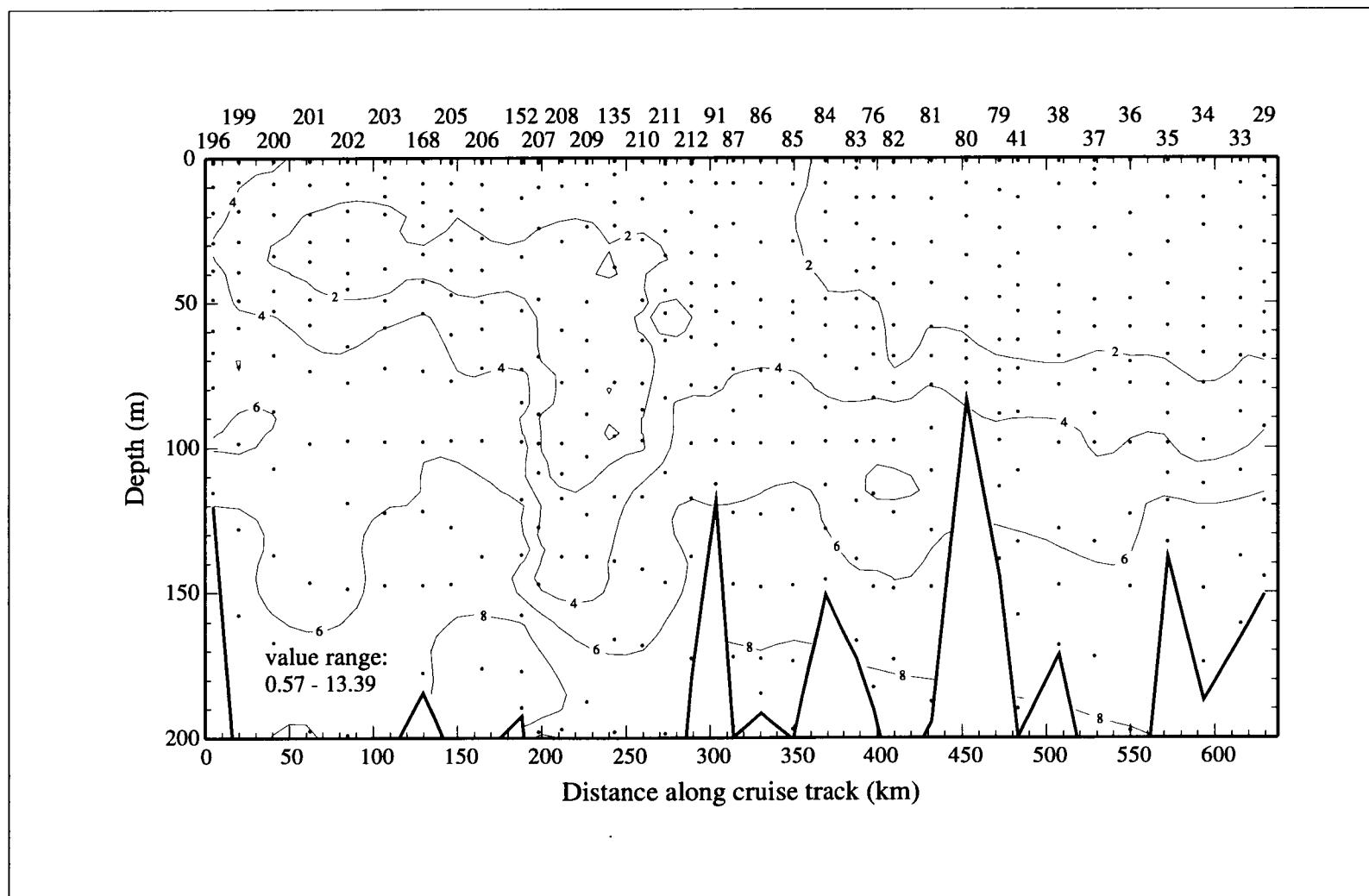


Figure 5.2-17. Vertical contours of bottle silicate ($\mu\text{mol}\cdot\text{l}^{-1}$) along 200-m isobath during hydrographic cruise H05. Dots indicate sample locations.

5.3 Dissolved oxygen distributions and hypoxia

Introduction

Ocean surface waters are commonly supersaturated by several percent with respect to dissolved oxygen concentrations, but, due to consumption by animals and bacteria, subsurface ocean waters are predominantly undersaturated (Broecker and Peng 1982). That is certainly the case for waters over the Texas-Louisiana shelf. Here we will refer to saturations greater than or equal to 110% as “highly supersaturated”.

Studies of stress in fish and invertebrates indicate that at dissolved oxygen concentrations less than $1.4 \text{ ml}\cdot\text{l}^{-1}$ there is too little oxygen to sustain healthy animal communities (Tyson and Pearson 1991). Such waters are classified as hypoxic. Fish and shrimp may be capable of moving to more oxygenated areas; less mobile members of the benthic community may experience varying degrees of stress and sometimes death. Thus, hypoxic conditions are environmentally and economically important, because benthic communities provide major sources of food for larger animals and are responsible for reworking the sediments. At locations where oxygen is extremely depleted and nitrate and organic substances are available, denitrification may occur (Wada and Hattori 1991).

In this section we present a brief overview of the observed distributions of dissolved oxygen on the Texas-Louisiana shelf. Then the relationships of oxygen saturation to both surface salinity and surface chlorophyll-a are examined. Next, we report the occurrence of hypoxic conditions in the bottom waters of the shelf as observed during the period April 1992 through November 1994. The relationship of bottom oxygen saturation to water column static stability and bottom nitrate correlations are examined. Finally, the effects of Loop Current eddies on shelf edge oxygen concentrations is illustrated by an example.

Surface oxygen distributions

In Figure 5.3-1 we show the surface dissolved oxygen saturations for each LATEX A hydrographic survey, H01-H10, arranged by season. The one winter cruise (H04 in February 1993; Figure 5.3-1a) shows supersaturated surface waters over the eastern shelf with the exception of the outer shelf between 91° and 94°W . Most of the nearshore region was highly supersaturated, with values greater than 120% (above 6.5 or $7 \text{ ml}\cdot\text{l}^{-1}$) near the Mississippi Delta. Mississippi-Atchafayala discharge during early 1993 was much above the long-term mean (Figure 2.3-1).

The three spring distributions of surface dissolved oxygen saturation are shown in Figure 5.3-1b. During cruise H01 (May 1992) highly supersaturated waters were confined to the inner shelf on line 1 and the adjacent nearshore region off Atchafayala Bay and to

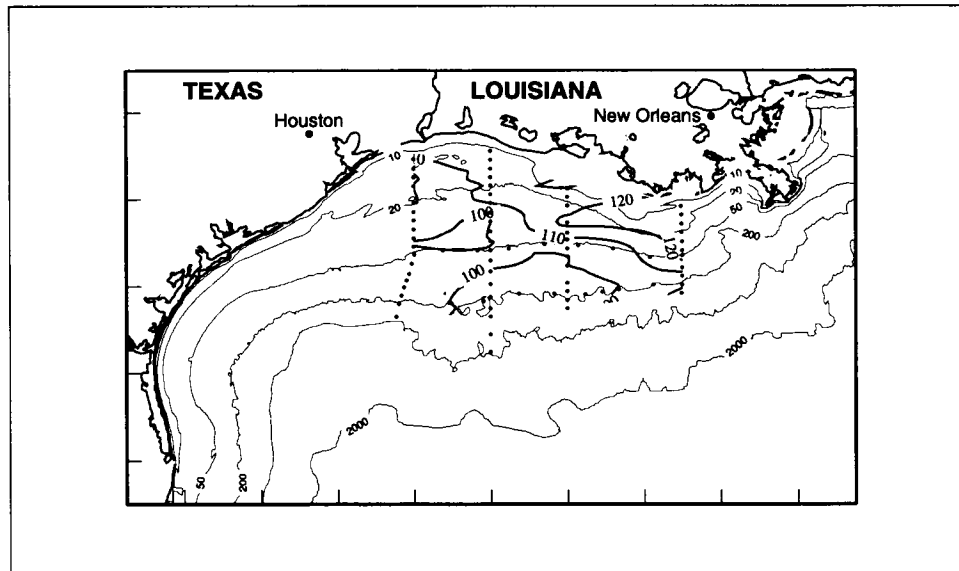


Figure 5.3-1a. Surface saturation (percent) of dissolved oxygen for winter cruise H04 (February 1993).

shallow waters off the Texas-Louisiana border. In both regions surface saturation values reached 140% ($> 7 \text{ ml}\cdot\text{l}^{-1}$). The May 1993 (cruise H05) distribution was similar to 1992 for the region east of 92°W ; elsewhere, values were everywhere within 10% of 100% saturation—no highly supersaturated waters were found off Texas. For May 1994 (cruise H08), all values over the shelf were near 100% saturation, including those near the Mississippi Delta. Mississippi-Atchafayala discharge during the first quarter of 1992 was not particularly different from the long-term mean, while for the first and second quarters of 1993 and 1994, discharge was much above average as reflected in the surface salinity distributions. Surface oxygen saturation does not appear well correlated with just freshwater discharge and surface salinity.

Summer distributions (Figure 5.3-1c) picture values between 90 and 100% saturation almost everywhere. Slightly higher values are found shoreward of the 20-m isobath in a few locations. For summers the upcoast flow held low salinity water over the eastern shelf, and salinities < 30 extended across the entire shelf at line 1 in May 1993 and 1994. November distributions showed surface oxygen slightly higher than during summer (4.5 to $6 \text{ ml}\cdot\text{l}^{-1}$ versus 4 to $5 \text{ ml}\cdot\text{l}^{-1}$) with saturation between 90 and 110% (Figure 5.3-1d).

Figure 5.3-2 shows the relationship of the surface dissolved oxygen saturation and surface salinity for the spring, summer, and fall seasons of 1992 (upper panels), 1993 (middle panels), and 1994 (lower panels). Most of the oxygen saturation values are near 100% saturation

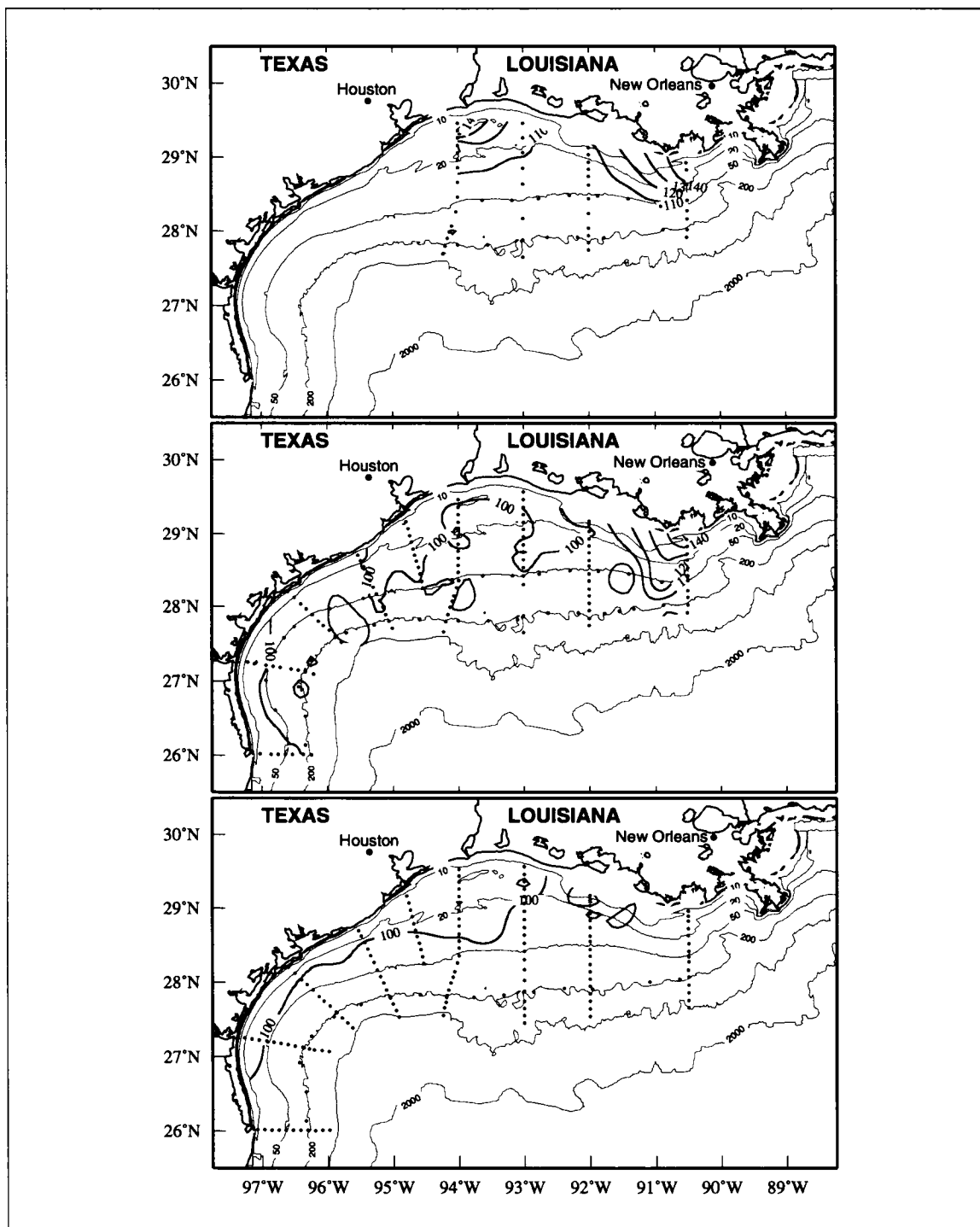


Figure 5.3-1b. Surface saturation (percent) of dissolved oxygen for spring cruises (upper panel) H01 (May 1992), (middle panel) H05 (May 1993), and (lower panel) H08 (May 1994).

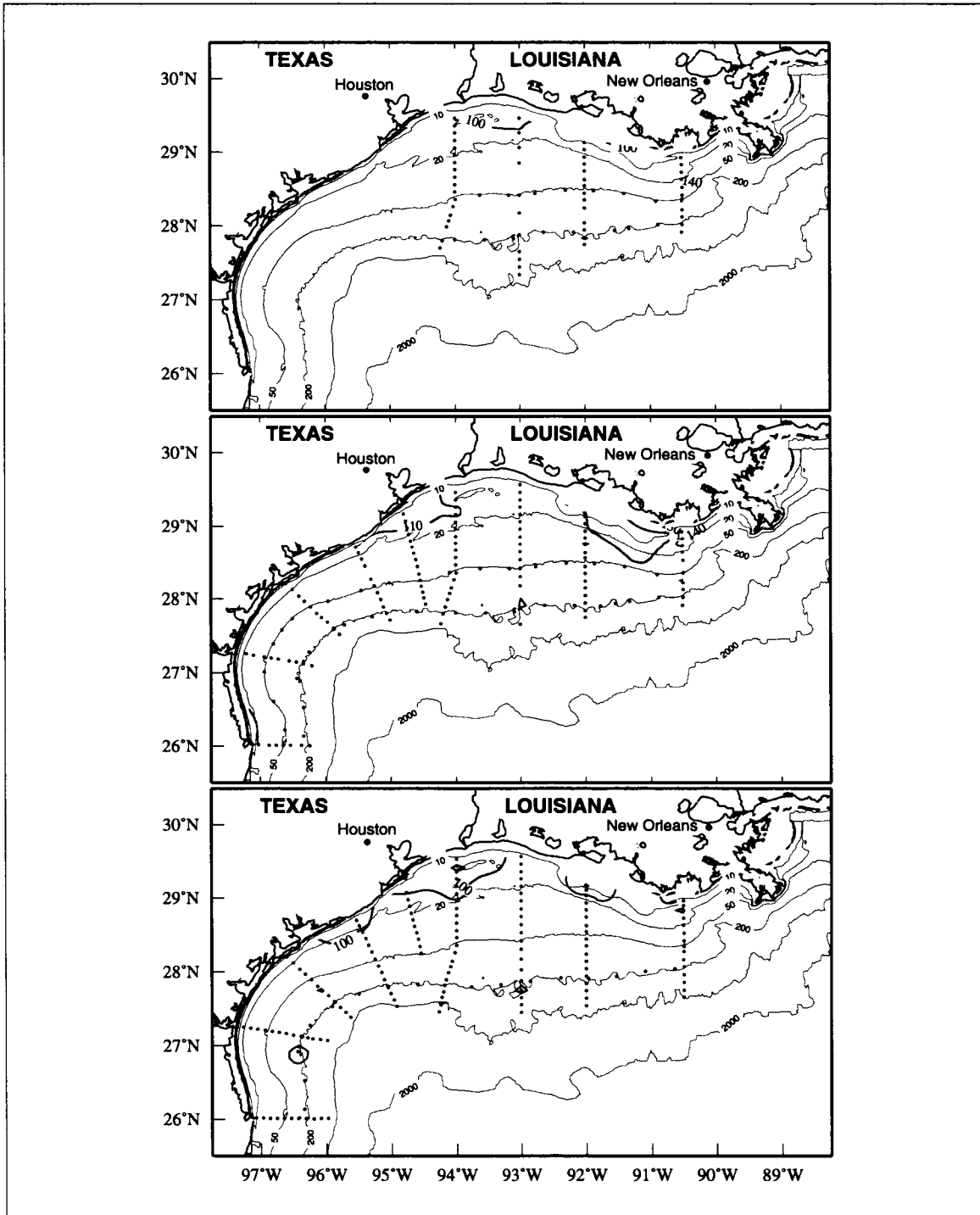


Figure 5.3-1c. Surface saturation (percent) of dissolved oxygen for summer cruises (upper panel) H02 (July-August 1992), (middle panel) H06 (July-August 1993), and (lower panel) H09 (July-August 1994).

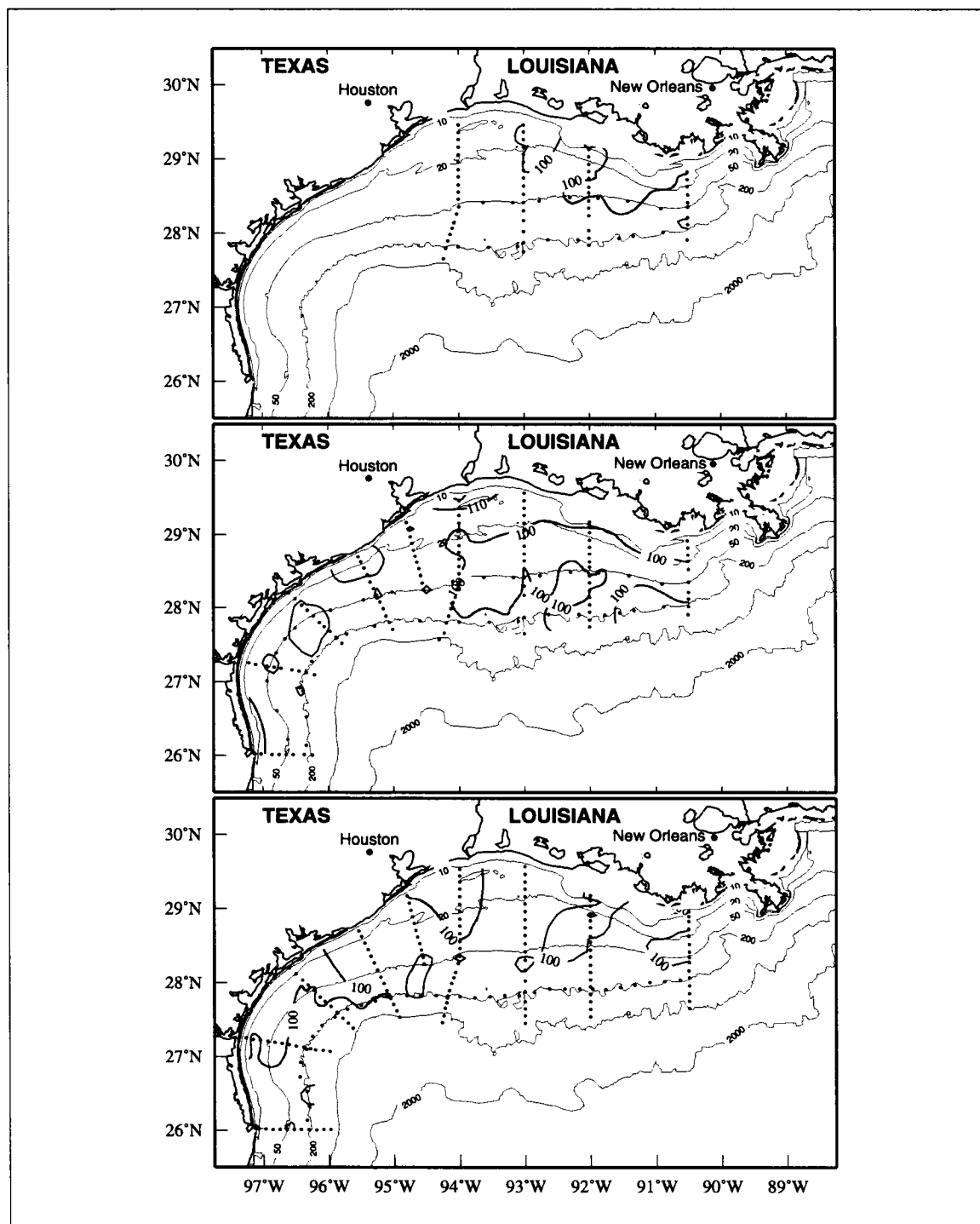


Figure 5.3-1d. Surface saturation (percent) of dissolved oxygen for fall cruises (upper panel) H03 (November 1992), (middle panel) H07 (November 1993), and (lower panel) H10 (November 1994).

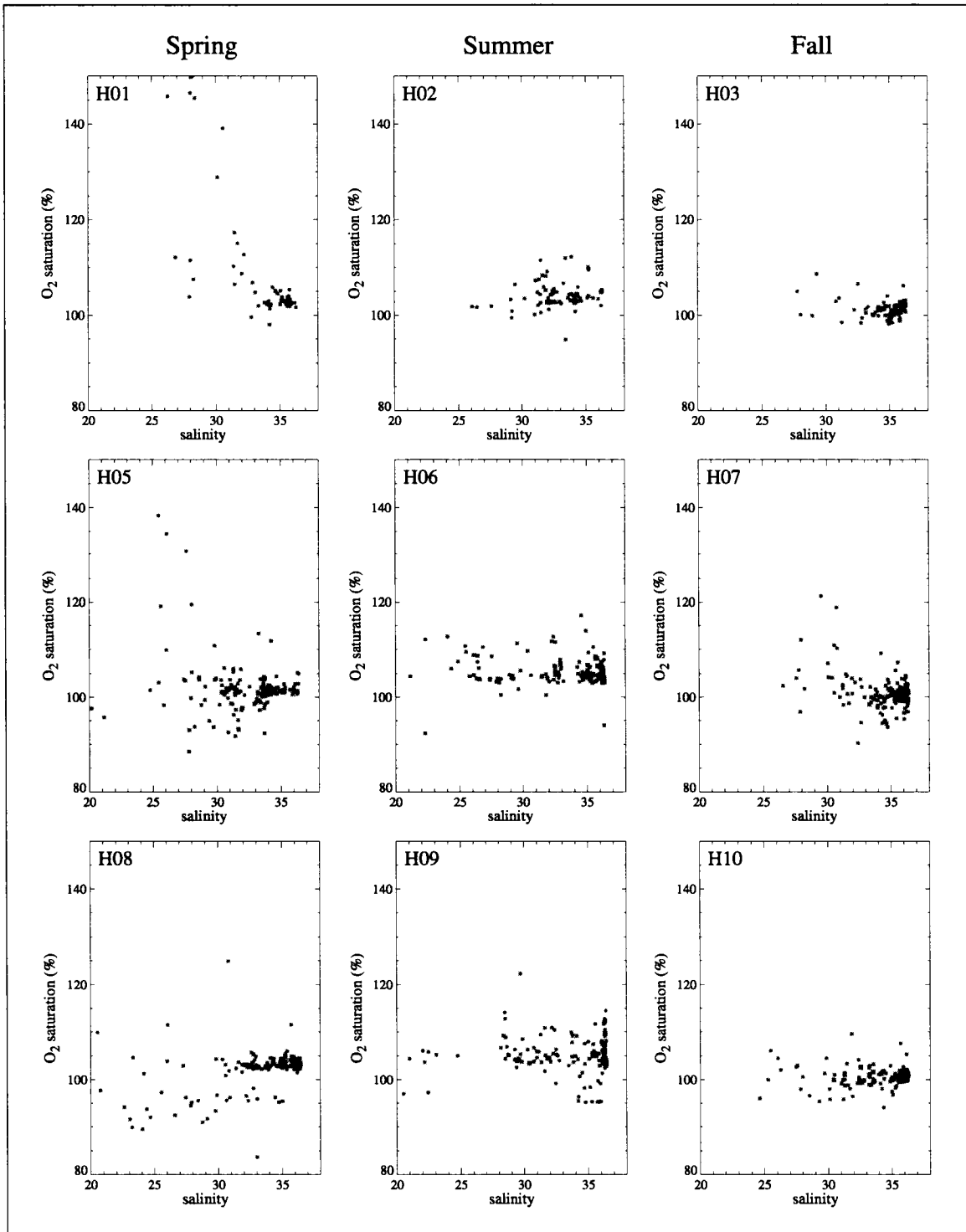


Figure 5.3-2. Surface dissolved oxygen saturation (percent) versus surface salinity for all samples for the spring, summer, and fall of 1992, 1993, and 1994.

($\pm 5\%$) and occur over the full range of fresh and salty waters in all three seasons. All saturation values are above 80%. Stations with highly supersaturated values occur in all three seasons, but less in fall, and most are located east of 94°W. The spring season has the stations with the highest surface oxygen saturation values. These values occur in waters with low (≤ 32) salinity, suggesting that highly supersaturated oxygen values are related to discharge of river water, although low salinities are observed on other spring and summer cruises for which highly supersaturated oxygenation is not seen. The squared correlation coefficients for surface oxygen saturation and surface salinity in stations located on the eastern inner shelf are less than 0.5 except for winter cruise H04. (Table 5.3-1). The correlations on the winter, two spring and two fall cruises are significant at the 95% level. The significant correlations are negative, indicating that low surface salinities are correlated with high surface oxygen saturation.

The river water carries a high nutrient content (Section 5.2) which enhances phytoplankton growth, which, in turn, adds oxygen to the water. Figure 5.3-3 shows the relationship of the surface dissolved oxygen saturation and the surface chlorophyll-a concentrations ($\text{ng}\cdot\text{l}^{-1}$) for the spring, summer, and fall seasons of 1992 (upper panels), 1993 (middle panels), and 1994 (lower panels). Most of the surface oxygen saturation values in all three seasons are about $100\% \pm 5\%$ over a wide range of chlorophyll-a concentrations. This is consistent with the major source of oxygen being the atmosphere, not the phytoplankton. Spring, however, is the season with the most stations with highly supersaturated surface oxygen. These highly supersaturated values occur with high concentrations ($> 1000 \text{ ng}\cdot\text{l}^{-1}$) of surface chlorophyll-a, indicating that the phytoplankton blooms can be major contributors to oxygen concentrations in the surface waters. High phytoplankton activity, indicated by high chlorophyll-a values, however, does not guarantee that the surface oxygen values will be highly supersaturated. This can be seen in the large number of stations with high chlorophyll-a concentrations but with oxygen saturation values between 90% and 110%. The squared correlation coefficients for surface oxygen saturation and surface chlorophyll-a in stations located on the eastern inner shelf are all less than 0.5, with correlations of all three spring cruises, the winter cruise and one fall cruise at the 95% significance level (Table 5.3-1). The significant correlations are positive, indicating high surface chlorophyll-a concentrations are correlated with high surface oxygen saturation.

General subsurface distributions

Here we present dissolved oxygen in vertical section along line 1 (approximately 90.5°W) for all ten LATEX A hydrographic surveys in chronological order. Distributions for the first four cruises, representing our seasons, are shown in Figures 5.3-4 through 5.3-7. For each cruise two vertical sections are pictured: one showing only the upper 50 m of the water column, and the other showing the contoured distributions in the upper 200 m. For subsequent cruises and other lines the vertical distributions show only the upper 50 m of the water

Table 5.3-1. Squared correlation coefficients for surface oxygen saturation with surface salinity and surface chlorophyll-a values over the eastern inner shelf.

Cruise	Squared correlation coefficient	Significance level (%)
<i>Surface oxygen saturation with surface salinity over the eastern inner shelf</i>		
H01	0.32117	99
H02	0.13594	90
H03	0.02964	50
H04	0.54082	99.9
H05	0.29217	99.5
H06	0.09140	90
H07	0.26512	99.5
H08	0.00012	<50
H09	0.04765	70
H10	0.26410	99.5
<i>Surface oxygen saturation with surface chlorophyll-a over the eastern inner shelf</i>		
H01	0.42723	99.5
H02	0.00466	<50
H03	0.00646	<50
H04	0.36842	99.5
H05	0.41564	99
H06	0.01581	50
H07	0.29711	99.9
H08	0.18069	98
H09	0.00043	<50
H10	0.09844	90

column. We believe that is where the changes of most significance to ecosystems occur—in particular, the occurrence of hypoxia.

Spring surface dissolved oxygen values on line 1 for cruise H01 (Figure 5.3-4) ranged from less than 5 ml·l⁻¹ over the continental rise to greater than 7 ml·l⁻¹ at the shallowest station. At the shelf break values decreased monotonically with depth to about 3 ml·l⁻¹ at 200 m. Below 10 m, the oxygen isopleths decreased with depth and sloped slightly upward toward the coast. At stations 71 and 73, very low bottom values (less than 2 ml·l⁻¹) were found. In summer 1992 (cruise H02, Figure 5.3-5), surface values along line 1 were somewhat greater than 4.5 ml·l⁻¹, considerably less than in spring. Offshelf values again decreased with depth to about 3 ml·l⁻¹ near 200 m. Bottom values were generally lower than in spring by about

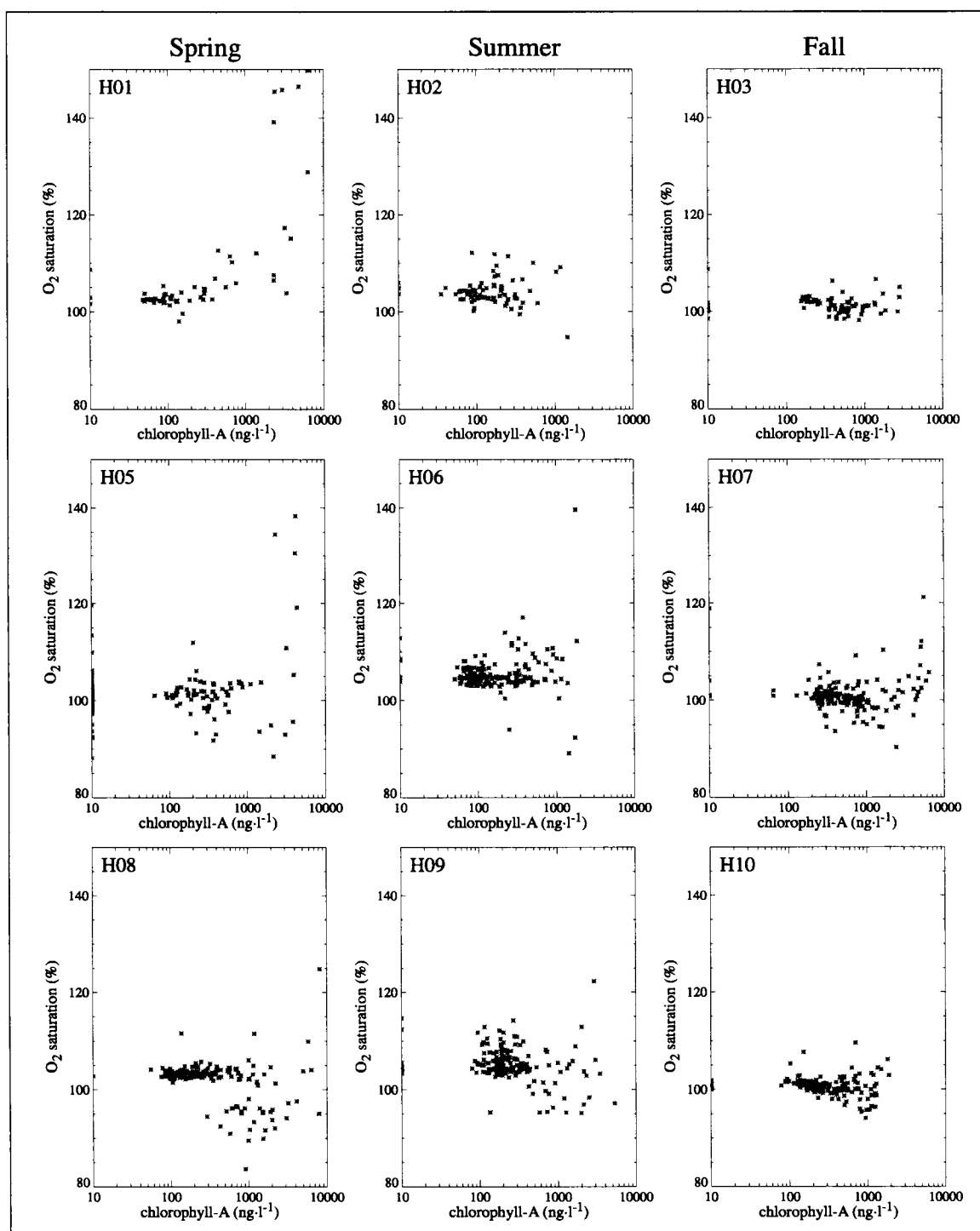


Figure 5.3-3. Surface dissolved oxygen saturation (percent) versus surface chlorophyll-a concentration (ng·l⁻¹) for all samples for the spring, summer, and fall of 1992, 1993, and 1994.

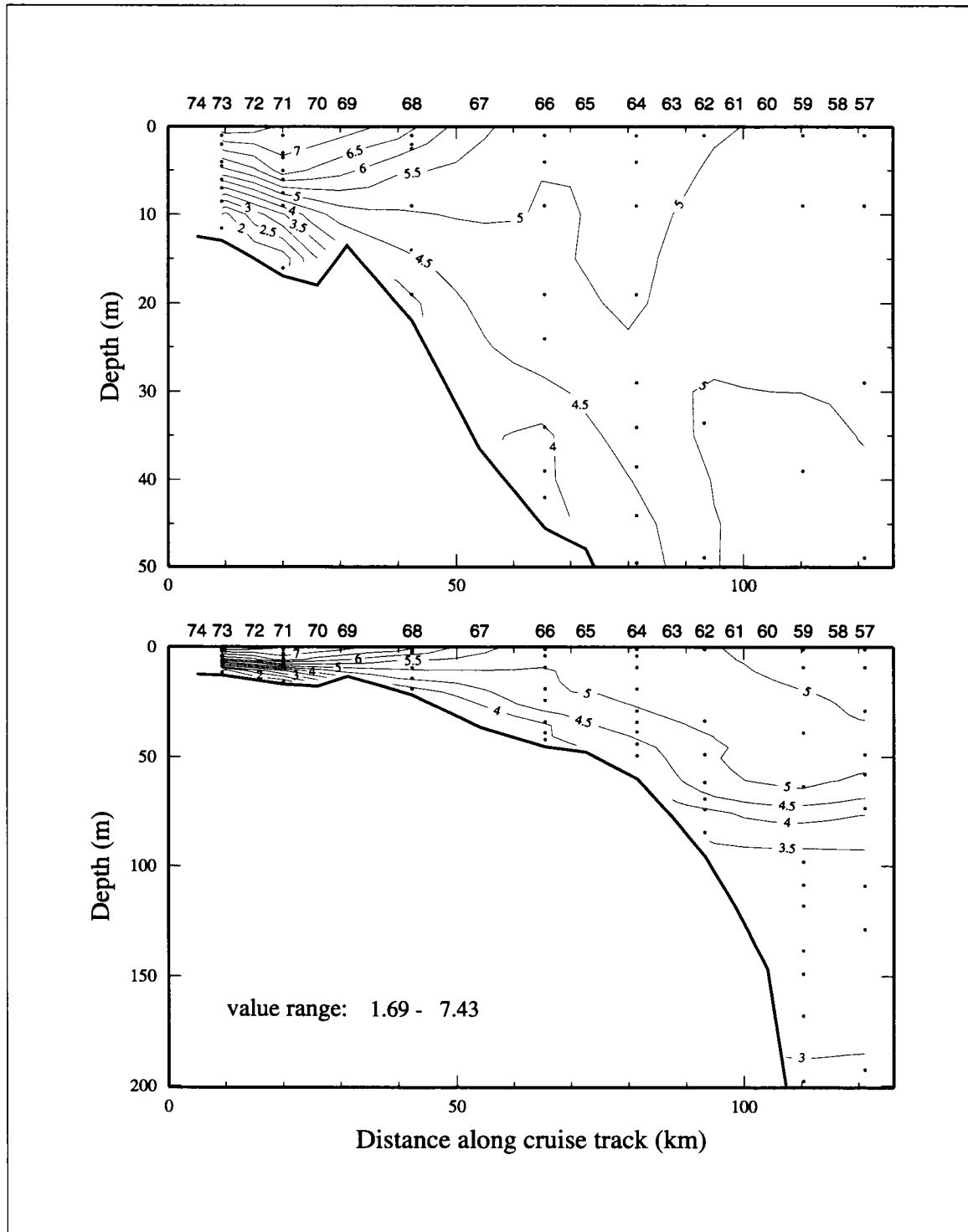


Figure 5.3-4. Contours of bottle dissolved oxygen ($\text{ml}\cdot\text{l}^{-1}$) along line 1 during cruise H01, 30 April-9 May 1992.

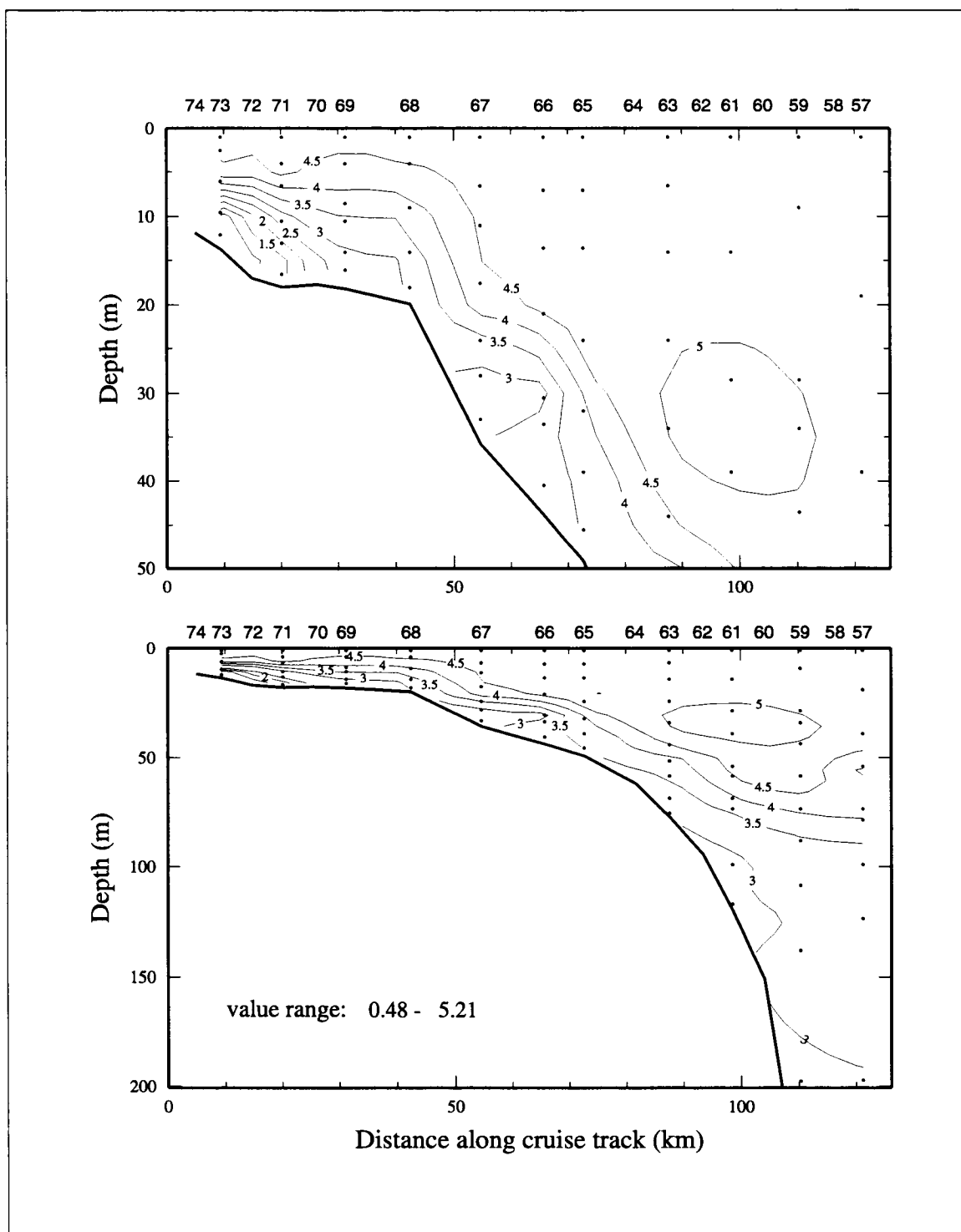


Figure 5.3-5. Contours of bottle dissolved oxygen ($\text{ml}\cdot\text{l}^{-1}$) along line 1 during cruise H02, 31 July-9 August 1992.

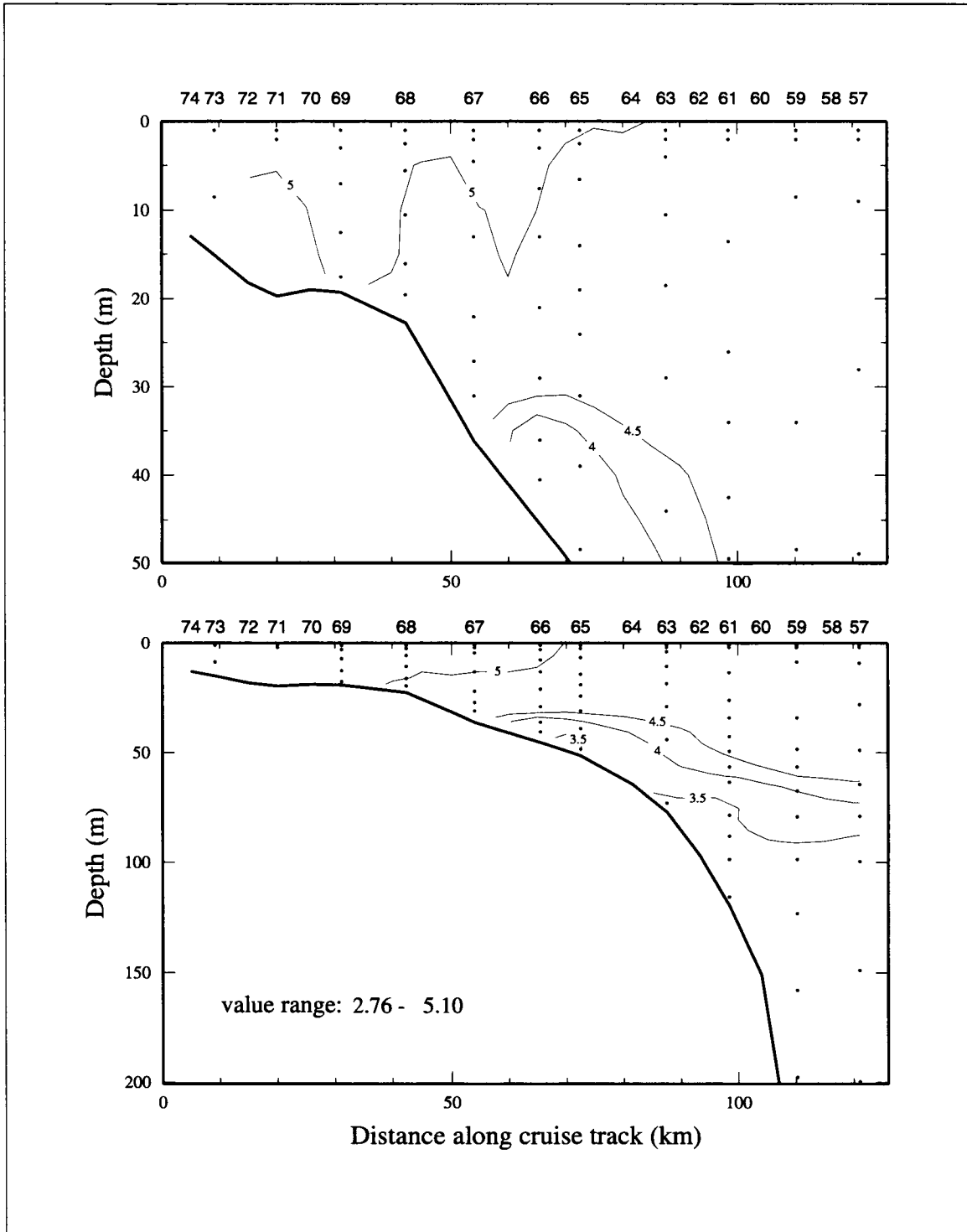


Figure 5.3-6. Contours of bottle dissolved oxygen ($\text{ml}\cdot\text{l}^{-1}$) along line 1 during cruise H03, 4-13 November 1992.

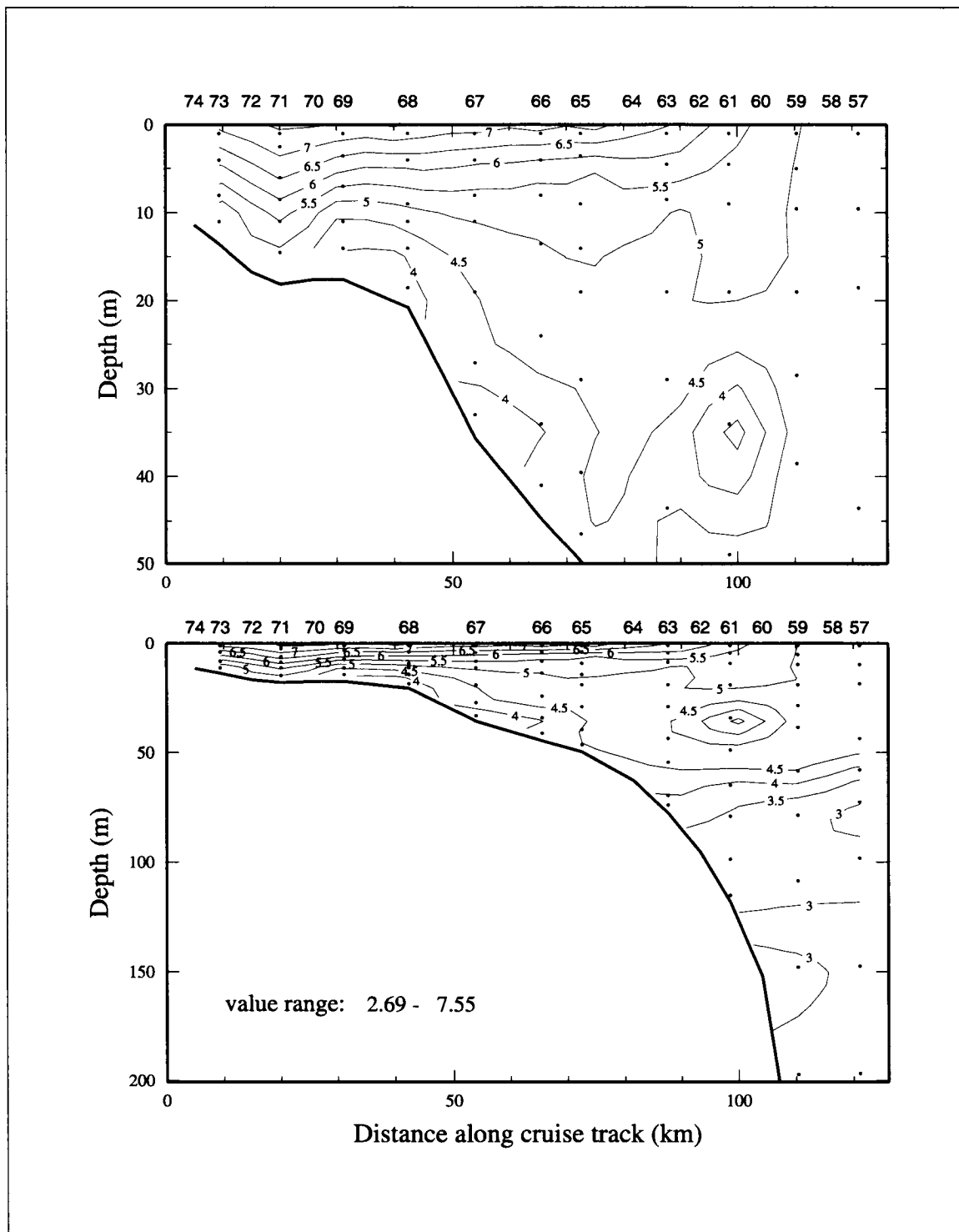


Figure 5.3-7. Contours of bottle dissolved oxygen ($\text{ml}\cdot\text{l}^{-1}$) along line 1 during cruise H04, 4-13 February 1993.

1 ml·l⁻¹. Hypoxic bottom conditions were seen at stations 71-73. By November 1992 (cruise H03, Figure 5.3-6), surface values had increased to somewhat more than 5 ml·l⁻¹, and those values were found to depths of about 20 m over the inner shelf. Oxygen values near the shelf edge were similar to those in July-August. Bottom values over the outer shelf were 3.5 to 4.5 ml·l⁻¹, about 1 ml·l⁻¹ higher than in summer; no hypoxia was present. By February 1993 (cruise H04, Figure 5.3-7), surface oxygen over the shelf had increased to between 5 and 7.5 ml·l⁻¹, increasing onshore. There was relatively strong vertical stratification over the inner shelf with bottom values between 4 and 5 ml·l⁻¹, increasing onshore with an upward onshore slope to isopleths.

The spring, summer, and fall dissolved oxygen distributions along line 1 for 1993, shown in Figure 5.3-8, are quite similar to those for 1992. They will not be discussed here except to note that there were hypoxic conditions at the bottom over the inner shelf during spring as well as summer in 1993.

Spring, summer, and fall dissolved oxygen distributions along line 1 for 1994 are shown in Figure 5.3-9. The principal differences from 1992 and 1993 occurred in spring. In 1994, spring surface oxygen values were lower by 1-2 ml·l⁻¹ than in the previous years. There was no hypoxia in the bottom waters over the inner shelf in 1994.

Spring, summer, and fall distributions of dissolved oxygen concentrations within the upper 50 m along line 4 (approximately 94°W) are shown for 1992, 1993, and 1994 in Figures 5.3-10, 5.3-11, and 5.3-12, respectively. Hypoxic conditions were not found on line 4 in those years. However, relatively low oxygen values were found in the bottom waters at one or more stations over the inner shelf during spring 1992 and 1994 and during summer 1993. In general, the distributions at line 4 evidence less vertical stratification in spring and summer than those on line 1. In November 1992 there was very little vertical structure, with values everywhere near 5 ml·l⁻¹. This was true, too, for February 1993 (cruise H04, not shown), for which values were between 5 and 6 ml·l⁻¹ everywhere. The November 1993 cruise (H07) also was marked by little spatial variability for dissolved oxygen.

The western shelf was surveyed only in 1993 and 1994. Figures 5.3-13 and 5.3-14 show distributions of dissolved oxygen along line 7 (approximately 27.3°N) for the spring, summer, and fall cruises of 1993 and 1994, respectively. Gradients are weaker on line 7 than on line 4. Distributions are somewhat more uniform on lines 4 and 7 than on line 1.

Incidences of hypoxia

Hypoxia has occurred on the Louisiana continental shelf during most summers since the first measurements were made in 1973 (Boesch and Rabalais 1991). This is the largest zone of hypoxic waters in U.S. coastal waters and may cover over 9000 km² (Rabalais et al.

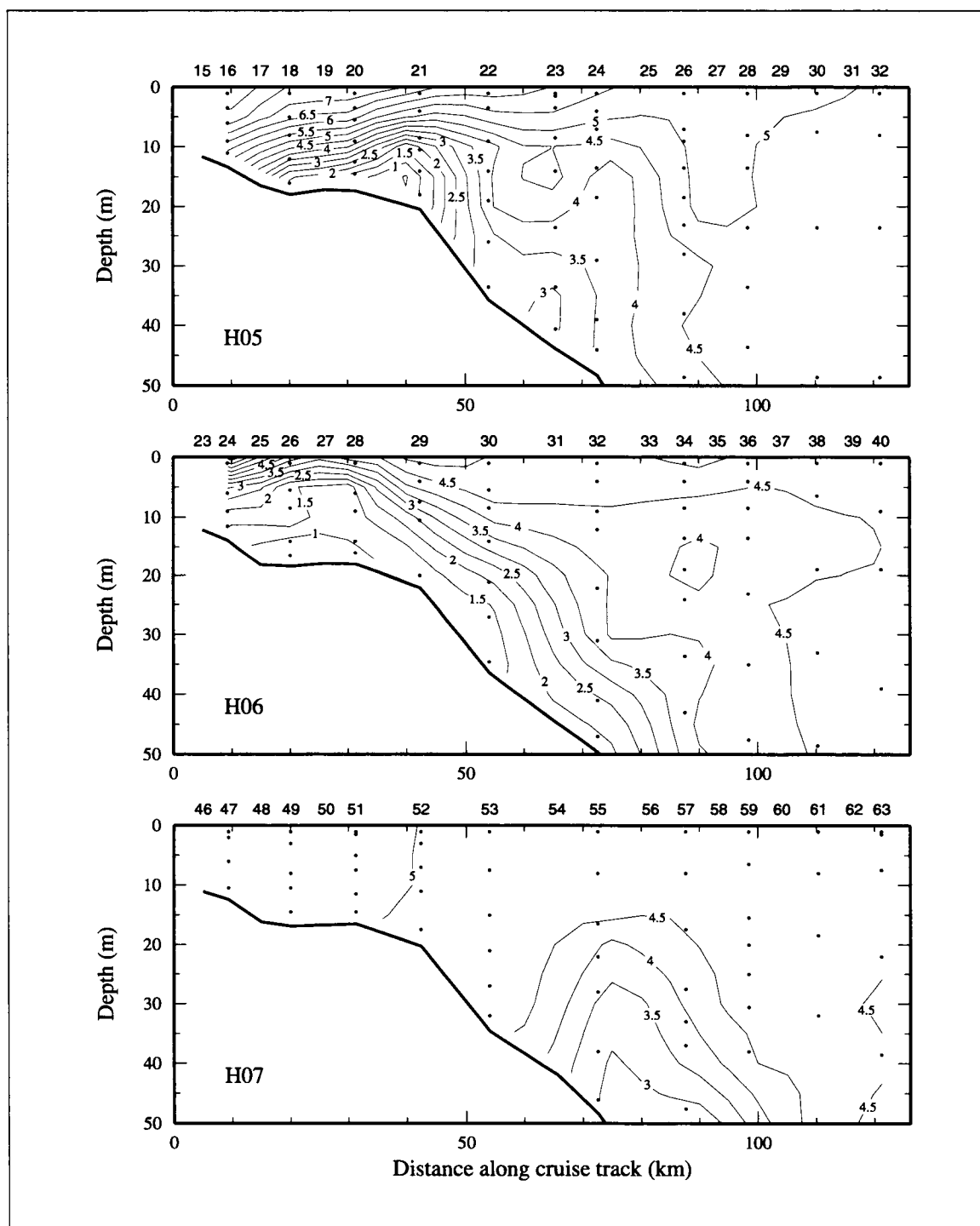


Figure 5.3-8. Contours of bottle dissolved oxygen ($\text{ml}\cdot\text{l}^{-1}$) along line 1 during cruises (upper panel) H05 (25 April-11 May 1993), (middle panel) H06 (25 July-7 August 1993), and (lower panel) H07 (6-22 November 1993).

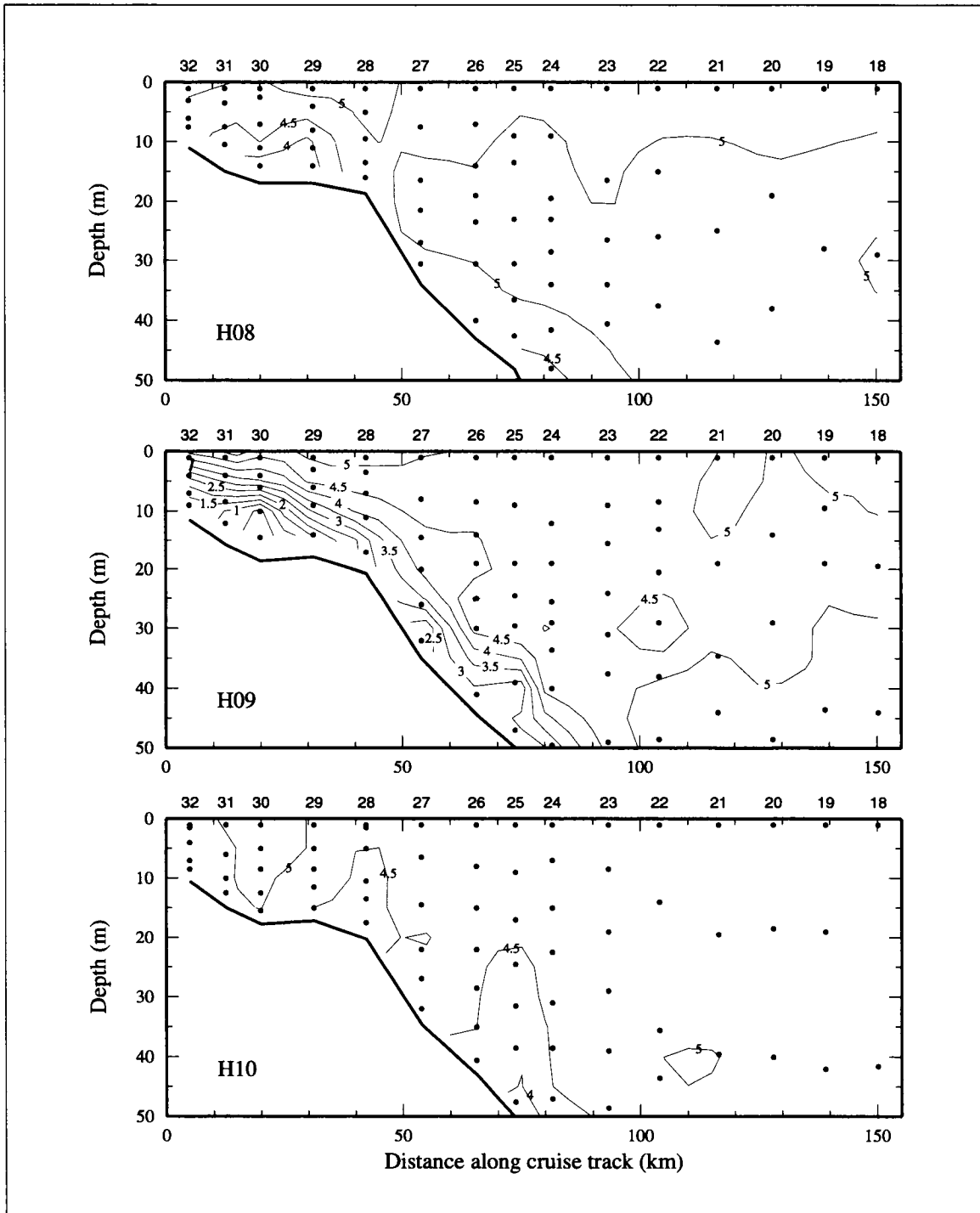


Figure 5.3-9. Contours of bottle dissolved oxygen ($\text{ml}\cdot\text{l}^{-1}$) along line 1 during cruises (upper panel) H08 (23 April-7 May 1994), (middle panel) H09 (26 July-7 August 1994), and (lower panel) H10 (2-14 November 1994).

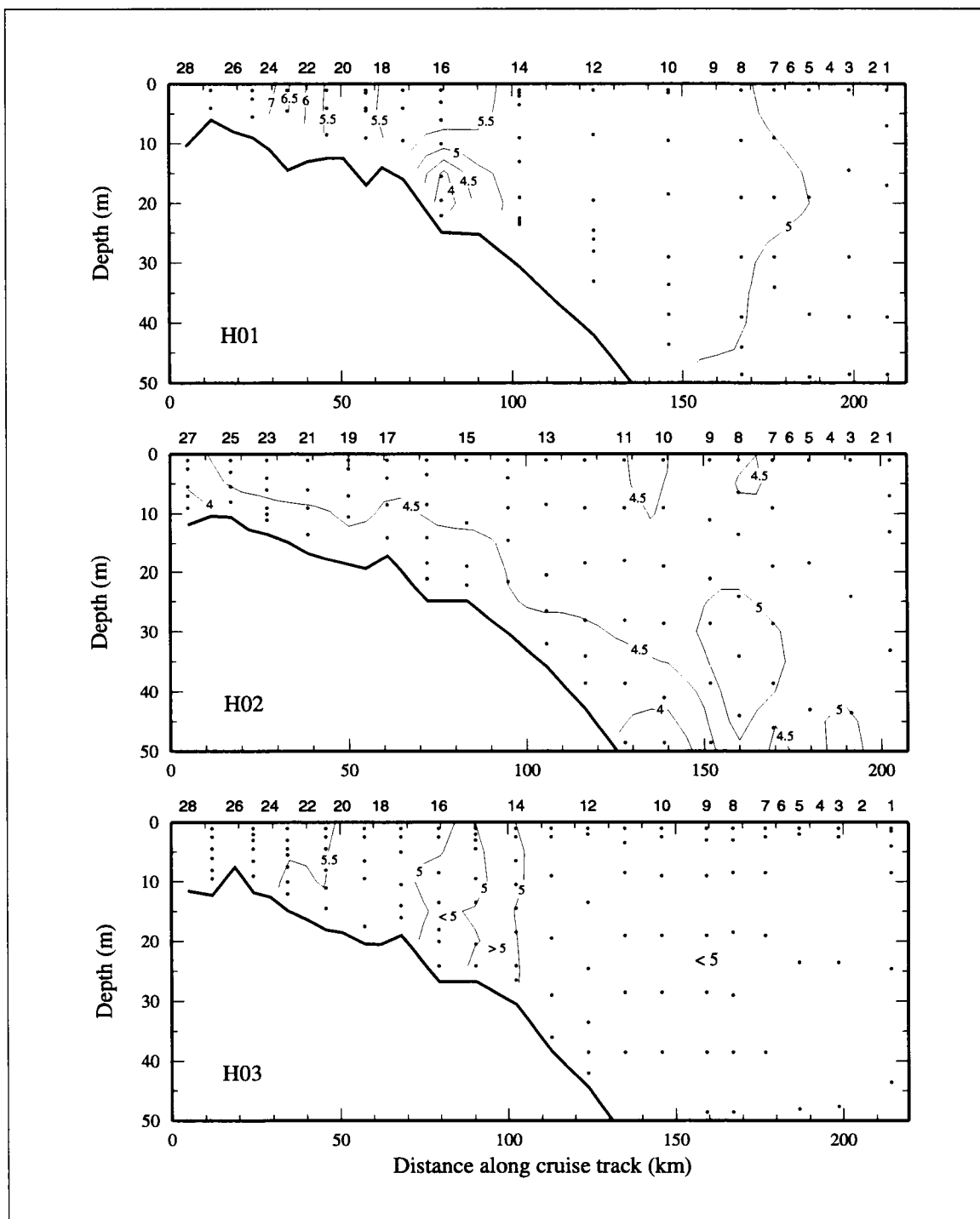


Figure 5.3-10. Contours of bottle dissolved oxygen ($\text{ml}\cdot\text{l}^{-1}$) along line 4 during cruises (upper panel) H01 (30 April-9 May 1992), (middle panel) H02 (31 July-9 August 1992), and (lower panel) H03 (4-13 November 1992).

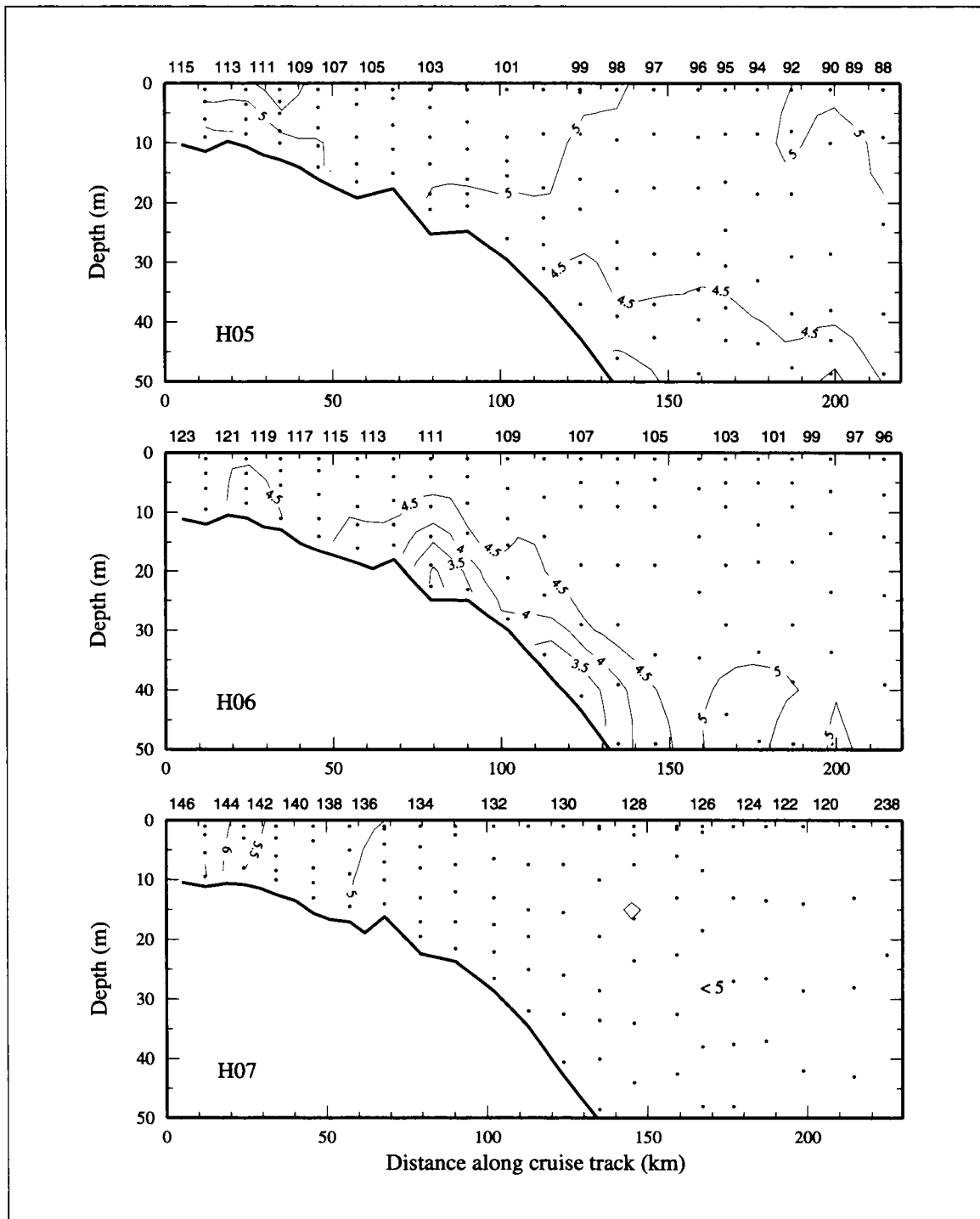


Figure 5.3-11. Contours of bottle dissolved oxygen ($\text{ml}\cdot\text{l}^{-1}$) along line 4 during cruises (upper panel) H05 (25 April-11 May 1993), (middle panel) H06 (25 July-7 August 1993), and (lower panel) H07 (6-22 November 1993).

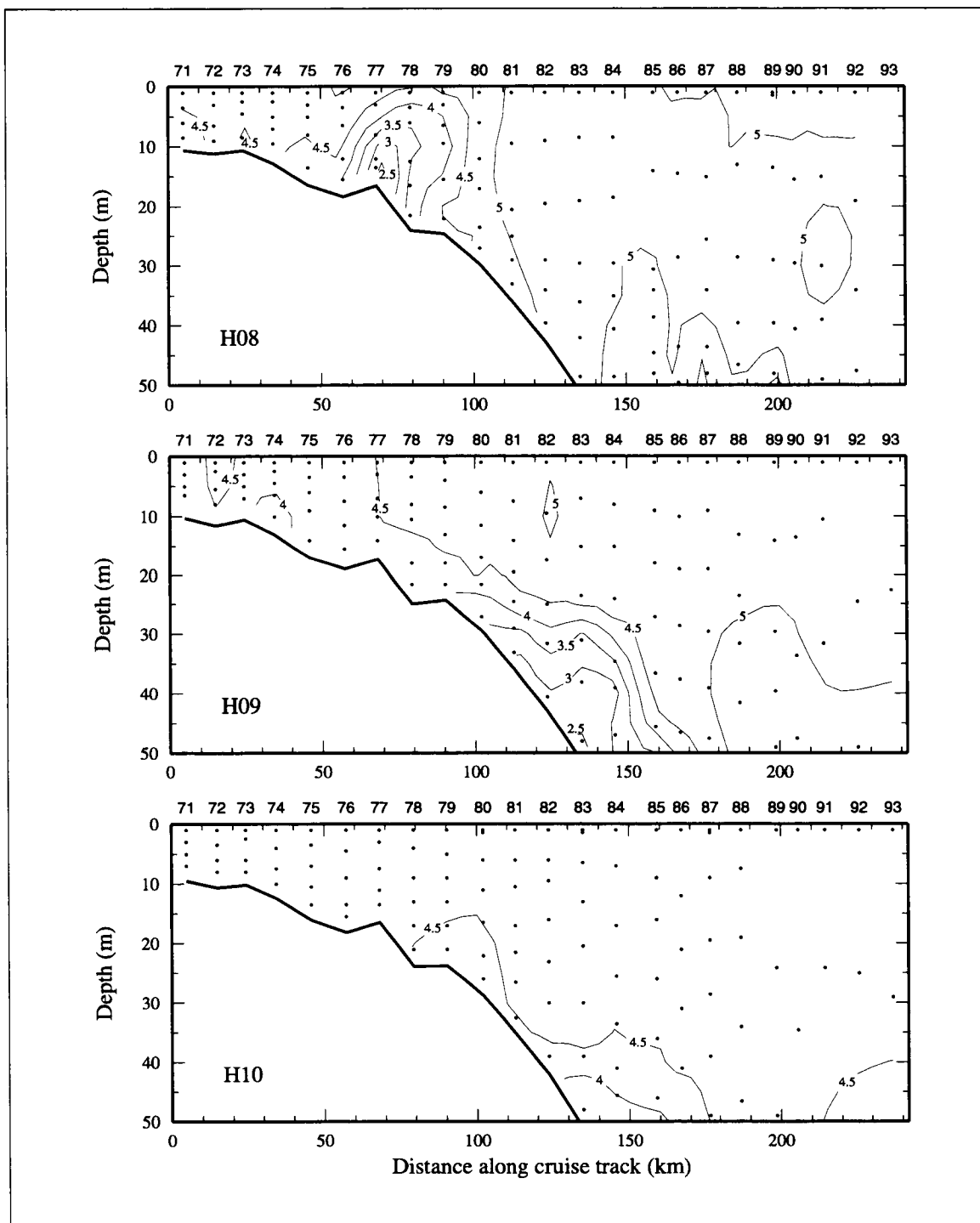


Figure 5.3-12. Contours of bottle dissolved oxygen ($\text{ml}\cdot\text{l}^{-1}$) along line 4 during cruises (upper panel) H08 (23 April-7 May 1994), (middle panel) H09 (26 July-7 August 1994), and (lower panel) H10 (2-14 November 1994).

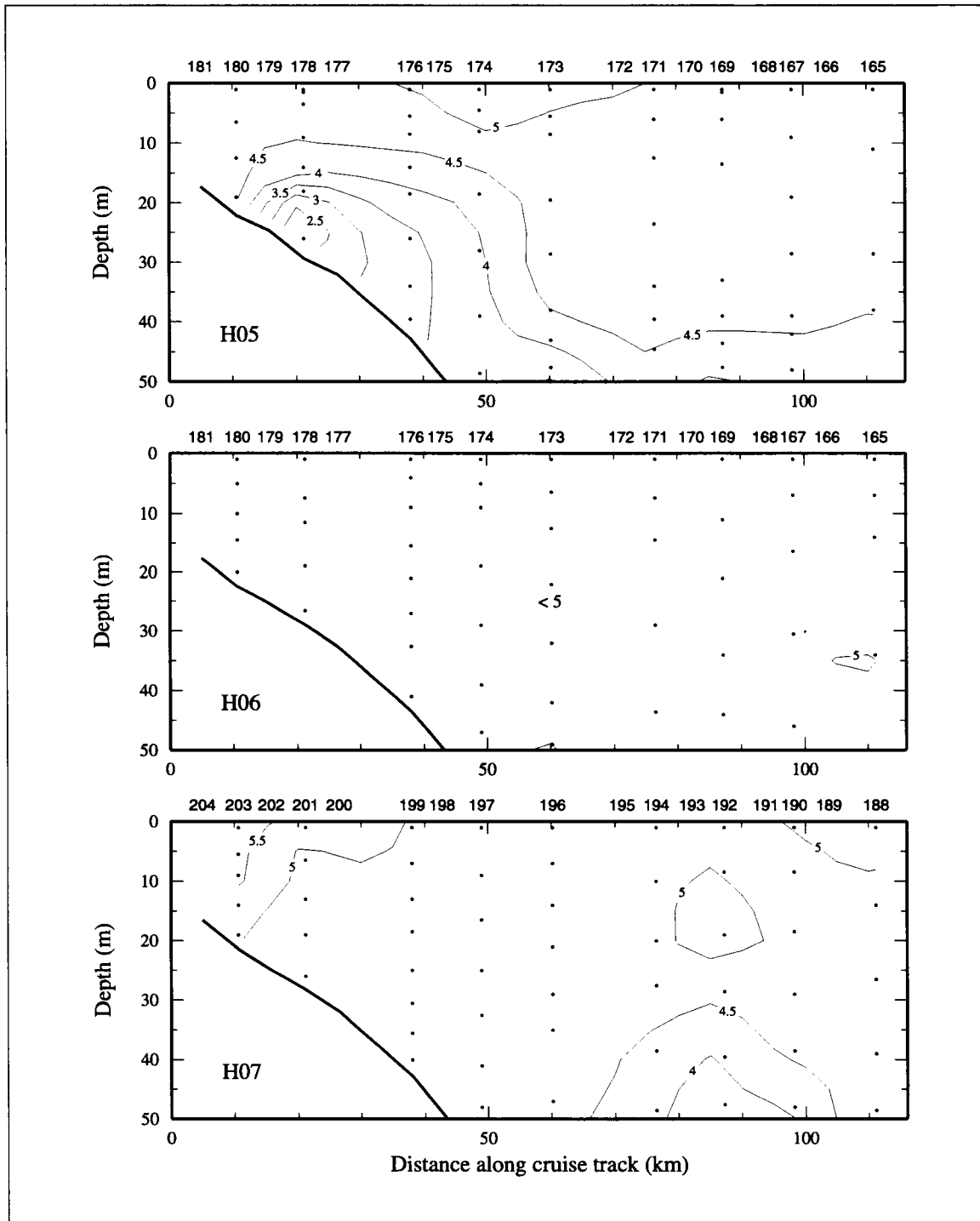


Figure 5.3-13. Contours of bottle dissolved oxygen ($\text{ml}\cdot\text{l}^{-1}$) along line 7 during cruises (upper panel) H05 (25 April-11 May 1993), (middle panel) H06 (25 July-7 August 1993), and (lower panel) H07 (6-22 November 1993).

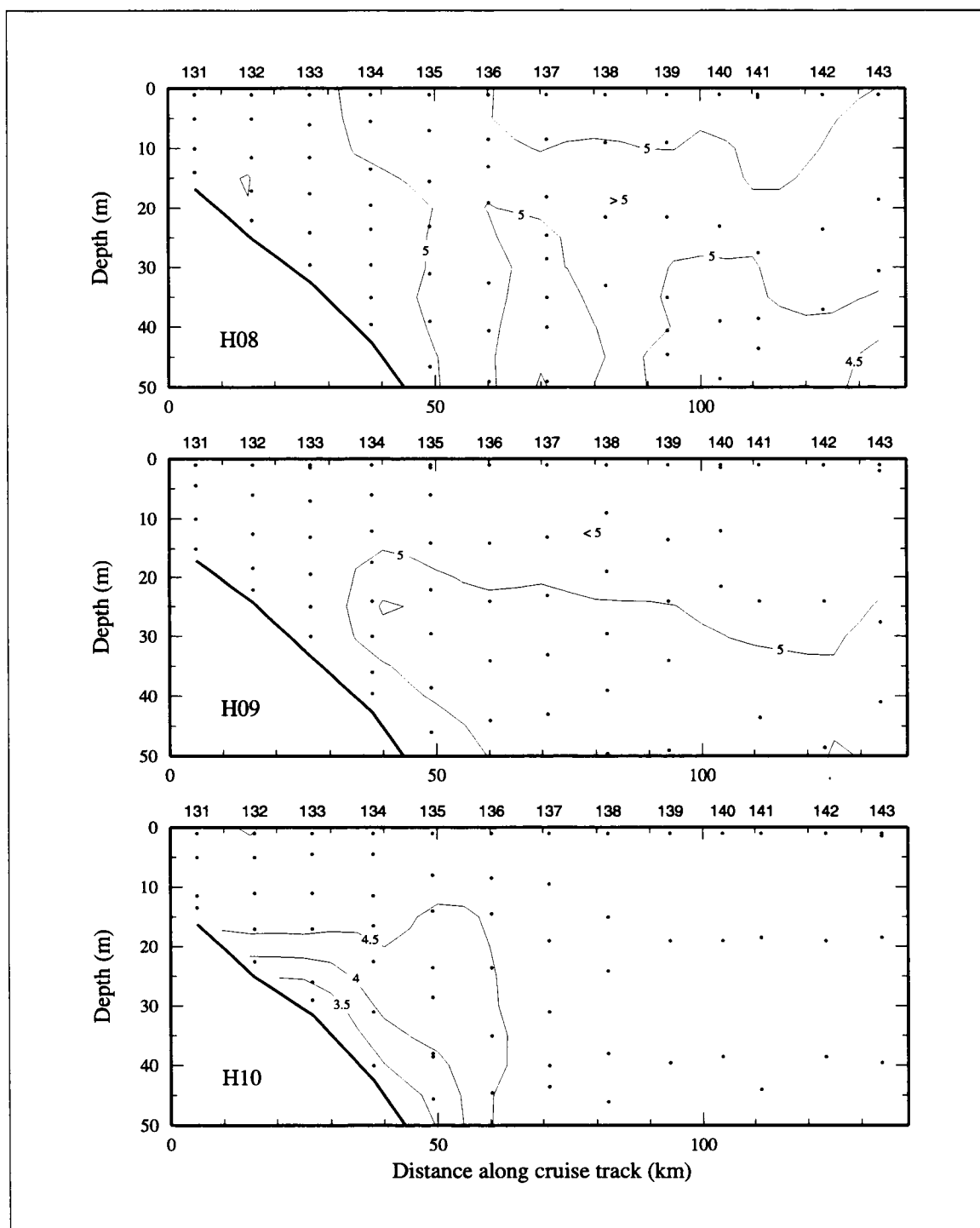


Figure 5.3-14. Contours of bottle dissolved oxygen ($\text{ml}\cdot\text{l}^{-1}$) along line 7 during cruises (upper panel) H08 (23 April-7 May 1994), (middle panel) H09 (26 July-7 August 1994), and (lower panel) H10 (2-14 November 1994).

1991). Hypoxic conditions have been observed on the Texas shelf (Harper et al. 1981), but not with the frequency seen on the Louisiana shelf.

To document the occurrence of hypoxic conditions, we examined the bottom distributions of dissolved oxygen based on the deepest bottle oxygen measurement at each station. The ranges and spatial means of dissolved oxygen measurements for spring and summer cruises are given in Table 5.3-2. Hypoxic conditions were observed in bottom waters over the eastern shelf in four of our ten cruises: summer 1992, spring and summer 1993, and summer 1994. Near hypoxic conditions were found on line 1 during spring 1992.

Bottom distributions are shown for 1992 cruises H01 (spring) and H02 (summer) in Figure 5.3-15. On H01 near hypoxic conditions were found only at the two inshore stations on line 1. For the summer cruise H02, however, hypoxia was recorded inshore on lines 1 and 3; near hypoxic conditions existed on line 2. On line 1 in water depths from 14 to 18 m, bottom values were from 0.5 to 1.3 ml·l⁻¹; in 18 m water depth, values less than 1.3 ml·l⁻¹ were measured over the lower 5 m of the water column oxygen (Figure 5.3-5). On line 3, hypoxic conditions were detected at the shallowest station with a water depth of 14 m, where the bottom 3 m were hypoxic with values at least as low as 0.9 ml·l⁻¹.

In spring 1993, hypoxia was found on lines 1 and 2, but not at the innermost stations (Figure 5.3-16). Bottom values were 0.7 to 1.1 ml·l⁻¹ for stations in water depths 17-21 m; values between 0.5 and 0.7 ml·l⁻¹ extended through the lower 10 m of the column at station 21 (Figure 5.3-8). The bottom oxygen distribution gives evidence for a pool of low oxygen water oriented along shelf. Low oxygen bottom waters also occur at nearshore station 178 on line 7 of the western shelf (Figure 5.3-13).

Evidence for a pool of low oxygen water oriented along shelf is also seen for summer 1993 cruise H06, for which hypoxic bottom waters stretched from line 1 past line 2 (Figure 5.3-16). Bottom values at stations with depths from 14 to 36 m on line 1 were 0.5 to 1.3 ml·l⁻¹; at 18 m water depth, the lower 7 m of the column had values between 0.8 and 1.3 ml·l⁻¹ (Figure 5.3-8). On line 2, hypoxic conditions (0.1-0.7 ml·l⁻¹) were found in water depths from 16 to 40 m. Also seen in Figure 5.3-16 are hypoxic conditions (< 0.7 ml·l⁻¹ in the lowest 2 m of the water column) at the shallowest station on line 3.

Figure 5.3-17 pictures the bottom oxygen distribution during summer 1994 cruise H09. The pattern of bottom hypoxia is very similar to that for summer 1993. On line 1 bottom values between 0.2 and 1.3 ml·l⁻¹ were in water depths from 11 to 35 m (Figure 5.3-9); on line 2 bottom values of 0.02 to 1.3 ml·l⁻¹ were found in water depths of 12 to 27 m.

A stratified water column facilitates the formation of hypoxic bottom waters by restricting the resupply of oxygen from the surface. The Mississippi-Atchafalaya river discharge,

Table 5.3-2. Bottom bottle dissolved oxygen measurements ($\text{ml}\cdot\text{l}^{-1}$).

	Range of bottom values	Spatial average
<i>Spring Cruises</i>		
H01, 1992	1.7 to 7.5	4.0
H05, 1993	0.7 to 5.5	3.7
H08, 1994	2.0 to 6.0	4.0
<i>Summer Cruises</i>		
H02, 1992	0.5 to 4.4	3.2
H06, 1993	0.1 to 5.1	3.3
H09, 1994	0.02 to 4.8	3.3

together with a reduction in wind stress and a seasonal thermocline in summer, contributes to the stratification observed on the continental shelf of the Gulf of Mexico (Rabalais et al. 1991; Justic et al. 1993).

We computed stability using

$$\text{Stability} = \frac{\sigma_{\theta_{\text{bottom}}} - \sigma_{\theta_{\text{surface}}}}{\text{water depth}}.$$

Values were not normalized by density. Figures 5.3-18 and 5.3-19 show bottom oxygen saturation versus stability for the spring, summer, and fall cruises in 1992 (upper panel), 1993 (middle panel), and 1994 (bottom panel). The data were plotted by location relative to east and west regions, with the east region being east of and including 94°W . Note that a small number of stations were sampled near but west of 94°W on the half-shelf cruises H01 through H04. Data from these stations are plotted as part of the west shelf. For the purposes of this discussion, a high stability is defined to be values $\geq 0.1 \text{ kg}\cdot\text{m}^{-4}$. All hypoxic stations have bottom saturation values of $\leq 30\%$.

Consider first the relationship of bottom oxygen saturation to stability in the fall season, which has no hypoxia, over both the east and the west shelf regions (Figures 5.3-18 and 5.3-19). All three years have a pattern consisting of two basic regimes. The deep stations of the outer shelf are clustered near stability values centered about $0.01 \text{ kg}\cdot\text{m}^{-4}$ and oxygen saturation values centered about 50%. This cluster is present in the spring and summer seasons as well. Thus, the deep stations are relatively stable throughout the year. The added group of points in this cluster that form a hook in 1994 reflect the addition of stations

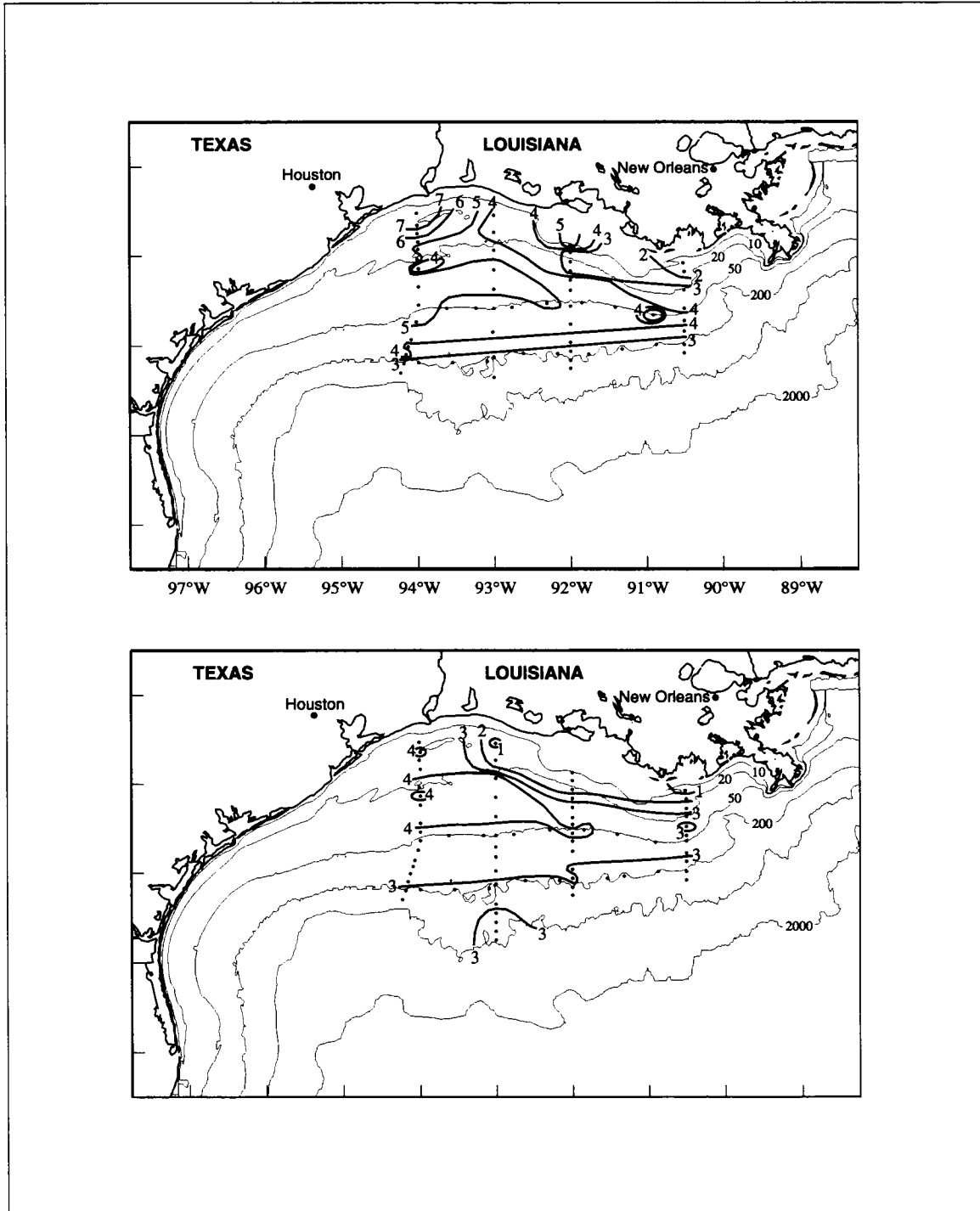


Figure 5.3-15. Bottom bottle dissolved oxygen ($\text{ml}\cdot\text{l}^{-1}$) for (upper panel) spring cruise H01 (30 April-9 May 1992) and (lower panel) summer cruise H02 (31 July-9 August 1992).

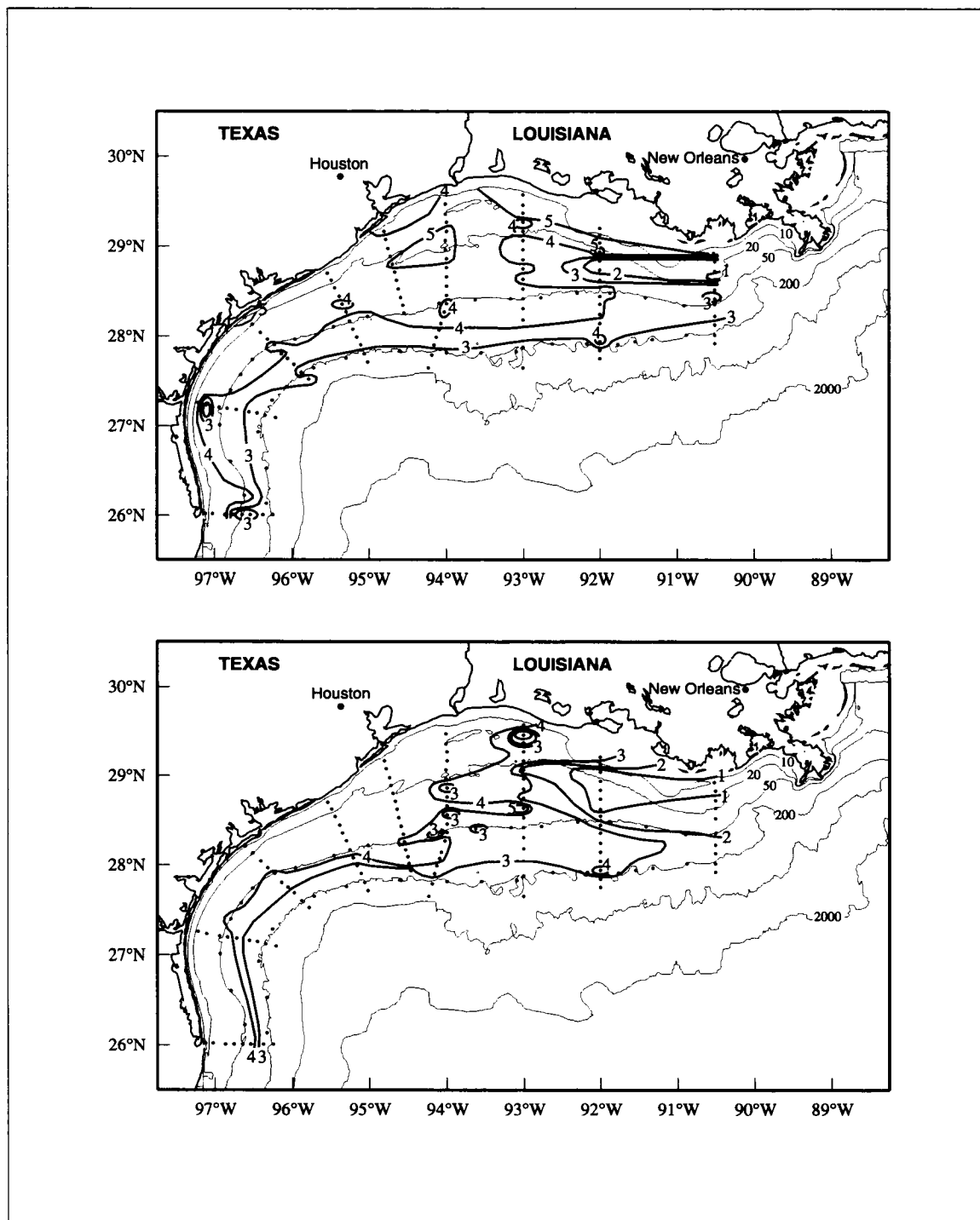


Figure 5.3-16. Bottom bottle dissolved oxygen ($\text{ml}\cdot\text{l}^{-1}$) for (upper panel) spring cruise H05 (25 April-11 May 1993) and (lower panel) summer cruise H06 (25 July-7 August 1993).

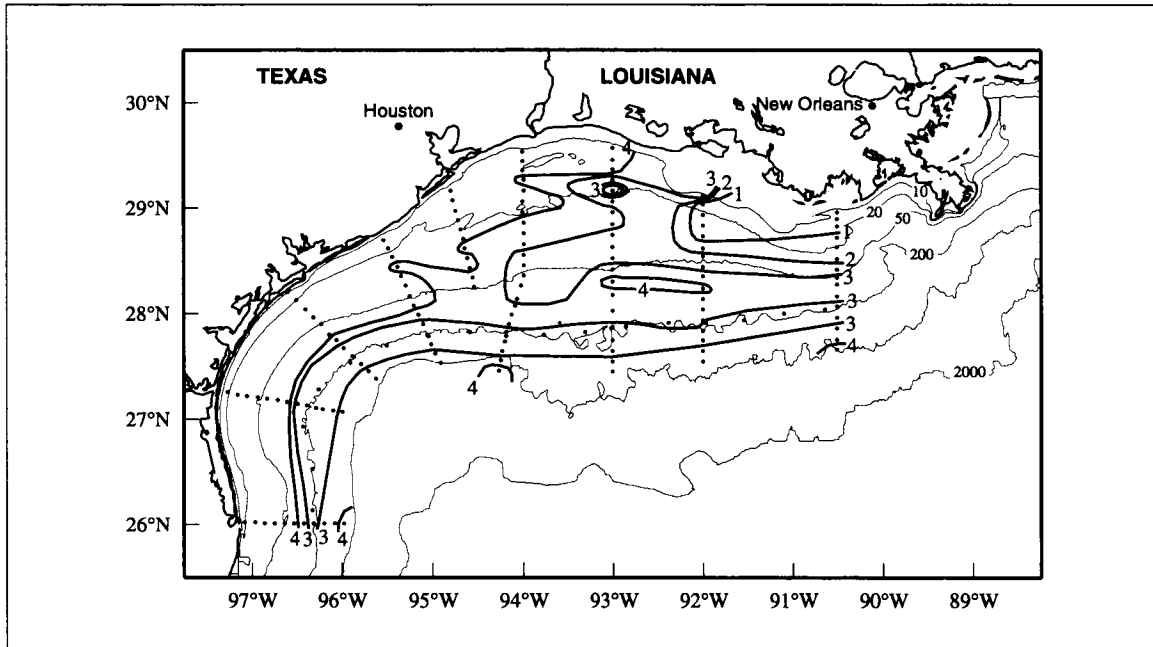


Figure 5.3-17. Bottom bottle dissolved oxygen ($\text{ml}\cdot\text{l}^{-1}$) for summer cruise H09 (26 July-7 August 1994).

between the 500- and 1000-m isobaths with deeper bottom samples than on the 1992 or 1993 cruises. The second regime in fall consists of stations with bottom oxygen saturation about 100%, but with stability values ranging from low ($< 0.001 \text{ kg}\cdot\text{m}^{-4}$) to high ($> 0.1 \text{ kg}\cdot\text{m}^{-4}$) values. This regime consists of the stations over the inner shelf where the depths are shallow and the waters are relatively well mixed to the bottom. The stations in this regime are subject to substantial change during the spring and summer seasons.

Over the west shelf, the general outline of the two regime structure of fall is present in spring, but with more scatter in saturation values and a shift to higher stability for the inner shelf stations (Figure 5.3-18). Note that the only station on the western shelf with a saturation value of less than 40% is the spring 1993, inner shelf station 178 noted previously. This station has high stability. In summer, all stations have bottom oxygen saturation values of $\geq 40\%$ and most have a stability approaching $0.1 \text{ kg}\cdot\text{m}^{-4}$. The stability of the inner shelf stations has increased and the oxygen saturation values have a wider range than in spring or fall. Summer 1994 exhibits more variability in stability. Correlations of bottom oxygen saturation with stability for stations over the inner shelf show spring and summer values that are negative and significant at the 95% level, but all have $r^2 < 0.5$ (Table 5.3-3). There is little difference in linear fit lines through the stations of 50 m and less; the largest slopes occur during the two summer cruises.

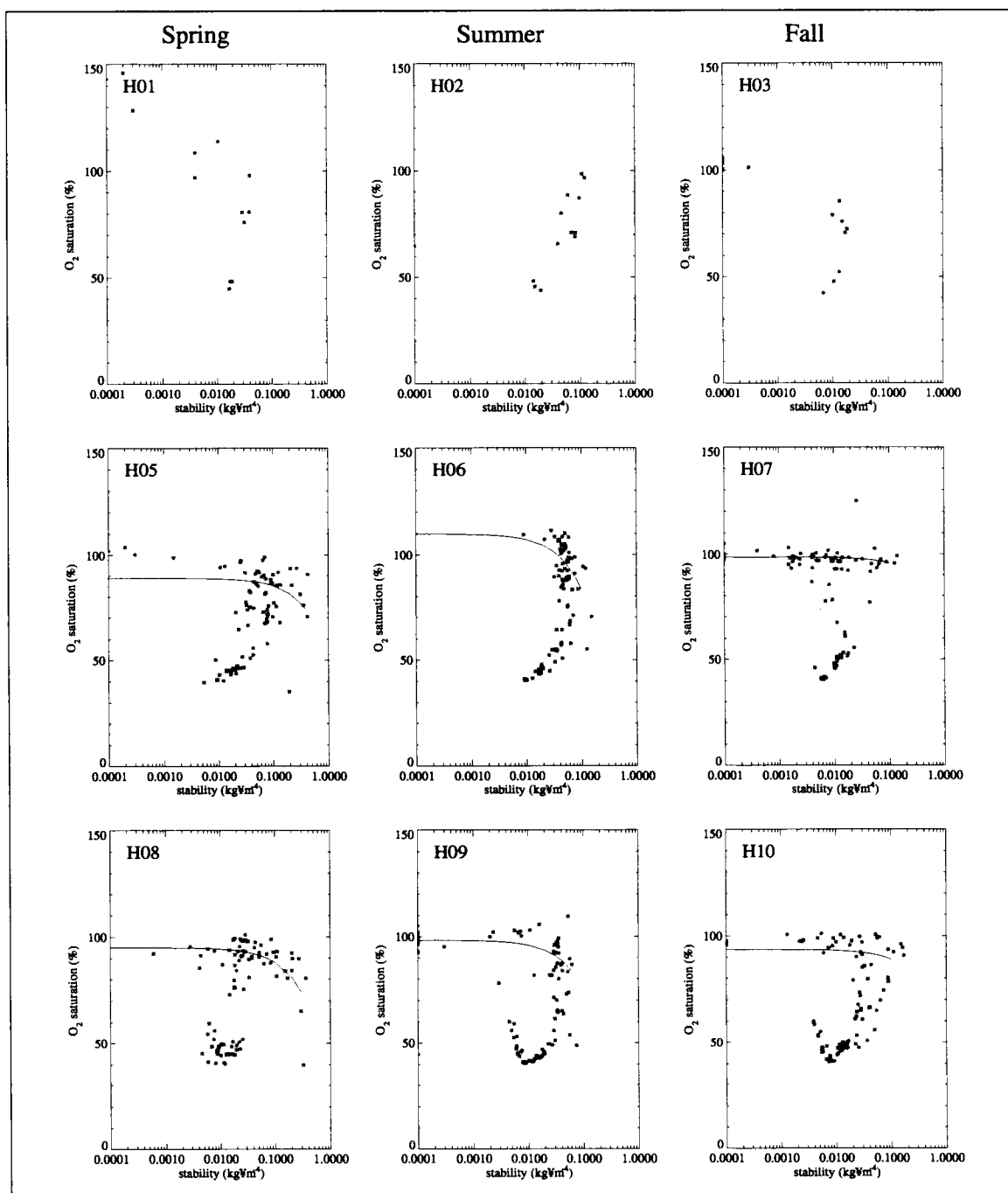


Figure 5.3-18. Bottom dissolved oxygen saturation (percent) versus stability ($\text{kg}\cdot\text{m}^{-4}$) over the shelf to the west of 94°W for the spring, summer, and fall of 1992, 1993, and 1994. A linear fit line is drawn through the stations in water depths of 50 m or less.

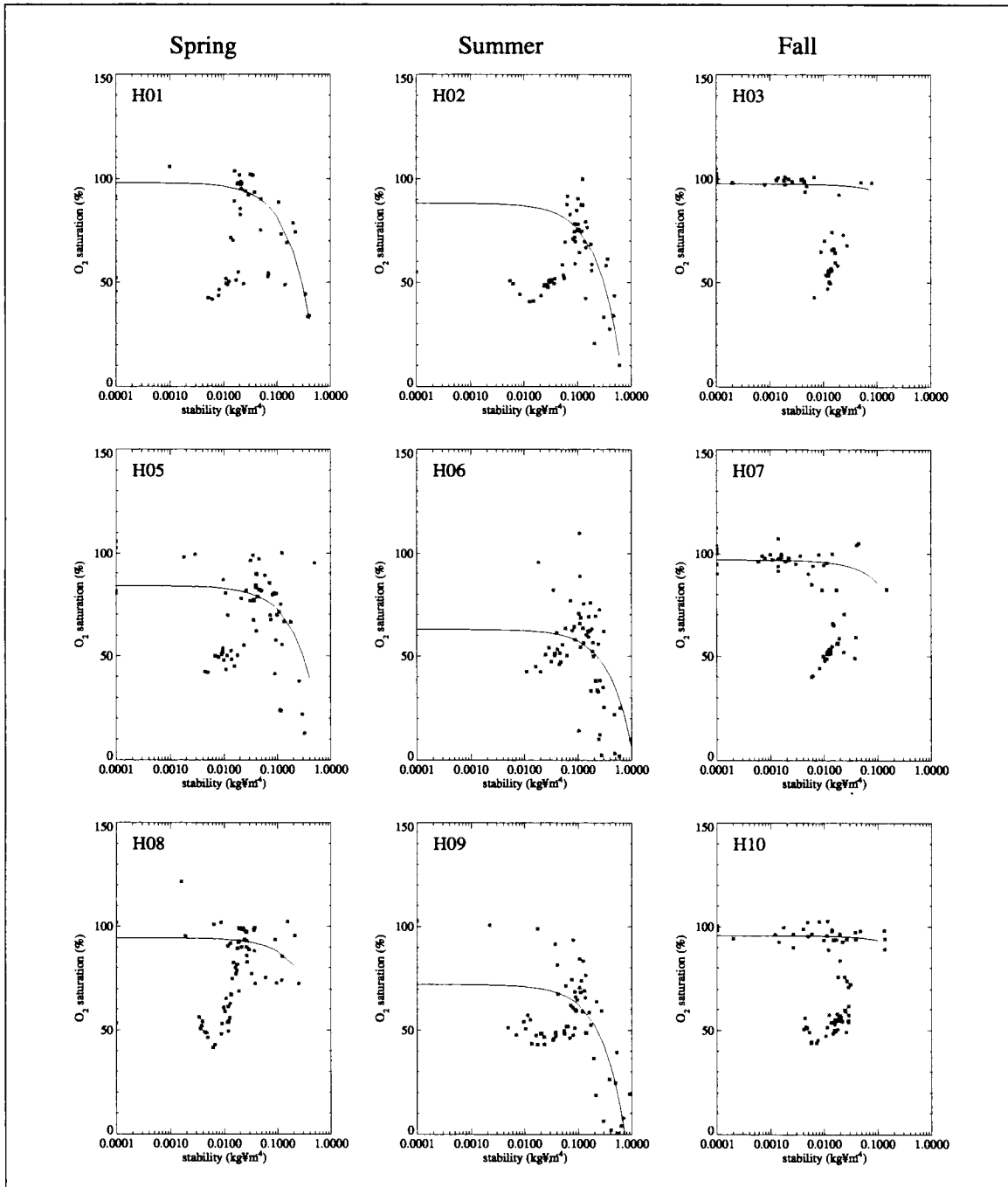


Figure 5.3-19. Bottom dissolved oxygen saturation (percent) versus stability ($\text{kg}\cdot\text{m}^{-4}$) over the east shelf of and including 94°W for the spring, summer, and fall of 1992, 1993, and 1994. A linear fit line is drawn through the stations in water depths of 50 m or less.

Table 5.3-3. Squared correlation coefficients for bottom oxygen saturation with west shelf stability, east shelf stability, and east shelf bottom nitrate.

Cruise	Squared correlation coefficient	Significance level (%)
<i>Bottom oxygen saturation with stability over the western inner shelf</i>		
H05	0.08824	95
H06	0.31260	99.9
H07	0.02473	60
H08	0.37976	99.9
H09	0.21747	99
H10	0.05014	80
<i>Bottom oxygen saturation with stability over the eastern inner shelf</i>		
H01	0.74667	99.9
H02	0.61958	99.9
H03	0.00603	<50
H04	0.58820	99.9
H05	0.18431	98
H06	0.29903	99.5
H07	0.13220	90
H08	0.12198	90
H09	0.60628	99.9
H10	0.02095	50
<i>Bottom oxygen saturation with bottom nitrate over the eastern inner shelf</i>		
H01	0.19202	90
H02	0.11431	90
H03	0.59734	99.9
H04	0.53685	99.9
H05	0.71685	99.9
H06	0.34789	99.9
H07	0.31911	99.9
H08	0.15557	95
H09	0.30355	99.5
H10	0.54317	99.9

Over the eastern shelf, the two regime structure of fall breaks down in spring and summer, although the deeper water regime is maintained in all seasons (Figure 5.3-19). All stations with hypoxia have high stability. The linear fit lines for the inner shelf stations, given on the figure, show that as stability increases, the bottom oxygen saturation values decrease. The smallest slopes for these lines occur in the fall of 1992 and 1994. The slope for fall 1993 was anomalously large and may be related to the large river discharge of that year. The correlations are significant at the 95% level for all cruises with hypoxia and for the winter cruise (Table 5.3-3). All correlations in Table 5.3-3 are negative. The hypoxic stations all are associated with fresh (< 31) surface waters from river runoff. The correlations of bottom oxygen saturation with surface salinity for the inner shelf stations are significant at the 95%

level and are 0.3 or higher for all cruises with hypoxia, except H05, and for the winter cruise. The significant correlations are positive. Because the low oxygen saturation values occur with high stability and low surface salinity, the river discharge contributes to the stratification that results in hypoxic conditions.

There is evidence of an enhanced flux of organic material to the bottom and resulting oxygen depletion from decomposition of that material. Figure 5.3-20 shows the bottom oxygen saturation levels versus the bottom nitrate concentration for the full shelf on the spring, summer, and fall cruises in 1992 (upper panel), 1993 (middle panel), and 1994 (bottom panel). In all seasons, as the station depth increases, bottom nitrate concentrations increase. This is clearly evident in the fall plots. There the lowest, near-zero bottom nitrate values occur at the shallowest stations as shown by the bottom oxygen saturation values of around 100% in the well-mixed waters of fall. At deeper stations, the bottom oxygen saturations decrease to between 40 and 50%; concurrently the bottom nitrate concentrations increase substantially. Note that the bottom nitrate concentrations decrease and the bottom oxygen saturations increase in the waters below 500-m represented by the hook shape at about $30 \mu\text{mol}\cdot\text{l}^{-1}$ nitrate in the 1994 cruises. The fall structure also is present in the spring and summer cruises. In addition, at some shallow stations, there is an enhanced bottom nitrate concentration of 2 to $15 \mu\text{mol}\cdot\text{l}^{-1}$ that corresponds to a decrease in bottom oxygen saturation levels to below 40%. This condition occurs most prevalently in spring 1993 and in all three summers. The enhanced bottom nitrate concentrations occur at the hypoxic and near hypoxic stations. The correlations for cruises H01 and H02 are not significant at the 95% level; the correlations for all other cruises are significant and negative (Table 5.3-3).

Effect of Loop Current eddies on oxygen

During April-May 1993, anticyclonic Loop Current Eddy V_n adjoined the western shelf edge (Section 2.5.1). Associated with the eddy to its west was a cyclonic eddy. Figure 5.3-21 shows the dissolved oxygen profiles along the 200-m isobath at three hydrographic stations from cruise H05. Station 209 was located in the northern periphery of Eddy V_n . Station 205 was in the western side of the cyclone. No Loop Current eddies were located to the east of about 94°W . Station 81, at the eastern shelf edge, was in the far field.

On the shelf, dissolved oxygen concentrations are higher in the upper waters, where oxygen is input by the atmosphere and photosynthesis, than in the deeper waters, where oxygen is consumed. Thus, the dissolved oxygen profiles for all three stations exhibit generally decreasing oxygen concentrations with depth (Figure 5.3-21). The principal difference in the profiles is related to the circulation associated with the cyclone and anticyclone. The cyclonic circulation raised oxygen-poor deeper water upward in the water column, while the anticyclonic circulation pushed oxygen-rich upper water downward. Thus, at a given depth, the waters of the anticyclone generally are higher in dissolved oxygen than those of

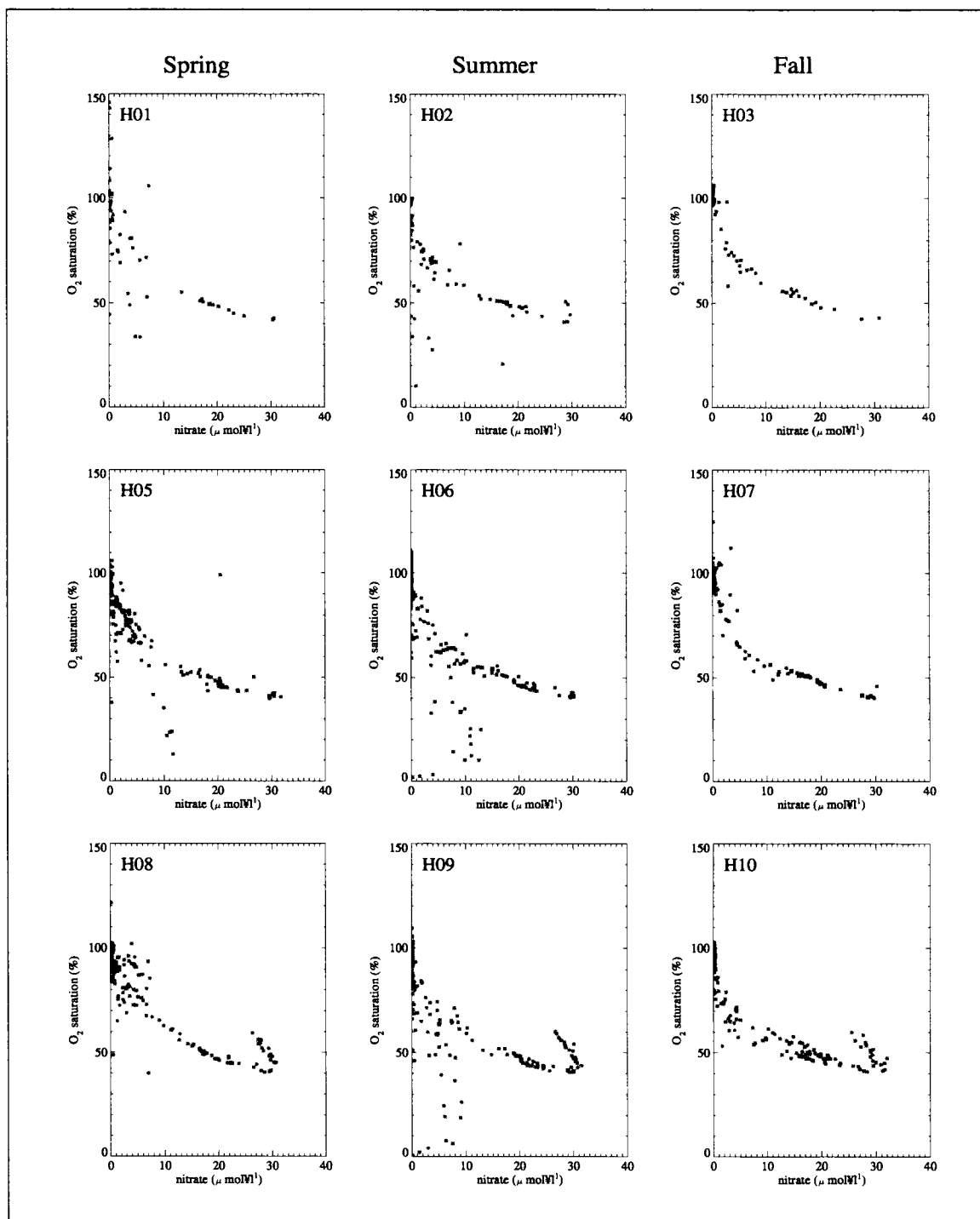


Figure 5.3-20. Bottom dissolved oxygen saturation (percent) versus bottom nitrate ($\mu\text{mol}\cdot\text{l}^{-1}$) over the full shelf sampled for the spring, summer, and fall of 1992, 1993, and 1994.

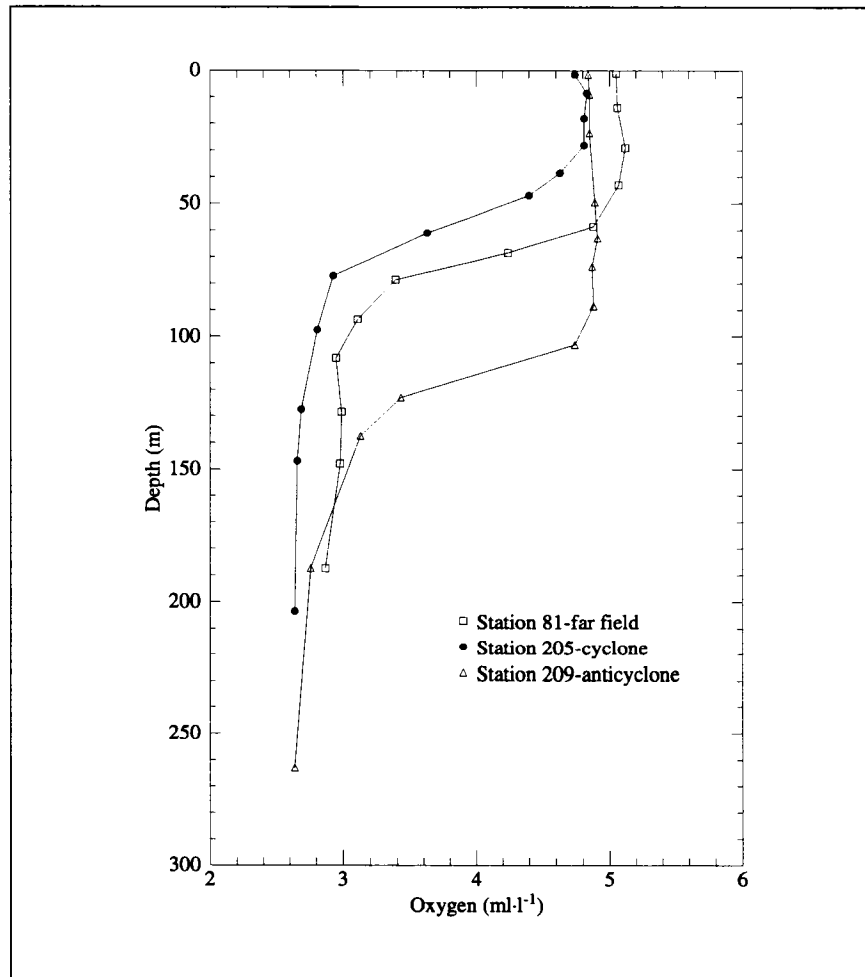


Figure 5.3-21. Dissolved oxygen profiles using bottle data for stations along the 200-m isobath during LATEX A cruise H05.

the cyclone. Below the mixed layer, the dissolved oxygen concentration of the anticyclone is greater at a given depth than that of the far field. Below about 150 m, the profiles of all three stations trend toward similar low values.

The raised and lowered structure of the oxygen isopleths also is seen in Figure 5.3-22, which shows the vertical section of dissolved oxygen along the 200-m isobath from cruise H05. Stations 206 to 212, under the influence of Eddy V_n along its northern periphery, exhibit the deepening oxygen isopleths that are characteristic of anticyclones. The $3.5 \text{ ml}\cdot\text{l}^{-1}$ contour reaches 125 m at stations 207 and 209. Stations 200 to 206 are on the western side of the cyclone; they show the upwelling of the oxygen-poor waters at the

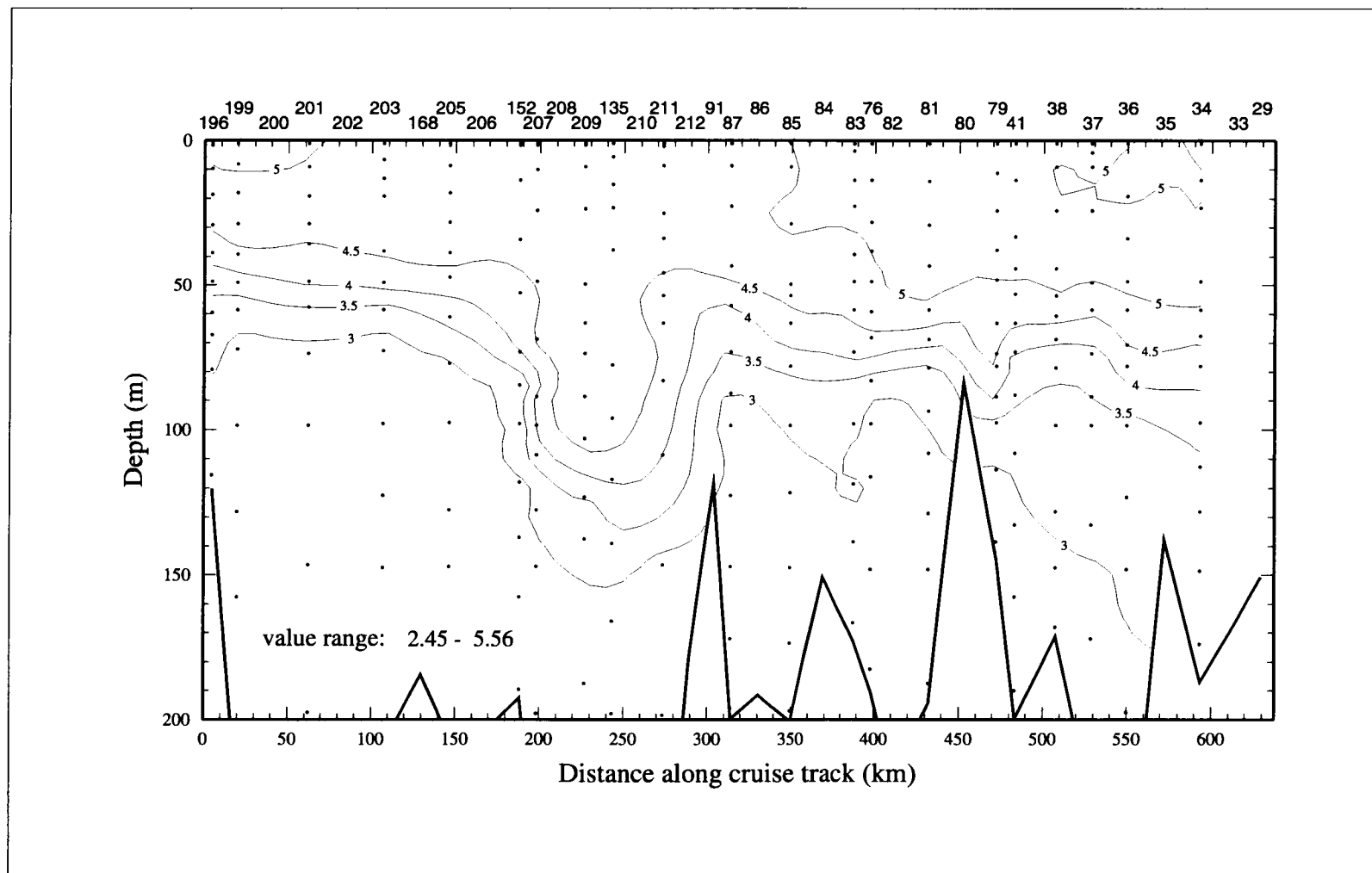


Figure 5.3-22. Dissolved oxygen ($\text{ml}\cdot\text{l}^{-1}$) from bottle data on line 9 along the 200-m isobath on LATEX A cruise H05. Dots indicate sample locations.

50- to 150-m depths; the $3.5 \text{ ml}\cdot\text{l}^{-1}$ isopleth extends upward to approximately 50 m. The far field extends from station 85 to station 33. There the $3.5 \text{ ml}\cdot\text{l}^{-1}$ contour generally is between 85 and 100 m.

5.4 Phytoplankton pigments

Several studies have been undertaken to delineate the factors controlling seasonal fluctuations in chlorophyll-a and phytoplankton biomass in the Mississippi River plume and the northwest Gulf of Mexico (Lohrenz et al. 1990, Sklar and Turner 1981, Thomas and Simmons 1960; El-Sayed et al. 1972; Fucik and El-Sayed 1979). They found seasonal fluctuations in phytoplankton production correlated with flow of the Mississippi-Atchafalaya river system. Before the LATEX A study, synoptic seasonal measurements of chlorophyll-a distributions over the Texas-Louisiana shelf had not been made, and the influence of freshwater input on the distribution of chlorophyll-a over the shelf was unclear.

The Mississippi-Atchafalaya river system provides most of the fresh water entering the Texas-Louisiana shelf (Section 2.3). Large annual differences in Mississippi-Atchafalaya discharge were observed during the LATEX study period. Previous studies correlated high freshwater inflow and high phytoplankton biomass in the plume with high levels of nutrients (Riley 1937; Thomas and Simmons 1960). Seasonal changes in the physical environment affect nutrient and light, critical to phytoplankton growth. Thus, distribution of chlorophyll-a reflects changes in circulation and river discharge.

Phytoplankton pigment data collected during the LATEX A Program were examined along with physical data to recognize seasonal and interannual patterns of chlorophyll-a on the Texas-Louisiana shelf and to identify relevant physical features contributing to the distribution. Interannual differences in chlorophyll-a were determined by comparing seasonal mean chlorophyll-a and the chlorophyll maximum calculated for each transect. Principal component analysis (PCA) of pigments, nutrients, temperature, and salinity was used to separate stations into groups with common characteristics. Accessory pigments helped identify phytoplankton assemblages.

First in this section we briefly describe the methods used to estimate pigment concentrations, the PCA analysis performed on the data, and the four water-typing groups developed from that analysis. The four PCA groups are used to characterize water types found at the sampled locations. The occurrence of chlorophyll-a maxima at the surface is discussed relative to the summer/nonsummer current regimes on the Texas-Louisiana shelf. Finally, we describe chlorophyll-a distributions inferred from the PCA analysis, along with algal class distributions, by season.

Methods and PCA analysis

Data were collected on the ten LATEX A hydrography cruises during the 32-month period from 1992-1994. Details of the cruise tracks, data collection, and sampling methods can be found in Jochens and Nowlin (1994, 1995) and Reap et al. (1996). Phytoplankton pigment analysis was performed in the laboratory at Texas A&M University, following the methods of Bidigare (1991) for high performance liquid chromatography (HPLC) and Smith et al. (1981) for Turner fluorescence. As part of a Master's thesis (Neuhard 1994), accessory pigments were measured by HPLC (Mantoura and Llewellyn 1983) for cruises H01-H05. That information has been incorporated in this study to describe algal class distributions.

PCA analysis. Chlorophyll-a, accessory pigments, nutrients, salinity, and temperature were analyzed together using PCA to delineate patterns among the variables in sea surface and chlorophyll maximum (chl max) data sets for each of the ten hydrographic cruises. Using the MATLAB software package, an eigenanalysis was performed on a normalized correlation matrix containing 18 (cruise H01-H05) or 8 (cruise H06-H10) variables. Variables considered for cruises H01-H05 were chlorophyllide-a, chlorophyll-c, peridinin, 19'-butanoyloxyfucoxanthin (19'-but), fucoxanthin, 19'-hexanoyloxyfuco-xanthin (19'-hex), diadinoxanthin, alloxanthin, zeaxanthin, chlorophyll-b, chlorophyll-a, carotene, silicate, nitrate, nitrite, phosphate, temperature, and salinity. Variables for cruises H06-H10 were chlorophyll-a, phaeopigments, silicate, nitrate, nitrite, phosphate, temperature and salinity. PCA analyses were performed separately on data from the surface and chlorophyll maximum for every cruise.

Principal component scores were produced for each variable. Eigenvectors provided weights for each variable; eigenvalues indicated percent standardized variance for each principal component. PCA is most useful if a large proportion of the variance is explained by two or three principal component axes (Pielou 1984). The first two principal component axes, PC1 and PC2, accounted for 56-80% of the variance in the data for both the surface and the chlorophyll maximum (Table 5.4-1). PC1 essentially separated the high and low chlorophyll-a groups; PC2 refined those two groups by considering the relationships among accessory pigments, nutrients, and temperature.

Sampled stations fell into four groups based on the relationships of variables extracted from the PCA analysis. Stations falling close to the origin of the PCA axes were not included in a group. Characteristics were assigned to each group based on the most heavily weighted variables (Table 5.4-2). Between one and five variables carried high or nearly equal weights in each PCA analysis. Groups were projected on station maps for each cruise. The four groups (I-IV) will be used in discussion of results.

Table 5.4-1. Percent variance accounted for by the first and second principal components for the chlorophyll maximum (chl max) and the sea surface for cruises H01-H10.

Cruise	PC1	Chl max PC2	PC1+PC2	PC1	Surface PC2	PC1+PC2
H01	46.8	13.7	60.5	43.5	12.8	56.3
H02	44.4	15.9	60.3	49.2	8.9	58.1
H03	54.0	10.7	64.7	55.3	12.4	67.7
H04	55.4	11.8	71.2	55.0	14.8	69.8
H05	38.0	18.9	56.9	43.6	15.0	58.6
H06	50.3	18.9	69.2	64.2	19.8	84.0
H07	52.9	18.0	70.9	62.2	14.8	77.0
H08	51.2	17.5	68.7	58.4	14.2	72.6
H09	50.3	18.9	69.2	58.0	16.8	74.8
H10	45.1	17.3	62.4	67.4	12.6	80.0

Table 5.4-2. Characteristics of PCA groups I, II, III, and IV for cruises H01-H10. The listed characteristics were common to each group on every cruise of that season. Accessory pigments were analyzed for cruises H01 through H05; where delineation of PCA groups could be further refined by that data, it is included by cruise.

Season	PCA Group	Characteristics
Spring	I and IV	salinity; low nutrients H01: 19'-hex, zeaxanthin H05: 19'-hex, 19'-but, zeaxanthin, chlorophyll-b, chlorophyllide
	II and III	chlorophyll-a, nutrients, peridinin, alloxanthin H01: chlorophylls -b and -c, 19'-but, fucoxanthin, carotene, chlorophyllide H05: chlorophylls -b and -c, alloxanthin, carotene
Summer	I and IV	salinity; low nutrients, temperature H02: 19'-but, 19'-hex
	II and III	chlorophyll-a, nutrients, zeaxanthin, chlorophyllide, diadinoxanthin, peridinin, alloxanthin, chlorophyll-b H02: 19'-hex, 19'-but, fucoxanthin, carotene
Fall	I and IV	salinity, temperature, zeaxanthin, 19'-but, 19'-hex
	II and III	chlorophylls -a, -b, and -c; nutrients, diadinoxanthin, fucoxanthin, alloxanthin, carotene H03: peridinin
Winter	I and IV	temperature, salinity, 19'-hex, 19'-but, zeaxanthin
	II and III	chlorophylls -a, -b, and -c, nutrients, peridinin, alloxanthin, fucoxanthin, diadinoxanthin, chlorophyllide

Lower salinity and higher nutrients separated the high chlorophyll-a groups (II and III) from the low (I and IV). Groups II and III fell mainly on the inner shelf, with the widest distribution occurring during periods of high river flow. Low chlorophyll-a groups (I and IV), were mainly found on the middle and outer shelf. High chlorophyll-a waters were usually grouped with high nutrient values in the first principal component. This relationship is attributed to the supply of nutrient-rich waters from the Mississippi-Atchafalaya system. Temperature patterns varied by season.

The PCA station separations revealed patterns among cruises. The first principal axis always separated chlorophyll-rich inner shelf water (water depths < 50 m) from chlorophyll-poor (relative to the inner shelf) outer shelf water (depths between 50 and 200 m). Salinity was also characterized by the first principal axis; chlorophyll-rich water was generally low in salinity. The second principal component axis defined nutrient and temperature characteristics. The temperature variable was seasonal and bore no relationship to the distribution of chlorophyll-a.

Chlorophyll-a maximum at the surface

Not every station on the hydrographic cruises was sampled for pigments. For those that were, chlorophyll-a concentrations were assessed for the surface and for the level in the water column that registered the chlorophyll maximum. Sometimes the chlorophyll maximum occurred at the surface. This was more likely to happen over the eastern shelf than the western. Table 5.4-3 shows the percentage of stations where chlorophyll maxima were found at the surface by line, by whole cruise, and by shelf region (east and west of 94°W). Table 5.4-4 lists the concentrations of chlorophyll-a at the chlorophyll maximum for each line by cruise.

Tables 5.4-3 and 5.4-4 support the conclusion of earlier investigators that phytoplankton productivity is controlled by river discharge. Proximity to the largest source of river water on the shelf is the most important factor controlling the primary productivity of a given location on the Texas-Louisiana shelf. In the spring, cross-shelf lines 1 through 4 registered chlorophyll maxima at the surface during every cruise; 75% of the stations sampled for pigments on line 1 during cruise H05 were so classified. River discharge generally decreases during summer, and this was reflected in fewer stations with chlorophyll maxima at surface, although, again, lines 1 and 2, being closer to the river outflow, showed higher percentages in this regard than do other lines. There being almost no maxima at the surface over the western shelf in summer can be explained by the upcoast current regime along the Texas coast, which prevents the nutrient-rich, fresh water from flowing into the region. With the return to downcoast flow in the fall, the number of maxima-at-surface stations increased over the western shelf, but still never approached the number in the east. Percentages for the lone winter cruise, H04, were highest of all the cruises over the eastern shelf, a reflection of

Table 5.4-3. Number and percentage of chlorophyll maxima (cmax) observed at the surface and the number of stations per line at which pigments samples were taken, with averages for cruises and eastern and western shelves.

line	1992			1993			1994		
	cmax @ sfc	# stn	% cmax @ sfc	cmax @ sfc	# stn	% cmax @ sfc	cmax @ sfc	# stn	% cmax @ sfc
<i>Winter</i>									
					H04				
1				4	4	100.0			
2				5	8	62.5			
3				5	11	45.5			
4				6	20	30.0			
eastern shelf average						46.5			
<i>Spring</i>									
		H01			H05			H08	
1	6	12	50.0	6	8	75.0	2	15	13.3
2	2	15	13.3	3	8	37.5	3	18	16.7
3	1	17	5.9	1	9	11.1	3	20	15.0
4	6	20	30.0	1	11	9.1	5	23	21.7
11				2	6	33.3	1	11	9.1
5				0	6	0.0	3	14	21.4
6				0	5	0.0	1	12	8.3
7				1	4	25.0	3	13	23.1
8				0	4	0.0	4	11	36.4
cruise average		23.4			23.0			18.2	
eastern shelf average			23.4			30.6			17.1
western shelf average						12.0			19.7
<i>Summer</i>									
		H02			H06			H09	
1	0	12	0.0	8	11	72.7	8	15	53.3
2	2	15	13.3	2	16	12.5	1	18	5.6
3	0	21	0.0	2	18	11.1	1	20	5.0
4	2	20	10.0	0	20	0.0	3	23	13.0
5				0	12	0.0	0	12	0.0
6				0	10	0.0	1	11	9.1
7				0	9	0.0	0	12	0.0
8				0	8	0.0	0	10	0.0
cruise average		5.8			10.3			12.1	
eastern shelf average			5.8			18.5			17.1
western shelf average						0.0			5.4
<i>Fall</i>									
		H03			H07			H10	
1	4	12	33.3	3	11	27.3	6	15	40.0
2	4	15	26.7	5	16	31.3	3	18	16.7
3	1	10	10.0	3	18	16.7	5	20	25.0
4	3	19	15.8	6	20	30.0	4	23	17.4
11				2	10	20.0	1	11	9.1
5				0	12	0.0	0	14	0.0
6				3	10	30.0	0	12	0.0
7				2	9	22.2	2	13	15.4
8				1	7	14.3	1	11	9.1
cruise average		21.4			22.1			16.1	
eastern shelf average			21.4			26.2			23.7
western shelf average						16.7			6.6

Table 5.4-4. Mean chlorophyll-a ($\text{ng}\cdot\text{l}^{-1}$) calculated at the chlorophyll maximum by cross-shelf transect line by cruise. Lines are listed from east (1) to west (8); see Figures 1.2-2, 1.2-3, and 1.2-4 for cruise tracks. Averages for the eastern and western shelves are given. Chlorophyll-a data for line 1, cruise H04, were only available from the inner shelf; no low chlorophyll-a waters were included, thus the extremely high mean value.

Line	H01	H02	H03	H04	H05	H06	H07	H08	H09	H10
1	2126	1086	818	16514	3935	1273	2699	1278	1470	615
2	1188	914	1032	9153	1665	970	1437	2484	1315	714
3	855	891	757	2613	949	951	1733	1308	1309	1108
4	2162	1178	1083	2680	1557	921	1963	1603	1116	866
11					1804	285	1849	810	1507	1156
5					924	644	399	851	811	727
6					796	745	1688	1026	1021	651
7					1052	686	1468	742	757	637
8					638	813	1124	1118	716	653
avg east	1586	1017	923	7740	2026	1029	1958	1668	1302	825
avg west					903	627	973	910	963	765

remarkable productivity following above average river discharge in the months prior to the cruise.

Chlorophyll-a and accessory pigment distributions by season

Omitting the lone winter cruise (H04), ranking values of average chlorophyll-a at the chlorophyll maximum by cruise (Table 5.4-5) shows that chlorophyll production was highest on the eastern shelf in spring. Of exceptional note was the fall 1993 cruise (H07), which showed the second highest average chlorophyll maximum of all the cruises over the eastern shelf. The three summer cruises also grouped together by their chlorophyll maxima. The remaining two fall cruises, H06 and H10, showed the lowest chlorophyll numbers. For the western shelf, a pattern is less discernible. Of the six cruises that covered the western shelf, the two spring cruises in 1993 and 1994 rank in the middle, with summer 1993 and fall 1994 on the low side, and summer 1994 and fall 1993 on the high.

In addition to chlorophyll-a, a number of accessory marker pigments were chosen as PCA variables for cruises H01-H05. Delineations of algal class distribution were made between areas of high and low chlorophyll-a using accessory pigment data. The division of inner shelf waters from outer shelf waters by the first principal component axis separated algal classes into inner and outer shelf groups.

Table 5.4-5. Mean chlorophyll (ng·l⁻¹) at the chlorophyll maximum ranked by cruise for the eastern and western shelves. Winter cruise H04 is not considered.

Eastern Shelf			Western Shelf	
Rank	Mean chl	Cruise	Rank	Mean chl
4	1583	H01 Spr 92		
7	1017	H02 Sum 92		
8	923	H03 Fall 92		
1	2026	H05 Spr 93	4	903
6	1029	H06 Sum 93	6	627
2	1958	H07 Fall 93	1	973
3	1668	H08 Spr 94	3	910
5	1302	H09 Sum 94	2	963
9	825	H10 Fall 94	5	765

Fucoxanthin, in diatoms, dominated high chlorophyll-a waters across the shelf in all seasons. Alloxanthin was found mainly on the inner shelf where chlorophyll-a levels were high. Peridinin, found exclusively in dinoflagellates, followed a pattern similar to alloxanthin. 19'-hex was generally higher on the middle and outer shelf in low chlorophyll-a water. 19'-but increased towards the outer shelf on all transects, similar in distribution to 19'-hex. Levels of zeaxanthin and chlorophyll-b were variable across the shelf and no clear distribution existed for these pigments.

Spring distributions. High chlorophyll-a waters were found near the coast the whole length of the shelf where the nonsummer downcoast transport of low salinity water occurred (Figure 5.4-1). Stations characterized by PCA groups II and III (high chlorophyll-a, low salinity, high nutrients) were restricted to the inner and middle shelf (Figure 5.4-2). Groups I and IV were distinguished by low chlorophyll-a, high salinity, and low nutrients. These groups covered the middle and outer shelf stations where surface salinity was above 32. This pattern was especially clear during cruise H08.

The spring cruises all had high mean chlorophyll-a at the chlorophyll maximum (Table 5.4-4). Surface chlorophyll maxima were observed in low salinity surface water on the eastern shelf and near major riverine sources (Table 5.4-5). Interannual variability of average chlorophyll-a appeared to be related to the amount of fresh water on the shelf. High river flow from the Mississippi-Atchafalaya resulted in elevated mean chlorophyll-a in spring cruises H05 and H08. Both H05 and H08 surveyed the shelf during periods of above average river flow compared to the 64-year mean (Figure 2.3-1). Fresh water extended farthest from shore, and mean chlorophyll-a levels were highest of the spring cruises, during cruise H05. Mean chlorophyll-a for H01 was lowest among the three cruises, probably because average

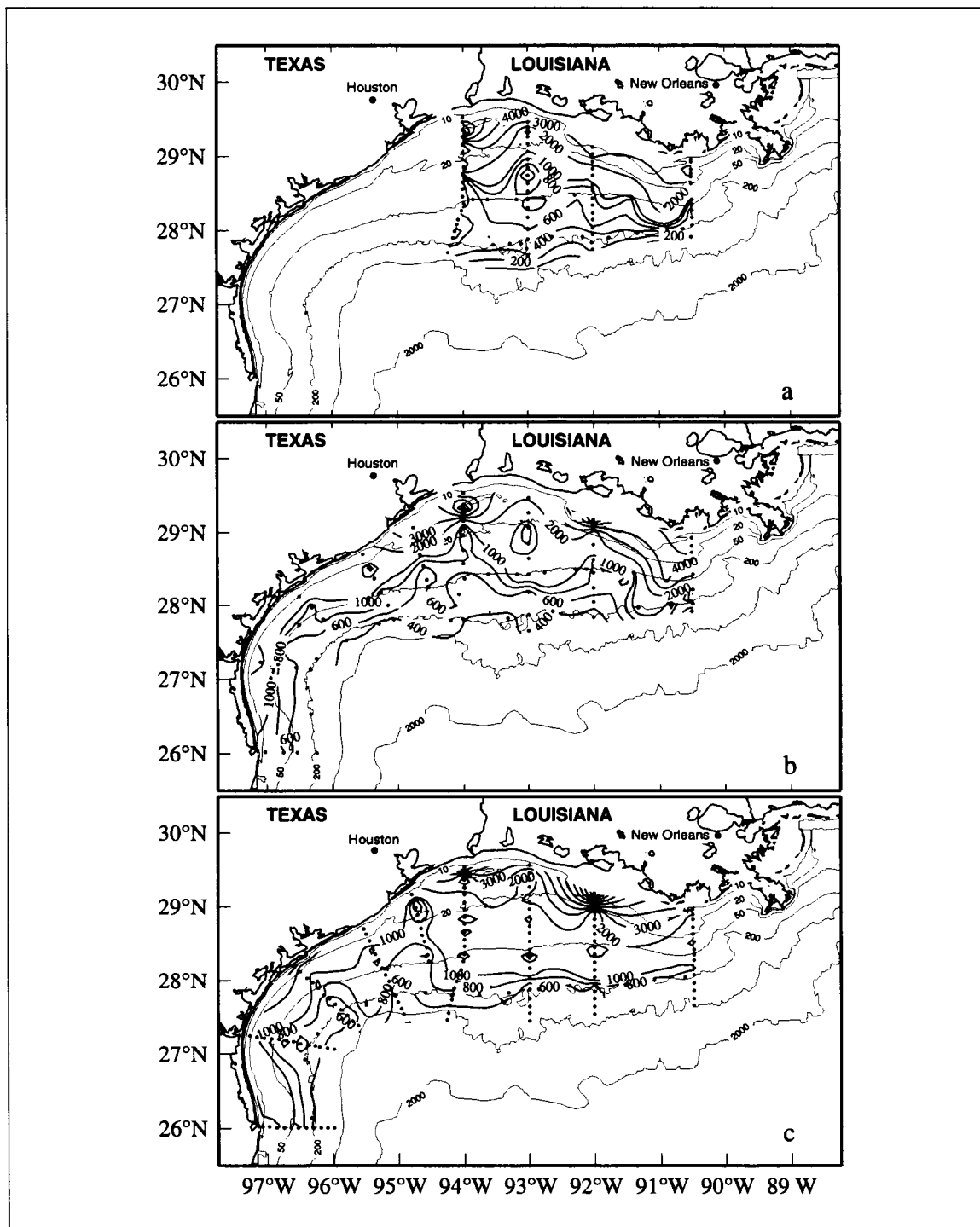


Figure 5.4-1. Spring distributions of chlorophyll maximum (ng·l⁻¹) for LATEX A hydrographic cruises (a) H01 in May 1992, (b) H05 in May 1993, and (c) H08 in May 1994.

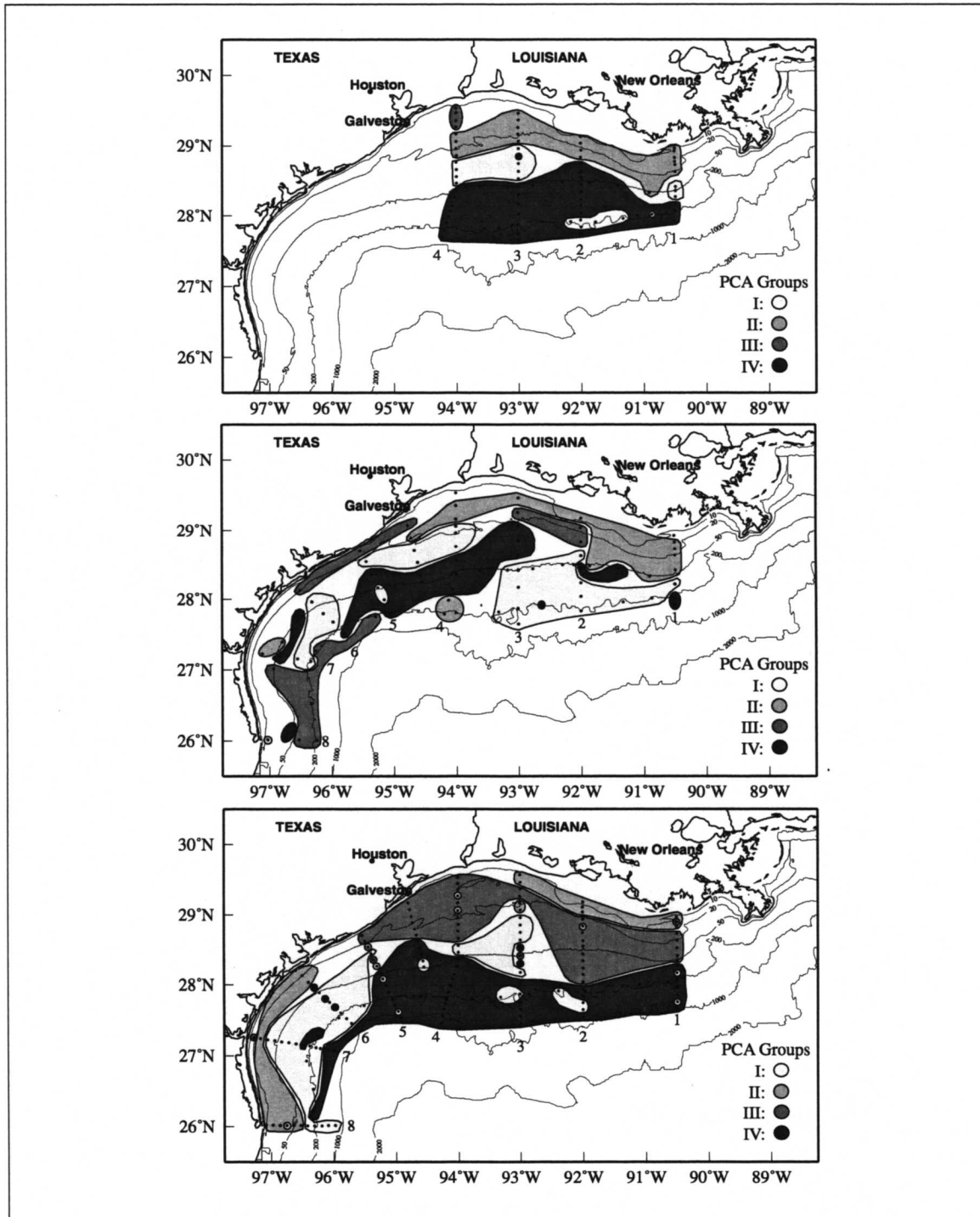


Figure 5.4-2. Principal component groups for the chlorophyll maximum (top) H01, 1-8 May 1992; (middle) H05, 26 April-11 May 1993; and (bottom) H08, 24 April-7 May 1994.

daily river discharge during cruise H01 was slightly below average, and the months before the cruise were near or slightly below the 64-year mean.

Accessory pigments and algal classes. Accessory pigments for cruises H01 and H05 were divided by the first PCA axis into inner and outer shelf groups. Pigments in diatoms, dinoflagellates, and cryptophytes dominated the low salinity, high chlorophyll-a groups II and III in spring on the inner shelf. Pigments that mark prymnesiophytes, chrysophytes, and cyanobacteria were the main constituents of low chlorophyll-a waters in groups I and IV at both the surface and the chlorophyll maximum. Chlorophyll-b (characteristic of green algae) appeared in surface groups II and III and in groups I and IV in the chlorophyll maximum. In the low chlorophyll, high salinity waters on both cruises H01 and H05, chlorophyll-b concentrations were higher at the chlorophyll maximum. Bontempi (1995) substantiated by cell counts the algal class distributions at the surface and chlorophyll maximum over the eastern shelf during cruises H01 and H05.

Summer distributions. Summertime chlorophyll-a patterns typified by the four PCA groups differed dramatically from spring as a result of the seasonal decrease in Mississippi-Atchafalaya discharge and the change to the summer upcoast current regime (Figures 5.4-3 and 5.4-4). Chlorophyll maxima occurred less frequently at the surface, and high chlorophyll-a groups were found mainly on the Louisiana shelf in low surface salinity water. The summertime surface patterns of the PCA groups show most clearly the effect low-frequency circulation on chlorophyll distribution. Most western shelf stations were characterized by the low chlorophyll-a groups I and IV. High chlorophyll-a groups II and III were restricted mainly to the inner and middle Louisiana shelf.

The magnitude of river flow affected chlorophyll-a distribution. High chlorophyll-a waters (groups II and III) covered the greatest area of the three summer cruises during cruise H06 (Figures 5.4-3 and 5.4-4) corresponding to high river output. Even outer shelf stations of easternmost line 1, where the chlorophyll maximum were at the surface (Table 5.4-4) fell into group II. The areal extent of high chlorophyll-a during cruise H06 probably resulted from the large amount of fresh surface water extending over the shelf. High mean chlorophyll-a levels, however, were not realized on cruise H06 (Table 5.4-5) despite the extent of fresh water. Summer temperatures were warmest during H06, and, combined with large volumes of low salinity water held on the shelf, conditions were right for a stable water column, thus slowing the mixing of nutrients between layers and resulting in a lower mean chlorophyll-a compared to other summer cruises.

During cruise H06, stations in group III (high chlorophyll-a) were found in the chlorophyll maximum near the 50-m isobath on most of the Texas-Louisiana shelf (Figure 5.4-3). Vertical sections of salinity prepared for cruise H06 (Figure 3.1-8) do not support the group III identification of those waters, particularly on the western shelf. This conflict is unresolved.

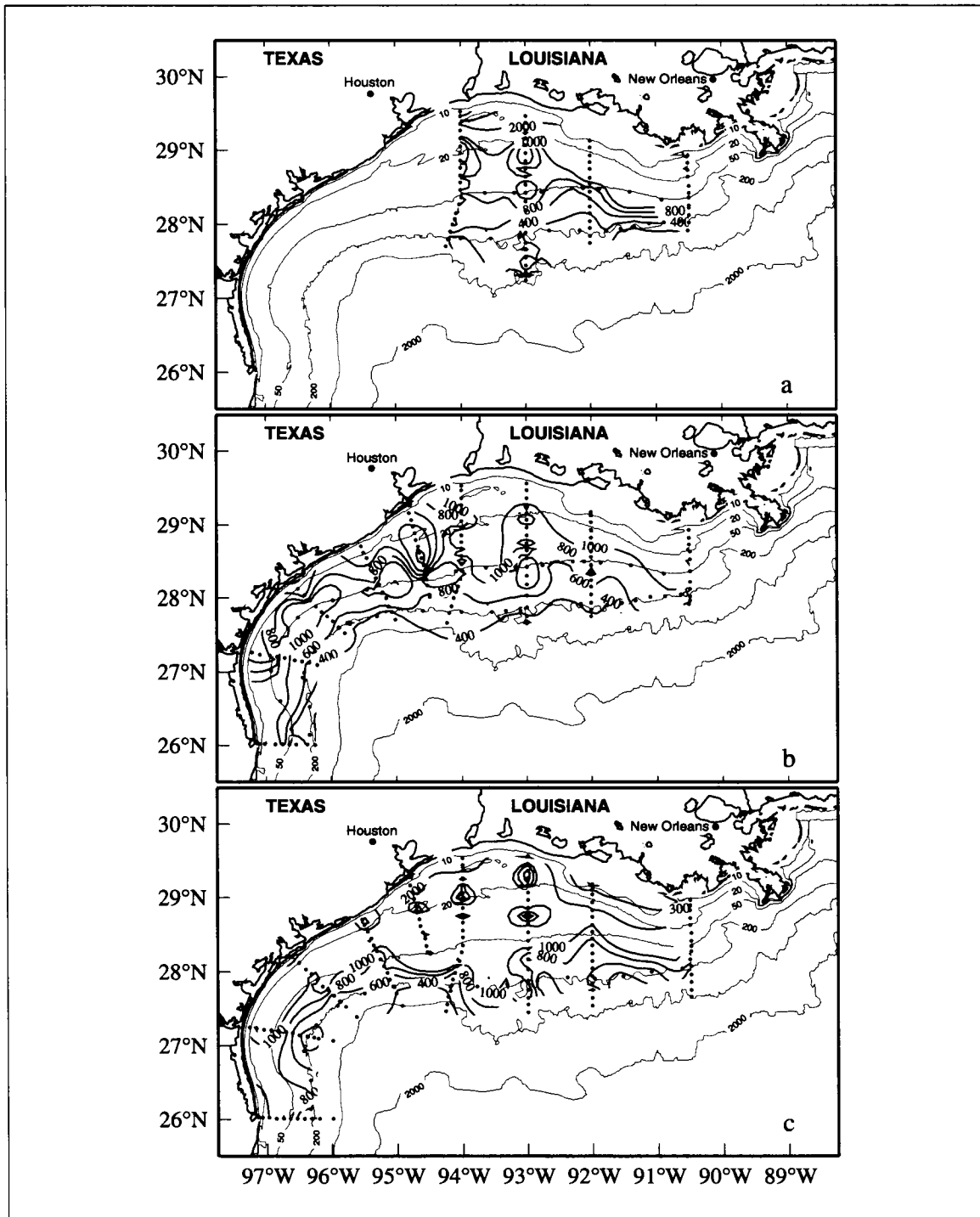


Figure 5.4-3. Summer distributions of chlorophyll maximum (ng·l⁻¹) for LATEX A hydrographic cruises (a) H02 in August 1992, (b) H06 in August 1993, and (c) H09 in August 1994.

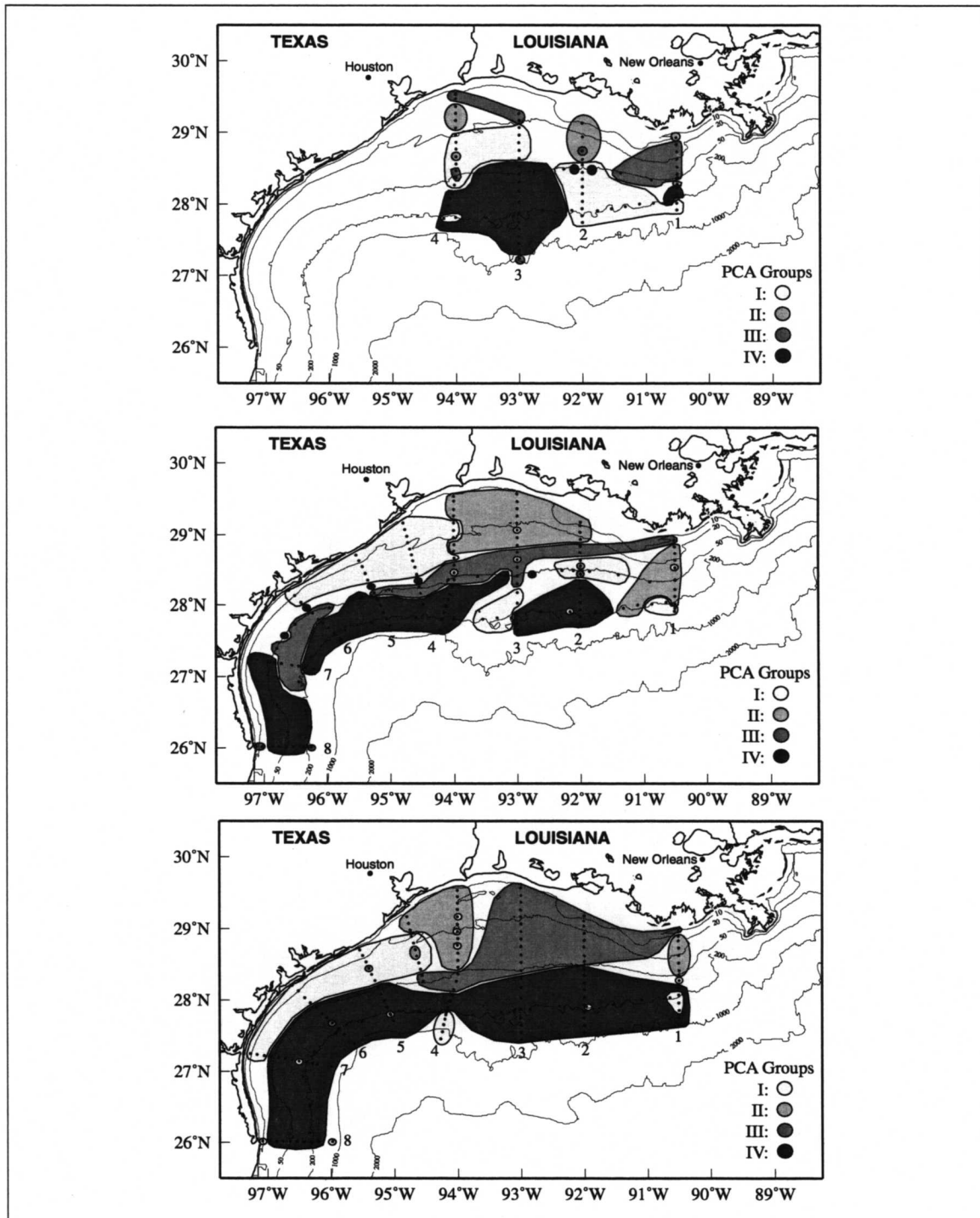


Figure 5.4-4. Principal component groups for the chlorophyll maximum (top) H02, 1-8 August 1992; (middle) H06, 26 July-7 August 1993; and (bottom) H09, 27 July-7 August 1994.

In contrast to H06 and H09, surface salinity was not low (salinity was ≥ 35) on the western Louisiana shelf during cruise H02. Chlorophyll-rich groups II and III were confined to the inner eastern shelf. Cruise H02 supported the lowest mean chlorophyll-a over the eastern shelf of the three summer cruises, and a surface chlorophyll maximum rarely occurred (Tables 5.4-4 and 5.4-5). As in spring, highest average chlorophyll maximum chlorophyll-a in summer was observed during above average river flow. Cruise H02 took place during an average river flow period and was not preceded by high river flow.

Accessory pigments and algal classes. Marker pigments of prymnesiophytes, chrysophytes, green algae, and cyanobacteria were found group III-type waters in the surface. This grouping indicated that more prymnesiophytes, chrysophytes, green algae, and cyanobacteria were present in summer in the high chlorophyll-a surface waters than in spring. In the chlorophyll maximum, 19'-but and 19'-hex (prymnesiophytes and chrysophytes) were grouped in the high salinity outer shelf water, as expected. These marker pigments increased in the chlorophyll maximum on the outer shelf during all seasons. Summertime zeaxanthin levels were higher on the inner shelf, indicating the presence of cyanobacteria and/or prochlorophytes.

The combined effect of low summer Mississippi River flow and upcoast currents was reflected by a shift in the inner shelf surface phytoplankton population—the summer surface inner shelf was characterized by greater levels of pigments from prymnesiophytes, chrysophytes, cyanobacteria and green algae than were found in spring or fall.

Fall distributions. The return to downcoast circulation carried low salinity, chlorophyll-rich water along the inner shelf (Figure 5.4-5) and chlorophyll contours reflect this return to springlike circulation. High chlorophyll groups II and III were located in low salinity water found shoreward in a narrow band characteristic of the nonsummer circulation (Figure 5.4-6). Low chlorophyll groups I and IV were located on the middle and outer shelf during the three fall cruises. These waters were characterized by low nutrients, warmer temperatures, and high salinity. Group I covered the outer western shelf where there were the lowest chlorophyll-a and most saline waters. Warmer temperatures and low nutrients characterized group IV on the eastern shelf.

Group III covered a large portion of the Louisiana shelf in the chlorophyll maximum of cruise H10 (Figure 5.4-6). Group II waters extended onto the outer Louisiana shelf (line 3), unusual compared to other cruises. Characterized by higher nutrients and cooler temperatures, the chlorophyll maximum at stations in group II was as much as 20 m shallower than of surrounding stations (lines 2 and 4). The chlorophyll maximum at stations in group II were found at the interface between 35 and 36 salinity waters. No surface water with salinity of 35 was found on any other transect on outer stations of the Louisiana shelf (lines 1-4). It is possible that a Loop Current eddy created upwelling conditions, resulting in increased

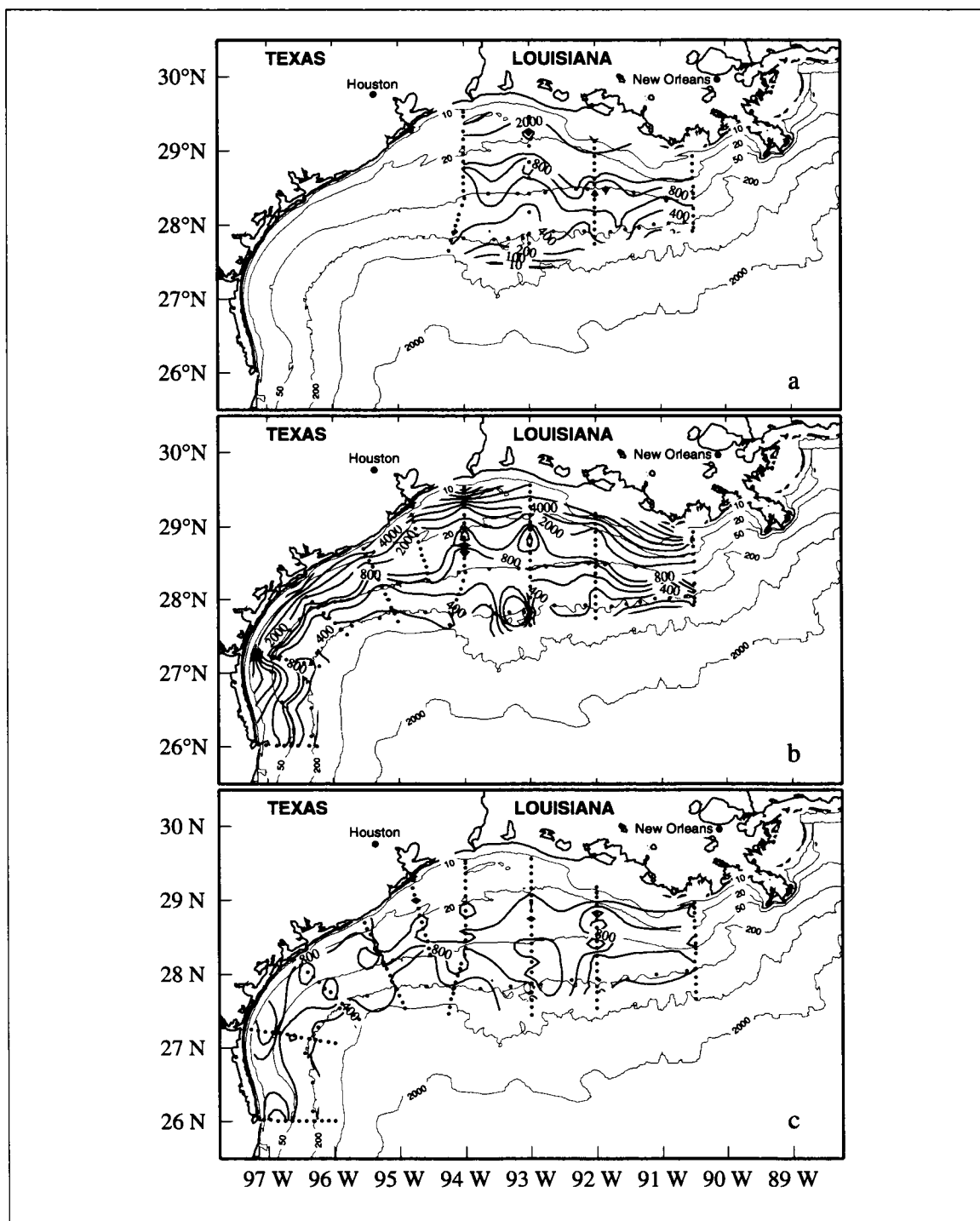


Figure 5.4-5. Fall distributions of chlorophyll maximum (ng·l⁻¹) for LATEX A hydrographic cruises (a) H03 in November 1992, (b) H07 in November 1993, and (c) H10 in November 1994.

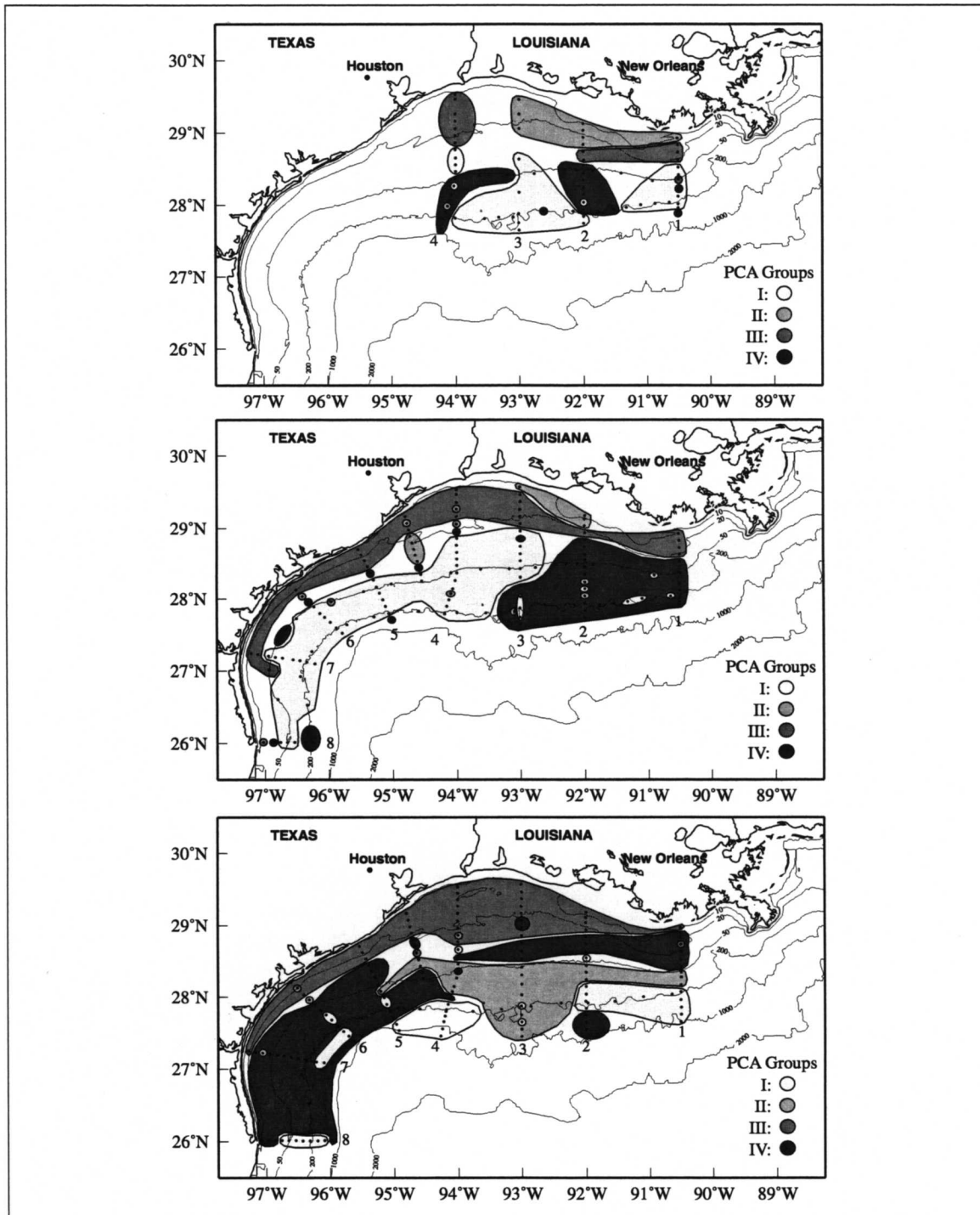


Figure 5.4-6. Principal component groups for the chlorophyll maximum of cruise (top) H03, 5-13 November 1993; (middle) H07, 7-21 November 1993; and (bottom) H10, 2-13 November 1994.

chlorophyll-a in the chlorophyll maximum; increased chlorophyll-a was not observed in the surface here.

Very high mean chlorophyll-a measurements were recorded during cruise H07. Higher (relative to summer) inner shelf chlorophyll-a on the Texas shelf reflected a return to downcoast circulation. Cruise H07 followed three record high seasons of freshwater discharge on the eastern shelf. Some of the highest levels of chlorophyll-a of the ten cruises were observed at the innermost stations during H07 (Tables 5.4-3, 5.4-4, and 5.4-5). Surface chlorophyll maxima were observed in low salinity water on both eastern and western shelves during cruise H07.

Accessory pigments and algal classes. Shelfwide algal class distributions were comparable between spring and fall. Spring and fall have similar circulation patterns; river flow characteristics differed widely, however. Highest average river flow occurs in spring and lowest in fall. Fall pigment data (cruise H03) were collected during an average river flow year, and fucoxanthin (prymnesiophytes and chrysophytes) and chlorophyll-a levels were all much lower compared to spring. The patterns in algal class distribution were similar to spring.

Diatoms, cryptophytes, dinoflagellates, and green algae were represented by their respective marker pigments in group II- and III-type waters. Pigments for prymnesiophytes, chrysophytes, and cyanobacteria were found in low chlorophyll-a waters with groups I and IV in both the surface and the chlorophyll maximum, located on the outer and middle shelf.

Winter distribution. The chlorophyll maximum distribution for cruise H04 is shown in Figure 5.4-7. This was the only winter cruise conducted during the 32-month LATEX study, so interannual comparisons are not possible. This cruise took place near the beginning of a long period of above average river flow. PCA group patterns were as expected (Figure 5.4-8). Groups II and III were seen in inner shelf, low salinity, high chlorophyll-a water, characterized by higher nutrients. Mean chlorophyll-a levels were dramatically higher, however, than any of the spring, summer, or fall cruises. Chlorophyll maxima at the surface were prevalent (Table 5.4-4); along line 1, every station sampled for pigments showed the maximum at the surface. The very high mean chlorophyll-a observed during cruise H04 was likely the result of unusually heavy winter runoff.

Accessory pigments and algal classes. High chlorophyll-a groups II and III were characterized by pigments typical of spring and fall. Diatoms, dinoflagellates, cryptophytes and green algae were significant in concentration in the high chlorophyll-a waters of the inner shelf. Marker pigments for prymnesiophytes, chrysophytes, and cyanobacteria were found in low chlorophyll-a waters in groups I and IV in both the surface and the chlorophyll maximum during this cruise. These algal class distributions became interesting when examining inner shelf pigment concentrations.

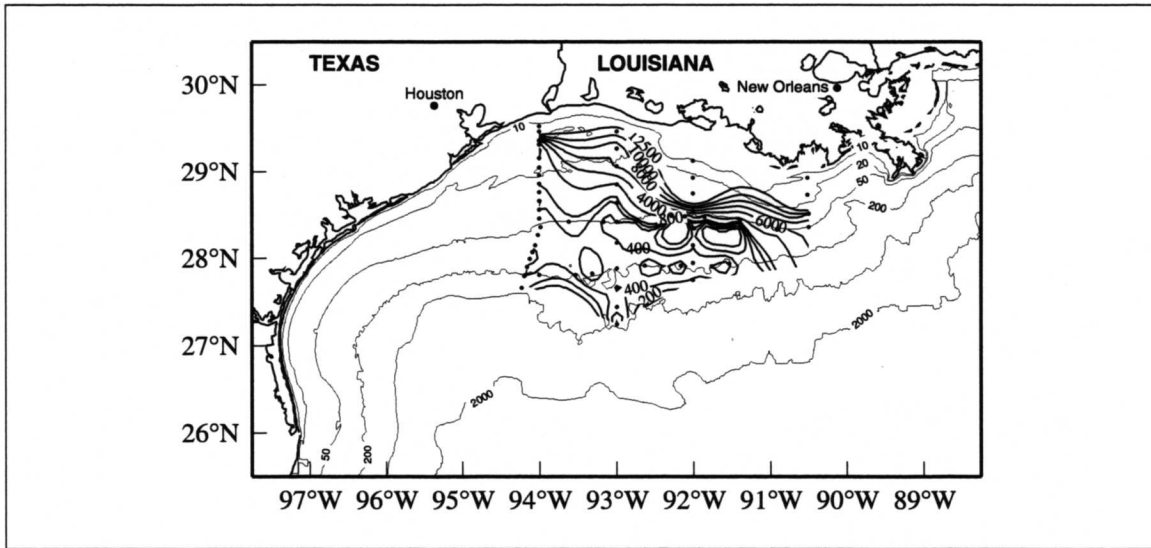


Figure 5.4-7. Winter distributions of chlorophyll maximum ($\text{ng}\cdot\text{l}^{-1}$) for LATEX A hydrographic cruise H04 in February 1993.

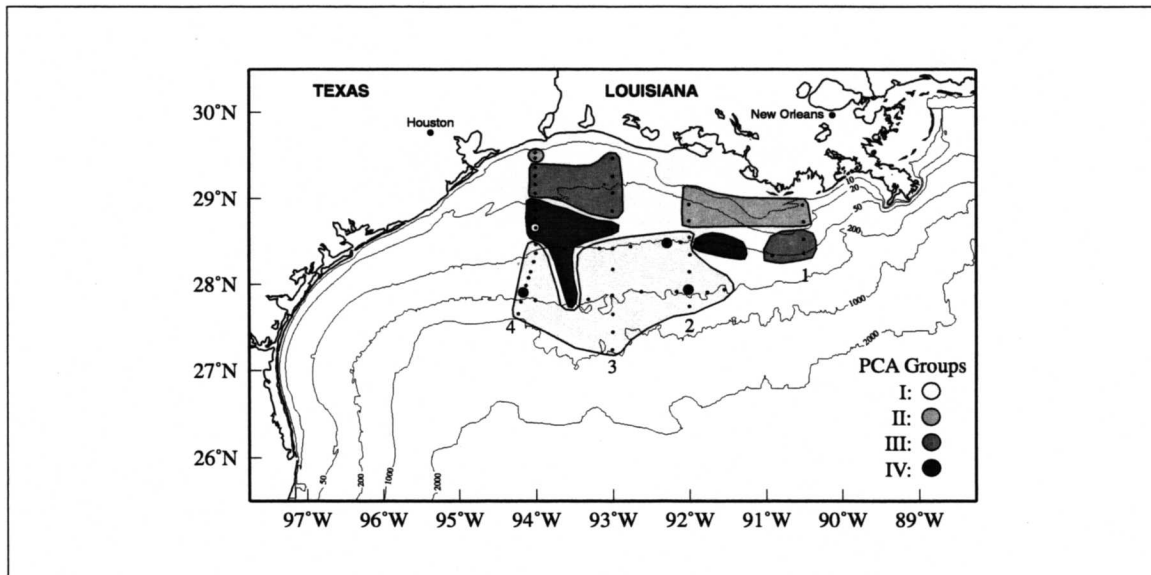


Figure 5.4-8. Principal component groups for the chlorophyll maximum of cruise H04, 6-13 February 1993.

Mean chlorophyll-a was shown to be extremely high during this winter cruise, before which river flow had reached above average levels. Examination of horizontal pigment plots revealed that diatom, cryptophyte, and dinoflagellate pigments measured in the chlorophyll-a maximum were more than two times higher than the other cruises on the inner shelf. Pigments typical of the outer shelf flora exhibited a normal distribution during H04. The inner shelf algal groups, principally diatoms, were the main contributors to the high chlorophyll-a concentrations observed during this cruise. High river flow appears to have contributed to the increase in inner shelf pigment concentrations. Diatom pigments increased most dramatically.

Summary

From the high and low chlorophyll-a areas distinguished by PCA analysis, it is clear that low frequency circulation over the inner shelf first described by Cochrane and Kelly (1986) and now supported by LATEX data is an important mechanism in the distribution of chlorophyll-a on the Texas-Louisiana shelf. Annual differences in mean concentrations of chlorophyll-a were related to the magnitude of fresh water on the shelf. High mean chlorophyll-a was observed on the shelf in all seasons when Mississippi-Atchafalaya discharge was above average. Winter and spring mean chlorophyll-a levels were highest on the eastern shelf. Spring and fall chlorophyll-a were highest in low salinity inner shelf water carried downcoast by the prevailing circulation.

Localized affects on the distribution of chlorophyll-a bear investigation. Unusual features in cruise H06 manifested high chlorophyll-a on the middle Texas shelf, which is unexplained by vertical sections of salinity and temperature. A surface chlorophyll maximum in high chlorophyll-a groups was observed during summer cruise H06, where low salinity surface water extended onto the eastern Louisiana outer shelf (line 1). During fall cruise H10, high chlorophyll-a groups were found on the outer middle Louisiana shelf, where temperature and salinity measurements indicated a lower salinity water mass. These features may have been caused by a Loop Current eddy influencing the local circulation and providing opportunities for production of higher than expected chlorophyll-a. A similar feature was observed off the outer shelf of line 4 in spring 1992 (Neuhard 1994), but the effect was not strong enough to be discerned by PCA analysis.

The distribution of phytoplankton pigments on the Texas-Louisiana shelf reflected the environment in which they were found; the highest overall chlorophyll-a levels were found during highest river flow periods. Areas of high chlorophyll-a followed the circulation and distribution of low salinity water. High levels of chlorophyll-a and fucoxanthin dominated coastal waters where diatoms thrived in the nutrient-rich inner shelf environment. Algal class distributions were predictable based on the distribution of high and low chlorophyll-a. Diatom pigments were always grouped in low salinity, high chlorophyll-a waters.

Cryptophyte pigments (alloxanthin) and peridinin-containing dinoflagellates were usually grouped with diatoms. Prymnesiophytes, chrysophytes, and cyanobacterial pigments were more prevalent where the water column most resembled open ocean conditions on the outer shelf.

6 REFERENCES

- Adams, C.E., Jr., J.T. Wells, and J.M. Coleman. 1982. Sediment transport on the central Louisiana continental shelf: implications for the development of the Atchafalaya River delta. *Contrib. Mar. Sci.* 25:133-148.
- Al-Abdulkader, K.A. 1996. Spatial and temporal variability of phytoplankton standing crop and primary production along the Texas-Louisiana continental shelf. PhD dissertation. Texas A&M University, Dept. of Oceanography, College Station, TX. 177 pp.
- Barnard, W. R. and P. N. Froelich, Jr. 1981. Nutrient geochemistry of the Gulf of Mexico, p. 127. NOAA/AOML Conference: Environmental research needs in the Gulf of Mexico, 30 September - 5 October 1979, Key Biscayne, FL. Miami, FL.
- Barrett, B.B., J.L. Merrel, T.P. Morrison, M.C. Gillespie, E.J. Ralph, and J.F. Burdon. 1978. A study of Louisiana's major estuaries and adjacent offshore waters. Louisiana Department of Wildlife and Fisheries. Tech. Bull. 27. Baton Rouge, LA. 197 pp.
- Bender, L.C. III, and F.J. Kelly. 1998. LATEX Shelf Data Report: Acoustic Doppler current profiler, July 1992 through November 1994. Texas A&M University, Dept. of Oceanography, College Station, TX. Reference No. 96-3-T. 372 pp.
- Berger, T.J., P. Hamilton, J.J. Singer, and R.R. Leben. 1996. Louisiana/Texas Shelf Physical Oceanography Program: Eddy Circulation Study, Final Synthesis Report. OCS Study MMS 96-0051. U.S. Department of the Interior, Minerals Management Service, Gulf of Mexico OCS Region, New Orleans, LA. 324 pp.
- Bidigare R.R. 1991. Analysis of algal chlorophyll and carotenoids, pp. 119-123. In D.C. Hurd and D.W. Spencer, eds. *Marine particles: analysis and characterization*. Geophysical Monograph 63. Amer. Geophys. Union. Washington, D.C.
- Biggs, D.C., G.S. Fargion, P. Hamilton, and R.R. Leben. 1996. Cleavage of a Gulf of Mexico Loop Current eddy by a deep water cyclone. *J. Geophys. Res.* 101(C9): 20,629-20,641.
- Bloomfield, P. 1976. *Fourier analysis of time series: An introduction*. John Wiley & Sons, Inc. New York, NY. 258 pp.
- Boesch, D.F., and N.N. Rabalais. 1991. Effects of hypoxia on continental shelf benthos: comparisons between the New York Bight and the northern Gulf of Mexico, pp. 27-34. In R. V. Tyson and T.H. Pearson, eds. *Modern and ancient continental shelf anoxia*. Geological Soc. Special Publ. London, England. 470 pp.

- Bontempi, P.S. 1995. Phytoplankton distributions and species composition across the Texas-Louisiana continental shelf during two flow regimes of the Mississippi River. MS thesis. Texas A&M University, Dept. of Oceanography, College Station TX. 274 pp.
- Bretherton, F.P., R.E. Davis, and C.B. Fandry. 1976. A technique for objective analysis and design of oceanographic experiments applied to MODE-73. *Deep-Sea Res.* 23:559-582.
- Broecker, W.S., and T.H. Peng. 1982. *Tracers in the sea*. Eldigio Press. New York, NY. 690 pp.
- Brooks, D.A. 1984. Current and hydrographic variability in the northwestern Gulf of Mexico. *J. Geophys. Res.* 89(C5):8022-8032.
- Brooks, J.M. 1980. Determining seasonal variations inorganic nutrient composition and concentration of the water column. *In* W.B. Jackson and G.M. Faw, eds. *Biological/chemical survey of Texoma and Capline salt dome brine disposal sites off Louisiana, 1978-1979*. NOAA Tech. Mem. No. NMFS-SEFC-32. 31 pp.
- Bryden, H.L., and R.D. Pillsbury. 1977. Variability of deep flow in the Drake Passage from year-long current measurements. *J. Phys. Oceanogr.* 7:803-810.
- Carter, E.F., and A.R. Robinson. 1987. Analysis models for the estimation of oceanic fields. *J. Atmos. Oceanic. Technol.* 4:49-73.
- Chen, H.-W. 1995. Variability and structure of currents over the Texas-Louisiana shelf—a view from a shipboard acoustic Doppler current profiler. PhD dissertation. Texas A&M University, Dept. of Oceanography, College Station, TX. 117 pp.
- Chen, H.-W., R.O. Reid, and S.F. DiMarco. (1998.) Spatial correlation scales of streamfunction over the Texas-Louisiana continental shelf based on ADCP data. *In* revision.
- Chen, X., S.E. Lohrenz and D.A. Wiesenburg. 1996. Seasonal variations of plankton photosynthetic parameters and primary production in the shelf region along the Louisiana and Texas coasts. *Eos Trans. Am. Geophys. Union.* 76:OS32.
- Cho, K. 1996. Three-dimensional structure and variability of low-frequency currents on the Texas-Louisiana shelf based on moored current meter data. Ph.D. Dissertation. Texas A&M University, Dept. of Oceanography, College Station, TX. 121 pp.

- Cho, K., R.O. Reid, and W.D. Nowlin, Jr. (1998.) Objectively mapped streamfunction fields on the Texas-Louisiana shelf based on 32 months of moored current meter data. *J. Geophys. Res.* In press.
- Clarke, A.J., and K.H. Brink. 1985. The response of stratified, frictional flow of shelf and slope waters to fluctuating large-scale, low-frequency wind forcing. *J. Phys. Oceanogr.* 15:439-453.
- Cochrane, J.D., M.K. Howard, and L.L. Lee. 1995. Coastal upwelling and related currents in the western Gulf of Mexico. Collected abstracts of AGU Chapman Conference on Circulation of the Intra-Americas Sea, La Parguera, Lajas, Puerto Rico, January 22-26, 1995. Amer. Geophys. Union. Washington, D.C.
- Cochrane, J.D., and F.J. Kelly. 1986. Low-frequency circulation on the Texas-Louisiana continental shelf. *J. Geophys. Res.* 91:10,645-10,659.
- Cochrane, J.D., and F.J. Kelly. 1994. Anticyclonic eddy encroaching on the continental shelf south of Freeport, Texas, in May 1993. Abstract. *Eos Trans. Am. Geophys. Union.* 75(3):51.
- Crisp, C.A., and J.M. Lewis. 1992. Return flow in the Gulf of Mexico. Part I: A classificatory approach with a global historical perspective. *J. Appl. Meteor.* 31:868-881.
- Csanady, G.T. 1981. Circulation in the coastal ocean, pp. 101-183. *In* *Advances in Geophysics*, Vol. 23. Academic Press. New York, NY. 279 pp.
- Csanady, G.T. 1982. *Circulation in the Coastal Ocean*. Reidel Publ. Dordrecht, Neth. 279 pp.
- Curray, J.R. 1960. Sediments and history of the Holocene transgression, continental shelf, northwest Gulf of Mexico, pp. 221-266. *In* *Recent sediments, northwest Gulf of Mexico: a symposium summarizing the results of work carried on in Project 51 of the American Petroleum Institute, 1951-1958*. American Association of Petroleum Geologists, Tulsa, OK.
- Current, C.L. 1996. Spectral model simulation of wind driven subinertial circulation on the inner Texas-Louisiana shelf. PhD dissertation. Texas A&M University, Dept. of Oceanography, College Station, TX. 144 pp.
- Dagg, M.J. 1988. Physical and biological responses to the passage of a winter storm in the coastal and inner shelf of the northern Gulf of Mexico. *Cont. Shelf Res.* 8:167-178

- Denman, K.L., and H.J. Freeland. 1985. Correlation scales, objective mapping and a statistical test of geostrophy over the continental shelf. *J. Mar. Res.* 43:517-539.
- Dey, C.H. 1989. Evolution of objective analysis methodology at the National Meteorological Center. *Weather and Forecasting.* 4:297-312.
- DiMarco, S.F. 1996. LATEX Shelf Data Report: SeaData 635-8 wave gauge, April 1992 through July 1993. Texas A&M University, Dept. of Oceanography, College Station, TX. Reference No. 96-7-T. 58 pp.
- DiMarco, S.F. 1998. LATEX Technical Report: On the use of the method of cyclic descent to estimate principal tidal constituents. Texas A&M University, Dept. of Oceanography, College Station, TX. Reference No. 98-1-T. 33 pp.
- DiMarco, S.F., A.E. Jochens, and M.K. Howard. 1997. LATEX Shelf Data Report: Current meters, April 1992 through December 1994; 10 volumes. Texas A&M University, Dept. of Oceanography, College Station, TX. Reference No. 97-1-T.
- DiMarco, S.F., and F.J. Kelly. 1995. LATEX Shelf Data Report: MiniSpec directional wave gauges. Volume II: September 1993 through December 1994. Texas A&M University, Dept. of Oceanography, College Station, TX. Reference No. 95-4-T. 245 pp.
- DiMarco, S.F., F.J. Kelly, and N.L. Guinasso, Jr. 1995. LATEX Shelf Data Report: MiniSpec directional wave gauges. Volume I: April 1992 through August 1993. Texas A&M University Dept. of Oceanography, College Station, TX. Reference No. 95-4-T. 331 pp.
- DiMego, G.J., L.F. Bosart, and G.W. Endersen. 1976. An examination of the frequency and mean conditions surrounding frontal incursions into the Gulf of Mexico and Caribbean Sea. *Mon. Weather Rev.* 104:709-718.
- Dinnel, S.P., and W.J. Wiseman, Jr. 1986. Fresh water on the Louisiana and Texas shelf. *Cont. Shelf Res.* 6(6):765-784.
- El-Sayed, S.Z., W.M. Sackett, L.M. Jeffrey, A.D. Fredericks, R.P. Saunders, P.S. Conger, G.A. Fryxell, K.A. Steidinger, and S.A. Pearle. 1972. Primary productivity and standing crop of phytoplankton, pp. 8-13. *In* V.C. Bushnell, ed. *Chemistry, primary productivity, and benthic algae of the Gulf of Mexico.* Amer. Geophys. Soc. New York, NY.
- Etter, P.C. 1975. A climatic heat budget study of the Gulf of Mexico. MS thesis. Dept of Oceanography, Texas A&M University, College Station TX. 87 pp.

- Etter, P.C. 1983. Heat and freshwater budgets of the Gulf of Mexico. *J. Phys. Oceanogr.* 13 (11):2058-2069.
- Etter, P.C. 1996. LATEX Shelf Data Report: Heat and freshwater budgets of the Texas-Louisiana shelf, April 1992 through November 1994. TAMU Oceanography Tech. Rpt. No. 96-1-T. Texas A&M University, College Station TX. 174 pp.
- Etter, P.C., and J.D. Cochran. 1975. Water temperature on the Texas-Louisiana shelf. Texas A&M University Sea Grant Program, Mar. Adv. Bull. SG 75-604. 22 pp.
- Etter, P.C., P.J. Lamb, and D.H. Portis. 1987. Heat and freshwater budgets of the Caribbean Sea with revised estimates for the Central American seas. *J. Phys. Oceanogr.* 17(8):1232-1248.
- Etter, P.C, W.F. Ulm, and J.D. Cochran. 1985. The relationship of wind stress to heat flux divergence of Texas-Louisiana shelf waters. *Cont. Shelf Res.* 4(5):547-552.
- Flint, R.W., and N.N. Rabalais, eds. 1981. Environmental studies of a marine ecosystem. South Texas outer continental shelf. Univ. of Texas Press. Austin, TX. 240 pp.
- Florida A&M University. 1988. Meteorological database and synthesis for the Gulf of Mexico. OCS Study MMS 83-0064. Dept of the Interior, Minerals Management Service, New Orleans. 486 pp.
- Francis, R., G. Graf, P.G. Edwards, M. McCaig, C. McCartney, P. Dubock, A. Lefevre, B. Pieper, P.-I. Pouvreau, R. Wall, F. Wechsler, J. Louet, and R. Zobl. 1991. The ERS-1 spacecraft and its payload. *European Space Agency Bull.* 65:27-48.
- Freilich, M.H., and R.S. Dunbar. 1993. A preliminary C-band scatterometer model function for the ERS-1 AMI instrument, pp. 79-84. Proceedings of the 1st ERS-1 Symposium: Space at the Service of Our Environment, Cannes, 4-6 November 1992, European Space Agency, Paris.
- Fucik, K.W., and S.Z. El-Sayed. 1979. Effect of oil production and drilling operations on the ecology of phytoplankton in the OEI study area. *Rice University Studies*, Houston, TX. 65:325-353.
- Gandin, L.S. 1965. Objective analysis of meteorological fields. Israel Program for Scientific Translations. Jerusalem. 242 pp.
- Grant, W.D., and O.S. Madsen. 1979. Combined wave and current interaction with a rough bottom. *J. Geophys. Res.* 84:1797-1808.

- Grant, W.D., A.J. Williams, III, and S.M. Glenn. 1984. Bottom stress estimates and their prediction on the northern California continental shelf during CODE-1: The importance of wave-current interaction. *J. Phys. Oceanogr.* 14:506-527.
- Hamilton, P. 1992. Lower continental slope cyclonic eddies in the central Gulf of Mexico. *J. Geophys. Res.* 97(C2):2185-2200.
- Harper, D., Jr., L. McKinney, R. Salzer, and R. Case. 1981. The occurrence of hypoxic bottom water off the upper Texas coast and its effect on the benthic biota. *Contrib. Mar. Sci.* 24:53-79.
- Hastenrath, S., and P. Lamb. 1978. Heat budget of the tropical Atlantic and eastern Pacific Oceans. *Bull. Amer. Meteorol. Soc.* 60(2):131-132.
- Henry, W.K. 1979. Some aspects of the fate of cold fronts in the Gulf of Mexico. *Mon. Weather Rev.* 107:1078-1082.
- Henry, W.K., and A.H. Thompson. 1976. An example of polar air modification over the Gulf of Mexico. *Monthly Weather Review.* 104:1324-1327.
- Ho, C.L., and B.B. Barrett. 1977. Distribution of nutrients in Louisiana's coastal waters influenced by the Mississippi River. *Estuar. Coastal Marine Sci.* 5:173-195.
- Howard, M.K., and S.F. DiMarco. (1998.) LATEX Shelf Data Report: Drifting buoys, August 1992 through December 1994. Dept of Oceanography Tech. Rpt. No. unassigned. Texas A&M University, Dept. of Oceanography, College Station, TX. CD-ROM.
- Hsu, S.A. 1988. *Coastal Meteorology*. Academic Press, San Diego, CA. 260 pp.
- Hsu, S.A. 1993. The Gulf of Mexico—a breeding ground for winter storms. *Mariners Weather Log.* 37(2):4-11.
- Hsu, S.A. 1994. On the incorporation of wave characteristics into drag coefficient formulation at sea, pp. 237-238. Preprint: 2nd International Conference on Air-Sea Interaction and Meteorology and Oceanography of the Coastal Zone, September 1994, Lisbon, Portugal. American Meteorol. Soc., Boston, MA.
- Hsueh, Y., and J.J. O'Brien. 1971. Steady coastal upwelling induced by an along-shore current. *J. Phys. Oceanogr.* 1(7):180-186.

- Huh, O.K., L.J. Rouse, Jr., and N.D. Walker. 1984. Cold air outbreaks over the northwest Florida continental shelf: heat flux processes and hydrographic changes. *J. Geophys. Res.* 89(C1):717-726.
- Huh, O.K., W.J. Wiseman, Jr., and L.J. Rouse, Jr. 1978. Winter cycle of sea surface thermal patterns, northeastern Gulf of Mexico. *J. Geophys. Res.* 83:4523-4529.
- Isemer, H.-J., and L. Hasse. 1987. *The Bunker Climate Atlas of the North Atlantic Ocean. Volume 2: Air-Sea Interactions.* Springer-Verlag, Berlin. 252 pp.
- Jochens, A.E. 1997. Circulation over the Texas-Louisiana slope based on sea surface elevation and current velocity fields. PhD dissertation. Texas A&M University, Dept. of Oceanography, College Station, TX. 159 pp.
- Jochens, A.E., and W.D. Nowlin, Jr., eds. 1994. *Texas-Louisiana Shelf Circulation and Transport Processes Study: Year 1, Annual Report. Volume II: Technical Summary.* OCS Report MMS-94-0030, U.S. Dept. of the Interior, Minerals Management Service, Gulf of Mexico OCS Region, New Orleans, LA. 207 pp.
- Jochens, A.E., and W.D. Nowlin, Jr., eds. 1995. *Texas-Louisiana Shelf Circulation and Transport Processes Study: Year 2, Annual Report.* OCS Study MMS-95-0028, U.S. Dept. of the Interior, Minerals Management Service, Gulf of Mexico OCS Region, New Orleans, LA. 172 pp.
- Jochens, A.E., D.A. Wiesenburg, L.E. Sahl, C.A.N. Lyons, and D.A. DeFreitas. (1998.) *LATEX Shelf Data Report: Hydrography.* Texas A&M University Dept. of Oceanography, College Station, TX. Reference No. 96-6-T.
- Jones, I.S.F., and B.C. Kenney. 1977. The scaling of velocity fluctuations in the surface mixed layer. *J. Geophys. Res.* 82:1392-1396.
- Justic, D., N.N. Rabalais, R.E. Turner, and W.J. Wiseman, Jr. 1993. Seasonal coupling between riverborne nutrients, net productivity, and hypoxia. *Mar. Pollution Bull.* 26:184-189.
- Kamykowski, D., and J.L. Bird. 1981. Phytoplankton associations with the variable nepheloid layer on the Texas continental shelf. *Estuar. Coastal and Shelf Sci.* 13:317-326.
- Kanamitsu, M. 1989. Description of the NMC global data assimilation and forecast system. *Weather and Forecasting.* 4:335-342.

- Kelly, F.K. 1988. Physical Oceanography and Meteorology, pp. 45-132. *In* N.W. James and B.M. Phillips, eds. Offshore Texas and Louisiana Marine Ecosystem Data Synthesis, Vol. II, Chapter 4. OCS Study/MMS 88-0067. U.S. Dept. of the Interior, Minerals Management Service, Gulf of Mexico OCS Regional Office, New Orleans, LA. 477 pp.
- Kelly, F.J., S.F. DiMarco, N.L. Guinasso, Jr., R.C. Hamilton, and K.A. Kurrus. 1993. Calibration and performance of the pressure and temperature sensors in the Coastal Leasing, Inc., MiniSpec directional wave gauge. Texas A&M University Dept. of Oceanography, College Station, TX. Reference No. 93-7-T. 63 pp.
- Kelly, F.J., J.E. Schmitz, R.E. Randall, and J.D. Cochran. 1985. Physical Oceanography, Chapter 1. *In* R.W. Hann, Jr., C.P. Giammona, and R.E. Randall, eds. Offshore oceanographic and environmental monitoring services for the Strategic Petroleum Reserve: Annual report for the West Hackberry site from September 1983 through August 1984. Report to the U. S. Dept. of Energy, Washington, D.C. Report No. DOE/P010850-4.
- Konrad, C.E. II. 1996. Relationships between the intensity of cold-air outbreaks and the evolution of synoptic and planetary-scale features over North America. *Monthly Weather Review*. 124(6):1067-1083.
- Kundu, P.K., and J.S. Allen. 1976. Some three-dimensional characteristics of low frequency current fluctuations near the Oregon coast. *J. Phys. Oceanogr.* 6:181-199.
- Kundu, P.K., J.S. Allen, and R.L. Smith. 1975. Modal decomposition of the velocity field near the Oregon coast. *J. Phys. Oceanogr.* 5:683-704.
- Leben, R.R., G.H. Born, D.C. Biggs, D.R. Johnson, and N.D. Walker. 1993. Verification of TOPEX altimetry in the Gulf of Mexico. TOPEX/Poseidon Rec. Notes. 1:3-6.
- Lentz, S.J. 1994. Current dynamics over the northern California inner shelf. *J. Phys. Oceanogr.* 24:2461-2478.
- Lentz, S.J., and C.D. Winant. 1986. Subinertial currents on the southern California shelf. *J. Phys. Oceanogr.* 16:1737-1750.
- Lewis, J.K., A.D. Kirwan, Jr., and G.Z. Forristall. 1989. Evolution of a warm-core ring in the Gulf of Mexico: Lagrangian observations. *J. Geophys. Res.* 94(C6):8163-8178.
- Lewis, J.M., and C.A. Crisp. 1992. Return flow in the Gulf of Mexico. Part II: Variability in return-flow thermodynamics inferred from trajectories over the Gulf. *J. Appl. Meteor.* 31:882-898.

- Li, Y., W.D. Nowlin, Jr., and R.O. Reid. 1996. Spatial-scale analysis of hydrographic data over the Texas-Louisiana continental shelf. *J. Geophys. Res.* 101(C9):20,595-20,605.
- Li, Y., W.D. Nowlin, Jr., and R.O. Reid. 1997. Mean hydrographic fields and their interannual variability over the Texas-Louisiana continental shelf in spring, summer, and fall. *J. Geophys. Res.* 102(C1):1027-1049.
- Little, J.N., and L. Shore. 1992. *Signal Processing Toolbox user's guide*. The MathWorks, Inc. Natick, MA. 166 pp.
- Liu, Q., J.M. Lewis, and J.M. Schneider. 1992. A study of cold air modification over the Gulf of Mexico using in situ data and mixed-layer modeling. *J. Appl. Meteor.* 31:909-924.
- Lohrenz, S.E., M.J. Dagg, and T.E. Whitledge. 1990. Enhanced primary production at the plume/oceanic interface of the Mississippi River. *Cont. Shelf Res.* 10:639-664.
- Mantoura, R.F.C., and C.A. Llewellyn. 1983. The rapid determination of algal chlorophyll and carotenoid pigments and their breakdown products in natural waters by reverse-phase high-performance liquid chromatography. *Analitica Chimica Acta.* 151:297-314.
- Mariano, A., and O.B. Brown. 1992. Efficient objective analysis of dynamically heterogeneous and nonstationary fields via the parameter matrix. *Deep-Sea Res.* 39:1255-1271.
- McWilliams, J.C., W.B. Owens, and B.L. Hua. 1986. An objective analysis of the POLYMODE local dynamics experiment, Part I: general formalism and statistical model selection. *J. Phys. Oceanogr.* 16:483-504.
- Mellor, G.L. 1993. *User's guide for a three-dimensional, primitive equation, numerical ocean model*. Princeton University. Princeton, NJ. 35 pp.
- Meindl, E.A, and G.D. Hamilton. 1992. Programs of the National Data Buoy Center. *Bull. Amer. Meteor. Soc.* 73(7):985-993.
- Mitchum, G.T., and A.J. Clarke. 1986. The frictional nearshore response to forcing by synoptic scale winds. *J. Phys. Oceanogr.* 16:934-946.
- Morrison, J.M., W.J. Merrell, Jr., R.M. Key, and T.C. Key. 1983. Property distributions and deep chemical measurements within the western Gulf of Mexico. *J. Geophys. Res.* 88(C3):2601-2608.

- Morrison, J.M., and W.D. Nowlin, Jr. 1977. Repeated nutrient, oxygen, and density sections through the Loop Current. *J. Mar. Res.* 35(1): 105-128.
- Morrison, J.M., and W.D. Nowlin, Jr. 1982. General distribution of water masses within the eastern Caribbean Sea during the winter of 1972 and the fall of 1973. *J. Geophys. Res.* 87(C6):4207-4227.
- Mortimer, E.B., G.A. Johnson, and H.W.N. Lau. 1988. Major arctic outbreaks affecting Louisiana. *National Weather Digest.* 13(1):5-13.
- Murray, S.P., and J. Donley. 1995. Mississippi River plume hydrography: Second annual report. OCS Study MMS 96-0022. U.S. Dept. of the Interior, Minerals Management Service, Gulf of Mexico OCS Region, New Orleans, LA. 175 pp.
- Neuhard, C.A. 1994. Phytoplankton distributions across the Texas-Louisiana shelf in relation to coastal physical processes. MS thesis. Texas A&M University, Dept. of Oceanography, College Station, TX. 204 pp.
- Njoku, D.W., T.P. Barnett, R.M. Laurs, and A.C. Vastano. 1985. Advances in satellite sea surface temperature measurements and oceanographic applications. *J. Geophys. Res.* 90:11,573-11,586.
- North, G.R. 1984. Empirical orthogonal functions and normal modes. *J. Atmos Sci.* 41:879-887.
- North, G.R., T.L. Bell, R.F. Cahalan, and F.J. Moeng. 1982. Sampling errors in the estimation of empirical orthogonal functions. *Monthly Weather Rev.* 110:699-706.
- Nowlin, W.D., Jr. 1972. Winter circulation patterns and property distributions, pp. 3-52. In L.R.A. Capurro and J.L. Reid, eds. *Contributions on the Physical Oceanography of the Gulf of Mexico.* Gulf Publishing Co., Houston, TX.
- Nowlin, W.D., Jr., A.E. Jochens, N.L. Guinasso, Jr., D.A. Weisenburg, R.O. Reid, S.A. Hsu, and R.C. Hamilton. 1991. Louisiana-Texas Shelf Physical Oceanography Program Task A: A Technical Proposal. Texas A&M University Dept. of Oceanography, College Station, TX. Ref. No. 93-6-T. 196 pp.
- Nowlin, W.D., Jr., and C.A. Parker. 1974. Effects of a cold-air outbreak on shelf waters of the Gulf of Mexico. *J. Phys. Oceanogr.* 4(3):467-486.
- Oey, L.-Y. 1995. Eddy- and wind-forced shelf circulation. *J. Geophys. Res.* 100:8621-8637.

- Pielou, E.C. 1984. The interpretation of ecological data: a primer on classification and ordination. John Wiley and Sons, Inc., New York, NY. 263 pp.
- Press, W.H., B.P. Flannery, S.A. Teukolsky, and W.T. Vetterling. 1986. Numerical recipes. Cambridge University Press. Cambridge, England. 818 pp.
- Preisendorfer, R.W. 1988. Principal Component Analysis in Meteorology and Oceanography. Elsevier. Amsterdam, Neth. 425 pp.
- Rabalais, N.N., R.E. Turner, D. Justic, Q. Dortch, W.J. Wiseman, Jr., and B.K. Sen Gupta. 1996. Nutrient changes in the Mississippi River and system responses on the adjacent continental shelf. *Estuaries*. 19(2B):386-407.
- Rabalais, N.N., R.E. Turner, W.J. Wiseman, Jr., and D.F. Boesch. 1991. A brief summary of hypoxia on the northern Gulf of Mexico continental shelf: 1985-1988, pp. 35-47. In R.V. Tyson and T.H. Pearson, eds. Modern and ancient continental shelf anoxia. Geological Soc. Special Publ. London, England. 470 pp.
- Rabin, R.M., L.A. McMurdie, C.M. Hayden, and G.S. Wade. 1993. Evaluation of the atmospheric water budget following an intense cold air outbreak over the Gulf of Mexico—application of a regional forecast model and SSM/I observations. *J. Appl. Meteor.* 32:3-16.
- Reap, M.E., A.E. Jochens, and W.D. Nowlin, Jr., eds. 1996. Texas-Louisiana Shelf Circulation and Transport Processes Study: Year 3, Annual Report. OCS Study MMS-96-0030, U.S. Dept. of the Interior, Minerals Management Service, Gulf of Mexico OCS Region, New Orleans, LA. 82 pp.
- Rhines, P.B. 1975. Waves and turbulence on a β -plane. *J. Fluid. Mech.* 69:417-443.
- Rhines, P.B. 1977. Marine Modeling, pp. 189-318. In E.D. Goldberg, I.N. McCave, J.J. O'Brien, and J.H. Steele, eds. The sea, ideas and observations in the progress in the study of the seas, Volume 6. John Wiley & Sons, New York, NY.
- Rhines, P.B., and F.P. Bretherton. 1974. Topographic Rossby-waves in a rough-bottomed ocean. *J. Fluid. Res.* 61:583-607.
- Rienecker, M.M., C.N.K. Mooers, and A.R. Robinson. 1987. Dynamical interpolation and forecast of the evolution of mesoscale features off northern California. *J. Phys. Oceanogr.* 17:1189-1213.

- Riley, G.A. 1937. The significance of the Mississippi River drainage for biological conditions in the northern Gulf of Mexico. *Journal of Marine Research*. 1:60-74.
- Rouse, R.J., Jr. 1996. Short time scale variability (3-7 days) of the Mississippi River plume. Abstract. AGU Ocean Sciences Meeting, 12-16 February 1996, San Diego, CA. *Eos. Trans. Am. Geophys. Union*. 76(3):OS64.
- Sahl, L.E., W.J. Merrell, and D.C. Biggs. 1993. The influence of advection on the spatial variability of nutrient concentrations on the Texas-Louisiana continental shelf. *Cont. Shelf Res.* 13:233-251.
- Sahl, L.E., W.J. Merrell, D.W. McGrail, and J.A. Webb. 1987. Transport of mud on continental shelves: evidence from the Texas shelf. *Mar. Geol.* 76:33-43.
- Sahl, L.E., D.A. Wiesenburg, and W.J. Merrell. 1997. Interaction of mesoscale features with Texas shelf and slope waters. *Cont. Shelf Res.* 17(2):117-136.
- Sheng, J., and K.R. Thompson. 1996. A robust method for diagnosing regional shelf circulation from scattered density profiles. *J. Geophys. Res.* 101(C11):25,647-25,659.
- Shideler, G.L. 1981. Development of the benthic nepheloid layer on the south Texas continental shelf, western Gulf of Mexico. *Mar. Geol.* 41:37-61.
- Sklar, F.H., and R.E. Turner. 1981. Characteristics of phytoplankton off Barataria Bay in an area influenced by the Mississippi River. *Contributions to Marine Science*. 24:93-106.
- Smith, N.P. 1979. An investigation of vertical structure in shelf circulation. *J. Phys. Oceanogr.* 9:624-630.
- Smith, R.C, K.S. Baker, and P. Dustan. 1981. Fluorometric techniques for the measurement of oceanic chlorophyll in the support of remote sensing, pp. 1-14. SIO ref. 81-71, Scripps Institute of Oceanography, University of California, San Diego, CA.
- Smith, S. 1988. Coefficients for sea surface wind stress, heat flux, and wind profiles as a function of wind speed and temperature. *J. Geophys. Res.* 93:15,467-15,472.
- Smith, W.H.F., and P. Wessel. 1990. Gridding with continuous curvature splines in tension. *Geophysics*. 55:293-305.
- Tennekes, H. 1973. Similarity laws and scale relations in planetary boundary layers, pp. 177-216. *In* D. Haugen, ed. *Workshop on Micrometeorology*. Amer. Meteor. Soc. Boston, MA.

- Thomas, W.H., and E.G. Simmons. 1960. Phytoplankton production in the Mississippi Delta, pp. 103-116. *In* F. Shephard, ed. Recent sediments, northwest Gulf of Mexico. Amer. Assoc. of Petroleum, Tulsa, OK.
- Tyson and Pearson. 1991. Modern and ancient continental shelf anoxia: an overview, pp. 1-24. *In* R.V. Tyson and T.H. Pearson, eds. Modern and ancient continental shelf anoxia. Geological Soc. Special Publ. London, England. 470 pp.
- Ulm, W.F. 1983. A volumetric temperature-salinity census for the continental shelf of the northwestern Gulf of Mexico. MS thesis. Dept of Oceanography, Texas A&M University, College Station TX. 56 pp.
- U.S. Army Corps of Engineers. 1974. Deep draft access to the ports of New Orleans and Baton Rouge. Draft Environmental Statement. Corps of Engineers, New Orleans District.
- Vastano, A.C., and R.O. Reid. 1985. Sea surface topography estimation with infrared satellite imagery. *J. Atmos. Oceanic Technol.* 2:393-400.
- Velasco, G.G., and C.D. Winant. 1996. Seasonal patterns of wind stress and wind stress curl over the Gulf of Mexico, 1990-1993. *J. Geophys. Res.* 101:18,127-18,140.
- Vidal, V.M.V., F.V. Vidal, and J.M. Perez-Molero. 1992. Collision of a Loop Current anticyclonic ring against the continental shelf slope of the western Gulf of Mexico. *J. Geophys. Res.* 97(C2):2155-2172.
- Vukovich, F.M., and B.W. Crissman. 1986. Aspects of warm rings in the Gulf of Mexico. *J. Geophys. Res.* 91:2645-2660.
- Vukovich, F.M., and E. Waddell. 1991. Interaction of a warm ring with the western slope in the Gulf of Mexico. *J. Phys. Oceanogr.* 21(7):1062-1074.
- Wada, E. and A. Hattori. 1991. Nitrogen in the sea: forms, abundances, and rate processes. CRC Press. Boca Raton, FL. 208 pp.
- Walker, N.D. 1996. Satellite assessment of Mississippi plume variability: causes and predictability. *Remote Sensing of Environment.* 58:21-35
- Wang, W. 1996. Analyses of surface meteorological fields over the northwestern Gulf of Mexico and wind effects on the circulation over the LATEX shelf. PhD dissertation. Texas A&M University, Dept. of Oceanography, College Station, TX. 120 pp.

- Wang, W., M.K. Howard, W.D. Nowlin, Jr., and R.O. Reid. 1996. LATEX Shelf Data Report: Meteorology, April 1992 through December 1994. Texas A&M University, Dept. of Oceanography, College Station, TX. Reference No. 96-2-T. 499 pp.
- Wang, W., W.D. Nowlin, Jr., and R.O. Reid. (1998a.) Analyzed surface meteorological fields over the northwestern Gulf of Mexico for 1992-1994; mean, seasonal, and monthly patterns. *Mon. Weather Rev.* In press.
- Wang, W., W.D. Nowlin, Jr., and R.O. Reid. 1998b. A comparison among LATEX, NCEP, and ERS-1 scatterometer winds over the northwestern Gulf of Mexico. *J. Atmos. Ocean. Tech.* 15(5):1205-1215.
- Washburn, L., M.S. Swenson, J.L. Largier, P.M. Kosro, and S.R. Ramp. 1993. Cross-shelf sediment transport by an anticyclonic eddy off Northern California. *Science.* 261:1560-1564.
- Wessel, P., and W.H.F. Smith. 1991. Free software helps map and display data. *Eos Trans. Am. Geophys. Union.* 72:441, 445-446.
- White, W.B., and R.L. Bernstein. 1979. Design of an oceanographic network in the mid-latitude North Pacific. *J. Phys. Oceanogr.* 9:592-606.
- Wilkin, J.L., and D.C. Chapman. 1990. Scattering of coastal-trapped waves by irregularities in coastline and topography. *J. Phys. Ocean.* 20(3):396-421.
- Winant, C.D., and R.C. Beardsley. 1979. A comparison of some shallow wind-driven currents. *J. Phys. Oceanogr.* 9:218-220.
- Winant, C.D., R.C. Beardsley, and R.E. Davis. 1987. Moored wind, temperature and current observations made during CODE-1 and CODE-2 over the northern California shelf and upper slope. *J. Geophys. Res.* 76:1569-1604.



The Department of the Interior Mission

As the Nation's principal conservation agency, the Department of the Interior has responsibility for most of our nationally owned public lands and natural resources. This includes fostering sound use of our land and water resources; protecting our fish, wildlife, and biological diversity; preserving the environmental and cultural values of our national parks and historical places; and providing for the enjoyment of life through outdoor recreation. The Department assesses our energy and mineral resources and works to ensure that their development is in the best interests of all our people by encouraging stewardship and citizen participation in their care. The Department also has a major responsibility for American Indian reservation communities and for people who live in island territories under U.S. administration.



The Minerals Management Service Mission

As a bureau of the Department of the Interior, the Minerals Management Service's (MMS) primary responsibilities are to manage the mineral resources located on the Nation's Outer Continental Shelf (OCS), collect revenue from the Federal OCS and onshore Federal and Indian lands, and distribute those revenues.

Moreover, in working to meet its responsibilities, the **Offshore Minerals Management Program** administers the OCS competitive leasing program and oversees the safe and environmentally sound exploration and production of our Nation's offshore natural gas, oil and other mineral resources. The **MMS Minerals Revenue Management** meets its responsibilities by ensuring the efficient, timely and accurate collection and disbursement of revenue from mineral leasing and production due to Indian tribes and allottees, States and the U.S. Treasury.

The MMS strives to fulfill its responsibilities through the general guiding principles of: (1) being responsive to the public's concerns and interests by maintaining a dialogue with all potentially affected parties and (2) carrying out its programs with an emphasis on working to enhance the quality of life for all Americans by lending MMS assistance and expertise to economic development and environmental protection.